ASME
SETTING THE STANDARD
1880 2005

Journal of Engineering for Gas Turbines and Power

Published Quarterly by ASME

VOLUME 127 • NUMBER 4 • OCTOBER 2005

Editor
LEE S. LANGSTON (2006)

Assistant to the Editor
LIZ LANGSTON

Associate Editors
Fuels and Combustion Technologies
K. M. BRYDEN (2008)

Internal Combustion Engines
J. C. COWART (2008)
M. S. WOOLDRIDGE (2008)

International Gas Turbine Institute
IGTI Review Chair
H. R. SIMMONS (2003)
A. J. STRAZISAR (2004)
K. C. HALL (2005)

Combustion and Fuels
P. MALTE (2006)

Structures and Dynamics
N. ARAKERE (2007)
M. MIGNOLET (2005)

PUBLICATIONS DIRECTORATE
Chair, ARTHUR G. ERDMAN

OFFICERS OF THE ASME
President, RICHARD E. FEIGEL

Executive Director,
VIRGIL R. CARTER

Treasurer,
T. PESTORIUS

PUBLISHING STAFF

Managing Director, Publishing
PHILIP DI VIETRO

Production Coordinator
JUDITH SIERANT

Production Assistant
MARISOL ANDINO

Transactions of the ASME, Journal of Engineering for Gas Turbines and Power (ISSN 0742-4795) is published quarterly (Jan., April, July, Oct.) by The American Society of Mechanical Engineers, Three Park Avenue, New York, NY 10016. Periodicals postage paid at New York, NY and additional mailing offices. POSTMASTER: Send address changes to Transactions of the ASME, Journal of Engineering for Gas Turbines and Power, c/o THE AMERICAN SOCIETY OF MECHANICAL ENGINEERS, 22 Law Drive, Box 2300, Fairfield, NJ 07007-2300.
CHANGES OF ADDRESS must be received at Society headquarters seven weeks before they are to be effective. Please send old label and new address.
STATEMENT from By-Laws. The Society shall not be responsible for statements or opinions advanced in papers or ... printed in its publications (B7.1, par. 3).
COPYRIGHT © 2005 by the American Society of Mechanical Engineers. For authorization to photocopy material for internal or personal use under circumstances not falling within the fair use provisions of the Copyright Act, contact the Copyright Clearance Center (CCC), 222 Rosewood Drive, Danvers, MA 01923, Tel: 978-750-8400, www.copyright.com.
Canadian Goods & Services Tax Registration #126148048

TECHNICAL PAPERS

Gas Turbines: Aircraft Engine

697 Comparison of Computational Fluid Dynamics and Particle Image Velocimetry Data for the Airflow in an Aeroengine Bearing Chamber
C. W. Lee, P. C. Palma, K. Simmons, and S. J. Pickering

Gas Turbines: Combustion and Fuels

704 Optimization of Wall Cooling in Gas Turbine Combustor Through Three-Dimensional Numerical Simulation
R. Gordon and Y. Levy

724 Observations of Flame Behavior in a Laboratory-Scale Premixed Natural Gas/Air Gas Turbine Combustor From Planar Laser Induced Fluorescence Measurements of OH, Laser Doppler Anemometer Velocity Measurements, and Coherent Anti-Stokes Roman Spectrometer Temperature Measurements
Paul O. Hedman, Thomas H. Fletcher, Daniel V. Flores, Stewart G. Graham, Jason K. Haslam, Robert L. Murray, and G. Wayne Timothy

740 Demonstration of a Reheat Combustor for Power Production With CO_2 Sequestration
Ben Chorpening, Geo. A. Richards, Kent H. Casleton, Mark Woike, Brian Willis, and Larry Hoffman

748 Active Instability Control: Feedback of Combustion Instabilities on the Injection of Gaseous Fuel
M. P. Auer, C. Gebauer, K. G. Mösl, C. Hirsch, and T. Sattelmayer

755 Unsteady Flow Structures in Radial Swirler Fed Fuel Injectors
Kris Midgley, Adrian Spencer, and James J. McGuirk

Gas Turbines: Cycle Innovations

765 Thermodynamic and Economic Investigation of an Improved Graz Cycle Power Plant for CO_2 Capture
Wolfgang Sanz, Herbert Jericha, Mathias Moser, and Franz Heitmeir

773 Effect of the Specific Heat Ratio on the Aerodynamic Performance of Turbomachinery
Stephen K. Roberts and Steen A. Sjolander

Gas Turbines: Heat Transfer

781 Analysis of Tangential-Against-Rotation Injection Lomakin Bearings
Mihai Arghir, Mathieu Hélène, and Jean Frene

791 Influence of Fluid Dynamics on Heat Transfer in a Preswirl Rotating-Disk System
Gary D. Lock, Michael Wilson, and J. Michael Owen

798 A Novel Cooling Method for Turbine Rotor-Stator Rim Cavities Affected by Mainstream Ingress
Y. Okita, M. Nishiura, S. Yamawaki, and Y. Hironaka

(Contents continued on inside back cover)

This journal is printed on acid-free paper, which exceeds the ANSI Z39.48-1992 specification for permanence of paper and library materials. ♾™
♻ 85% recycled content, including 10% post-consumer fibers.

Downloaded 03 Jun 2010 to 171.66.16.160. Redistribution subject to ASME license or copyright; see http://www.asme.org/terms/Terms_Use.cfm

Journal of Engineering for Gas Turbines and Power OCTOBER 2005

Volume 127, Number 4

Gas Turbines: Manufacturing, Materials, and Metallurgy

807 Mechanical Properties of Overaluminized MCrAlY Coatings at Room Temperature
Yoshiyasu Itoh and Masahiro Saitoh

Gas Turbines: Structures and Dynamics

814 Life Prediction for Complex Structures
S. C. Forth, B. S. Annigeri, and W. D. Keat

820 Application of Computational Fluid Dynamics Analysis for Rotating Machinery—Part II: Labyrinth Seal Analysis
Toshio Hirano, Zenglin Guo, and R. Gordon Kirk

827 Modeling Oil Flows on Seal Runners and Engine Sump Walls
Masayoshi Shimo, James V. Canino, and Stephen D. Heister

835 Sensitivity of Tuned Bladed Disk Response to Frequency Veering
J. A. Kenyon, J. H. Griffin, and N. E. Kim

843 Rotordynamic Coefficients for a Tooth-on-Stator Labyrinth Seal at 70 Bar Supply Pressures: Measurements Versus Theory and Comparisons to a Hole-Pattern Stator Seal
Arthur Picardo and Dara W. Childs

856 Characterization of Turbine Blade Friction Dampers
K.-H. Koh, J. H. Griffin, S. Filippi, and A. Akay

863 Combined Fatigue Life Test and Extrapolation of Turbine Disk Mortise at Elevated Temperature
Rongqiao Wang, Chongdu Cho, and Jingxu Nie

Internal Combustion Engines

869 Methods for Specific Emission Evaluation in Spark Ignition Engines Based on Calculation Procedures of Air-Fuel Ratio: Development, Assessment, and Critical Comparison
Stefano d'Ambrosio, Ezio Spessa, and Alberto Vassallo

883 Multidimensional Predictions of In-Cylinder Turbulent Flows: Contribution to the Assessment of k-ε Turbulence Model Variants for Bowl-in-Piston Engines
Mirko Baratta, Andrea E. Catania, Ezio Spessa, and Rui L. Liu

897 Coupled Simulations of Nozzle Flow, Primary Fuel Jet Breakup, and Spray Formation
Eberhard von Berg, Wilfried Edelbauer, Ales Alajbegovic, Reinhard Tatschl, Martin Volmajer, Breda Kegl, and Lionel C. Ganippa

909 Feasibility Study of an On-Board Natural Gas to Dimethyl Ether Reactor for Dimethyl Ether Preinjection and Enhanced Ignition
David Horstman, Duane Abata, Jason Keith, and Leroy Oberto

918 An Analysis of Turbocharged Diesel Engine Dynamic Response Improvement by Electric Assisting Systems
Tomaž Katrašnik, Ferdinand Trenc, Vladimir Medica, and Stojan Markič

927 Author Index

The ASME Journal of Engineering for Gas Turbines and Power is abstracted and indexed in the following:

AESIS (Australia's Geoscience, Minerals, & Petroleum Database), Applied Science & Technology Index, Aquatic Sciences and Fisheries Abstracts, Civil Engineering Abstracts, Compendex (The electronic equivalent of Engineering Index), Computer & Information Systems Abstracts, Corrosion Abstracts, Current Contents, Engineered Materials Abstracts, Engineering Index, Enviroline (The electronic equivalent of Environment Abstracts), Environment Abstracts, Environmental Science and Pollution Management, Fluidex, INSPEC, Mechanical & Transportation Engineering Abstracts, Mechanical Engineering Abstracts, METADEX (The electronic equivalent of Metals Abstracts and Alloys Index), Pollution Abstracts, Referativnyi Zhurnal, Science Citation Index, SciSearch (The electronic equivalent of Science Citation Index), Shock and Vibration Digest

Downloaded 03 Jun 2010 to 171.66.16.160. Redistribution subject to ASME license or copyright; see http://www.asme.org/terms/Terms_Use.cfm

Comparison of Computational Fluid Dynamics and Particle Image Velocimetry Data for the Airflow in an Aeroengine Bearing Chamber

C. W. Lee
P. C. Palma
K. Simmons
S. J. Pickering

University Technology Centre in Gas Turbine Transmission Systems,
University of Nottingham,
University Park,
Nottingham NG7 2RD, UK

Investigations into the single-phase velocity field of a model aeroengine bearing chamber are presented. Adequately resolving the airflow field is important to subsequent computational modeling of two-phase fluid transport and heat transfer characteristics. A specially designed test rig, representing the features of a Rolls Royce Trent series aeroengine bearing chamber, was constructed. Experimental data for the airflow field was obtained using particle image velocimetry (PIV). The results show a strong influence of shaft rotation and chamber geometry on the flow features within the bearing chamber. A computational fluid dynamics (CFD) simulation was carried out using the commercial CFD code FLUENT 6. Flow features were adequately modeled, showing the features of secondary velocities. Turbulence modeling using the differential Reynolds stress (RSM) model shows good agreement with the experimental data. [DOI: 10.1115/1.1924635]

Introduction

The evolution of bearing chamber designs has largely been based on correlation databases derived from empirical knowledge collated over the years through expensive and time consuming experiments. Continual development of aeroengines towards lighter weight and more compact designs, while not sacrificing performance, leads to ever increasing demand on the lubrication system. Increase in engine operating efficiency demands an increase in turbine inlet temperatures. Turbine blades face a higher input temperature and cooling air taken from the compressor via an internal air system to the bearing chamber is also at a higher temperature. This leads to a reduction of the temperature difference that drives the cooling process. Larger proportions of total engine mass flow of air are required for cooling the lubrication system, which represents a power loss to the engine. An increase in cooling requirements can also lead to requirements for larger pumps, filters and heat exchangers, and consequently higher engine power requirements, as well as additional weight. Therefore, an adequate assessment of bearing chamber flows in terms of internal air systems and lubrication systems is essential when considering aero engine performance.

The high pressure (HP) turbine shaft and the intermediate pressure (IP) turbine shaft are housed together in the HP–IP bearing chamber, situated after the combustion chamber. The bearing chamber consists of shafts rotating at engine representative speeds within a stationary casing. A sectioned view of the HP–IP bearing chamber is shown in Fig. 1. Air is supplied to the chamber for sealing and leaves via vent and scavenge ports from an annular chamber wrapped around the main bearing chamber. Incorporated within the bearing chamber are the turbine roller bearings, which permit the different rotation of the two shafts. These bearings are lubricated and cooled by injection of oil through targeted jets from an injector block, situated in the middle of the bearing chamber main cavity. The oil supplied to the bearing chamber consists of lubricating oil to the jets and oil supply to the squeeze film dampeners for the bearings. Lubricating oil is targeted at oil catchers (known as scallops) on the inside of the stubshaft, and channeled through the oil feed holes to the roller bearings. The lubricant is then scavenged through a return at the bottom of the chamber while the air and oil mist mixture in the chamber pass through a vent pipe into a centrifugal breather that separates and retain the oil, discharging the filtered air. The sealing air in the chamber is drawn from the compressor system, maintaining a positive pressure through the labyrinth seals.

The work presented here is part of ongoing study to understand and model the complex multiphase phenomena and heat transfer characteristics of the HP–IP bearing chamber. It is of paramount importance that an accurate representation of the airflow field is achieved as this has significant impact on the oil phase transport and heat transfer characteristics, influencing the lubrication and cooling efficiencies of the engine.

Background

Recent studies into bearing chambers have examined the heat transfer characteristics with specific focus on oil fires and engine coking problems [1]. Ignition mechanisms were identified and a strong dependence on the air/oil mixture characteristics was concluded. Earlier investigations into bearing chamber flows [2] involved using an ultrasonic film thickness measurement technique. It was demonstrated that the heat transfer characteristics depended on rotational speed and mass flow ratio of oil into the chamber. An extension of this work was carried out to include film velocity measurements [3] where the air flow regime is fundamental to the calculation procedure of film flows. Oil droplet flow investigations [4] also showed a strong dependence of the oil phase motion on the air flow. The strength of the secondary airflow and recirculation regions ensuing in the complex shape could have an effect on the flow of the oil in the form of droplets. Droplet size distributions and droplet entrainment from oil films have also been identified [5]. It was shown that the dispersed oil phase is

Contributed by the International Gas Turbine Institute (IGTI) of THE AMERICAN SOCIETY OF MECHANICAL ENGINEERS for publication in the ASME JOURNAL OF ENGINEERING FOR GAS TURBINES AND POWER. Paper presented at the International Gas Turbine and Aeroengine Congress and Exhibition, Vienna, Austria, June 13–17, 2004. Paper No. GT2004-53281. Manuscript received by IGTI, October 1, 2003; final revision, March 1, 2004. IGTI Review Chair: A. J. Strazisar.

Copyright © 2005 by ASME

Downloaded 02 Jun 2010 to 171.66.16.98. Redistribution subject to ASME license or copyright; see http://www.asme.org/terms/Terms_Use.cfm

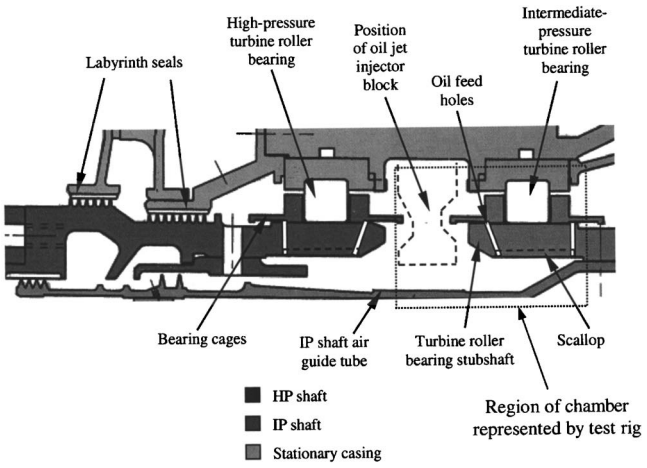

Fig. 1 Section view of HP–IP bearing chamber

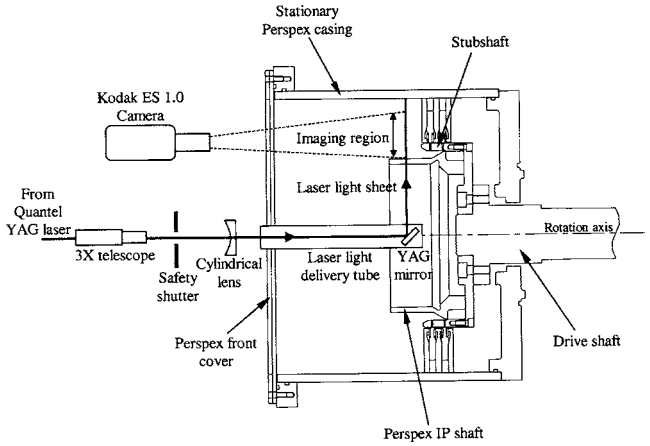

Fig. 2 Experimental set-up

greatly affected by the air phase flow patterns, which have implications on the lubrication and cooling of bearing chambers. In these studies, the authors employed only a numerical procedure to calculate the airflow and concluded that any successful numerical analysis of two-phase flow phenomena in bearing chambers requires a thorough understanding of the airflow to derive a relation for the coupling between the air and oil phase.

In addition, measurements of the heat transfer characteristics [6] and an attempt at a generalized description of bearing chamber heat transfer are presented in the literature. Various parameters such as chamber height, rotational speed and lubrication oil flow were examined. One study of the chamber air flow [7] examined a simplified chamber geometry of two coaxial cylinders. Well-known instabilities in the form of toroidal cells known as Taylor vortices were observed. From these measurements, local heat transfer coefficients were obtained and condensed into correlation functions. Other attempts at correlation [8–10] were faced with great difficulty due to the lack of material available in open literature.

Results obtained thus far have been encouraging and the increased knowledge base in bearing chamber flows is important in building towards a physics-based design process, moving away from purely empirical approaches, as has been the case until recently. Modeling work [11–13] aimed to provide an insight into bearing chamber flows has been successful, but experimental data is still required to substantiate these results. Previous single-phase experimental results using PIV obtained for rotating flow geometries [14,15] have been successful. These studies were carried out in geometries specific to the particular application.

This paper presents PIV results obtained from single-phase airflow field measurements in a rig designed to simulate the IP end of a Trent style HP–IP bearing chamber, with the oil jet injector absent, forming an axisymmetric geometry. Comparisons to CFD simulations of the rig geometry using FLUENT 6 are included. The information obtained adds to the present knowledge of flows within these complex environments and also provides high quality data for validation of simulation codes. A thorough understanding of the single-phase flow features will provide valuable insight into the subsequent effects of two-phase flow transport and heat transfer effects.

Experimental Details

The general layout of the test rig and measurement apparatus is shown in Fig. 2. The IP end formed by the coupling of the IP shaft and stubshaft are contained in a stationary Perspex casing. The rotating parts are driven through a drive shaft connected to a 4 kW motor. As is clear from Fig. 1, the seal is well away from the region of interest and sealing air has not been included in this study. The results presented in this paper are for a shaft speed of 4600 rpm. The IP shaft radius is designated R_i and the gap outer radius (Perspex casing or stubshaft) is R_o. Figure 3 shows an enlargement of the measurement region. The gap width between the IP shaft and the Perspex casing is defined as, $d=R_o-R_i$, where $d_A=d_B=0.78R_i$ and $d_C=0.1R_i$. The gap ratio, which is defined as R_i/R_o, is 0.56 for planes A and B, and 0.91 for plane C (Fig. 3).

The Reynolds number, Re=220,000, is based on the shaft velocity and distance between the IP shaft and the outer stationary Perspex wall. The corresponding Taylor number [16], is Ta=2.7 $\times 10^{10}$. The rotation speed encountered in the present experiment is many times larger than the critical value for the first instability of viscous Couette flow [16]. In this regime, the flow is expected to be turbulent and the presence of coherent Taylor cells are not expected [17].

A commercial PIV system (Dantec Flowmap 1100) was set up to measure the circumferential velocity in the region of the IP end as shown in Fig. 3. The output from a 150 mJ/pulse Nd:YAG laser (Quantel Twins) was focused with a telescopic lens adjusted to form a focused beam at the imaging region. The beam was then passed through a cylindrical lens to form a laser light sheet of 1.0 mm thickness. The laser produces two pulses and the pulse separation, Δt, was 38 μs, with pulse duration of 5 ns. Subsequently, a portion of the laser light sheet is transmitted down the purpose built laser light delivery tube, which contains a mirror

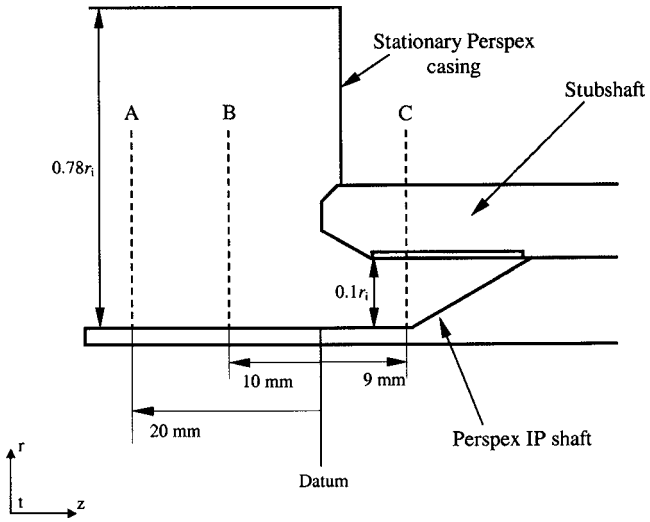

Fig. 3 PIV measurement planes

Downloaded 02 Jun 2010 to 171.66.16.98. Redistribution subject to ASME license or copyright; see http://www.asme.org/terms/Terms_Use.cfm

that turns the laser light sheet by 90 deg to form a sheet perpendicular to the IP shaft. The IP shaft is constructed out of Perspex to allow transparency to the laser light.

The images are captured with a digital camera (Kodak Megaplus ES 1.0) viewing through the front Perspex cover and focused at the plane of the laser sheet. The camera is a progressive interline transfer CCD with 1008(H) by 1018(V) pixels. The distance of the camera lens from the front Perspex cover is approximately 250 mm. Thus, the size of imaged region (field of view) is approximately 70 mm and the imaging magnification factor, is $M=0.14$.

The laser light delivery tube was inserted into the working section through the middle of the front cover and was moved accordingly to form the laser light sheet at various axial positions from the end of the stubshaft. This ensured that flow disruption was minimal as the flow is expected to be symmetrical about this point. Also, with the probe situated inside the confines of the IP shaft any influence of the probe on the imaging region tends to be negated. The imaging planes, labeled A, B, and C, and their respective distances from the stubshaft are shown in Fig. 3. The flow velocities in these planes are mainly in the circumferential direction due to the rotation of the shaft. The lubricating jet was removed from this set-up to form an axisymmetric geometry and hence it was only necessary to perform the PIV measurements at one circumferential location.

The flow was seeded with oil droplets of the order of 1 μm diameter, using an in-house design of air pressure atomizer, similar to designs reported previously [18]. The output from the seeding generator couples onto the end of the Perspex cover. Only low levels of seeding were found to be necessary and the seeding was introduced intermittently at a time when data was not being collected thus creating a negligible effect on the test chamber flow field.

The laser light sheet illuminated these particles and a pair of image maps was captured on the CCD camera. The images were divided into interrogation regions ($D_I=1\times 8$ mm corresponding to 16×128 pixels), with a 50% overlap between adjacent interrogation regions, and spatially cross-correlated to produce a mean vector for each region. The velocity of the fluid is thus derived from measuring the mean particle displacement within each interrogation region. This was performed on the entire image across the gap width of the measurement planes shown in the radial direction. Velocity vectors were determined across the radial distance only as the geometry is axisymmetric. This reduces the data processing time. For each measurement plane, more than 100 image map pairs were collected. This is considered adequate for deriving components of mean velocity to within 1% [19], whereas turbulence measurements require sample sizes of at least an order of magnitude larger to achieve the same level of accuracy. The vectors produced were validated and all the image maps averaged to yield the time-averaged velocity data. In addition, velocity fluctuations in the sample dataset are recorded to give information of the turbulence statistics. The uncertainty of the derived turbulence quantities is estimated to be not more than 8%, depending on the radial position of measurement. Further details on the PIV technique applied can be found in the literature [18,20].

Modeling Details

The rig geometry was modeled as an axisymmetric case with the commercial CFD software FLUENT 6, which uses a finite-volume formulation. A structured grid was used, as shown in Fig. 4. The computational domain is enclosed within walls that are stationary (casing) and rotating (shaft) with no-slip conditions applied at the walls. The scallops and oil feed holes were omitted from the model for simplification. The domain represents a slice of the circumferential rig geometry and hence was solved in 2D axisymmetric polar coordinates, using a segregated solver. The rotating walls were given an angular velocity, ω_s, of 481.6 rad s^{-1}.

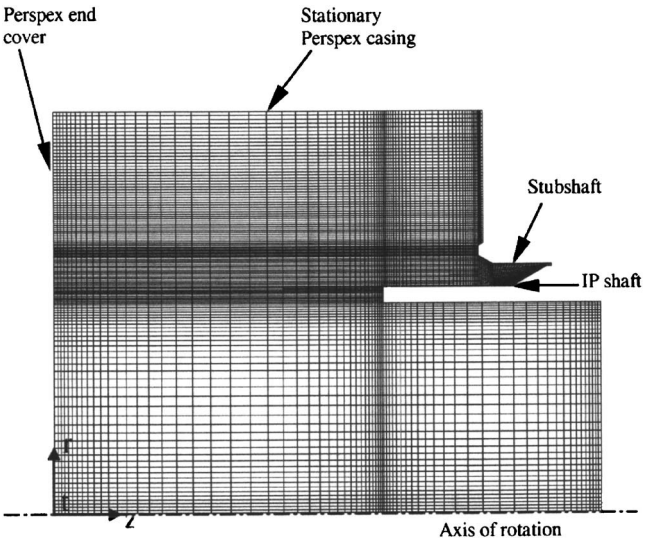

Fig. 4 Computational domain

The fluid in the computational domain was air at room temperature and pressure (density 1.225 kg m^{-3}, viscosity 1.789×10^{-5} kg m^{-1} s^{-1} and absolute pressure 101,325 Pa), as in the rig. The fluid was considered as incompressible and material properties were constant. Heat transfer effects are not thought to be significant and were not modeled. The computational grid used in the calculation contained 9600 cells.

Two turbulence modeling approaches were applied: a standard $k-\varepsilon$ (SKE) [21] method where the Reynolds-averaged Navier–Stokes equations are modeled using the Boussinesq approximation; and a Reynolds stress transport model (RSM) [22] where the turbulent fluctuations are solved directly.

The discretization scheme for all the solution equations required the use of second-order upwind schemes, first-order schemes led to problems of numerical diffusion. The SIMPLE algorithm [23] was used for pressure-velocity coupling. Convergence criteria dictated a reduction of scaled residuals of at least 3 orders of magnitude and that point values were stable.

Standard wall functions were employed where the y^+ values at the walls were between 11.25 and 100 to ensure validity of the application of the logarithmic law-of-the-wall approximation. This involved iterations of the computational grid to obtain a final fixed size of the first cell. The cell density in the region of interest was subsequently varied in order to investigate the solution dependency on the cell resolution and it was found that 20 cells between the IP shaft and the stubshaft was adequate. An increase in cell density resulted in a solution where the difference was less than 0.1%. It was found that the solution stability benefited from solving the flow without rotation to begin with and subsequently ramping up the speed of the rotating boundaries. The solution of the standard $k-\varepsilon$ model was used as the initial solution for the RSM model.

Results and Discussion

The averaged tangential velocity profiles are shown for planes A, B, and C in Fig. 5, scaled to the shaft linear velocity, U_s. The typical uncertainty bars shown were calculated from the standard deviation of velocities at each measurement point. The uncertainties are generally less than 2% of the local velocity but larger values are encountered in regions where laser scatter affected the estimation of the displacement vector. This caused erroneous correlations, which resulted in a greater uncertainty in the estimation of velocity vectors. This is reflected in the uncertainty bars shown, and is more pronounced in plane B due to the proximity to the end

Downloaded 02 Jun 2010 to 171.66.16.98. Redistribution subject to ASME license or copyright; see http://www.asme.org/terms/Terms_Use.cfm

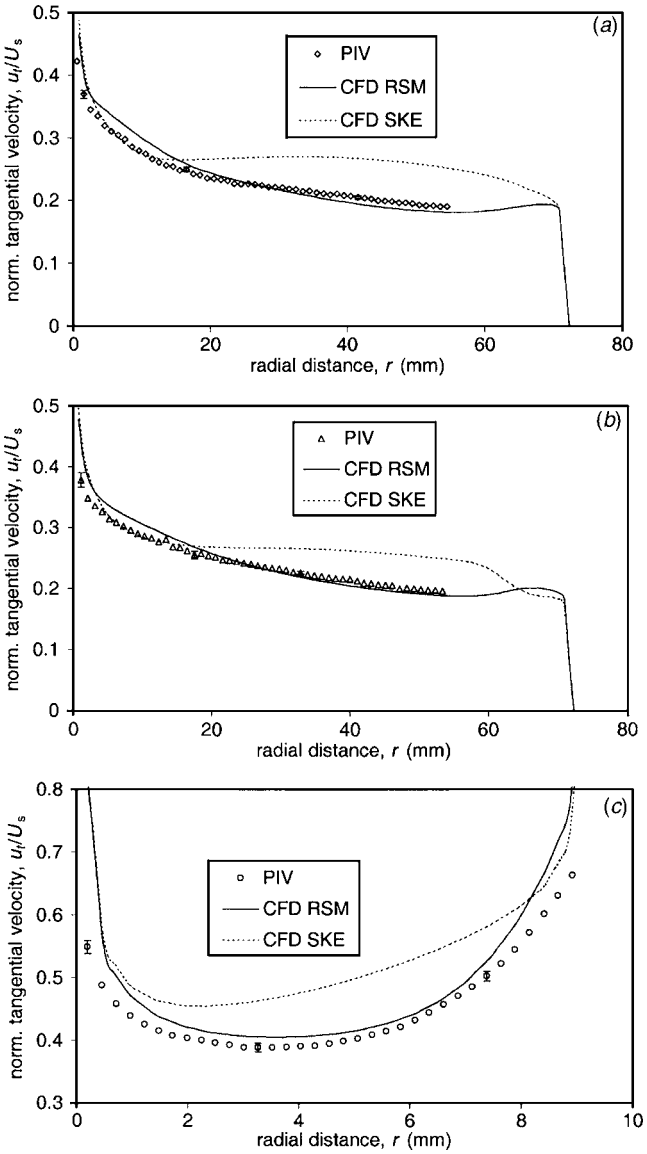

Fig. 5 Normalized tangential velocity (*a*) plane *A*; (*b*) plane *B*; (*c*) plane *C*

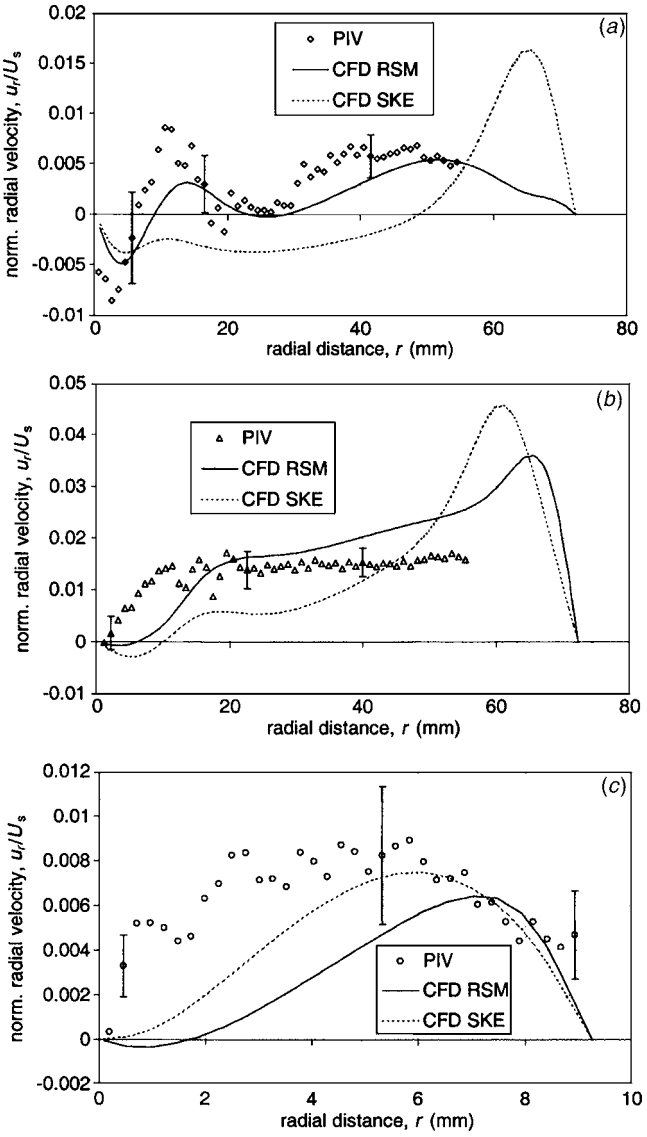

Fig. 6 Normalized radial velocity (*a*) plane *A*; (*b*) plane *B*; (*c*) plane *C*

of the stubshaft, causing greater scatter. The maximum uncertainty for any data point shown is 2.5%, except for the first boundary point, where it is up to 6%.

The plots in Fig. 5 show a comparison of the PIV experimental data to results from CFD simulations using the two turbulence models. The flow velocities in planes *A* and *B* were approximately constant for the SKE model between $r/d=0.25$ and 0.83 whereas the RSM showed a progressive decrease in tangential velocity. The SKE model predicts a much greater effect of the shaft rotation on flow velocities in the core flow region. The RSM result shows good agreement with the PIV data with at most 8% discrepancy whereas the SKE model differed from the PIV data by as much as 35% ($r/d=0.7$) in plane *A*. In plane *C*, the RSM model performed well, capturing the greater velocity drop between the two rotating surfaces in the IP gap. At $r/d=0.54$, the discrepancy between the PIV data and the RSM and SKE models are 3% and 21%, respectively. The data suffers from lack of measurements of velocity near boundaries ($r/d<0.04$). This is caused by velocity gradients within interrogation regions leading to velocity bias errors. In addition, surface flare as the laser passes through the Perspex can lead to data loss. The data is particularly augmented in the IP gap region. In addition, it was not possible to obtain PIV data beyond $r/d=0.76$ in planes *A* and *B* as the rig end cover restricted camera access. Good agreement was also found in tests for rotation speeds up to 7042 rpm (737.6 rad/s), but with greater uncertainties in the experimental data. This data has not yet been presented.

The radial velocities, shown in Fig. 6, are scaled to the shaft velocity to provide a comparison with the tangential velocity magnitudes. The normalized radial velocities are generally much smaller (<0.02) than the tangential velocities. The larger uncertainties in the radial measurements using the PIV technique are due to the smaller particle displacements in the radial direction. Smaller displacements result in a larger fraction of the measured velocity that could be attributed to random error in estimating particle displacements and the resulting velocity estimates. This problem is most pronounced in the velocity measurements in plane *C* where particle displacements are smallest.

The magnitudes are larger in plane *B* compared to plane *A* due to the proximity of the end of the stubshaft. This indicates that fluid is flung out of the IP gap. The velocity is constant through most of measurement plane *B* whereas a variation is observed in plane *A*. Close to the shaft in plane *A*, the velocity is negative. This indicates a suction effect close to the shaft drawing fluid in

Downloaded 02 Jun 2010 to 171.66.16.98. Redistribution subject to ASME license or copyright; see http://www.asme.org/terms/Terms_Use.cfm

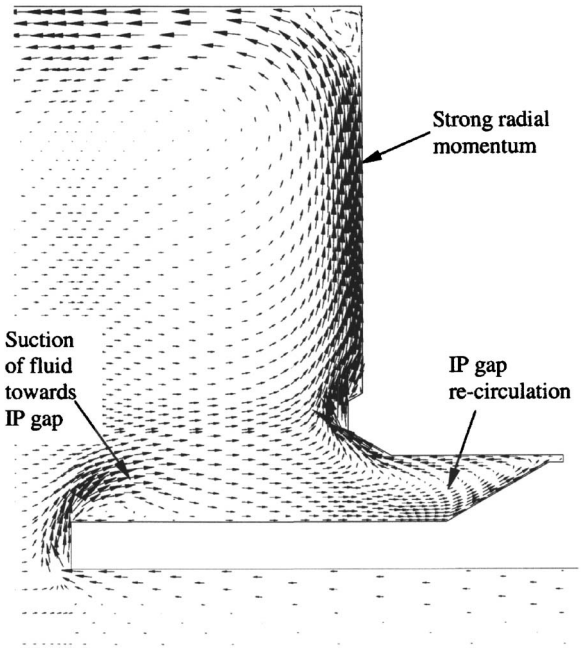

Fig. 7 Secondary flow vectors

towards the IP gap. Fluid is also flung out at an oblique angle from the IP gap shown by a maximum velocity at $r/d=0.21$ in plane *A*. Fluid can be thought of as being ejected from the gap close to the chamfered stubshaft end. Most of the faster moving fluid travels along the end wall in a radial direction. Radial velocities in the gap are of a small magnitude and approach zero near the walls.

The radial velocity profile predicted for plane *A* by the SKE model is largely negative, indicating that fluid is drawn in towards the IP gap. However, this is not the case in the PIV data where the negative velocity only occurs near the IP shaft surface. This indicates fluid being drawn into the IP gap along the surface of the IP shaft. This is captured more accurately with the RSM model.

For planes *A* and *B* the radial velocities computed using the RSM turbulence model are in good agreement with the PIV data. The agreement between model and experiment is less good in plane *C*, with the CFD underpredicting the radial velocity component and largely falling outside the PIV uncertainty bars. The secondary flow behavior is best observed in a vector plot from the CFD simulation (with RSM turbulence model) shown in Fig. 7, where a close-up of the IP gap region is displayed. The figure shows that fluid is drawn towards the IP gap from as far as the end of the shaft. This suction effect causes a recirculation near the end of the shaft. The fluid is drawn into the gap along the IP shaft surface and the flow is reversed in the IP gap and ejected along the stubshaft. Most of the fluid has a strong radial momentum along the end wall and it is this recirculation that is captured by the plane *C* data.

In the CFD model the scallops are not included and considering Fig. 7 it is likely that their inclusion would affect both the location and magnitude of the IP gap recirculation, increasing the outwards radial component at plane *C*. It is suggested that this accounts for the lower predicted radial velocity components of Fig. 6(*c*). The results show that air is ejected from the IP gap along the stubshaft surface and this could have an effect on the efficiency of the scallops to capture oil and deliver it to the bearings.

The RSM model calculates the turbulence fluctuations in each direction whereas the assumption of isotropic turbulence in the SKE model yields single turbulence intensity for all three orthogonal directions. A comparison of the turbulence intensity profiles is shown in Fig. 8.

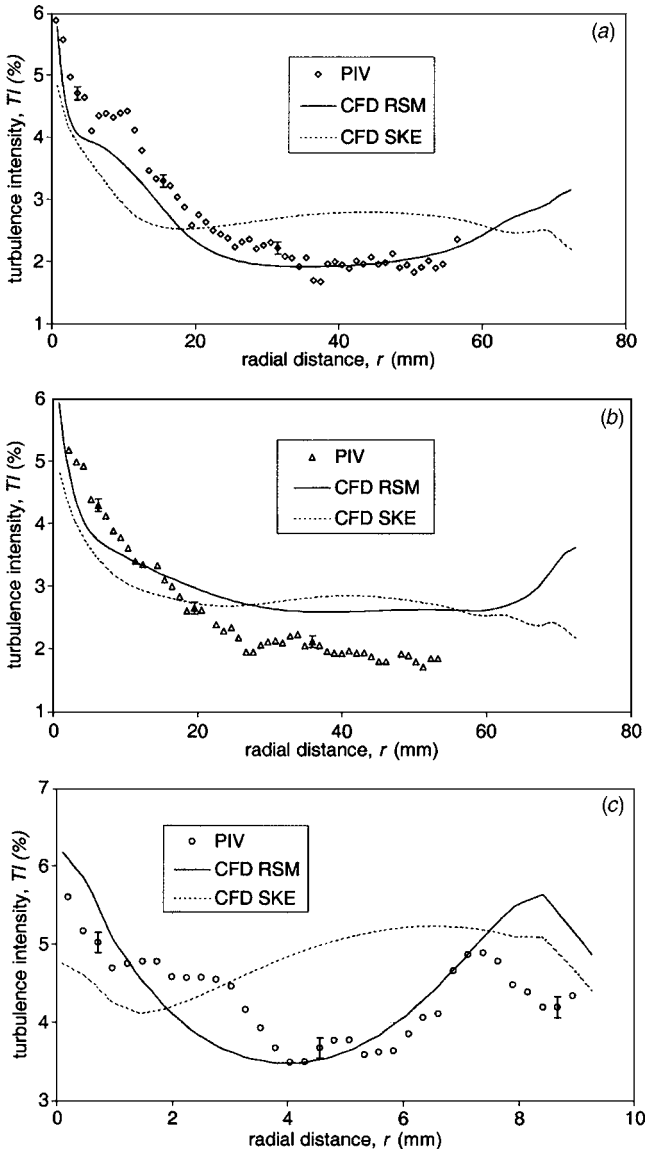

Fig. 8 Turbulence intensity profiles (*a*) plane *A*; (*b*) plane *B*; (*c*) plane *C*

The turbulence measurements are presented in terms of turbulence intensity (TI), where measurements of the fluctuating velocity component in the tangential direction ($u'_{t,\mathrm{rms}}$) are scaled to the shaft velocity, U_s. The tangential velocity fluctuations were measured with less uncertainty compared to radial velocity fluctuations. The measured velocity fluctuations could be attributed to random errors in the measurement and turbulence. Uncertainty analysis shows that with all systematic errors neglected, random errors accounted for less than 5% of the velocity fluctuations. Therefore, the variation in velocity throughout the sampled data can be attributed to turbulent fluctuations. The uncertainty in the radial velocity fluctuations was much greater due to the smaller particle displacements in the radial direction. This introduced an uncertainty of around 50% for turbulence measurements in the radial direction and is not presented here. Superior agreement is observed in all three planes of measurement for the RSM model as opposed to the SKE model. The agreement is particularly good in plane *A* for the RSM model, whereas the SKE model overpredicts the turbulence levels in the core region and under predicts close to the rotating wall. The discrepancy with the PIV measurements is as much as 50% in some regions for the SKE model. The

Downloaded 02 Jun 2010 to 171.66.16.98. Redistribution subject to ASME license or copyright; see http://www.asme.org/terms/Terms_Use.cfm

agreement is less striking in plane B for the RSM model. The CFD results show a greater effect of the stubshaft end on the generation of turbulence. This is reflected in the higher turbulence levels in plane B for both turbulence models as compared with those of plane A. There is less difference in measured turbulence levels in the experimental results. The higher turbulence levels around $r/d=0.14$ are attributed to the suction effect observed in the secondary flow illustrated in Fig. 7. This generates greater turbulence, which is captured adequately by the RSM model but not by the SKE model. The fidelity of the RSM model is further confirmed in comparisons for plane C. The turbulence levels are predicted more accurately with the RSM model, with the SKE model predicting an incorrect profile and magnitude. However, the experimental data could be improved by increasing the sample data to smooth the experimental profiles, which suffered from noise.

The observations in the present study are in agreement with previous work [15,24] on rotating and swirling flows. The widely used SKE is inadequate in modeling turbulent flows of this configuration due to the assumptions of isotropy. The modeling of near-wall flows using the RSM and standard wall functions are known to have certain limitations [25], such as underpredicting the near-wall stress. However, it is shown here that turbulence profiles are adequately captured, which will allow reasonable estimates of the effect of the single-phase flow on bearing chamber studies.

Conclusion

Single-phase flow field investigations were carried out in a rig built to model part of an aero-engine bearing chamber. The PIV technique gave highly accurate measurements of the dominant tangential flow velocity with good spatial resolution. The radial velocity component was also obtained although the measurement uncertainty was greater. CFD results for the same geometry showed reasonable agreement with the PIV data. Comparison between turbulence models showed superior agreement of velocity profiles for the RSM model over the SKE model. Comparison of turbulence intensity again indicates greater accuracy of the RSM model, suggesting the importance of anisotropic turbulence in rotating flows of this kind.

A vector plot showing the secondary flow features revealed the strong effect of chamber geometry on the flow field. Air is drawn towards the IP gap along the surface of the IP shaft, and ejected out of the IP gap at velocities up to 5% of the shaft velocity. This secondary flow component may have an effect on the transport of lubricating oil in the form of films and droplets. These effects will have implications for the efficiency of the scallops in channeling oil through to the bearings. This very much depends on the structure of the oil phase and will be investigated in future studies.

Acknowledgment

The authors are grateful for the financial support of Rolls Royce plc. In addition the technical support of Barry Hatch and John Chapman of The University of Nottingham are gratefully acknowledged.

Nomenclature

D_I = interrogation region size
M = magnification
P = absolute pressure (kPa)
Re = Reynolds number, $=U_s d/\nu$
Ta = Taylor number
TI = turbulence intensity ($=u'_{t,\mathrm{rms}}/U_s$)
U = velocity (m s^{-1})
d = gap width, $=R_o-R_i$ (m)
r = gap distance$=R-R_i$ (m)
R = radius (m)
Δt = laser pulse separation (s)
ν = kinematic viscosity (m s^{-1})
ω = angular velocity (rad s^{-1})

Subscripts

A = plane A
B = plane B
C = plane C
i = inner cylinder
o = outer cylinder
r = radial direction
rms = root-mean-square
s = shaft
t = tangential direction
z = axial direction

References

[1] Willenborg, K., Busam, S., Roßkamp, H., and Wittig, S., 2002, "Experimental Studies of the Boundary Conditions Leading to Oil Fire in the Bearing Chamber and in the Secondary Air System of Aeroengines," ASME Turbo EXPO, Amsterdam, The Netherlands.

[2] Wittig, S., Glahn, A., and Himmelsbach, J., 1994, "Influence of High Rotational Speeds on Heat Transfer and Oil Film Thickness in Aero-Engine Bearing Chambers," ASME J. Eng. Gas Turbines Power, **116**, pp. 395–401.

[3] Glahn, A., and Wittig, S., 1996, "Two-Phase Air/Oil Flow in Aero Engine Bearing Chambers: Characterization of Oil Film Flows," ASME J. Eng. Gas Turbines Power, **118**, pp. 578–583.

[4] Glahn, A., Kurreck, M., Willmann, M., and Wittig, S., 1996, "Feasibility Study on Oil Droplet Flow Investigations inside Aero Engine Bearing Chambers-PDPA Techniques in Combination with Numerical Approaches," ASME J. Eng. Gas Turbines Power, **118**, pp. 749–755.

[5] Glahn, A., Busam, S., Blair, M. F., Allard, K. L., and Wittig, S., 2002, "Droplet Generation by Disintegration of Oil Films at the Rim of a Rotating Disk," ASME J. Eng. Gas Turbines Power, **124**, pp. 117–124.

[6] Busam, S., Glahn, A., and Wittig, S., 2000, "Internal Bearing Chamber Wall Heat Transfer as a Function of Operating Conditions and Chamber Geometry," ASME J. Eng. Gas Turbines Power, **122**, pp. 314–320.

[7] Jakoby, R., Kim, S., and Wittig, S., 1999, "Correlations of the Convection Heat Transfer in Annular Channels with Rotating Inner Cylinder," ASME J. Eng. Gas Turbines Power, **121**, pp. 670–677.

[8] Zimmermann, H., Kutz, J., and Fischer, R., 1998, "Air Systems Correlation, Part 2: Rotating Holes and Two Phase Flow," International Gas Turbine and Aeroengine Congress and Exhibition, Stockholm, Sweden.

[9] Zimmermann, H., and Wolff, K. H., 1998, "Air Systems Correlations, Part 1: Labyrinth Seals," International Gas Turbine and Aeroengine Congress and Exhibition, Stockholm, Sweden.

[10] Zimmermann, H., Kammerer, A., Fischer, R., and Rebhan, D., 1991, "Two-Phase Flow Correlations in Air/Oil Systems of Aero Engines," International Gas Turbine and Aeroengine Congress and Exposition, Orlando, FL.

[11] Wang, Y., Hibberd, S., Simmons, K., Eastwick, C., and Care, I., 2001, "Application of CFD to Modelling Two-Phase Flow in a High-Speed Aero-Engine Transmission Chamber," ASME Fluids Engineering Division Summer Meeting, New Orleans, LA.

[12] Farrall, M., Hibberd, S., and Simmons, K., 2003, "Modelling Oil Droplet/Film Interaction in an Aero-Engine Bearing Chamber," ICLASS, Sorento, Italy.

[13] Farrall, M. B., Hibberd, S., and Simmons, K., 2000, "Computational Modelling of Two-Phase Air/Oil Flow within an Aero-Engine Bearing Chamber," ASME Fluids Engineering Division Summer Meeting, Boston, MA.

[14] Wernet, M. P., 2000, "A Flow Field Investigation in the Diffuser of a High-Speed Centrifugal Compressor Using Digital Particle Imaging Velocimetry," Meas. Sci. Technol., **7**, pp. 1007–1022.

[15] Zhou, M., and Garner, C. P., 1996, "Particle Image Velocimetry Measurements of the Flow Field within an Enclosed Rotating Disc-Stator System and Comparisons with Computational Fluid Dynamics Results," Optical Diagnostics in Engineering (Part 2), **1**, pp. 9–21.

[16] Coles, D., 1965, "Transition in Circular Couette Flow," J. Fluid Mech., **21**, pp. 385–425.

[17] Smith, G. P., and Townsend, A. A., 1982, "Turbulent Couette Flow between Concentric Cylinders at Large Taylor Numbers," J. Fluid Mech., **123**, pp. 187–217.

Downloaded 02 Jun 2010 to 171.66.16.98. Redistribution subject to ASME license or copyright; see http://www.asme.org/terms/Terms_Use.cfm

[18] Raffel, M., Willert, C., and Kompenhans, J., 1998, *Particle Image Velocimetry: A Practical Guide* Springer-Verlag, Berlin.
[19] Ullum, U., Schmidt, J. J., Larsen, P. S., and McCluskey, D. R., 1997, "Statistical Analysis and Accuracy of PIV Data," 2nd International Workshop on PIV, Japan.
[20] Grant, I., 1997, "Particle Image Velocimetry: A Review," Proc. Institution Mech. Eng., Vol. 221, C.
[21] Launder, B. E., and Spalding, D. B., 1972, *Lectures in Mathematical Models of Turbulence*, Academic, London.
[22] Launder, B. E., and Spalding, D. B., 1974, "The Numerical Computation of Turbulent Flows," Comput. Methods Appl. Mech. Eng., **3**(2), pp. 269–289.
[23] Patankar, S. V., and Spalding, B. E., 1972, "A Calculation Procedure for the Heat, Mass and Momentum Transfer in Three-Dimensional Parabolic Flows," Int. J. Heat Mass Transfer, **15**, pp. 17–87.
[24] Parker, J., and Merati, P., 1996, "An Investigation of Turbulent Taylor-Couette Flow Using a Laser Doppler Velocimetry in a Refractive Index Matched Facility," ASME J. Fluids Eng., **118**, pp. 810–818.
[25] Jakirlić, S., Hanjalić, K., and Tropea, C., 2002, "Modelling Rotating and Swirling Turbulent Flows: A Perpetual Challenge," AIAA J., **40**(10), pp. 1984–1997.

Downloaded 02 Jun 2010 to 171.66.16.98. Redistribution subject to ASME license or copyright; see http://www.asme.org/terms/Terms_Use.cfm

Optimization of Wall Cooling in Gas Turbine Combustor Through Three-Dimensional Numerical Simulation

R. Gordon
e-mail: rgordon@tx.technion.ac.il

Y. Levy
e-mail: leoyy@alrodyne.technion.ac.il

Faculty of Aerospace Engineering,
Technion—Israel Institute of Technology,
Haifa 32000, Israel

This paper is concerned with improving the prediction reliability of CFD modeling of gas turbine combustors. CFD modeling of gas turbine combustors has recently become an important tool in the combustor design process, which till now routinely used the old "cut and try" design practice. Improving the prediction capabilities and reliability of CFD methods will reduce the cycle time between idea and a working product. The paper presents a 3D numerical simulation of the BSE Ltd. YT-175 engine combustor, a small, annular, reversal flow type combustor. The entire flow field is modeled, from the compressor diffuser to turbine inlet. The model includes the fuel nozzle, the vaporizer solid walls, and liner solid walls with the dilution holes and cooling louvers. A periodic 36 deg sector of the combustor is modeled using a hybrid structured/unstructured multiblock grid. The time averaged Navier-Stokes (N-S) equations are solved, using the k-ϵ turbulence model and the combined time scale (COMTIME)/PPDF models for modeling the turbulent kinetic energy reaction rate. The vaporizer and liner walls' temperature is predicted by the "conjugate heat transfer" methodology, based on simultaneous solution of the heat transfer equations for the vaporizer and liner walls, coupled with the N-S equations for the fluids. The calculated results for the mass flux passing through the vaporizer and various holes and slots of the liner walls, as well as the jet angle emerging from the liner dilution holes, are in very good agreement with experimental measurements. The predicted location of the liner wall hot spots agrees well with the position of deformations and cracks that occurred in the liner walls during test runs of the combustor. The CFD was used to modify the YT-175 combustion chamber to eliminate structural problems, caused by the liner walls overheating, that were observed during its development.
[DOI: 10.1115/1.1808432]

Introduction

The design operating conditions of new gas turbine engines have put more emphasis on developing affordable, lightweight, advanced liner cooling technology, as well as prediction methodologies of combustor exit temperature field, liner wall temperature, and film cooling. The thermal loads and gradients prevailing in a gas turbine engine determine the lifetime of the engine's parts. Thus, accurate prediction of the exit temperature profiles, liner wall temperature, and film cooling effects of various film cooling geometries are of major importance to the gas turbine industry.

In recent years, computational fluid dynamics (CFD) methods have become an important tool in the aero-turbine industry. Significant advances in CFD algorithms, physical models, as well as improvements in processing speed and storage capacity of computers, were the driving force behind the adaptation of CFD as a design tool of gas turbines.

The main objectives of the present paper are validation of the CFD results and demonstration of the feasibility of CFD as a practical and better design tool. This is achieved through the application of the conjugate heat transfer methodology for the simultaneous calculation of the liner wall temperature, numerical simulations of several alternative film cooling geometries for reduction of the liner wall temperature and temperature gradients, and comparison of the calculated results with experimental data.

Contributed by the Combustion and Fuels Division of THE AMERICAN SOCIETY OF MECHANICAL ENGINEERS for publication in the ASME JOURNAL OF ENGINEERING FOR GAS TURBINES AND POWER. Manuscript received by the C&F Division April 28, 2003; final revision received May 5, 2004. Associate Editor: P. C. Malte.

Many of the previous CFD models of gas turbine combustors included only calculation of reacting flows within the combustor liner while assuming profiles at the various liner inlets; see, for example, Refs. [1–6]. Structured grids were usually used in these CFD models.

Danis et al. [1] used the proprietary code CONCERT for calculating the inner chamber flow of five modern turbo-propulsion engine combustors. The N-S equations were solved for turbulent reacting flows, including spray modeling. The 3D CFD models were first calibrated with correlations based on design database for one combustor. The anchored models were then run successfully for the other four combustors. A structured single-block grid was used in this research with suitable meshing around the internal obstacles. Two-dimensional results for the exit velocity profiles, along with measured spray quality, were used as the swirl cup (atomizer) inlet conditions for the 3D calculations. The turbulence properties at the swirl cup were calibrated using design database.

Lawson [2] calculated the reacting flow inside the combustor liner. A structured single-block grid was used in this study. Lawson was able to successfully match the calculated radial temperature profile at the combustor exit with experimental data, and then used the calibrated CFD model to predict the radial temperature profile that resulted from different cooling and dilution air patterns. Lawson used a one-dimensional code to predict flow splits, and a two-dimensional CFD model to predict the flow profile at the exit plane of the swirl cup. This profile was then applied as a boundary condition in the 3D model.

 Copyright © 2005 by ASME

Downloaded 02 Jun 2010 to 171.66.16.98. Redistribution subject to ASME license or copyright; see http://www.asme.org/terms/Terms_Use.cfm

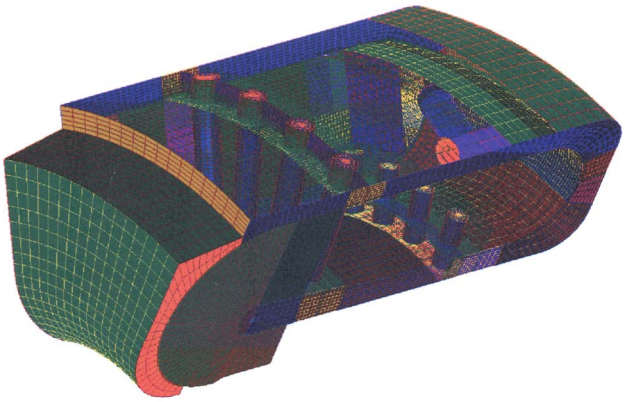

Fig. 1 A 36 deg sector of the YT-175 combustion chamber

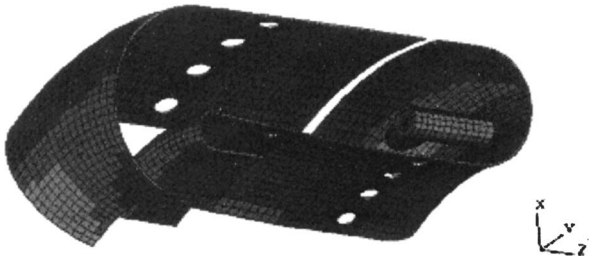

Fig. 2 The YT-175 combustor liner

Fuller and Smith [3] predicted the exit temperature profiles of an annular direct flow combustor that were in fairly good agreement with measurements. They used a structured multiblock grid in their calculations, which is essential for modeling complex geometries. They also used a two-dimensional model to provide the boundary conditions at the exit plane of the swirl nozzle.

Gulati et al. [5] measured the exit plane mean and rms temperature and mole fraction of the major species of a 3D full-scale 10-cup double-annular research combustion sector. Calculations were carried out for the same geometry and operating conditions, using the CONCERT-3D CFD code. A single block structured grid was used for calculating the flow inside the combustor liner. The predicted exit plane mean and rms temperature and mole fraction of the major species were then compared with the measured data, and were found to be in fair agreement. The effect of various inner/outer dilution air jets combinations on the exit plane mean temperature (radial distribution of the circumferentially averaged temperature) and major species mole fractions were also studied and compared with the experimental results. The calculated results were found to recover the trends of these geometry variations fairly well.

Lai [6] modeled the inner chamber of a gas turbine combustor similar to that of the Allison 570KF turbine used by the Canadian Navy. A 22.5 deg periodic sector of the combustor was modeled using a structured multiblock grid. Lai included the swirler passages in his model, which is an important step in reducing the uncertainty in the boundary conditions. He was able to predict liner and dome hot spots, based on near-wall gas temperatures that corresponded to locations in the combustor that had experienced deterioration. No comparison was made, in his work, with experimental results for the combustor flow fields.

In a recent study, Gosselin et al. [7] simulated steady, 3D turbulent reacting flows with liquid spray, in a generic type gas turbine combustor using a hybrid structured/unstructured multiblock grid. The commercial FLUENT code was used in this study. The calculation allowed for detailed combustor geometry, including the inner chamber, external channel, and the various liner film cooling holes and dilution ports. The N-S equations were solved using the k-ε/RNG turbulence model and the PDF turbulent kinetic energy reaction rate model. The calculated results for the gas temperatures, mass functions of CO/CO_2, and velocity fields were compared with experimental measurements. However, no prediction of the wall temperature was included in this work.

Great emphasis has been placed in recent years on the development of liner wall temperature prediction methodologies. A representative sample of works on liner wall temperature calculation are those of Mongia and co-workers [8–13] and Croker et al. [14]. The majority of the first generation design-related liner wall temperature calculations were quasi-one-dimensional, similar to the approach described by Lefebvre [15]. According to this approach, standard empirical film effectiveness and heat transfer coefficients were used. A typical example of the use of this approach is the work by Mongia and Brands [8].

The second generation of liner wall temperature prediction was based on a ''hybrid'' modeling approach [9]. According to this approach, the 3D CFD reacting flow-field results of the combustor inner flow were combined with empirical correlations for film effectiveness to give the liner wall temperature. This methodology was later replaced by use of 3D CFD reacting flow-field results, of the combustor internal flow calculations, as input data for a finite element thermal code [10]. The CFD calculations were run on a structured coarse grid, for an adiabatic wall, and were first calibrated to ensure that they resemble the physical process as much as possible [1]. Within the thermal code, the heat transfer coefficient was determined from the wall function. In recent studies [11,12] the 3D CFD reacting flow results of the combustor internal flow simulations were combined with fine unstructured grid CFD simulations of the flow through a small domain surrounding multihole cooling configurations. The complex flow field exiting

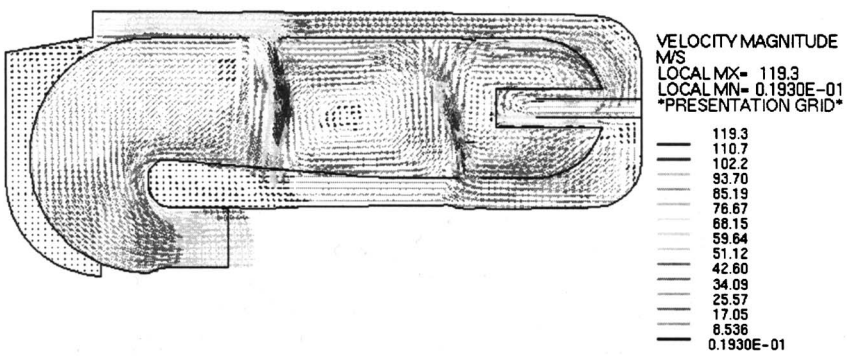

Fig. 3 Cold flow velocity vector field along a longitudinal cross section

Downloaded 02 Jun 2010 to 171.66.16.98. Redistribution subject to ASME license or copyright; see http://www.asme.org/terms/Terms_Use.cfm

Table 1 Mass flux comparison for a cold flow

	STAR-CD Results with "UW" Scheme and coarse mesh				STAR-CD Results with 'MARS' scheme and fine mesh				NPT measured results $\dot{m}$ [%]	CTC-Solver results $\dot{m}$ [%]
	$\dot{m}$ [kg/s]	$\dot{m}$ [%]	Corrected $\dot{m}$ [%]	error	$\dot{m}$ [kg/s]	$\dot{m}$ [%]	Corrected $\dot{m}$ [%]	error		
Sum of 4 upper liner dilution holes – A	0.04342	35.21	31.97	1.54	0.04435	35.96	32.54	0.86	33.4	30.5
Slot – B	0.01904	15.44	13.97	1.87	0.02033	16.485	14.91	2.81	12.1	11.8
Sum of 4 first inner liner dilution holes – C	0.02985	24.21	21.91	2.59	0.03142	25.47	23.05	1.45	24.5	26.5
Sum of 2 last inner liner dilution holes – D	0.02048	16.61	15.03	0.73	0.02035	16.50	14.94	0.64	14.3	15.6
Vaporizer – E	0.01053	8.54	7.73	1.53	0.00688	5.58	5.05	1.15	6.2	6.1
Cooling holes – F									9.5	9.4
Total	0.1233	100%	90.5%			100%	90.5%		100%	99.9%

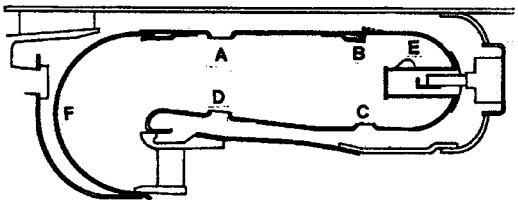

the nuggets was now calculated, instead of using assumed nugget exit profiles as input data as in previous CFD attempts.

The basic assumption behind the approach of Mongia and his co-workers [8–13] in calculating film cooling effectiveness and liner wall temperature is that the interaction of a cooling film with the hot gas inside the combustor is dealing with small details of the flow field. Thus, the film cooling and liner wall temperature calculation is constrained to a small domain around the cooling holes/slots. This approach may be appropriate for large combustors. However, it is the authors' opinion that in small to medium range combustors the cooling holes/slots influence not only their immediate vicinity, but the entire combustion chamber flow field as well. Thus, the entire flow field must be modeled as a whole, from compressor diffuser to turbine inlet, with full coupling of the flow inside and outside the combustor liner.

In a recent study, Crocker et al. [14] modeled a gas turbine combustor from compressor exit to turbine inlet with a structured multiblock grid. The calculations were carried out using the commercial CFD-ACE code. Their model included an air-blast fuel nozzle, dome, and liner walls with dilution holes and cooling louvers. Liner wall temperature was predicted by conjugate heat transfer through the solid liner walls and included radiation effects. Since their combustor was a representative model, they did not have experimental data to compare with the calculated results. The emphasis in their paper was placed on the modeling methodology.

The present paper describes a CFD simulation of the YT-175 combustor, designed by the Noel Penny Turbine (NPT) Company and manufactured by BSE Ltd., from compressor diffuser to turbine inlet. Detailed combustor geometrical configuration is used, including the vaporizer walls and liner walls with dilution holes and cooling slots. The wall temperature of the vaporizer and the liner is predicted by the conjugate heat transfer methodology. Comparison is made between the calculated results and experimental data for the mass flux through the vaporizer and various holes and slots of the liner wall. The angle of the air jets emerging from these holes is compared with experimental measurements. The predicted locations of the liner wall hot spots are compared with the locations in the combustor liner walls that had experienced deformations and cracks during test runs of the engine. Numerical simulations of several alternative film cooling geometries are performed in order to reduce the liner wall temperature and temperature gradients that were observed in the YT-175 combustor experiments.

Combustor Description

The YT-175 combustor used for the simulations is a small size (diameter about 30 cm) reverse flow type combustor, designed by the NPT Company (see Fig. 1). The combustor has 10 L-shaped vaporizers. Hence, a 36 deg periodic sector of the combustor was analyzed. The combustor configuration is essentially made up of three zones: the primary zone, the secondary zone, and the dilution zone. The function of the primary zone is to provide the conditions needed for stable combustion, namely a nearly stoichiometric fuel to air ratio and a low velocity region (typically at the core of a large vortex). It also accommodates the igniter for the initiation of the combustion process. The secondary zone is used to complete the combustion. Air is added to the mixture in this region in order to lean it. This enables burning of the remaining fuel. The dilution zone is used to mix the hot gases with the remaining air in order to reduce their temperature to the level sustained by the turbine blades. The primary zone of the 36 deg sector of the combustor includes the vaporizer, through which about 6% of the combustor air is admitted, a row of louvers and three rows of tiny holes (''porous media'') on the outer liner. For simplicity, the row of louvers and three rows of tiny holes are simulated in the present calculations by a 7.5 deg opening. The secondary zone of the sector consists of a single row of four holes on the inner liner. The dilution zone of the sector consists of a single row of four dilution holes (see Fig. 2) on the outer liner, two dilution holes on the inner liner, and a region of porous media on the outer liner, next to the combustor exit, through which about 9.5% of the combustor air is admitted.

Combustor Geometry Modeling

A 36 deg periodic sector of the combustor was simulated. A multiblock, hybrid structured/unstructured grid was generated using the GRIDGEN code from PointWise Ltd. The generation of a grid for such complex geometry is a time-consuming process. The

Downloaded 02 Jun 2010 to 171.66.16.98. Redistribution subject to ASME license or copyright; see http://www.asme.org/terms/Terms_Use.cfm

use of GRIDGEN simplifies the grid generation and enables easy introduction of geometrical changes. The hybrid grid of structured and unstructured blocks is connected in STAR-CD, in a finite-element fashion, using unstructured grid numbering. A coupling procedure implemented in STAR-CD was used for connecting blocks of different nodes at their interfaces. The use of hybrid structured/unstructured blocks with block coupling can dramatically reduce the total number of required cells.

Most CFD codes [14] utilize a multiblock approach of structured grid topology. It is possible to model virtually any geometry using a structured multiblock approach with block mesh coupling. However, for complex geometries this process is quite laborious. Unstructured grids are generally easier to generate for complex geometries, and the potential for automation is greater. However, unstructured grids may sometimes require many more grid cells, for example, near wall boundaries. In Ref. [7] Gosselin et al. tried to reduce the number of cells required by an unstructured mesh, with the FLUENT/UNS code (version 4.2), by using a hybrid structured/unstructured grid. However, again they ended up with the same problem of a large number of cells. This was due to the lack of a coupling procedure between blocks of different nodes at their interfaces, within the code. The ability of STAR-CD to use hybrid structured/unstructured blocks with mesh coupling simplifies grid generation and reduces the number of required grid cells, thus reducing the overall run time of the numerical simulations.

The vaporizer and liner solid walls, made of 0.7 mm steel, were simulated by a grid of one cell thickness (see Fig. 2). The film cooling louvers and tiny holes at the primary zone were modeled by a continuous slot of equivalent area and opening angle, since it was not practical to model these ports individually. The solid wall thermal conductivity, density, and heat coefficient were assumed to be 43 W/(m-K), 7800 kg/m^3, and 473KJ/(kg-K), respectively, the values for steel.

Two grids were used in the present study: a coarse grid of about 119,000 nodes and a fine grid of about 200,000 cells (see Fig. 1). The fine grid was used to ensure proper resolution of the grid near the walls, with $30<Y_+<200$. The 36 deg sector of the YT-175 combustor was built of 85 blocks. Detailed structures such as the liner wall dilution holes and vaporizer's fuel nozzle were modeled with fine grid blocks, which were coupled with the neighboring blocks, without transferring the high density grid into the entire combustor. The dilution holes were modeled as cylindrical fine mesh blocks, with fine grid blocks in the immediate vicinity, as seen in Fig. 1. This type of grid ensures grid independence while keeping the total number of grid cells to a manageable level.

Combustor Numerical Simulation

The commercial STAR-CD code, version 3.15, from Computational Dynamics Ltd. was used in the present studies. The calculations were carried out on an SGI Octane workstation and on a parallel Origin 200 machine with four processors. The time averaged Navier-Stokes (N-S) equations were solved, with the standard *k-ϵ turbulence model. Results were obtained with both the combined time scale (COMTIME) and the PPDF models for modeling the turbulent kinetic energy reaction rate.*

The COMTIME model is based on the assumption that the reaction time scale is the sum of the turbulent time scale (used by the eddy breakup model) and the chemical time scale. This model was proposed in order to alleviate the problem encountered by the eddy breakup model of overprediction of the reaction rates in near-wall regions. Similar to the EBU model, the COMTIME model is applicable to both premixed and unpremixed systems.

The presumed-PDF (PPDF) model was developed to predict unpremixed (diffusion) flames formed at the interface between totally separate fuel-bearing and oxidant-bearing streams. This model employs the ''fast-kinetics'' or ''mixed is burnt'' assumption; thus, the reaction rate is determined by the turbulent mixing between the streams. For more details see Refs. [16,17].

The effect of radiation on the combustor gas temperature was not modeled in the present study. Previous studies [14,18], on a simplified small model combustor have shown that the effect of radiation is rather small; with radiation, the predicted gas temperature was about 50 K lower than without the incorporation of radiation in the predictions. Also, the fuel was assumed to be in gaseous phase. All effort was focused here on studying the physical phenomena that have the strongest effect on the calculated results. Further study will include radiation and simulation of liquid spray of fuel and will be reported separately.

Calculations were performed for nonreactive and reactive conditions. The nonreactive calculations were carried out for a cold flow, with fuel injection but without combustion. The predicted values for the cold flow were validated by comparison with experimental isothermic flow results.

The reactive flow calculations were then carried out with a two-step reaction of propane fuel according to

step A: $C_3H_8+3.5O_2\rightarrow 3CO+4H_2O$
step B: $CO+0.5O_2\rightarrow CO_2$

It should be mentioned that in the experiments, kerosene fuel was used. However, for simplicity, the calculation was performed with a fuel that has a simpler molecular structure and is easier to model. Liquid fuel will be incorporated in the modeling in the near future and will be reported separately.

The effect of the difference scheme on the calculated results were first studied using different schemes: the first-order ''Up-Wind'' (UW) scheme and the second order ''MARS'' scheme of STAR-CD. The MARS scheme was selected for further use based on these results and on previous comparisons [19] of calculated results with experimental data of the flow in a small cylindrical combustion chamber. In Ref. [19] both, the first-order Up-Wind scheme and the second-order MARS scheme were examined for cold flows. The calculated results for the velocity profiles with the MARS scheme were in very good agreement with the experimental results, while those of the UW scheme were inferior. Also, the MARS scheme is the one preferred by STAR-CD code developers, as its accuracy is less affected by the mesh structure and skewness.

The total airflow through the combustor was prescribed by a single boundary condition at the compressor diffuser. The fuel mass flow was prescribed at the inlet of the fuel nozzle. The calculations were carried out for an ideal gas. The standard k-ε/ high Reynolds number turbulence model was used with the wall function approximation near the walls. The following constants were used for the solid, steel-made walls:

k=43 W/(m K)
ρ=7800 kg/m^3
Cp=473 KJ/(kg K)

Boundary Conditions. Cyclic boundary condition was used on the longitudinal cross-section surfaces: θ=constant. The following boundary conditions were imposed at the inlet and exit boundaries:

Main Air Inlet:
$\dot{m}$=1.2141 kg/s (for the whole combustor)
Ts=480.8 °K
ρ=3.1576 kg/m^3
Fixed mass flux boundary condition.

Fuel Inlet:
$\dot{m}$=0.00197 kg/s (at each vaporizer)
Ts=373°K
ρ=6.1821 kg/m^3
Fixed mass flux boundary condition.

Exit:
''pressure'' boundary condition
Ps=427,900 N/m^2
Zero turbulence gradient.

Downloaded 02 Jun 2010 to 171.66.16.98. Redistribution subject to ASME license or copyright; see http://www.asme.org/terms/Terms_Use.cfm

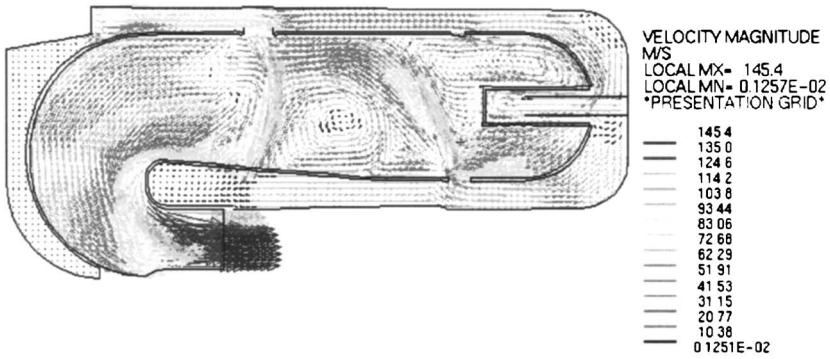

a) Velocity vector field along a longitudinal cross-section.

b) Temperature field along a longitudinal cross-section.

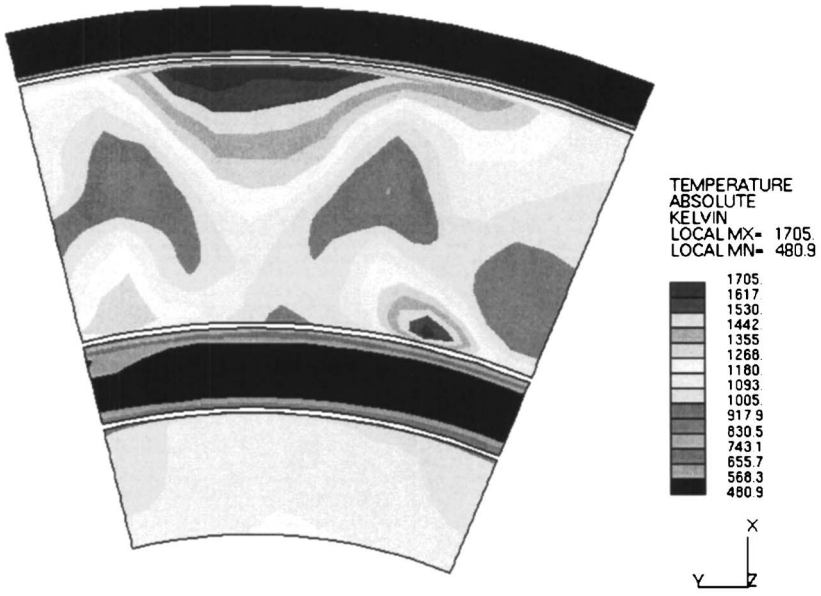

c) Temperature field at the combustor exit cross-section.

Fig. 4 Calculated results using a fine grid, MARS scheme and COMTIME model. (*a*) Velocity vector field along a longitudinal cross section. (*b*) Temperature field along a longitudinal cross section. (*c*) Temperature field at the combustor exit cross section. (*d*) Temperature field along the vaporizer cross section. (*e*) Velocity vector field along the vaporizer cross section. (*f*) CO concentration field at the combustor exit cross section.

Downloaded 02 Jun 2010 to 171.66.16.98. Redistribution subject to ASME license or copyright; see http://www.asme.org/terms/Terms_Use.cfm

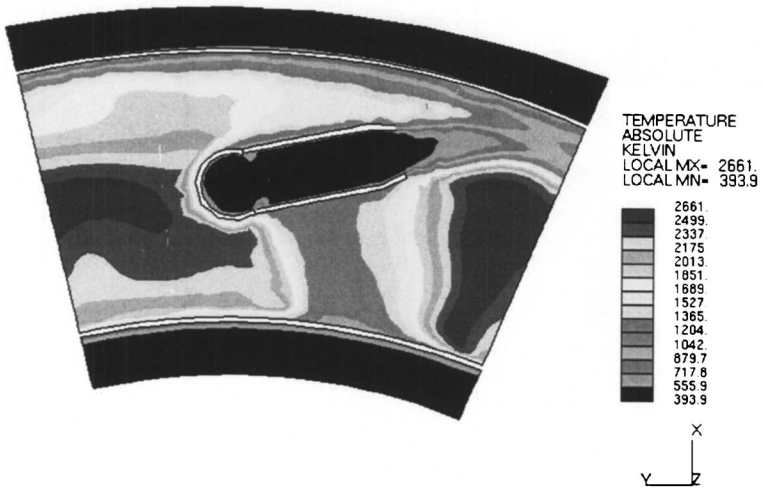

d) Temperature field along the vaporizer cross-section.

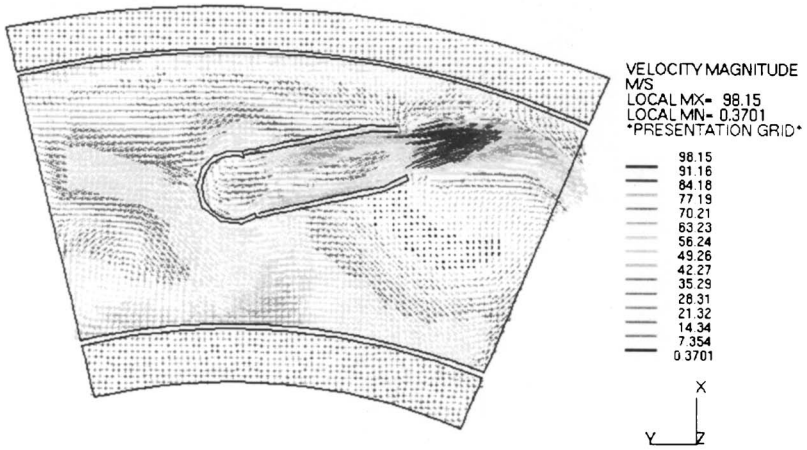

e) Velocity field along the vaporizer cross-section.

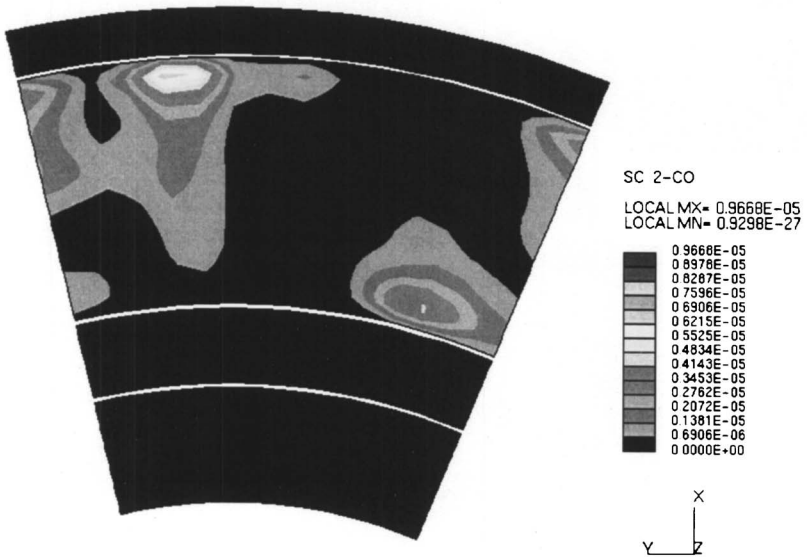

f) CO concentration at the exit cross-section.

Fig. 4 (***continued***)

Downloaded 02 Jun 2010 to 171.66.16.98. Redistribution subject to ASME license or copyright; see http://www.asme.org/terms/Terms_Use.cfm

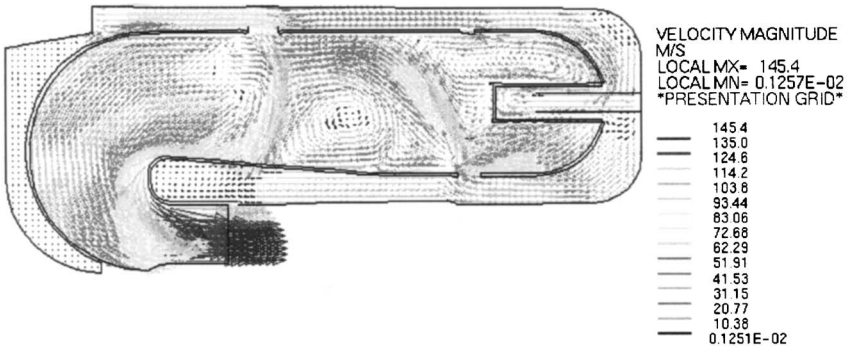

a) Velocity vector field.

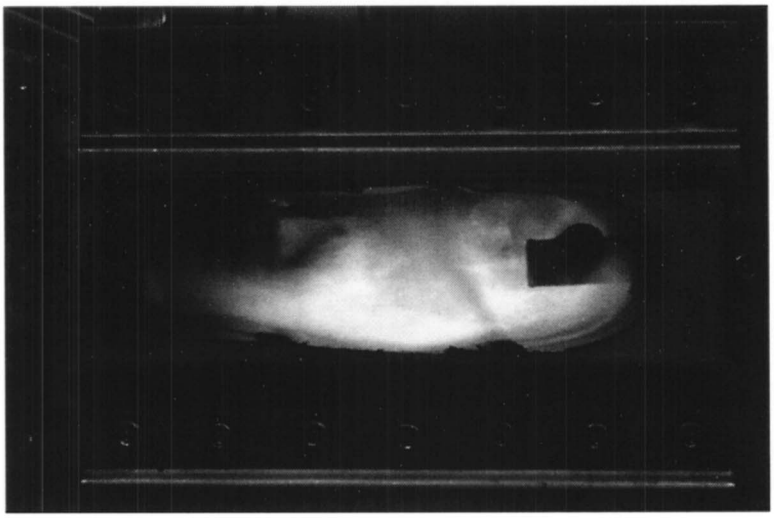

b) Photo image of the flow.

Fig. 5 Comparison of the calculated and measured airflow through the combustor. (*a*) Velocity field along a longitudinal cross section. (*b*) Photo image of the flow.

Results and Discussion

1 Flow Analysis and Validation. In order to validate the computational results, calculations were first carried out for an isothermic flow. Figure 3 presents the cold flow velocity flow field results along a longitudinal cross section. As seen from this figure, the air emanating from the liner holes and slots penetrates deeply into the combustion chamber and generates recirculation of air in the primary and secondary zones. Table 1 presents the results for the mass flux through the various combustor ports, as obtained by a. STAR-CD results using coarse mesh with upwind scheme; b. STAR-CD results using fine mesh with MARS scheme; c. experimental data; and d. semi-empirical results obtained by CTC-AIT (UK). In Table 1 the STAR-CD results present the mass flux in kg/s and in percentages, as well as the corrected results (percentages) and errors. The corrected results were obtained by taking into account the 9.5% of mass flux emanating from the outer liner porous media next to the combustor exit, which was not simulated. The error is defined as

$$\text{error} = |\text{predicted value}[\%] - \text{measured value}[\%]|$$

As seen from this table there is a very good agreement between the calculated and the experimental results. The calculated error for the row of louvers and tiny holes has a somewhat higher value due to inaccurate simulation by slot B. Also, the results for the fine mesh with MARS scheme are significantly better than those obtained for the coarse mesh with the UW scheme.

The reacting flow velocity and temperature fields along a longitudinal cross section are presented in Figs. 4(*a*) and (*b*), respectively. These results were obtained using a fine grid with the MARS scheme and the COMTIME turbulent reaction rate model. Figures 4(*c*) and (*f*) present the temperature and CO concentration fields, respectively, at the combustor exit cross section, and Figs. 4(*d*) and (*e*) present the temperature and velocity fields along the vaporizer cross section. Similar to the cold flow results, the air emanating from the primary zone liner holes and slots penetrates deeply into the combustion chamber and forms a large circumferential toroidal vortex, which embraces the fuel vaporizers within it. The vortex creates the basic condition needed for stabilized combustion. The air added in the secondary region assists in completing the combustion process. The dilution zone cooling holes add cold air to the mixture to reduce the hot gas temperature to the level and distribution pattern required for the turbine blades. Good penetration of the dilution zone air jets is seen, resulting in a rather uniform temperature field at the combustor exit. Figures 5(*a*) and (*b*) present the calculated results for the air flow through the combustion chamber along a longitudinal cross section and the corresponding photo image, as observed in experiments carried out at the Technion Turbo & Jet Propulsion Laboratory, for a periodic section of the combustor. The agreement between the

Downloaded 02 Jun 2010 to 171.66.16.98. Redistribution subject to ASME license or copyright; see http://www.asme.org/terms/Terms_Use.cfm

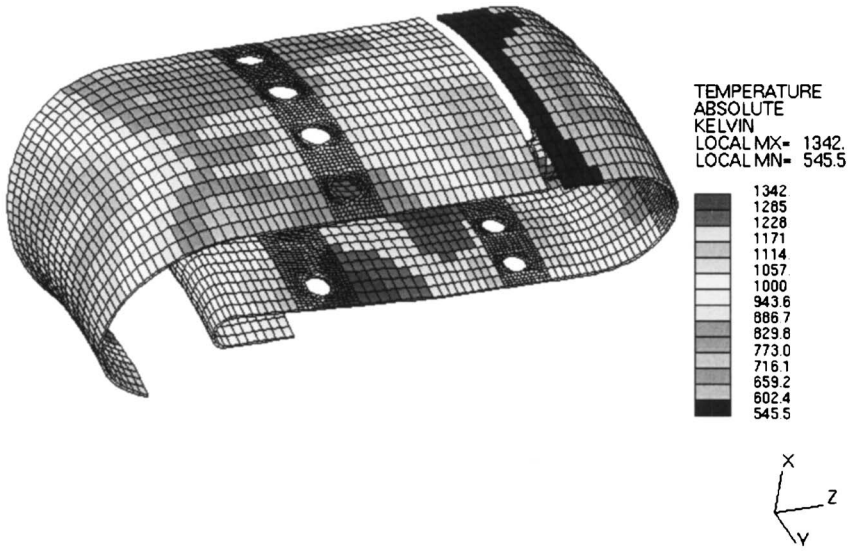

a) Line wall temperatures.

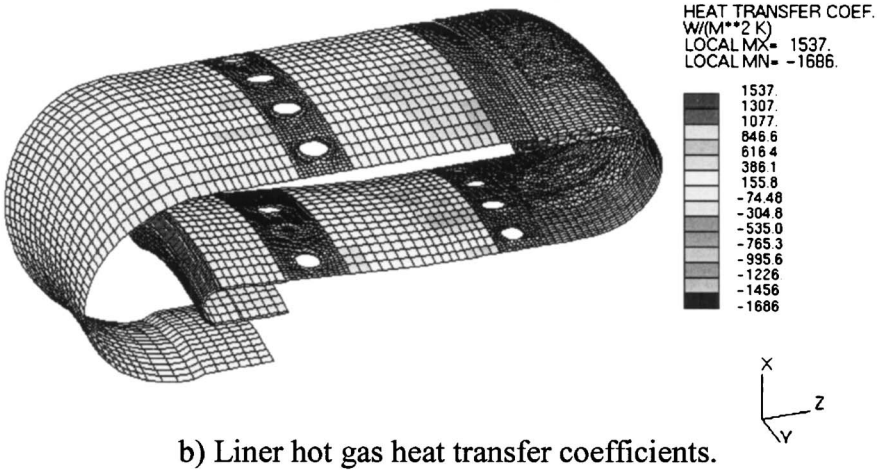

b) Liner hot gas heat transfer coefficients.

Fig. 6 Calculated results for the fine grid, MARS scheme and COMTIME model. (*a*) Liner wall temperatures. (*b*) Liner hot gas heat transfer coefficients.

calculated and the experimental results for the air jet angle emerging from the combustor liner holes is very good. Figures 6(*a*) and (*b*) present the liner wall temperatures and liner hot gas heat transfer coefficients, respectively. As observed from Fig. 6(*a*) high temperatures and temperature gradient are predicted on the outer and inner liner walls. The predicted locations of the outer liner hot spots agree well with the position of deformations and cracks, which occurred in the outer liner walls during test runs of the combustor. Deformations were not observed in the experiments on the inner liner, probably due to the higher strength of the inner wall resulting from its small radius. Figure 6(*b*) presents the distribution of the liner hot gas convective heat transfer coefficient (hot side), defined as

$$h = \frac{Q_{wall}}{T_{wall} - T_{bulk}}$$

where Q_{wall} is the heat flux from the wall to the fluid, T_{wall} is the local liner wall temperature, and the "bulk temperature" of the combustor was defined as

$$T_{bulk} = \frac{\sum \text{volume}_i \cdot T_i}{\sum \text{volume}_i}$$

where volume_i is the volume of cell i at the inner part of the combustor (without the annulus). T_i is the cell's temperature and the summation is over the inner chamber cells. The bulk temperature was calculated for this flow case and found to be: $T_{bulk} = 1498$ K. This value was used here. The range of the heat transfer coefficient spans between -1700 to 1550 $[w/(m^2 K)]$ approximately. Negative values are seen around the holes where the incoming air is cooler than the liner metal. The metal near the holes is heated by conduction from the nearby hotter part of the liner which is heated by the hot combustion gases, and therefore heat is being transferred from the metal to the gas (positive Q).

The execution time for the fine grid calculations with the MARS scheme and COMTIME model is about 80 h on an SGI Octane single processor machine, having an R12000 360 MHz processor. It is expected that this calculation would have taken

Downloaded 02 Jun 2010 to 171.66.16.98. Redistribution subject to ASME license or copyright; see http://www.asme.org/terms/Terms_Use.cfm

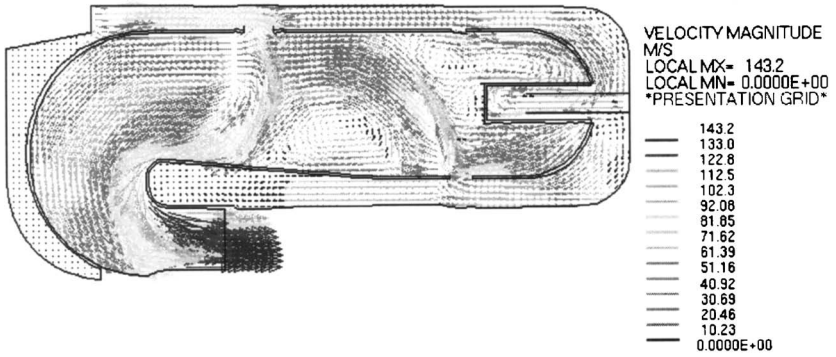

a) Velocity vector field along a longitudinal cross-section.

b) Temperature field along a longitudinal cross-section.

Fig. 7 Calculated results using a coarse grid, MARS scheme and COMTIME model. (*a*) Velocity vector field along a longitudinal cross section. (*b*) Temperature field along a longitudinal cross section. (*c*) Temperature field at the combustor exit cross section. (*d*) Temperature field along the vaporizer cross section.

about one-third or less of that time on current available PC machine having a 3.0 GHz Intel processor. The calculation time may be drastically reduced by using the parallel version of STAR-CD on a parallel machine.

2 Parametric Studies. Initial runs were carried out on a coarse grid of about 116,000 cells using the MARS difference scheme and the COMTIME turbulent reaction rate model. Figures 7(*a*) and (*b*) present the calculated velocity and temperature fields in a longitudinal cross section, respectively. Figure 7(*c*) presents the temperature field at the combustor exit cross section and Fig. 7(*d*) presents the temperature field along the vaporizer cross section. Figure 8 presents the corresponding liner wall temperatures. Observation of the liner wall temperatures and temperature gradients and the values of Y_+ near the wall of these calculations revealed the need for a finer mesh. Thus, a finer grid was built with about 200,000 cells. Comparison of Figs. 4(*a*)–(*d*) and 6(*a*) of the fine grid results with Figs. 7(*a*)–(*d*) and 8 of the coarse grid results shows that the overall flow pattern is quite similar, though the maximum field temperature of the coarse grid is about 50 K higher than that of the fine grid. Also, the liner wall temperatures of the fine and coarse grids are of similar pattern, but with a higher maximum temperature of about 30 K for the fine grid.

To study the effect of the difference scheme, calculations were carried out with the coarse grid, using the COMTIME model with two finite difference schemes: the first-order UW scheme and the second-order MARS scheme. Figures 9(*a*) and (*b*) present the velocity and temperature fields in a longitudinal cross section as obtained with the UW scheme, respectively. Figure 9(*c*) presents the temperature field at the combustor exit cross section and Fig. 9(*d*) presents the temperature field along the vaporizer cross section. Figure 10 presents the corresponding liner wall temperature. Comparison of Figs. 7(*a*)–(*d*) with Figs. 9(*a*)–(*d*) shows that although the velocity and temperature fields look quite similar, there is a significant difference between the maximum gas temperatures obtained with the two schemes of about 240 K. The liner wall temperature of the MARS scheme is about 170 K higher than that of the UW scheme. It should be noted that the use of the MARS scheme considerably increases the computation time.

To study the effect of the turbulent reaction rate model, we ran the same case with the PPDF combustion model. Figures 11(*a*) and (*b*) present the velocity and temperature fields in a longitudinal cross section as calculated with the fine grid MARS scheme and PPDF model. Figures 11(*c*) and (*f*) present the temperature and CO concentration fields, respectively, at the combustor exit cross section. Figures 11(*c*) and (*e*) present the temperature and velocity fields along the vaporizer cross section, respectively, and Fig. 12 presents the liner wall temperature of this calculation. Comparison of Figs. 11(*a*)–(*f*) and 12 with Figs. 4(*a*)–(*f*) and 6(*a*) of the COMTIME model (MARS scheme, fine grid) shows that there is a significant difference between the temperature fields,velocity fields, and liner wall temperatures of the two models. Also, the angle of the air jets emanating from the liner cooling holes is different. The air jets angle of the PPDF model is almost perpendicular to the liner wall, while that of the COMTIME model forms a moderate angle with the normal to the liner wall surface. However, the most prominent difference is the reaction that takes place within the vaporizer itself, while using the PPDF model.

The reaction within the vaporizer results in high vaporizer wall temperature, very high gas temperature inside the vaporizer, and acceleration of the gas velocities within the vaporizer. Velocity values as high as 206 m/s at the tip of the vaporizer are recorded.

Downloaded 02 Jun 2010 to 171.66.16.98. Redistribution subject to ASME license or copyright; see http://www.asme.org/terms/Terms_Use.cfm

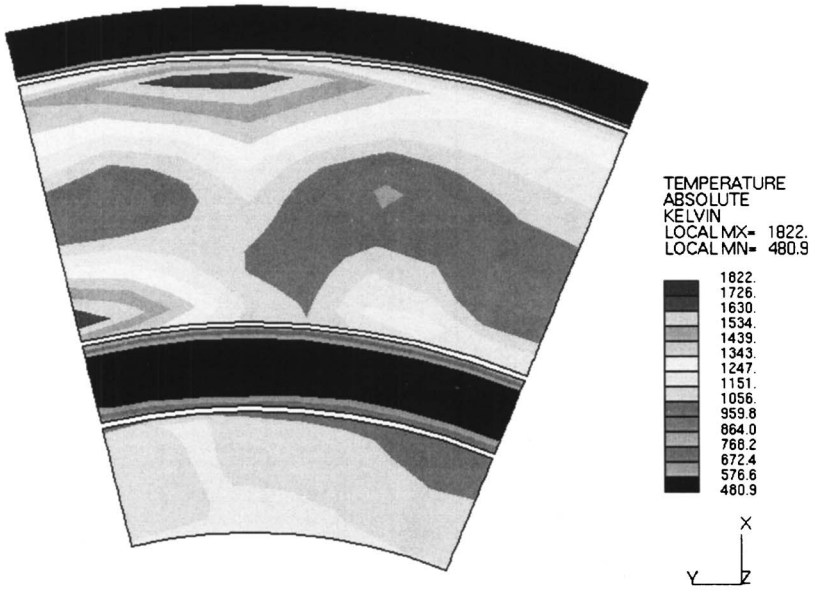

c) Temperature field at the combustor exit cross-section.

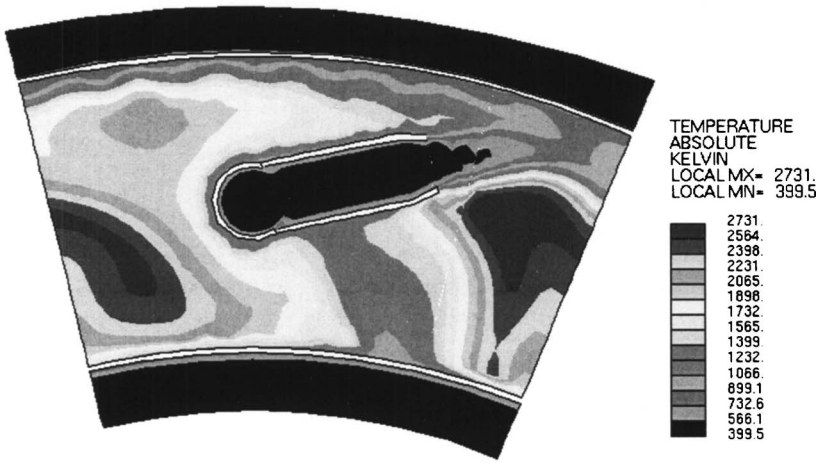

d) Temperature field along the vaporizer cross-section.

Fig. 7 (***continued***)

This is probably the result of the PPDF model assumption of ''fast kinetics'' or ''mixed is burnt.'' As air and fuel are mixed within the vaporizer, although under very rich conditions, reaction under the PPDF assumption is taking place, the gas temperature is increased, and high velocities are obtained. Such phenomenon is rarely the reality. Typically, no reaction takes place inside the vaporizer. Also, the effect of the high velocities emerging from the vaporizer is increase of the liner wall temperature at the base side of the vaporizer, where values over 2000 K are observed. Thus, it can be concluded that the PPDF model is probably not suitable for the present simulations.

Table 2 presents comparisons of the average, maximal, and minimal temperatures at the combustor exit plane and of the liner wall for the various cases that were studied here. The average exit plane/liner wall temperature is defined as

$$T_{av} = \frac{\sum \text{area}_i \cdot T_i}{\sum \text{area}_i}$$

where area_i is the area of cell i at the exit plane/liner wall. T_i is the cell's temperature and the summation is over the exit plane/liner wall cells. The table presents also the pattern factor P_f, defined as

$$P_f = \frac{T_{max} - T_{av}}{T_{av} - T_{inlet}}$$

As seen from Table 2 the average exit temperature of the COM-

Downloaded 02 Jun 2010 to 171.66.16.98. Redistribution subject to ASME license or copyright; see http://www.asme.org/terms/Terms_Use.cfm

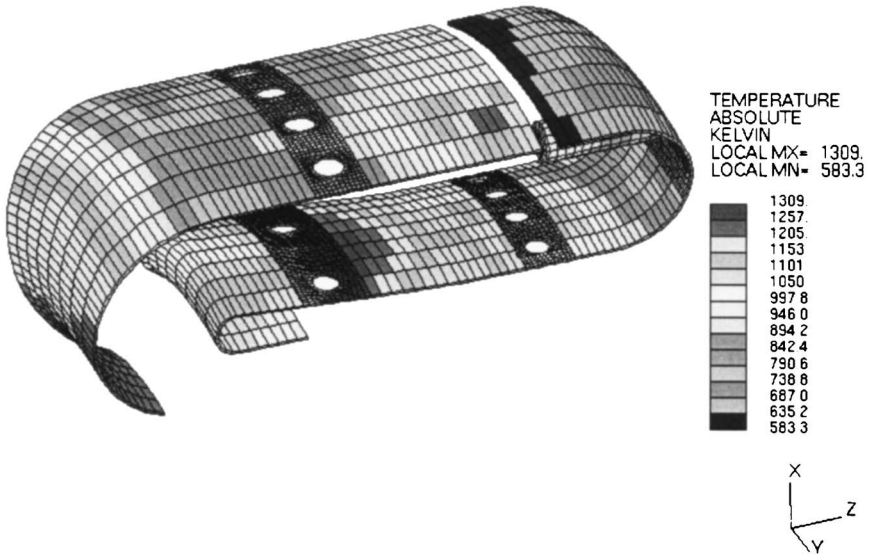

Fig. 8 Liner wall temperatures calculated with a coarse grid, MARS scheme and COMTIME model

TIME model for the various cases studied here (fine grid with MARS scheme/coarse grid with MARS scheme/coarse grid with UW scheme), are the same, while the average exit temperature of the PPDF model (fine grid and MARS scheme) is about 60 K lower. Hence, the predicted efficiency of the combustor with the PPDF model is lower than that with the COMTIME model. This lower efficiency is due to the partial burning of the fuel with the PPDF model, which can be seen from Fig. 11(*f*) presenting the CO

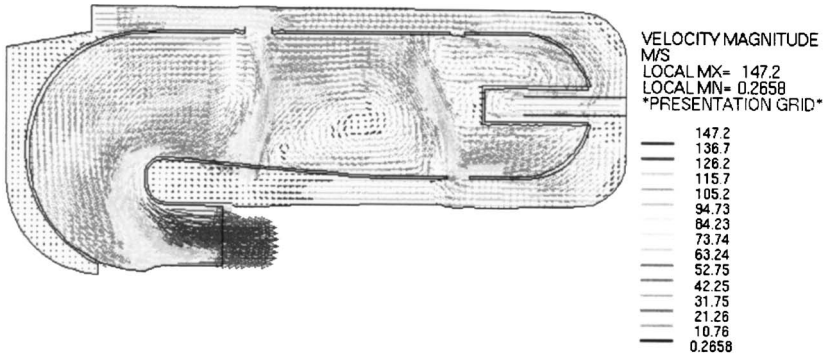

a) Velocity field along a longitudinal cross-section.

b) Temperature field along a longitudinal cross-section.

Fig. 9 Calculated results using a coarse grid, UW scheme and COMTIME model. (*a*) Velocity vector field along a longitudinal cross section. (*b*) Temperature field along a longitudinal cross section. (*c*) Temperature field at the combustor exit cross section. (*d*) Temperature field along the vaporizer cross section.

Downloaded 02 Jun 2010 to 171.66.16.98. Redistribution subject to ASME license or copyright; see http://www.asme.org/terms/Terms_Use.cfm

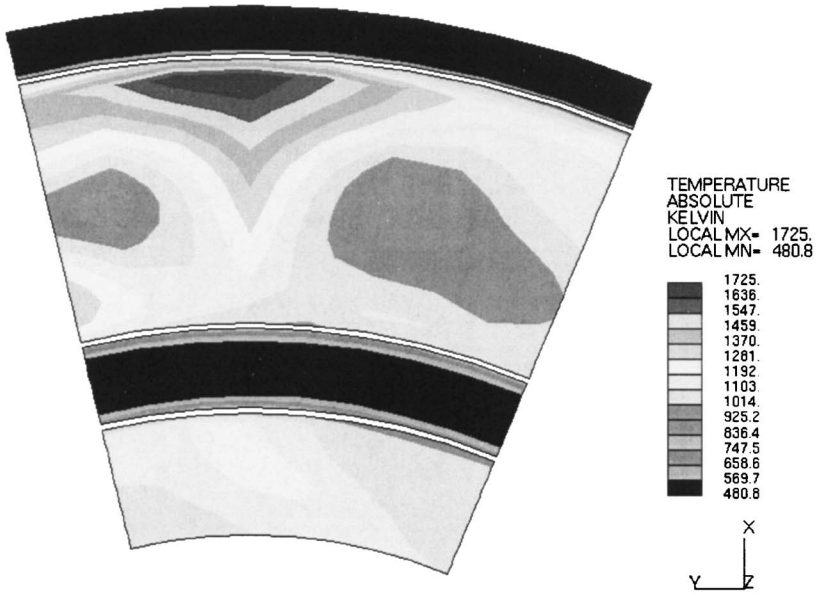

c) Temperature field at the combustor exit cross-section.

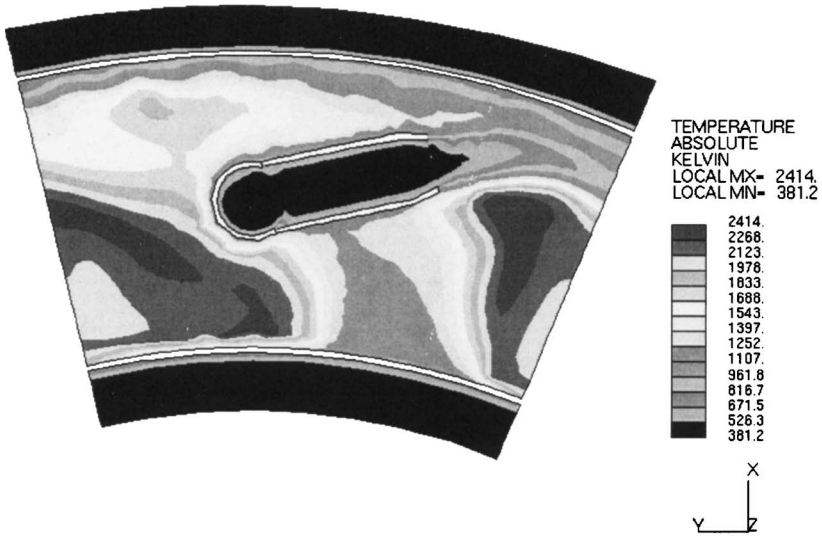

d) Temperature field along the vaporizer cross-section.

Fig. 9 (***continued***)

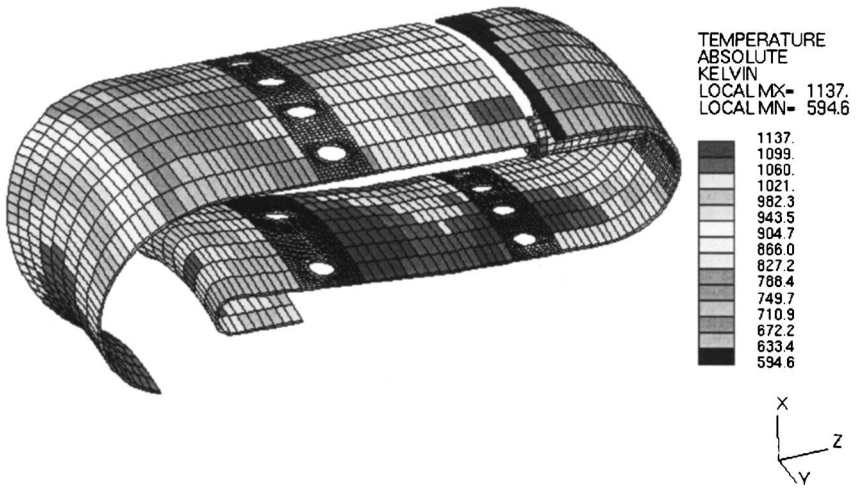

Fig. 10 Liner wall temperatures calculated with a coarse grid, UW scheme and COM-TIME model

Downloaded 02 Jun 2010 to 171.66.16.98. Redistribution subject to ASME license or copyright; see http://www.asme.org/terms/Terms_Use.cfm

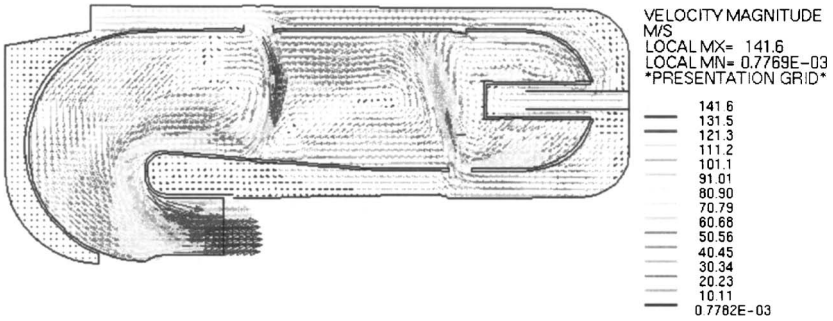

a) Velocity vector field along a longitudinal cross-section.

b) Temperature field along a longitudinal cross-section.

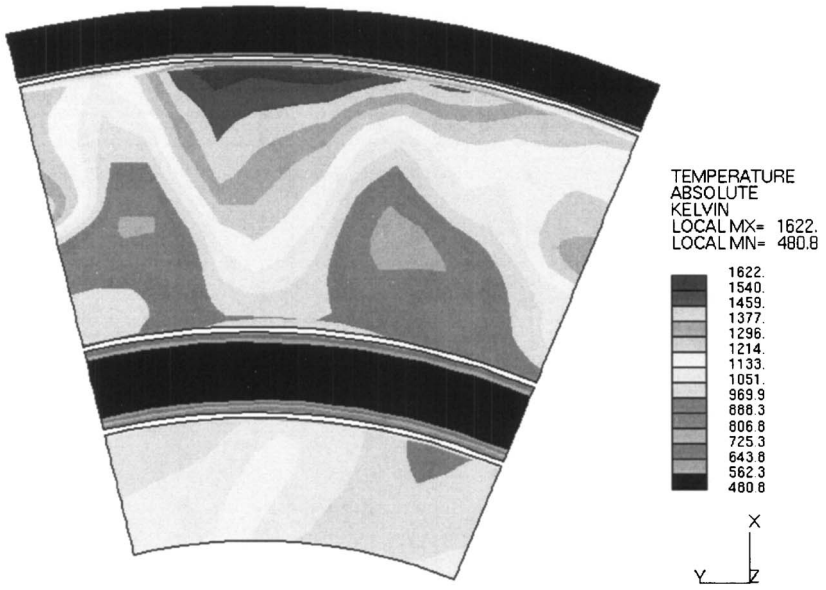

c) Temperature field at the combustor exit cross-section.

Fig. 11 Calculated results using a fine grid, MARS scheme and PPDF model. (*a*) Velocity vector field along a longitudinal cross section. (*b*) Temperature field along a longitudinal cross section. (*c*) Temperature field at the combustor exit cross section. (*d*) Temperature field along the vaporizer cross section. (*e*) Velocity vector field along the vaporizer cross section. (*f*) CO concentration field at the combustor exit cross section.

Downloaded 02 Jun 2010 to 171.66.16.98. Redistribution subject to ASME license or copyright; see http://www.asme.org/terms/Terms_Use.cfm

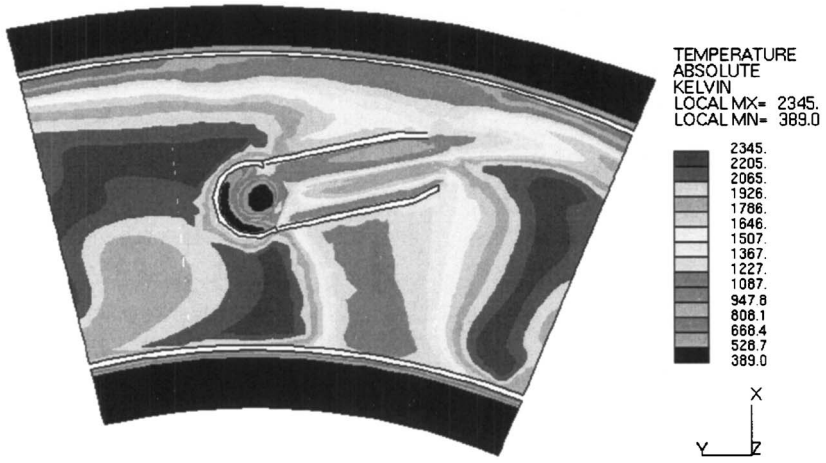

d) Temperature field along the vaporizer cross-section.

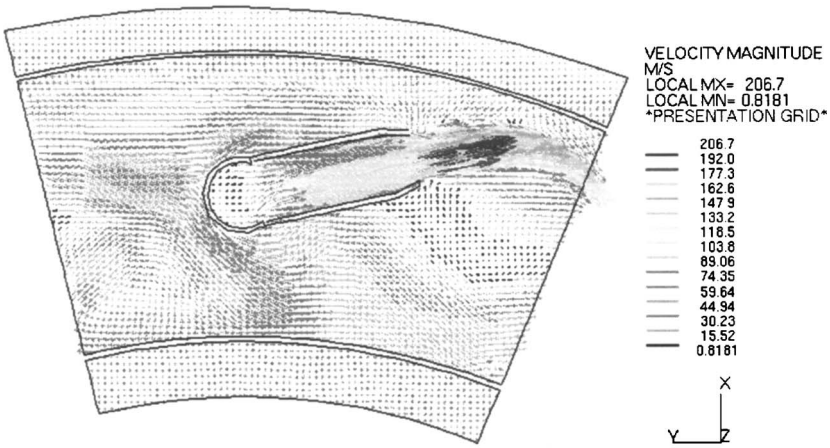

e) Velocity field along the vaporizer cross-section.

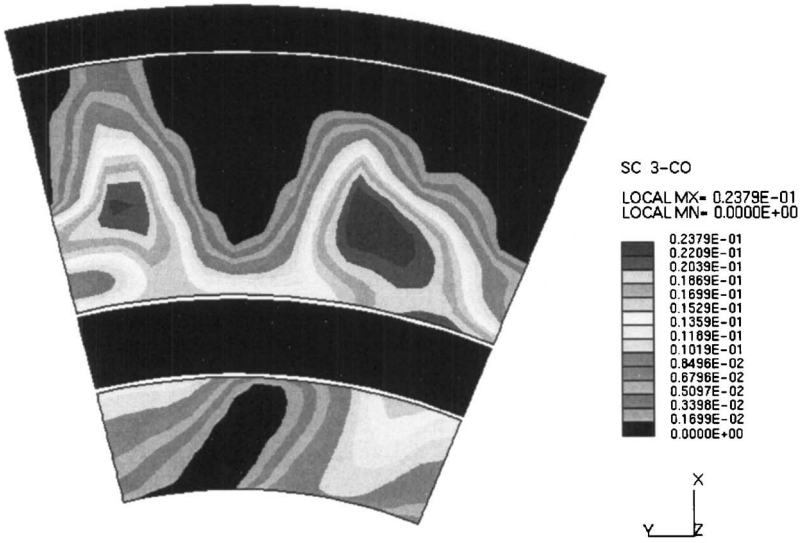

f) CO concentration at the exit cross-section.

Fig. 11 (***continued***)

Downloaded 02 Jun 2010 to 171.66.16.98. Redistribution subject to ASME license or copyright; see http://www.asme.org/terms/Terms_Use.cfm

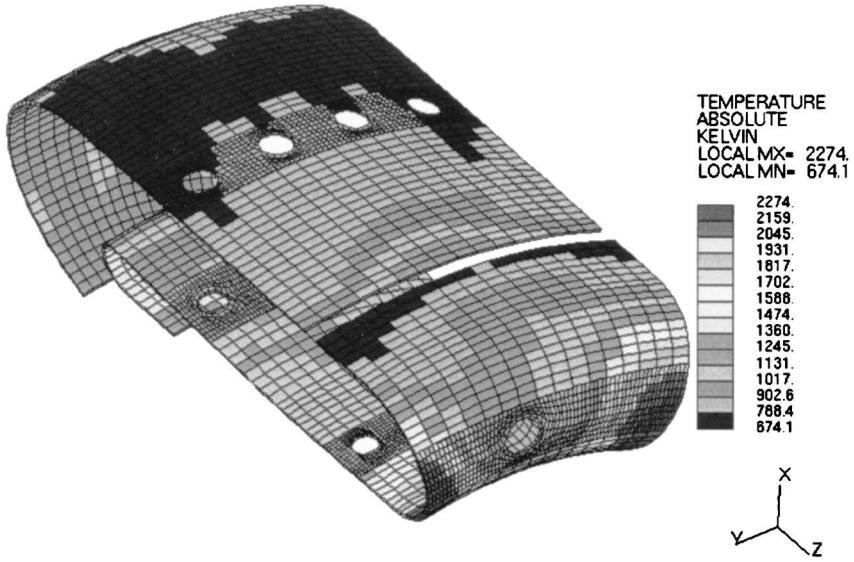

Fig. 12 Liner wall temperatures calculated with a fine grid, MARS scheme and PPDF model

Table 2 Comparison of the calculated exit and liner wall temperatures of the various parametric studies

	Exit Temperatures				Liner Temperatures		
	T_{av} [°K]	T_{max} [°K]	T_{min} [°K]	P_f	T_{av} [°K]	T_{max} [°K]	T_{min} [°K]
Fine grid, 'MARS' scheme, COMTIME model	1115	1237	981	0.192	983	1342	543
Coarse grid, 'MARS' scheme, COMTIME model	1115	1221	1016	0.167	958	1309	583
Coarse grid, 'UW' scheme, COMTIME model	1116	1239	995	0.194	911	1137	595
Fine grid, 'MARS' scheme, PPDF model	1057	1153	929	0.167	1148	2274	674

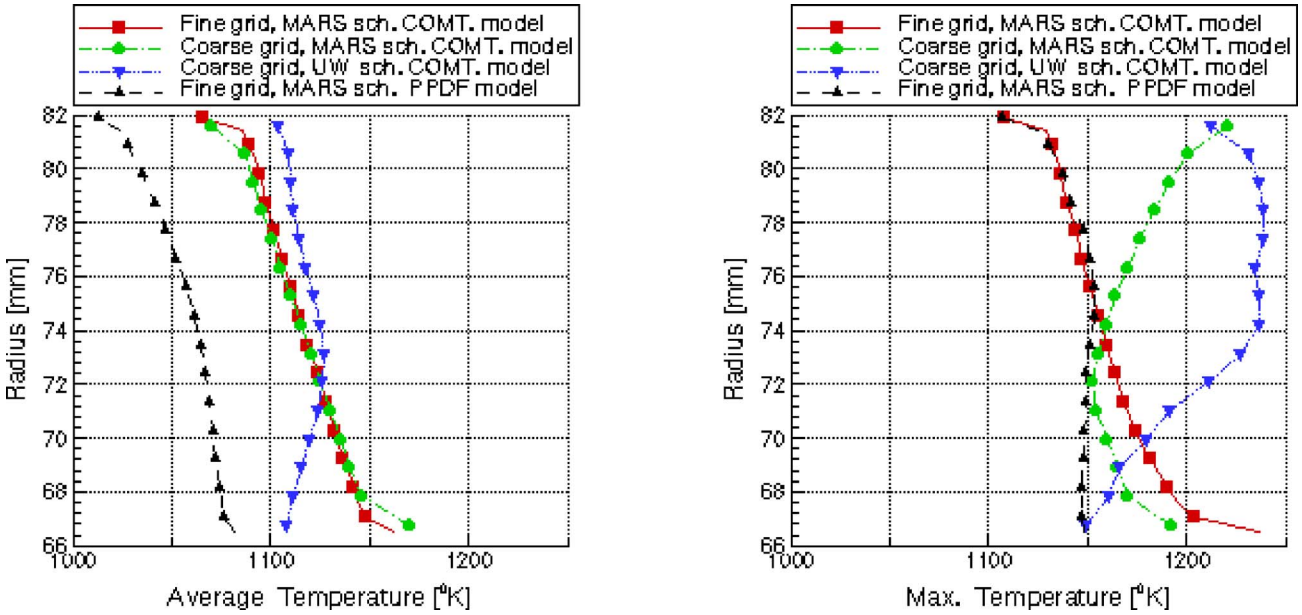

Fig. 13 Comparison of the radial exit plane temperature profiles of the various case studies. (*a*) Circumferentially averaged temperature. (*b*) Maximum temperature.

Downloaded 02 Jun 2010 to 171.66.16.98. Redistribution subject to ASME license or copyright; see http://www.asme.org/terms/Terms_Use.cfm

Fig. 14 Alternative I configuration geometry along a longitudinal cross section

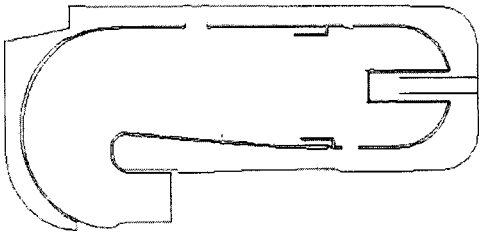

Fig. 15 Alternative II configuration geometry along a longitudinal cross section

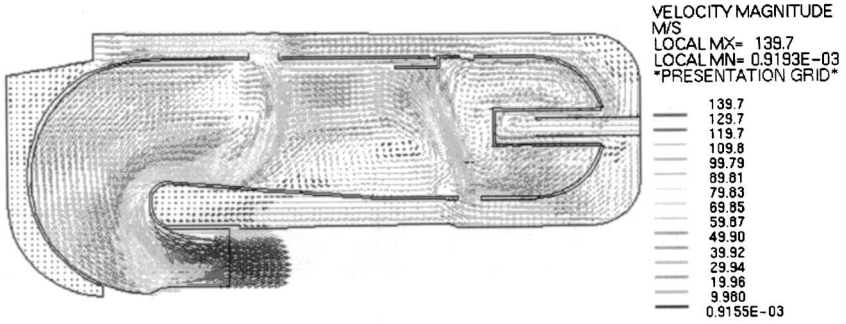

a) Velocity vector field along a longitudinal cross-section.

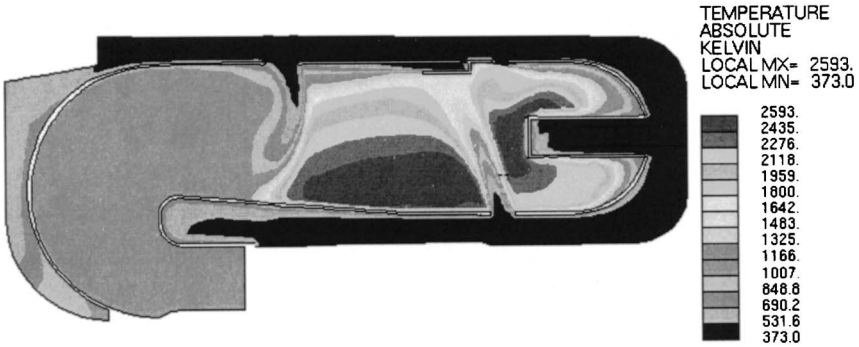

b) Temperature field along a longitudinal cross-section.

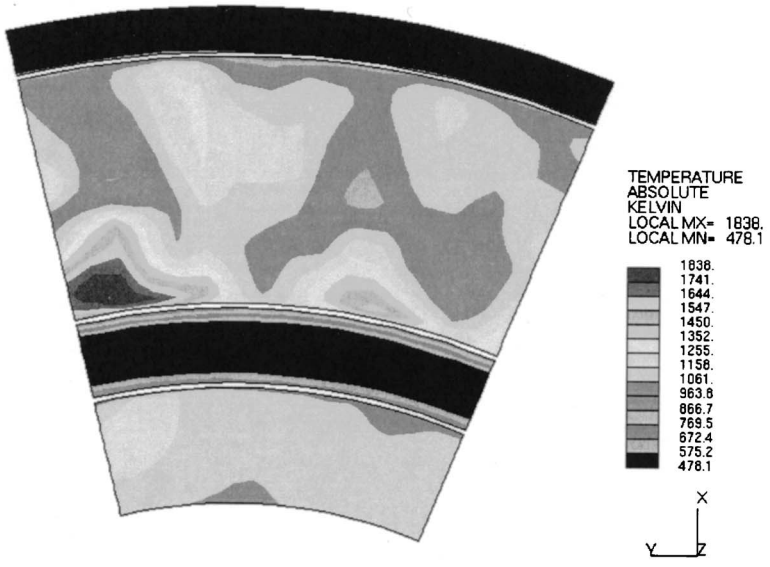

c) Temperature field at the exit cross-section.

Fig. 16 Calculated results of alternative I using a fine grid, MARS scheme and COMTIME model. (*a*) Velocity vector field along a longitudinal cross section. (*b*) Temperature field along a longitudinal cross section. (*c*) Temperature field at the combustor exit cross section.

Downloaded 02 Jun 2010 to 171.66.16.98. Redistribution subject to ASME license or copyright; see http://www.asme.org/terms/Terms_Use.cfm

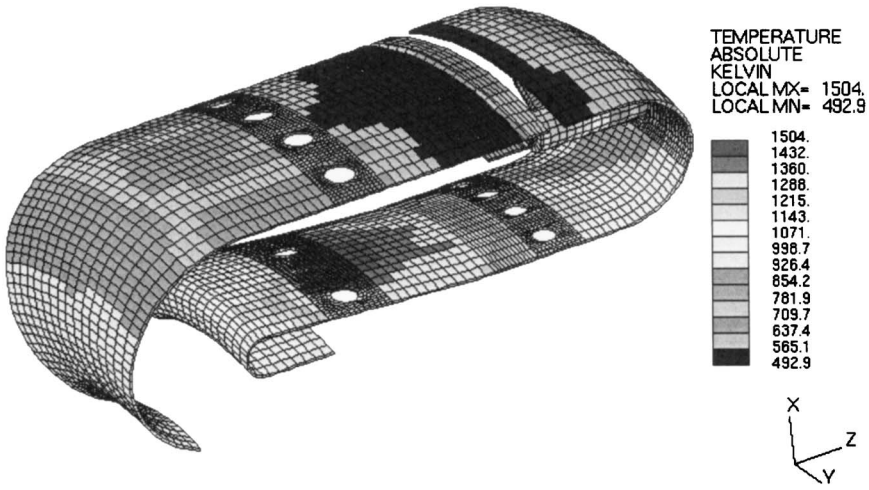

Fig. 17 Liner wall temperatures of alternative I using a fine grid, MARS scheme and COMTIME model

concentration at the exit plane. As seen from this figure, a high-percentage of CO exits the combustor unburnt. This is contrary to the COMTIME model results, where the fuel is almost completely burnt at the exit plane. Figure 4(*f*) presents the CO concentration at the exit plane for the COMTIME model (fine grid, MARS scheme) for comparison.

The average gas temperature in the inner sector of the combustor (i.e., the bulk temperature defined earlier) was calculated from the COMTIME prediction (fine grid, MARS scheme) and was found to be 1498 K. The value under PPDF predictions was found to be only 1414 K. Thus, the PPDF model predicts lower gas temperatures in the inner part of the combustor. Similar results were obtained by Gosselin et al. [7], who used the FLUENT/UNS code with the PDF model for the prediction of the flow in a gas turbine combustor. Comparison of the calculated results with experiments in Ref. [7] showed that the numerical results underpredicted the gas temperatures by about 18% to 25% depending on the various combustor zones.

Figures 13(*a*) and (*b*) present a comparison of the radial circumferentially averaged temperature and maximal temperature profiles at the combustor exit plane, respectively, for the various case studies. As seen from Fig. 13(*a*), the radial distribution of the circumferentially averaged temperatures of the PPDF model is lower than that of the COMTIME model by about 60 K. Comparison of the various COMTIME model predictions reveals that the radial distribution of the circumferentially averaged temperature of the UW scheme is almost uniform across the exit plane. Also, the radial distribution of the circumferentially averaged temperature of the MARS scheme with the fine grid is similar to that of the coarse grid, except for a somewhat higher temperature at the turbine root and lower temperature at its tip. These differences are due to the better resolution obtained with the fine grid near the combustor walls. Comparison of Figs. 13(*a*) and (*b*) reveals that the radial maximal temperature profiles of the coarse grid, for both the MARS and UW schemes, differ considerably from their corresponding radial average temperature profiles. Thus, large tangential variations at the exit plane are predicted with the coarse-grid. This is due to the low resolution of the coarse grid results. Also, the radial maximal temperature profiles of the fine grid, for both the COMTIME and PPDF models, differ only by a small amount from the corresponding radial average temperature profiles.

Improvements to the YT-175 Gas Chamber

Experiments performed using the YT-175 combustor revealed deformations and distortions of the gas chamber liner walls operating at sea level and M=0 flow conditions. These deformations and distortions are due to local high temperature peaks and sharp temperature gradients in the liner walls. High liner wall temperatures and temperature gradients were also predicted by the CFD calculations (with the COMTIME model). To reduce the hot spot's temperature and temperature gradients the CFD was utilized as a design tool to redesign the liner wall cooling. The basic requirement of the redesign was minimal modifications of the combustor geometry to avoid major changes in the combustor air distribution. Also, the temperature field across the combustor exit should be as uniform as possible, with maximum value at about 2/3 of the exit cross-section radius.

Two alternative geometry modifications were examined:

Alternative (configuration) I: Obtained by adding a 0.5 mm compact series of holes (or split) on the upper liner wall, with a 12 mm shelf at 2 mm from the upper wall.

Alternative (configuration) II: Obtained by adding two 0.5 mm splits, one on the upper liner wall and the other on the lower liner wall, with 12 mm shelves, at 2 mm from the walls. Figures 14 and 15 present the two alternatives. Calculations were carried out with the MARS scheme and COMTIME model using the fine mesh with slight modifications to accommodate the new geometries.

Figures 16(*a*) and (*b*) present the velocity and temperature fields in a longitudinal cross section, respectively, as calculated for the first alternative (I), and Figs. 16(*c*) and 17 present the combustor exit cross-section temperature field and liner wall temperatures for this flow case. The corresponding results for alternative II are presented in Figs. 18(*a*)–(*c*) and 19. As observed from Figs. 16(*a*)–(*b*) and 17, alternative I resulted in cooling of the upper liner wall. However, it resulted in overheating of the lower liner wall. Thus, the introduction of the upper liner-cooling split affects the flow not only in the vicinity of the split, but also throughout a large portion of the combustion chamber. Also, the temperature field at the exit, as calculated for alternative I, does not satisfy the requirements for uniform temperature across the exit with a maximum value at about 2/3 of the radius. Figures 18(*a*) and (*b*) and 19 show that alternative II resulted in cooling of both the upper and lower liner wall temperatures, with nearly uniform temperature across the exit, and maximal temperature value at about 2/3 of the exit cross-section radius. Table 3 presents

Downloaded 02 Jun 2010 to 171.66.16.98. Redistribution subject to ASME license or copyright; see http://www.asme.org/terms/Terms_Use.cfm

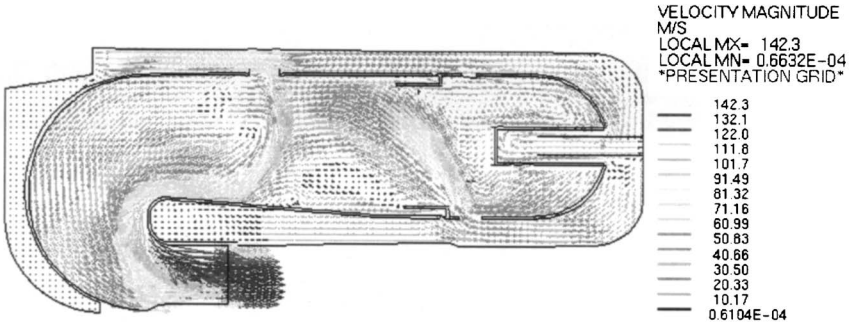

a) Velocity vector field along a longitudinal cross-section.

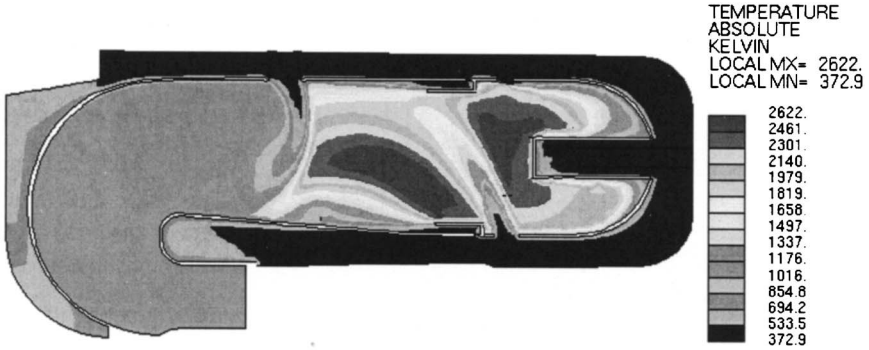

b) Temperature field along a longitudinal cross-section.

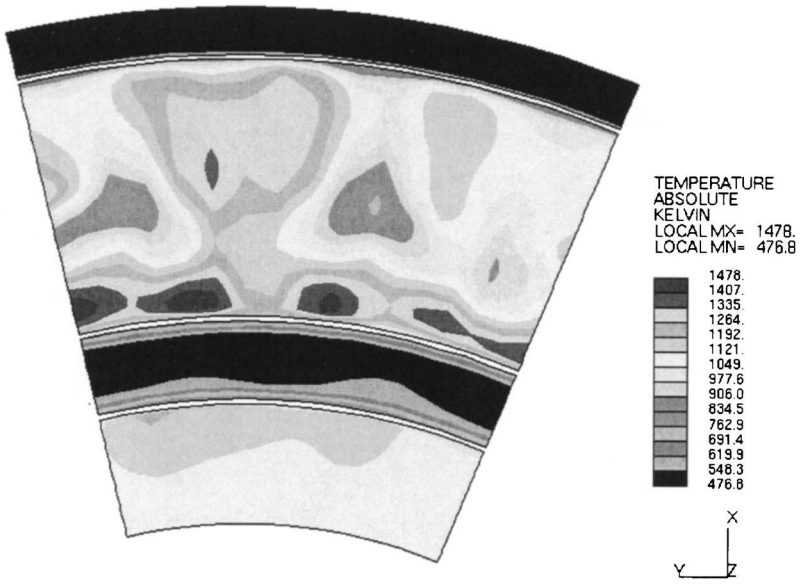

c) Temperature field at the exit cross-section.

Fig. 18 Calculated results of alternative II using a fine grid, MARS scheme and COMTIME model. (*a*) Velocity vector field along a longitudinal cross section. (*b*) Temperature field along a longitudinal cross section. (*c*) Temperature field at the combustor exit cross section.

Downloaded 02 Jun 2010 to 171.66.16.98. Redistribution subject to ASME license or copyright; see http://www.asme.org/terms/Terms_Use.cfm

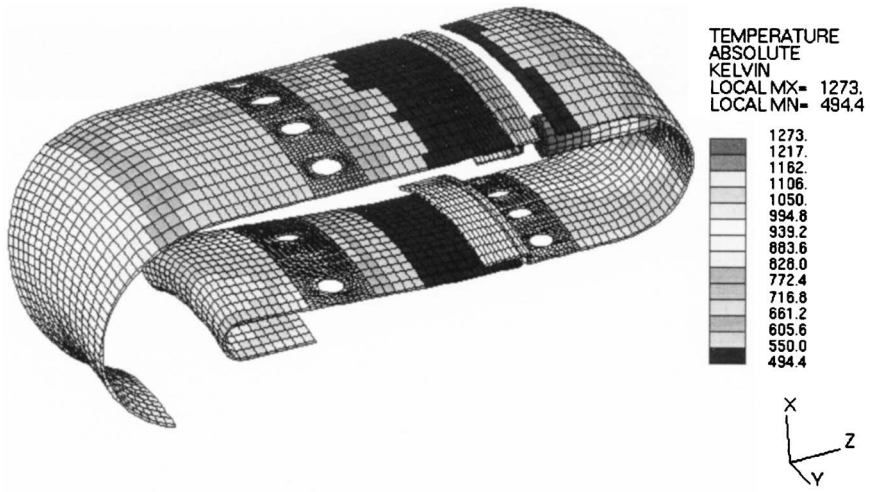

Fig. 19 Line wall temperatures of alternative II using a fine grid, MARS scheme and COMTIME model

Table 3 Mass flux comparison of the original and two alternative configurations

	Original Configuration		Configuration I with 1 added top slot		Configuration II with 2 added slots	
	kg/sec	%	kg/sec	%	kg/sec	%
Sum of all 4 top dilution holes - A	0.04517	36.63	0.04043	32.75	0.03684	29.88
Slot - B	0.01833	14.87	0.01533	12.42	0.01426	11.565
Sum of the 4 low, first dilution holes - C	0.03109	25.215	0.02872	23.26	0.02601	21.09
Sum of the 2 low dilution holes - D	0.01934	15.685	0.01822	14.76	0.01796	14.57
Premixed air - E	0.00937	7.60	0.00882	7.14	0.00818	6.63
Added top slot - F			0.01194	9.67	0.01090	8.84
Added bottom slot - G					0.00915	7.42

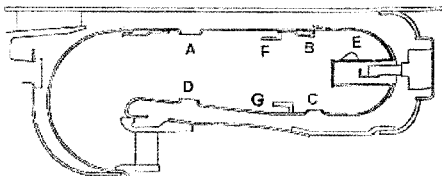

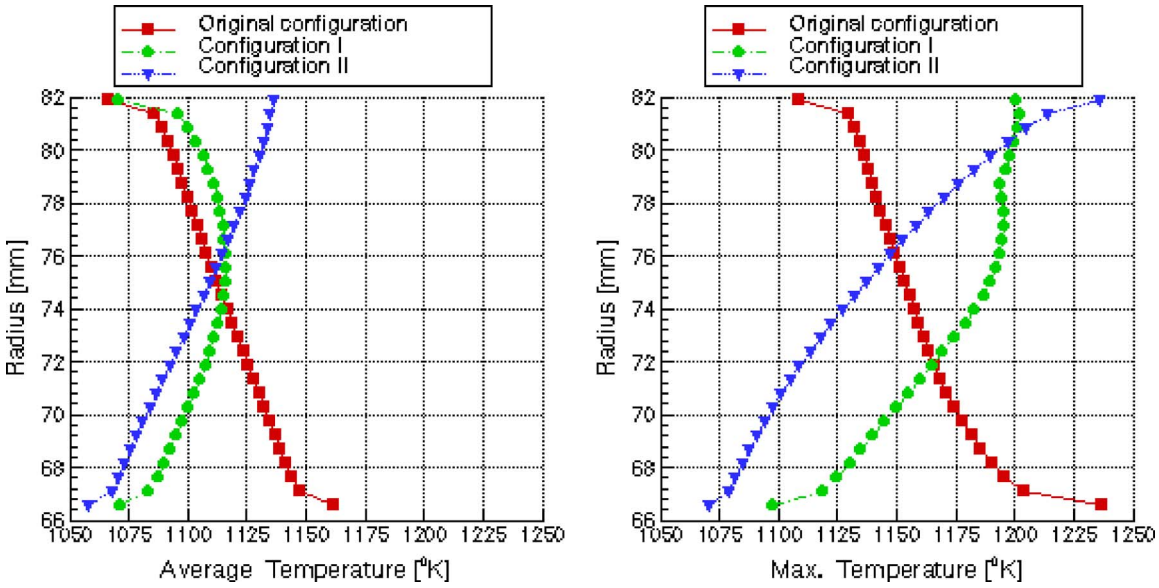

Fig. 20 Comparison of the radial exit plane temperature profiles of the original and modified configurations. (*a*) Circumferentially averaged temperature profiles. (*b*) Maximal temperature profiles.

Downloaded 02 Jun 2010 to 171.66.16.98. Redistribution subject to ASME license or copyright; see http://www.asme.org/terms/Terms_Use.cfm

Table 4 Comparison of the calculated exit and liner wall temperatures of the original and two alternative configurations

	Exit Temperatures				Liner Temperatures		
	T_{av} [°K]	T_{max} [°K]	T_{min} [°K]	P_f	T_{av} [°K]	T_{max} [°K]	T_{min} [°K]
Original configuration	1115	1237	981	0.192	983	1342	543
Configuration I	1104	1202	993	0.157	896	1504	493
Configuration II	1105	1236	1032	0.210	824	1273	494

comparisons of the mass flow through the various liner holes, slots, and vaporizer of the original configuration, and of alternatives I and II. As seen from this table, the mass flux distribution of both alternatives changes only slightly with respect to that of the original configuration, as required.

Figures 20(*a*) and (*b*) present a comparison of the radial circumferentially averaged temperature and maximal temperature profiles at the combustor exit plane, respectively, of the original configuration and the two alternatives studied here. As seen from Fig. 20(*a*) the effect of the film cooling slots incorporated in these alternatives is a reduction of the average temperature at the exit plane inner side, by about 100 K, shift of the average temperature profile peak location outward, and decrease of its peak value. As seen from Fig. 20(*b*), the radial maximal temperature profiles of the original configuration and of alternative II are similar to the corresponding radial average temperature profiles, differing by less than 60 K, while for alternative I, the maximal temperature profile differs from the radial average temperature profile considerably; up to 130 K at the tip (larger radius). Thus, for alternative I the exit plane temperature varies quite a lot circumferentially.

Table 4 presents comparisons of the average, maximal, and minimal temperatures at the combustor exit plane, and liner wall, for the original configuration and two alternatives.

Conclusions and Further Research

The paper presents a 3D numerical simulation of a small gas turbine combustor. The entire flow field is modeled from the compressor diffuser to turbine inlet. A periodic 36 deg sector of the combustor is modeled using a hybrid structured/unstructured multiblock grid. The liner wall temperature is predicted by the ''conjugate heat transfer'' methodology, based on simultaneous solution of the heat transfer equations for the vaporizer and liner walls, coupled with the N-S equations for the fluids. Calculations were carried out for both the COMTIME and the PPDF turbulent reaction rate models. The calculated results with the COMTIME model agreed well with experimental data. These results represent a significant achievement for the simulation of a gas turbine combustor. Additional experiments of the gas turbine temperatures would assist in the validation and improvement of physical modeling of reacting flows in gas turbines.

The CFD was utilized as a design tool to redesign the liner cooling, to prevent deformations and distortions that were observed during test runs of the YT-175 engine.

Several subjects that were not addressed in the present study still need to be resolved for complete combustor modeling. These include droplet evaporation and trajectory calculations, gas radiation, and soot effect prediction.

References

[1] Danis, A. M., Burrus, D. L., and Mongia, H. C., 1997, ''Anchored CCD for Gas Turbine Combustor Design and Data Correlation,'' ASME J. Eng. Gas Turbines Power, **119**, pp. 535–545.

[2] Lawson, R. J., 1993, ''Computational Modeling of an Aircraft Engine Combustor to Achieve Target Exit Temperature Profiles,'' ASME Paper-93GT-164.

[3] Fuller, E. J., and Smith, C. E., 1993, ''Integrated CFD Modeling of Gas Turbine Combustors,'' AIAA paper 93-2196.

[4] Tolpadi, A. K., Burrus, D. L., and Lawson, R. J., 1995, ''Numerical Computation and Validations of Two-Phase Flow Downstream of a Gas Turbine Combustor Dome Swirl Cup,'' ASME J. Eng. Gas Turbines Power, **117**, pp. 704–712.

[5] Gulati, A., Tolpadi, A. K., VanDeusen, G., and Burrus, D. L., 1995, ''Effect of Dilution Air on Scalar Flowfield at Combustor Sector Exit,'' J. Propul. Power, **11**, pp. 1162–1169.

[6] Lai, M. K., 1997, ''CFD Analysis of Liquid Spray Combustion in a Gas Turbine Combustor,'' ASME Paper 97-GT-309.

[7] Gosselin, P., DeChamplain, S., Kalla, and Kretschmer, D., 2000, ''Three-Dimensional CFD Analysis of a Gas Turbine Combustor,'' AIAA-2000-3466 paper, 36th AIAA/ASME/SAE/ASEE Joint Propulsion Conf. and Exhibit, 16–19 July, 2000, Huntsville, Alabama.

[8] Mongia, H. C., and Brands, D. J., 1982, ''Design Documentation Report Counter Flow Film-Cooled Combustor Program,'' NASA CR-167922 June 1982.

[9] Rizk, N. K., and Mongia, H. C., 1991, ''Three-Dimensional Analysis of Gas Turbine Combustors,'' J. Propul. Power, **7**, No. 3, pp. 603–611.

[10] Mongia, H. C., 1998, ''Aero-thermal Design and Analysis of Gas Turbine Combustion Systems: Current Status and Future Direction,'' AIAA Paper 1998-3982.

[11] Kumar, G. N., and Mongia, H. C., 2000, ''Validation of Near-wall Turbulence Models for Film Cooling Applications in Combustors,'' AIAA Paper 2000-0480.

[12] Kumar, G. N., Duncan, B. S., and Mongia, H. C., 2000, ''Results of a DOE on Film Cooling Effectiveness of a Modern Combustor With Machined Ring,'' AIAA Paper 2000-3354, 36th AIAA/ASME/SAE/ ASEE Joint Propulsion Conf. and Exhibit, 16–19 July, 2000, Huntsville, Alabama.

[13] Mongia, H. C., 2001, ''Gas Turbine Combustor Liner Wall Temperature Calculation Methodology,'' AIAA Paper 2001-3267, 36th AIAA/ASME/SAE/ASEE Joint Propulsion Conference and Exhibit, 16–19 July, 2000, Huntsville, Alabama.

[14] Crocker, D. S., Nickolaus, D., and Smith, C. E., 1999, ''CFD Modeling of a Gas Turbine Combustor From Compressor Exit to Turbine Inlet,'' ASME J. Eng. Gas Turbines Power, **121**, pp. 89–95.

[15] Lefebvre, A. H., 1980, *Gas Turbine Combustion*, Taylor & Francis, London, Chap. 8: Heat Transfer.

[16] *Methodology*—STAR-CD *Version 3.15*, Computational Dynamics Ltd., 2001.

[17] Richardson, J. M., Howard, H. C., Jr., and Smith, R. W., 1953, ''The Relation Between Sampling Tube Measurements and Concentration Fluctuations in a Turbulent Gas Jet,'' 4th Symp. On Combustion, pp. 814–817.

[18] Magnussen, B. F., and Hjertager, B. W., 1981, ''On the Structure of Turbulence and a Generalized Eddy Dissipation Concept for Chemical Reaction in Turbulent Flow,'' 19th AIAA Aerospace Meeting, St. Louis, MO.

[19] Gordon, R., and Levy, Y., 2000, ''Evaluation of Results of CFD Calculations Applied to Combustion Chambers,'' Report No. 27645985-01, Technion-IIT Haifa, Israel, Sept. 2000.

Downloaded 02 Jun 2010 to 171.66.16.98. Redistribution subject to ASME license or copyright; see http://www.asme.org/terms/Terms_Use.cfm

Observations of Flame Behavior in a Laboratory-Scale Premixed Natural Gas/Air Gas Turbine Combustor From Planar Laser Induced Fluorescence Measurements of OH, Laser Doppler Anemometer Velocity Measurements, and Coherent Anti-Stokes Roman Spectrometer Temperature Measurements

Paul O. Hedman
Thomas H. Fletcher
Daniel V. Flores
Stewart G. Graham
Jason K. Haslam
Robert L. Murray
G. Wayne Timothy

Department of Chemical Engineering and Advanced Combustion Engineering Research Center,
Brigham Young University,
Provo, UT 84602

Instantaneous planar laser induced fluorescence (PLIF) images of OH, simultaneous axial/radial and axial/tangential velocity measurements with an LDA (laser Doppler anemometer), and instantaneous gas temperature measurements using a coherent anti-Stokes Raman spectrometer (CARS) were obtained in a pre-mixed, swirl-stabilized laboratory-scale combustor, fired with natural gas. Four operating conditions were examined (two swirl conditions and equivalence ratios of 0.80 and 0.65). The instantaneous PLIF images of OH illustrate the chaotic nature of the turbulent flame eddies. Mean and standard deviations of each variable were measured at different locations in the flame, along with probability density functions. Stability of the flame at each condition is related to measurements in the central and side recirculation zones. [DOI: 10.1115/1.1914804]

Introduction

Lean, premixed combustion is being used as a means to meet severe NO_x and CO emission regulations on stationary gas turbines. A series of laser-diagnostic experiments was performed in a lean-premixed combustion apparatus at the same lean operating conditions. Planar laser-induced fluorescence (PLIF) was used to image OH, two-component laser Doppler anemometry (LDA) [1] was used to measure velocity, and coherent anti-Stokes Raman spectroscopy (CARS) [2] was used to measure temperature. These data were obtained principally for evaluation of comprehensive gas turbine combustion models [3–5]. The laser diagnostic data presented in this paper were obtained in a laboratory-scale, gas-turbine combustor (LSGTC) with a pre-mixed, swirl-stabilized, natural gas flame. The LSGTC was operated at two swirl conditions [high swirl (HS) and medium swirl (MS)] and two fuel equivalence ratios (0.80 and 0.65) at atmospheric pressure. The LSGTC simulates many of the key combustor characteristics of commercial gas turbines [6], and provides a realistic flame where model predictions and in situ measurements can be compared. Use of advanced optical diagnostics permits near-instantaneous (about 10-ns resolution), nonintrusive measurements that provide insight into the physical processes that govern the combustion processes. This set of data is thought to be among the most complete for lean premixed combustion applicable to gas turbines, and therefore serves as a good test set for modern computer models.

Contributed by the Fuels and Combustion Division of THE AMERICAN SOCIETY OF MECHANICAL ENGINEERS for publication in the ASME JOURNAL OF ENGINEERING FOR GAS TURBINES AND POWER. Manuscript received by the F&C Division July 30, 2003; final revision received May 5, 2004. Associate Editor: P. C. Malte.

Combustor Test Facility

The combustion facility used for this study is the same used by Hedman and co-workers [7–11]. The facility was further modified for this study to allow investigation of a premixed natural gas/air flame. This premixed natural gas/air combustor was developed with support from the US/DOE Advanced Turbine Systems program, and is referred to as the ATS burner. The laboratory-scale, gas-turbine combustor (LSGTC), illustrated in Fig. 1, was designed to reproduce the characteristics found in a modern annular combustor [6]. The combustor, which was provided to BYU by Wright Laboratory [12], consists of a four-sided chamber with metal corner fillets to more nearly simulate an axisymmetric combustor while maintaining adequate optical access. A metal plate or a quartz window can be placed in each wall, depending on the optical access required. The exit of the reactor was restricted by a flat plate with a 92-mm hole in the center.

The premixed swirl injector, illustrated in Fig. 2, is located in the center of the combustion chamber base. The injector consists of a stainless steel tube with a honeycombed brass insert. The brass insert serves to smooth the flow as well as provide a flame arrestor in case of flashback in the premixed fuel/air mixture. Inserts are installed in the injector to provide different magnitudes of swirl to the inlet flow. The swirler inserts are placed 40 mm

 Copyright © 2005 by ASME

Downloaded 02 Jun 2010 to 171.66.16.98. Redistribution subject to ASME license or copyright; see http://www.asme.org/terms/Terms_Use.cfm

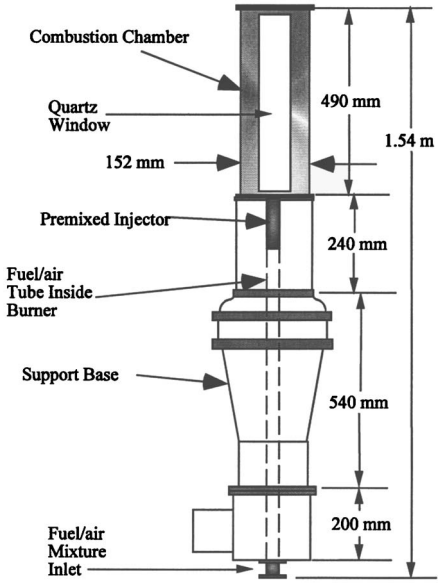

Fig. 1 Schematic of premixed combustor (adapted from Schmidt and Hedman [11])

above the brass honeycomb and secured by a threaded post that anchors the swirler to the brass honeycomb. A cap with an 18-mm hole in the center and beveled walls is placed on the top of the steel tube to coalesce the swirling flow at the injector exit. This cap was needed in order to make the burner operate successfully.

Figure 2 shows a schematic of the two swirl inserts used in this study. The inserts are labeled high swirl (HS) and medium swirl (MS) to coincide with the 60- and 45-deg slot angles. The swirl number (SN) indicated in Fig. 2 is a nondimensional number defined by the ratio of the axial flux of tangential momentum divided by the product of the axial flux of axial momentum and the equivalent nozzle radius [13].

Fuel flow to the burner was measured with a variable area flow meter and is reported in slpm (standard liters per minute, or 10^{-3} standard m^3/min) referenced to 1 atm (101 kPa) and 70 °F

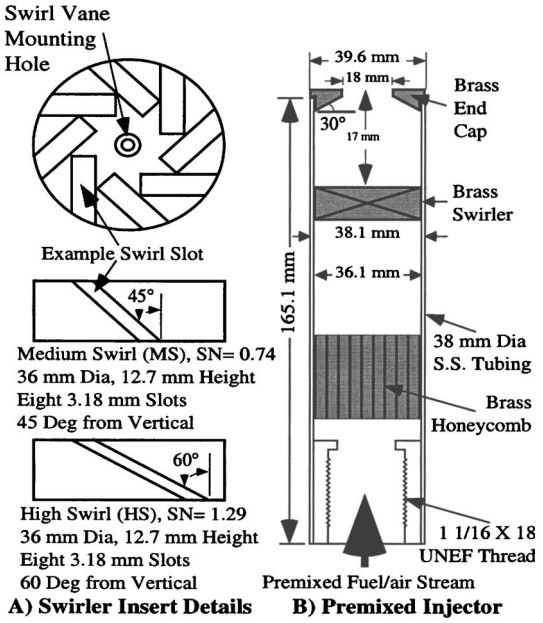

Fig. 2 Schematic of premixed injector and medium and high swirl block inserts (adapted from Schmidt and Hedman [11])

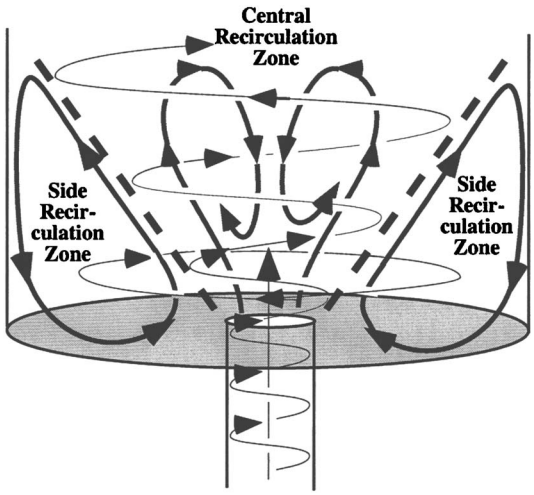

Fig. 3 Flow patterns in a confined, bluff-base, premixed, swirl-stabilized combustor (adapted from Gupta et al. [13])

(21.1 °C). Airflow was controlled by varying the upstream pressure of a choked flow nozzle. The diameter of the nozzle used for this study was 0.1485 in. (3.77 mm) providing airflow rates from 250 to 1000 slpm, depending on upstream pressure. Uniform mixing of gaseous fuel and air was assured by (a) the length of the tube from the mixing point to the burner, (b) a jet mixer in the feed system, and (c) a honeycomb flame arrestor. The air flow rate for the four test conditions used in this study was 500 slpm.

Visual Flame Characterization. Figure 3 presents a schematic drawing of the flow patterns present in the swirl-stabilized flame. The swirling flow creates a funnel or tornado-like vortex flow centered on the injector exit. A central recirculation zone and a side recirculation zone accompany the tornadolike flow. Both recirculation zones have been found to influence flame stability. Depending on swirl number and fuel equivalence ratio, one or the other of the recirculation zones may dominate the flame stability [1].

Wide variations in flame shape have been observed in the ATS burner for different combinations of swirl number and fuel equivalence ratio. These structures were studied both visually, through photographic and video recordings, with the PLIF images, and with the velocity and temperature results obtained in this study. Such observations have yielded insight into the location of the flame front, variation of flame structure with operating conditions, and the presence and strength of the recirculation zones. These flame shapes are primarily a result of the effect of the swirl intensity and fuel equivalence ratio on the flow field, with the magnitude of the airflow rate being of secondary importance. The equivalence ratio was varied by changing the fuel flow rate while maintaining a constant 500 slpm air flow rate. The changes in flame shape were characterized using the point of attachment, the location of the flame front, the structure of the vortex, and the visible intensity of the flame.

An example of a visual image of the flame structure is presented in Fig. 4 for a stoichiometric ($\phi=1.0$), MS case. The $\phi=1.0$ image was included in the paper to provide a photographic illustration of the flame structure. The $\phi=1.0$ image was used because this image was brighter, more visual, and reproduced better than images from flames with $\phi<1.0$. It was visually observed that the flame at $\phi=0.80$ was more stable than at $\phi=0.65$. The flame with the HS injector was more coalesced and closer to the injector than with the MS injector. At $\phi=0.65$, the flame was near the lean flammability limit, and was quite unstable for both swirl injectors. When using the MS injector, the flame would oscillate between two different flame structures, one that was more or less

Downloaded 02 Jun 2010 to 171.66.16.98. Redistribution subject to ASME license or copyright; see http://www.asme.org/terms/Terms_Use.cfm

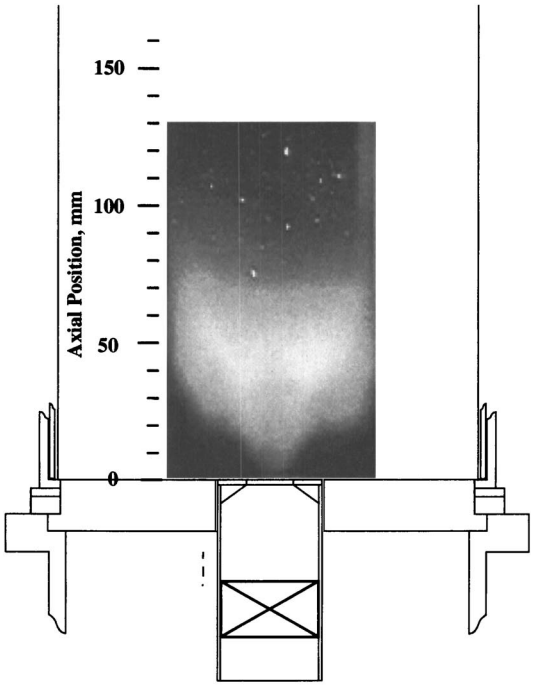

Fig. 4 Example video image of premixed natural gas/air flame (MS burner, 500-slpm air flow rate, ϕ=1.0)

attached to the vortex funnel, and one that was lifted well above the vortex funnel. The MS case at ϕ=0.65 was at the very edge of the lean flammability limit, and on occasion would actually extinguish.

Planar Laser-Induced Fluorescence. Planar laser-induced fluorescence (PLIF) is a valuable tool for studying combustion phenomena. Flame propagation is partly governed by the diffusion and transport of important combustion intermediates like OH and CH. Laser-induced fluorescence has the potential of measuring trace amounts of these short-lived combustion species at near instantaneous temporal resolution (10–100 ns). Likewise, because PLIF is laser-based, probing of the burner is nonintrusive. Laser-induced fluorescence measurements are often made at the focal point of a converging excitation laser [14]. However, due to the advances in detector and laser performance, fluorescence can be captured instantaneously over a two-dimensional area for many species. The two-dimensional image area captured resembles an instantaneous photograph-like image directly related to the concentration distribution of the combustion species being probed. The flame is probed with a thin sheet of laser light tuned to the appropriate wavelength. The PLIF images of OH provide detailed information regarding the location and shape of the flame structure. This structural information is very useful in analyzing burner designs, understanding combustion phenomena, and validating combustion computer models.

The use of PLIF to determine flame properties has become more popular in the last few years. For instance, use of PLIF and acetone tracers is a popular method to determine mixing characteristics [15–18]. Measurements of NO using PLIF are reviewed by Cooper and Laurendeau [19]. Measurements of OH using PLIF to determine flame structure in natural gas/air flames [20–25] and kerosene spray flames [26,27] related to gas turbine combustors have also been reported recently reported. However, none of these previous measurements have been combined with detailed laser-based measurements of velocities and/or temperature.

The excitation source used to pump the OH radical (283 nm) came from frequency doubling 566-nm laser light from a tunable dye laser (Spectra Physics PDL-3) with a KD^*P crystal in the wave extender. The tunable dye laser used a frequency doubled Nd:YAG laser (Quantaray) as a pump source. The final exiting laser beam at 283 nm was formed into a thin sheet approximately 0.5 mm thick and 13.0 cm wide. No attempt was made to determine exactly which OH transition was being pumped. For the purposes of this study, it was sufficient to simply scan across the OH transitions and select the one that gave the most intense OH image. This setting was then maintained for images at all test conditions so that the detector counts would be proportional to OH concentration. As the laser beam passed through the flame, an electronic camera (Princeton Instruments, ICCD-5765/RB-E) that uses an intensified charge coupled display (ICCD) with an electronic shutter speed of 100 ns was used to capture the induced fluorescence (308 nm) of OH. The ICCD camera was set up orthogonal to the laser beam and was fitted with appropriate filters to block unwanted light and with a Nikon f/1.2 quartz lens that would pass the uv light. A detailed schematic of the PLIF apparatus used here is found elsewhere [28]. Captured images were digitally transferred to computer memory for subsequent analysis.

Since the optical setup was identical for all test conditions, the actual detector counts may be proportional to the concentration of OH present at a given diagnostic location. Eckbreth [14] has suggested that in the linear regime the fluorescence signal power is proportional to the laser irradiance and the species population prior to laser excitation. However, the effects of saturation and quenching may cause the counts to be nonlinear. It is beyond the scope of this study to try to quantify this effect.

Figure 5 presents four example instantaneous OH images for each of the four test conditions. Images were selected that represent: (A) the least intense (i.e., lowest image counts, and most fragmented image) flame structure, (B) a flame structure of near average intensity, and (C) the most intense (highest image counts, and the most well-defined image). The fourth image (column D) was selected and included because of its oddity. The computer processing of the counts from each pixel into the false color images presented is somewhat misleading. For each image, the detector counts for each pixel were normalized to the peak detector count, and the image was scaled using Lab-View software to a false color image, with red scaled to the peak normalized value and black scaled to the minimum value. The false color images were converted to gray-scale images for publication. The detector counts were normalized to the peak relative intensity for that image whether the value of the peak detector count was 400 or 4000. Nevertheless, the instantaneous structure is well represented. Actual detector counts for representative locations within selected images are tabulated below (see Fig. 8) on normalized probability distribution functions (PDFs) for that location.

The observations about flame structure noted from the visual and camera images are confirmed with the instantaneous PLIF images. Operation at ϕ=0.80 produced stable flames with both the HS and MS injectors (e.g., Fig. 5, Images B-101 and B-126). The flame with the HS injector was more coalesced and closer to the injector than that with the MS injector. At ϕ=0.65, the flame was near the lean flammability limit, and was quite unstable for both swirl injectors. As noted visually, the flame would oscillate between two different flame structures, one that was more or less attached to the vortex funnel, and one that was lifted well above the vortex funnel. Visual observations showed that the MS case at ϕ=0.65 was at the very edge of the lean flammability limit. Figure 5, Image A-062, supports this observation, showing little OH in the central vortex and the flame being nearly extinguished. Even the image near the average structure (Fig. 5, Image B-105) shows little of the OH needed to support flame propagation.

The PLIF diagnostic capability allowed the collection of a significant number of separate instantaneous OH images (256 images at each test condition). Consequently, images of the mean and the standard deviation in the fluorescence signal were obtained by applying the appropriate statistical analysis to the collection of images, pixel by pixel. Figure 6 presents the average image of the

Downloaded 02 Jun 2010 to 171.66.16.98. Redistribution subject to ASME license or copyright; see http://www.asme.org/terms/Terms_Use.cfm

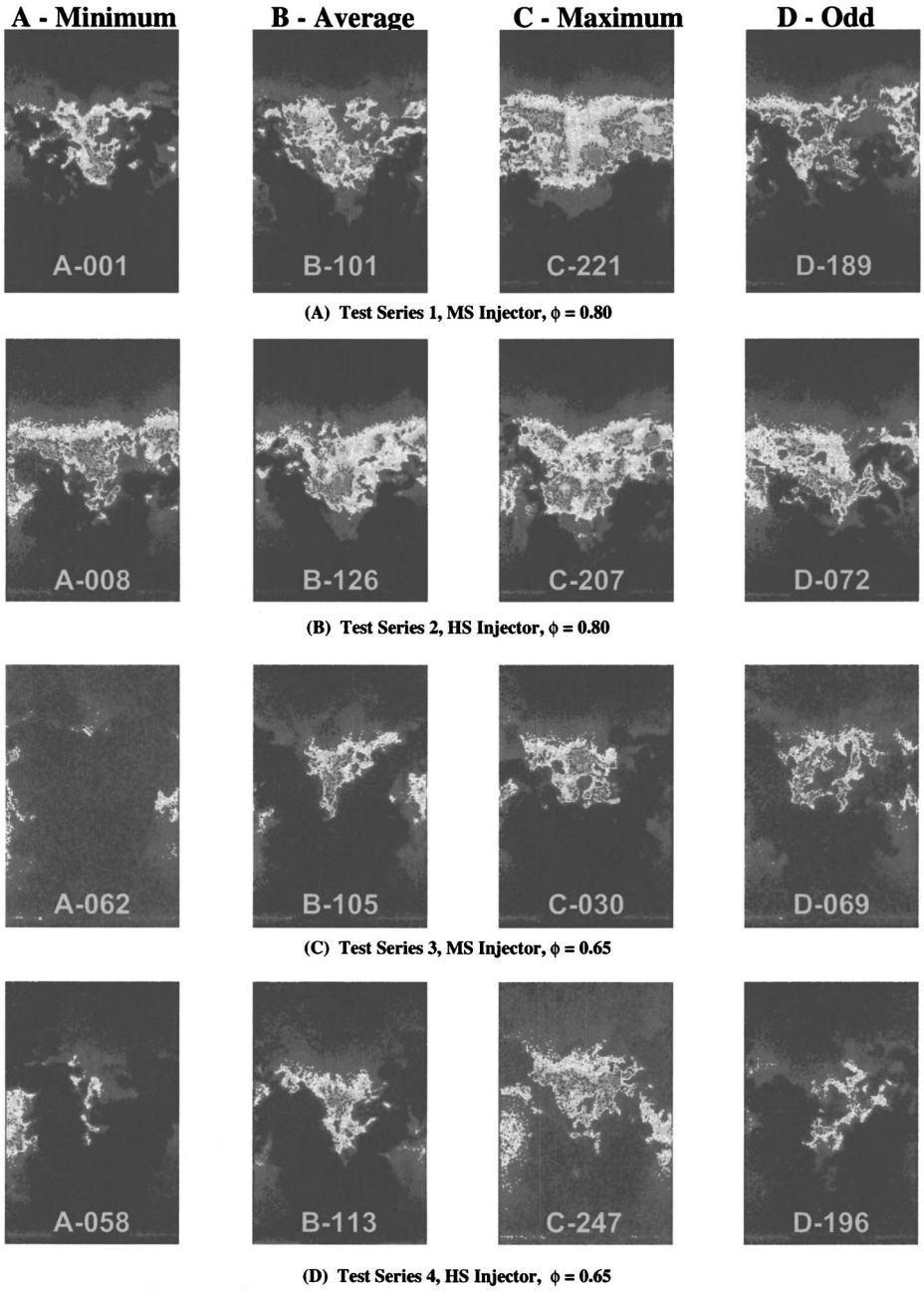

Fig. 5 Instantaneous PLIF OH images of flame structure

256 separate laser shots for the OH species for the four test conditions. The mean image is very similar to the observed video images. However, the variation in pixel count, as reflected in the normalized gray image, allows more insight into the structure of the flame and the character of the two different recirculation zones. As with the video images and instantaneous PLIF images, the mean PLIF images from the ϕ=0.80 cases indicate a very structured stable flame for both the HS and MS injectors. The vortex for the HS case is narrower, and the top of the flame zone is closer to the injector than in the MS case. The ϕ=0.65 cases reflect a narrower vortex and lower flame zone for the HS configuration. Both configurations are near lean blowout at ϕ=0.65, but the MS case is more unstable, and consequently more likely to extinguish than the HS case. Standard deviation PLIF images were also calculated pixel by pixel and are shown in Fig. 7 for the four cases. The standard deviation gives insight into the amount of large-scale turbulence and zones where ignition/extinction occur within the flame. The greater coalescence in the flows with the HS injector is more readily apparent in the standard deviation images (see Fig. 7, images B and D compared to images A and C, respectively). The greater instability associated with the MS ϕ=0.65 case is also apparent in Fig. 7, image C. As noted above, the normalized transform from the detector counts has a different maximum value for each image. These normalized images therefore provide means for comparison of the shape of the flow field, as depicted by the standard deviation calculation, rather than the relative intensity.

The actual detector counts at selected pixel locations have been used to create PDFs within the flame structure. The average count and peak count, and the shape of the PDFs provide additional insights into the flame characteristics, and have provided a measure of the effect of operating condition on the relative level of OH in the flame. Examples of PDF distributions for the most stable test case (HS, ϕ=0.80) and for the least stable test case

Downloaded 02 Jun 2010 to 171.66.16.98. Redistribution subject to ASME license or copyright; see http://www.asme.org/terms/Terms_Use.cfm

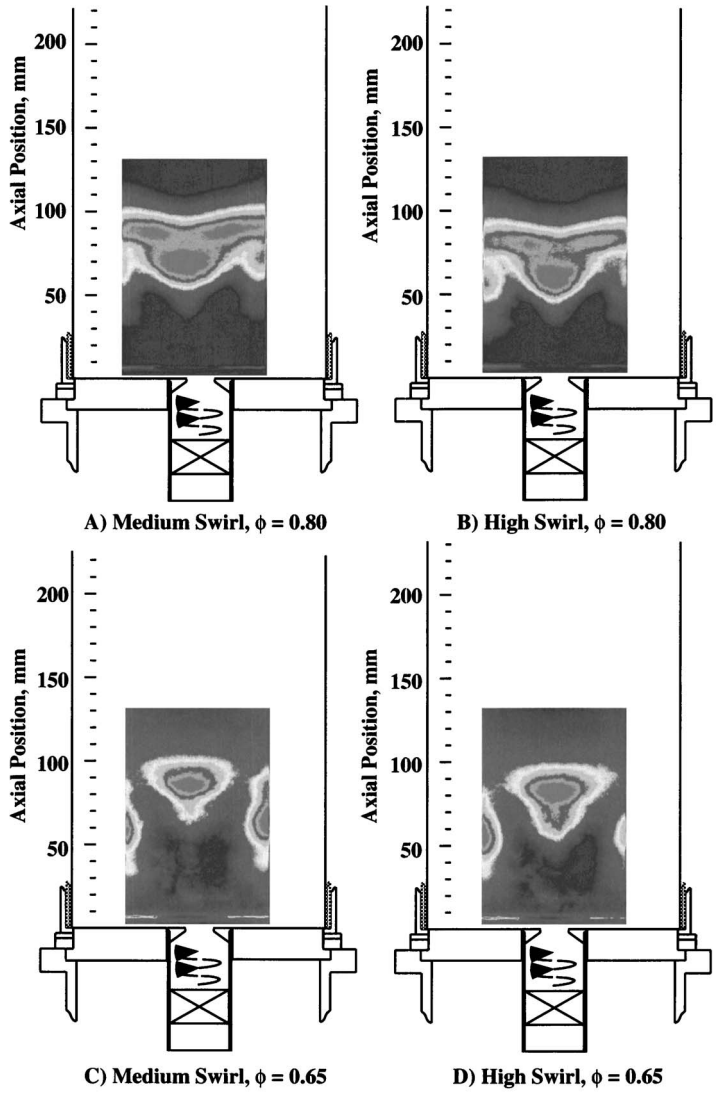

Fig. 6 Mean PLIF images of OH in the ATS burner (premixed natural gas/air, air flow=500 slpm)

(MS, ϕ=0.65) are presented in Figs. 8 and 9, respectively. Eight locations where the PDFs have been determined are superimposed on the mean PLIF image for both cases presented. The eight locations shown in Figs. 8 and 9 are identical for both cases. Locations were selected above the flame, in the most intense regions of the flame, and below the flame. The PDF plots appear to be more similar to beta distributions rather than Gaussian distributions. In every case, the PDF shows that there is a significant amount of time that no OH exists at that location (e.g., Fig. 8), even in the most intense part of the flame zone. Likewise, significant levels of OH are seen even in regions that are predominately outside, but near the flame zone. In Fig. 8 (HS, ϕ=0.80) the maximum detector count (4633 counts at maximum, 1652 counts at average) occurs at a location inside the intense part of the flame (location D). In Fig. 9 (MS, ϕ=0.65), the maximum detector count in the intense part of the flame (1926 counts at maximum, 402 counts at average) occurs at location B. This suggests that the concentration of OH in the MS, ϕ=0.65 case is about one fourth that of the HS, ϕ=0.80 case. The nonlinear PLIF response and the possibility of fluorescence saturation may alter the interpretation of concentration slightly. Nevertheless, the magnitude of the detector counts, as well as the corresponding PDFs, provides considerable insight into the character of the turbulent, reacting flame.

Figure 9 further quantifies the unstable nature of the MS, ϕ=0.65 case. Even in the most intense region (location B), there is a considerable amount of time when no OH is detected in the central vortex region. It is apparent that the stabilization process in the turbulent, swirl-stabilized flame is a very complicated process. The PLIF images obtained have provided some insight into this process, but must be considered with the velocity and temperature data to provide a more complete understanding about the turbulent combustion process and flame stability.

LDA Velocity Measurements. The LDA setup used in this study is a two-color system in forward scattering mode [1,29] originally developed by Schmidt and Hedman [11]. The argon-ion laser was operated in multi-line mode lasing at several frequencies simultaneously. The multi-frequency laser beam was passed through a collimator to reduce beam divergence, and then polarized. A color separator and mirrors were used to select the two strongest wavelengths, 488 nm (blue) and 514.5 nm (green). The green beam was split into two beams in the horizontal plane, and the blue beam was split into two beams in the vertical plane. One green and one blue beam were passed through separate Bragg cells which allowed negative velocities to be obtained. The four beams were passed through a beam expander and focused into two superimposed elliptical probe volumes with major axes of about 2.3 mm and minor axes of about 0.13 mm. The focal length of the

Downloaded 02 Jun 2010 to 171.66.16.98. Redistribution subject to ASME license or copyright; see http://www.asme.org/terms/Terms_Use.cfm

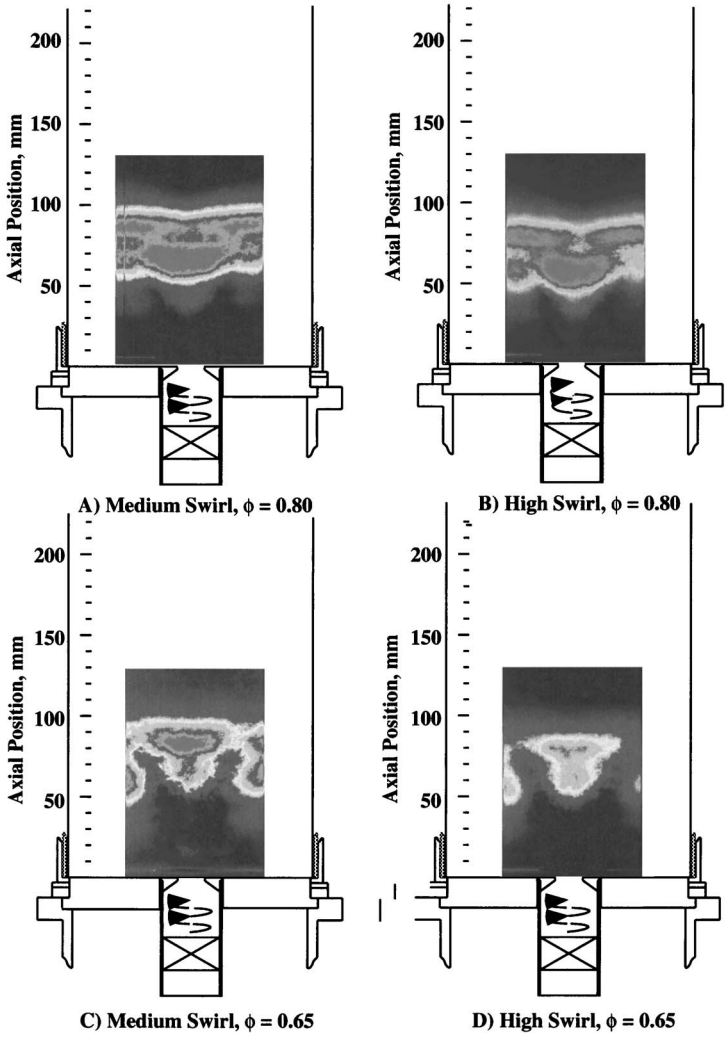

Fig. 7 Standard deviation PLIF images of OH in the ATS burner (premixed natural gas/air, air flow=500 slpm)

transmitting lens was 762 mm with the beams intersecting at a half angle of 3.1 deg. The diameter of the laser beam at the lens face was approximately 4 mm. This two-color, four-beam LDA configuration formed a probe volume with two fringe patterns at right angles to each other, with a blue fringe spacing of 4.44 μm and a green fringe spacing of 4.68 μm.

The airflow was seeded with about 6-μm diameter hollow aluminum oxide micro-spheres. The aerodynamic diameter of these particles was such that they followed the gas flow patterns, even in the recirculation zones. The seeding of the airflow occurred prior to the fuel addition point and well before the fuel injector. A particle traversing the probe volume produced two Doppler signals. The fringes of the blue beams gave Doppler signals for the axial velocity component and the fringes of the green beams gave the Doppler signals that corresponded to either the radial or tangential velocity component. Sample rates ranged from 400 counts per second to 10,000 counts per second, depending on where the probe volume was positioned in the flame. Sample rates were significantly lower in the high-temperature regions of the flame. The Doppler signals were collected in two different photomultiplier tubes (PMT). Each PMT was connected to a signal processor [30] for filtering and validation. Valid velocity signals were recorded and stored by computer using a direct memory access (DMA) digital I/O card from TSI and a data acquisition program [31] also developed by TSI.

Figures 10 and 11 provide example axial, radial, and tangential iso-velocity contour plots for the HS ϕ=0.80 and the MS ϕ =0.65 cases, respectively. The results for the other two cases are reported by Murray [1]. The analysis of the approximately 4000 instantaneous velocities obtained at each measurement location in the flame zone allows statistical investigation into the turbulent character of the flame to be made. Example standard deviations (in m/s) for the axial, radial, and tangential velocities were calculated at each location in the combustion chamber, and corresponding contour plots are shown in Figs. 12 and 13 for the HS ϕ=0.80 and MS ϕ=0.65 cases, respectively. Maximum and minimum standard deviation velocities are also presented.

Comparison of the standard deviation velocity maps with the corresponding mean velocity maps (Figs. 10 and 11) show that the highest standard deviation axial, radial, and tangential velocities occur in the positive velocity flow channel where the fastest positive mean axial, radial, and tangential velocities occur. In addition, the lowest standard deviation velocities occurred in the upper region of the combustion chamber and in the side recirculation zone (SRZ). Lower mean velocities were present in these areas. Past studies have suggested that a large standard deviation correlated with high turbulence regions [9,11]. In this study, the largest standard deviations occurred in the same location as the largest mean velocity.

Probability distribution functions (PDFs) have been used to describe the flow characteristics and to confirm the accuracy of the

Downloaded 02 Jun 2010 to 171.66.16.98. Redistribution subject to ASME license or copyright; see http://www.asme.org/terms/Terms_Use.cfm

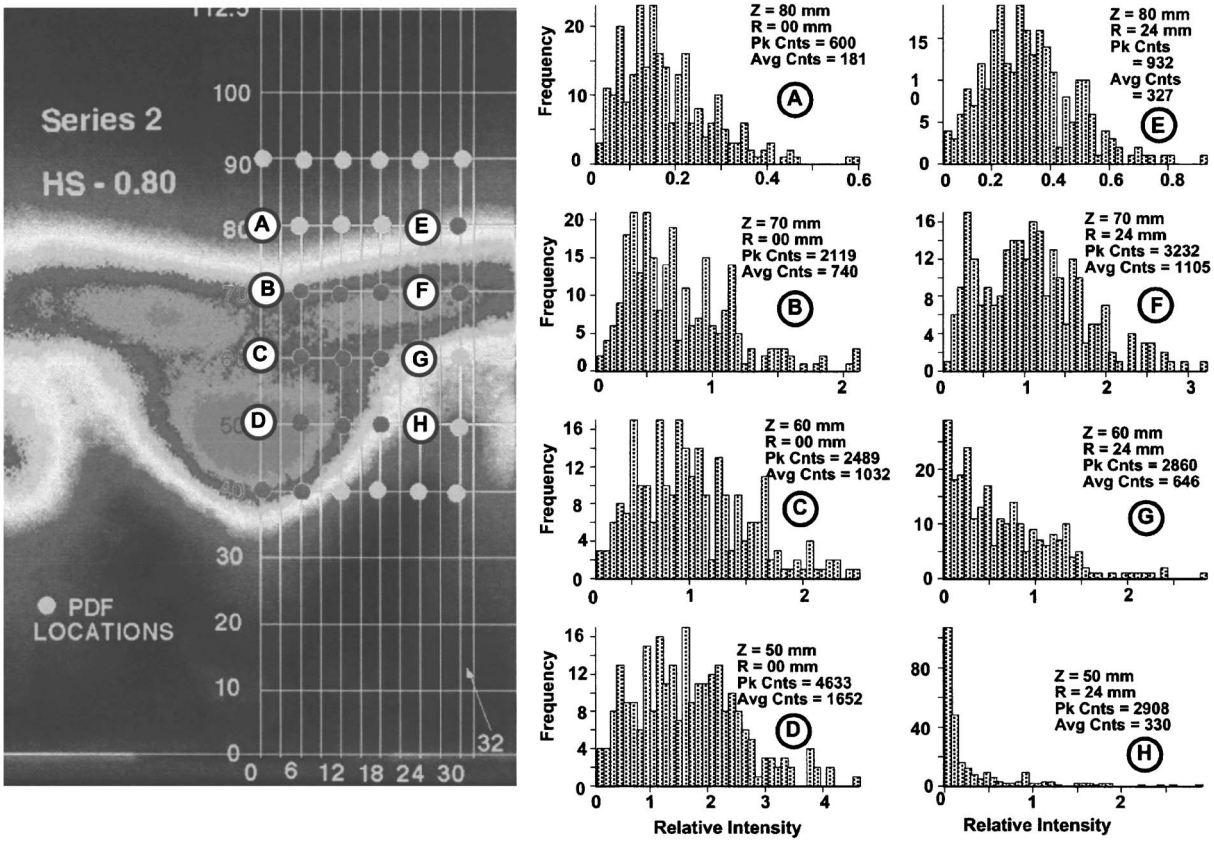

Fig. 8 Example PDFs from OH-PLIF images (HS injector, ϕ=0.80)

data. Figures 14 and 15 show examples of axial velocity PDFs at an axial position of 80 mm and radial positions from near the centerline to about a 40-mm radial location for the HS ϕ=0.80 and MS ϕ=0.65 cases, respectively. Additional PDF results are provided by Murray [1]. Labeled on the PDF are the axial position, radial position, mean axial velocity, and standard deviation. Generally, the axial velocity PDFs have a near Gaussian distribution in an identifiable flow zone. However, these PDFs had a bimodal distribution when gas velocities were measured across the shear layer between two different identifiable flow zones. Typically, this can be seen at a position near the zero velocity contour. These measurements have velocity components from both sides of the zero velocity boundary.

In Fig. 14, starting at a radial position of −1 mm, the PDF has a basic Gaussian profile with a slightly increased gradient in the positive velocity region. As measurements move to a radial position of 11 mm, the PDF became less Gaussian, with the positive velocity region of the PDF increasing in size, the negative velocity region decreasing in size, and the standard deviation increasing. At 17 mm, the positive velocity region of the PDF has increased significantly. At radial positions of 23 and 29 mm, the positive velocity region of the PDF continues to increase, the mean axial velocity becomes positive overall, the standard deviation continues to increase, and the bimodal peaks are about equal in size and shape. It should be noted that these two positions (23 and 29 mm) straddle the zero axial velocity contour, and hence have velocity components from both sides of the zero velocity boundary. At a radial position of 35 mm, the bimodal distribution continues, the positive region of the PDF increases, the positive mean axial velocity increases in magnitude, and the standard deviation remains fairly constant. At a radial position of 41 mm, the negative velocity region of the PDF has nearly disappeared, the mean positive velocity dominates the distribution, and the standard deviation has decreased slightly. Similar observations regarding the changes in PDF distributions as one moves from near centerline past the zero axial velocity contour can be seen in Fig. 15 for the MS ϕ=0.65 case.

As expected, the observations regarding the PDFs support the conclusion of strong shear layers in the combustion chamber. Bimodal distributions across the shear layer (zero axial velocity contour) were typically found from an axial position of 60 mm to an axial position of 100 mm. Below an axial position of 60 mm bimodal distributions were sometimes seen, but the spacing between measurements was too great to get a good progression of PDFs. At axial positions above 125 mm, the measured velocities across the shear layer were not high enough to demonstrate the bimodal distributions in the PDFs. Instead, the PDF usually represented a near Gaussian distribution with the peak of the distribution being at or near the axial centerline.

Discussion of Recirculation Zones. Recirculation zones play a major role in stabilizing a turbulent, premixed natural gas combustor. In this study, it was assumed that gas moving down into the ignition zone and radially towards the axial centerline improved the stability of the flame. In other words, the incoming premixed fuel and air needed a source of heat and/or radicals from the recirculated products to stabilize the flame. The intensity of the recirculation zones was based on how well the recirculation zones moved hot gases to the middle of the combustion chamber and down into the ignition zone. Examination of the zero axial velocity and zero radial velocity contours helps define recirculation regions. Zero velocity contours for both the axial and radial velocity maps are shown in both Fig. 10 and 11. The sizes of the recirculation zones are directly related to the heights and widths of the zero velocity contours. For convenience, a set of dimensions is defined in Fig. 10 and 11. The maximum height of the zero axial velocity contour, measured from the combustor base plate is labeled "h_{cu}" for the central recirculation zone (CRZ) and "h_{su}" for

Downloaded 02 Jun 2010 to 171.66.16.98. Redistribution subject to ASME license or copyright; see http://www.asme.org/terms/Terms_Use.cfm

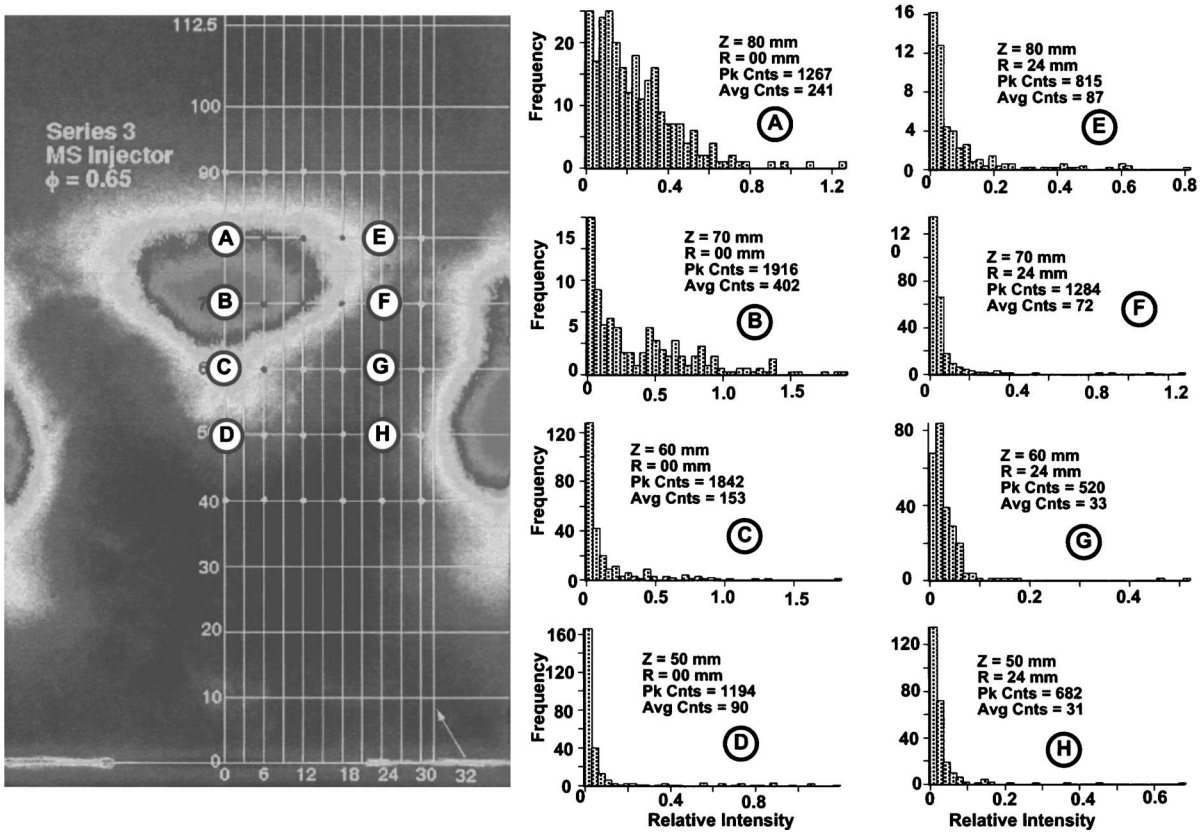

Fig. 9 Example PDFs from OH-PLIF images (MS injector, ϕ=0.65)

the side recirculation zone (SRZ). The maximum horizontal distance between the zero axial velocity contours for the CRZ is the width of the axial flow channel (w_{cu}), with a similar value (w_{su}) for the SRZ. Murray and co-workers [1,29] have used the heights and widths to quantitatively investigate the effect of flow recirculation on flame stability. The measured axial velocities were radially averaged inside both the central and side recirculation zones for each case. The resultant volumetric flow rates are shown at each axial position in Fig. 16 and 17.

The conclusions drawn are (1) the MS cases had a higher flow rate in the CRZ at an axial position of 120–150 mm than observed in the corresponding HS cases, (2) the HS cases had a higher Q_c at

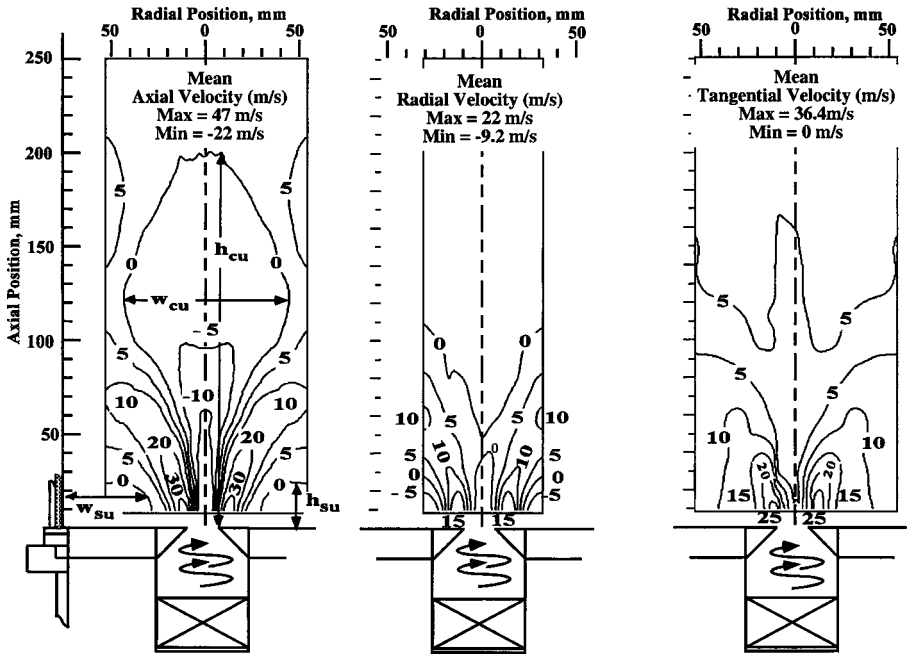

Fig. 10 Iso-contour maps of mean axial, radial, and tangential velocity (HS injector, ϕ=0.80)

Downloaded 02 Jun 2010 to 171.66.16.98. Redistribution subject to ASME license or copyright; see http://www.asme.org/terms/Terms_Use.cfm

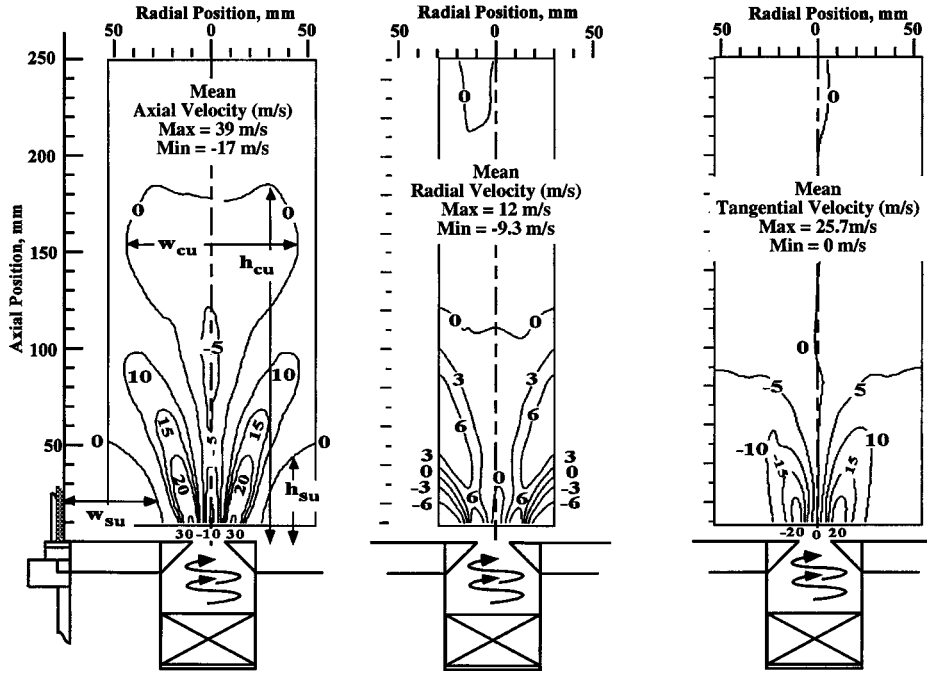

Fig. 11 Iso-contour maps of mean axial, radial, and tangential velocity (MS injector, ϕ=0.65)

an axial position of 50–120 mm than observed in the corresponding MS cases, and (3) the MS ϕ=0.80 case had about the same CRZ flow rate as the MS ϕ=0.65 case up to an axial position of 105 mm above the base of the combustion chamber.

The flow rates through the SRZ were much greater and extended higher up into the combustion chamber for the MS cases than the HS cases. The flow rates were only calculated out to a radial position of about 40–45 mm. Some of the cases had a SRZ that extended beyond a radial position of 40–45 mm. For these cases, the flow rate could only be determined up to the farthest radial position where data were taken, hence the values shown in Fig. 17 should be larger in most cases. Figure 17 shows that the MS cases had greater SRZ flow rates than the HS cases, with the largest flow rate in the MS ϕ=0.80 case. The MS ϕ=0.80 case was the only case that had the SRZ extend up into the visible flame zone.

The HS cases had larger CRZ flow rates than the MS cases at axial positions of 10–110 mm. The ignition zone was located below an axial position of 50 mm and the lower half of the visible flame zone was located from 50 to 110 mm. Therefore, HS cases had a larger CRZ flow rate, recirculating hot gases down through the lower half of the visible flame zone and into the ignition zone

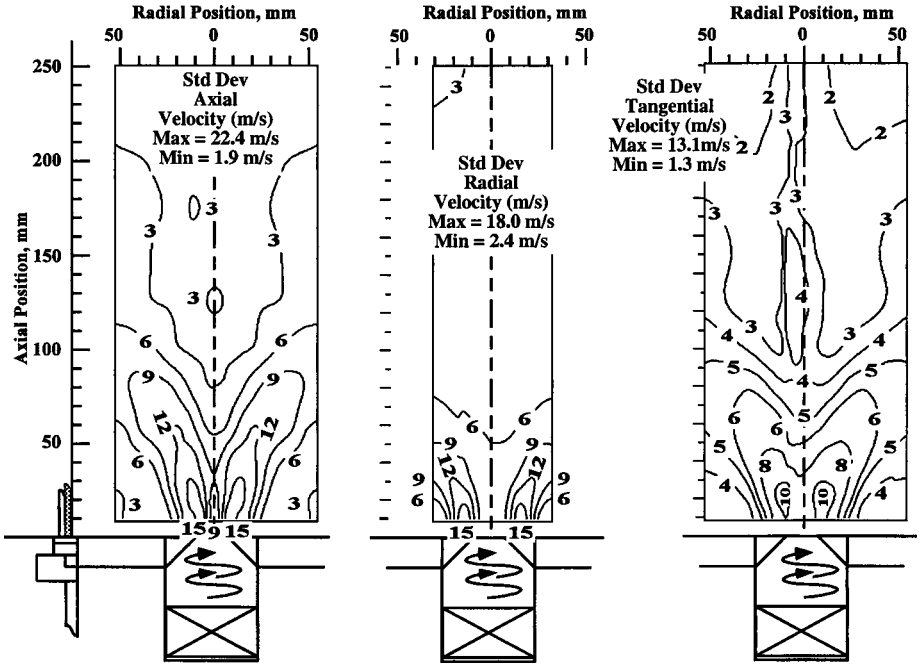

Fig. 12 Iso-contour maps of standard deviations of axial, radial, and tangential velocity (HS injector, ϕ=0.80)

Downloaded 02 Jun 2010 to 171.66.16.98. Redistribution subject to ASME license or copyright; see http://www.asme.org/terms/Terms_Use.cfm

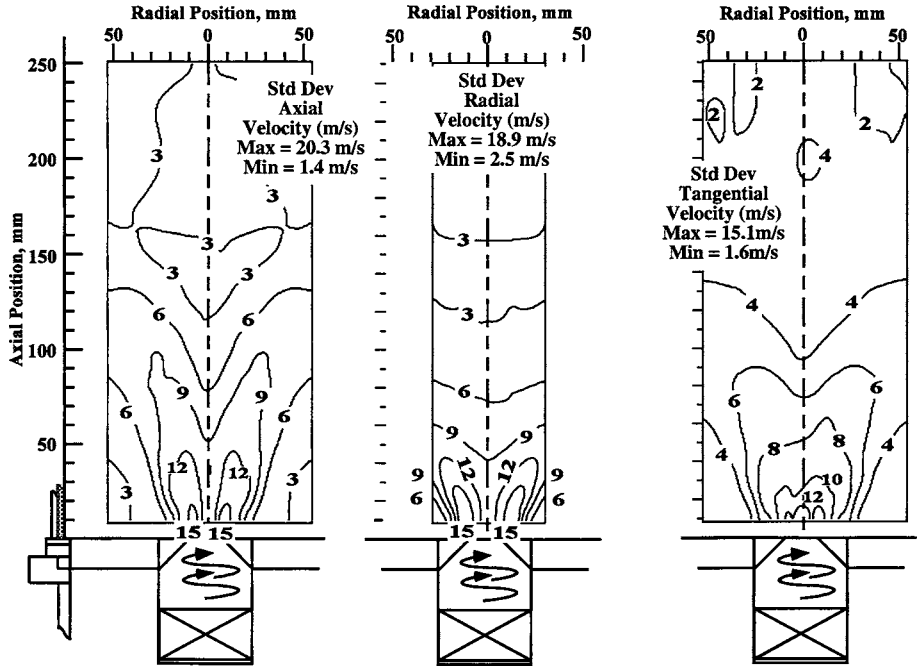

Fig. 13 Iso-contour maps of standard deviations of axial, radial, and tangential velocity (HS injector, ϕ=0.65)

than for the MS cases. In addition, the MS case did not have a change in the CRZ until after an axial position of 105 mm. This suggested that the CRZ played only a small role in stabilizing the MS cases. Large increases in the CRZ flow rate appear to occur in the visible flame zone. These large increases in the CRZ flow rate could partly be due to an increase in temperature. Further studies need to be made to identify the relationship between recirculated flow rates and temperature.

The MS cases had much larger SRZ flow rates than the HS cases in spite of limitations in completely calculating the SRZ flow rates for the MS cases. The MS ϕ=0.80 case was the only case where the SRZ extended up into the visible flame zone. It appears that the MS cases needed to have more recirculated hot gases coming down into the ignition zone to stabilize the flame. These conclusions support observations made earlier. However, only the MS ϕ=0.80 case extended up into the visible flame zone and thus only the MS ϕ=0.80 case had improved stability from the stronger side recirculation.

Gas Temperature Measurements

Coherent anti-Stokes spectroscopy (CARS) is based on Raman scattering of high-energy, coherent, laser beams. In general, a pump beam is split into two beams of equal intensity, and crossed with a Stokes beam that is tuned to the particular Raman resonance for the species being probed (e.g., 2331 cm^{-1} for N_2 and 2143 cm^{-1} for CO). Nonlinear wave mixing occurs in the diagnostic volume where the three probe beams cross, and a fourth beam is generated at the anti-Stokes frequency for the species being probed. The anti-Stokes spectra contain information that relates to gas temperature and species concentration. The nonlinear wave mixing is a vector process, and the laser-like anti-Stokes signal leaves the diagnostic volume in a prescribed direction that depends on the vector angles of the pump and Stokes beams. Since the signal is laser-like, it can be focused into a spectrometer for analysis. A detailed discussion of CARS theory and application can be found in Eckbreth [14].

Several types of CARS setups have been explored previously by Hedman and co-workers [32–35] in combustion systems. The current BYU CARS instrument [2,36] uses a frequency doubled ND:Yag laser (532 nm) to supply the two pump beams. A portion of the 532-nm laser energy is split off and used to excite the Stokes laser. A broadband, dual pyromethene dye laser (pyromethene 597 and 650 from Exciton) is used to simultaneously excite the Raman frequencies of N_2, CO, O_2, and CO_2. The spectrometer used in this study was patterned after the one used by Eckbreth at UTRC [14,37]. The diagnostic volume had a 200 -μm waist and a 1-mm length. The spectra were imaged onto an intensified photodiode array (IPDA) of an EG&G PARC 1421B camera, and recorded to a computer via an EG&G OMA model 1461. The specific characteristics of the IPDA and OMA system were determined by Boyack and co-worker [32,33]. Gas temperatures were determined from the N_2 CARS spectra using the FTCARS code [38] from SANDIA National Laboratories with modified input and output interfaces. Spectra that were too noisy or that could not be fit well with the FTCARS code were discarded. Flores and co-workers [2,36] conducted temperature calibration measurements on air in an electrically heated tube furnace equipped with a type-K thermocouple and a digital readout. Measurements in the range of 300–1000 K resulted in an average error of 30 K and standard deviations of 50 K. Accuracy of the temperature measurements at higher temperatures is thought to be within the usual ±50 K generally assumed for the CARS technique. Additional details of the instrumentation and calibration are given by Flores [2,36]. This study used the N_2 anti-Stokes spectra to deduce the gas temperatures presented herein.

Figure 18 presents the iso-contour mean gas temperature maps for the four cases tested in this study (HS and MS and ϕ=0.65 and 0.80). Figure 18(*a*) presents the results for the MS ϕ=0.65 (least stable flame) case and Figure 18(*d*) presents the results for the HS ϕ=0.80 (most stable flame) case. Comparison of these two figures shows the broadest effect of both swirl level and stoichiometry. The definition of stability used here is in regards to flame extinction rather than the amount of turbulent fluctuations present. The MS ϕ=0.65 (least stable flame) case was quite unstable, and the visible flame would move from a flame attached to the injector inlet to a flame that was lifted up into the combustion chamber. The mean temperature map does not show this effect because of the averaging involved. The average temperature contours do

Downloaded 02 Jun 2010 to 171.66.16.98. Redistribution subject to ASME license or copyright; see http://www.asme.org/terms/Terms_Use.cfm

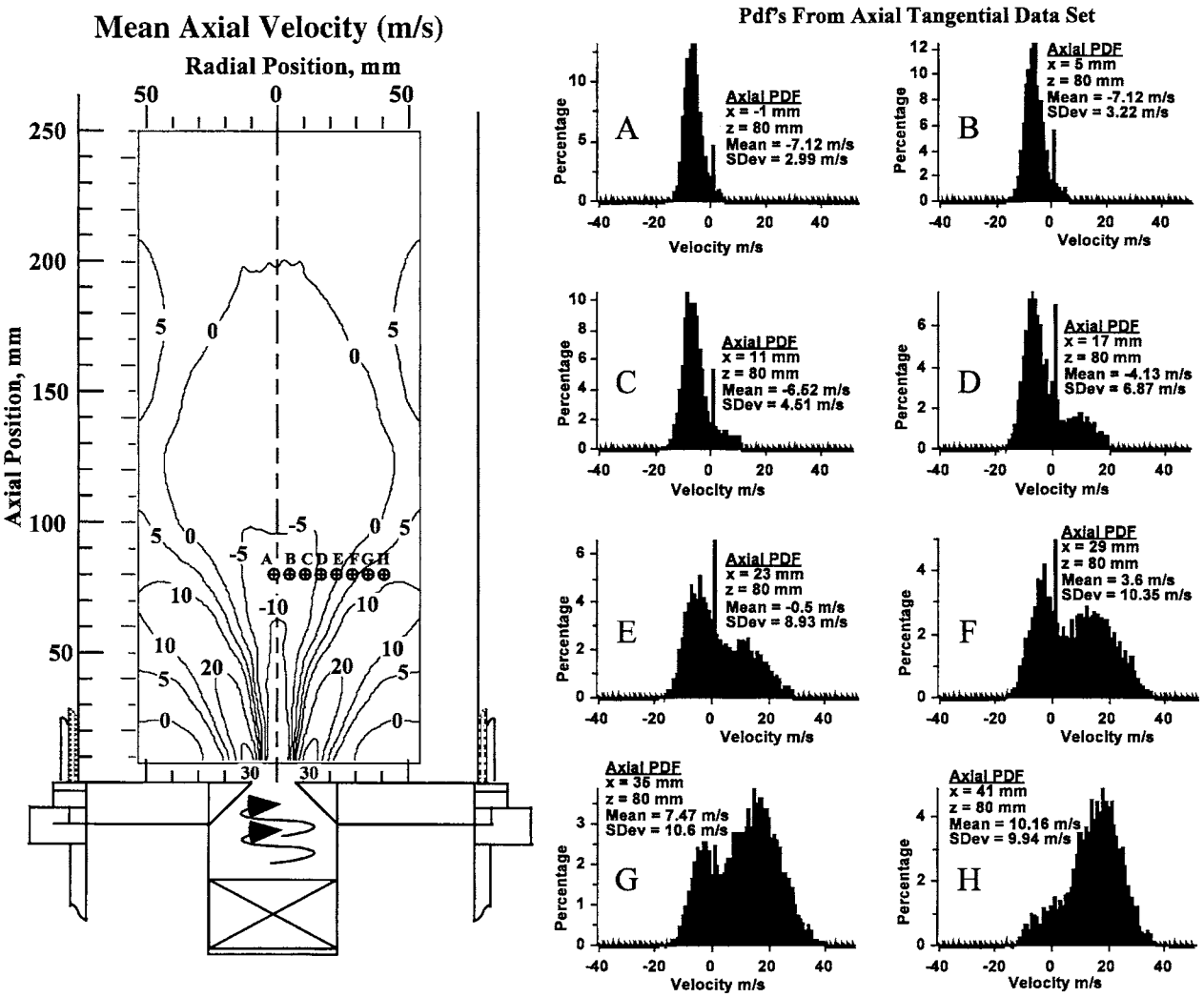

Fig. 14 Mean axial velocity contour map and example velocity PDFs (HS injector, ϕ=0.80)

show that the flame in the MS ϕ=0.65 case is higher in the combustion chamber when compared to the HS ϕ=0.80 (most stable flame) case. The peak temperature of the MS ϕ=0.65 (least stable flame) case was also lower (1449 versus 1648 K) than the HS ϕ =0.80 case. The adiabatic flame temperatures were 2000 and 1750 K for the ϕ=0.80 and ϕ=0.65 cases, respectively. The differences between measured and adiabatic flame temperature are attributed to the heat losses from the burner.

Comparison of Figs. 18(*a*) and 18(*b*), or Figs. 18(*c*) and 18(*d*) show that the increased heat release associated with the higher fuel equivalence ratio (0.80 versus 0.65) had the effect of increasing flame stability, causing the vortex core to be closer to the injector inlet. The increased heat release also causes a significant increase in the peak flame temperature.

The effect of swirl on flame structure can be seen by comparing Figs. 18(*a*) and 18(*c*) or Figs. 18(*b*) and 18(*d*). The higher swirl level has increased flame stability as evidenced by (1) the location of the flame vortex (HS moves the vortex closer to the injector), and (2) the higher peak flame temperatures associated with the higher swirl level (1550 versus 1449 K for the ϕ=0.65 cases, and 1648 versus 1603 K for the ϕ=0.80 cases).

As noted above, recirculation zones play a major role in stabilizing a turbulent, premixed natural gas combustor. Gas moving down into the ignition zone and radially towards the axial centerline improved the stability of the flame. The intensity of the recirculation zones was based on how well the recirculation zones moved hot gases to the middle of the combustion chamber and down into the ignition zone. The vortex structures shown in the gas temperature maps are consistent with the previous observations of OH-PLIF images, and the similar iso-velocity contours above.

The analysis of the approximately 1000 instantaneous gas temperature measurements obtained at each in situ measurement location in the flame zone allowed statistical investigation into the turbulent character of the flame to be made. Standard deviations for the gas temperatures were calculated at each location in the combustion chamber. Iso-contour plots of standard deviation (σ_T) temperature are shown in Fig. 19 for all four test cases. The actual values of σ_T were normalized by the local mean temperature, and the normalized standard deviation results are presented as percents. This treatment is analogous treatments of fluctuating velocity data to determine local turbulent intensities. Maximum and minimum mean temperatures are also included in Fig. 19.

The effects of swirl level and stoichiometry on gas temperature fluctuations are apparent in these maps. The effect of swirl level on flame structure and stability can be obtained by comparing Figs. 19(*a*) and 19(*c*) or Figs. 19(*b*) and 19(*d*). In general, the maximum values of σ_T are close to the same for all four cases. Within the flame, the highest levels of σ_T follow the high velocity shear zone that separates the central recirculation zone with the side recirculation zone. This is consistent with the velocity observations. In the velocity study, the highest values of σ_u correlated directly with the high velocity channel that was associated with the vortex flow. Past studies have suggested that a large standard

Downloaded 02 Jun 2010 to 171.66.16.98. Redistribution subject to ASME license or copyright; see http://www.asme.org/terms/Terms_Use.cfm

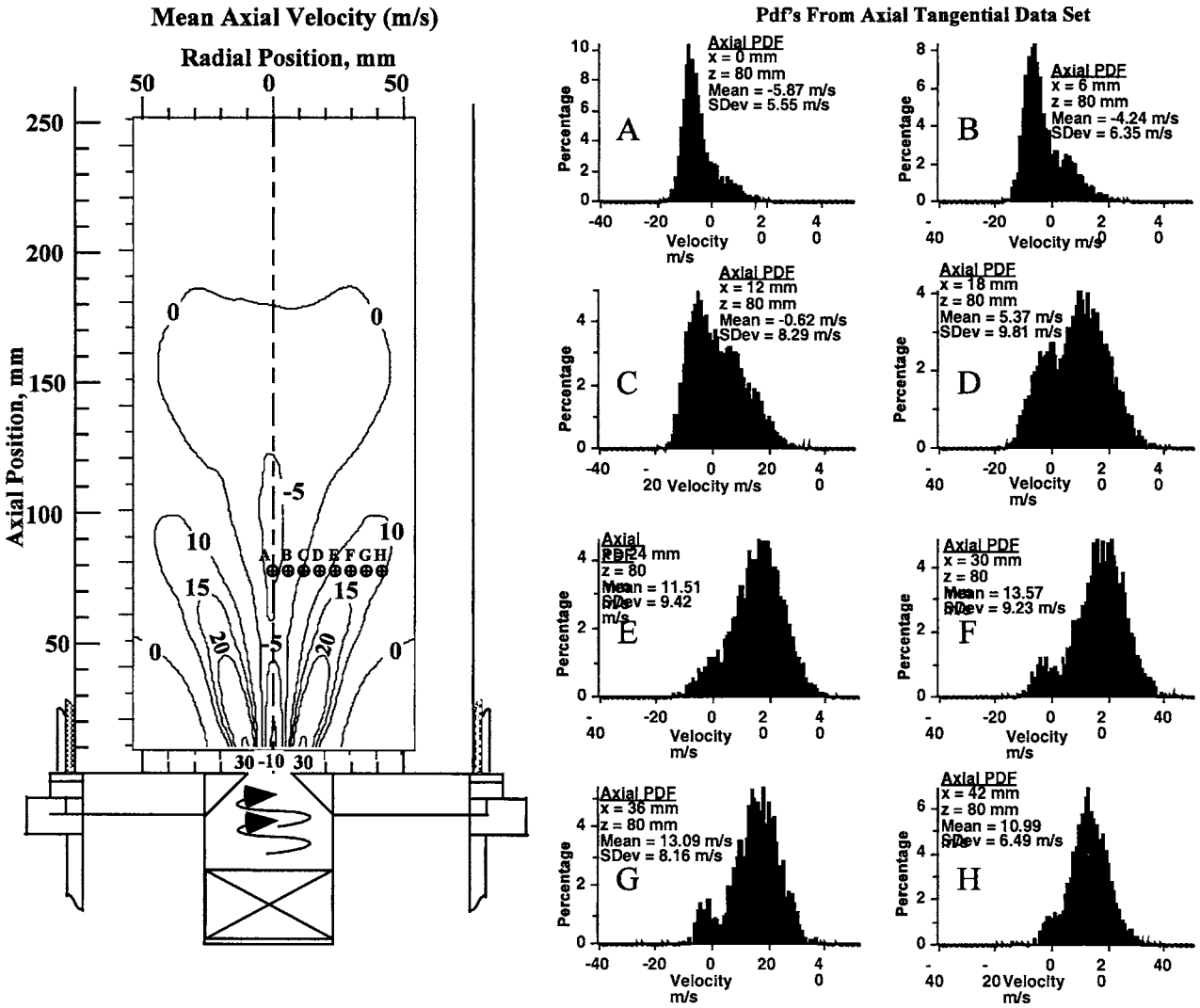

Fig. 15 Mean axial velocity contour map and example PDFs (MS injector, ϕ=0.65)

deviation correlated with high turbulence regions [8,11]. In this study, the largest values of σ_T occurred in the same location as the largest values of mean velocity.

The effect of stoichiometry on flame structure and stability can be obtained by comparing Figs. 19(*a*) and 19(*b*) or Figs. 19(*c*) and 19(*d*). In general, the higher heat release associated with the ϕ =0.80 cases resulted in (1) a reduction of the size of the highly fluctuating zone, and (2) a movement of that zone closer to the injector inlet.

Probability distribution functions (PDFs) have been used to de-

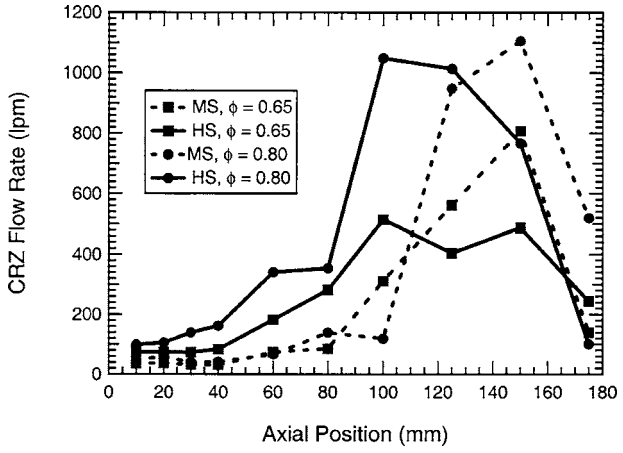

Fig. 16 Volumetric flow rates in the central recirculation zone, computed from axial velocities

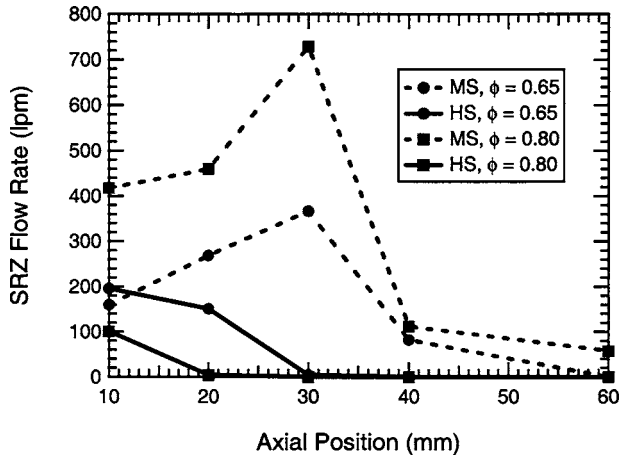

Fig. 17 Volumetric flow rates in the side recirculation zone, computed from axial velocities

Downloaded 02 Jun 2010 to 171.66.16.98. Redistribution subject to ASME license or copyright; see http://www.asme.org/terms/Terms_Use.cfm

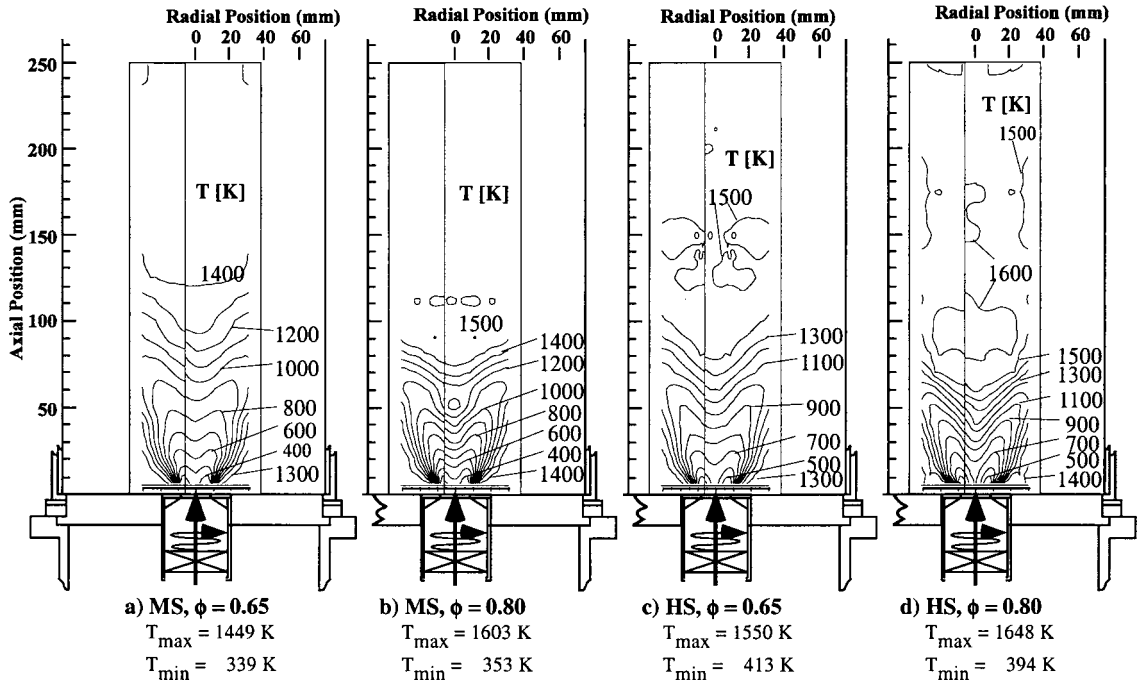

Fig. 18 Contour maps of mean gas temperatures for the four test conditions

scribe the characteristics of the fluctuating temperature. Figures 20 and 21 show examples of gas temperature PDFs at axial locations of 40, 60, and of 80 mm and radial positions from the centerline to a 30-mm radial location for the HS ϕ=0.80 and MS ϕ=0.65 cases. Additional PDF results are included in the dissertation by Flores [2]. Labeled on the PDF are the axial position radial position mean gas temperature (K) standard deviation temperature (K) and normalized standard deviation temperature, σ_T (%).

In Fig. 20, the PDFs generally do not exhibit a Gaussian distribution. The distributions in a single identifiable zone (i.e., in either the central recirculation zone or the side recirculation zone) seem to follow a Beta distribution. As with the velocity distributions, the distributions that bridged the two recirculation zones tended to have a bimodal PDF. Comparison of distributions E and F (40 mm) in Fig. 20 show that these two PDF distributions are clearly on opposite sides of the boundary between the central and side recirculation zones. At a higher position (80 mm), distributions M, N, and O all exhibit a wide distribution that has a bimodal character. This suggests that in the higher part of the flame there was a significant side to side fluctuation, even though the σ_T was not large, that shifted the side and central recirculation zones back and forth across the diagnostic locations.

Figure 21 presents similar PDF results for the HS ϕ=0.80 case.

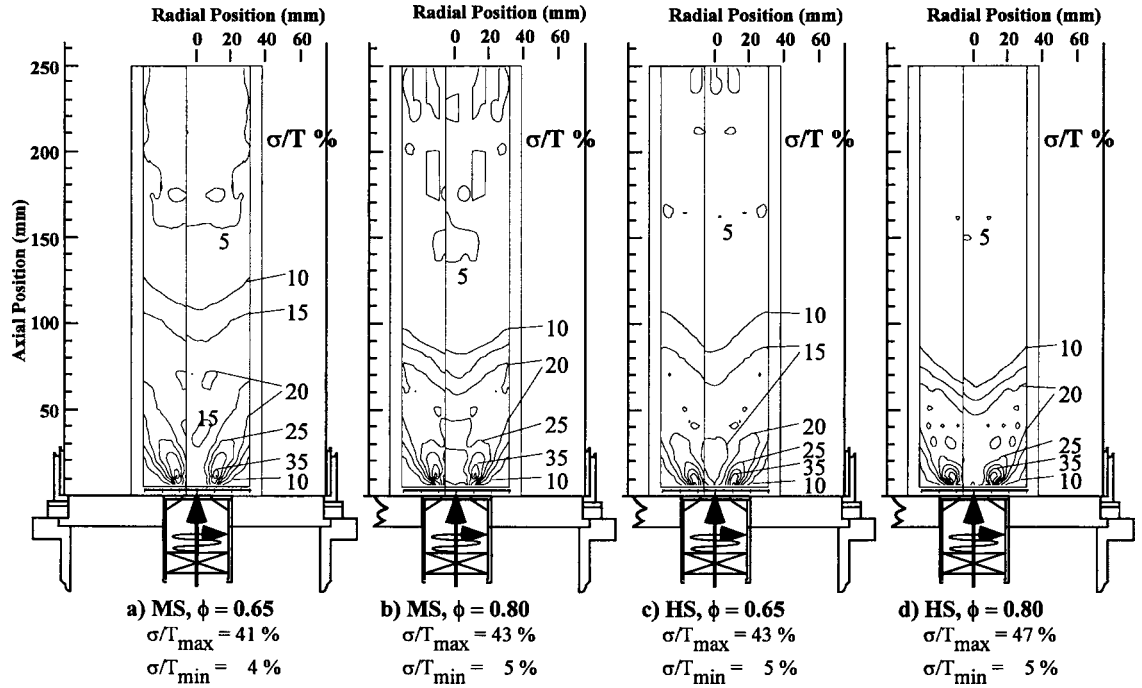

Fig. 19 Contour maps of normalized σ/T% for the four test conditions

Downloaded 02 Jun 2010 to 171.66.16.98. Redistribution subject to ASME license or copyright; see http://www.asme.org/terms/Terms_Use.cfm

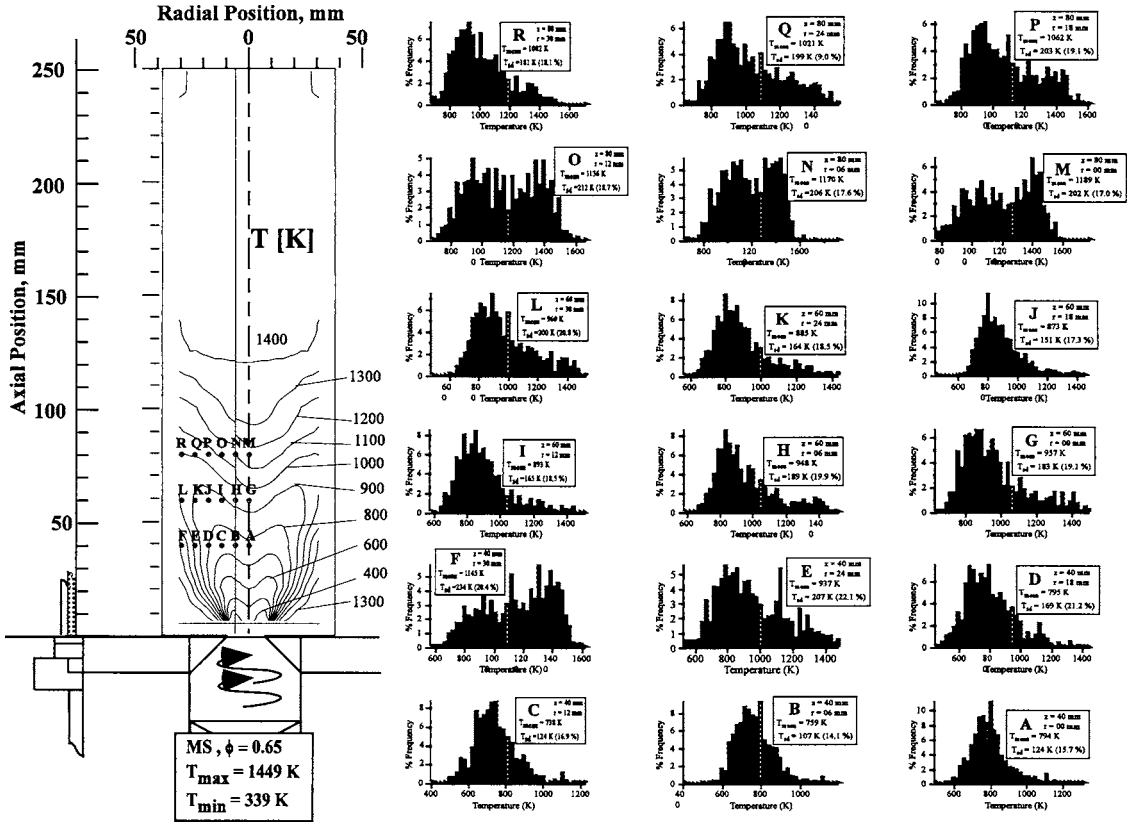

Fig. 20 Mean gas temperature contour map and example temperature PDFs (HS injector, ϕ=0.80)

Since the vortex is more coalesced near the injector for the HS ϕ=0.80 case, the bimodal character is easier to identify. Attention is drawn to locations A and B (z=40 mm) where there is a bimodal character to the PDF distribution even though these locations are near the centerline. Locations C, D, and E (also at 40 mm) reflect distributions in the high velocity region where cooler unreacted gases are being brought into the combustion chamber. Location F shows a bimodal character, but seems to be dominated by a higher temperature region associated with the side recirculation zone. The distributions at locations G, H, and I (z=60 mm) are dominated by a high-temperature zone associated with the central recirculation zone. However, at locations J, K, and L (also at 60 mm), the distributions have the bimodal character associated with components from both the central and side recirculation zones. Higher in the burner (z=80 mm) the distributions are nearly Gaussian in shape, and of nearly the same magnitude. This suggests that for this test condition, the combustion was nearly complete and near uniform flow had been achieved. In Fig. 20 at z=80 mm, the mean temperatures showed greater variation with radius, and were much below the final peak temperature in the burner. The location of the PDFs with bimodal distributions is shown in Fig. 22, showing that the bimodal distributions occur in the strong shear layers between the central and side recirculation zones.

Summary and Conclusion

A laboratory-scale gas turbine combustor (LSGTC) was used to reproduce the characteristics found in a modern annular gas turbine combustor. This laboratory scale gas turbine combustor was used to investigate the characteristics of a premixed natural gas/air flame using PLIF, LDA, and CARS at four operating conditions (two swirl conditions, HS and MS, and two equivalence ratios, ϕ=0.65 and 0.80). These data comprise one of the most complete characterizations of flames in lean premixed systems, and therefore present an important benchmark for testing computer models.

Data from all four types of measurements (video, PLIF, LDA, and CARS) showed that the least stable case was the MS ϕ=0.65 case, and that the most stable case was the HS ϕ=0.80 case. This was confirmed by heights of recirculation zones, location of OH, intensity of the OH measurements, PDF distributions of OH (showing the fraction of time when no OH was present), maximum temperatures, location of maximum temperatures, and standard deviations in OH and temperatures. The MS ϕ=0.65 flame would oscillate between two different flame structures, one that was more or less attached to the vortex funnel, and one that was lifted well above the vortex funnel. The MS case at ϕ=0.65 was at the very edge of the lean flammability limit, and would occasionally extinguish.

The variations in flame shapes were primarily a result of the effect of the swirl intensity and fuel equivalence ratio on the flow field, with the magnitude of the airflow rate being of secondary importance.

Probability density functions were generated at each measurement location for all three components of velocity, for OH intensity, and for temperatures. In general, PDF shapes were Gaussian in the downstream region after the main flame zone, were bimodal in the shear layer between the central and side recirculation zones, and followed a beta distribution inside the recirculation zones. The PDF plots show that there is a significant amount of time that no OH is detected in the most intense part of the flame zone. Likewise, significant levels of OH are seen even in regions that are predominately outside, but near the flame zone. The detector counts suggest that the maximum and average concentrations of OH for the MS, ϕ=0.65 case are about one fourth that of the HS, ϕ=0.80 case.

Boundaries of the recirculation zones were determined from the zero velocity contours, and the axial velocity was integrated radi-

Downloaded 02 Jun 2010 to 171.66.16.98. Redistribution subject to ASME license or copyright; see http://www.asme.org/terms/Terms_Use.cfm

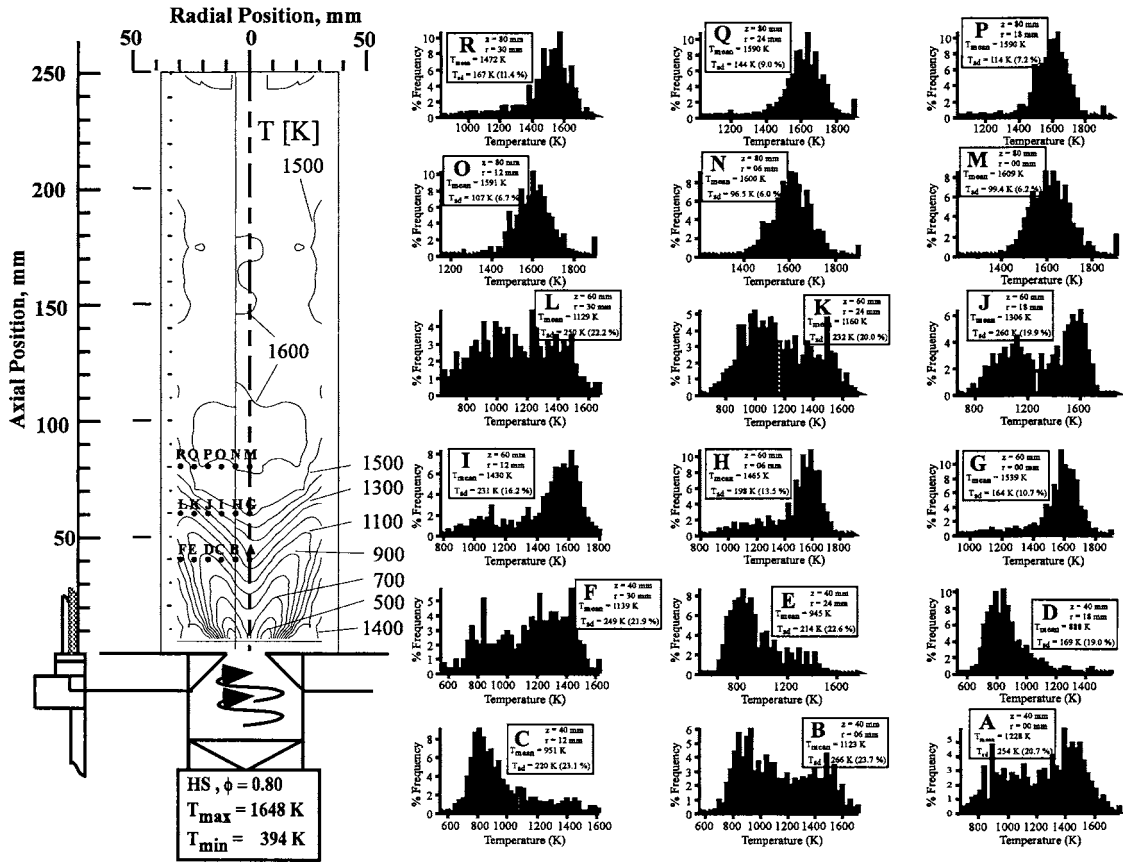

Fig. 21 Mean gas temperature contour map and example temperature PDFs (HS injector, ϕ=0.65)

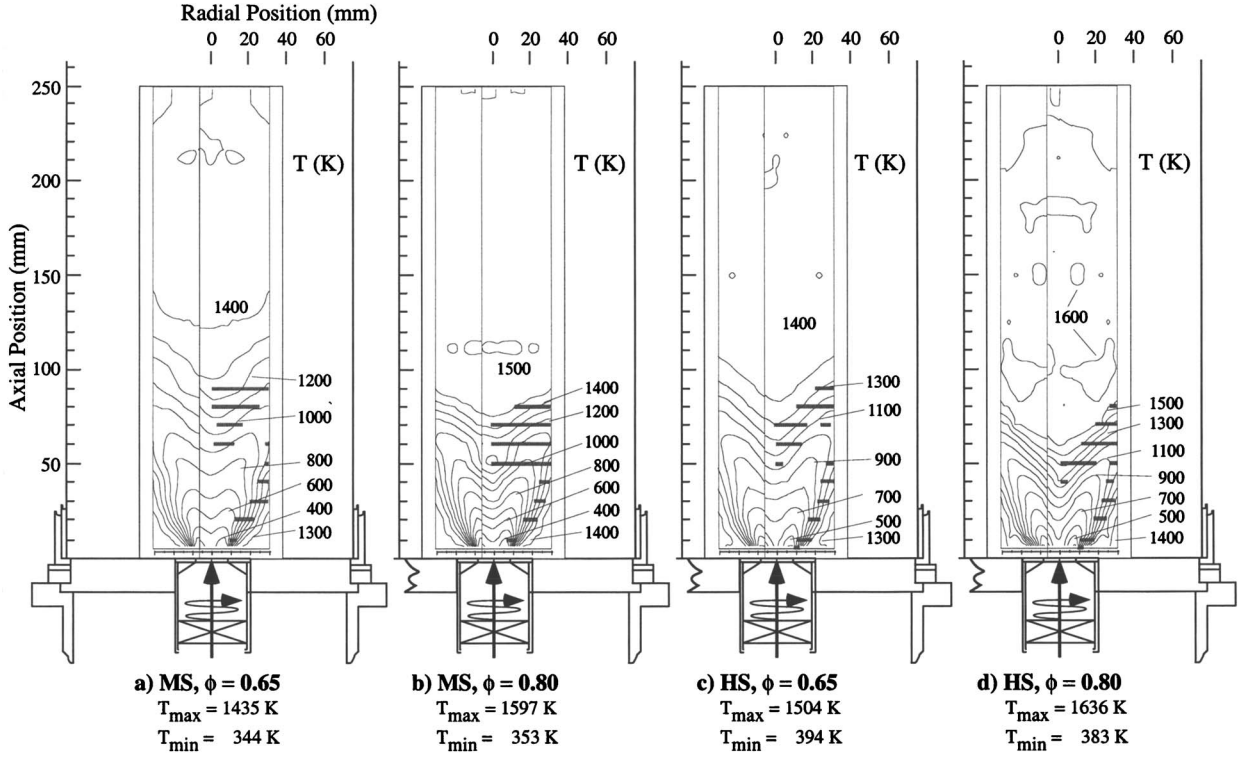

Fig. 22 Location of the bimodal distribution PDFs for all combustion cases, as indicated by horizontal lines

Downloaded 02 Jun 2010 to 171.66.16.98. Redistribution subject to ASME license or copyright; see http://www.asme.org/terms/Terms_Use.cfm

ally across the two zones to provide a volumetric flow rate in the reverse direction in each recirculation zone. This analysis showed that the flame stabilization was strongly influenced by the central recirculation zone for the HS ϕ=0.80 case, and by the side recirculation zone for the MS ϕ=0.65 case.

Acknowledgment

This paper presents results from a study that was funded in part by a U.S. Department of Energy's (DOE) Advanced Turbine Systems (ATS) program, with additional support by the Brigham Young University (BYU) Advanced Combustion Engineering Research Center (ACERC).

Nomenclature

CRZ = central recirculation zone
h = height
HS = HS condition
lpm = liters per minute
MS = MS condition
PDF = probability density function
Q = flow rate
r = radius
SN = swirl number
SRZ = side recirculation zone
w = width
ϕ = equivalence ratio

Subscripts

c = central (referring to central recirculation zone)
s = side (referring to side recirculation zone)
u = axial velocity
v = radial velocity
w = tangential velocity
x = horizontal distance from centerline
z = vertical distance from burner surface

References

[1] Murray, R. L., 1998, "Laser Doppler Anemometry Measurements in a Turbulent, Premixed, Natural Gas/Air Combustor," M.S. thesis, Chemical Engineering Department, Brigham Young University, Provo, UT.
[2] Flores, D. V., 2003, "Analysis of Lean Premixed Turbulent Combustion Using Coherent Anti-Stokes Raman Spectroscopy Temperature Measurements," Ph.D. dissertation, Chemical Engineering Department, Brigham Young University, Provo, UT.
[3] Cannon, S. M., Brewster, B. S., and Smoot, L. D., 1998, "Stochastic Modeling of CO and NO in Premixed Methane Combustion," Combust. Flame, **113**, pp. 135–146.
[4] Cannon, S. M., Brewster, B. S., and Smoot, L. D., 1999, "PDF Modeling of Lean Premixed Combustion Using In Situ Tabulated Chemistry," Combust. Flame, **119**, pp. 233–252.
[5] Mallampalli, H. P., Fletcher, T. H., and Chen, J. Y., 1998, "Evaluation of CH_4/NO_x Reduced Mechanisms Used for Modeling Lean Premixed Turbulent Combustion of Natural Gas," ASME J. Eng. Gas Turbines Power, **120**, pp. 703–712.
[6] Sturgess, G. J., Sloan, D. G., Lesmerises, A. L., Heneghan, S. P., and Ballal, D. R., 1992, "Design and Development of a Research Combustor for Lean Blowout Studies," ASME J. Eng. Gas Turbines Power, **114**, pp. 13–19.
[7] Hedman, P. O., Sturgess, G. J., Warren, D. L., Goss, L. P., and Shouse, D. T., 1995, "Observations of Flame Behavior from a Practical Fuel Injector Using Gaseous Fuel in a Technology Combustor," ASME J. Eng. Gas Turbines Power, **117**, pp. 441–452.
[8] Hedman, P. O., and Warren, D. L., 1995, "Turbulent Velocity and Temperature Measurements from a Gas-Fueled Technology Combustor with a Practical Fuel Injector," Combust. Flame, **100**, pp. 185–192.
[9] Warren, D. L., and Hedman, P. O., 1997, "Differential Mass and Energy Balances in the Flame Zone from a Practical Fuel Injector in a Technology Combustor," ASME J. Eng. Gas Turbines Power, **119**, pp. 352–361.
[10] Pyper, D. K., 1994, "The Study of Non-Swirl and Swirl Non-Premixed Flame Stability Near Lean Blow Out and the Design of a Research Combustion Facility," M.S. thesis, Mechanical Engineering Department, Brigham Young University, Provo, UT.
[11] Schmidt, S. E., and Hedman, P. O., 1995, "CARS Temperature and LDA Velocity Measurements in a Turbulent, Swirling, Premixed Propane/Air Fueled Model Gas Turbine Combustor," ASME Paper No. 95-GT-64.
[12] Roquemore, W. M., 1992, personal communication, Wright Laboratory, Wright Patterson Air Force Base, Dayton, OH.
[13] Gupta, A. K., D. G. Lilley, and N. Syred, 1994, *Swirl Flows*, Abacus Press, Kent, United Kingdom.
[14] Eckbreth, A. C., 1996, *Laser Diagnostics for Combustion Temperature and Species*, 2nd Ed., Gordon and Breach Publishers, Amsterdam, The Netherlands.
[15] Tait, N. P., and Greenhalgh, D. A., 1993, "PLIF Imaging of Fuel Fraction in Practical Devices and LH Imaging of Soot," Ber. Bunsenges. Phys. Chem., **97**(12), pp. 1619–1625.
[16] Campbell, R. P., Checkel, M. D., and Wilson, D. J., 1996, "Measurements of Time-Varying Jet Isopleths Using Dual Light Sheet PLIF," ASME Paper No. 96-GT-28.
[17] McDonell, V. G. and Samuelson, G. S., 2000, "Measurement of Fuel Mixing and Transport Processes in Gas Turbine Combustion," Meas. Sci. Technol., **11**, pp. 870–886.
[18] Thomsen, D. D., Ravikrishna, R. V., Cooper, C. S., Jiang, Y., and Laurendeau, N. M., 2001, "Concentration Measurements in a Mixing Module for Lean, Premixed, Gas-Turbine Combustors," J. Propul. Power, **17**, pp. 218–222.
[19] Cooper, C. S., and Larendeau, N. M., 2000, "Laser-Induced Fluorescence Measurements in Direct-Injection Spray Flames: Technique Development and Application," Meas. Sci. Technol., **11**, pp. 902–911.
[20] Broda, J. C., Seo, S., Santoro, R. J., Shirhattikar, G., and Yang, V., 1998, "An Experimental Study of Combustion Dynamics of a Premixed Swirl Injector," *Proceedings of the Combustion Institute*, **27**, pp. 1849–1856.
[21] Lee, S.-Y., Seo, S., Broda, J. C., Pal, S., and Santoro, R. J., 2000, "An Experimental Estimation of Mean Reaction Rate and Flame Structure During Combustion Instability in a Lean Premixed Gas Turbine Combustor," *Proceedings of the Combustion Institute*, **28**, pp. 775–782.
[22] Hicks, Y. R., Locke, R. J., and Anderson, R. C., 2000, "Optical Measurement and Visualization in High-Pressure, High-Temperature, Aviation Gas Turbine Combustors," Proc. SPIE **4076**, pp. 66–77.
[23] Birouk, M., and Gupta, A. K., 2001, "Structure of Lean Premixed Swirling Flames Using PLIF Imaging," J. Flow Visualization Image Process., **8**(4), pp. 341–353.
[24] Kobayashi, H, 2002, "Experimental Study of High-Pressure Turbulent Premixed Flames," Exp. Therm. Fluid Sci. **26**, pp. 375–387.
[25] Griebel, P., Scharen, R., Siewert, P., Bombach, R., Inauen, A., and Kreutner, W., 2003, "Flow Field and Structure of Turbulent High-Pressure Premixed Methane/Air Flames," ASME Paper No. GT-2003-38398.
[26] Hicks, Y. R., Locke, R. J., Anderson, R. C., Zaller, M., and Schock, H. J., 1998, "Imaging Fluorescent Combustion Species in Gas Turbine Flame Tubes: On Complexities in Real Systems," NASA Technical Memorandum No. 113157, 1074.
[27] Locke, R. J, Zaller, M. M., Hicks, Y. R., and Anderson, R. C., 1999, "Non-Intrusive Laser-Induced Imaging for Speciation and Patternation in High Pressure Gas Turbine Combustors," Proc. SPIE, **3783**, pp. 332–338.
[28] Hedman, P. O., Fletcher, T. H., Graham, S. G., Timothy, G. W., Flores, D. V., and Haslam, J. K., 2002, "Observations of Flame Behavior in a Laboratory-Scale Pre-Mixed Natural Gas/Air Gas Turbine Combustor from PLIF Measurements of OH," ASME Paper No. GT-2002-20052.
[29] Hedman, P. O., Murray, R. L., and Fletcher, T. H., 2002, "Observations of Flame Behavior in a Laboratory-Scale Pre-Mixed Natural Gas/Air Gas Turbine Combustor from LDA Velocity Measurements," ASME Paper No. GT-2002-20053.
[30] Laser Velocimetry Systems, 1990, TSI Inc., St. Paul, MN.
[31] *Find Software*, 1996, TSI Inc., St. Paul, MN.
[32] Boyack, K. W., and Hedman, P. O., 1990, "Dual-Stokes CARS System for Simultaneous Measurement of Temperature and Multiple Species in Turbulent Flames," *Twenty-Third Symposium (International) on Combustion*, The Combustion Institute, Pittsburgh, PA.
[33] Boyack, K. W., 1990, "A Study of Turbulent Nonpremixed Jet Flames of CO/N_2 Using Coherent Anti-Stokes Raman Spectroscopy," Ph.D. dissertation, Chemical Engineering Department, Brigham Young University, Provo, UT.
[34] Haslam, J. K., and Hedman, P. O., 1996, "The Use of Two Pyromethene Dyes in a Single Stokes Dye Laser to Make CARS Temperature and Multiple Species (CO, CO_2, O_2, and N_2) Concentration Measurements," Paper No. WSS/CI 96F-086, Fall Meeting of the Western States Section of the Combustion Institute, The University of Southern California, Los Angeles, CA, October 28-29.
[35] Dawson, R. W., and Hedman, P. O., 1996, "A Technique for Determining Instantaneous N_2, CO, O_2, CO_2, and H_2O Species Concentrations Using Multiplex CARS in Premixed Gaseous Flames," Paper No. WSS/CI 96F-087, Fall Meeting of the Western States Section of the Combustion Institute, The University of Southern California, Los Angeles, CA, October 28-29.
[36] Hedman, P. O., Flores, D. V., and Fletcher, T. H., 2002, "Observations of Flame Behavior in a Laboratory-Scale Pre-Mixed Natural Gas/Air Gas Turbine Combustor from CARS Temperature Measurements," ASME Paper No. GT-2002-20054.
[37] Eckbreth, A. C., 1985, personal communication.
[38] Palmer, R. E., 1989, "The CARSFT Computer Code for Calculating Coherent Anti-Stokes Raman Spectra: User and Programmer Information," Sandia Report No. SAND89-8206, Sandia National Laboratories, Livermore, CA.

Downloaded 02 Jun 2010 to 171.66.16.98. Redistribution subject to ASME license or copyright; see http://www.asme.org/terms/Terms_Use.cfm

Ben Chorpening
e-mail: Benjamin.chorpening@netl.doe.gov

Geo. A. Richards

Kent H. Casleton

U.S. Department of Energy,
National Energy Technology Laboratory,
Morgantown, WV 26507-0880

Mark Woike[1]

Brian Willis

NASA Glenn Research Center,
Plum Brook Station,
Sandusky, OH 44870

Larry Hoffman
Clean Energy Systems, Inc.,
Rancho Cordova, CA 95742-7500

Demonstration of a Reheat Combustor for Power Production With CO_2 Sequestration

Concerns about climate change have encouraged significant interest in concepts for ultralow or "zero"-emissions power generation systems. In a concept proposed by Clean Energy Systems, Inc., nitrogen is removed from the combustion air and replaced with steam diluent. In this way, formation of nitrogen oxides is prevented, and the exhaust stream can be separated into concentrated CO_2 *and water streams. The concentrated* CO_2 *stream could then serve as input to a* CO_2 *sequestration process. In this study, experimental data are reported from a full-scale combustion test using steam as the diluent in oxy-fuel combustion. This combustor represents the "reheat" combustion system in a steam cycle that uses a high and low-pressure steam expansion. The reheat combustor serves to raise the temperature of the low-pressure steam turbine inlet, similar to the reheat stage of a conventional steam power cycle. Unlike a conventional steam cycle, the reheat enthalpy is actually generated by oxy-fuel combustion in the steam flow. This paper reports on the unique design aspects of this combustor, as well as initial emissions and operating performance.* [DOI: 10.1115/1.1924633]

Introduction

The ultraclean fossil fuel-based energy plants of the future will be expected to effectively remove all environmental concerns traditionally associated with fossil fuels. Development of the technology for these plants is being supported by the U.S. Department of Energy, and includes support for revolutionary technologies which will facilitate CO_2 sequestration [1].

One technology that would enable CO_2 sequestration is oxy-fuel combustion. By removing the nitrogen from the oxidant stream, NO_x formation is prevented. Combustion of a mixture of oxygen and fuel produces an exhaust stream of H_2O and CO_2. By condensing the H_2O from the exhaust stream, the CO_2 is easily separated and may be sequestered. Additional water is added to the system to provide a greater volume of working fluid and to limit the working fluid temperature because of material limitations.

The proposal for such a cycle has been explained elsewhere [2–4] and is shown in Fig. 1. Fuel, oxygen, and diluent steam or water are supplied to a high-pressure gas generator (i.e., combustor). This high-pressure combustor drives a turbine similar to the high-pressure stage of a conventional steam power plant. As in steam power cycles, expansion through the high-pressure turbine is limited by the steam quality that would occur if directly expanded to the lowest cycle pressure. Thus, expansion occurs in sequential high and low-pressure stages, with a reheat combustor added between stages. The reheat combustor serves to increase the temperature of the steam before entering the low-pressure turbine, allowing expansion to the exit conditions with high steam quality. The operating pressure and temperatures shown in Fig. 1 are representative of the conditions proposed by Anderson et al. [3,4].

The combustors necessary for implementing this unique cycle had not been built before. Clean Energy Systems, Inc., is developing the combustion technology needed for the high-pressure gas generator, and this work will be described elsewhere. This paper reports on the unique design aspects and initial operating data from an oxy-fuel steam reheat combustor, built by DOE/NETL and tested at NASA Glenn Research Center-Plum Brook Station. The reheat combustor was investigated for both operating behavior and emissions data. Although the proposed power cycle shown in Fig. 1 would sequester all the noncondensable gases (mostly CO_2), information was sought on incomplete combustion (CO), as well as trace NO_x (from nitrogen impurities in the oxygen supply or in the fuel). Although trace emissions from this cycle are expected to be negligible, operating emissions data reported here are useful to evaluate this technology for applications where sequestration may be initially excluded.

Other cycles using dilute oxy-fuel combustion have also appeared in the literature, all aimed at producing power with an exhaust stream that could be directly sequestered. Some cycles use recycled CO_2 as a diluent, rather than H_2O [5,6]. An alternative strategy is to "decarbonize" the fuel by reforming and shifting hydrocarbons to produce hydrogen fuel. In this case, CO_2 is exhausted from the fuel reformer, and hydrogen can be used directly with air combustion in a nearly conventional power cycle. However, to achieve very high thermal efficiencies Bannister et al. [7] propose using steam-diluted oxy-fuel combustion, even with pure hydrogen fuel. These authors propose intermediate stage reheat combustors similar to those shown in Fig. 1. Although many power cycles for dilute oxy-fuel combustion have been proposed, no prior studies have demonstrated actual development of needed combustion hardware. Although the results presented here are specific to the conditions proposed by Anderson et al.[3,4], the issues discussed may be relevant to high-pressure oxy-fuel combustion for other cycle configurations. These tests are not intended to evaluate thermodynamic performance of cycles which sequester CO_2, but instead demonstrate that dilute oxy-fuel combustion can be successfully deployed in proposed reheat cycles. The thermodynamic and economic viability of such cycles is expected to benefit from advances in oxygen separation that are being developed through the U.S. Department of Energy [8–10].

[1]Current address: NASA Glenn Research Center, Cleveland, OH 44135.

Contributed by the International Gas Turbine Institute (IGTI) of THE AMERICAN SOCIETY OF MECHANICAL ENGINEERS for publication in the ASME JOURNAL OF ENGINEERING FOR GAS TURBINES AND POWER. Paper presented at the International Gas Turbine and Aeroengine Congress and Exhibition, Atlanta, GA, June 16–19, 2003. Paper No. 2003-GT-38511. Manuscript received by IGTI, October 1, 2002, final revision, March 1, 2003. Associate Editor: H. R. Simmons.

 Copyright © 2005 by ASME

Downloaded 02 Jun 2010 to 171.66.16.98. Redistribution subject to ASME license or copyright; see http://www.asme.org/terms/Terms_Use.cfm

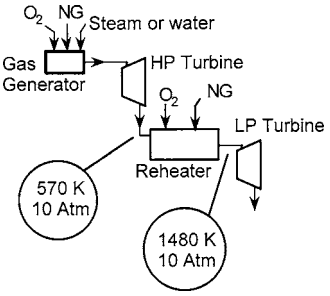

Fig. 1 Schematic of oxy-fuel reheat cycle as proposed by Anderson et al. [3], showing both high-pressure (HP) and low-pressure (LP) expansion stages. Fuel is natural gas (NG).

Table 1 Maximum flow capabilities or stored capacity of the NASA Plum Brook Hypersonic Tunnel Facility (HTF) and required maximum flow rates for this test.

Flow	HTF Max flow or stored capacity	Max flow required for this test
Steam	3.78 kg/s (30,000 lb/hr)	0.57 kg/s (4500 lb/hr)
Oxygen	9600 N m^3 @ 15.6 MPa (360,000 scf @ 2250 psi)	0.074 N m^3/s (10,000 scfh)
Natural gas	5400 N m^3 @ 13.9 MPa (200,000 scf @ 2000 psi)	0.037 N m^3/s (5000 scfh)
CO_2	Tube trailer as needed	0.019 N m^3/s (2600 scfh)
Nitrogen	20,000 N m^3 @ 33 MPa (750,000 scf @ 4800 psi)	0.0037 N m^3/s (<500 scfh)

Design Issues

Since this was the first test of a prototype combustor with significant differences from conventional systems, more details on the design of the combustor are provided than would ordinarily be expected. The design of the combustor provided some unique challenges because of both its reactant stream and because of its experimental goals. The reactant stream is unusual because of the use of pure oxygen and the very high steam loading (about 8:1 steam to oxygen by mole). The initial design goal was to develop a can-style combustor suitable for a 1 MW power cycle, such that the combustor could be replicated ten times, for example, to service a 10 MW power cycle. This requirement established the basic flow sizing of the combustor.

The design operating temperature and pressure were set by the cycle conditions (Fig. 1). It is notable that the operating conditions are very similar to early generation industrial gas turbine combustors. Thus, it would appear that the design could use standard gas turbine combustion methods. To some extent, this is true. In contrast to conventional gas turbine combustion, steam replaces the nitrogen. Furthermore, the intent of this design is to use zero excess oxygen, since oxygen generation reduces the net output power from the overall cycle. Finally, the oxygen must be fully mixed with diluent steam to avoid undiluted oxy-fuel combustion that would damage the combustion hardware. Thus, the combustor design needed to focus on three major issues: (1) test facility and combustor configuration; (2) oxygen-steam mixing; and (3) experimental operation and data acquisition in the steam environment. These issues are described below.

Test Facility

Testing was conducted at the NASA Glenn Research Center, Plum Brook Station, in Sandusky, Ohio. Testing was performed under an Interagency Agreement between the U.S. Department of Energy and NASA. The Plum Brook Hypersonic Tunnel Facility (HTF) had most of the needed flow services required for the tests described here. Table 1 shows the peak flow rate or storage capacity of the HTF. Both oxygen and steam flows are readily supplied at rates much greater than were needed for testing. The available oxygen storage allowed continuous testing at planned conditions for several hours. Natural gas was stored on site in high-pressure tube trailers; the composition is presented in Appendix A. The oxygen, CO_2, and natural gas were metered with Coriolis type mass flowmeters with factory calibrations assuring accuracies of ±0.35% of full-scale reading [0.151 kg/s (1200 lbm/hr) gaseous oxygen, 81.9 g/s (650 lbm/hr) CO_2, 37.8 g/s (300 lbm/hr) natural gas]. Steam flow was measured using a vortex shedding flow meter accurate to 34×10^{-6} m^3/s (0.072 $ft.^3$/min) or 1.35% of the measured flow rate, whichever is greater. This measurement required post-run adjustment for the steam density to obtain the correct mass flow rates, to accommodate a faulty setting found after initial testing. The density corrections adjusted the steam mass flow rates by 20%. Small quantities of nitrogen were used to purge the igniter and viewing windows. These flows were metered with fixed orifices operating at a given pressure drop (usually critical).

Combustor Configuration

The combustor needed to be designed with adequate residence time for CO oxidation to CO_2. This issue was examined first with stirred (PSR) and plug-flow reactor (PFR) studies, then CFD simulation. These studies, reported by Lewis et al. [11], concluded that the basic combustor flow splits could be arranged as shown in Fig. 2. For the purposes of initial design, the primary zone was treated as a well-stirred reactor followed by a plug flow reactor. Not all of the steam diluent that is needed to achieve the exit temperature of 1477 K (2200°F) is introduced at the front of the combustor. A steam to oxygen ratio near 8:1 (molar) is required to reach this exit temperature under adiabatic conditions; this ratio was lower during testing to account for heat losses (discussed later). The desired exit temperature is too low to sustain combustion, so the combustor was designed to divert 20% of the steam to dilution ports downstream of the primary zone. This allows the primary zone to operate at a higher temperature than would be possible if all the steam entered at the front end of the combustor. The dilution flow splits were established by Lewis et al. [11] as a tradeoff in primary zone conditions. Inadequate dilution would lead to the formation of CO by high-temperature equilibrium, but excessive dilution would result in CO production from slow oxidation kinetics at lower temperatures. It should be noted that the as-built dilution flow splits differ slightly from the planned split due to actual pressure drops across the fuel injector; this is described below. Finally, the calculations of Lewis et al. [11] suggested that 20 ms residence times in both the well-stirred and plug flow reactors would be ample to reach equilibrium CO concentrations in both zones. Assuming the stirred reactor was defined by a

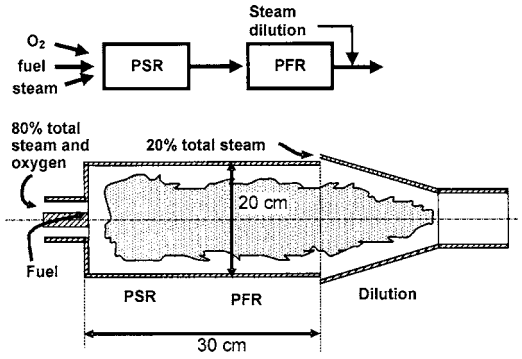

Fig. 2 Schematic of combustor design, showing stirred and plug flow representation of the primary zone and dilution region

Downloaded 02 Jun 2010 to 171.66.16.98. Redistribution subject to ASME license or copyright; see http://www.asme.org/terms/Terms_Use.cfm

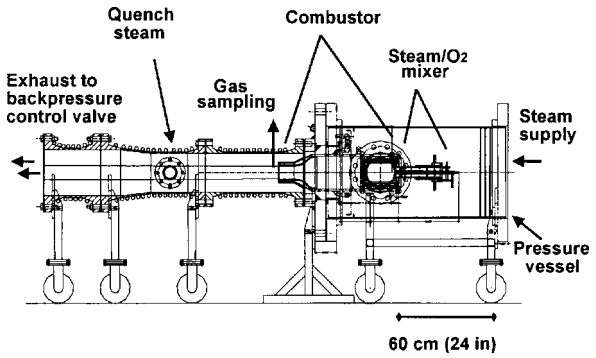

Fig. 3 Layout of pressure vessel and combustor (note scale at right). Flow is from right to left.

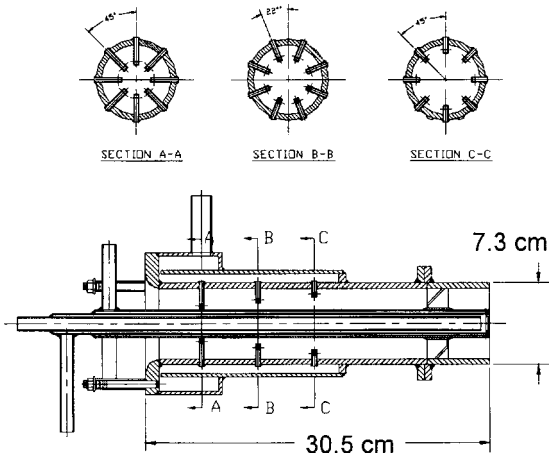

Fig. 5 Fuel/oxygen/steam mixer. Steam enters annulus at left, and flows to the right (orientation is reversed from previous figure). Oxygen is injected through spokes at locations A, B, and C. Natural gas is injected from centerbody tip at right, at the combustor inlet.

cylindrical portion of the combustor, with aspect ratio (diameter to length) of unity, it was possible to size the main features of the combustor, and then conduct CFD analyses of the proposed design. This was the approach used to design the combustor. The CFD analyses are not included here; they essentially confirmed the design concept based on the simpler modeling was adequate. Visual observations during testing confirmed the CFD prediction that the flame would anchor just downstream of the step expansion. Species measurements in the exhaust stream were near expected values from PSR-PFR calculations.

For the purposes of a proof-of-concept test, the combustor was designed with water cooled walls. Results presented here would not be expected to be dramatically different for a film cooled design as long as the cooling flows were developed to avoid CO quenching. A preliminary design using a convectively cooled liner was dismissed as too complicated for an initial study. The uncertainties associated with film cooling trajectories, and the need to characterize flow splits between cooling and combustion flow was thought to introduce too many variables into a first-of-a-kind test. Thus, although a commercial design would likely be film-cooled, these tests were conducted with water-cooled walls.

The combustor is shown in Figs. 3 and 4. The overall layout (Fig. 3) shows the combustor housed in a 61 cm (24 in.) diameter pressure vessel, mounted on the downstream flange. Flow is from right to left. Steam enters the combustor through the oxygen mixer described later, and through the dilution holes. The combustor is cylindrical with an i.d. of 20.3 cm (7.98 in.). As seen in Fig. 4, rectangular windows (18.1 cm $\times$ 11.8 cm, 7.13 in. $\times$ 4.65 in.) on the combustion liner provided optical access to the combustor dump plane. These windows were made from technical grade quartz, and were mounted such that they provided as little disruption to the cylindrical geometry as possible. Note that the combustor windows were subjected only to the pressure drop loading that exists across the combustor. A separate pressure-rated

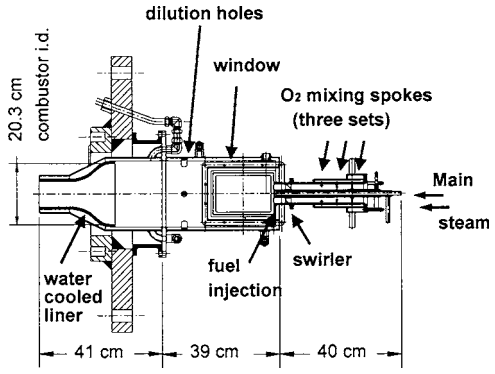

Fig. 4 Combustor layout. Flow is from right to left.

window was mounted on the pressure vessel to allow viewing into the pressure vessel and combustor. It was necessary to connect the pressure view port and the combustor window by a tube arrangement that was purged by nitrogen to prevent steam condensation from obscuring the windows.

The fuel injector and swirler design (Fig. 5) was based on conventional diffusion combustor nozzles for natural gas. While premixed combustion is advantageous for low NO_x production in conventional turbine combustion, there is no need to use premixed combustion here. Because the oxidant dilution is controlled by the amount of steam mixed with the oxygen, the temperature of the diffusion flame is controlled by the steam flow split. Furthermore, since only purge nitrogen, fuel nitrogen, or nitrogen from imperfect oxygen separation is present, the potential to create NO_x is very low in this system, even using diffusion flame combustion. For this reason, the simplicity of a diffusion flame arrangement was selected. The primary steam is mixed with oxygen in an annulus upstream of the swirler. The premixer annulus is 2.54 cm i.d. $\times$ 6.27 cm o.d. (1 in. $\times$ 2.47 in.). A ten vane straight-blade swirler is located upstream of the fuel injection. The vanes are oriented at 45 deg to the flow axis, and cover 2.04 cm (0.80 in.) of axial length. The natural gas is injected radially from ten holes (2.184 mm, 0.0860 in. diam) at the tip of the centerbody into the steam/oxygen mixture. Combustion is established at the dump plane of the combustor. The products are mixed with the remaining steam that enters through six 9.17 mm (0.361 in.) dilution holes located 30.5 cm (12 in.) downstream from the combustor dome (Fig. 4). The size and number of these dilution holes was established to meet two criteria. First, the effective flow area of the dilution holes was selected to produce the desired flow split for the steam. Second, the dilution jet mixing was optimized to produce well-mixed products downstream of the combustor. The latter requirement was met by following the dilution jet design procedures outlined by Lefebvre [12]. The former requirement was met by initial design based on calculated flow effective areas, followed by cold-flow tests of the as-built components. The cold flow tests were conducted using air as a surrogate for the steam flow, measuring the component pressure drops at the planned volume flow rates, and then making corrections for the properties of steam versus air. These calculations did not account for the pressure drop produced by the flame during actual operation. Neglecting the combustion pressure-drop, cold-flow testing indicated that the as-built flow split for steam was 75% steam flow into the primary zone, with 25% going into the dilution holes. Accounting for the combustion pressure-drop would shift more of the flow to

Downloaded 02 Jun 2010 to 171.66.16.98. Redistribution subject to ASME license or copyright; see http://www.asme.org/terms/Terms_Use.cfm

the dilution holes. The net effect would be a slightly hotter primary zone than investigated by the stirred-reactor/plug flow design, but this is somewhat offset by heat losses to the walls which were roughly estimated to be 10% of the total heat generated in combustion.

The oxygen addition to the steam supply, upstream of the combustor, includes special provision to meet several requirements. First, the oxygen must be spatially well-mixed with the steam to avoid undiluted oxy-fuel combustion. Second, it was recognized that the arrangement of a single oxygen-steam mixer would have the propensity to produce dynamic coupling with the heat release and combustor acoustics, potentially leading to combustor pressure oscillations, called dynamics. This issue is a prominent difficulty of premixed combustors, where the fuel is mixed with the oxidant upstream of the combustion zone [13]. Although no prior literature has considered the possibility of dynamics originating from oxidant-diluent mixing, it is a conceivable mechanism to produce damaging combustion oscillations. Therefore, steps were taken to reduce this possibility by distributing the oxygen axially at three stations along the mixer. This concept has been demonstrated as a successful method to reduce combustion dynamics originating in premixed fuel injection [14]. As shown in Fig. 5, and focusing on the oxygen mixer, three sets of oxygen injection spokes are inserted with 5.08 cm (2.0 in.) separation along the axis of the mixer. Each set of spokes supplies a different radius with oxygen. The jet trajectories were designed using standard jet penetration rules [12], followed by a CFD analysis of the entire assembly. The CFD analysis confirmed that oxygen would mix with steam with excellent uniformity before arriving at the swirl vanes. Although no experimental tests of the mixing were performed, prior experience using CFD and mixing designs suggested that sufficient accuracy could be expected to avoid large-scale mixing problems. Large-scale mixing problems could produce undiluted oxy-fuel combustion that would damage the fuel injector hardware. This type of damage was not observed in testing.

As noted above, the combustion liner was water cooled. Because the exterior walls of the combustor were colder than the dew point, condensate management was an issue. To reduce condensation, a layer of ceramic insulation was applied to the lines that supplied water cooling, and to the combustor exterior itself. Commercial steam traps were used on the pressure vessel for removal of the condensate while maintaining the chamber pressure. Even with ceramic insulation to reduce condensation, the test rig required careful attention to detail in anticipation of collection of condensate during operation or warmup (an hour-long process). Pressure taps and other connections to the vessel were installed to drain condensate back to the vessel whenever possible. Fuel and oxygen lines were purged with nitrogen during warmup to avoid collecting liquid water before flowing process gas in these lines.

During warmup, condensation was obvious inside the combustor itself from the video observation through the windows. The downstream steam dilution holes in the walls of the combustor limited condensate buildup in the combustor; however, a considerable "splash" was observed at light-off. The windows dried quickly after lightoff, with the exception of a small area of condensation on the water-cooled frame around the window holder.

Exhaust gas concentrations of CO, CO_2, O_2, and NO were measured following condensation of the steam. Gas samples were extracted from the combustor exhaust following the neck-down, as shown in Fig. 3. The gas sampling train extracted sample from the pressurized section of the exhaust, reduced the pressure, and condensed out the water vapor before the sample was sent to the gas analyzers (Fig. 6). Details of the gas sampling train are discussed in Appendix B. Despite the large fraction of the exhaust stream removed by the condensers (more than 90% by mole), the loss of measured gases remained small. At most, the dissolved CO_2 carried away by the condensate has been estimated to be 1%

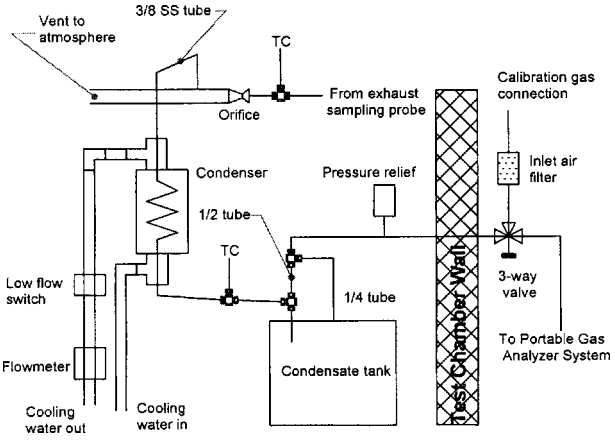

Fig. 6 Gas sampling train

of the measured CO_2 in the dry exhaust stream. The other measured gases are much less water soluble (see Appendix B).

Before the exhaust flow exits the pressure vessel, quench steam was added (Fig. 3) to reduce the temperature of the combustion products. The quenched products then flowed out through a back-pressure control valve used to establish the combustor pressure.

Temperature measurements were acquired with type *K* thermocouples except for the exhaust gas temperature, where type *B* thermocouples were used. These type *B* thermocouple readings were not corrected for radiation, but the downstream exhaust section is refractory lined, producing a radiative environment that minimizes the error due to radiation losses. These thermocouples were used to affirm that the combustor exit temperatures reached planned levels of 1480 K (2200°F).

Ignition was achieved with a spark-ignited natural gas/air torch. The torch was situated at a right angle to the flow axis, 2.5 cm (1.0 in.) downstream of the dump plane. The torch was a simple 12.5 mm (0.5 in.) stainless steel tube, inserted through both the pressure vessel and the combustion liner. An insulated center electrode extended to within 5.0 cm (2 in.) of the combustor walls, providing an ignition source. Stoichiometric natural gas and air were supplied to produce a 3 kW (10,000 Btu/h) flame, which was easily visible through the combustor windows prior to ignition of the main flows. Wetting of the ceramic insulator was a serious complication, and care was taken to avoid this problem. Without a continuous purge, the ceramic insulator would be wetted by steam condensate either during warm-up, or during combustion studies, making it impossible to re-light. Thus, a nitrogen purge of less than 0.15 g/s (about 20 scfh) was supplied to the torch at all times. While this flow rate is less than 0.1% oxygen flow at all test conditions, it was a significant factor in producing NO_x emissions, described later. Because the torch location is ideally situated at the position where the flame is anchored, and where temperatures are highest, NO_x production from unmixed purge nitrogen is likely. Future designs which seek to minimize NO_x formation will likely either use ignition methods which do not require purge at all, or use a purge other than nitrogen.

Combustor Acoustics

In addition to gas sampling, the combustor was continually monitored for thermoacoustic pressure oscillations (i.e., dynamics) using a high speed Kistler model 206 dynamic pressure transducer mounted on an infinite coil probe. See Mahan and Karchmer [15] for a description of this type of measurement. The pressure transducer was able to clearly indicate pressure signals associated with ignition or flame-out. However, thermoacoustic pressure oscillations were never encountered during the testing of this combustor.

Downloaded 02 Jun 2010 to 171.66.16.98. Redistribution subject to ASME license or copyright; see http://www.asme.org/terms/Terms_Use.cfm

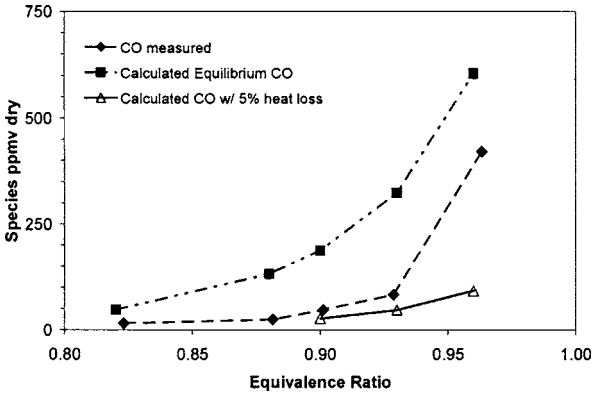

Fig. 7 CO in dry exhaust, calculated and measured for operation at 10 atm with CO_2 diluent added to the reactants

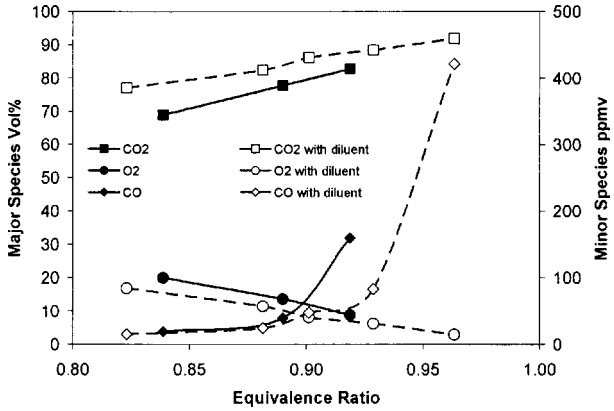

Fig. 8 Measured species concentrations in dry exhaust gas during 10 atm operation

Test Results

Initial shakedown and testing was conducted in a one-week test series. Because there was no prior experience operating this type of combustor, some uncertainty existed about the conditions needed for light-off and ramping to test conditions. Light-off was conducted near atmospheric pressure. It was shown, by repeated ignition attempts, that light-off was easier with excess oxygen ($\phi \sim 0.9$), and with a lower than planned steam to oxygen ratio (planned 8:1, actual 5.6:1, molar basis). These light-off conditions were obviously advantageous for establishing a flame because of the lower dilution and excess oxygen. The steam to oxygen ratio for the remainder of the tests was held at 5.6:1 (molar) to ensure flame stability. The combined effects of heat loss and substoichiometric conditions required lower steam dilution than the theoretical 8:1 needed at stoichiometric to produce exit temperatures of 1480 K (2200°F). Having achieved good light-off performance, pressurized test conditions were achieved by alternatively increasing the flow rates and closing the backpressure control valve. The diffusion flames emanating from the nozzle tip (where natural gas was injected) were readily visible through the combustor window. Once the diffusion jets reached the walls, typically about 5 cm downstream from the nozzle, the combustion region became much more uniform in appearance.

In Fig. 7, the measured CO levels from the combustor are compared with equilibrium CO levels for adiabatic operation, and with PSR-PFR calculations with 5% heat loss. The operating conditions shown were at 10 atm pressure, with a steam flow producing a plug-flow reference velocity of 20 m/s (65 ft/s) at the inlet of the oxygen mixer. Carbon dioxide was added to the steam flow as a diluent to mimic the products of the gas generator output (see Fig. 1). The CO_2 addition is sizeable, representing 5% of the total volume flow. A very significant effect of heat loss is demonstrated in Fig. 7, with 5% heat loss producing calculated CO levels about 1/6 of adiabatic equilibrium levels. The actual heat loss was estimated from the experimental data to be at most 23% of the theoretical sensible enthalpy gain of the mixture for the case of phi=0.96, and $P=10$ atm. This estimate assumed all the inlet gases enter at the steam inlet temperature. Chemkin [16] was used to determine the adiabatic flame temperature of the diluted mixture. The sensible enthalpy gains of the exhaust stream from the inlet temperature to the adiabatic and measured exhaust temperature were then compared to estimate the heat loss. The measured temperature of the exhaust was not corrected for radiation losses. The local nature of heat losses in the combustor adds to the difficulty in predicting the CO levels, as temperatures at the core of the product gases will be higher than near the wall. This makes it unlikely that a single temperature equilibrium calculation will accurately predict the resulting CO level. Nevertheless, it is interesting to note that the measured CO levels fall between the adiabatic and 5% heat loss curves from PSR-PFR calculations. If nonuniform mixing of oxygen with diluent were to occur, CO concentrations would be expected to be higher due to the increased local temperatures in regions with below-average dilution, if those regions remained segregated through the combustor. The combustor design, however, allowed for 20 ms of residence time, while the PSR-PFR calculations indicated that CO conversion to CO_2 would reach near-equilibrium in less than 1 ms. Figure 7 suggests that careful consideration must be given to the planned exit temperature to avoid significant levels of CO in the product stream. The strong sensitivity of the predicted CO concentration to the heat loss of this system demonstrates the need for accurate heat loss estimation. It is emphasized that the data on Fig. 7 are the **dry** CO concentrations. As noted above, the CO levels in the combustion products, before water condensation, are approximately 15 times lower than shown in Fig. 7. Thus, the higher CO concentration in the combustion products (at $\phi \sim 0.96$) would be around 30 ppm.

Dry gas concentrations measured from testing at 10 atm (147 psia) are shown in Fig. 8. These initial data sets were limited to fuel-lean cases ($0.83 < \phi < 0.96$). Results from subsequent tests covered a range of equivalence ratios including approximately stoichiometric. These results will be reported at a later time. Figure 8 also compares results with and without the addition of CO_2 as a diluent. Recall that the CO_2 was added to more accurately mimic the exhaust stream from the first stage gas generator, Fig. 1. All other operating parameters were unchanged between cases with and without the CO_2 addition, so that there was a lower combustion temperature when the CO_2 was added. As expected, the CO_2 diluent increased the volume fraction of CO_2 in the exhaust and decreased the fraction of O_2. Addition of CO_2 diluent also reduced the formation of CO, presumably by reducing the temperature of the combustion zone and the exhaust.

Experimental data were also obtained at half the design operating pressure, 5 atm (75 psia), as shown in Fig. 9. The range of stoichiometry investigated was $0.82 < \phi < 0.95$. The sharp upturn in CO concentrations occurred at a slightly higher equivalence ratio ($\phi \sim 0.93$) than during operation at 10 atm (upturn at $\phi \sim 0.90$). This behavior may have been due to the lower rate of heat generation competing with losses to the combustor walls resulting in lower combustion zone and exhaust temperatures. Figure 9 also shows predictions of the expected CO_2 and O_2, assuming complete combustion. Agreement between measured and expected concentrations of CO_2 is very good (typically within 1%). Similar agreement was achieved at the 10 atm conditions. The measured oxygen concentrations decreased with increasing equivalence ratio, but were several percent below expected values. This discrepancy may be attributed to some systematic calibration error at the low end of the flow loops, or due to uncertainties in

Downloaded 02 Jun 2010 to 171.66.16.98. Redistribution subject to ASME license or copyright; see http://www.asme.org/terms/Terms_Use.cfm

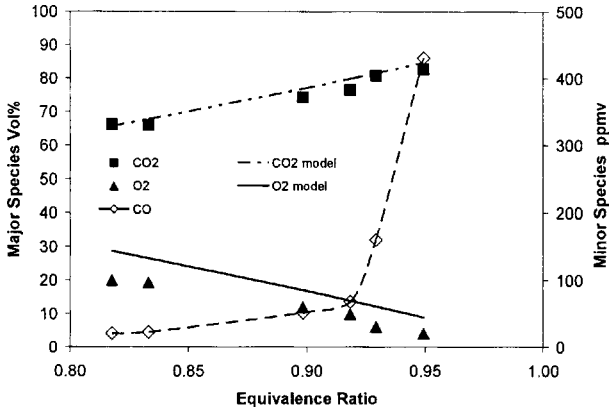

Fig. 9 Species concentrations in dry exhaust gas during 5 atm operation. Model for major species assumes complete combustion.

the natural gas composition. The complete species closure for a test of this scale was fairly good, and is shown in Fig. 10. These data are the mass closure at the 10 atm design point, both with and without the CO_2 diluent. Measured major species (CO_2 and O_2) are combined with calculated flow rates of purge nitrogen, nitrogen from the fuel (see Appendix A), and residual water vapor (Appendix B) to calculate the dry gas composition *measured* at the analyzers. Measured flow rates of all the *inputs* are then used to calculate a gas composition *expected* at the analyzers ignoring the trace species. The difference (*expected*−*measured*) is termed the "missing" mole fraction because it represents the species that are unaccounted for due to the collective inaccuracy of flow metering, fuel composition, and gas analysis. Referring to Fig. 10, less than 2%of the input mass is unaccounted for in the sample during operation at the higher equivalence ratios with the CO_2 diluent. The agreement is not as good at lower equivalence ratios, and in the absence of the CO_2 diluent. Figure 10 also shows the missing O_2, and it is clear that most of the species discrepancies are due to missing O_2. This is possibly due to a systematic error in oxygen metering, or in the oxygen gas analyzer calibration. The latter is likely because the initial oxygen analyzer calibrations were not selected for equivalence ratios below 0.9, where the discrepancy is most notable. Steps were taken in subsequent testing to improve the O_2 measurement and hence mass closure. Even so, the present data sets show remarkably good closure for an experiment of this size, and indicate that the major species can be readily sampled and analyzed with precautions to condense and remove the significant water content of the combustion products.

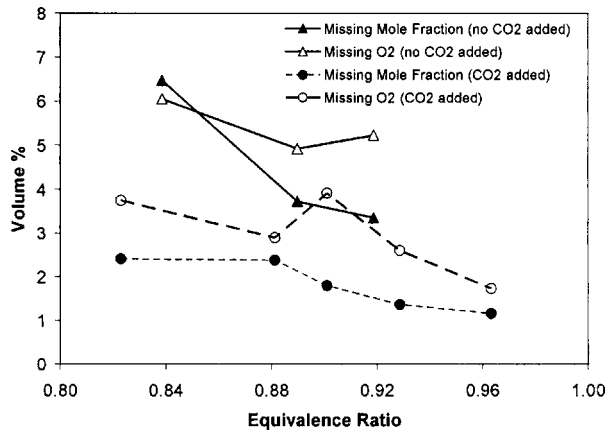

Fig. 10 Mass conservation at 10 atm

As noted in the Introduction, one of the objectives of this study was to characterize the NO_x production in this combustor. Although nitrogen is ideally absent from the oxy-fuel reactants, nitrogen may enter the combustor through imperfect oxygen separation, through the fuel composition (Appendix A), or deliberately to purge components. The resulting NO_x may be a consideration where the zero-emission concept is initially permitted without sequestering the exhaust stream. Initial estimates of the NO_x production (using Chemkin) from this combustor did not consider the potential of NO_x formed where the igniter purge N_2 entered the combustor, and this turned out to be significant. The small quantity of nitrogen (less than 0.1% of the oxygen flow) led to NO levels exceeding the original analyzer full-scale range of 20 ppmv. To confirm the contribution of the igniter purge flow, it was momentarily shut off at the 10 atm operating point, during which the measured NO concentration dropped to 17 ppmv. This measurement was on dry basis; the corresponding NO concentration in the wet combustor exhaust was 1.1 ppmv. While more testing is needed, these data suggest NO_x emissions can be very low, even with relatively high fuel nitrogen content.

A commercial design might use film cooling instead of water cooling of the combustor walls. A film cooled combustor design would be expected to result in higher wall temperatures and lower heat loss than the water-cooled design tested in this experiment. The resulting emissions would be impacted by two effects: localized quenching due to the film cooling and changes to the overall temperature. A film cooled combustor design could be developed that would minimize heat loss to the coolant. In this case, the CO levels would increase simply from higher equilibrium temperatures (Fig. 7). However, the diluent ratio could be increased to compensate, producing reduced equilibrium temperatures and CO levels similar to those reported here. As long as the film cooling was designed to avoid CO quenching, it is expected that a film-cooled version of this combustor could produce similar performance.

Initial testing of the system was terminated by the failure of one internal window on the combustor. While the potential for window failure introduced complications in the operation, it is emphasized that visual observations proved to be invaluable for troubleshooting the initial startup of the combustor. Additional testing of this combustor over a larger operating region has been completed and will be reported at a later date.

Conclusions

An oxy-fuel combustor with steam diluent has been demonstrated for the first time. The combustion system is appropriate for a steam power cycle with CO_2 sequestration. The combustor, designed for 1 MW thermal output, was operated at 10 atm with a molar steam-to-oxygen ratio of 5.6. Exhaust gas analysis provided CO_2 and O_2 results that followed expected values very well. CO concentrations were well below predictions of adiabatic PSR-PFR simulations; however, allowing for 5% heat loss reduces the calculated CO levels to below the measured levels.

Heat loss to the water-cooled combustor walls not only reduced the CO concentrations in the exhaust stream, but also reduced the maximum diluent ratio (steam/oxygen) achievable during initial tests. To achieve the designed exhaust temperature of 1480 K (2200°F), a steam/oxygen ratio of ~8:1 was expected to be required at stoichiometric conditions. During initial tests, a steam/oxygen ratio of 5.6 was maintained for combustion stability at slightly lean test conditions. This indicates the importance of careful accounting of heat loss to accurately plan diluent ratios for stable operation. In addition, careful consideration of the heat loss is also required to produce low CO concentrations in the exhaust.

During testing it was learned that the igniter purge nitrogen, necessary to keep the igniter dry, was contributing significantly to NO formation. This produced NO levels that exceeded the analyzer range. This limited valid NO_x measurements to only one operating condition, when the igniter purge was temporarily

Downloaded 02 Jun 2010 to 171.66.16.98. Redistribution subject to ASME license or copyright; see http://www.asme.org/terms/Terms_Use.cfm

Table 2 Natural gas composition from gas chromatography (error ±5% of measurement)

Component	Vol %
Methane	91.59%
Ethane	3.83%
Propane	0.76%
Butane	0.29%
Pentane	0.10%
Hexane	0.06%
Hydrogen	0.01%
Carbon dioxide	0.60%
Helium	0.04%
Oxygen or Argon	0.01%
Nitrogen	2.69%
Total	99.98%

turned off. Without the igniter nitrogen, NO levels were 1.1 ppmv in the combustion products, before condensing and removing the steam, and 17 ppmv after condensing the steam. The majority of this NO_x is attributed to the nitrogen which exists in the fuel supply.

In summary, these tests have shown that the concept of oxy-fuel combustion using steam dilution is viable. Endorsement or rejection of the full power generation and CO_2 sequestration cycle cannot be made from these tests. However, they do show that it is possible to construct and operate the steam reheater desired to improve the efficiency of the power cycle. These initial tests of an oxy-fuel-steam combustor are considered successful since ignition and extended operation (about 1 h) were achieved, and the low CO emissions measurements were in reasonable agreement with equilibrium calculations, indicating efficient mixing and combustion were achieved. Additional testing to further define the operating performance of this type of combustion, and provide a complete set of data over a wider range of stoichiometry and operating conditions has been completed and will be reported later.

Acknowledgment

This work was sponsored by the U.S. Department of Energy Turbines Program. The support of both past and current Product Managers (Ms. Abbie Layne and Mr. Richard Dennis) is gratefully recognized. The Plum Brook Operations Support Group is recognized for excellent experimental set-up and operation. Gas sampling system fabrication and support by Messrs. Randy Barnes, Mike Dera, and Mark Tucker, and combustor fabrication by Parsons Project Services at NETL are likewise acknowledged.

Nomenclature

A_j = ratio of moles of species j produced (consumed) per mole of natural gas input
N_i = moles of species i
X_i = mole fraction of species i
stoic = Stoichiometric
ϕ = Equivalence ratio; $(\text{fuel/oxygen})/(\text{fuel/oxygen})_{\text{stoic}}$

Appendix A: Natural Gas Composition

The natural gas used in the tests was analyzed at the Hastings Gas Analysis Laboratory of Dominion Transmission. The results of gas chromatography are summarized in Table 2.

The nitrogen content, in particular, is important to interpreting the experimental results. Due to the high moisture content of the exhaust stream (80%–90%), any impurities in the reactants are magnified in the on-line analysis of the exhaust gases when the water is condensed out.

Appendix B: Exhaust Gas Sampling

Gas Sampling System. The gas sample train is sketched in Fig. 6. A sample probe was inserted just downstream of the combustor neck-down (Fig. 3) so that samples were extracted before quench steam was added. Based on plug flow calculations, this probe position was more than 20 ms downstream of the dilution holes, meaning that sufficient time was available for completing mixing and oxidation reactions. The sample probe was a water-cooled tube positioned across the diameter of the exhaust with three 2.4 mm (0.094 in.) diameter holes facing the flow. Gas was carried by the inner tube of the sample probe (4.6 mm, 0.180 in. i.d.) to a 2.7 mm (0.1065 in.) diameter critical flow orifice that allowed a continuous 5 g/s flow of sample gas to bleed to an atmospheric vent line. As soon as the backpressure of the experiment exceeded 1 atm, the gas sample began to flow through the critical orifice to vent. Compared to more traditional sampling systems, which might be closed until needed, this venting approach was required to avoid condensing steam in the gas sample probe. Temperatures upstream of the orifice were monitored with a thermocouple to ensure that the sample was sufficiently cooled to quench any continuing CO oxidation. During sampling, the high pressure sample line temperature consistently measured near 170°C (340°F), which was low enough to quench any significant reactions. Gas samples were pulled from the critical orifice exit region by the sample train pump into a heat exchanger cooled with flowing water. The heat exchanger was designed (using the method described by Votta [17] and Perry and Chilton [18]) to cool the gas sample and condense the majority of the steam, producing a gas sample with a dew point near 20°C (70°F). As shown in Fig. 6, the condensate was separated from the flowing gas using a tee-arrangement, and stored in a closed tank. The tee-arrangement routed the flowing gas to the analyzer cart with minimal comingling with the gases occupying the empty volume of the condensate tank. Once the sample gas reached the analyzer cart, it passed through a thermoelectric sample conditioner achieving a dewpoint of 5°C (41°F). The final, dry sample then flowed to CO, CO_2, O_2, and NO_x analyzers. The analyzers were field calibrated on a daily basis with reference gas mixtures appropriate for the expected gas concentrations. Despite the large fraction of the exhaust stream removed by the condensers, the loss of measured gases remained small (discussed later). At most, the dissolved CO_2 carried away by the condensate has been estimated to be 1% of the measured CO_2 in the dry exhaust stream. The other measured gases were much less soluble.

Estimation of Dry Species Concentrations. Since the combustion products were predominantly water vapor that condensed out during gas sampling, the resulting dry concentrations were significantly different from those in the wet combustor exhaust. A model description of the change from wet exhaust to dry sample aids in understanding the results, including mass closure.

All the operating conditions tested were fuel-lean. The ratios of carbon dioxide, water, and oxygen produced or consumed by complete combustion of each fuel component i with oxygen was multiplied by the mole fraction of each component in the natural gas to calculate the production ratios A_j [Eq. (2)]. Additional quantities of water, nitrogen, and CO_2 brought in purposely as diluent, or unintentionally as part of the natural gas are also added. This is shown in Eqs. (1) and (2), where j is O_2, CO_2, N_2, or H_2O, and i refers to each component in the natural gas,

$$N_{j,\text{out}} = N_{j,\text{in}} + X_{j,\text{NG}} N_{\text{NG,in}} + A_j N_{\text{NG,in}} \tag{1}$$

$$A_j = \sum_i X_i \left(\frac{N_{j,\text{prod}}}{N_i} \right)_{\text{stoic},i} \tag{2}$$

These calculations provide the wet exhaust content of the major species. The content of the dry exhaust is then calculated by removing the water and calculating the remaining mole fractions. In

Downloaded 02 Jun 2010 to 171.66.16.98. Redistribution subject to ASME license or copyright; see http://www.asme.org/terms/Terms_Use.cfm

Table 3 Summary data of estimate of dissolved gas in condensate

Gas	α, $T=5°C$ ml_{gas}/ml_{water}	X_i	$V_{i,gas}$ ml/s	P_i kPa	$V_{i,dissolved}$ ml/s	V_{ratio}
CO_2	1.42400	0.9	99.58	91.17	1.089E+00	1.09E−02
CO	0.03149	0.005	0.5532	0.5065	1.338E−04	2.42E−04
N_2	0.02086	0.01	1.106	1.013	1.773E−04	1.60E−04
O_2	0.04287	0.1	11.06	10.13	3.644E−03	3.29E−04
NO	0.06461	3.00E−05	3.319E−03	3.039E−03	1.648E−06	4.96E−04

reality, not all of the water is removed; the remaining water vapor is estimated according to Eq. (3). The final condensation stage is at 5°C (41°F), at which water has a saturation pressure of 0.87 kPa. With an estimated total pressure of 88.2 kPa, this yields about 1% water vapor in the sample gas flowing to the analyzers.

$$X_{H_2O,sample} = \frac{P_{sat,condenser}}{P_{condenser}} = \frac{P_{sat,5°C}}{P_{condenser}} = \frac{0.87\ kPa}{88.2\ kPa} = 0.010 \quad (3)$$

The dry gas mole fractions are then adjusted for the residual water content, according to Eq. (4), to find the expected concentrations from the gas analyzers. This is a relatively small adjustment, but does improve the mass closure.

$$X_{j,sample} = X_{j,dry}(1 - X_{H_2O\ sample}) \quad (4)$$

Based on the equations above, the following "rule-of-thumb" can be made for gas species reported here. Because of the very high water content of the exhaust gases, on a volume basis, the measured dry gas concentrations are about 15 times larger than what existed in the combustor exhaust prior to water removal. For example, a CO concentration of 150 ppmv in the sample corresponds to approximately 10 ppmv in the combustor exhaust.

Dissolved Gases. The volume of dissolved gas with the gas at 1 atm pressure (without water vapor) is given in Table 3. The data come from Lange's Handbook of Chemistry [19].

The effect of dissolved gas on the dry gas measurements may be estimated from the flow rates and the solubility properties of the gases. A typical flow rate through the condenser provides 0.85 g/s of condensate and 0.21 g/s of dry gas. Henry's Law states that the solubility of a gas is directly proportional to the partial pressure exerted by the gas, or

$$P_i = kX_i \quad (5)$$

where P_i is the partial pressure of the species i in the gas phase, and X_i is the mole fraction of the gas dissolved in the liquid (in this case, water). The parameter α gives a slightly different version of this value, as the volume of dissolved gas at STP (0°C and 101.3 kPa), dissolved in 1 ml of water at a specific temperature. The choice of 5°C for the condensate temperature is conservative, since the solubility of all the gases in the table increases with decreasing water temperature. The primary condenser exit temperature is closer to 20°C, which is where most of the water is removed from the exhaust stream.

Following Henry's Law, the quantity of gas dissolved in the water is linearly proportional to the partial pressure of the gas. This adjustment may be made using

$$V_{gas,dissolved} = V_{water}\alpha\frac{P_i}{P_{ref}} \quad (6)$$

where P_{ref} is the pressure at which α has been measured. V_{water} is the volume flow rate of the water (condensate), and V_{gas} is the volume flow rate of the gas that dissolves in the water. Comparing the volume flow rate of dissolved gas with the flow rate of the undissolved gas gives an estimate of the impact of the dissolved gas on the measured value, as expressed in V_{ratio}. The result is that only CO_2 is significantly impacted by its water solubility, but even that impact is 1% or less.

References

[1] Coal and Power Systems Strategic and Multi-Year Program Plans, U.S. Dept. of Energy, National Energy Technology Laboratory, 2001, www.netl.doe.gov/coal/refshelf/for coal web mypp_2001_all.pdf.

[2] Bilger, R. W., 1999, "Zero Release Combustion Technologies and the Oxygen Economy," The Fifth International Conference on Technologies and Combustion for a Clean Environment, Lisbon, Portugal, 12–15 July, 1999.

[3] Anderson, R. E., Brandt, H., Doyle, S. E., Mueggenburg, H., Taylor, J., and Viteri, F., 2000, "A Unique Process for Production of Environmentally Clean Electric Power Using Fossil Fuels," 8th International Symposium on Transport Phenomena and Dynamics of Rotating Machinery, March 28, Honolulu, Hawaii.

[4] Anderson, R., Brandt, H., Mueggenburg, H., Taylor, J., and Viteri, F., 1998, "A Power Plant Concept Which Minimizes the Cost of Carbon Dioxide Sequestration and Eliminates the Emission of Atmospheric Pollutants," 4th International Conference On Greenhouse Gas Control Technologies, August 30–September 2, Interlaken, Switzerland.

[5] Staicovici, M. D., 2002, "Further Research Zero CO_2 Emission Power Production: The COOLENERG Process," Energy, **27**, pp. 831–844.

[6] Mathieu, P., and Nihart, R., 1999, "Zero-Emission MATIANT Cycle," ASME J. Eng. Gas Turbines Power, **121**, pp. 116–120.

[7] Bannister, R. L., Newby, R. A., and Yang, W. C., 1998, "Development of a Hydrogen-Fueled Combustion Turbine Cycle for Power Generation," ASME J. Eng. Gas Turbines Power, **120**, pp. 276–283.

[8] Balachandran, U., Ma, B., Maiya, P. S., Mieville, R. L., Dusek, J. T., Picciolo, J. J., Guan, J., Dorris, S. E., and Liu, M., 1998, "Development Of Mixed-Conducting Oxides For Gas Separation," Solid State Ionics, **108**, pp. 363–370.

[9] Prasad, R., Chen, J., van Hassel, B., Sirman, J., White, J., Apte, P., Aaron, T., and Shreiber, E., 2002, "Advances in OTM Technology for IGCC," 19th Annual Pittsburgh Coal Conference, Pittsburgh, PA, 23–27 September 2002.

[10] Dyer, P. N., Richards, R. E., Russek, S. L., and Taylor, D. M., 2000, "Ion Transport Membrane Technology For Oxygen Separation And Syngas Production," Solid State Ionics, **134**, pp. 21–33.

[11] Lewis, R. E., Casleton, K. H., Richards, G. A., Straub, D. L., and Rogers, W. A., 2001, "A Comparison of Turbine Combustion Concepts Suitable for Integration with CO2 Sequestration," 2001 Joint International Combustion Symposium, Kauai, HI, 10–12 September 2001.

[12] Lefebvre, A. H., 1999, *Gas Turbine Combustion*, 2nd ed., Taylor and Francis, Philadelphia.

[13] Richards, G. A., and Janus, M. C., 1998, "Characterization of Oscillations During Premix Gas Turbine Combustion," ASME J. Eng. Gas Turbines Power, **120**(2), pp. 294–302.

[14] Straub, D. L., and Richards, G. A., 1998, "Effect of Fuel Nozzle Configuration on Premix Combustion Dynamics," ASME 98-GT-492.

[15] Mahan, J. R., and Karchmer, A., 1991, "Combustion Core Noise," *Aeroacoustics of Flight Vehicles: Theory and Practice, Volume 1: Noise Sources*, NASA Langley Research Center, Available from AIAA Technical Library.

[16] Kee, R. J., Rupley, F. M., and Miller, J. A., 1989, Chemkin-II: A FORTRAN Chemical Kinetics Package for the Analysis of Gas-phase Chemical Kinetics, Sandia National Laboratories Report No. SAND89-8009.

[17] Votta, F., 1964, "Simplified Design Method for Condensers of Vapor-Gas Mixtures," Chem. Eng. (Rugby, U.K.), **71**, pp. 223–228.

[18] Perry, R. H., and Chilton, C. H., eds., 1973, *Chemical Engineers Handbook*, 5th ed., McGraw–Hill, New York, pp. 14.2–14.3.

[19] Dean, J. A., ed., 1985, *Lange's Handbook of Chemistry*, 13th ed., McGraw–Hill, New York, pp. 10.3–10.5.

Downloaded 02 Jun 2010 to 171.66.16.98. Redistribution subject to ASME license or copyright; see http://www.asme.org/terms/Terms_Use.cfm

Active Instability Control: Feedback of Combustion Instabilities on the Injection of Gaseous Fuel

M. P. Auer

C. Gebauer

K. G. Mösl

C. Hirsch

T. Sattelmayer
e-mail: sattelmayer@td.mw.tum.de

Lehrstuhl für Thermodynamik,
Technische Universität München,
85747 Garching, Germany

Modern low-emission premix combustion systems are often susceptible to combustion instabilities. Active instability control (AIC) systems are commonly used to attenuate these oscillations. For the control authority of AIC systems the effective amplitude and phase of the fuel modulation at the fuel outlet are as critical as the proper injection position. In typical cases the modulation of the fuel at the location of the actuator can be fundamentally different in amplitude and phase from the modulation of the fuel flow at the fuel outlet. In addition to the well-known effects stemming from the acoustics and Mach number of the fuel system, the fuel flow in the fuel system is also modulated by the oscillation of the pressure in the combustor in case of combustion instabilities. The superposition of the upstream modulation by the actuator and the modulation downstream by the combustion instability can result in an unexpected behavior of the fuel injection, from total compensation of the modulation to very high oscillations in the resonant case, accompanied by drastic phase shifts. This paper describes the influence of the secondary fuel modulation because of the combustion instability on the control authority of AIC systems on the basis of theoretical considerations and measurements for an atmospheric test rig with a natural gas-fired swirl burner. [DOI: 10.1115/1.1924718]

Introduction

Lean premixed combustion systems are highly susceptible to thermoacoustical combustion instabilities, which can penalize the system performance and lifetime considerably. A necessary condition for the feedback mechanism of thermoacoustic instabilities is given by Rayleigh's criterion, which admits self-sustained oscillation only if the fluctuation of the heat release rate correlates positively with the fluctuation of pressure in the combustor. This is the leverage point of all instability control methods, which aim at destroying this exciting correlation between heat release and pressure fluctuation, thus breaking up the feedback mechanism of the instability.

Instabilities may principally be eliminated by altering the combustion system acoustics, e.g., by resonators and baffles. This is a difficult task because the acoustic properties depend on the physical dimensions of the combustor as well as on the operating conditions. Therefore, this route is often blocked by technical constraints. Also, the effectiveness of these passive measures taken for one instability mode may be offset by a loss of stability of another mode. Although passive methods damp or detune the oscillating system, thus responding to the existing oscillation, active instability control (AIC) actively interferes with the feedback mechanism. Several approaches have been investigated and are summarized by McManus et al. [1]. In particular, AIC by secondary fuel injection has been observed to have the highest impact on instabilities, feeding only a small fraction of the fuel anti-cyclical to the heat release oscillation. With this method, the flame dynamics are addressed directly, thus altering phase and amplitude of the heat-release fluctuations relative to the pressure oscillations.

Numerous actuator types [2–4] and control algorithms [5–7] are described in the literature. Hathout et al. [8] state that the characteristics of the fuel injectors, including bandwidth, authority, and the form of modulation, have an effect on performance. Proportional injection seems to be more successful than on-off injection since proportional injection can modulate both amplitude and phase of the secondary fuel. However, Shcherbik et al. [9] successfully use noncoherent oscillatory fuel injection in order to break up the feedback loop. The attenuations reported in many publications vary widely and the damping effects often remain unexplained. Partly, this large variance in the control effectiveness may be related to the fact that the fuel-injection systems do not provide the desired modulation.

Some authors investigate the relation between fuel-line dynamics and combustion instability. Lieuwen and Zinn [10,11], Hobson et al. [12], and others show how fuel-system impedance can affect stability of combustion systems. This effect of modulation of a gas flow in a side branch is well known [13,14] and usually undesired in gas turbine fuel lines. Therefore, feed lines for main fuel injection as well as for piloting are usually choked in order to avoid coupling. For AIC the secondary fuel pipe needs an open boundary condition at the injection position to release intentionally modulated fuel into the combustion system. Here, the oscillation of the combustion system may negatively affect the desired modulation. Lee and Santavicca [15] and Richards et al. [16,17] took advantage of this side-branch coupling by adjusting the fuel-line impedance in order to allow the secondary fuel modulation by the combustion oscillation without an actuator.

Direct injection without a fuel line downstream of the actuator would doubtlessly be the best way to achieve control authority without concerns of fuel-line eigenfrequencies and delays. Unfortunately, this is not possible for the most practical combustion systems because the actuators are usually too bulky and too sensitive to temperature.

In this paper we demonstrate the importance of the fuel feed line dynamics for AIC because of secondary fuel injection. Based on experimental data an acoustical model of the feed line is formulated, which is then used to simulate its dynamical behavior.

Contributed by the International Gas Turbine Institute (IGTI) of THE AMERICAN SOCIETY OF MECHANICAL ENGINEERS for publication in the ASME JOURNAL OF ENGINEERING FOR GAS TURBINES AND POWER. Paper presented at the International Gas Turbine And Aeroengine Congress and Exhibition, Vienna, Austria, June 13–17, 2004. Paper No. GT2004-53055. Manuscript received by IGTI, October 1, 2003; final revision, March 1, 2004. IGTI Review Chair: A. J. Strazisar.

 Copyright © 2005 by ASME

Downloaded 02 Jun 2010 to 171.66.16.98. Redistribution subject to ASME license or copyright; see http://www.asme.org/terms/Terms_Use.cfm

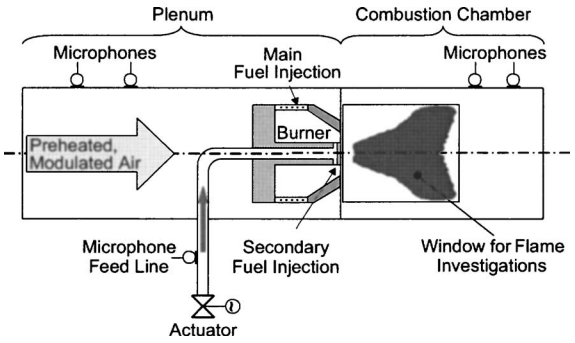

Fig. 1 Atmospheric single-burner test rig

From these results, conclusions are drawn with respect to necessary properties of an AIC by secondary fuel injection.

Experimental Setup

The experiments were performed using an atmospheric single-burner test rig fired with natural gas. A sketch of the test rig is shown in Fig. 1. It consists of an electrical air preheated with 312 kW, a 1235 mm long cylindrical supply tube (plenum) of 400 mm dia with a siren at its beginning, a swirl burner at its end, and a 735 mm rectangular combustor with a cross-sectional area of 350×350 mm and an open exit. The combustion chamber is air-cooled and has a quartz glass window of 250×200 mm open area.

The investigated TD^2 burner, shown in Fig. 2, is the second generation of a simple and highly flexible modular test burner kit, which captures the essential aerodynamics and acoustic features of gas turbine burners. The new TD^2 burner is an upscale version, and unlike the first version it permits technical premixing within the burner.

The preheated air enters the burner through a radial swirler with eight tangential inlet slots and is, subsequently, accelerated in a nozzle before entering the combustion chamber. The main fuel is injected through rows of small orifices perpendicular to the inlet slots of the swirler. The high pressure drop across the main fuel orifices leads to choked conditions; therefore, the feed line dynamics are decoupled from the combustion system. Secondary fuel can be injected at various positions of the burner. The preheated air mass flow can be forced by a siren. The amplitude of the forcing is adjusted by bypassing a part of the total preheated air mass flow. To modulate the secondary fuel mass flow a direct-drive servo valve (MOOG DDV 633) was mounted at the end of the secondary fuel feed line of 12 mm inner diameter. This proportional actuator with internal feedback system uses a position transducer for the spool to guarantee a precise and known movement up to 470 Hz. Since the actuator has a time delay to the input voltage, the position transducer signal was used for signal processing. Condenser microphones (G.R.A.S. GRA-40BP with preamplifier GRA-26AL) were used to measure the acoustic pressure distribution in the test rig. The microphones were inserted into water-cooled pressure taps, mounted flush with the plenum and combustion chamber walls, respectively. The microphones were calibrated relatively to a reference microphone, in order to minimize the phase and relative amplitude error. OH^*-radiation was measured by a photomultiplier (HAMAMATSU H5784-03) equipped with a bandpass filter (Schott UG11) around 307 nm. All signals were sampled simultaneously with a sample-and-hold PC card with a sampling rate of 10 kHz.

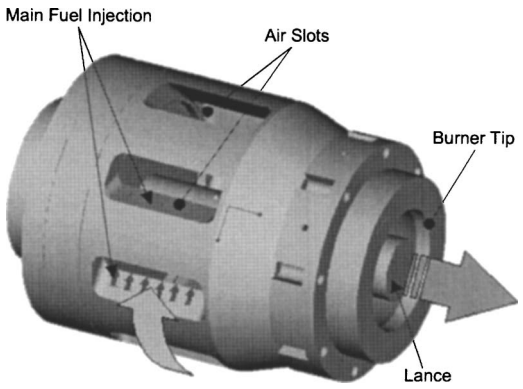

Fig. 2 TD^2 burner design

Experimental Procedure

As briefly outlined in the introduction self-excited thermoacoustic instabilities depend on all operational parameters of the system. Under typical self-excited operating conditions a frequency drift is observed for small changes of thermal power. Therefore, investigating AIC by secondary fuel injection is very difficult. Thus, a procedure was developed that allows measurement of the effects of secondary fuel injection on the flame with excellent reproducibility. The acoustic field in the rig is forced using the siren at a fixed frequency of 120 Hz, which is in the relevant frequency range of common instabilities and does not couple with the natural modes of the rig. Now the response of the flame transfer function to the AIC by secondary fuel injection in terms of flow rate, modulation amplitude, and phase, as well as the injection point, can be clearly discerned. In particular, no complex controller is needed because the frequency is fixed. In all cases the total amount of fuel was kept constant. When using secondary fuel injection, 5% of the fuel flow rate was passing through the secondary fuel pipe and modulated by the actuator. With modulation the actuator frequency was exactly the same as the forcing frequency of the siren but with adjustable amplitude and phase shift.

The experiments reported here were performed with 523 K air preheating, at an equivalence ratio of $\Phi=0.54$ and a thermal power of 380 kW. Radial secondary fuel injection through four orifices of 6 mm in the burner lance was used located $0.7D_{\text{Lance}}$ upstream of the lance tip. The focus of the experiments was the real modulation of the secondary fuel flow at the tip of the lance. However, the pressure was measured by a microphone 10% of the pipe length downstream of the actuator. This signal is labeled "Feed Line." The acoustic pressure in the combustion system was measured by microphones in the plenum upstream of the burner and downstream of the flame in the combustion chamber (denoted as "Combustor").

Experimental Results

AIC modulates secondary fuel that is injected into the combustion system to destroy the thermoacoustic feedback cycle as briefly outlined in the introduction. The effect of automodulated piloting will be demonstrated first. Then, the influence of the combustor oscillation on the modulation will be discussed in the next section.

Open and Choked Secondary Fuel Injection. The target of the first set of experiments was to assess the baseline influence of the acoustical field in the combustion system on the unforced secondary fuel injection. Therefore, the fuel line was in one case equipped with an orifice that provides choked flow at the desired fuel flow rate. This case is denoted as "choked." In the other case, called "open," which is representative for the AIC injection method, no orifice was present. The fuel injections in both conditions, open and choked, were identical, concerning average speed and injection position, because the orifice was integrated upstream into the feed line to guarantee the same flow field downstream of the injection position.

Figure 3 shows the pressure spectra from the fuel pipe (upper

Downloaded 02 Jun 2010 to 171.66.16.98. Redistribution subject to ASME license or copyright; see http://www.asme.org/terms/Terms_Use.cfm

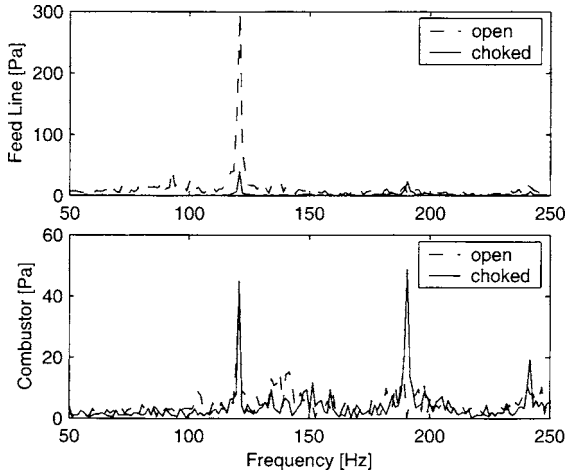

Fig. 3 Pressure amplitudes in the secondary fuel pipe and in the combustion chamber without secondary fuel injection: open pipe (dashed) and pipe with integrated orifice (solid line)

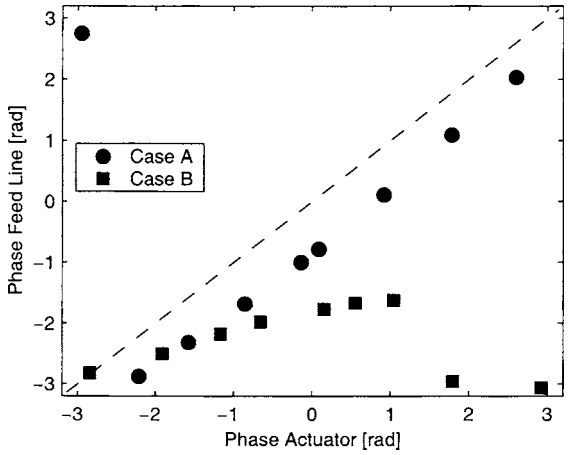

Fig. 5 Pressure phases in the feed line versus the corresponding phases of the actuator: Case A with high amplitudes of secondary fuel excitation, and case B with low amplitudes of secondary fuel excitation

half) and the combustor in the two cases without secondary fuel mass flow. For the open conditions (dashed line) significant oscillations in the secondary fuel pipe are induced by the combustor oscillations. This coupling is much weaker for the feed line with integrated orifice (solid line) because of the large area ratio of the orifice. The combustor microphone detects, in both cases, the same amplitude of ~40 Pa at the forced frequency of 120 Hz.

The results shown in Fig. 3 also illustrate the usefulness of the experimental procedure chosen. A weak self-excited combustor instability can be seen around 190 Hz in the measurement taken with the orifice in the fuel line, which is not so evident in the case of the open pipe. But both experiments were performed under equal nominal operation conditions. Thus, the difficulty arising from the sensitivity of the instability to small perturbations of the operational parameters when investigating the basic impact of AIC measures becomes clear. Considering, in contrast, the forced frequency at 120 Hz, the amplitudes in both cases are nearly identical.

The effect of unforced piloting (i.e., not actuated by the actuator) with 5% fuel through the secondary fuel-injection system is shown in Fig. 4. For the choked orifice case, there is no coupling of the fuel pipe acoustics with the combustion system and the pressure amplitude of the 120 Hz oscillation in the combustor is reduced by a factor of 1.6. The open secondary fuel pipe undergoes strong modulation from the combustor side, and an increase of the pressure amplitude is observed.

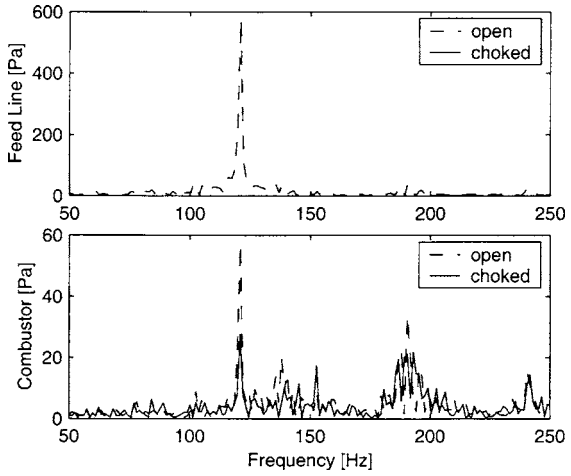

Fig. 4 Pressure amplitudes in the secondary fuel pipe and in the combustion chamber with 5% unforced secondary fuel injection: open pipe (dashed): and pipe with integrated orifice (solid line)

These two experiments demonstrate the feedback of pressure oscillations in the combustion system on the modulation of secondary fuel under open conditions. Having thus established the basic influence of automodulation because of combustion instability on piloting systems, we look next at the superposition of actuator- and combustor-driven oscillations in the fuel pipe to establish the resulting effect on the AIC control authority.

Modulation of Secondary Fuel

To quantify the interference of the modulation from the combustor downstream with the forcing by the actuator upstream was the aim of the next experiments reported here. The idea is to show the control authority of the actuator modulation on the flame by recording the flame response while changing the actuator phase relative to the combustor oscillation phase. Two cases A and B are discussed below that had equal nominal operation conditions. The only difference was that the amplitude of the harmonic forcing of the secondary fuel by the actuator was higher in case A than in case B. In the following graphs only the phases and amplitudes at the forcing frequency of 120 Hz are shown. The phase is measured relative to the pressure in the vicinity of the injection position, which was determined from the acoustics in the plenum with a low-order model.

In Fig. 5 the phase of the microphone in the secondary fuel line is plotted over the phase shift of the actuator. Ideally the data would follow the diagonal, meaning that the modulation of the secondary fuel mass flow is dictated by the actuator. In case A (marked by filled circles) with the higher actuator amplitude, the experimental data indeed follow the diagonal fairly well. Therefore, the wave field in the secondary fuel pipe is dominated by the actuator. In case B the smaller actuator amplitudes have a tremendous effect on the modulation of the secondary fuel. Now the effective phase range seen at the feed-line microphone is only 25% of one period despite the fact that the actuator phase covers 2π.

When looking at the amplitudes measured by the secondary fuel-line microphone, this loss of actuator influence becomes clear. In Fig. 6 the measured feed-line amplitudes are plotted over the actuator phase shift. To show the relative strength of the actuator forcing, the amplitude measured with actuator activity has been normalized with the combustor pulsation-induced amplitude, which was obtained before and after each actuator modulated se-

Downloaded 02 Jun 2010 to 171.66.16.98. Redistribution subject to ASME license or copyright; see http://www.asme.org/terms/Terms_Use.cfm

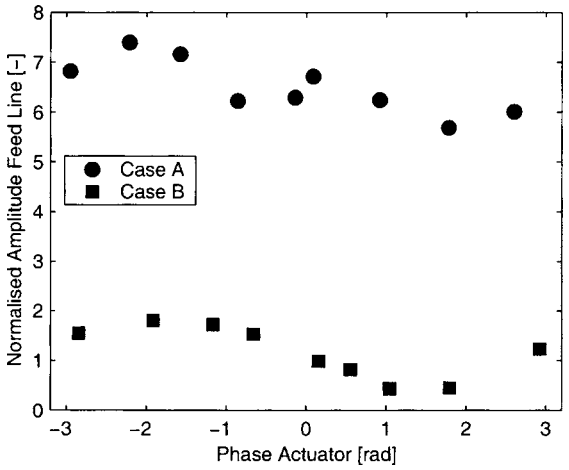

Fig. 6 Amplitude ratio of secondary fuel modulation in the pipe versus the corresponding phases of the actuator: Case A with high amplitudes of secondary fuel excitation and case B with low amplitudes of secondary fuel excitation

ries. In case A the amplitudes with actuator modulation increase by a factor of 5.7–7.4 over those driven only by the combustor. Therefore, it is plausible that the fuel-line modulation is dominated by the actuator. For case B actuator and combustor driven waves in the fuel pipe are of similar amplitude, such that the relative amplitude varies between close to zero and 2. Now the resulting wave field in the fuel line originates from modulations of the actuator and the combustor, leading to a weak control authority of the actuator.

To be able to draw conclusions from the data shown above on the achieved modulation of the secondary fuel mass flow, the response of the flame to the modulation was measured recording the intensity of the OH^*-chemiluminescence.

In Fig. 7 the phase delay between the feed-line pressure and the flame response as well as the phase difference between the actuator and the flame are shown. For both cases the phase differences between pressure and flame are nearly constant. In case A also the delay between actuator and flame is almost constant, whereas in case B it varies as had to be expected from the data shown above.

At this point it may be concluded that the fuel-line acoustics, as measured by the pressure in the fuel line, determine the effective flame control authority. Therefore, in an AIC strategy one must account for the fuel-line dynamics to asses the range of control

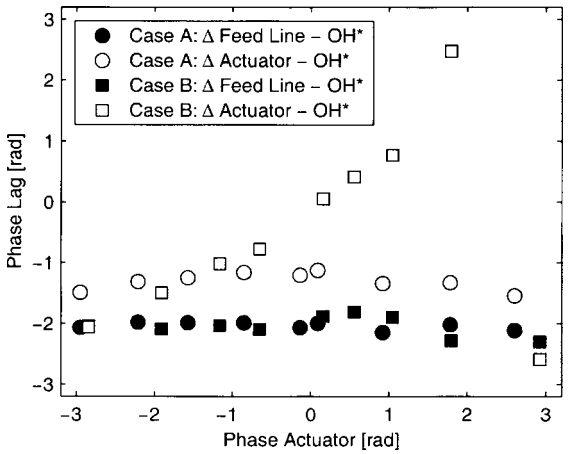

Fig. 7 Phase lags between flame response and feed-line pressure and actuator, respectively

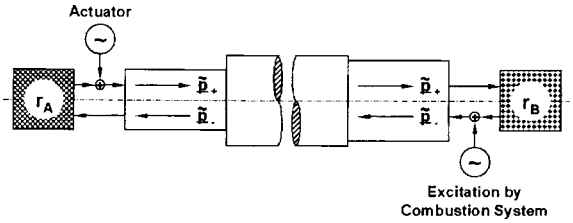

Fig. 8 Schematic of a network model

obtainable with the actuator. Below, a network model of the current fuel line is presented, which allows one to calculate the fuel-line behavior in the tests.

Acoustic Network Model

The following model is based on the mechanism presented in the preceeding section, which explains the experimentally observed fuel-line dynamics because of superposition of the waves generated by the actuator and the combustor oscillations.

In acoustic network modeling a pipe system is divided into single elements with constant parameters along its length, e.g., temperature, velocity, cross-sectional area, etc. These elements can be formulated in terms of "two ports" relating pressure and acoustic velocity at the input port to the corresponding output port [13,14]. Assuming that the plane-wave condition is fulfilled by the connected pipes, the acoustic pressure and velocity at the interfaces have to be equal. At the end of the network the downstream propagating wave will be reflected and heading upstream through all the pipe elements to the upstream end where it will be reflected again. The reflection conditions at the boundaries are defined by complex reflection factors. With a source in the model providing a harmonic signal the wave field in this network can be excited.

The current model consists of several pipe elements to account for the temperature gradient. The medium is pure methane with a constant mass flow. The reflection coefficients were set to $r_A=1$ (closed end) at the actuator side and $r_B=-0.6$ (nearly open end) at the burner-injection side. Harmonic wave generators are added on either side to simulate the actuator upstream and the pressure oscillations in the combustion system at the downstream end of the fuel pipe (Fig. 8).

The amplitude of the actuator in the simulation was set to 1, and the amplitude of the downstream excitation was varied from 0 to 1. The phase lag between both generators reflects the relative phase shift of the actuator to the acoustics in the vicinity of the injection position in the experiment. In order to validate the model the phases and amplitude ratios of the feed-line microphone were calculated and compared to the measured values. The Fig. 9 and 10 show this comparison, where the filled symbols are the experimental data points and the open symbols are the corresponding calculated values. Very good agreement is obtained. The oscillator amplitude ratio of $AR=0.02$ corresponds to case A and $AR=0.18$ to case B. After this validation the real fuel mass flow modulation at the injection position is determined using the network model. In particular we focus on the amplitude and phase of the secondary fuel mass flow modulation achieved at the injection point, which is normalized with the mean flow rate of the secondary fuel and then divided by the actuator-forcing amplitude. This data is referred to below as SFM. Thus, multiplying SFM with the forcing amplitude will result in the relative amplitude of the secondary mass flow oscillation at the injection location.

In Fig. 11 the predicted phase of the injected secondary fuel mass flow at the end of the fuel pipe is plotted versus the actuator phase. The phase at the injection position shows the same phase drift as the microphone upstream in the pipe but with a phase offset (compare $AR=0.02$ and $AR=0.18$ to Fig. 9). In general the model predicts a decreasing phase range available to the controller for increasing relative combustor amplitudes. In the current sys-

Downloaded 02 Jun 2010 to 171.66.16.98. Redistribution subject to ASME license or copyright; see http://www.asme.org/terms/Terms_Use.cfm

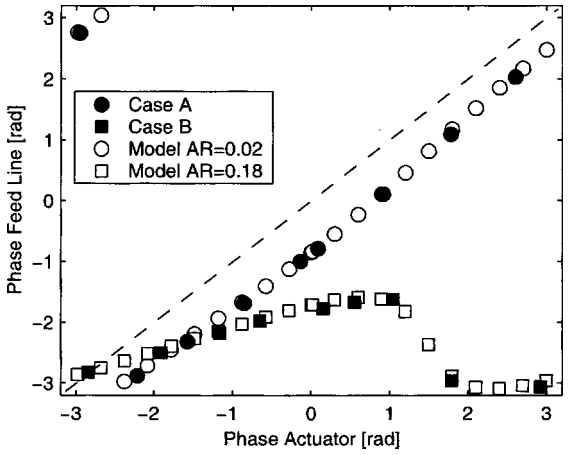

Fig. 9 Comparison of the experimental pressure phases (filled symbols) with the calculated model results (open symbols)

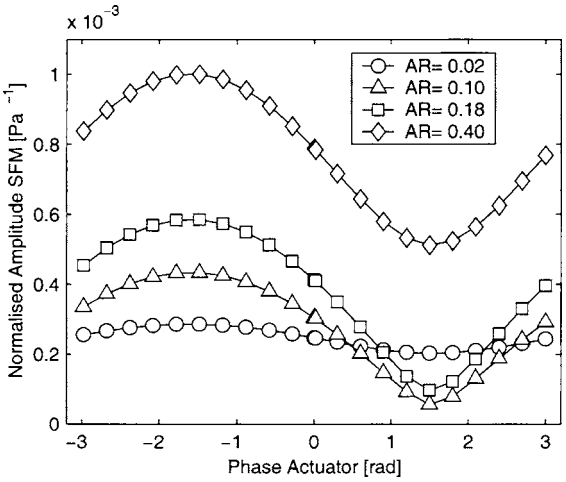

Fig. 12 Calculated amplitudes of the SFM at the injection position

tem an amplitude ratio of $AR=0.18$ already limits the phase to approx. $\pi/2$. For larger amplitudes phase control is lost. Figure 12 provides the corresponding amplitudes of the secondary fuel modulation. The smaller amplitude ratio of the excitation (e.g., $AR=0.02$), i.e., the actuator-dominated situation, gives the smaller relative modulation of the fuel mass flow at the injection point. In case of higher combustor influence (e.g., $AR=0.18$), a larger modulation is observed for certain actuator phase shifts but at the expense of a smaller achievable phase range.

In a sensitivity analysis of the feed-line dynamics of several parameters were considered. No noticeable effect was detected by small variations of the mean mass flow through the pipe, resulting in Mach numbers below 0.10. Different temperature profiles, changes of the geometry including variations of reflection coefficients, and a variation of the excitation frequency were also investigated. Because a change of these parameters alters the resonance frequency f^* of the fuel-line system, the results of the sensitivity analysis will be discussed briefly in terms of the variation of the excitation frequency with respect to the resonance frequency.

In Figs. 13 and 14 the phase and normalized amplitudes, respectively, of the secondary fuel modulation at the injection point for different frequencies are plotted over the phase of the actuator forcing for an amplitude ratio of $AR=0.18$. Both frequencies close to the resonance frequency (circles and squares) show equal behavior of phase and amplitude except for the achievable phase ranges of the SFM with equal bandwidth but different absolute values.

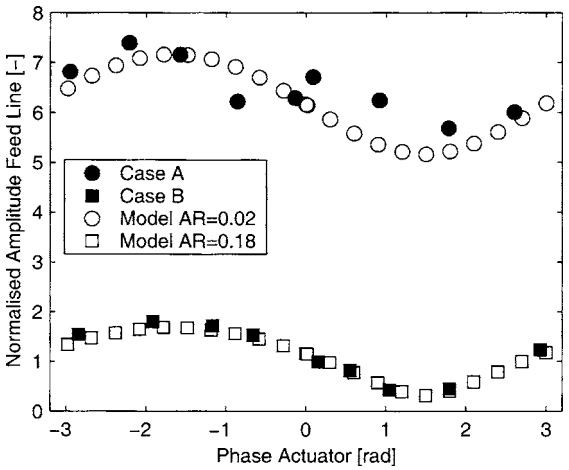

Fig. 10 Comparison of the experimental pressure amplitudes (filled symbols) to the calculated model results (open symbols)

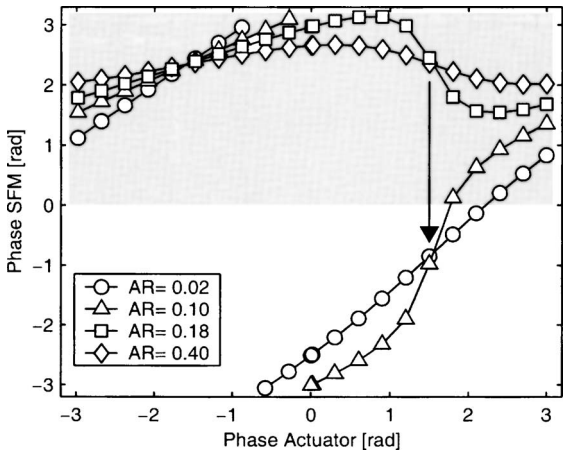

Fig. 11 Calculated phases of the secondary fuel modulation (SFM) at the injection position

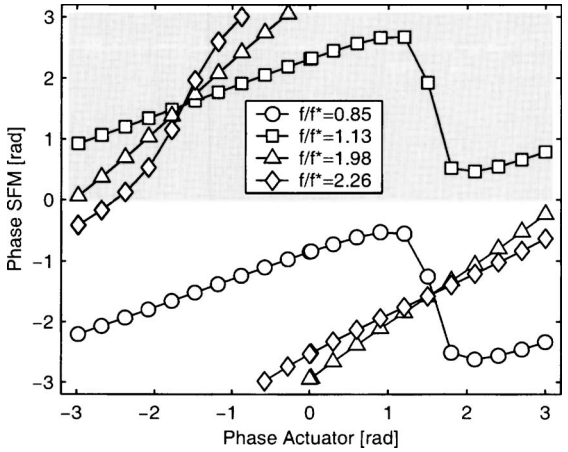

Fig. 13 Calculated phases of the SFM for different frequencies (normalized by the first resonance frequency) versus the corresponding phases of the actuator movement ($AR=0.18$)

Downloaded 02 Jun 2010 to 171.66.16.98. Redistribution subject to ASME license or copyright; see http://www.asme.org/terms/Terms_Use.cfm

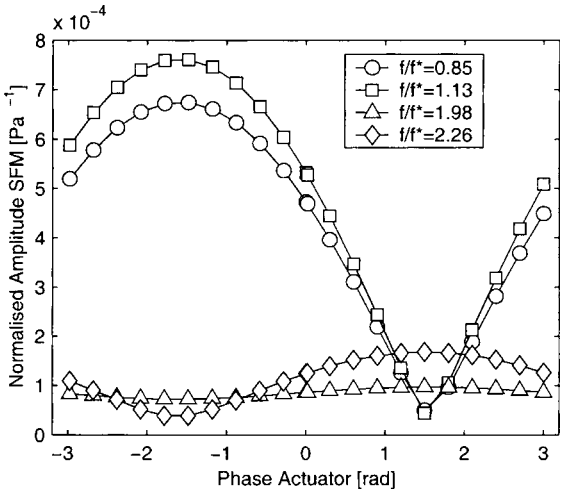

Fig. 14 Calculated amplitudes of the SFM for different frequencies (normalized by the first resonance frequency) versus the corresponding phase of the actuator movement (*AR* =0.18)

Near the first harmonic $f/f^*=2$ (triangles and diamonds) phase control is achieved by the actuator even for larger amplitude ratios (here $AR=0.18$) but with the drawback of low amplitudes of the SFM. Going to higher frequencies the amplitude response as a function of the actuator phase has been shifted by π comparing to the low-frequency results. Both, the decrease of amplitude and the phase shift characterize the fuel line as a second-order harmonic system.

Discussion of the Results

No general rules may be given for an effective AIC approach because several paths may lead to effective secondary fuel modulation. However, the following examples may serve to explain some of the necessary properties of such a system. Let us assume that we want to attenuate a combustor oscillation at a fixed frequency. According to the Rayleigh criterion and the specific time delay between secondary fuel injection and flame response, let this require the phase of the SFM to be within $\pi/2\pm\pi/2$. This phase area is shown in gray in Figs. 11 and 13.

In the current fuel-pipe system all amplitude ratios $AR\geqslant 0.18$ will fulfill this requirement at any phase of the actuator (Fig. 11) and even with very high amplitudes (Fig. 12) of the SFM, since the SFM phase is essentially constant. For all actuator-dominated amplitude ratios ($AR\rightarrow 0$), only a limited phase range of the actuator will provide the proper SFM phase for control and this only with low amplitudes. On the other hand, given the wrong phase window for attenuation because of, e.g., improper choice of the injection location, only the $AR\rightarrow 0$ mode may provide any control at all, if the resulting SFM amplitudes are sufficiently strong.

Let us now consider a simple phase-shift controller providing an actuator phase of $\pi/2$ and starting at $AR=0.40$. The modulated secondary fuel will damp the combustion instability, resulting in lower combustor amplitudes and therefore in a decrease of the amplitude ratio. When the amplitude ratio reaches the value $AR=0.10$, the achieved phase of the SFM will change by approximate π (shown by the arrow in Fig. 11) and, thus, enter the phase region in which the combustion instability is enhanced. Thus, the attenuation by a fixed phase-shift-controlled AIC is limited. A proportional controller in the same situation would keep the amplitude ratio and, thus, stay in the damping phase region, such that the achievable attenuation would not be limited by the feed-line dynamics.

With the feed-line dynamics considered, it turns out that some improvement of the phase-shift controller attenuation can be gained by proper phase adjustment. If in the current example the phase is set to $-\pi/2$, Fig. 11 shows that SFM phase does not change very much corresponding to the decrease of the combustion instability. Interestingly, now the effective modulation will decrease proportionally to the damping of the combustor oscillation ($AR\rightarrow 0$). So the simple phase-shift controller now will behave like a proportional controller with very high SFM amplitudes (Fig. 12).

As the highest SFM amplitude is expected at the resonance frequency of the feed line, it is common to adjust the feed system accordingly. But Fig. 13 illustrates that care must be taken, since the phase of secondary fuel modulation reacts very sensitively to small changes of frequency in the vicinity of the resonance frequency. Small frequency shifts are often observed by changing operation conditions, and in this example a small decrease of the frequency would put the AIC system out of the damping phase range (gray area).

Summary and Conclusions

In the current paper we have adressed the dynamics of the fuel line in AIC systems using secondary fuel injection.

An experimental procedure based on forced flame oscillations was used that allows one to study the basic mechanisms of secondary fuel injection in a very reproducible way. As no coupling between the forced oscillation and other natural instabilities was observed, it can be concluded that the procedure is adequate.

It was shown experimentally that the modulation achieved in the fuel line is a strong function of the relative phase and amplitude of the actuator and the combustor oscillation. A variation of this amplitude ratio shifts the phase in the injection fuel line.

A model of the secondary fuel line was formulated that compares well to the experimental data. With it, the realized modulation of the fuel mass flow at the injection location and the influence of the amplitude ratio on the effective control authority can both be calculated.

The demonstrated results lead to some important conclusions for the design of AIC systems with respect to the geometry of the injection system and the controller algorithm. The position of the secondary fuel injection is mainly governed by considerations concerning mixing and optimization of the time delay to achieve the best attenuation of the combustion instability. Thus, it is usually not possible to set the injection point close or into a pressure node in order to avoid a strong influence of the combustor oscillation on the SFM. Therefore, the feed-line dynamics must be considered for the active control strategy.

With an increasing amplitude ratio between the amplitude of the combustor oscillation and the actuator forcing the model predicts a decreasing phase range available. This explains why AIC actuators must follow the amplitude of the combustor oscillation closely in order to obtain optimum control. For similar strength of both excitations, the phase range is essentially zero and the effective phase of the modulation is given by the ratio of the excitation frequency and the resonance frequency of the pipe.

Acknowledgment

The work presented in this paper is supported within the program AG Turbo II, funded by the Bundesministerium für Wirtschaft und Technologie, Germany, and Alstom Power Generation, Switzerland, Förderkennzeichen 032706W/9.

References

[1] McManus, K. R., Poinsot, T., and Candel, S. M., 1993, "A Review of Active Control of Combustion Instabilities," Prog. Energy Combust. Sci., **19**, pp. 1–29.

[2] Yu, K. H., Wilson, K. J., and Schadow, K. C., 1998, "Liquid-Fueled Active Instability Suppression," *27th Symposium (International) on Combustion*, The Combustion Institute, Pittsburgh, PA.

[3] Hathout, J. P., Fleifil, M., Annaswamy, A. M., and Ghoniem, A. F., 2001, "Role of Actuation in Combustion Control," Combust. Sci. Technol., **167**, pp. 57–82.

Downloaded 02 Jun 2010 to 171.66.16.98. Redistribution subject to ASME license or copyright; see http://www.asme.org/terms/Terms_Use.cfm

[4] Sun, F., Cohen, J. M., and Anderson, T. J., 2002, "Liquid Fuel Modulation by Fluidic Valve for Active Combustion Control," ASME Paper No. GT2002-30607.
[5] Campos-Delgado, D. U., Zhou, K., Allgood, D., and Acharya, S., 2003, "Active Control of Combustion Instabilities Using Model-Based Controllers," Combust. Sci. Technol., **175**(1), pp. 27–53.
[6] Murugappan, S., Acharya, S., Allgood, D. C., Park, S., Annaswamy, A. M., and Ghoniem, A. F., 2003, "Optimal Control of a Swirl-Stabilized Spray Combustor Using System Identification Approach," Combust. Sci. Technol., **175**(1), pp. 55–81.
[7] Riley, A. J., Park, S., Dowling, A. P., Evesque, S., and Annaswamy, A. M., 2003, "Adaptive Closed-Loop Control on an Atmospheric Gaseous Lean-Premixed Combustor," ASME Paper No. GT2003-38418.
[8] Hathout, J. P., Fleifil, M., Annaswamy, A. M., and Ghomien, A. F., 2002, "Combustion Instability Active Control Using Periodic Fuel Injection," J. Propul. Power, **18**(2), pp. 390–399.
[9] Shcherbik, D., Lubarsky, E., Neumeier, Y., Zinn, B. T., McManus, K., Fric, T. F., and Srinivasan, S., 2003, "Supression of Instabilities in Gaseous Fuel High-Pressure Combustor Using Non-Coherent Oscillatory Fuel Injection," ASME Paper No. GT2003-38103.
[10] Lieuwen, T., and Zinn, B. T., 1998, "The Role of Equivalence Ratio Oscillations in Driving Combustion Instabilities in Low NO*x* Gas Turbines," *27th Symp. (Int.) on Combustion*, The Combustion Institute, Pittsburgh, PA.
[11] Lieuwen, T., Torres, H., Johnson, C., and Zinn, B. T., 1999, "A Mechanism of Combustion Instability in Lean Premixed Gas Turbine Combustors," ASME Paper No. 99-GT-003.
[12] Hobson, D. E., Fackrell, J. E., and Hewitt, G., 2000, "Combustion Instabilities in Industrial Gas Turbines: Measurements on Operating Plant and Thermoacoustic Modeling," ASME J. Eng. Gas Turbines Power, **122**(3), pp. 420–428.
[13] Fahy, F., 2001, *Foundations of Engineering Acoustics*, Academic Press, London.
[14] Munjal, M. L., 1987, *Acoustics of Ducts & Mufflers*, Wiley, New York.
[15] Lee, J. G., and Santavicca, D. A., 2003, "Experimental Diagnostics for the Study of Combustion Instabilities in Lean Premixed Combustors," J. Propul. Power, **19**(5), pp. 735–750.
[16] Richards, G., Straub, D., and Robey, E., 2001, "Dynamic Response of a Premix Fuel Injector," ASME Paper No. 2001-GT-0036.
[17] Richards, G., Straub, D., and Robey, E., 2003, "Control of Combustion Dynamics Using Fuel System Impedance," ASME Paper No. GT2003-3852.

Downloaded 02 Jun 2010 to 171.66.16.98. Redistribution subject to ASME license or copyright; see http://www.asme.org/terms/Terms_Use.cfm

Unsteady Flow Structures in Radial Swirler Fed Fuel Injectors

Kris Midgley
Adrian Spencer
James J. McGuirk

Department of Aeronautical and Automotive Engineering,
Loughborough University,
Loughborough,
Leiceestershire LE11 3TU, UK

Many fuel injector geometries proposed for lean-premixed combustion systems involve the use of radial swirlers. At the high swirl numbers needed for flame stabilization, several complex unsteady fluid mechanical phenomena such as vortex breakdown and recirculation zone precession are possible. If these unsteady aerodynamic features are strongly periodic, unwanted combustion induced oscillation may result. The present paper reports on an isothermal experimental study of a radial swirler fed fuel injector originally designed by Turbomeca, and examines the dynamical behavior of the unsteady aerodynamic flow structures observed. Particle Image Velocimetry (PIV) is used to capture the instantaneous appearance of vortex structures both internal to the fuel injector, and externally in the main flame-stabilizing recirculation zone. Multiple vortex structures are observed. Vector field analysis is used to identify specific flow structures and perform both standard and conditional time averaging to reveal the modal characteristics of the structures. This allows analysis of the origin of high turbulence regions in the flow and links between internal fuel injector vortex breakdown and external unsteady flow behavior. The data provide a challenging test case for Large Eddy Simulation methods being developed for combustion system simulation. [DOI: 10.1115/1.1925638]

Introduction

Fuel injector fluid mechanics has always played a major role in determining combustor performance, via control of fuel placement, fuel air mixing, primary zone aerodynamics, etc. Most fuel injectors contain components that introduce swirl into the flow, and there have been many studies into the influence of swirler design on combustor behavior. Merkle et al. [1], for example, have shown that the lean stability limits of a combustor depend strongly on the choice of swirler in the airblast atomiser used. However, it is not only the global, time-average performance that is of interest to combustor designers. Combustion dynamics is an increasingly important consideration, particularly driven by the interest in lean premixed systems. Swirl-induced central recirculation zones (CRZ) are a result of the vortex breakdown phenomenon known to occur when confined highly swirling flow encounters a region of adverse pressure gradient. This phenomenon has been studied for nearly 50 years (Brooke-Benjamin [2], Sarpkaya [3], Billant et al. [4]) but is still not fully understood. Recent measurements by Li and Gutmark [5] have shown how the dynamics of vortex breakdown cause interactions between vortical structures in the flow associated with breakdown and other (e.g., acoustical) instability modes. Their measurements show that the vortical structures are highly dependent on swirler geometry details and operating conditions and critically affect the thermoacoustic behavior of the system. The fuel injector studied by them represented a complex triple annular axial flow swirler and is typical of the complex designs being suggested for future lean primary zone fuel injectors. Similar observations on the sensitivity of combustion instability dynamics to fuel injector nozzle swirler details have been made by Broda et al. [6] and Cohen et al. [7]. Further features of swirling flows that can impact on combustor dynamics are vortex shedding from swirler vanes and the appearance of a processing vortex core (PVC), where the whole CRZ rotates around the combustor axis (Syred et al. [8] and Anacleto et al. [9]). The importance of these swirler-induced fuel injector phenomena in future combustor designs is likely to increase as more flow enters the combustor via the fuel injector, and more complex swirler designs are investigated (e.g., multiple axial or radial flow swirlers). The experimental study of swirling flow aerodynamics is therefore set to continue for some time, with an increased emphasis on the unsteady flow behavior.

Much previous work has also focused on the ability of CFD methods to predict swirl-induced phenomena, both steady (e.g., overall size and strength of the CRZ) and unsteady (e.g., onset of a PVC or higher frequency instability modes associated with small-scale swirler geometric features). Unsteady RANS-based CFD has been applied with some success to isothermal flow through a double radial-flow swirler by Noll et al. [10] and to combustor dynamics phenomena in lean premixed combustors by Canon et al. [11]. The latter authors, however, also examined the ability of the Large Eddy Simulation (LES) approach and concluded that only LES was capable of capturing the 3D time-dependent flow structures that have been observed experimentally. A similar LES-based approach has been adopted by Tang et al. [12] and Wang et al. [13]. These LES studies are highly promising, showing evidence of PVC capture, bimodal velocity pdf's, and detailed vortical flow structures that can all be related to vortex shedding and vortex breakdown processes. The simulations show how the time-dependent behavior depends strongly on the interaction and competition between various instability modes, and display the same sensitivity to swirler flow conditions that has been noted in experimental studies.

The above discussion has indicated the importance of improving our understanding of swirler-based fuel injector aerodynamics to allow more robust design of fuel injectors. It is clear that for fluid mechanical phenomena as complex as this, LES methods are likely to play a dominant role. Appropriate experimental data to validate such simulations is, however, rare, appropriate in this sense implies full knowledge of boundary conditions, and detailed characterisation of unsteady flow features as well as time-averaged flow. The purpose of the present work, therefore, is to report on an experimental study intended to serve as a benchmark test case for unsteady swirler dynamics relevant to fuel injectors. A radial swirler geometry from Turbomeca was chosen (Bissieres [14]) for the test case, since less work has been done on these systems, but their compact nature makes them interesting for lean premixed applications; Turbomeca's experience on such configu-

Contributed by the International Gas Turbine Institute (IGTI) of THE AMERICAN SOCIETY OF MECHANICAL ENGINEERS for publication in the ASME JOURNAL OF ENGINEERING FOR GAS TURBINES AND POWER. Paper presented at the International Gas Turbine and Aeroengine Congress and Exhibition, Vienna, Austria, June 13–17, 2004. Paper No. GT2004-53608. Manuscript received by IGTI, October 1, 2003; final revision, March 1, 2004. IGTI Review Chair: A. J. Strazisar.

Copyright © 2005 by ASME

Downloaded 02 Jun 2010 to 171.66.16.98. Redistribution subject to ASME license or copyright; see http://www.asme.org/terms/Terms_Use.cfm

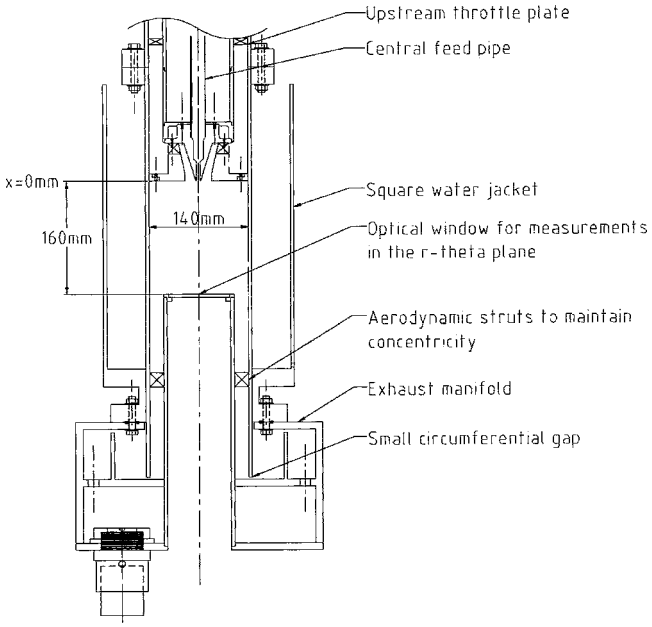

Fig. 1 Experimental rig

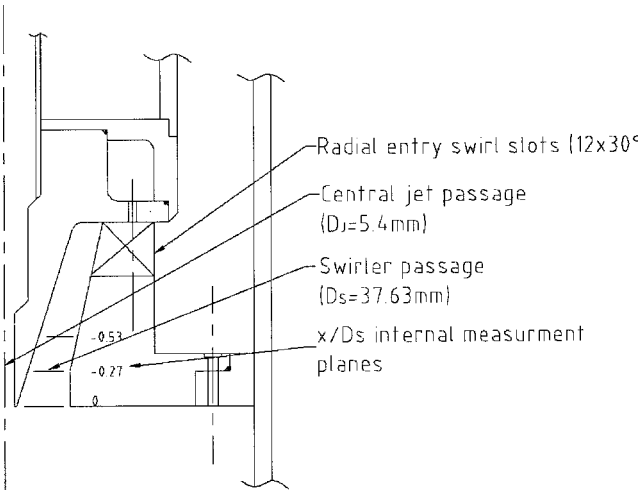

Fig. 2 Fuel injector geometry

rations confirms they are still of great current interest. The experiment has therefore been designed to create a simplified but generically representative flow-field typical of a radial swirler fed fuel injector in an aero gas turbine combustor. Particle Image Velocimetry (PIV) has been used to obtain 2D spatially resolved images of flow structures and their unsteady dynamics. An isothermal, water-based experiment was selected to ease seeding problems and reduce the magnitude of dynamically important frequencies, and to allow emphasis on the unsteady aerodynamics in the immediate vicinity of the fuel injector exit plane. The experimental set-up and instrumentation used are detailed in the following sections. Careful checks on statistical and spatial resolution accuracy were performed, particularly for turbulence statistics. Initial results of the study have been presented by Midgley et al. [15]; the present paper contains further analysis of the instantaneous and time-resolved information using time-series, spectra, pdf's, and in particular conditional averaging to understand the impact of vortical structures produced internal to the fuel injector on the turbulence field in the combustor main zone.

Experimental Facility

The experimental rig is shown in Fig. 1. The water flow through the rig came from a single constant head supply to feed two vertically oriented, concentric tubes. The fuel injector was mounted so that the inner tube fed a central jet (simulating a fuel stream) and the outer tube fed a single radial swirler (12 angled 30 deg slots). Both swirl and jet streams discharged into a larger diameter cylindrical duct ($D=140$ mm). The diameter of the duct relative to the fuel injector exit was chosen to be typical of the level of confinement found in aero-engine combustors. A valve in the return circuit from test section exit to a sump tank controlled the total flow rate. An upstream throttle plate controlled the flow split between swirl and jet streams. The flow rate was set to ensure the Reynolds number was sufficiently high to guarantee fully turbulent flow. A central axisymmetric blockage was introduced downstream to avoid problems with an overly elongated central recirculation zone, and provide a controlled exit boundary condition from the test section. The test section was surrounded by a square section water jacket to minimise refraction and distortion of the laser light sheet by curved surfaces. A calibration plate containing an accurately ruled Cartesian grid inserted inside the test section showed the distortion to be negligible except within 1 mm of the concave surface of the inner cylinder wall. The rig was illuminated from the side with a laser light sheet to allow measurements in the axial-radial ($x-r$) plane. In addition, a window was created in the downstream blockage to allow the camera to view an $r-\theta$ plane oriented light sheet. The distance of the downstream blockage from the fuel injector exit was varied in preliminary tests. The final position, chosen to provide sufficient blockage without changing the flow in the immediate vicinity of the fuel injector, was 160 mm. The fuel injector studied is shown in Fig. 2. The radially fed swirler produced an annular swirl stream (outer diameter $D_s=37.63$ mm) at the fuel injector exit. The inner diameter of the annulus was formed by the outer wall of a central jet nozzle (inner diameter $D_j=5.4$ mm). The test conditions corresponded to swirler and jet exit Reynolds numbers of 8×10^4 and 2.63×10^4, respectively. Re is here defined using D_s and D_j and the bulk mean velocities based on geometrical exit areas: $V_{x,j}=4.88$ m/s, $V_{x,s}=2.13$ m/s. Note, however, that the discharge coefficient of the swirl passage was measured to be 0.5, so the peak velocity in the swirl stream was about $1.5V_{x,s}$.

Instrumentation

The PIV instrument comprised a LaVision system with a twin Nd:YAG laser generating a 1 mm thick light sheet via spherical and cylindrical lenses, and a Kodak Megaplus ES 1.0 camera with 1008×976 pixel resolution, running at 15 Hz. Laser/camera synchronisation, image acquisition, and data processing using the cross-correlation technique were controlled by Davis software running on a dual processor Pentium III PC. 20 μm polyamide particles (almost neutrally buoyant in water) were used as light scattering particles. The PIV instrumentation parameter set-up was selected following the recommendations of Keane and Adrian [16]. The interframe time (particle shift) was set so that the in-plane displacement was less than $\frac{1}{4}$ of the PIV interrogation cell used for cross-correlation and, where possible, led to out-of-plane motion less than $\delta z/4$, where δz is the camera depth of field. The optimum particle image diameter is generally accepted to be around 2 pixels. For 20 μm particles this was achieved in the present experiment with a field of view (FoV) less than 80 $\times80$ mm^2. In most data collected there were at least 10 particle pairs per interrogation window. The interrogation cell used a deformed multi-pass grid (LaVision [17]) of initial size 64 $\times64$ pixels, reducing to a final size of 32×32 pixels (with 50% overlap). The inter-frame delay time was around 500 μs for the large FoV images, and 20–50 μs for the smallest FoV. This choice minimized out-of-plane data loss and maximized the in-plane displacement, which was typically from 3 to 8 pixels. To

Downloaded 02 Jun 2010 to 171.66.16.98. Redistribution subject to ASME license or copyright; see http://www.asme.org/terms/Terms_Use.cfm

provide a separate crosscheck on the PIV data collected, an LDA system was also used. This comprised a 20 mW He–Ne laser with Dantec optics, frequency shifting and photomultiplier, and a TSI IFA550 processor. Data were taken at a fixed sampling rate of 1 kHz and blocks of data of up to 25,000 points were used to allow time-histories, auto-correlations and spectra to be evaluated.

Data Validation

The axial-radial $(x-r)$ plane of the test section was initially captured using a large FoV of 160×160 mm^2. This allowed illumination of the entire flow field between fuel injector and downstream blockage in a single view, but resulted in an interrogation cell size of 5×5 mm^2. In a strongly swirling flow a large range of both positive and negative velocities exists, and out-of-plane velocities can be larger than in-plane velocities. It is clear that the optimization of PIV system parameters, as described above and required for accurate flow data, can only be achieved by allowing the FoV to be dependent on the local flow conditions. More details of this are given in Midgley et al. [15], but the end result is as follows:

(1) The large FoV (160×160 mm^2), which captures the whole flow domain did not allow confidence in the accuracy of the data gathered, particularly for turbulence statistics, although it was useful as a preliminary route to identifying flow structures;
(2) The use of a medium size FoV of (80×80 mm^2) was sufficient in the downstream region of the flow domain ($x/D_s>2$);
(3) In the region near the fuel injector, the medium FoV lead to instantaneous velocity gradients across the PIV interrogation cell in jet and shear layer regions which, for the interframe Δt used, produced variations in particle displacement across the cell of greater than 2 particle image diameters. In these regions it was therefore necessary to use a small FoV of 20×20 mm^2 (providing an interrogation cell size of 0.63×0.63 mm^2) in order to meet the PIV system parameter optimisation requirements.

In the results presented below therefore, when complete maps of the flow field are shown (or profiles across the whole flow field), it should be emphasized that these are composite images, patched together using appropriate size FoV information in various flow regions.

It is also well known that the turbulence energy measured using the PIV technique can be in error (underestimated) if the size of the interrogation cell is not small compared to the local integral length scale. Host-Madsen and Nielson [18] have analyzed this problem. It is related to loss of turbulence information due to the filtering applied to the set of particle pairs contained within a PIV interrogation cell. If most of the turbulence energy of the fluctuating motions is to be captured, Host-Madsen and Nielson [18] recommended that the interrogation cell should be no larger than about 1/5 of the local integral scale. Since the integral scale is unknown when the measurements are performed, and in any case varies across the flow field, the best data validation that can be done is either to take measurements of the same flow region with various FoVs (reducing in size), or to compare the turbulence data obtained from the PIV instrument with LDA measurements, which do not suffer from this problem. Both techniques have been adopted in the present work.

The local turbulence integral length scales have been estimated from the PIV data using the technique developed by Spencer and Hollis, and described in [19]. Essentially this involves calculation of the length scales from the spatial correlation function evaluated at each point within the PIV measurement plane:

$$\bar{R}_{ij}(\underline{x},\underline{r}) = \frac{\overline{u_i(\underline{x})u_j(\underline{x}+\underline{r})}}{\sqrt{\overline{u_i(\underline{x})^2}}\sqrt{\overline{u_j(\underline{x}+\underline{r})^2}}}$$

where $\underline{x}$ is any measurement point and $\underline{r}$ is the separation vector from that point. The integral length scale in the direction k is then calculated from the area under the correlation function as $\underline{r}$ increases in the k direction (in practice the region to the first zero crossing has been used to evaluate the area):

$$L^k_{ij}(\underline{x}) = \int_0^\infty \overline{R_{ij}}(\underline{x},\underline{r})d\underline{r}^k$$

For the present data, the two length scales that have been calculated are the longitudinal integral scale L^x_{xx} and the transverse length scale L^r_{rr}. Care is required close to the edges of the measurement region where no zero crossing of the spatial correlation function may be observed in the direction perpendicular to the edge. The practice adopted here was to assume a symmetric correlation function. When the length scales were evaluated from the PIV data in this way, it was observed that, as long as the appropriate choice of FoV for each flow region was made as described above, the indicated level of turbulence energy captured in the present data was greater than 95% of the expected true value implied by the Host-Madsen [18] correction formula.

Finally, to obtain converged, stationary time-averages, a large enough number of statistically independent samples must be gathered. The maximum number of instantaneous velocity vector images that could be stored in the PC memory was 650. The statistical convergence of the present data has therefore been examined. It is shown in Midgley et al. [15] that the convergence of time-averaged first and second moments for sample sizes from as few as 5 up to 650 frames agreed well with standard error estimates. A 650 frame average met the 99% confidence level for the percentage error in the mean velocity ($\varepsilon_{\bar{v}}/V_{x,s}$) to be less than 1% in most regions of the flow field, but as high as 10% in the jet shear layer where high local turbulence intensities were observed. The percentage error in the rms was around 7%. Further, Midgley et al. [15] compared selected turbulence intensity profiles taken using both PIV and LDA techniques and show that they are in very good agreement, even in the high shear near fuel injector exit region.

Results

Time-Averaged Measurements. Figure 3 shows a composite picture of time-averaged velocity vectors superimposed on a contour map of axial velocity for the whole cylindrical combustor volume. Note that in this and all subsequent figures, nondimensionalizing scales for velocities and lengths are the bulk average axial velocity at swirler exit $V_{x,s}$ and the swirler passage outer diameter D_s. The swirl number S evaluated from the axial and tangential profiles measured at swirler exit was 0.74. At this level of S the overall flow pattern is as expected. An aerodynamic "cone-angle" of around 60 deg is observed, which isolates a corner recirculation region when the annular swirling jet impinges on the cylindrical duct wall at around $x/D_s=1.2$. The central jet penetrates to around $x/D_s=0.75$ where a free stagnation point is found. The downstream flow field consist of a very slow moving recirculation zone whose "eye" is at around $x/D_s=2.0$, $r/D_s=1.4$. The reattaching annular shear layer forms a strong wall jet after impact, which then exits the duct through the annular gap around the downstream blockage. Close examination of the velocity vectors at swirl passage exit indicates a recirculation has formed near the inner wall of the annular passage, and the flow is actually directed into the fuel injector. This is more clearly illustrated in the 5 selected radial velocity profiles of the axial velocity shown in Fig. 4. The backflow into the swirler passage is now clearly seen, with the negative velocity region growing downstream and moving radially outward. At around $x/D_s=0.75$ this merges with the slow backflow zone in the central duct region.

Downloaded 02 Jun 2010 to 171.66.16.98. Redistribution subject to ASME license or copyright; see http://www.asme.org/terms/Terms_Use.cfm

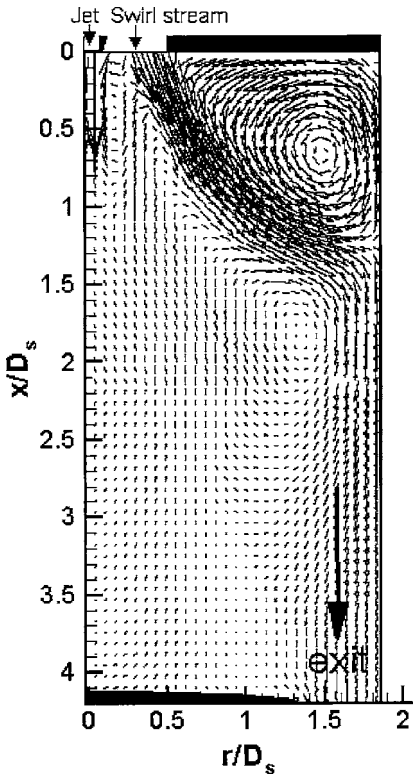

Fig. 3 Overall flow structure

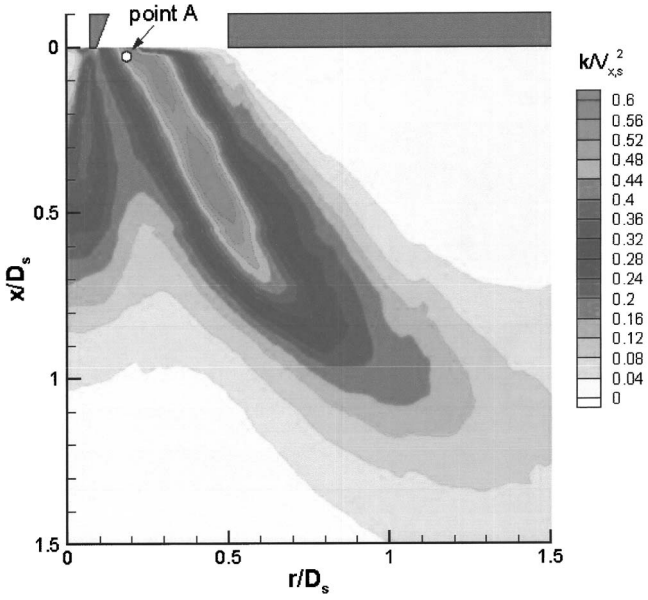

Fig. 5 Turbulence energy contours

The erosion of the high gradient shear layers by turbulence, for both central jet and swirler flow, is also visible, both disappearing at about $x/D_s=1.0$.

A close-up view of the fuel injector near-field nondimensional turbulence energy is given in Fig. 5. Note that to obtain the axial and radial normal stresses, the $x-r$ plane PIV data have been used, with the tangential normal stress interpolated onto the $x-r$ data from the r-θ plane PIV data. The high-shear regions identified in the time-mean velocity field are represented here by regions of high k. It is notable, however, that even though the shear is significantly stronger in the edge of the central jet than in either edge of the emerging annular swirler flow (see Fig. 4), the k level in the inner edge of the swirler flow is 100% higher. This is unexpected and cannot be related to direct turbulence production; it is the first indication of significant, localised turbulence events occurring in the inner swirl flow shear layer. Individual components of the turbulence energy are given in Figs. 6–8 (axial, radial, and tangential rms levels) at five stations. At fuel injector exit two peaks are present in the axial fluctuations, but only one dominant peak is visible in the radial and circumferential components. This highly anisotropic turbulent state persist down to $x/D_s=1.0$, but further downstream the turbulent normal stresses are approximately isotropic. Two further features of the turbulence may be pointed out. The tangential rms shows evidence of a maximum on the centreline at all stations downstream of $x/D_s=0.27$. This is usually associated with the presence of a PVC, so that the turbulence level measured from long time-averaged PIV data contains a contribution from the coherent periodic motion of the precession, enhancing the turbulence level implied by the time-average data. The strength of this feature has been noted by Midgley et al. [15] to be closely connected with the central jet. When this is present (as in the current data), the PVC is rather weak; without a central jet, the precession is much stronger (see [15]); the central jet has the effect of stabilising the flow, although not entirely as can be seen in Fig. 8. Secondly, a second region of strong turbulence

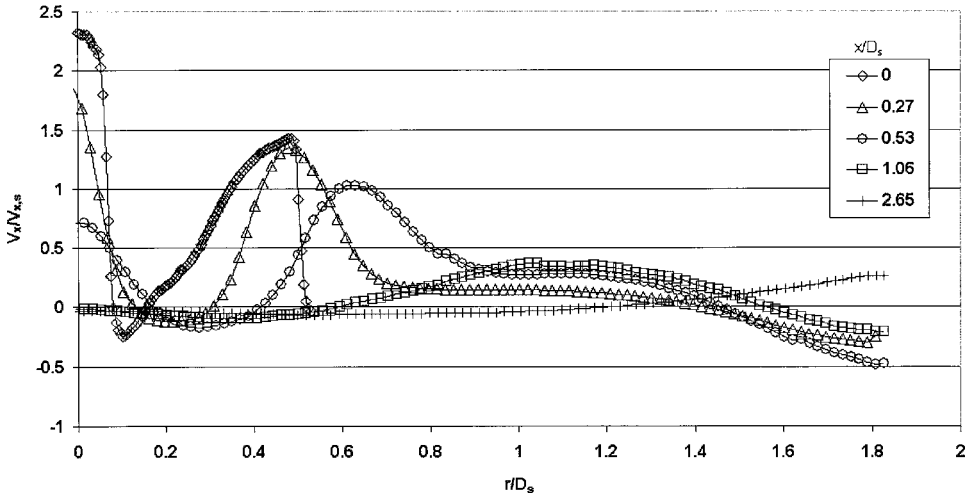

Fig. 4 Axial mean velocity profiles

Downloaded 02 Jun 2010 to 171.66.16.98. Redistribution subject to ASME license or copyright; see http://www.asme.org/terms/Terms_Use.cfm

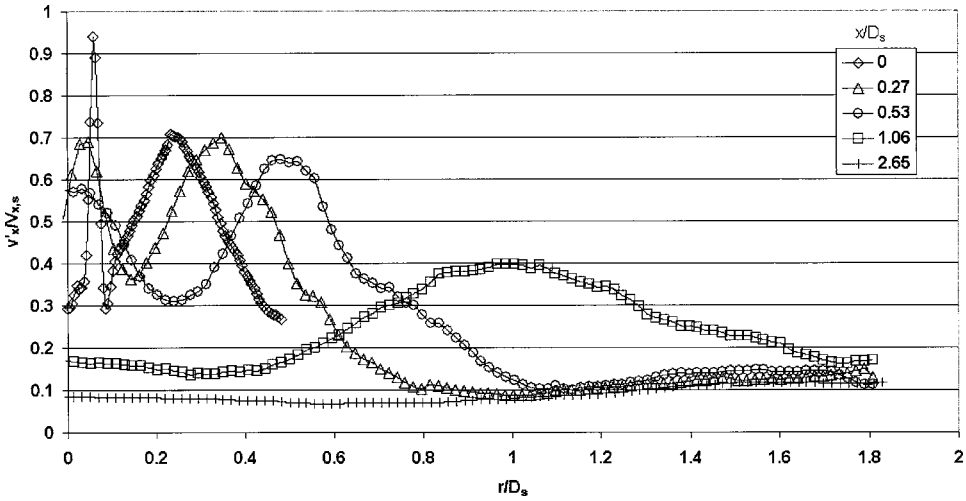

Fig. 6 Axial rms profiles

anisotropy is observed in the outflowing annular wall jet, where the radial rms decreases more rapidly as the wall is approached. To complete the time-averaged data in the combustor duct, the turbulence length scales that have been evaluated using the methodology described are presented in Figs. 9 (longitudinal) and 10 (transverse). Once again, although localized regions show length

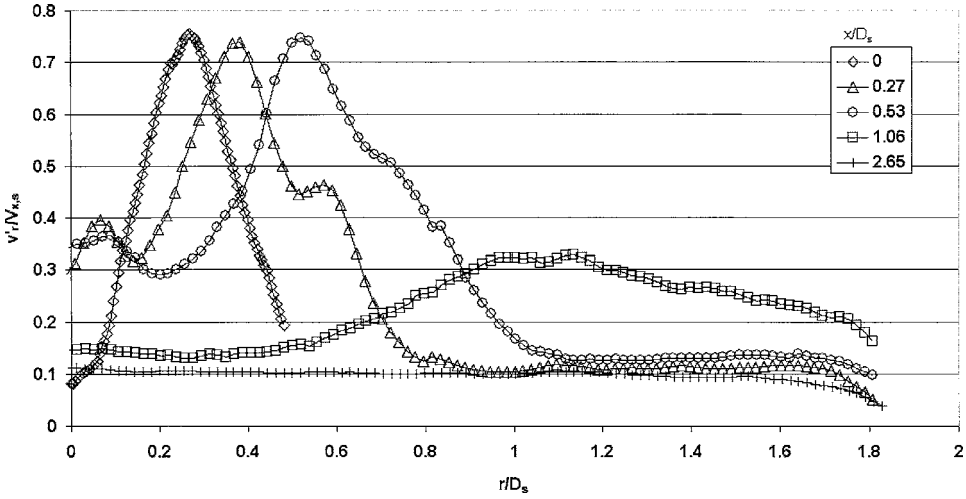

Fig. 7 Radial rms profiles

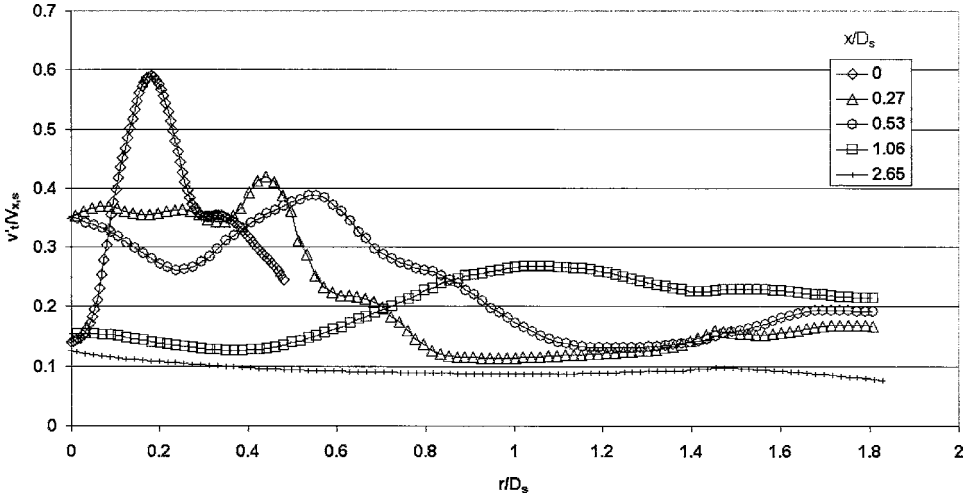

Fig. 8 Tangential rms profiles

Downloaded 02 Jun 2010 to 171.66.16.98. Redistribution subject to ASME license or copyright; see http://www.asme.org/terms/Terms_Use.cfm

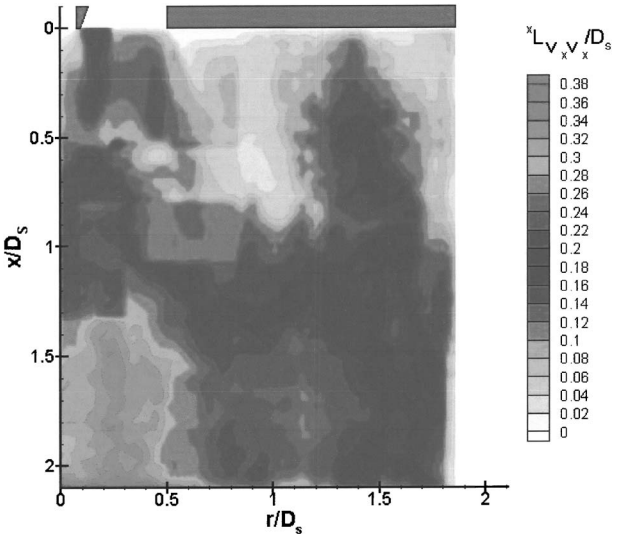

Fig. 9 Longitudinal length scale

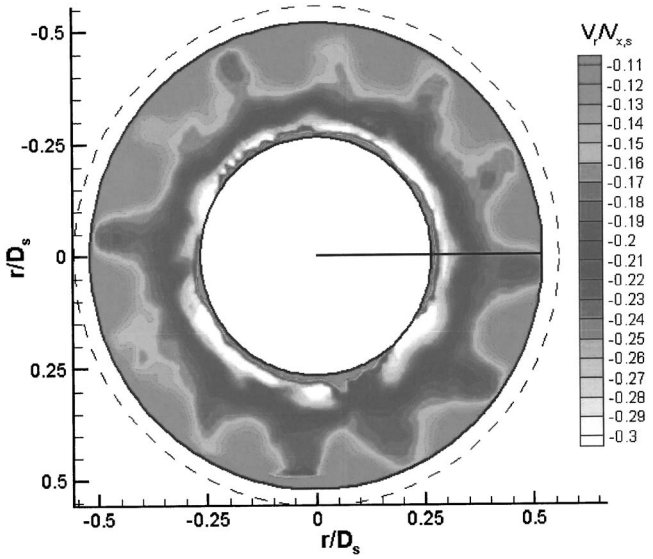

Fig. 11 Radial velocity field at $x/D_s=-0.53$

scales approximately the same in both x and r directions, these are relatively rare. In the vicinity of the free stagnation point ($x/D_s=1.75$) both length scales show very rapid growth as the turbulence structures adjust to the large-scale recirculation zone from the upstream smaller shear layer widths. The large differences in length scale imply this flow will be very difficult to predict for all RANS-based CFD models that rely on a single length scale.

Measurements in the $r-\theta$ plane were also possible inside the fuel injector, in particular in the swirl passage. This is fed from 12 tangential slots in the radial swirler (see Fig. 2), and evidence of these can be seen in the radial velocity field measured at $x/D_s=-0.53$, Fig. 11 (note that glare from the outer wall prevented measurements being taken near that region). Twelve zones of inflowing fluid can be seen; the high radial inflow velocities near the inner circle are merely connected to the shape of the centrebody. This strong 3D effect has disappeared by $x/D_s=-0.27$ where, quite surprisingly, the radial velocities are now all positive (Fig. 12). This picture of radially outward moving fluid near the centrebody persists all the way to swirler exit. The likely conclusion is that this is evidence of a separation process taking place somewhere between the two planes shown. It implies that the axial backflow velocities identified above at fuel injector exit (Figs. 3 and 4) penetrate further upstream than $x/D_s=-0.27$. Further discussion on the flow events taking place inside the fuel injector is deferred until after consideration of unsteady measurements.

Unsteady Measurements. Time-averaged data are informative, but do not reveal the full flow characteristics. To this end, the instantaneous data provided by PIV have been analysed. For example, we may examine the location of the instantaneous "free" stagnation point represented by the furthest penetration of the central jet into the combustor duct; or we may identify the instantaneous reattachment point of the swirl shear layer on the outer duct wall. Although the time resolution of the PIV instrument (15 Hz) is insufficient to capture a true time history (even with the low frequency nature of a water flow experiment), the 650 frame data set can be processed to give a probability density function (pdf) of these locations. These are illustrated in Figs. 13 and 14. The mean central jet penetration was noted in Fig. 3 to be about $x/D_s=0.75$. This is borne out by the pdf shown, but this also indicates

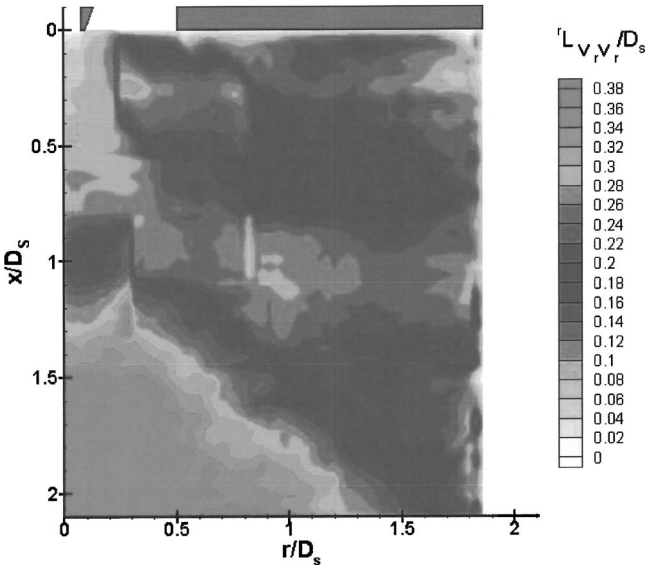

Fig. 10 Transverse length scale

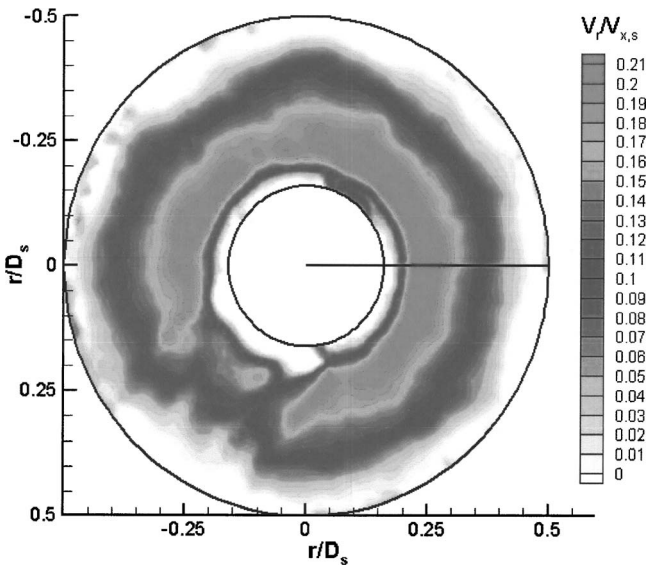

Fig. 12 Radial velocity field at $x/D_s=-0.27$

Downloaded 02 Jun 2010 to 171.66.16.98. Redistribution subject to ASME license or copyright; see http://www.asme.org/terms/Terms_Use.cfm

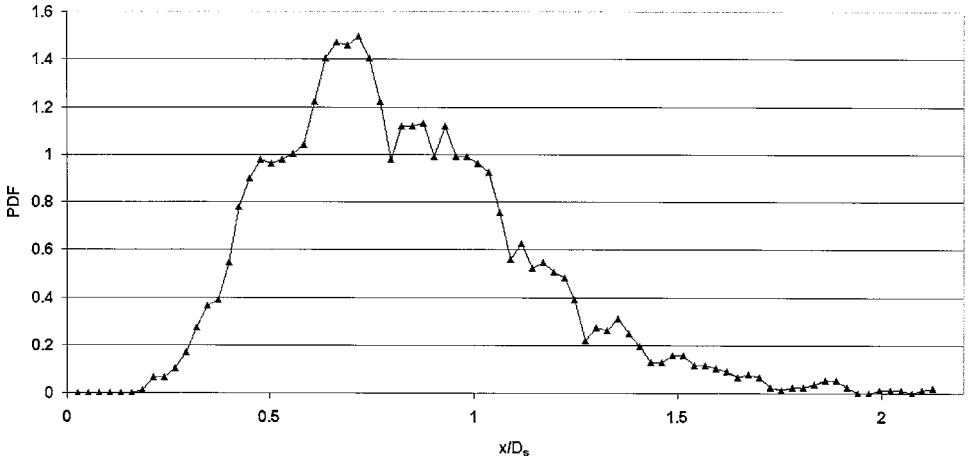

Fig. 13 Pdf of central, jet penetration distance

that the variation of the free stagnation point position is large, ranging from $x/D_s=0.2$ to 1.5, with a very long "tail" on the high penetration side. A similar observation may be made for the wall reattachment point (Fig. 14); this occurs at around $x/D_s=1.2$ most of the time but wanders around by $\pm 0.3D_s$ or $\pm 25\%$. These figures indicate the strength of the large scale motions in controlling these global flow features. This data is ideal for validation of LES predictions of this flow, since only a time-dependent method like LES can predict the behavior observed in Figs. 13 and 14 (URANS CFD might, but it is thought unlikely given the single length scale argument mentioned above).

A further unsteady feature of the flow is presented in Fig. 15. This shows an instantaneous velocity vector image of the swirler shear layer in the $x-r$ plane. Vortex structures are clearly visible in the inner shear layer edge. A video made from the whole 650 image data set indicates that these vortex structures propagate in time, and provides the first clue as to the origin of the high turbulence levels in this shear layer noted in the time-averaged data. To explore the origin of these vortex structures further, instantaneous vector maps in the $r-\theta$ plane were examined. Figure 16 shows one such map at $x/D_s=0.0$. It is clear that streamwise vortices are being formed inside the fuel injector in the annular swirl passage near the centrebody wall. These are obviously related to the separation event noted above in Figs. 11 and 12. In Fig. 16 two vortices are observed. Adrian et al. [20] have discussed various data processing techniques for identifying vortex structures. One alternative to examining the instantaneous data (Fig. 16) is to adopt a Reynolds decomposition and subtract the time-averaged velocity field in the same plane. This is shown in Fig. 17. Now it is possible to identify 4 vortices, 2 strong and 2 weak. The origin of these vortex structures is likely to be a vortex breakdown event inside the fuel injector. As the swirling flow encounters the adverse pressure gradient associated with the area variation of the swirl passage (see the corner in Fig. 2), vortex breakdown can occur as noted by Sarpkaya [3]. It is also clear that, since at most 4 vortices are present, the breakdown is not associated with the number of wakes (12) emerging from the radial swirler slots. The pictures in Figs. 16 and 17 are of course single time snapshots. The vortex pattern rotates with the swirling flow. The frequency of this rotation cannot easily be captured from the PIV data because of the poor time resolution. LDA data (sampling rate 1 kHz) were taken in the same flow (at position A marked in Fig. 5) and the power spectral density (PSD) deduced from this data is given in Fig. 18. This shows that strong periodic events are occurring at frequencies well within the energy containing range of the turbulence (i.e., no spectral gap exists). The strongest peak is at 75 Hz (St=1.32), with a second, weaker, peak at 154 Hz (St=2.71). These motions are extremely energetic and will obviously contribute significantly to the long time-averaged turbulence in this region. The periodic contributions arise from the rotating vortex pattern emerging from the fuel injector, which follow a helical pattern after entering the combustor zone. These same vortices are observed in the inner swirl shear layer edge every time the helical path crosses the $x-r$ plane. Midgley et al. [15] have analyzed the frequency content of these measurements and concluded that the

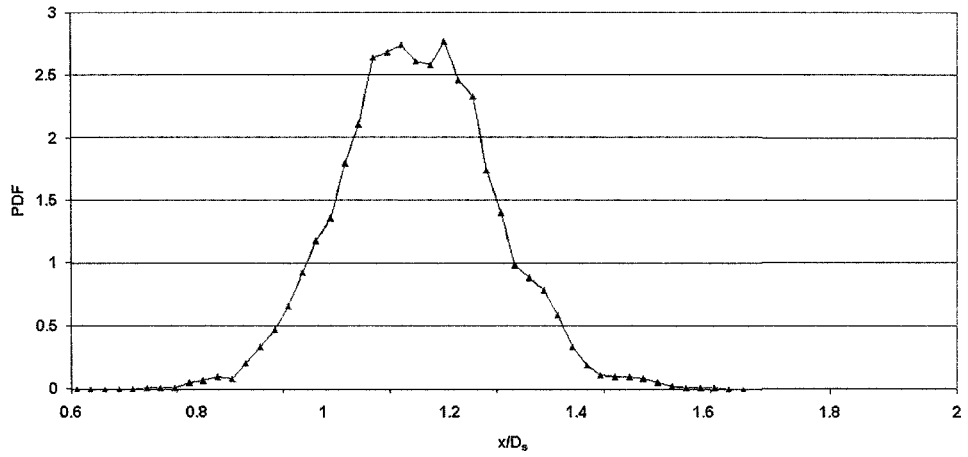

Fig. 14 Pdf of wall reattachment point

Downloaded 02 Jun 2010 to 171.66.16.98. Redistribution subject to ASME license or copyright; see http://www.asme.org/terms/Terms_Use.cfm

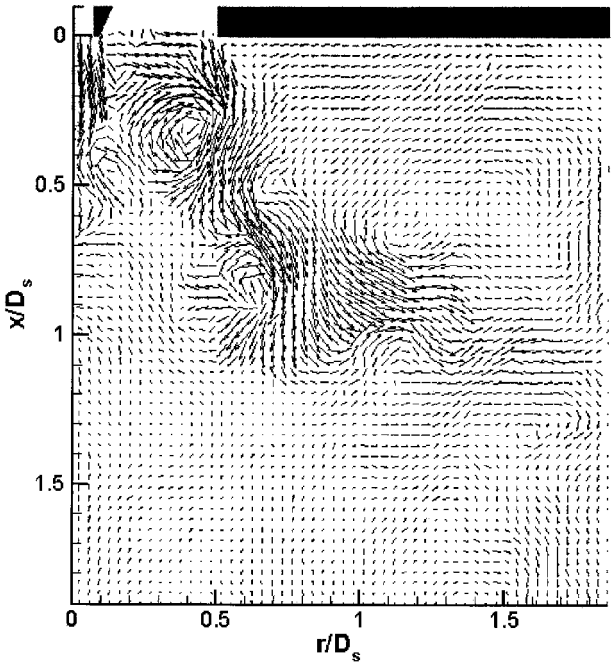

Fig. 15 Instantaneous vector map in the $x-r$ plane

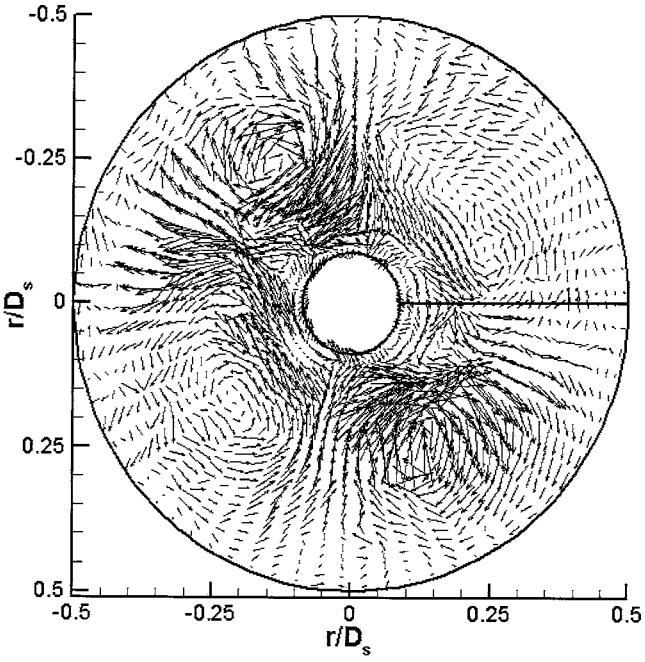

Fig. 17 Reynolds decomposition vector map at $x/D_s=0.0$

75 Hz frequency is caused by the strongly coherent two vortex pattern rotating past a fixed point, whilst the higher frequency is caused by the less coherent 4 vortex pattern. This data again form an excellent test case for LES methods. It is also interesting to point out that this process could also cause a combustion induced oscillation scenario, since the mixing rate of central jet fluid (i.e., fuel) and swirling jet fluid (i.e., air) will be strongly periodic due to these vortices.

Conditionally Averaged Measurements. The point has been made above that the rotating vortex structure will contribute to the turbulence energy measured on a long time-averaged basis. It is of interest to quantify this contribution, since in some respects this allows a decomposition of the time-averaged data into "true" turbulence and "apparent" or "pseudo" turbulence due to the large scale rotation. To perform this decomposition it is first necessary to identify a frame of reference that rotates with the vortex pattern, and then conditionally average the instantaneous data relative to this frame. A similar procedure was followed by Graftieaux et al. [21] in order to extract the contribution of a PVC to the measured time-averaged turbulence in a rotating cylinder flow. The vortex cente′rs present in any instantaneous flow image must first be identified. As noted above, Adrian [20] has compared several methods to achieve this. This cannot unambiguously be achieved by merely calculating the instantaneous vorticity in the flow, since vorticity distributions are notoriously "noisy" and also identify regions of shear as well as discrete vortex structures. Reynolds decomposition, as shown above, is helpful in extracting vortex structures, since, in many flows, the vortex centers are moving approximately with the local mean velocity. Once Reynolds decomposition has been applied to each PIV frame, the swirl strength parameter identified by Zhou et al. [22] is used to locate the precise center of each vortex. This method identified in each frame two nearly equally strong vortex centers. To provide a unique definition of the frame of reference, the following procedure was adopted. The angular location on the first frame of one vortex was selected (say vortex A); vortex B had a location approximately 180 deg out of phase (±5 deg standard deviation). In subsequent frames vortex A was identified by assuming initially a frequency of rotation of half the frequency of the first peak in the PSD shown in Fig. 18. Once both vortex A and B were identified, the average rotation angle (relative to the first frame) was calculated. With this data, all 650 frames could be conditioned by rotating with the appropriate angle, and then time-averaged to form the conditional average. Figure 19 shows the conditional average of the Reynolds decomposed velocity field, together with superimposed contours of the swirl strength parameter. It is clear from this figure that the 2 strong/2 weak vortex picture described above is correct. The 2 weak vortices may be formed merely as a consequence of the 2 strong vortices and the need to preserve continuity in the $r-\theta$ plane. Figure 20 shows the conditionally averaged radial turbulence rms. This illustrates graphically that only two regions of high turbulence are present at swirl passage exit. The intensity in these regions (approx 0.67) is nearly three times

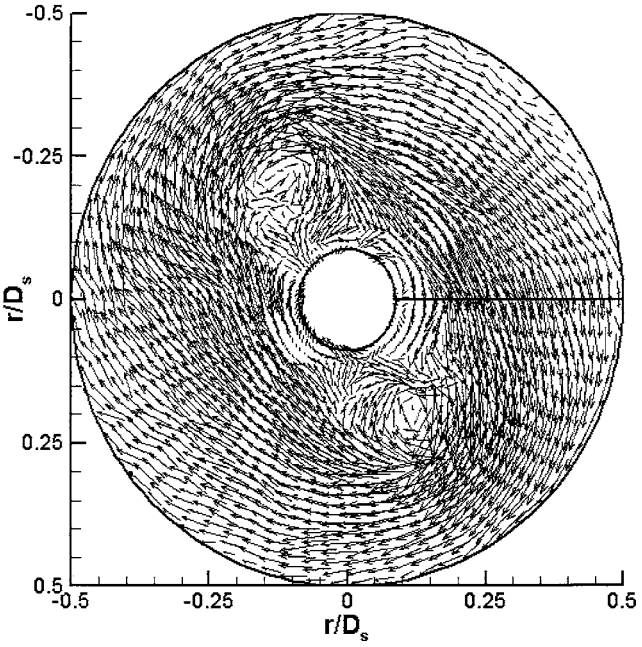

Fig. 16 Instantaneous vector map at $x/D_s=0.0$

Downloaded 02 Jun 2010 to 171.66.16.98. Redistribution subject to ASME license or copyright; see http://www.asme.org/terms/Terms_Use.cfm

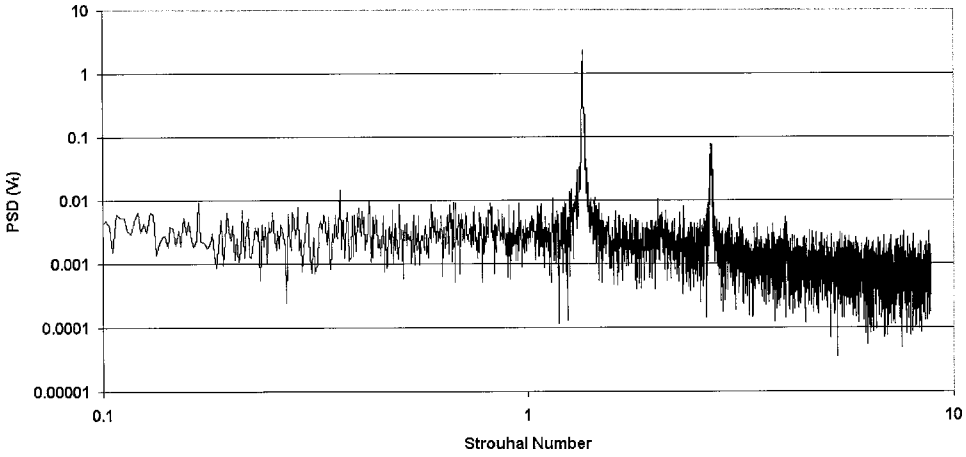

Fig. 18 PSD of tangential velocity at point A

that of the background turbulence outside the two vortices (approx 0.24). Hence, the picture provided by the long-time-averaged data (Fig. 21) of a ring of high turbulence at fuel injector exit is quite misleading. Once again the point is made that for this flow type, RANS methods are unlikely to prove sufficient, LES methods are needed and the present data form an excellent benchmark data set for validating LES methods for fuel injector flows. As a final comment, perhaps a better method of performing this analysis would be the proper orthogonal decomposition (POD) technique described by Adrian [20]; this method is being applied to the present data and will be the subject of a future paper.

Conclusions

The work presented here was aimed at conducting a benchmark experiment for fuel injectors containing radially fed swirlers. The test data presented have covered both time-averaged information, suitable for RANS CFD model validation, but, more importantly, have also quantified the unsteady characteristics of the flow. Evidence of unsteadiness in the global flow field was documented in the form of pdfs of important locations such as maximum jet penetration distance and reattaching shear layer position. Evidence of high turbulent mixing was revealed in the swirling shear layer, and this lead to the identification of energetic discrete vortex structures. The origin of these was traced back to a suggested vortex breakdown and separation process inside the fuel injector. This caused a twin vortex pattern to form and emerge from the fuel injector in a helical path as it passed down the combustor. The current investigation has concentrated on isothermal flow only; however, a study undertaken as part of the same project by Janus et al. [23] has shown very similar behavior of both time-averaged and unsteady flow. The data presented here is detailed, of high quality, representative of radial fed swirler flows, and is put forward as a test case for LES prediction methods under development for combustor applications.

Acknowledgment

The work reported here was carried out in the Loughborough UTC in Combustion Aerodynamics with funding provided by EU project "MOLECULES" (G4RD-CT-2000-00402).

Nomenclature

D = cylindrical combustor duct diameter
D_j = central jet diameter
D_s = annular swirler passage diameter
f = frequency of periodic motion peaks in PSD data
k = turbulence kinetic energy, or direction k

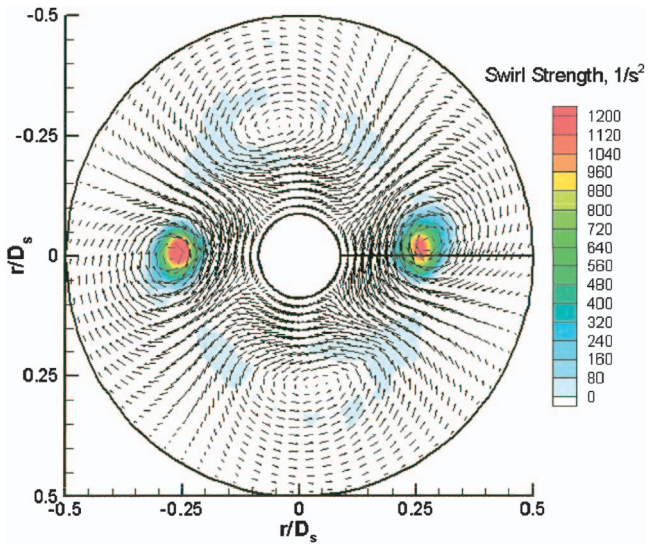

Fig. 19 Conditionally averaged velocity field at $x/D_s=0.0$

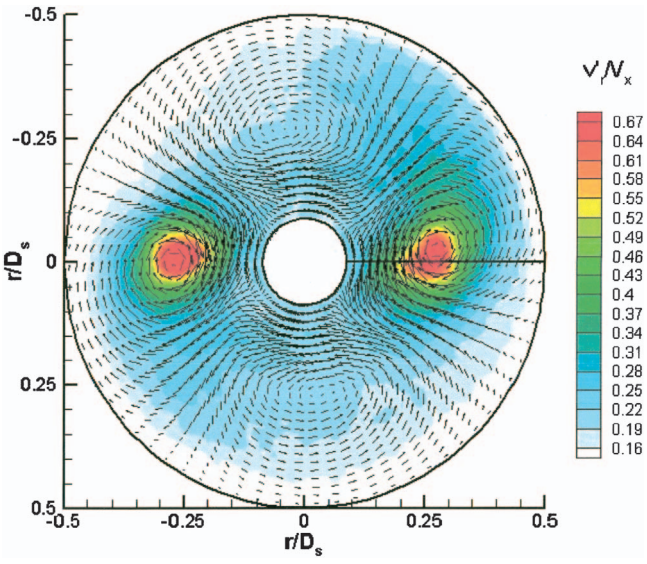

Fig. 20 Conditionally averaged radial rms at $x/D_s=0.0$

Downloaded 02 Jun 2010 to 171.66.16.98. Redistribution subject to ASME license or copyright; see http://www.asme.org/terms/Terms_Use.cfm

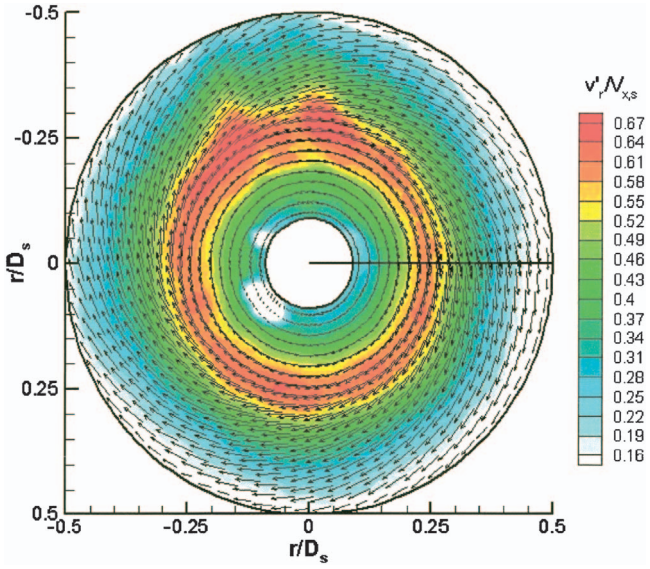

Fig. 21 Long time-averaged radial rms at $x/D_s=0.0$

L_{ij}^{k} = integral length scale
$\underline{r}$ = separation vector
$\overline{R_{ij}}$ = spatial correlation function
St = dimensionless Strouhal number ($fD_s/V_{x,s}$)
u_i, u_j = velocity fluctuations in i, j directions
V_x, V_r, V_t = mean velocities in x, r, θ directions
v_x', v_r', v_t' = rms turbulence intensities in x, r, θ directions
x, r, θ = cylindrical polar coordinates (axial, radial, tangential)
Δt = interframe time
δz = camera depth of field

References

[1] Merkle, K., Buechner, H., Zarzalis, N., and Sara, O. N., 2003, "Influence of Co and Counter Swirl on Lean Stability Limits of an Airblast Nozzle," ASME GT-2003-38004.

[2] Brooke-Benjamin, T., 1962, "Theory of the Vortex Breakdown Phenomenon," J. Fluid Mech., **14**, pp. 593–628.

[3] Sarpkaya, T., 1971, "On Stationary and Travelling Vortex Breakdowns," J. Fluid Mech., **45**, pp. 545–559.

[4] Billant, P., Chomaz, J.-M., and Huerre, P., 1998, "Experimental Study of Vortex Breakdown in Swirling Jets," J. Fluid Mech., **376**, pp. 183–219.

[5] Li, G., and Gutmark, E. J., 2003, "Geometry Effects on the Flow Field and the Spectral Characteristics of a Triple Annular Swirler," ASME G-2003-38799.

[6] Broda, J. C., Seo, S., Santoro, R. J., Shirhattikar, G., and Yang, V., 1998, "An Experimental Study of Combustion Dynamics of a Premixed Swirl Injector," 27th Symposium Int. on Combustion, The Combustion Institute, pp. 1849–1856.

[7] Cohen, J. M., Hibshman, J. R., Proscia, W., Rosfjord, T. J., Wake, B. E., McVey, J. B., Lovett, J., Ondas, M., DeLaat, J., and Breisacher, K., 2000, "Longitudinal Mode Combustion Instabilities: Modelling and Measurements," NASA/TM-2000-210067.

[8] Syred, N., Fick, W., O'Doherty, T., and Griffiths, A. J., 1997, "The Effect of the Precessing Vortex Core on Combustion in a Swirl Burner," Combust. Sci. Technol., **125**, pp. 139–157.

[9] Anacleto, P. M., Fernandes, E. C., Heitor, M. V., and Shtork, S. I., 2001, "Characteristics of a Precessing Vortex Core in an LPP Combustor Model," in Proc. of 2nd TSFP Symp., Stockholm, Sweden.

[10] Noll, B., Schueltz, H., and Aigner, M., 2001, "Numerical Simulation of High Frequency Flow Instabilities Near an Airblast Atomizer," ASME 2001-GT-0041.

[11] Cannon, S. M., Adumitroaie, V., and Smith, C. E., "3D LES Modelling of Combustion Dynamics in Lean Premixed Combustors," ASME 2001-GT-375.

[12] Tang, G., Yang, Z., and McGuirk, J. J., "Large Eddy Simulation of Isothermal Confined Swirling Flow with Recirculation," *Proceedings of 5th International Symposium on Engine Turbine Models and Measurements*, pp. 885–894.

[13] Wang, S., Hsieh, S.-Y., and Yang, V., 2001, "Numerical Simulation of Gas-Turbine Swirl-Stabilized Injector Dynamics," AIAA 2001-0334.

[14] Bissieres, D., 1998, "Final Report on the Design with Numerical Simulation of the MAKLIA DLN Combustor," Turbomeca Technical Report No. 13294.

[15] Midgley, K., Spencer, A., and McGuirk, J. J., 2003, "PIV Measurements of Confined Swirling Flow," in Proceedings of the 3rd TSFP Symposium, Sendai, Japan.

[16] Keane, R. D., and Adrian, R. J., 1992, "Theory of Cross-Correlation Analysis of PIV Images," Appl. Sci. Res., **49**, pp. 191–215.

[17] La Vision GmbH, 2000, "PIV Flowmaster Manual."

[18] Host-Madsen, A., and Neilson, A. H., 1998, "Accuracy of PIV Measurements in Turbulent Flows," in Proceedings of the 7th European Symposium on Particle Characterisation, Nurnberg, G.

[19] Hollis, D., 2004, "Particle Image Velocimetry in Gas Turbine Combustor Flow Fields," PhD thesis, Laughborough University, UK.

[20] Adrian, R. J., Christensen, K. T., and Liu, Z.-C., 2000, "Analysis and Interpretation of Instantaneous Turbulent Velocity Fields," Exp. Fluids, **29**, pp. 275–290.

[21] Graftieaux, L., Michard, M., and Grosjean, N., 2002, "Combining PIV, POD and Vortex Identification Algorithms for the Study of Unsteady Turbulent Swirling Flows," Meas. Sci. Technol., **12**, pp. 1422–1429.

[22] Zhou, J., Adrian, R. J., Balachandar, S., and Kendall, T. M., 1999, "Mechanisms for Generating Coherent Packets of Hairpin Vortices in Channel Flow," J. Fluid Mech., **387**, pp. 353–396.

[23] Janus, B., Dreizler, A., and Janicka, J., 2004, "Flow field and Structure of Swirl Stabilized Non-Premixed Natural Gas Flames at Elevated Pressure," ASME GT-2004-53340.

Downloaded 02 Jun 2010 to 171.66.16.98. Redistribution subject to ASME license or copyright; see http://www.asme.org/terms/Terms_Use.cfm

Thermodynamic and Economic Investigation of an Improved Graz Cycle Power Plant for CO_2 Capture

Wolfgang Sanz
e-mail: wolfgang.sanz@tugraz.at

Herbert Jericha

Mathias Moser

Franz Heitmeir

Institute for Thermal Turbomachinery and Machine Dynamics,
Graz University of Technology,
Inffeldgasse 25,
A-8010 Graz, Austria

Introduction of closed-cycle gas turbines with their capability of retaining combustion generated CO_2 can offer a valuable contribution to the Kyoto goal and to future power generation. Therefore, research and development at Graz University of Technology since the 1990s has lead to the Graz Cycle, a zero emission power cycle of highest efficiency. It burns fossil fuels with pure oxygen, which enables the cost-effective separation of the combustion CO_2 by condensation. The efforts for the oxygen supply in an air separation plant are partly compensated by cycle efficiencies far higher than 60%. In this work a further development, the S-Graz Cycle, which works with a cycle fluid of high steam content, is presented. Thermodynamic investigations show efficiencies up to 70% and a net efficiency of 60%, including the oxygen supply. For a 100 MW prototype plant the layout of the main turbomachinery is performed to show the feasibility of all components. Finally, an economic analysis of a S-Graz Cycle power plant is performed showing very low CO_2 mitigation costs in the range of \$10/ton CO_2 captured, making this zero emission power plant a promising technology in the case of a future CO_2 tax.
[DOI: 10.1115/1.1850944]

Introduction

In the last hundred years the concentration of some greenhouse gases in the atmosphere has markedly increased. There is a wide consensus in the scientific community that this seems to influence the Earth's surface temperature and, thus, the world climate.

Therefore, in 1997 the Kyoto conference defined the goal of global greenhouse gas emission reduction of about 5% in the next years compared to the 1990 emission level. CO_2 is the main greenhouse gas because of the very high overall amount emitted by human activities. About one-third of the overall human CO_2 emissions are produced by the power generation sector. In the EU there is a strong pressure on utilities and industry to reduce the CO_2 emissions by power generation. In 2003 the European Parliament passed a directive on emission trading. In 2005 emission allowances will be assigned to about 10,000 companies in 25 countries within the EU, which will cover about 46% of the overall EU CO_2 emissions. Companies that do not need their full amount can sell it to companies that need more than assigned. As emission allowances become scarce they will have an increasing value, estimates vary between 10 and 20 euro/ton CO_2 by 2010 and even more by 2015 [1].

So there is a strong driving force to develop commercial solutions for the capture of CO_2 from power plants. The main technologies are [2]:

- postcombustion CO_2 capture, e.g., by washing of exhaust gases using amines
- precombustion decarbonization of fossil fuels to produce pure hydrogen
- chemical looping combustion
- oxy-fuel cycles with internal combustion of fossil fuels with pure oxygen

The authors believe that oxy-fuel cycles are a very promising technology and that their Graz Cycle can be the most economic solution for CO_2 capture from fossil power generation once the development of the new turbomachinery components needed are done. Oxygen needed in a large amount for this kind of cycle can be generated by air separation plants, which are in use worldwide with great outputs in the steelmaking industry and even in enhanced oil recovery. The largest air separation plant, already in operation for some years in the Gulf of Mexico, produces nitrogen for the injection in the gas dome of a large oil field offshore [3]. The equivalent amount of this oxygen could feed a Graz Cycle plant of 1300 MW.

The basic principle of the so-called Graz Cycle has been developed by Jericha in 1985 [4]. Improvements and further developments since then were presented at many conferences [5–10]. Any liquid or gaseous fossil fuel (preferably with low nitrogen content) is proposed to be combusted with oxygen so that mainly only the two combustion products CO_2 and H_2O are generated. The cycle medium of CO_2 and H_2O allows an easy and cost-effective CO_2 separation by condensation. Furthermore, the oxygen combustion enables power cycles that are far more efficient than current air-based cycles, thus, largely compensating the additional efforts for oxygen production.

At the ASME IGTI Conference 2003 in Atlanta, a Graz Cycle power plant with a cycle efficiency of 63% was presented and the general layout of all components for a 90 MW prototype plant were discussed [9]. In this paper this cycle is compared to a modified cycle scheme, which promises efficiencies up to 70%, thus allowing one to fully compensate the efforts of oxygen supply. The general layout of all turbomachinery components of this new Graz Cycle as well as the general arrangement with gears and electric generators is discussed. An economical investigation shows that this new Graz Cycle is a very cost-effective solution of a zero-emission power plant, which is thought to be worth pursuing in the future.

Contributed by the International Gas Turbine Institute (IGTI) of THE AMERICAN SOCIETY OF MECHANICAL ENGINEERS for publication in the ASME JOURNAL OF ENGINEERING FOR GAS TURBINES AND POWER. Paper presented at the International Gas Turbine and Aeroengine Congress and Exhibition, Vienna, Austria, June 13–17, 2004, Paper No. 2004-GT-53722. Manuscript received by IGTI, October 1, 2003; final revision, March 1, 2004. IGTI Review Chair: A. J. Strazisar.

Copyright © 2005 by ASME

Downloaded 02 Jun 2010 to 171.66.16.98. Redistribution subject to ASME license or copyright; see http://www.asme.org/terms/Terms_Use.cfm

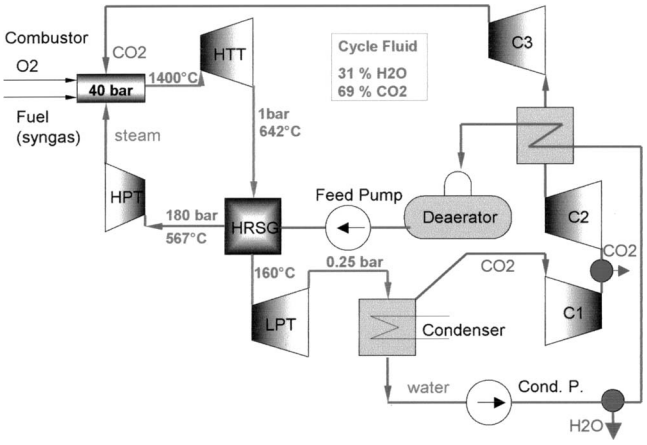

Fig. 1 Principle flow scheme of Graz Cycle power plant

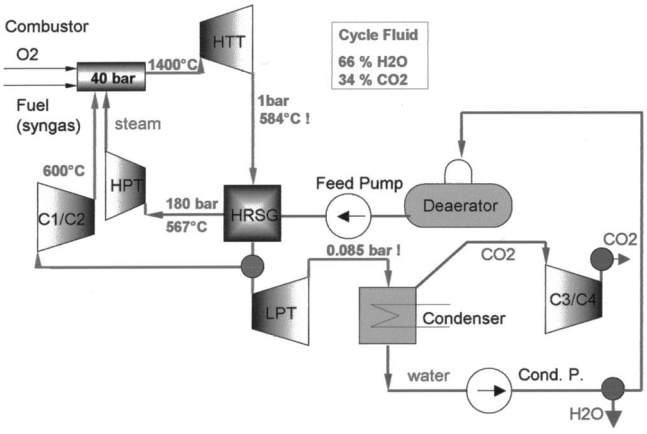

Fig. 2 Principle flow scheme of S-Graz Cycle power plant

Cycle Configurations and Thermodynamic Layout

All thermodynamic simulations were performed using the commercial software IPSEpro by SIMTECH Simulation Technology [11]. This software allows one to implement user-defined fluid properties to simulate the real gas properties of the cycle medium. The physical properties of water and steam are calculated using the IAPWS_IF97 formulations [12], the CO_2 properties are calculated using [13]. Furthermore, a turbine module was developed for the calculation of cooled turbine stages. A simple stage-by-stage approach similar to [14] is assumed that allows one to calculate the amount of cooling steam needed per stage.

Although the Graz Cycle is suited for all kinds of fossil fuels, for natural gas fuel it seems more economical to reform CH_4 to $CO+H_2$. Hydrogen can then be separated and burned in an air-breathing gas turbine, a solution that reduces the oxygen requirements considerably. But in using oxygen-blown coal gas as a fuel, a Graz Cycle plant is most effective in retaining CO_2 and in use of oxygen. So the thermodynamic data presented are for a cycle fired with a typical fuel gas composition from an oxygen-blown coal gasification plant (syngas mole fractions: $0.1\,CO_2$, 0.4 CO, $0.5\,H_2$).

The thermodynamic simulation is based on the following assumptions on efficiencies and losses: (i) the isentropic efficiency of turbines is 92% (90% for HPT); (ii) the isentropic efficiency of CO_2 compressors is 90% and of CO_2/H_2O compressors 88%; (iii) the mechanical efficiency of the turbomachinery is 99%; (iv) the generator efficiency is 98.5%; (v) HRSG: cold side pressure loss is 5 bar; hot side pressure loss is neglected; (vi) the pinch point of the heat exchangers is limited to 5°C; (vii) the cooling water temperature in the condenser is 15°C; (viii) fuel and oxygen is supplied at 40 bar; (ix) CO_2 is released at 1 bar, efforts of a further compression to 100 bar (275 kJ/kg) is considered in the power balance; and (x) the power consumption of oxygen production is 900 kJ/kg (0.25 kWh/kg) and of oxygen compression is 455 kJ/kg.

Graz Cycle. At first the flow scheme of the Graz Cycle as published in [8,9] will be presented before the modification leading to enhanced efficiency will be discussed. Figure 1 shows the principle flow scheme with the main components and will be used to explain the main characteristics of this zero emission power cycle. Detailed cycle data for a 92 MW pilot plant, such as mass flow, pressure, temperature, enthalpy, or cycle fluid composition, as well as the details of the thermodynamic simulation can be found in [9].

Basically the Graz Cycle consists of a high-temperature Brayton cycle [compressors C2, C3, combustion chamber, and high-temperature turbine (HTT)] and a low-temperature Rankine cycle [low-pressure turbine (LPT), condenser, heat recovery steam generator (HRSG), and high-pressure turbine (HPT)]. The fuel together with the stoichiometric mass flow of oxygen is fed to the combustion chamber, which is operated at a pressure of 40 bar. Steam as well as CO_2 is supplied to cool the burners and the liner. A mixture of about three-quarters of CO_2 and one-quarter of steam leaves the combustion chamber at a mean temperature of 1400°C. The fluid is expanded to a pressure of 1 bar and 642°C in the HTT. Due to the addition of cooling steam in the HTT, the steam content in the cycle medium increases to 31%. It is quite clear that a further expansion down to condenser pressure would not end at a reasonable condensation point for the water component, so that the hot exhaust gas is cooled in the following HRSG to vaporize and superheat steam for the HPT. Then it is further expanded in the LPT to a condenser pressure of 0.25 bar. For a mixture of a condensable (steam) and a noncondensable gas (CO_2), the condensation temperature depends on the partial pressure of steam, which continuously decreases during the condensation. Assuming a minimum cooling water temperature of 20°C and condensation of 93% of the water content results in a minimum condenser pressure of 0.25 bar due to the steam content of 31%.

In the condenser the separation of CO_2 and H_2O takes place by water condensation. The water is preheated and in the HRSG va-

Table 1 Graz Cycle power balance

Total turbine power [MW]	111
Total compression power [MW]	18.8
Net shaft power [MW]	92.2
Total heat input [MW]	143.4
Thermal cycle efficiency [%]	**64.3**
Electrical power output [MW]	90.4
Electrical cycle efficiency [%]	**63.3**
O_2 generation and compression [MW]	11.95
Net efficiency [%]	**55.0**
CO_2 compression to 100 bar [MW]	3.7
Net efficiency if CO_2 at 100 bar [%]	52.5

Table 2 S-Graz Cycle power balance

Total turbine power [MW]	150.4
Total compression power [MW]	50.5
Net shaft power [MW]	99.9
Total heat input [MW]	143.4
Thermal cycle efficiency [%]	**69.6**
Electrical power output [MW]	98.4
Electrical cycle efficiency [%]	**68.6**
O_2 generation and compression [MW]	11.95
Net efficiency [%]	**60.3**
CO_2 compression to 100 bar [MW]	3.7
Net efficiency if CO_2 at 100 bar [%]	57.7

Downloaded 02 Jun 2010 to 171.66.16.98. Redistribution subject to ASME license or copyright; see http://www.asme.org/terms/Terms_Use.cfm

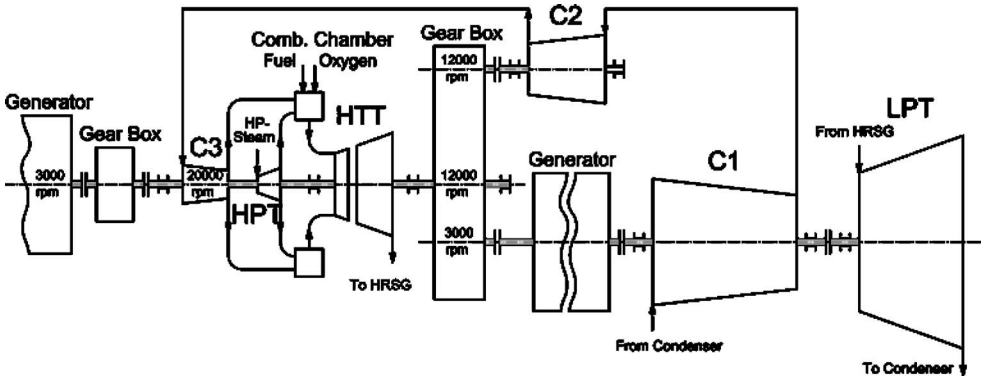

Fig. 3 Schematic arrangement of turbomachinery for a 92 MW Graz Cycle power plant

porized and superheated while doing the necessary cooling of the HTT exhaust flow. The steam is then delivered to the HPT with 180 bar and 567°C; after the expansion, it is used to cool the burners and the first and second HTT stages. The CO_2 from the condenser is compressed to atmospheric pressure; the combustion CO_2 is then separated for further use or storage at 1 bar. The remaining CO_2 is compressed and fed to the combustion chamber to cool the liners.

The cycle arrangement of the Graz Cycle offers several advantages. On one hand, it allows heat input at very high temperature, whereas on the other hand, expansion takes place till to vacuum conditions, so that a high thermal efficiency according to Carnot can be achieved. The dual medium CO_2 and H_2O results also in very low compression work. With both medium components in use over the full temperature range, the cycle gives this beneficial effect because only the gas CO_2 requires turbo compressors (C1,C2,C3), whereas feed water can be pumped to form high-pressure steam. High-pressure steam can be expanded to generate additional power in the high-pressure turbine HPT, before being united with the CO_2 flow in the combustion chamber. Further beneficial effects are the possibility to create burner vortices and to cool the hottest nozzles and blades of the HTT first and second stage using the exhaust steam of the HPT, which is of suitable pressure and temperature.

Table 1 gives an overview of the power balance of the Graz Cycle. For a 92 MW pilot plant the total turbine power adds up to 111 MW, 90 MW of it are supplied by the HTT [9]. On the other side, the total compression power mostly used for CO_2 compression is 18.8 MW. Considering generator mechanical and electrical losses, an overall thermal cycle efficiency of 63.3% can be evaluated. But considering the efforts for oxygen production and compression from atmosphere to combustion pressure results in an efficiency reduction to 55.0%. For comparison a combined cycle with a single pressure steam cycle was calculated using the same main cycle data and assumptions. The resulting thermal efficiency of 53% is below the Graz Cycle efficiency considering the efforts of oxygen production and compression. If CO_2 is compressed to 100 bar for liquefaction, the efficiency further reduces to 52.5%.

High Steam Content Graz Cycle (S-Graz Cycle). The authors have tested various compositions of the cycle medium (about 20% CO_2 and 80% H_2O) in the publications of 1995 [5,6], where only approximate designs for turbomachinery arrangement, rotor, and blading configuration were shown. In the following years intensive work on an innovative cooling system and a test stand for transonic turbine stages were completed, so that in Refs. [7–9] an optimized compressor design and a first transonic turbine stage could be presented. These design features are associated with a cycle medium composition of about 75% CO_2 and 25% H_2O being on the other boundary of the admissible medium composition range.

The work presented here aims again for a much higher water content, now called the ''high Steam content Graz Cycle'' or shortly ''S-Graz Cycle.'' This cycle differs from the 1995 cycle [5,6] only by different cycle parameters, which result in a remarkable efficiency increase and promises a still more viable turbomachinery arrangement. When previous solutions are referred to in the following, the result of Refs. [8,9] are nominated as the original Graz Cycle.

Figure 2 shows the principal flow scheme with the main components. Similar to the original Graz Cycle, the fuel together with the stoichiometric mass flow of oxygen is fed to the combustion chamber, which is operated at a pressure of 40 bar. Steam as well as a CO_2/H_2O mixture is supplied to cool the burners and the liner. A mixture of about 62% steam and 38% CO_2 leaves the combustion chamber at the same mean temperature of 1400°C. The fluid is expanded to a pressure of 1 bar in the HTT. But the turbine exit temperature is now about 60°C lower due to the different cycle medium. It contains 66% steam after the HTT. The hot exhaust gas is also used in the following HRSG to vaporize and superheat steam for the HPT; the pinch point of the HRSG is 9.4°C at the superheater exit. But after the HRSG only 43% of the

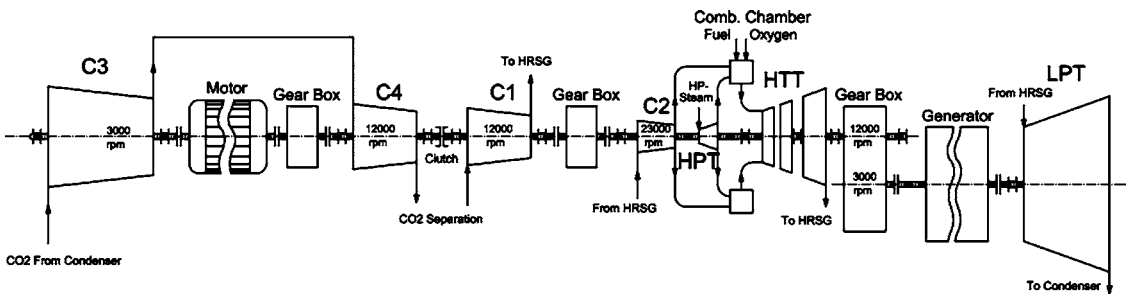

Fig. 4 Schematic arrangement of turbomachinery for a 100 MW S-Graz Cycle power plant

Downloaded 02 Jun 2010 to 171.66.16.98. Redistribution subject to ASME license or copyright; see http://www.asme.org/terms/Terms_Use.cfm

Table 3 Main turbomachinery data of S-Graz Cycle

Turbines: Total turbine power 150,387 kW						
Turbine name		HPT	HPT cool	HTT stage 1	HTT st. 2–4	LPT
m	kg/s	21.31	1.79	82.26	90.81	37.12
V_{inlet}	m^3/s	0.416	0.117	12.37	30.78	81.05
V_{exit}	m^3/s	1.401	0.349	30.78	298.74	589.21
P	kW	8553	508	40,835	86,919	13,572
n	rpm	23,000	23,000	23,000	12,000	3000
z	···	4		1	3	4
$D_{m,inlet}$	m	0.190	···	0.389	0.554	1.29
L_{inlet}	m	0.02	···	0.050	0.118	0.27
$D_{m,exit}$	m	0.192	···	0.477	0.958	1.85
L_{exit}	m	0.02	···	0.066	0.272	0.58
Compressors and pumps: Total power 50,524 kW						
Compressor name		C1	C2	C3	C4	Feed pump
m	kg/s	52.34	52.34	14.24	14.24	21.31
V_{inlet}	m^3/s	78.12	11.40	109.5	54.35	0.0221
V_{exit}	m^3/s	12.49	6.56	67.81	10.71	0.0219
P	kW	27,157	20,466	608	1864	427
n	rpm	12,000	23,000	3000	12,000	3000
z	···	9	7+1 rad	8	4	
$D_{o,inlet}$	m	0.842	0.304	1.071	0.659	
L_{inlet}	m	0.168	0.053	0.214	0.132	
D_i/D_o	···	0.60	0.65	0.60	0.60	
$M_{rel\ tip}$	···	1	1	1	1.3	
$D_{o,exit}$	m	0.754	0.322	0.956	0.607	
L_{exit}	m	0.080	0.025	0.100	0.080	

cycle mass flow is further expanded in the LPT. The exit and, thus, condenser pressure is 0.085 bar, significantly lower than for the Graz Cycle because of the higher steam content of the cycle medium (see above).

CO_2 and steam are separated in the condenser. From there on, the CO_2 mass flow, which is equal to the combustion CO_2, is compressed to atmosphere and supplied for further use or storage. After segregating the combustion H_2O, the water is preheated and vaporized and superheated in the HRSG. The steam is then delivered to the HPT with 180 bar and 575°C, and after the expansion, it is used to cool the burners and the HTT stages. The cooling mass flow for the HTT turbine is 12.6% of the HTT inlet mass flow.

The major part of the cycle medium, which is separated after the HRSG, is compressed using an intercooled compressor and fed to the combustion chamber with a maximum temperature of 600°C. The detailed flow sheet used for the thermodynamic simulation is included in the Appendix (Fig. 9) and gives mass flow, pressure, temperature, and enthalpy of all streams.

Table 2 gives the power balance of the S-Graz Cycle for the same heat input as before. Turbine and compressor power are 150.4 MW and 50.5 MW, respectively, and thus are considerably higher than in the original Graz Cycle. The high compressor power of the S-Graz Cycle results from the compression of more than half of the cycle steam in the gaseous phase which is avoided in the Graz Cycle. The resulting net shaft power of 99.9 MW leads to a thermal cycle efficiency of 69.6% and electrical cycle efficiency of 68.6% including generator losses. If considering the efforts for oxygen production and compression from atmosphere to combustion pressure a net efficiency of 60.3% can be evaluated which is nearly 6 percentage points higher than for the original Graz Cycle, higher than for state-of-the-art combined cycles and far beyond the efficiencies which are reported for other technologies of a zero emission power plant. If CO_2 is compressed to 100 bar for liquefaction, the efficiency further reduces to 57.7%.

The original Graz Cycle strives for minimum compression work, which is achieved insofar as only the noncondensable gas CO_2 in its return flow to the combustion chamber is compressed by compressors. The second component, liquid water, is only mixed into the combustion chamber by way of evaporation, superheating, and expansion in the HPT. The advantage of minimal compression work is counteracted by the disadvantage of the higher heat input that is therefore required to the combustion chamber.

The second solution, the S-Graz Cycle, uses a very high steam content, from which less than the half releases its heat of vaporization by condensation. The major part is compressed in the gaseous phase and takes its high heat content back to the combustion chamber. A second advantage of the high steam content is the lower possible condenser pressure for the same cooling medium temperature. This leads to a higher power output of the LPT despite of a much lower mass flow. Both features contribute to the remarkable efficiency increase compared to the original Graz Cycle.

Methane-Fired S-Graz Cycle. If instead of syngas, methane is fired in a S-Graz Cycle power plant, the cycle medium contains nearly 75% H_2O at the combustion chamber exit. This different composition leads to an electrical cycle efficiency of 67.6%, which is 1 percentage point below the syngas-fired version. Methane needs more oxygen per heat input to the combustion chamber, so that the effort for oxygen production and compression is 15.5 MW. This results in a net efficiency of 56.8%, about 4.5 percentage points below the syngas-fired version. If CO_2 compression to 100 bar is considered (2.15 MW), the efficiency further decreases to 55.3%.

Turbomachinery Design

Compression and expansion in large power cycles can only be affected with modern turbomachinery. The gases we have to deal with, in our case CO_2 and H_2O steam, are very compressible at the given high enthalpy heads or pressure ratios. The resulting high changes in volume flow in the individual compressors and turbines require a multishaft arrangement connected by gears.

The design decision of having the high-temperature flow channel with minimum surface and minimum heat loss and also with minimum cooling flow supply leads to the arrangement of turbomachinery for the original Graz Cycle as given in Fig. 3, which is intensively discussed in [8,9]. Two overhang disks of different speed provide the shortest possible high-temperature annular flow

Downloaded 02 Jun 2010 to 171.66.16.98. Redistribution subject to ASME license or copyright; see http://www.asme.org/terms/Terms_Use.cfm

Table 4 Estimated investment costs

Component	Scale Parameter		Specific Costs
Reference plant [15]			
Investment costs	Electric power	$\$/kW_{el}$	414
S-Graz Cycle plant			
Investment costs	Electric power	$\$/kW_{el}$	414
Air separation unit [16]	O_2 mass flow	$\$/(kg\ O_2/s)$	1,500,000
Other costs (piping, CO_2-recirc.) [16]	CO_2 mass flow	$\$/(kg\ CO_2/s)$	100,000
CO_2-compression system [16]	CO_2 mass flow	$\$/(kg\ CO_2/s)$	450,000

channel. So power end drive has to be on opposite sides. At 20,000 rpm HPT and C3 can be optimally connected. At the 12,000 rpm side main power is delivered via gears to the main generator. On the other side of the generator, C1 and low pressure turbine LPT are arranged running at 3000 rpm.

The power produced by HTT first stage and HPT greatly surpasses the power demand of C3, so a second electric generator is necessary. The only alternative would have been an outside gear shaft connecting to the main gear box and the main generator. The electric shaft proposed here seems to be a superior solution because, for much larger units, the same type of arrangement can be kept. Since gears with a power of about 100 MW are in successful operation in standard gas turbine units, the output of this Graz Cycle prototype unit could be doubled, still retaining high-speed turbomachinery design.

The S-Graz Cycle differs from the original Graz Cycle insofar as only two compressors of high power (C1 and C2) are needed for the compression of the cycle medium and that the effort for the CO_2 delivery is much reduced. This leads to a different turbomachinery arrangement as shown in Fig. 4, which also includes the compressors C3 and C4, compressing the separated CO_2 to atmosphere.

The HTT turbine needs four instead of three stages due to the higher heat capacity of the now optimized cycle medium. Again the HTT is split into two shafts, where the first stage runs at 23,000 rpm, the other three stages at 12,000 rpm. A bearing is arranged between the second and third stages. In order to reduce the number of generators, the power of all four compressors is balanced with the HTT first stage and the HPT. Both turbines drive the cycle medium compressors C1 and C2 and in normal operation the CO_2 delivering compressors C3 and C4 also. These compressors are connected via a self-synchronizing clutch and are disconnected from the main high-speed shaft during startup. Then they are driven by a separate electric motor in a mode similar to the vacuum pump in a steam plant. This arrangement needs two gear boxes because the compressors C1 and C4 run at 12,000 rpm and the compressor C3 at 3000 rpm.

Stages 2, 3, and 4 of the HTT run at 12,000 rpm and deliver their power via the main gear to the generator, which is driven on the other side by the LPT in a way quite similar to very large steam turbines.

Table 3 gives the main turbomachinery data and their dimensions for the S-Graz Cycle. Corresponding data for the original Graz Cycle are given in [9]. Due to the small volume flow of the

Table 5 Economical data for syngas firing

	Reference plant [15]	S-Graz Cycle	S-Graz Cycle $+CO_2$ at 100 bar
Plant capital costs $[\$/kW_{el}]$	414	414	414
Addit. capital costs $[\$/kW_{el}]$		148	209
CO_2 emitted $[kg/kWh_{el}]$	0.629	0.0	0.0
Net plant efficiency [%]	56.2	60.3	57.7
COE for plant amort. $[¢/kWh_{el}]$	0.96	1.3	1.44
COE due to fuel $[¢/kWh_{el}]$	6.22	5.8	6.06
COE due to O&M $[¢/kWh_{el}]$	0.7	0.8	0.8
Total COE $[¢/kWh_{el}]$	**7.88**	**7.9**	**8.30**
Comparison			
Differential COE $[¢/kWh_{el}]$		0.02	0.42
Mitigation costs [\$/ton CO_2 capt.]		0.3	6.7

Table 6 Economical data for methane firing

	Reference plant [15]	S-Graz Cycle	S-Graz Cycle $+CO_2$ at 100 bar
Plant capital costs $[\$/kW_{el}]$	414	414	414
Addit. capital costs $[\$/kW_{el}]$		177	221
CO_2 emitted $[kg/kWh_{el}]$	0.37	0.0	0.0
Net plant efficiency [%]	56.2	56.8	55.3
COE for plant amort. $[¢/kWh_{el}]$	0.96	1.36	1.47
COE due to fuel $[¢/kWh_{el}]$	2.31	2.29	2.35
COE due to O&M $[¢/kWh_{el}]$	0.7	0.8	0.8
Total COE $[¢/kWh_{el}]$	**3.97**	**4.45**	**4.62**
Comparison			
Differential COE $[¢/kWh_{el}]$		0.48	0.65
Mitigation costs [\$/ton CO_2 capt.]		13.0	17.5

Downloaded 02 Jun 2010 to 171.66.16.98. Redistribution subject to ASME license or copyright; see http://www.asme.org/terms/Terms_Use.cfm

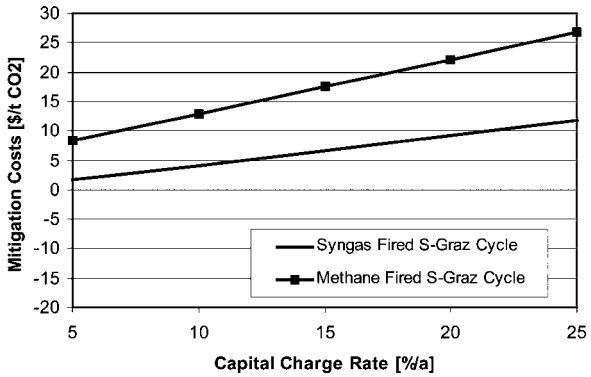

Fig. 5 Influence of capital charge rate on the mitigation costs (CO_2 provided at 100 bar)

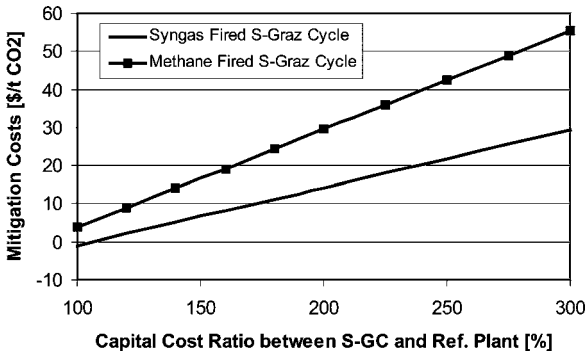

Fig. 8 Influence of capital costs on the mitigation costs (CO_2 provided at 100 bar)

HPT, it is designed in the form of a four-stage partial admission impulse steam turbine. Its arrangement immediately ahead of the HTT allows it to affect cooling of the HTT first-stage disk in a very effective way. Exhaust steam is fed via labyrinth seals to the front side of the disk, thus, holding the shaft and the disk at a temperature of around 300°C. The disk is bell shaped with broad width in the center, leading to a strong fir-tree root blade attachment, which contains the cooling steam inlet ports to the hollow blades.

On the other side the space between the HTT first- and second-stage disks is again filled with cooling steam from outside, cooling both disks and providing in a form of a stationary steam bearing additional damping to both shafts. Again from here cooling steam is fed into the second disk and its blades.

The compressors C1 and C2 have to act on a medium consisting of CO_2 and steam. The high volume change requires a change of speed (C1 at 12,000 rpm, C2 at 23,000 rpm) with relatively high Mach numbers at the tip of their respective first blades. But relatively long last blades result in low clearance loss and low deterioration of meridional flow profile. In order to keep the high-speed shaft short and to reduce the number of stages in C2, a radial final stage is proposed which can replace three or four axial stages due to its higher diameter and at the same time delivers the medium radially outward, making the inflow to the combustion chamber easier.

The number of stages of the LPT increased from two for the original Graz Cycle to four for the S-Graz Cycle, due to the lower condenser pressure and the higher heat capacity of the cycle medium.

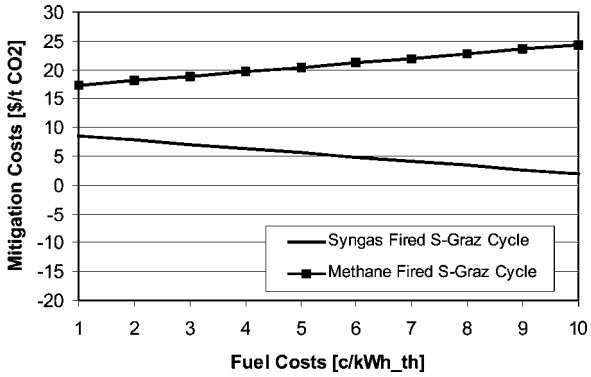

Fig. 6 Influence of fuel costs on the mitigation costs (CO_2 provided at 100 bar)

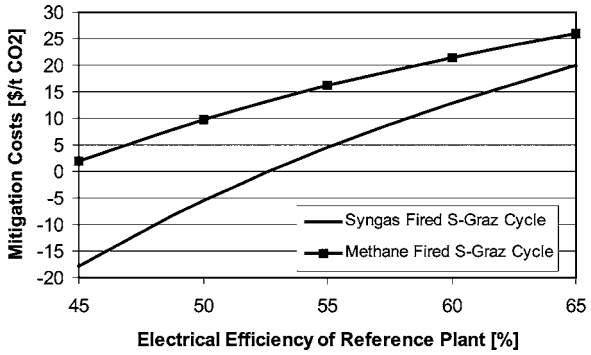

Fig. 7 Influence of reference plant efficiency on the mitigation costs (CO_2 provided at 100 bar)

Startup of a S-Graz Cycle Power Plant. At startup all machines are thought to be filled with steam from a foreign source fed into the turbomachinery high-pressure side. All labyrinths are sealed with steam, and the turning gears on both shafts are operating. The electric motor of C3 and C4 starts turning and creates vacuum in the condenser. Now the self-synchronizing clutch is coupled, and thus the electric motor drives the high-speed shaft. Steam flows throughout the interior of all turbomachinery and is condensed in the condenser. The feed water flow is started toward the feed water tank. This should go so far that the turbosets run out of turning gear and reach about 25% nominal speed. Now oxygen and fuel gas can be fed to the combustion chamber, and ignition of the combustion chamber burner pilot flames is tried. Putting in more fuel and oxygen should allow one to run the machines up to speed. In case of flame out or ignition failure, oxygen and fuel supply stop immediately, steam supply is restarted, compressors C3 and C4 are disconnected, and ventilating the interior of the combustion chamber and all turbomachinery is repeated.

When ignition is successful, the turboset will run up to higher speed and the generator can be synchronized. Compressors C3 and C4 are again connected to the high-speed shaft and start delivering noncondensable gases outside, first to a gas cleaning unit and then into the CO_2 delivery line at 1 bar.

Economic Evaluation

Despite the high efficiency and positive impact on the environment of a S-Graz Cycle power plant, a future application of this technology and an erection of a power plant mainly depends on the economical balance. Therefore, an economic comparison with a high-efficiency state-of-the-art combined cycle power plant is performed, whose economical data are reported in [15].

Downloaded 02 Jun 2010 to 171.66.16.98. Redistribution subject to ASME license or copyright; see http://www.asme.org/terms/Terms_Use.cfm

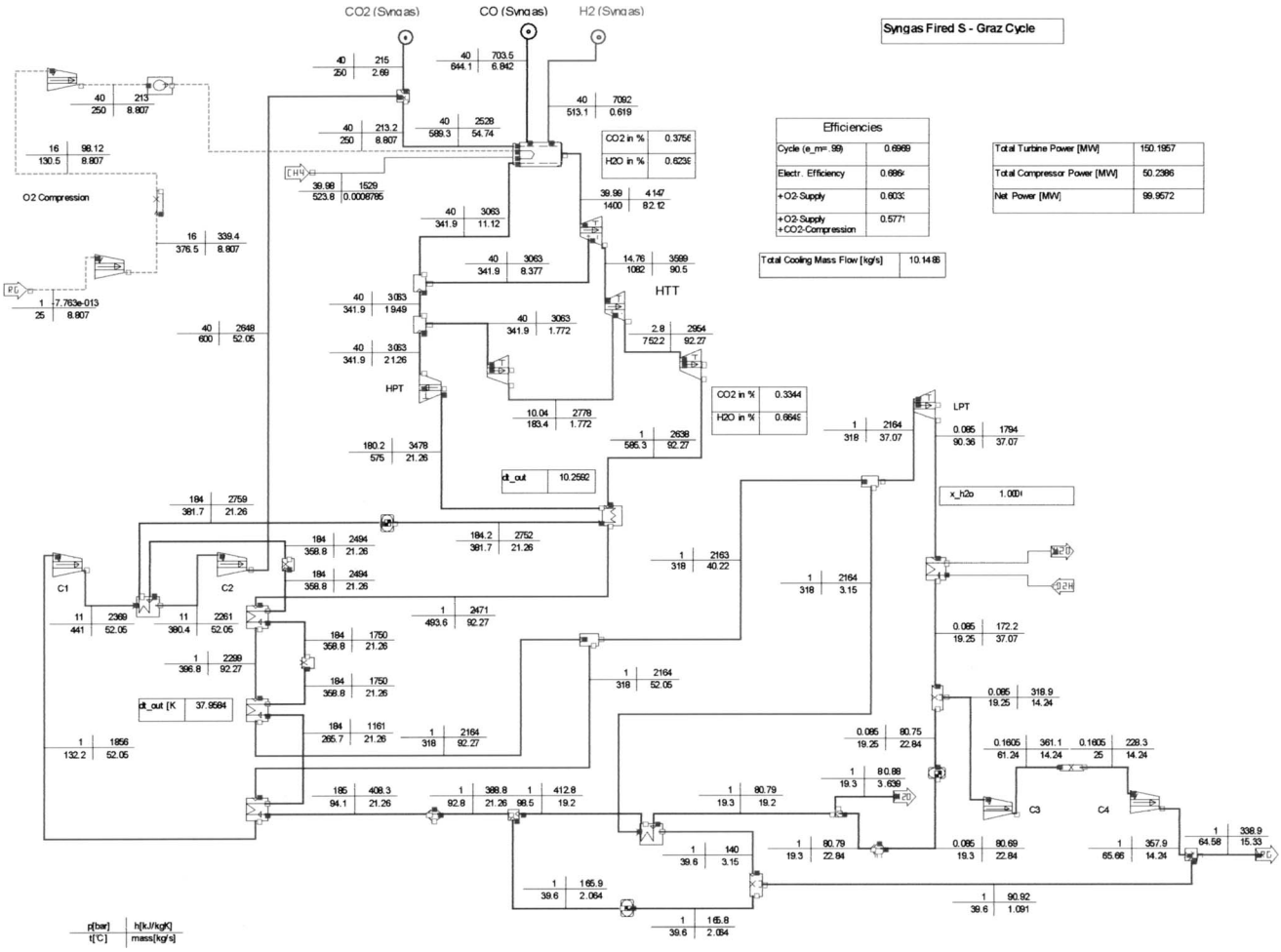

Fig. 9 Detailed thermodynamic cycle data of a 100 MW S-Graz Cycle power plant fired with syngas

The economical analysis is based on following assumptions: (i) the yearly operating hours is assumed at 6500 hr/yr; (ii) the capital charge rate is 15%/yr; (iii) fuel is either syngas or methane; (iv) methane fuel costs are $1.3¢/kWh_{th}$ according to [15]; (v) syngas is supplied by a syngas producer at $3.5¢/kWh_{th}$, so no efficiency penalty for the production is considered; (v) an efficiency decrease of the reference plant due to syngas firing and a higher fuel compression effort for the Graz Cycle due to a higher combuster pressure are not considered (but these influences are discussed later by the sensitivity analysis of Fig. 7); (vi) the investment costs per kilowatt are the same for the reference plant and the S-Graz Cycle plant; (vii) additional investment costs are assumed for the air-separation unit and for additional equipment (see Table 4, [16]); (viii) additional investment and operating costs for the compression of CO_2 to 100 bar for liquefaction are considered alternatively (the effort for CO_2 compression is 275 kJ/kg CO_2); (ix) the costs of CO_2 transport and storage are not considered because they depend largely on the site of a power plant.

Three indicators characterizing the economical performance of a power plant for CO_2 capture are estimated:

- the costs of electricity (COE) for both plants
- the differential COE representing the additional costs of electricity due to CO_2 capture
- the mitigation or capture costs representing the additional costs incurred by CO_2 capture per ton CO_2

Tables 5 and 6 show the result of the economical evaluation for syngas and methane firing, respectively. Compared to the reference plant, the capital costs are about 50% higher only by considering the additional components for O_2 generation and CO_2 compression. The fuel costs have the major influence on the COE, especially for syngas firing. The S-Graz Cycle has lower fuel costs in most cases due to its high efficiency. The O&M costs are assumed 15% higher for a S-Graz Cycle plant due to the operation of additional equipment.

Based on these assumptions, the COE of a syngas-fired S-Graz Cycle plant is with $0.02¢/kWh_{el}$ and $0.42¢/kWh_{el}$, respectively, only slightly higher than for the reference plant. The mitigation costs are \$0.3/ton CO_2 and \$6.7/ton of CO_2 captured, if the CO_2 liquefaction is considered and thus are far below the height of a CO_2 tax currently discussed.

If methane is used as fuel, then the mitigation costs are higher because of the reduced CO_2 emission of methane ($0.37\ kg/kWh_{el}$ compared to $0.629\ kg/kWh_{el}$), the higher need of oxygen per heat input and the lower efficiency of the S-Graz Cycle as discussed above. Assuming lower fuel costs as for the syngas cycle (1.3 instead of $3.5¢/kWh_{el}$), the mitigation costs are \$13.0/ton CO_2 and \$17.5/ton of CO_2 captured, if the CO_2 liquefaction is considered. These values are still promising and show the potential of the S-Graz Cycle. But as discussed above, it has to be investigated if, for methane, the steam reforming and subsequent H_2 separation is the more economical option.

The results of the economic study depend mainly on the assumptions about investment costs, fuel costs, and capital charge rate as well as on the choice of the reference plant. Therefore, a cost-sensitivity analysis is performed in order to study the influ-

Downloaded 02 Jun 2010 to 171.66.16.98. Redistribution subject to ASME license or copyright; see http://www.asme.org/terms/Terms_Use.cfm

ence of the different parameters. Figures 5–8 show the resulting changes of the mitigation costs for the S-Graz Cycle considering also the CO_2 liquefaction costs.

The capital charge rate considers the payback period and the capital interests. If it varies between 5% and 25%, the mitigation costs change from \$1.5 to \$12/ton CO_2 captured for the syngas fired S-Graz Cycle and from \$8 to \$27/t CO_2 captured for the methane fired version (Fig. 5). If a CO_2 tax of at least \$20/ton is assumed, then an investment in a syngas-fired S-Graz Cycle plant is reasonable even for a strongly varying capital charge rate.

The variation of the fuel costs (Fig. 6) between 1 and $10¢/kWh_{th}$ does not strongly change the mitigation costs because of the small efficiency difference between S-Graz Cycle and reference plant. Therefore, the investment decision is not influenced by the fuel costs. Because of higher electrical efficiency of the syngas-fired S-Graz Cycle compared to the reference plant, the mitigation costs decrease with increasing fuel costs.

On the other hand the electrical efficiency of an alternative plant has a higher impact on the investment decision (Fig. 7). This parameter also covers the influence of an efficiency decrease of the reference plant due to syngas firing or of the S-Graz Cycle plant due to a higher fuel compression effort or component efficiencies lower than assumed. A reference plant of 60% efficiency, which has just been achieved by a H-technology combined cycle plant, increases the mitigation costs to \$13/ton CO_2 captured for the syngas fired S-Graz Cycle and to \$26/ton CO_2 captured for the methane fired S-Graz Cycle.

It is rather difficult to estimate the capital costs for a S-Graz Cycle power plant due to some new turbomachinery components (i.e., the HTT and the fuel-oxygen combustion chamber). If only the investment costs for the air separation unit and the CO_2 compression is considered, then the capital costs increase by approximately 50%. For the syngas-fired S-Graz Cycle investment costs twice as high as for a reference combined cycle plant lead to mitigation costs of \$15/ton CO_2, three times higher investment costs to \$30/ton CO_2 captured (see Fig. 8). Considering that currently a CO_2 tax of this height is discussed, then a syngas-fired S-Graz Cycle power plant seems a reasonable investment even at remarkably higher capital costs compared to a conventional power plant. The economical situation is less promising for the methane-fired S-Graz Cycle; double investment costs lead to mitigation costs of \$30/ton CO_2 captured.

In these considerations about the height of additional investment costs, a further advantage of the S-Graz Cycle, the almost NO_x-free combustion was not evaluated. According to [17] exhaust flow NO_x and CO catalytic reduction to achieve single-digit emissions (in strict attainment areas) can increase gas turbine genset plant costs by 40–50%.

Conclusion

The Graz Cycle is an oxy-fuel power cycle with the capability of retaining all the combustion generated CO_2 for further use. In this work a further development, the S-Graz Cycle, has been presented, which works with a cycle fluid of higher steam content and promises thermal efficiencies of up to nearly 70%. Even considering the costs of oxygen supply, the net efficiency is in the range of most modern combined cycle power plants.

In the S-Graz Cycle about one-third of the total turbine power is used for compression, so that a new arrangement of the turbomachinery components is proposed. The general layout of all components for a 100 MW prototype plant is presented verifying the feasibility of all components.

In an economical analysis a S-Graz Cycle power plant is compared to a reference plant. Due to the very high efficiency of the S-Graz Cycle, the CO_2 mitigation costs of the syngas-fired version are less than \$10/ton CO_2 captured, so that the investment in such a zero-emission power plant seems very reasonable considering stronger CO_2 taxation in the future.

Acknowledgment

Support came from project Y57-TEC "Non-Intrusive Measurement in Turbomachinery," funded by the Austrian Science Foundation (FWF, START-program, J. Woisetschläger).

Nomenclature

D = diameter (m)
L = blade length (m)
$M_{rel,tip}$ = relative tip Mach number
m = mass flow (kg/s)
n = speed (rpm)
P = power (kW)
V = volume flow (m^3/s)
z = number of stages

Subscripts

o = outer, tip
m = mean
i = inner, hub

Appendix

Please see Fig. 9.

References

[1] Strömberg, L., 2003, "Overview of CO_2 Capture and Storage—Technology and Economics for Coal Based Power Generation," VGB Congress 2003, Copenhagen.

[2] Gabbrielli, R., and Singh, R., 2002, "Thermodynamic Performance Analysis of New Gas Turbine Combined Cycles With No Emissions of Carbon Dioxide," ASME Paper No. GT-2002-30117.

[3] Turanskyj, L., and Keenan, B. A., 2001, "Turbomachinery for the World's Largest Nitrogen Plant: Enhanced Oil Recovery to Increase the Output in the Cantarell Oil Field, Mexico," Exposición Latinoamericana del Petróleo, Maracaibo, Venezuela.

[4] Jericha, H., 1985, "Efficient Steam Cycles With Internal Combustion of Hydrogen and Stoichiometric Oxygen for Turbines and Piston Engines," CIMAC Conference Paper, Oslo, Norway.

[5] Jericha, H., Sanz, W., Woisetschläger, J., and Fesharaki, M., 1995, "CO_2—Retention Capability of CH_4 /O_2 Fired Graz Cycle," CIMAC Conference Paper, Interlaken, Switzerland.

[6] Jericha, H., and Fesharaki, M., 1995, "The Graz Cycle—1500°C Max Temperature Potential H_2-O_2 Fired CO_2 Capture With CH_4-O_2 Firing," ASME Paper No. 95-CTP-79.

[7] Jericha, H., Lukasser, A., and Gatterbauer, W., 2000, "Der "Graz Cycle" für Industriekraftwerke gefeuert mit Brenngasen aus Kohle- und Schweröl-vergasung" (in German), VDI Berichte 1566, VDI Conference Essen, Germany.

[8] Jericha, H., and Göttlich, E., 2002, "Conceptual Design for an Industrial Prototype Graz Cycle Power Plant," ASME Paper No. 2002-GT-30118.

[9] Jericha, H., Göttlich, E., Sanz, W., and Heitmeir, F., 2003, "Design Optimization of the Graz Cycle Prototype Plant," J Eng. Gas Turbines Power, **126**, pp. 733–740.

[10] Heitmeir, F., Sanz, W., Göttlich, E., and Jericha, H., 2003, "The Graz Cycle—A Zero Emission Power Plant of Highest Efficiency," XXXV Kraftwerkstechnisches Kolloquium, Dresden, Germany.

[11] SimTech Simulation Technology, 2003, "IpsePro Overview," http://www.simtechnology.com/IPSEpro

[12] Wagner, W., and Kruse, A., *Properties of Water and Steam*, Springer-Verlag, Berlin, 1998.

[13] Sievers, U., 1984, *Die thermodynamischen Eigenschaften von Kohlendioxid* (in German), VDI Verlag, Düsseldorf, Fortschritt-Berichte VDI, Reihe 6, Energietechnik, Nr. 155.

[14] Jordal, K., Bolland, O., and Klang, A., 2003, "Effects of Cooled Gas Turbine Modelling for the Semi-Closed O2/CO_2 Cycle With CO_2 Capture," ASME Paper No. 2003-GT-38067.

[15] David, J., 2000, "Economic Evaluation of Leading Technology Options for Sequestration of Carbon Dioxide," Master thesis, Massachusetts Institute of Technology, Cambridge, MA.

[16] Göttlicher, G., 1999, *Energetik der Kohlendioxidrückhaltung in Kraftwerken* (in German), VDI Verlag, Düsseldorf. Fortschritt-Berichte VDI, Reihe 6, Energietechnik, Nr. 421.

[17] Gas Turbine World, 2003, *2003 Handbook for Project Planning, Design and Construction*, Pequot Publishing, New Haven, CT.

Downloaded 02 Jun 2010 to 171.66.16.98. Redistribution subject to ASME license or copyright; see http://www.asme.org/terms/Terms_Use.cfm

Effect of the Specific Heat Ratio on the Aerodynamic Performance of Turbomachinery

Stephen K. Roberts
e-mail: sroberts@mae.carleton.ca

Steen A. Sjolander
e-mail: ssjoland@mae.carleton.ca

Department of Mechanical and Aerospace Engineering,
Carleton University,
3135 MacKenzie Building,
Ottawa, ON K1S 5B6, Canada

Many gases, including carbon dioxide and argon, have been considered as alternative working fluids to air in a number of design studies for closed and semi-closed gas turbine engines. In many of these studies, it has been assumed that if the gas constant R and specific heat ratio γ are included in the speed and flow parameters, the compressor map or turbine characteristic is applicable to other working fluids. However, similarity arguments show that the isentropic exponent itself is a criterion of similarity and that the turbomachinery characteristics, even when appropriately nondimensionalized, will, in principle, vary as the γ of the working fluid varies. This paper examines the effect of γ on turbomachinery characteristics, mainly in terms of compressors. The performance of a centrifugal compressor stage was measured using air (γ=1.4), CO_2 (γ=1.29), and argon (γ=1.67). For the same values of the nondimensional speed, the pressure ratio, efficiency, and choking mass flow were found to be significantly different for the three test gases. The experimental results have been found to be consistent with a CFD analysis of the impeller. Finally, it is shown that the changes in performance can be predicted reasonably well with simple arguments based mainly on one-dimensional isentropic flow. These arguments form the basis for correction procedures that can be used to project compressor characteristics measured for one value of γ to those for a gas with a different value. [DOI: 10.1115/1.1995767]

Introduction

Although gas turbine engines used in power generation are relatively clean burning, the carbon dioxide emitted by open-cycle gas turbine engines contributes to the greenhouse gas content of the earth's atmosphere. Growing concern about global warming and climate change make it desirable to reduce the greenhouse gas emissions from all fossil fuel combustion, including that in gas turbine engines.

The use of CO_2 as the primary working fluid in a semi-closed cycle has been proposed as one method for eliminating the emission of CO_2 from gas turbine engines in some applications. A clean hydrocarbon fuel and the oxygen needed for combustion would be injected into the combustion chamber. The only products of combustion would be water vapor and CO_2. The water can be condensed and removed, and the excess CO_2 generated by the combustion of the fuel can be bled from the circuit and safely disposed of, or used industrially.

A number of design studies have been conducted to determine the viability of semi-closed O_2/CO_2 combustion gas turbine cycles [1–6]. These studies address many important issues about the plant performance. However, the authors have generally assumed that if the fluid properties are retained in the speed and flow parameters, then a component performance map is valid for any fluid that can be modeled as an ideal gas. As will be shown in the next section, similarity arguments indicate that for an ideal gas the performance of a turbomachine is, in fact, a function of four nondimensional parameters: appropriately nondimensionalized speed and flow parameters, the Reynolds number, and the specific heat ratio γ. The influence of the Reynolds number is reasonably well understood, and standard corrections are available for predicting the performance of a turbomachine from performance data obtained for the same machine at a different Reynolds number. However, there seems to be very little discussion in the literature of the influence of γ on compressor and turbine aerodynamic characteristics. In a couple of studies [4,6], the authors appear to be aware that matching of the speed and flow parameters for a given compressor using two different working fluids will not necessarily result in the same pressure ratio and efficiency, but they do not quantify the effect and implicitly assume that it is small.

The ASME Power Test Code for compressors and exhausters (ASME PTC 10) [7] provides an approximate method for predicting the speed at which a compressor must be operated to produce the same pressure ratio using a different gas. The method can be modified to approximately predict the pressure ratio that would result for a compressor operating at the same speed parameter using a substitute working fluid, but the underlying assumption is that there is no effect of the isentropic exponent on the losses. Thus, the results of such an analysis do not necessarily permit engineers to predict component performance with sufficient accuracy for design purposes when substitute gases are used.

The present study was conducted to clarify the influence of γ on turbomachinery characteristics. It is part of a larger study related to semi-closed gas turbines using CO_2 as the primary working fluid. The turbomachinery in such engines will see values of γ significantly different from that in air: about 1.29 for the compressor and as low as 1.18 at the turbine inlet condition.

Three approaches were used in the study. First, the characteristics of a small centrifugal compressor stage were measured for three different working fluids: air (γ=1.4), CO_2 (γ=1.29), and argon (γ=1.67). Second, computational fluid dynamics (CFD) calculations were conducted for the rotor for the same working fluids. The computations were conducted for constant Reynolds number, which was not achievable in the experiment. In addition, the computations allowed the choking mass flow rate to be determined, whereas it was not possible to achieve choking in the test rotor. Finally, an attempt was made to devise simple arguments,

Contributed by the International Gas Turbine Institute (IGTI) of THE AMERICAN SOCIETY OF MECHANICAL ENGINEERS for publication in the ASME JOURNAL OF ENGINEERING FOR GAS TURBINES AND POWER. Paper presented at the International Gas Turbine and Aeroengine Congress and Exhibition, Amsterdam, The Netherlands, June 3–6, 2002. Paper No. 2002-GT-30410. Manuscript received by IGTI, December 1, 2001, final revision, March 1, 2002. Associate Editor: E. Benvenuti.

Copyright © 2005 by ASME

Downloaded 02 Jun 2010 to 171.66.16.98. Redistribution subject to ASME license or copyright; see http://www.asme.org/terms/Terms_Use.cfm

based mainly on one-dimensional and isentropic flow, to explain the performance differences observed in both the measurements and the CFD computations.

Similarity Considerations

Assuming the working fluid is a perfect gas, it requires eight independent parameters to fully specify the performance of a particular member of a family of geometrically similar turbomachines

$$N, D, \dot{m}, \begin{pmatrix} a_{01} \\ or \\ T_{01} \end{pmatrix}, \begin{pmatrix} P_{01} \\ or \\ \rho_{01} \end{pmatrix}, \mu, R, \gamma$$

With eight independent parameters and four basic dimensions (mass, length, time, and temperature) Buckingham's Π theorem indicates that the independent parameters can be grouped into four nondimensional independent groups (or criteria of similarity) [8]:

i. Speed parameter:

$$\Pi_N = \frac{ND}{a_{01}} = \frac{ND}{\sqrt{\gamma R T_{01}}} = \frac{N}{\sqrt{T_{01}}} \frac{D}{\sqrt{\gamma R}} \tag{1}$$

The speed parameter is effectively the Mach number based on the rotor tip speed.

ii. Flow parameter:

$$\Pi_m = \frac{\dot{m}}{\rho_{01} a_{01} D^2} = \frac{\dot{m}}{\frac{P_{01}}{RT_{01}} \sqrt{\gamma R T_{01}} D^2} = \frac{\dot{m}\sqrt{T_{01}}}{P_{01}} \sqrt{\frac{R}{\gamma}} \frac{1}{D^2} \tag{2}$$

The flow parameter can also be interpreted as the Mach number based on the axial velocity through the machine.

It is worth noting that the speed and flow parameters (Eqs. (1) and (2)) would still represent valid nondimensional parameters if the isentropic exponent was omitted. However, they could then no longer be interpreted as Mach numbers, thus losing their physical significance.

iii. Reynolds number:

$$\mathrm{Re}_D = \frac{\rho_{01} N D^2}{\mu} \tag{3a}$$

For centrifugal compressors, the blade speed at the impeller tip U_2 and the vane height at the tip b_2 are sometimes used as the velocity and length scales in the Reynolds number. Thus,

$$\mathrm{Re}_{b2} = \frac{\rho_{01} U_2 b_2}{\mu} \tag{3b}$$

iv. Specific heat ratio (which is already nondimensional):

$$\gamma = \frac{c_p}{c_v} \tag{4}$$

γ relates changes in pressure to ideal changes in density and temperature in a compressible flow and therefore is also referred to as the isentropic exponent.

All other performance parameters are then functions of these four independent parameters

$$\frac{P_{02}}{P_{01}}, \eta, etc. = fns\left(\frac{N}{\sqrt{T_{01}}} \frac{D}{\sqrt{\gamma R}}, \frac{\dot{m}\sqrt{T_{01}}}{P_{01}} \sqrt{\frac{R}{\gamma}} \frac{1}{D^2}, \mathrm{Re}_{b2}, \gamma \right)$$

In turbomachinery, compressor performance is normally presented on a compressor map, with the pressure ratio plotted against the mass flow parameter, and with lines of constant speed parameter and efficiency also shown. Since compressors are normally designed and tested using the same working fluid, the fluid properties are usually omitted from the speed and flow parameters, and the isentropic exponent is not included as a criterion of similarity. However, such a map is only valid for fixed values of both the Reynolds number and the isentropic exponent. There is not normally a strong effect of the Reynolds number on the performance of the compressor, except at very low values of machine Reynolds number (typically $\mathrm{Re}_{b2} < 90{,}000$ for centrifugal compressors). Also, empirical corrections to the efficiency are widely available in the literature, and minor corrections can also be made to the pressure ratio and flow parameter [9] to account for differences in machine Reynolds number between the test and operating conditions. On the other hand, the literature provides virtually no guidance on the influence of γ on the performance map.

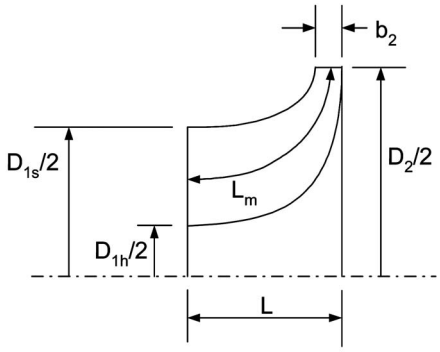

Z	Number of full vanes	6
Z_s	Number of splitter vanes	6
D_2	Impeller tip diameter	76.2 mm
b_2	Vane width at impeller tip	4.8 mm
D_{1h}	Inlet hub diameter	18.3 mm
D_{1s}	Inlet shroud diameter	54.0 mm
β_1'	Vane inlet angle at mean line	50°
β_2'	Backsweep Angle	27°
L	Impeller axial length	25 mm
L_m	Meridional length at meanline	44 mm

Fig. 1 Summary of centrifugal impeller geometry

Experimental Apparatus

Test Compressor. The centrifugal compressor from a Turbonetics T04-E 50 trim turbocharger was selected for the performance tests. The compressor geometry is summarized in Fig. 1; drawings for the rotor were not available, and the dimensions were estimated from the actual rotor. The aerodynamic performance of turbocharger components is generally lower than that of the turbomachines found in gas turbine engines, but they provide an inexpensive option for generic performance investigations. In addition, the compressor map, complete with efficiency contours, was available from the supplier, providing a means of benchmarking the compressor test stand. The compressor rotor is followed by a short vaneless diffuser and a volute.

Test Stand. The compressor was driven using the attached radial turbine as an air turbine. The compressed air to drive the air turbine was obtained from four large storage tanks that were pressurized to approximately 8 bar prior to a test. Rotational speed was maintained by using a feedback control to provide constant pressure at the air turbine inlet. For the majority of the tests, the compressed air supply allowed for steady-state operation of the compressor for the minimum 15 min duration recommended in ASME PTC 10.

Downloaded 02 Jun 2010 to 171.66.16.98. Redistribution subject to ASME license or copyright; see http://www.asme.org/terms/Terms_Use.cfm

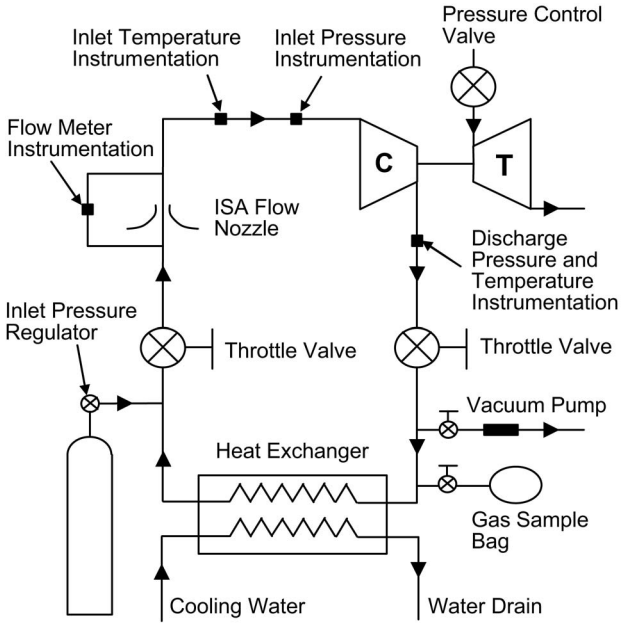

Fig. 2 Schematic of test rig

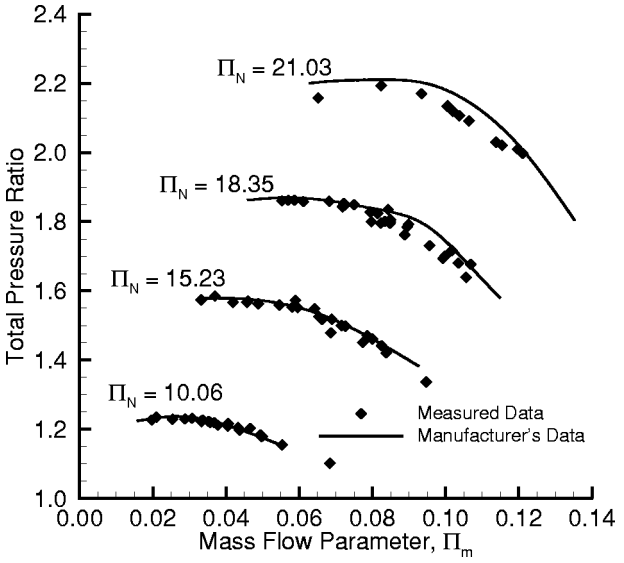

Fig. 3 Comparison of measured pressure ratio with manufacturer's data for air

The test stand (shown schematically in Fig. 2) was constructed to comply with the guidelines of ASME PTC 10. It consists of a closed-loop test circuit that was instrumented to measure the compressor rotational speed, flow rate, and the inlet and discharge pressures and temperatures. These measurements provide sufficient data to evaluate the pressure ratio, mass flow parameter, speed parameter, machine Reynolds number, and the isentropic efficiency.

Flow rate was measured using an ISA short radius flow nozzle. The inlet static pressure was measured using four static taps spaced at 90 deg, and the inlet stagnation temperature was measured using a total temperature probe with a Type-E thermocouple. The discharge stagnation conditions were measured using a combination probe incorporating a Type-E thermocouple and a Kiel-type total pressure probe. Rotational speed was measured using an infrared tachometer and frequency counter.

The flow meter differential pressure was measured with an Omega PX-139 ±5 psi (±35 kPa) differential transducer. All other pressures was measured by using a Scanivalve connected to an Omega PX-613 0–60 psig (0–400 kPa) pressure transducer.

The data were collected using an HP 3852A data acquisition system. For each data point, 200 pressure and temperature samples were collected at a sampling rate of 2 kHz, and five discrete speed measurements of 1 s duration were taken and averaged. The measured speed varied up to 60 rpm for a given test point, compared with typical absolute speeds of about 40,000–95,000 rpm. The compressor casing, inlet, and discharge were insulated to minimize any heat transfer between the compressor and the temperature measurement stations.

It was found that a small amount of gas could leak into or out of the test circuit through the shaft bearings at the compressor and turbine. Therefore, for the tests with CO_2 and argon, the test gas was continually supplied to the circuit upstream of the flow meter, through a pressure regulator, to keep the circuit above atmospheric pressure and to compensate for leakage out of the circuit. This resulted in a very high concentration of the desired test gas in the test circuit and also, through the choice of circuit pressure level, allowed limited control over the machine Reynolds number. Gas samples were taken frequently during the non-air test runs and analyzed using gas chromatography. The majority of the samples were found to have in excess of 99.5% molar fraction of the desired test gas.

Commissioning of the Test Stand. In order to verify the proper functioning of the test stand, it was operated first using air as the working fluid, and the experimental results were compared to the manufacturer's published data. Figures 3 and 4 show the measured pressure ratio and isentropic efficiency versus the mass flow parameter and compare the results to data supplied by the manufacturer. For reference, the maximum value of the speed parameter (Π_N) corresponds to an absolute speed of about 96,000 rpm for air, 89,000 rpm for argon and 75,000 rpm for CO_2. The measurements for a given speed line include data obtained on different days to check the repeatability of the results.

The measured results are seen to have an acceptable level of scatter and to be in good agreement with the manufacturer's data. The differences between the measured performance and the manufacturer's data, particularly at high pressure ratios, may be due to

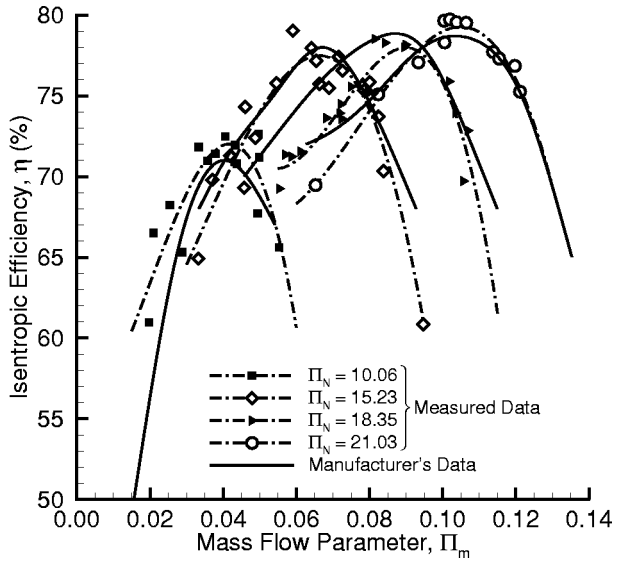

Fig. 4 Comparison of measured efficiency with manufacturer's data for air

Downloaded 02 Jun 2010 to 171.66.16.98. Redistribution subject to ASME license or copyright; see http://www.asme.org/terms/Terms_Use.cfm

normal manufacturing tolerances and variability. The compressor volute was delivered as cast, and it can be expected that there would be some variation in performance for different machines of the same model because of manufacturing differences in the passage area and surface roughness of the volute.

In the tests conducted using air, changes in relative humidity were found to have a noticeable effect on both the flow rate and efficiency measurements. This is believed to be the main source of scatter in Figs. 3 and 4. Essentially pure, dry CO_2 and argon were used in the subsequent tests and the scatter in the results for these gases was found to be noticeably less.

Computational Approach

In addition to the measurements, CFD computations were made for the rotor. Since only the approximate rotor geometry was known, and the diffuser and volute were not modeled, the CFD results were not intended for direct comparison to the measurements. Instead, they were intended to investigate two aspects of the performance that could not be examined experimentally.

In the first place, because of the need to control the circuit leakage it was not possible to maintain constant Reynolds number, for a given speed parameter, for all three test gases. However, the Reynolds number could be fixed in the computations, and the calculations were therefore used to provide supporting evidence that the performance differences observed in the measurements were due to the differences in γ, not the modest variations in Reynolds number. Second, Fig. 3 shows that the losses in the test circuit are too high to allow choking of the present rotor. In addition to the pressure ratio and efficiency, the choking mass flow rate for a given speed parameter is also an important aspect of the performance. This is particularly true for the turbines in gas turbine engines: the choking mass flow rate for the turbine plays an important part in determining the steady state operating line of the compressor to which it is connected. The CFD computations were used to investigate the effect of γ on the choking mass flow rate.

The computations were performed using CFX-BLADEGEN+, which is a two-part code consisting of a geometric design module and a CFD module. The CFD module is based on the CFX-5 Navier-Stokes code. Some features of the Navier-Stokes code have been disabled or supplied with default values to allow rapid specification of the computational case. For example, only one turbulence model is available, and the unstructured grid is generated semi-automatically based on the specification of a single grid refinement factor that controls the general grid density. The CFD module is intended to allow rapid aerodynamic screening of trial turbomachine geometries generated with the CAD module, rather than to give the final, detailed aerodynamic performance estimates. In the present context, use of this code also answered the question of whether the aerodynamic analysis tools currently used in turbomachinery design satisfactorily capture the influence of fluid properties, such as γ.

For the present calculations, an approximate geometric model of the rotor was created based on the dimensions given in Fig. 1. The computational domain included a short length of channel upstream and downstream of the rotor and extended circumferentially over one main vane spacing. Thus, it also included one of the splitter vanes. An intermediate grid density was used, giving about 250,000 tetrahedral and prismatic cells. Both the grid density and convergence criterion were varied to confirm that the overall performance results were adequately converged and reasonably grid independent.

Results and Discussion

Effect of γ on Pressure Ratio and Choking Mass Flow Rate. Figure 5 shows the measured pressure ratios as a function of flow parameter and speed parameter for the three test gases. The results for air from Fig. 3 are represented by a mean line to avoid clutter.

There is clearly a very noticeable effect of the working fluid on the pressure ratio. In the middle of the mass flow range, argon gave the highest pressure ratio and CO_2 the lowest. However, the CO_2 operating line crosses the line for air, suggesting that the choking mass flow rates may also be different for the different gases. As noted, this effect could only be investigated computationally. Figure 6 shows the rotor pressure ratios predicted by CFD for the three gases at a speed parameter of 21.03. Since the predictions do not include the losses in the diffuser and volute, the pressure ratios are higher than the stage pressure ratios shown in Fig. 5.

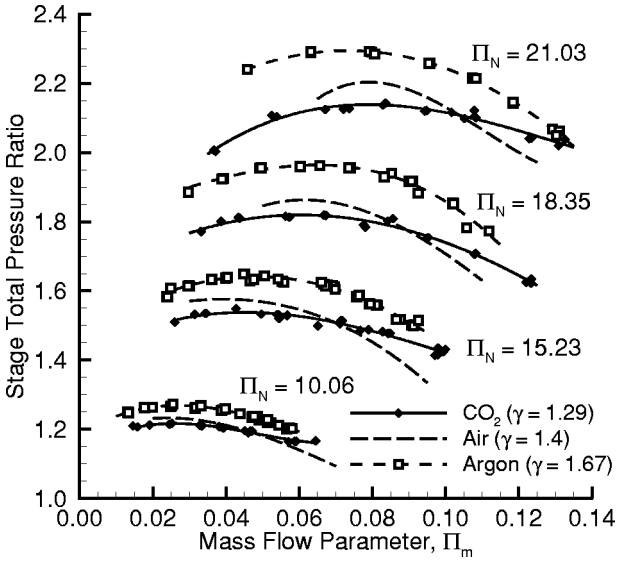

Fig. 5 Measured stage pressure ratio as function of γ

As mentioned earlier, it was not possible to maintain the same experimental Reynolds numbers, for a given value of speed parameter, for the three different gases. For example, for the Π_N =21.03 speed lines, the average Reynolds numbers (Re_{b2}) for air, CO_2, and argon were, respectively, about 82,000, 190,000, and 135,000. By comparison, the corresponding CFD calculations were all performed at a Reynolds number of 132,000. The good agreement between the computations and measurements, in both the trends and magnitudes of the changes in pressure ratio with

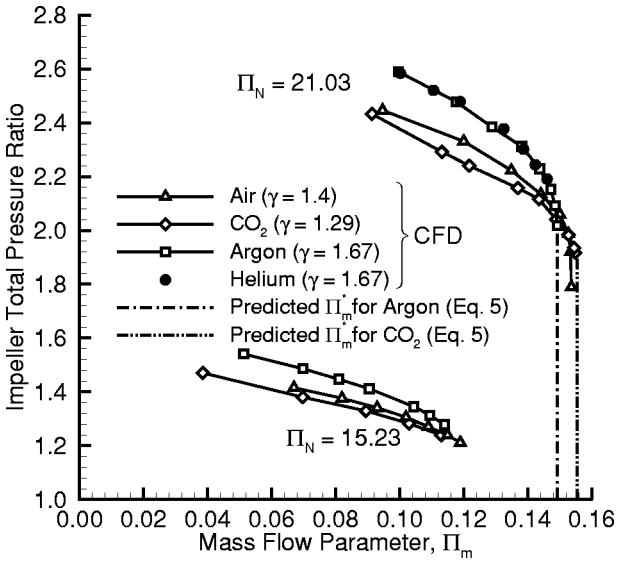

Fig. 6 CFD prediction of rotor pressure ratio and choking mass flow rate as function of γ

Downloaded 02 Jun 2010 to 171.66.16.98. Redistribution subject to ASME license or copyright; see http://www.asme.org/terms/Terms_Use.cfm

working fluid, demonstrates that the differences in behavior seen in Fig. 5 are predominantly due to the differences in γ, rather than Reynolds numbers. Also shown in Fig. 6 is the predicted performance with helium. Helium has the same γ as argon, but all other fluid properties are significantly different; for example, the values of R, c_p, and thermal conductivity k differ by about a factor of 10. The close agreement between the results for helium and argon lends support to the conclusion that the observed variations in behavior with working fluid are due exclusively to the differences in γ.

The CFD calculations also confirm that the crossing of the characteristics seen in Fig. 5 is the result of differences in the choking mass flow parameters. As seen from Fig. 6, the CFD indicates that the value of the mass flow parameter at choking varies inversely with γ, with argon having the lowest and CO_2 the highest values of Π_m^*.

Considering the question of choking further, for one-dimensional, isentropic flow of a perfect gas, the continuity equation can be written as follows:

$$\dot{m} = \frac{P_0}{\sqrt{T_0}} \sqrt{\frac{\gamma}{R}} AM \left(1 + \frac{\gamma - 1}{2}\right)^{-(1/2)[(\gamma+1)/(\gamma-1)]}$$

where A is the area of the channel and M the flow Mach number. Rewriting this in the form used for the present mass flow parameter and setting $M=1$ so that it corresponds to choked flow in the throat, the ratio of the values of Π_m^* for the same machine operating with two different working fluids A and B can be expressed as follows:

$$\frac{\Pi_{mB}^*}{\Pi_{mA}^*} = \frac{\left(\frac{\gamma_B + 1}{2}\right)^{-(1/2)[(\gamma_B+1)/(\gamma_B-1)]}}{\left(\frac{\gamma_A + 1}{2}\right)^{-(1/2)[(\gamma_A+1)/(\gamma_A-1)]}} \tag{5}$$

Equation (5) predicts that at choking the value of Π_m for CO_2 will be 1.012 times that for air, and that for argon this factor is 0.972. The projected values for CO_2 and argon, starting from the computed Π_m at choking for air, are shown in Fig. 6. In a centrifugal compressor, the throat typically occurs near the vane leading edges, where the flow is certainly not one-dimensional. Nevertheless, Eq. (5) appears to provide very reasonable estimates of the changes in choking mass flow parameter with γ.

The effect of γ on the pressure ratio can also be approximately predicted by considering an idealized compression process. Assuming there are no losses (i.e., isentropic compression) and no slip at the impeller discharge, it can be shown that matching of the speed and flow parameters also implies similarity of the flow coefficient ϕ and work coefficient ψ where

$$\phi = \frac{C_{a1}}{U_2}, \quad \psi = \frac{\Delta h_0}{U_2^2} \tag{6}$$

and Δh_0 is the total enthalpy rise across the compressor. It seems reasonable to assume that the work coefficients for two different working fluids would still be roughly equal when the losses and slip factor are considered, although this assumption is not strictly valid. A similar simplifying assumption is made in the ASME Power Test Code [7] for predicting the speed at which a compressor should be operated at to obtain the same pressure ratio using a substitute gas.

For a perfect gas, Δh_0 is related to the pressure ratio by

$$\Delta h_0 = \frac{c_p T_{01}}{\eta} (\mathrm{PR}^{\gamma-1/\gamma} - 1) \tag{7}$$

where η is the compressor isentropic efficiency. Then equating the work coefficients ψ, substituting from Eq. (7) for Δh_0, and using the equality of the speed parameters to relate the values of U_2, it can be shown that for two perfect gases A and B:

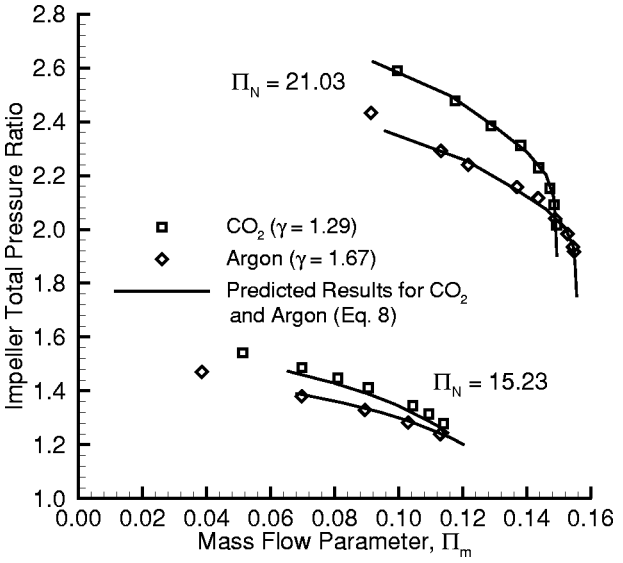

Fig. 7 Predicted pressure ratios for argon and CO_2 using correction Eq. (8)

$$\mathrm{PR}_B = \left[\frac{\gamma_B - 1}{\gamma_A - 1}\left(\frac{\eta_B}{\eta_A}\right)(\mathrm{PR}_A^{\gamma_A - 1/\gamma_A} - 1) + 1\right]^{\gamma_B/\gamma_B - 1} \tag{8}$$

Note that γ is the only fluid property that appears in both correction formulas, Eqs. (5) and (8).

Direct application of Eq. (8), for a given value of the mass flow parameter Π_m, ignores the fact that choking occurs for different values of Π_m for different working fluids. Better results are obtained if the values of Π_m for fluid A are first normalized on the observed value at choking Π_{mA}^*. Equation (5) is used to predict Π_{mB}^* from Π_{mA}^*, and Eq. (8) is then used to predict PR_B from PR_A at the same values of Π_m/Π_m^*.

The procedure just outlined has been applied to project the impeller characteristic for argon from the computed characteristic for air shown in Fig. 6. The results are shown in Fig. 7, using typical values of the efficiency ratio from the next section. The projected pressure ratio is seen to be in good agreement with the CFD calculations.

Effects of γ on Efficiency. In addition to the changes in the pressure ratio and the mass flow parameter at choking, there is also a significant effect of γ on the efficiency of the compressor. Figures 8 and 9 show the measured efficiency values for argon and CO_2, respectively. In general, higher values of efficiency were measured for lower values of the isentropic exponent. To make this clearer, the estimated peak values of measured efficiency are plotted in Fig. 10. The results in Fig. 10 have been corrected to a common Reynolds number for each value of the speed parameter (e.g., $\mathrm{Re}_{b2}=110{,}000$ for $\Pi_N=21.03$) using the method of Strub et al. [9]. Comparison to Figs. 8 and 9 shows that the corrections were typically only a few tenths of a percentage point. This further supports the assertion that the performance differences are predominantly due to the differences in γ.

One anomalous case occurs with the lowest speed line for argon, for which higher values of efficiency were measured than for air. This is believed to be an experimental problem. In particular, heat transfer from the hot duct between the impeller and the location of the discharge total temperature measurement will result in erroneously high values of efficiency. Because the highest discharge temperatures were recorded for argon, and also because argon has the lowest specific heat (c_p) of the three test gases, heat transfer through the insulation will have the greatest impact on the measured efficiency for argon, particularly at low mass flow rates, such as those seen for the lowest speed line.

Downloaded 02 Jun 2010 to 171.66.16.98. Redistribution subject to ASME license or copyright; see http://www.asme.org/terms/Terms_Use.cfm

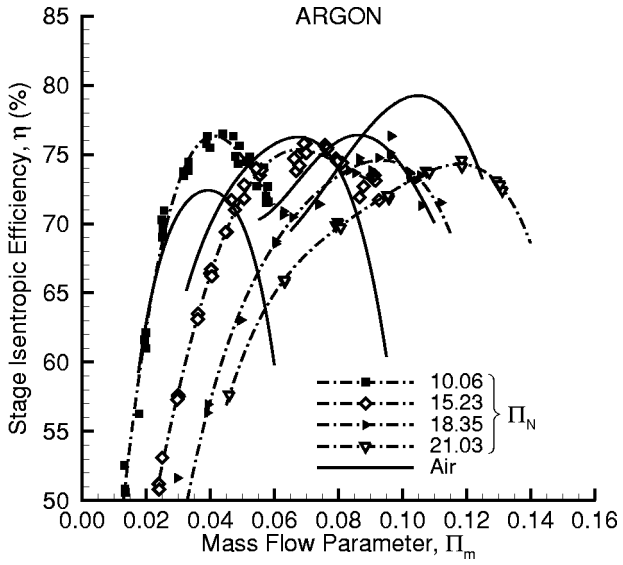

Fig. 8 Measured stage isentropic efficiency for argon; comparison with results for air

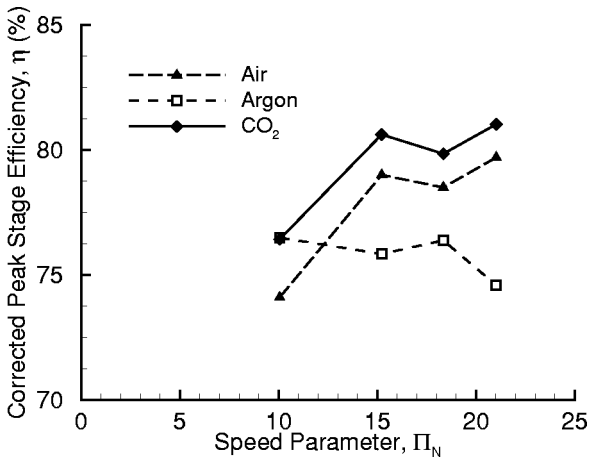

Fig. 10 Variation of measured peak stage efficiency with speed parameter (corrected for Reynolds number)

It is also noticeable that the peak efficiencies for both argon and CO_2 occur at slightly higher values of the mass flow parameter than for air. The reason for this is not known.

Figure 11 shows the corresponding impeller efficiencies as computed for $\Pi_N=15.23$ and $\Pi_N=21.03$. The trend in efficiency with γ is seen to be consistent with that in the measurements. Figure 11 also includes the computed results for helium. As with the pressure ratio, the results are almost identical for helium and argon. This again supports the conclusion that γ is the dominant fluid property that determines the variation in turbomachinery performance with changing working fluid.

For an isentropic compression, the ideal compression ratio is related to the pressure ratio as follows:

$$\frac{\rho_{02}}{\rho_{01}} = \left(\frac{P_{02}}{P_{01}}\right)^{1/\gamma} \tag{9}$$

Thus, for two identical compressors with the same inlet density and operating at the same pressure ratio, but with different working fluids, the fluid with the higher value of γ will have a lower discharge density. In order to satisfy continuity, the discharge velocity must, therefore, be higher. Since many of the contributions to the losses vary as the square of the velocity, the higher discharge velocity should result in higher losses in the impeller and all downstream components. This is consistent with the changes in efficiency with working fluid seen in the experiment and the computations.

Starting from Eq. (9) and assuming that the losses (and therefore the efficiency) scale on the dynamic pressure based on the impeller outlet relative velocity, it is possible, with the help of several other simplifying assumptions, to derive the following expression relating the efficiencies for the same machine operating with two different working fluids A and B [10]:

$$\frac{1-\eta_A}{1-\eta_B} = \frac{\gamma_A}{\gamma_B} \tag{10}$$

Figure 12 shows the results of using Eq. (10) to predict the efficiency for argon and CO_2 from the computed variation for air. Equation (10) is seen to somewhat overpredict the changes in efficiency compared to those predicted by the CFD. The overprediction is probably because of violation of some of the simplifying

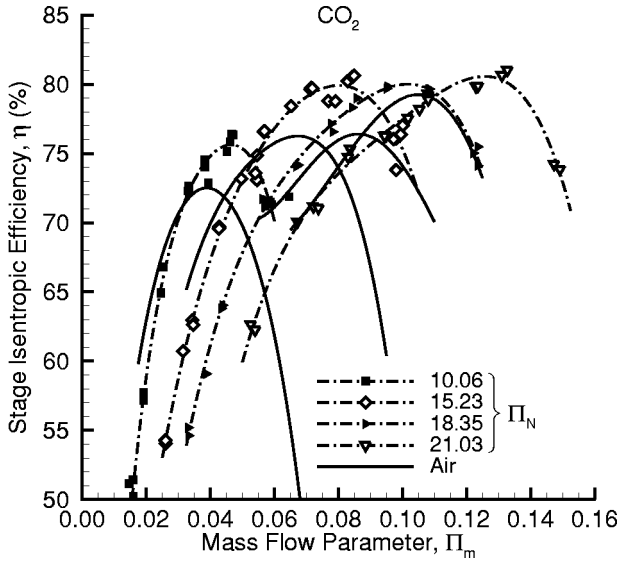

Fig. 9 Measured stage isentropic efficiency for CO_2; comparison with results for air

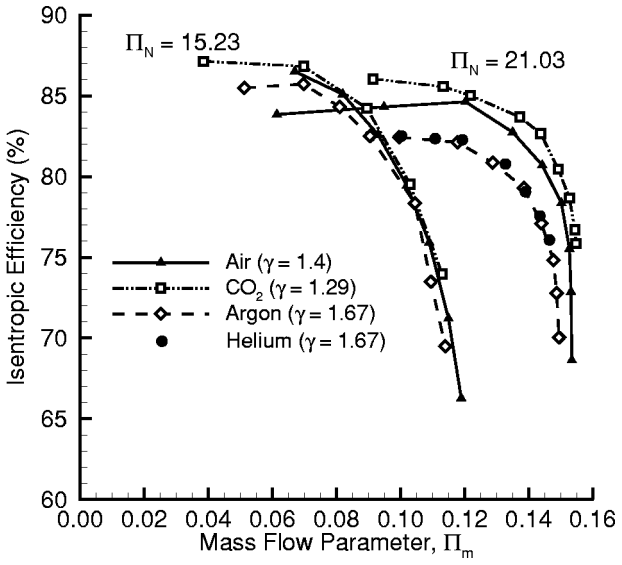

Fig. 11 Impeller efficiencies for air, argon, and CO_2 as predicted by CFD

Downloaded 02 Jun 2010 to 171.66.16.98. Redistribution subject to ASME license or copyright; see http://www.asme.org/terms/Terms_Use.cfm

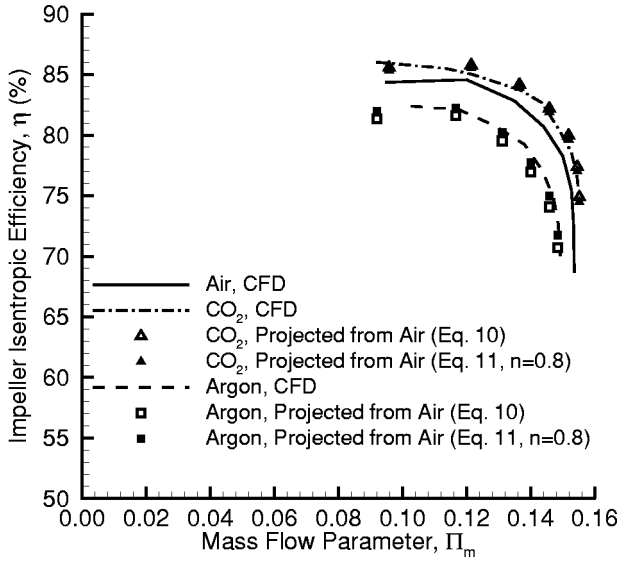

Fig. 12 Predicted impeller efficiencies using correction Eqs. (10) and (11)

assumptions used to derive at Eq. (10). In particular, there are a number of loss mechanisms present in the stage that do not depend on the impeller outlet conditions. For example, the inlet shock losses and losses due to incidence at the impeller leading edge are dependent on the flow conditions at the stage inlet. Therefore, it is plausible that Eq. (10) will tend to overpredict the influence of γ.

The following modified formula is tentatively proposed:

$$\frac{1-\eta_A}{1-\eta_B}=\left(\frac{\gamma_A}{\gamma_B}\right)^n \tag{11}$$

where a value of $n<1.0$ will reduce the influence of γ. An expression of this form has often been used to correct efficiency for the effects of varying Reynolds number [7,9]. As shown in Fig. 12, a value of $n=0.8$ appears to work well for both argon and CO_2.

Figure 13 shows the results of applying Eqs. (10) and (11) to the measured peak stage efficiencies. Although the scatter in the experimental data makes the assessment less clear, Eq. (11) with $n=0.8$ appears to give reasonable corrections for these data as well.

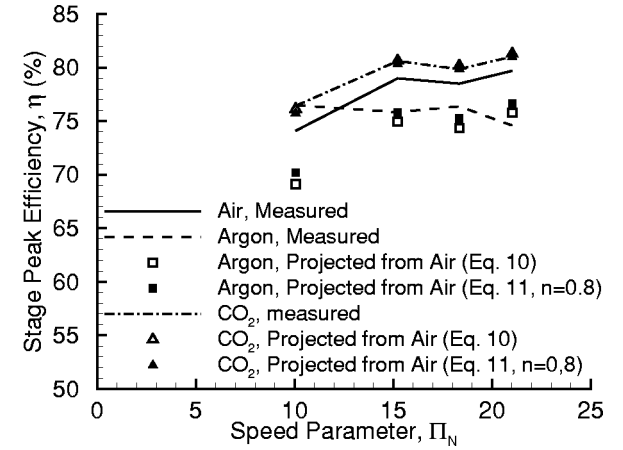

Fig. 13 Predicted stage efficiencies using correction Eqs. (10) and (11)

Conclusions

The effect of the isentropic exponent γ on the aerodynamic performance of turbomachinery has been investigated both experimentally and computationally. The results of the investigation have confirmed that γ is an important criterion of similarity in the performance of turbomachinery. For compressors, in particular, the pressure ratio, the choking mass flow rate, and the isentropic efficiency were all found to be significantly affected by changes in γ.

Based on simple arguments, methods have been developed for predicting the changes in performance of compressors when substitute gases are used. The correction formulas for the pressure ratio and choking mass flow rate produced very good results without apparent need for further empirical adjustments. The initial correction formula for efficiency appeared to overestimate the changes with γ. A simple modification, involving a single empirical factor, improved the results noticeably. The value of the empirical factor was determined from the present limited data, and it would be desirable to confirm it using a larger body of data.

In semi-closed O_2/CO_2 gas turbine engines, the turbines will also see values of γ that differ substantially from those experienced by the turbines in conventional open-cycle engines or in the typical rotating rigs used for prototype turbine testing and development. Thus, there is a need to conduct a similar investigation to the present one for turbines.

Acknowledgment

The financial support of the CANMET Energy Technology Centre (Natural Resources Canada) and of the Natural Science and Engineering Research Council of Canada is gratefully acknowledged.

Nomenclature

a = speed of sound
b_2 = centrifugal compressor vane height at outlet
C = absolute fluid velocity
c_p = specific heat at constant pressure
c_v = specific heat at constant volume
D = impeller diameter
h_0 = total enthalpy ($\Delta h_0=c_p\Delta T_0$ for a perfect gas)
L = impeller axial length
L_m = impeller vane meridional length
$\dot{m}$ = mass flow rate
N = rotational speed (usually rpm)
P = pressure
PR = pressure ratio
R = perfect gas constant of the working fluid
Re = Reynolds number (Eqs. (3*a*) and (3*b*))
T = temperature
U = blade speed
β' = blade angle relative to meridional direction
γ = c_p/c_v=specific heat ratio (or isentropic exponent)
ϕ = flow coefficient (Eq. (6))
η = isentropic efficiency
ρ = fluid density
μ = fluid viscosity
ψ = work coefficient (Eq. (6))
Π_m = nondimensional mass flow parameter (Eq. (2))
Π_N = nondimensional speed parameter (Eq. (1))

Subscripts

a = axial component
h = value at hub
s = value at shroud
1 = impeller inlet
2 = impeller or stage outlet

Downloaded 02 Jun 2010 to 171.66.16.98. Redistribution subject to ASME license or copyright; see http://www.asme.org/terms/Terms_Use.cfm

01 = inlet stagnation condition
02 = outlet stagnation condition

Superscript

* = choked condition

References

[1] Navaratnam, M., 1994, "The Investigation of an Aero Derivative Gas Turbine Using Alternative Working Fluids in Closed/Semi Closed Cycles," M.Sc. thesis, Cranfield University, Cranfield, UK.

[2] Hunter, I. H., 1994, "Design of Turbomachinery for Closed and Semi-Closed Gas Turbine Cycles," M.Sc. thesis, Cranfield University, Cranfield, UK.

[3] Zhou, M., and Gauthier, J. E. D., 1998, "A Literature Survey on the Use of O_2/CO_2 Mixtures as the Primary Working Fluid in Combustion Engines," Mech. Eng. Report No. 980503, Royal Military College of Canada, Kingston, Canada.

[4] Mathieu, P., Dechamps, P., and Distelmans, M., 1994, "Concepts and Applications of CO_2 Gas Turbines," Technical Report, Université de Liège, Liège, Belgium.

[5] Ulizar, I., and Pilidis, P., 1999, "Handling of a Semiclosed Cycle Gas Turbine With a Carbon Dioxide-Argon Working Fluid," ASME Paper No. 99-GT-374.

[6] Jackson, J. B., Neto, A. C., Whellens, M. W., and Audus, H., 2000, "Gas Turbine Performance Using Carbon Dioxide as Working Fluid in Closed Cycle Operation," ASME Paper No. 2000-GT-153.

[7] Performance Test Code on Compressors and Exhausters, ASME PTC 10-1997.

[8] Kline, S. J., 1986, *Similitude and Approximation Theory*, Springer-Verlag, New York.

[9] Strub, R. A., Bonciani, L., Borer, C. J., Casey, M. V., Cole, S. L., Cook, B. B., Kotzur, J., Simon, H., and Strite, M. A., 1987, "Influence of the Reynolds Number of the Performance of Centrifugal Compressors," ASME J. Turbomach., **109**, pp. 541–544.

[10] Roberts, S. K., 2002, "Effects of Fluid Properties on the Aerodynamic Performance of Turbomachinery for Semi-Closed Cycle Gas Turbine Engines Using O_2/CO_2 Combustion," M.A.Sc. thesis, Carleton University, Ottawa, Canada.

Downloaded 02 Jun 2010 to 171.66.16.98. Redistribution subject to ASME license or copyright; see http://www.asme.org/terms/Terms_Use.cfm

Analysis of Tangential-Against-Rotation Injection Lomakin Bearings

Mihai Arghir
e-mail: mihai.arghir@lms.univ-poitiers.fr

Mathieu Hélène

Jean Frene

LMS, Université de Poitiers,
UFR Sciences SP2MI, Téléport 2,
Blvd. Pierre et Marie Curie, BP 30719,
86962 Futuroscope Chasseneuil Cedex, France

This work presents a thin film flow model for analyzing the static and dynamic characteristics of centered, eccentric or misaligned tangential-against-rotation injection Lomakin bearings. The Lomakin bearing is a recent device intended for use in modern turbomachinery and having characteristics similar to hybrid bearings. It can be described as an ensemble of two opposing straight annular seals separated by a circumferential feeding groove. The fluid is supplied to the groove via orifice restrictors. Their tangential inclination generates an against-rotation circumferential flow in the groove that further penetrates into the thin film. This effect, known from annular seals as the prerotation speed, improves the dynamic characteristics of the bearing. A good description of the flow in the circumferential groove and the thin film is obtained from a full Navier–Stokes calculation of the centered bearing. The zero and first order analyses are then carried out by recognizing the crucial importance of taking into account the interaction between the flow in the thin film lands, the circumferential groove and the supply orifices. Due to the high Reynolds number regime, the land flow is governed by the two-dimensional thin film inertia equations (the "bulk flow" model). A one-dimensional circumferential flow dominated by inertia forces is assumed to take place in the groove and is described by an appropriate bulk flow equation. The flows in the supply orifices, the groove and the thin film lands are linked together by the same mass flow rate balance algorithm as used for hydrostatic and hybrid bearings analysis. The algorithm is extended to Lomakin bearings by considering the groove areas surrounding each orifice as a row of intercommunicating feeding pockets. This approach enables the analysis of centered, eccentric or misaligned Lomakin bearings. Comparisons with water-lubricated test results are used to validate the present model. For the zero eccentricity case a good agreement is obtained for the cross-coupled stiffness and for the whirl frequency ratio. A parametric study shows the variation of the bearing characteristics with increasing static eccentricity or misalignment. [DOI: 10.1115/1.1924632]

Introduction

The answer to the question as to why a rotating journal supported by a fluid bearing might induce machinery vibrations has been known for a long time. Experience has shown that sealing devices are also responsible for instabilities to the same extent as rotor supporting devices. This unwanted effect is an intrinsic part of the flow mechanism acting between the journal and the bearing or more generally between the rotor and the stator of rotating machinery. For a centered journal, the circumferential flow between its surface and a closely spaced housing is of the Couette-type with a velocity averaged over the film thickness equal to half the speed of the rotor. By using a simple flow rate balance, Hagg [1] showed that this flow can be the source of self-induced vibrations with a frequency equal to half the rotation speed of the journal. This is due to the fact that the sinusoidal-like pressure field that is generated when the rotor is slightly displaced from its centered position has a component normal to the direction of the perturbation. A more or less significant additional axial flow, as encountered in annular seals or finite length bearings, will not modify this destabilizing feature. Therefore the discouraging conclusion is that the destabilizing character of the perturbation-induced pressure field is intrinsically linked to the Couette flow engendered by a centered journal rotating inside a very closely-spaced housing. The question is then how to modify the sinusoidal-like pressure field in order to eliminate (or at least to diminish) its destabilizing feature. A partial answer is given by the cavitation effect that inherently modifies the pressure field and renders the journal bearing stable. The constraints and limitations are that, in order to have cavitation, the journal bearing must possess a static eccentricity which only a load can provide. Moreover, in most situations, cavitation can only be avoided and its occurrence can barely be controlled. Cavitation is therefore more an unexpected bonus than a real solution to stability problems.

Solutions for Improving the Stability of Bearings and Seals. Real solutions to stability problems were found by voluntarily modifying the sinusoidal-like pressure field of a circular journal bearing. The first solutions, represented by the step bearing and by the lobed bearing, modified the pressure field in a favorable manner by adding many active zones which stabilized the bearing. They were closely followed by tilting pad journal bearings that represented a better but a far more elaborate technical solution. An extensive description of these bearings can be found for example in [2,3]. The source of the stabilizing effect was the same and was to be found in the partition of the bearing circumference into preloaded or offset lobes or pads. Many active zones are thus created even at very low eccentricities and the sinusoidal-like pressure field is eliminated. None of these technical solutions tried to modify the circumferential flow, each lobe or pad being dominated by the Couette flow characteristics.

A second category consists of technical solutions that try to modify the $0.5R\Omega$ circumferential flow. A conceptually very simple solution would be to manufacture an artificially roughened

Contributed by the International Gas Turbine Institute (IGTI) of The American Society of Mechanical Engineers for publication in the ASME Journal of Engineering for Gas Turbines and Power. Paper presented at the International Gas Turbine and Aeroengine Congress and Exhibition, Atlanta, GA, June 16–19, 2003. Paper No. 2003-GT-38411. Manuscript received by IGTI, October 1, 2002, final revision, March 1, 2003. Associate Editor: H. R. Simmons.

Copyright © 2005 by ASME

Downloaded 02 Jun 2010 to 171.66.16.98. Redistribution subject to ASME license or copyright; see http://www.asme.org/terms/Terms_Use.cfm

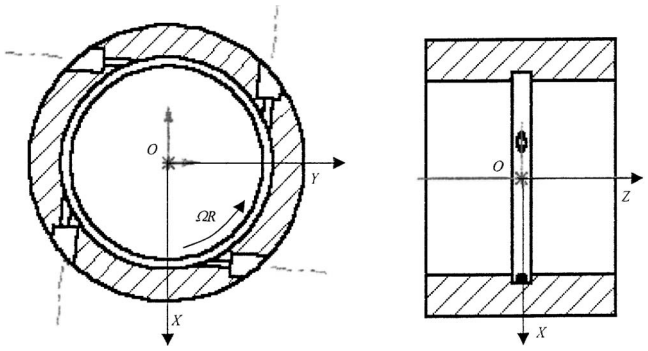

Fig. 1 Lomakin bearing geometry and coordinate system

bearing and a smooth journal. The high friction factor of the stationary surface would then obviously diminish the circumferential flow. For annular seal problems, the favorable effects of hole-pattern machined stators (named honeycomb surfaces when the hole-pattern density is maximum) were first described by von Pragenau [4] and are now extensively presented in the literature [3]. If the flow rate is high enough, a tangential-against-rotation supply might be an efficient solution. This is the case with straight or labyrinth annular seals. Thus, the swirl-brake [5] is an efficient device located just before the inlet section of the annular seal and this enables the circumferential component of the entering flow (usually known as swirl) to be controlled. In other cases, a tangential-against-rotation flow rate is supplied directly into the annular seal immediately after the inlet section [6]. The efficiency of these solutions will depend on the seal length and on the angular velocity of the rotor because in all cases the circumferential flow will develop towards a Couette one. This is why combining two means of reducing the circumferential flow (for example, the swirl-brake and the honeycomb stator) could be a very effective solution. A different solution for reducing the circumferential flow is the use of stator helical grooves arranged so as to oppose fluid rotation [7]. The solution is somewhat dissimilar because in this case it is the pressure field generated by the helically inclined grooves that slows down the development of the Couette circumferential flow.

The Lomakin Bearing. The device analyzed here is the so-called Lomakin bearing (LB), presented in Figs. 1 and 2, which is considered as an alternative to pocket hybrid journal bearings (HJB) for use in cryogenic turbopumps. From a design standpoint, the LB is close to squeeze film dampers with a central groove [8]. It consists of two opposing straight annular seals separated by a circumferential feeding groove. The fluid is supplied to the groove via orifice restrictors. The LB has characteristics similar to hybrid bearings such as load capacity at zero or very low rotation speeds and a supplementary load capacity at high rotation speeds. For zero or very low rotation speeds, its load capacity is due to the Lomakin effect, which is also responsible for the centering capabilities and the direct stiffness of annular seals. In order to improve its stability characteristics, the orifices are tangentially inclined against rotation. Globally, this will generate a corresponding circumferential flow in the groove that will go on to penetrate into the two straight annular parts of the LB. From this standpoint, the circumferential groove in conjunction with the tangential-against-rotation inclined orifices act in the same way as the previously mentioned swirl-brake device. It should be mentioned that tangential-against-rotation inclined orifices were also used for improving the stability characteristics of pocket hybrid bearings [9,10]. However it seems that in that case the mechanism involve din modifying the stability characteristics belonged more to the class described at the beginning of this paragraph than to the category based on the circumferential flow.

Theoretical Models for the LB. Test results for angle injection LB were obtained in [11] and were used in [12] for comparisons with theoretical predictions. The theoretical model introduced in [12,13] is a bulk-flow analysis that accounts for the interaction between the feeding orifices, the circumferential groove, and the thin film lands. The flow in the groove is considered as being one-dimensional and dominated by the circumferential direction. Corresponding continuity and circumferential momentum equations are introduced. The circumferential momentum equation is dominated by viscous effects and convective inertia forces are neglected. The circumferential velocity in the groove is considered as being entirely convected towards the thin film lands for which it represents an entrance swirl. The thin film land flow is then modeled by using the classical two-dimensional bulk-flow equations [14].

The present work introduces an alternative bulk-flow model for the LB. The model is similar to the previous one in accepting a one-dimensional circumferential flow in the groove, the same model for the thin film lands and for its coupling with the groove. Two aspects distinguish the present model. First the one-dimensional circumferential momentum equation in the groove is considered as being dominated by convective inertia forces and a corresponding form is proposed. The second aspect resides in a numerical treatment of the groove flow that is based on "macro" control volumes centered around each orifice restrictor. Handling the groove in this way enables the LB to be treated as a pocket hybrid bearing with all the benefits which can result (natural treatment of eccentric or misaligned working conditions, rapidity in coding by using the same iterative algorithms for satisfying the mass flow balance, etc.). The comparisons and the good agreement with test results taken from [12] show the ability of the present model to handle centered working conditions. A parametric study is then performed for investigating the variation of the bearing characteristics with increasing static eccentricity or misalignment.

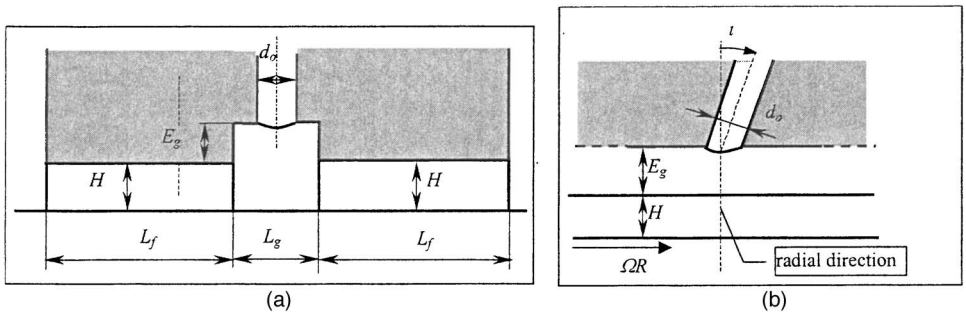

Fig. 2 The geometric characteristics of the Lomakin bearing: (a) axial section, (b) circumferential section

Downloaded 02 Jun 2010 to 171.66.16.98. Redistribution subject to ASME license or copyright; see http://www.asme.org/terms/Terms_Use.cfm

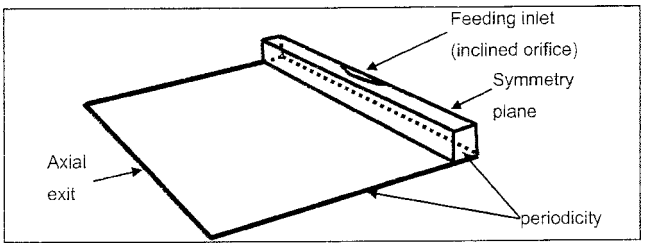

Fig. 3 Computational domain used for the full Navier–Stokes calculation of the Lomakin bearing

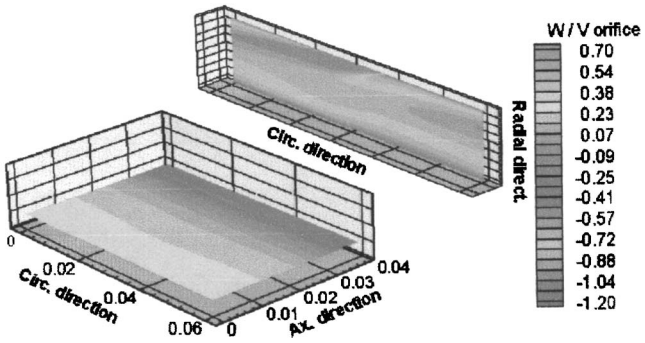

Fig. 5 Axial velocity in the Lomakin bearing (NS calculation)

Navier–Stokes Analysis of the 3D Flow in the Centered LB

A full Navier–Stokes analysis of the three-dimensional turbulent flow in the centered LB was performed for understanding the coupling between the groove and the thin film of the bearing. In accordance with Fig. 2, the analyzed Lomakin bearing had the following geometric characteristics: $R=38.23$ mm, $L_f=34.29$ mm, $C_0=0.1$ mm, $L_g=7.62$ mm, $E_g=3.81$ mm. The rotor and the stator surfaces were considered hydraulically smooth. The LB had 4 equally-spaced orifice restrictors with $d_o=3.175$ mm and $\iota=85°$. The LB was fed with water ($\rho=984.5$ kg/m^3, $\mu=0.5\cdot10^{-3}$ Pa s) at a supply pressure of 55.3 bar. The exit pressure was taken as 1 bar and the rotor speed was 17,400 rpm.

The computational domain is depicted in Fig. 3. Due to the very small ratio C_0/R the curvature effects are neglected and the bearing surface is assimilated with a plane. Advantage was also taken of the symmetry of the thin film lands and only half of the LB was considered. Centered working conditions and equally spaced feeding restrictors enable the analysis of a domain containing only one orifice with periodicity boundary conditions. In Fig. 3, the upper and the lower surfaces correspond to the stator and to the rotor, respectively. The spinning of the rotor is modeled as the ΩR velocity of the lower wall directed from one periodic surface to the other. The mass flow rate is imposed at the feeding orifice. The inclination of the restrictors was taken into account by considering an elliptical intersection of the orifice with the groove and by imposing a tangential component of the feeding velocity. The ambient pressure was imposed at the axial exit. Turbulence was taken into account by using the standard $k-\varepsilon$ model with the logarithmic wall law. The domain was discretized by using parallelepiped and prismatic control volumes and the solution of the three-dimensional averaged Navier–Stokes equations was obtained by using the SIMPLE algorithm. The mesh was refined until grid independent results were obtained. A similar analysis is detailed in [15] for HJB analysis.

Two pressure surfaces are depicted in Fig. 4. The horizontal surface is the rotor plane and the vertical one is the symmetry plane. From the symmetry plane one can see that the pressure is not constant in the groove. Pressures from the symmetry plane are averaged over the groove height and are depicted on the left-hand graph showing a sinusoidal variation along the circumference. As shown by the rotor surface pressure distribution, the variation of the groove pressure is not transmitted to the thin film land where the pressure is constant in the circumferential direction and decreases linearly towards the exit. On the other hand, the circumferential variation of the groove pressure is correlated with the axial velocity at the thin film land inlet section. Figure 5 depicts two axial velocity surfaces. The horizontal surface is a plane, equally spaced from the rotor and from the stator. The second surface is a plane, equally spaced from the symmetry plane and from the groove wall. The axial velocities depicted in the vertical plane have very low values. They show that the axial groove flow is almost negligible. In the horizontal plane representing the thin film land, the axial velocities are nonconstant close to the inlet section and their variations are correlated with the groove pressure. Thus, the groove pressure peaks correspond to the lower (light blue) and to the higher (dark blue) axial velocity zones. This leads to the idea that the pressure drop coefficient used in the generalized Bernoulli equation might also have a nonconstant value.

Figure 6 depicts surfaces of the circumferential velocity. The horizontal surface is a plane equally-spaced from the rotor and from the stator. The vertical surface is the symmetry plane. The circumferential velocities in this latter plane show that complicated mixing phenomena occur in the groove. As for the pressure, these effects are eliminated when the fluid enters the thin film. The circumferential velocity is transported without any apparent loss from the groove to the thin film. The horizontal plane shows that U in the thin film land is constant in the circumferential direction and its evolution corresponds to the normal effect produced by the spinning of the rotor.

From Figs. 4–6 it can be concluded that apart from the axial velocity variation in the first half, the thin film land behaves as an annular seal. The complicated mixing effects that occur in the

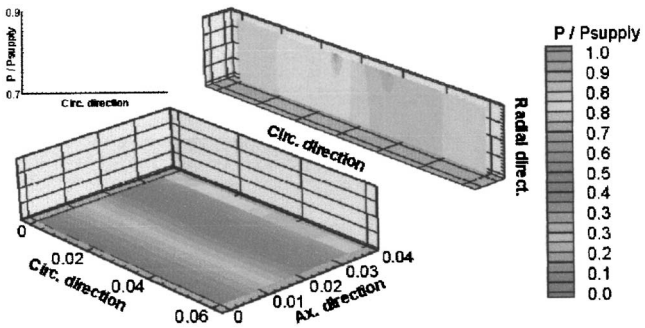

Fig. 4 Pressure variation in the Lomakin bearing (NS calculation)

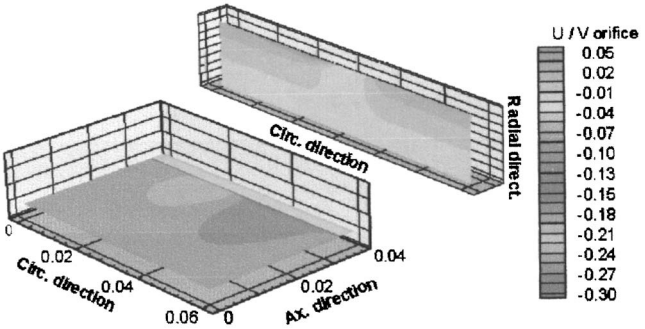

Fig. 6 Circumferential velocity in the Lomakin bearing (NS calculation)

Downloaded 02 Jun 2010 to 171.66.16.98. Redistribution subject to ASME license or copyright; see http://www.asme.org/terms/Terms_Use.cfm

groove are rapidly eliminated by the reduced passage from the groove into the thin film. It then follows that at least the land region of the Lomakin bearing can be described by the thin film model. A second conclusion is that due to the high ratio between the groove depth and the thin film thickness, the groove flow can be considered as a 1D circumferential flow with negligible axial velocity.

The Theoretical Model

The Thin Film Land Flow. The flow in the thin film lands is described by the bulk flow system of equation for an incompressible fluid.

$$\frac{\partial H}{\partial t} + \frac{\partial (HW)}{\partial z} + \frac{\partial (HU)}{\partial x} = 0 \tag{1}$$

$$\rho \left[\frac{\partial (HW)}{\partial t} + \frac{\partial (HWW)}{\partial z} + \frac{\partial (HUW)}{\partial x} \right] = -H \frac{\partial P}{\partial z} + \tau_{Sz} + \tau_{Rz} \tag{2}$$

$$\rho \left[\frac{\partial (HU)}{\partial t} + \frac{\partial (HWU)}{\partial z} + \frac{\partial (HUU)}{\partial x} \right] = -H \frac{\partial P}{\partial x} + \tau_{Sx} + \tau_{Rx} \tag{3}$$

where the wall shear stresses are given by a friction law.

$$\tau_{Sz} = \tau_S \frac{W}{V_S}, \quad \tau_{Sx} = \tau_S \frac{U}{V_S}, \quad \tau_{Rz} = \tau_R \frac{W}{V_R}, \quad \tau_{Rx} = \tau_R \frac{U - R\Omega}{V_R} \tag{4}$$

$$\tau_S = \frac{\rho V_S^2}{2} f_S, \quad \tau_R = \frac{\rho V_R^2}{2} f_R \tag{5}$$

$$V_S = \sqrt{W^2 + U^2}, \quad V_R = \sqrt{W^2 + (U - R\Omega)^2} \tag{6}$$

The friction factor is given by one of the available laws (Blasius, Moody, Colebrook, etc.). For example:

$$f_i = 1.375 \cdot 10^{-3} \left[1 + \left(2 \cdot 10^4 \frac{h_i}{D_h} + \frac{10^6}{\mathrm{Re}_i} \right)^{1/3} \right], \quad i = R,S \tag{7}$$

$$D_h = 2H, \quad \mathrm{Re}_i = \frac{\rho V_i D_h}{\mu} \tag{8}$$

The boundary conditions for this system of equations are given in terms of pressure and tangential velocity. If the fluid enters the thin film land, then the pressure and the tangential velocity on the boundary must be imposed. If the fluid leaves the thin film land, only the boundary pressure must be imposed and the tangential velocity is convected outwards. The passage in and out of the thin film land is accompanied by visco-inertia effects that cannot be described by the thin film equation. These effects are characterized by a very rapid pressure drop or recovery generally described by a generalized Bernoulli law. The exit pressure recovery is seldom to be taken into account, but the inlet pressure drop is always to be considered.

$$P^0 = P + (1 + \xi) \frac{\rho W^2}{2} \tag{9}$$

The Circumferential Groove Flow. The feeding pockets of HJB and the circumferential groove of the LB are zones where the thin film model is no longer applicable due to the significant depth. Even if these zones are excluded from the thin film analysis, they still remain coupled with the bulk flow system of equation via the boundary conditions. Some modeling of the flow inside the pockets of HJB and in the groove of the LB is necessary. The flow inside an HJB recess is described by using a given parametrical "pressure pattern" [16]. The pattern describes the recess pressure surface and is based on some strong simplifying assumptions. For example, for a rectangular recess, the pressure is constant in the axial direction and the velocity component tangential at the recess boundary is zero (which means the flow leaves the recess normally towards the thin film land). The only pressure variation inside the pocket is in the circumferential direction and should be taken into account for shallow recesses. The parameters governing the pressure pattern are a reference pressure and the normal velocity at the recess boundary. The reference pressure is the value at the exit of the orifice restrictor and is linked to the supply pressure common to all restrictors via an appropriate hydraulic resistance law. For an orifice restrictor,

$$\dot{M}_o = C_D \frac{\pi D_o^2}{4} \sqrt{2\rho (P_{\mathrm{Supply}} - P_r)}, \quad V_o = \frac{4\dot{M}_o}{\rho C_D \pi D_o^2} \tag{10}$$

Once P_r can be specified, the pattern gives the total pressures at the recess boundaries. For example, if a constant pressure pattern holds in the recess then $P^0 = P_r$. The pressure boundary conditions of the thin film land are then calculated by using the generalized Bernoulli law (9).

One of the strongest simplifying hypotheses in modeling the HJB recess flow is that the tangential velocity at the pocket boundary is zero. This means that the tangential component of the velocity is uncoupled from the recess pressure pattern. This cannot be the case for the LB. Figures 4–6 indicate that the thin film flow is strongly coupled with the groove flow not only via the pressure but also via the tangential (circumferential) velocity. The inclined restrictors generate a circumferential flow in the groove. Under the effect of the pressure difference between the supply and the exit section, the circumferential momentum is convected from the groove into the thin film lands. The circumferential groove and the inclined restrictors then act as a means of imposing a prerotation velocity in the two annular thin film parts of the LB. For a proper inclination of the restrictors, this is strongly affecting the swirl flow in the thin film land and can effectively lead to the improvement of the dynamic characteristics. Compared to the degree of modeling used for HJB, it therefore follows that a "pressure pattern" is insufficient for reproducing the groove flow. A transport equation must be added. Based on the information obtained from the full Navier–Stokes calculation the pressure and the circumferential velocity are considered to be constant in the axial direction inside the groove. It is then assumed that groove flow takes place only in the circumferential direction. With these simplifying assumptions, the flow in the groove of the LB is one-dimensional and is described by the following convective transport equation:

$$\rho L_g \frac{\partial (H_g U_g)}{\partial t} + \frac{\partial}{\partial x} (\dot{M}_x U_g) = -H_g L_g \frac{\partial P_g}{\partial x} + S_g^\tau + \frac{\delta}{\delta x} [\dot{M}_o V_o \cos(t)] - \frac{\partial}{\partial x} (\dot{M}_{\partial g} U_g) \tag{11}$$

$$H_g = E_g + H \tag{12}$$

$$\dot{M}_x = \rho H_g U_g L_g \tag{13}$$

$$S_g^\tau = (\tau_{Sx} + \tau_{Rx})_g L_g \tag{14}$$

The derivative $\delta / \delta x$ is considered in the sense of distributions. As for the bulk flow momentum equation, the viscous forces are lumped in the algebraic source term S_g^τ where τ_{S,R_θ} are calculated with the above-mentioned friction laws and depend only on U_g. The use of a convection dominated transport equation is advocated by the fact that large reduced Reynolds numbers of the circumferential groove flow are expected. Indeed, as suggested by Fig. 6, a very rough estimate of the circumferential bulk velocity in the groove is $U_g = -\Omega R \cdots -0.5\Omega R$. By considering the lower limit module it yields $|U_g| \approx 35$ m/s. The reduced Reynolds number relative to the stator is

Downloaded 02 Jun 2010 to 171.66.16.98. Redistribution subject to ASME license or copyright; see http://www.asme.org/terms/Terms_Use.cfm

$$\mathrm{Re}_S^* = \frac{\rho |U_g| E_g}{\mu} \frac{E_g}{R} = 26{,}167$$

One could argue that a better estimation of the relative importance of the inertia forces versus the viscous ones would be given by a reduced Reynolds number taking into account the turbulent flow regime, $\mathrm{Re}_S^{**} = 12/k_S \cdot \mathrm{Re}_S^* = 386$, where $k_S = f_S \mathrm{Re}_S = 814$. Both Re_S^* and Re_S^{**} are much larger than one and show that the inertia forces are dominant in the circumferential groove flow.

The unknown of the one-dimensional transport equation is the circumferential groove velocity $U_g(x)$. The groove pressure P_g coincides with P_r at the location of each orifice and its variation between restrictors undertakes the role of the pressure pattern.

The second equation for the circumferential groove is its algebraic mass flow balance.

$$\sum_{\text{all orifices}} \dot{M}_o = \dot{M}_{\partial g} + \rho \frac{\partial \vartheta_g}{\partial t} \tag{15}$$

$$\dot{M}_{\partial g} = \int_{\partial g} \rho W H \, d\gamma \tag{16}$$

$$\vartheta_g = L_g \int_0^{2\pi R} H_g \, dx \tag{17}$$

Following the definition of the orifice mass flow rate (10), the unknowns intervening in (15) are the pressures P_r for each restrictor. The groove mass flow balance then offers an equation for obtaining the groove pressure variation.

The thin film boundary conditions are then given by the groove pressure (together with the generalized Bernoulli equation) and by the groove circumferential velocity. It is assumed that the passage of the circumferential velocity from the groove flow towards the thin film occurs without any loss.

$$P^0 = P_g(x) \tag{18}$$

$$U = U_g(x) \tag{19}$$

Numerical Solution of the LB Model

The numerical solution of the LB has two aspects. The first is the solution of the thin film bulk flow equations provided that groove boundary conditions are given. The thin film land is discretized by using rectangular control volumes and the resulting system of equations is then completely solved. The solution is obtained by using the SIMPLE algorithm. The numerical method is extensively described in the literature [16–18] and will not be presented in this work.

The second aspect of the numerical solution of the LB model is the solution of the groove flow. This solution consists of groove pressures and groove circumferential velocities. The groove velocities can be obtained from Eq. (11) provided that groove pressures are known. The main difficulty in the solution of the LB compared to the solution of the HJB is that the groove is fed via many restrictors. Indeed, the fact that each recess of the HJB is fed via a single restrictor enables the development of a generally accepted non-linear algorithm for deducing the recess pressures. In this way, the mass flow balance of each recess is regarded as an algebraic equation for variables P_r, $r = 1 \cdots \mathrm{NR}$ (NR is the total number of recesses). A system of NR nonlinear algebraic equations with NR unknowns is then obtained. A Newton–Raphson algorithm enables the finding of P_r in a reasonable number of steps.

The fact that the LB has only one groove enables a single mass flow balance equation to be written having for unknowns the pressures at the location of each restrictor. A solution can be found only if these pressures have a priori identical values. Such a situation can be encountered in the singular case when the restrictors are identical and equally spaced on the groove circumference and for centered working conditions. (Zero misalignment working conditions and a nondamaged bearing surface can be added to the above mentioned restrictions.) It then follows that for general working conditions, the LB model cannot be directly dealt with as an HJB. Some supplementary hypotheses are therefore required.

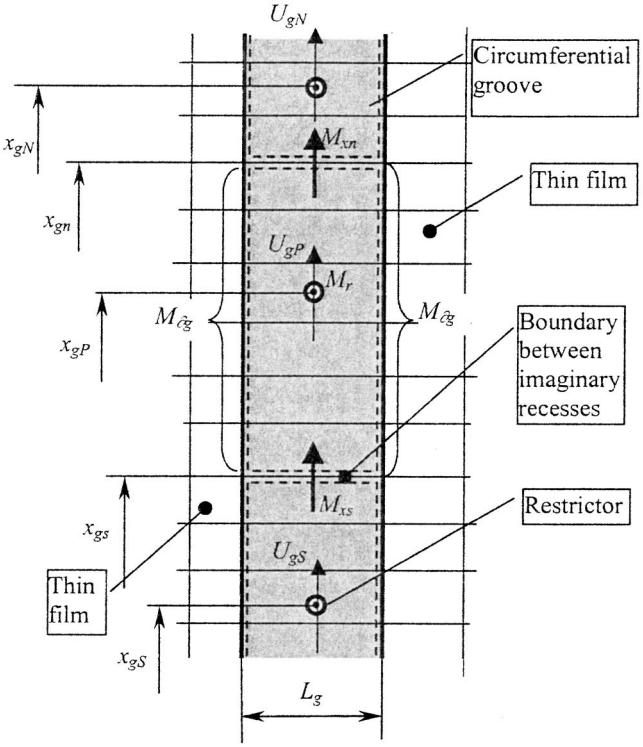

Fig. 7 The discretization of the circumferential groove of the Lomakin bearing

Figure 7 depicts a detail of the circumferential groove and of the thin film land. The circumferential groove is discretized by using a single row of rectangular control volumes. It is then assumed that the control volumes in the groove can be conventionally grouped around each restrictor and the circumferential groove can be regarded as a row of imaginary recesses. This heuristic hypothesis is aimed at enabling the use, without any modification, of the Newton–Raphson algorithm used for HJB. The continuity equation in the circumferential groove can then be cast as a system of mass conservation equations for each imaginary recess.

$$\dot{M}_o = \dot{M}_{\partial g} + \Delta \dot{M}_x + \rho \frac{\partial \vartheta_r}{\partial t} \tag{20}$$

$$\Delta \dot{M}_x = \dot{M}_{xn} - \dot{M}_{xs}, \quad \dot{M}_{xn,s} = \rho (H_g U_g)_{n,s} L_g \tag{21}$$

$$\dot{M}_{\partial r} = - \sum_{i \in \partial r} \rho_i W_i H_i \gamma_i \tag{22}$$

$$\vartheta_r = L_g \int_{x_{g_s}}^{x_{g_n}} H_g \, dx \tag{23}$$

As for HJB, each imaginary recess is fed via a single restrictor. It should be emphasized that due to the circumferential periodicity, the sum of the mass conservation equations for all the imaginary recesses is identical with the groove continuity equation

Downloaded 02 Jun 2010 to 171.66.16.98. Redistribution subject to ASME license or copyright; see http://www.asme.org/terms/Terms_Use.cfm

$$\sum_{\substack{\text{imaginary}\\ \text{recesses}}} \dot{M}_{\partial r} = \dot{M}_{\partial g}, \qquad \sum_{\substack{\text{imaginary}\\ \text{recesses}}} \Delta \dot{M}_x = 0, \qquad \sum_{\substack{\text{imaginary}\\ \text{recesses}}} \vartheta_r = \vartheta_g \tag{24}$$

The Newton–Raphson algorithm applied to the system of mass conservation equations for the imaginary recesses enables the calculation of the pressures P_r at the location of each restrictor. The groove pressure and its derivative at any circumferential location are then interpolated by using periodic cubic spline functions. (DCSPER and DCSDER are subroutines of the IMSL mathematical library.)

$$P_g(x) = \mathrm{DCSPER}(P_r, r = 1 \cdots \mathrm{NR}+1 | P_{\mathrm{NR}+1} = P_1, \mathrm{NR} \geqslant 3) \tag{25}$$

$$\frac{\partial P_g}{\partial x} = \mathrm{DCSDER}(P_r, r = 1 \cdots \mathrm{NR}+1 | P_{\mathrm{NR}+1} = P_1, \mathrm{NR} \geqslant 3) \tag{26}$$

First, the groove pressures $P_g(x)$ in conjunction with the generalized Bernoulli equation (9) are used as boundary conditions for the thin film land. Second, knowing the groove pressure gradient makes the numerical solution of the groove circumferential momentum equation possible. Therefore each imaginary recess is considered as a macro-control volume. Conforming to the control volume discretization method, the circumferential velocity and the pressure are considered to be constant in each macro-volume and their values are associated with the circumferential location of the restrictor. The groove circumferential velocities $U_{g_{n,s}}$ needed for expressing $\dot{M}_{x_{n,s}}$ are given by periodic cubic spline interpolation. The groove circumferential momentum equation is integrated over each macro-control volume.

$$(\dot{M}_x U_g)_n - (\dot{M}_x U_g)_s = \left[-H_{g_P} L_g \left(\frac{\partial P_g}{\partial x} \right)_P + S^{\tau}_{g_P} \right] (x_{g_n} - x_{g_s}) + \dot{M}_{o_P} V_{o_P} \cos(t) - \dot{M}_{\partial g_P} U_{g_P} \tag{27}$$

The momentum rates on the upper and on the lower macro-control volume boundary are estimated by using a first order of precision upwind approach.

$$(\dot{M}_x U_g)_n = \frac{\dot{M}_{x_n} + |\dot{M}_{x_n}|}{2} U_{g_P} + \frac{\dot{M}_{x_n} - |\dot{M}_{x_n}|}{2} U_{g_N} \tag{28}$$

$$(\dot{M}_x U_g)_s = \frac{\dot{M}_{x_s} + |\dot{M}_{x_s}|}{2} U_{g_S} + \frac{\dot{M}_{x_S} - |\dot{M}_{x_S}|}{2} U_{g_P} \tag{29}$$

A linear system of equation for U_g is then obtained.

$$-a_S U_{g_S} + a_P U_{g_P} - a_N U_{g_N} = S_P^{U_g} \tag{30}$$

$$a_S = \frac{\dot{M}_{x_s} + |\dot{M}_{x_s}|}{2}, \quad a_N = \frac{|\dot{M}_{x_n}| - \dot{M}_{x_n}}{2}, \quad a_P = a_S + a_N \tag{31}$$

$$S_P^{U_g} = \left[-H_{g_P} L_g \left(\frac{\partial P_g}{\partial x} \right)_P + S^{\tau}_{g_P} \right] (x_{g_n} - x_{g_s}) + \dot{M}_{o_P} V_{o_P} \cos(t) - \dot{M}_{\partial g_P} U_{g_P} - (\dot{M}_{x_n} - \dot{M}_{x_s}) U_{g_P} \tag{32}$$

The linear system is solved by using a Gauss–Seidel-type iterative procedure.

$$U_{g_P} = U_g^{(k-l)}{}_P + r_{U_g} \left[\frac{a_S U_{g_S} + a_N U_{g_N} + S_P^{U_g^{(k-l)}}}{a_P} - U_g^{(k-l)}{}_P \right] \tag{33}$$

The mass flow rates $\dot{M}_{x_{n,s}}$ and the coefficients of the linear system are updated after each iteration and therefore an underrelaxation factor $r_{U_g} = 0.1$ was necessary in all cases. The iterative procedure is repeated up to 10^{-3} reduction of the initial error. In order to accelerate the convergence of the iterative algorithm (33), the diagonal dominance of the linear system (30) must be enhanced as much as possible. This can be done by checking the sign of $\dot{M}_{\partial g_P}$ and of $(\dot{M}_{x_n} - \dot{M}_{x_s})$ in (32) and by permuting these from the source term to the main diagonal coefficient a_P. Finally, the variation of the groove circumferential velocity needed as boundary condition for the thin film land is obtained by periodic cubic spline interpolation of U_{g_P}.

$$U_g(x) = \mathrm{DCSPER}(U_{g_i}, i = 1 \cdots \mathrm{NR}+1 | P_{\mathrm{NR}+1} = P_1, \mathrm{NR} \geqslant 3) \tag{34}$$

Perturbation Analysis. The dynamic operating regime is traditionally described as a small amplitude motion of the rotor about an equilibrium position [3]. For a displacement perturbation, the thin film thickness has the following form:

$$H = H^{(0)} - \exp(j\omega t)(e_X^{(1)} \cos\theta + e_Y^{(1)} \sin\theta) \tag{35}$$

$$H^{(0)} = C_0 - (e_X^{(0)} \cos\theta + e_Y^{(0)} \sin\theta) \tag{36}$$

and leads to the perturbation of the flow variables. Following the traditional small perturbation approach, all variables are decomposed as $\Phi = \Phi^{(0)} + \varepsilon \Phi^{(1)}$ where ε is the perturbation parameter. The introduction of this decomposition into the unsteady flow equations gives two systems of equations. The zeroth order part is the original system with the exception of the unsteady terms. The perturbed (first order) system consists of linear equations and has exactly the same form as the original equations. The problem is extensively described in the lubrication related literature and will not be further detailed here. The system of the first order bulk flow equations is solved using the same SIMPLE algorithm. Forces arising from perturbation are obtained by integrating the first order pressure field and are expressed via the dynamic coefficients.

$$-\begin{Bmatrix} F_X^{(1)} \\ F_Y^{(1)} \end{Bmatrix} = \begin{bmatrix} K_{XX} & K_{XY} \\ K_{YX} & K_{YY} \end{bmatrix} \begin{Bmatrix} e_X^{(1)} \\ e_Y^{(1)} \end{Bmatrix} + \begin{bmatrix} C_{XX} & C_{XY} \\ C_{YX} & C_{YY} \end{bmatrix} \begin{Bmatrix} \dot{e}_X^{(1)} \\ \dot{e}_Y^{(1)} \end{Bmatrix} + \begin{bmatrix} M_{XX} & M_{XY} \\ M_{YX} & M_{YY} \end{bmatrix} \begin{Bmatrix} \ddot{e}_X^{(1)} \\ \ddot{e}_Y^{(1)} \end{Bmatrix} \tag{37}$$

The dynamic coefficients are evaluated from a least square procedure by using the results obtained for two perturbation frequencies (generally zero and synchronous whirl).

Validations and Results

The analyzed Lomakin bearing has the same geometric characteristics as the one used for the full Navier–Stokes analysis. The LB was fed with water ($\rho = 984.5\ \mathrm{kg/m^3}, \mu = 0.5 \cdot 10^{-3}\ \mathrm{Pa\,s}$) at three supply pressures, namely 41.4 bar, 55.3 bar, and 69.1 bar. Three rotation speeds (10,200 rpm, 17,400 rpm, and 24,600 rpm) were considered. One can now recognize that the working conditions selected for the full Navier–Stokes calculations corresponded to the medium pressure and medium speed test case. The coefficients needed for the theoretical analysis were $\xi = 0.1$ and $C_D = 0.9$. The exit pressure was taken as 1 bar with no recovery effect. These empirical coefficients were taken in the same way as in [11] where they were triggered in order to match the flow rate measured for $P_{\mathrm{Supply}} = 55.3$ bar and $\Omega = 17{,}400$ rpm.

The results in the following paragraphs are presented in dimensionless form with the numerical prediction of the case $P_{\mathrm{Supply}} = 55.3$ bar and $\Omega = 17{,}400$ rpm taken as reference values. All stiffness, damping and added-mass coefficients were divided by K_{XX}, C_{XX}, and M_{XX}, respectively, calculated for the reference case.

Downloaded 02 Jun 2010 to 171.66.16.98. Redistribution subject to ASME license or copyright; see http://www.asme.org/terms/Terms_Use.cfm

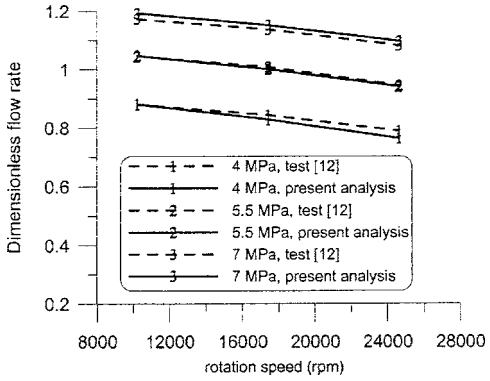

Fig. 8 Flow rate variation for centered working conditions

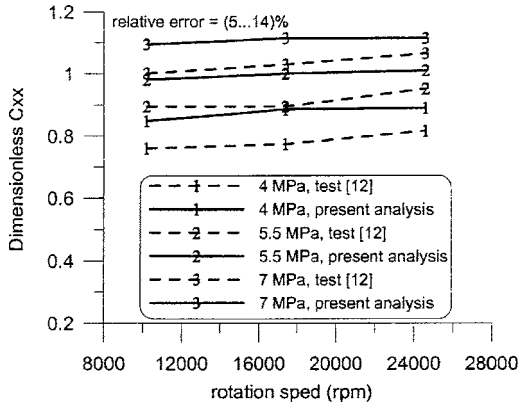

Fig. 11 Direct damping for centered working conditions

Validations for Centered Working Conditions (Figs. 8–15). Figure 8 compares the measured and the calculated flow rates. It can be seen that the theoretical predictions are very close to the measured values. Only the results of the case P_s=69.1 bar are slightly overestimated. The relative errors are less than 3%. The excellent agreement is obviously due to the adjustment of the empirical coefficients ξ and C_D. Another validating result is the groove pressure level. The average value of the sinusoidal pressure variation depicted in Fig. 4 is 4.46 MPa and is very well correlated with the pressure groove value of 4.13 MPa deduced with the present bulk flow model.

Figure 9 depicts the direct stiffness coefficients. Calculated values are systematically larger than measured ones. The differences could be explained by the Navier–Stokes results that showed the link that exists between the variation of the axial velocity in the inlet section of the thin film and the sinusoidal groove pressure. This effect is not coped with by the present bulk-flow model and might be the source of disagreements encountered between the calculated and the measured K_{XX}. The calculated direct stiffness depicted in Fig. 9 increases with increasing supply pressure but it shows a decreasing trend with increasing rotation speed which is different from measured results. The decrease of the direct stiffness with increasing Ω might be due to the augmentation of circumferential inertia forces and is a typical annular seal type be-

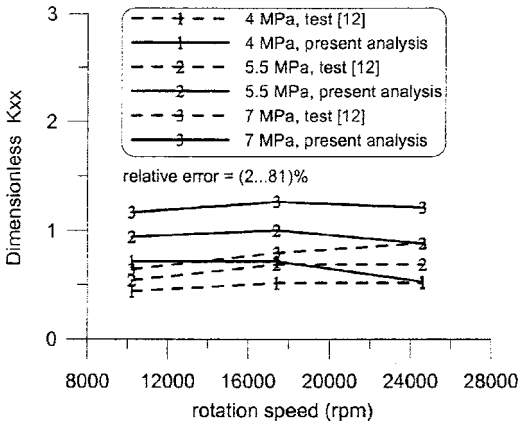

Fig. 9 Direct stiffness for centered working conditions

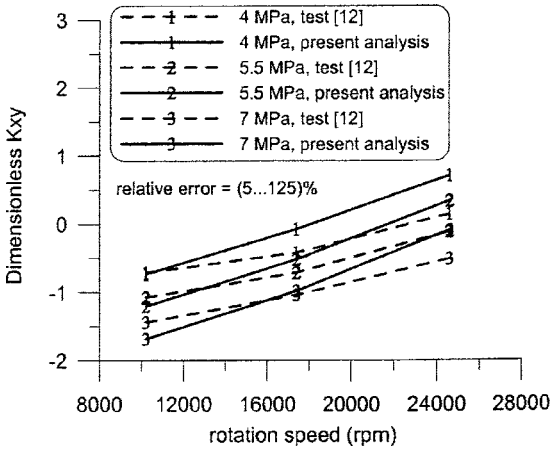

Fig. 10 Cross-coupled stiffness for centered working conditions

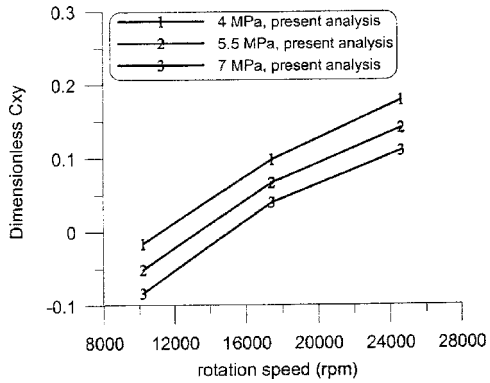

Fig. 12 Cross-coupled damping for centered working conditions

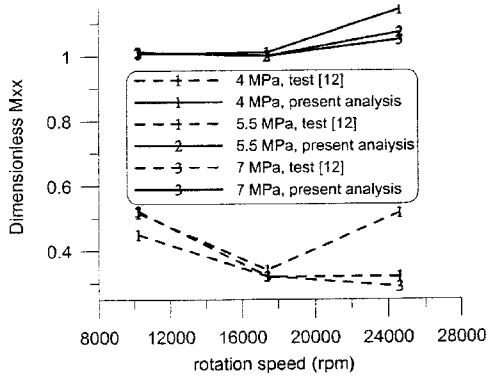

Fig. 13 Direct added-mass for centered working conditions

Downloaded 02 Jun 2010 to 171.66.16.98. Redistribution subject to ASME license or copyright; see http://www.asme.org/terms/Terms_Use.cfm

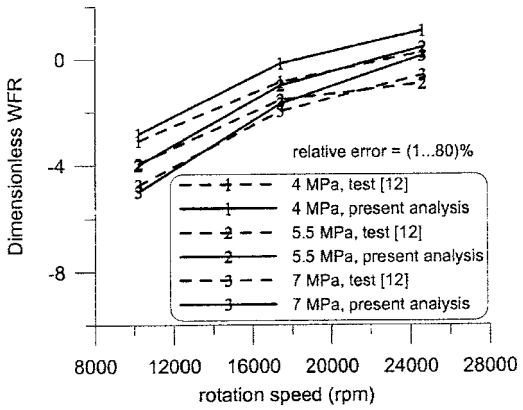

Fig. 14 Whirl frequency ratio for centered working conditions

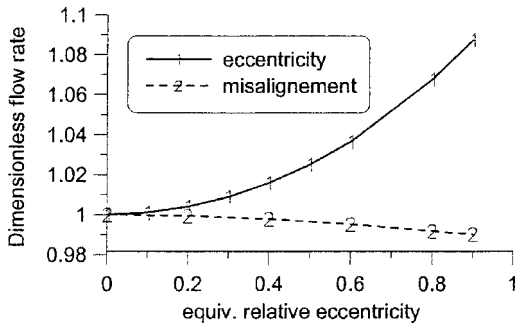

Fig. 16 Variation of the flow rate with equivalent eccentricity

havior of two thin film lands of the LB.

The cross-coupled stiffness is depicted in Fig. 10 and shows a fair agreement between calculated and measured values. The calculated coefficients are smaller than the measured values for $\Omega = 10{,}200$ rpm and are larger for $\Omega = 17{,}400$ rpm and 24,600 rpm but show the same trends: K_{XY} increases with increasing rotation speed and decreases with increasing supply pressure. These trends confirm the fact that K_{XY} is controlled by the against-rotation circumferential velocity in the groove. Indeed, increasing the supply pressure will increase the flow rate and for a tangential inclined restrictor this will lead to an augmentation of the circumferential groove velocity which takes on the role of the prerotation for the thin film lands. A tangential-against-rotation inclination of the orifice will then generate a favorable (in terms of dynamic stability) prerotation velocity that will decrease the value of the cross-coupled stiffness. The increase of K_{XY} with increasing rotation speed is a normal result taking into account the annular seal-type behavior of the thin film lands. Nevertheless, the calculated increase of K_{XY} with increasing velocity is more significant than for the test values leading to overestimated coefficients for the highest rotation speed.

The calculated direct damping coefficients are compared with measured values in Fig. 11. Theoretical coefficients have the same trends as test results but are systematically shifted to higher values. This result must be correlated with the overestimation of the slopes of K_{XY} with increasing velocity. Figure 12 depicts the calculated C_{XY} coefficient. Experimental values of the cross-coupled damping were not presented in [12] so Fig. 12 presents only the coefficients stemming from the present analysis. Added-mass values are compared in Fig. 13. The difference between the experimental and the calculated coefficients is important but the discrepancy is difficult to appreciate because it is usually accepted that added-masses are largely influenced by measurement errors.

The whirl frequency ratio for centered working conditions $\mathrm{WFR} = K_{XY}/(C_{XX}\Omega)$ is depicted in Fig. 14. A quite good agreement between calculated and measured values can be observed for low rotating speeds. With increasing Ω the calculated values overestimate the whirl frequency ratio. This is due to the cross-coupled stiffness coefficient which is larger than the measured value for $\Omega = 24{,}600$ rpm and cannot be balanced by the overestimation of the direct damping. Nevertheless, the trends are correctly predicted showing an increase of the WFR with increasing rotation speed and a decrease with increasing supply pressure. These are exactly the variation trends of the cross-coupled stiffness, thus showing that LB stability is mainly governed by K_{XY}.

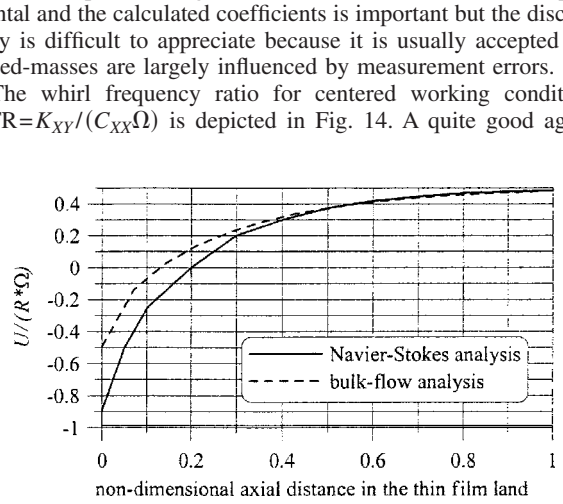

Fig. 15 Average circumferential velocity in the thin film land

The differences between the calculated and the measured cross-coupled stiffness can be explained by analyzing the circumferential velocity in the thin film which is known to have a crucial influence. Figure 15 depicts the comparison between circumferentially averaged U velocities stemming from the Navier–Stokes and from the bulk-flow analyses, respectively. In the thin film land inlet section, the bulk-flow calculation gives $-0.5R\Omega$ while the value calculated with the Navier–Stokes analysis is $-0.9R\Omega$. The circumferential velocities are identical beyond 40% of the thin film land length. One can conclude that the 27% overprediction of the K_{XY} coefficient given by the bulk-flow analysis compared to the measured value is mainly due to the difference in the U variations depicted in Fig. 15. In the meantime, it should be emphasized that the Navier–Stokes results depicted in Fig. 15 are circumferential velocities in a plane equally spaced from the rotor and from the stator and not values averaged over the film thickness as for the bulk-flow analysis. The circumferential velocities considered in this plane tend to be identical to the averaged values only for a pure Couette flow.

Results for Eccentric and Misaligned Working Conditions (Figs. 16–19). The LB characteristics for eccentric and misaligned working conditions were investigated for only one case from amongst the preceding nine others, namely, for $P_{\mathrm{Supply}} = 55.3$ bar and $\Omega = 17{,}400$ rpm. The eccentricity was assumed to be directed toward the orifice located on the positive X axis. The tilting point of the rotor axis was taken in the symmetry plane XOY of the LB. Then XOZ was considered as the misalignment plane containing the stator and the rotor axes. Finally, the misalignment amplitude was characterized by the eccentricity measured on the LB right exit section and will be referred to as the "equivalent eccentricity" in what follows. This description enables eccentricity and misalignment effects to be characterized by a single parameter.

Figure 16 depicts the variation of the flow rate with increasing equivalent eccentricity. The flow rate increases slightly with increasing eccentricity and decreases very slightly with increasing misalignment. It should be noted that due to the large E_g/C_0 ratio of the analyzed LB configuration and due to the selection of the tilting point in the XOY plane, which is also the symmetry plane of the circumferential groove, the groove pressure is almost unaffected by misalignment effects. This result is not reproduced for pure eccentricity effects for which case, despite the large E_g/C_0 ratio, the groove pressure are strongly influenced by the static

Downloaded 02 Jun 2010 to 171.66.16.98. Redistribution subject to ASME license or copyright; see http://www.asme.org/terms/Terms_Use.cfm

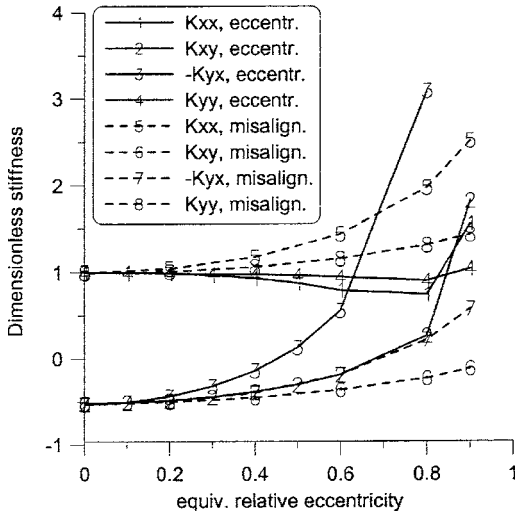

Fig. 17 Variation of the stiffness coefficients with equivalent eccentricity

eccentricity and show a circumferential variation.

Stiffness coefficients are depicted in Fig. 17. The direct coefficients are almost constant up to 0.3 equivalent relative eccentricity. For pure eccentricity effects K_{XX} and K_{YY} are first of all very slowly decreasing and then rapidly increase for relative eccentricities larger than 0.8, the K_{YY} coefficient being slightly larger than K_{XX}. The cross-coupling coefficients K_{XY} and K_{YX} show a much more rapid increase with increasing eccentricity with $-K_{YX}$ larger than K_{XY}. The stiffness coefficients calculated for static misaligned working conditions show a steady increase with increasing equivalent eccentricity. In this case K_{XX} is larger than K_{YY} and $-K_{YX}$ remains larger than K_{XY}.

Figure 18 depicts the variation of the damping coefficients with equivalent eccentricity. As for the stiffness, the damping coefficients are almost constant up to 0.3 equivalent relative eccentricity. The direct damping coefficients C_{XX} and C_{YY} then show an increase with increasing eccentricity. The increase is more pronounced for coefficients obtained for static eccentric working conditions. For both eccentricity and misalignment, C_{XX} shows larger values than C_{YY}. The cross-coupling damping coefficients are almost an order of magnitude lower than those of the direct coefficients. This difference, also obtained for centered working conditions, is not changed by static eccentricity or misalignment working conditions. In both cases $-C_{YX}$ is larger than C_{XY} and the former coefficient shows an increase while the latter coefficient is decreasing with increasing equivalent eccentricity.

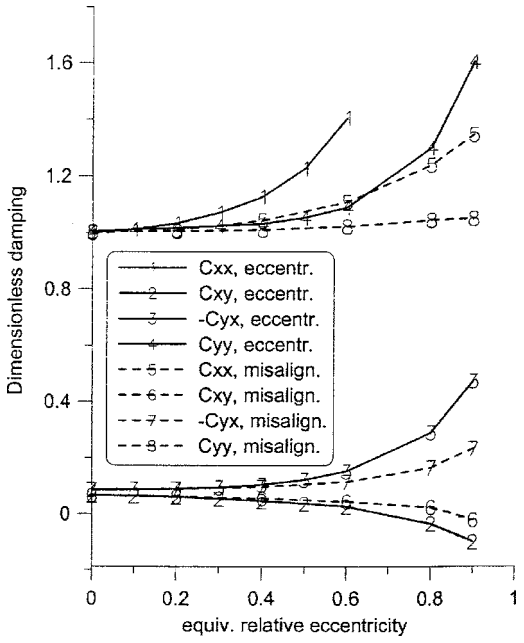

Fig. 18 Variation of the damping coefficients with equivalent eccentricity

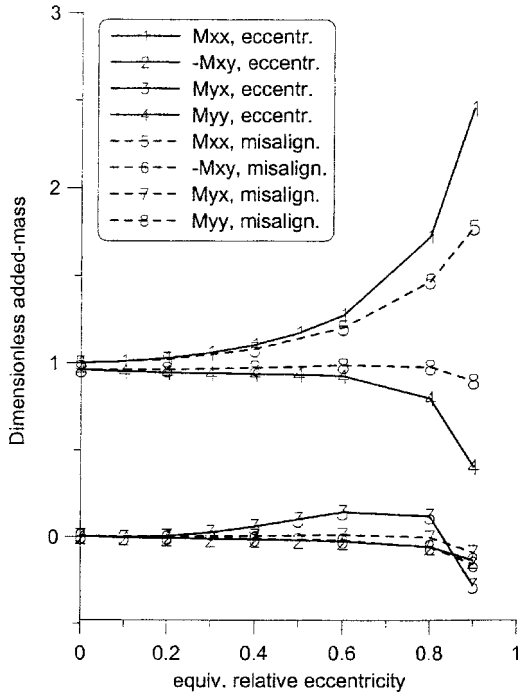

Fig. 19 Variation of the added mass coefficients with equivalent eccentricity

Added mass coefficients are depicted in Fig. 19. The values are almost constant up to 0.5 equivalent relative eccentricity. The M_{XX} coefficient is then increasing while M_{YY} is decreasing with increasing relative eccentricity. The cross-coupled coefficients are very close to zero.

Summary and Conclusions

The present work introduces a bulk-flow model for the LB. A full Navier–Stokes calculation show that although complicated mixing phenomena take place in the groove, the high aspect ratio makes the thin film flow close to the characteristics of an annular seal. In accordance with the high Reynolds numbers that are expected in the bearing, the land flow is then governed by the two-dimensional thin film inertia equations (the "bulk flow" model). Simplifying assumptions enabled the description of the groove flow by a one-dimensional momentum equation dominated by inertia forces. The interaction between the flow in the thin film lands, the circumferential groove and the supply orifices is taken into account by satisfying the global mass flow balance and by considering appropriate boundary conditions for the thin film. Therefore, the groove areas surrounding each orifice are considered as a row of intercommunicating feeding pockets. This heuristic hypothesis enables the use of the same algorithm for HJB and for LB and the analysis of centered, eccentric and misaligned working conditions. Test results for a water lubricated LB taken from [12] are used to validate the present model. For the zero eccentricity case a fair agreement is obtained for the cross-

Downloaded 02 Jun 2010 to 171.66.16.98. Redistribution subject to ASME license or copyright; see http://www.asme.org/terms/Terms_Use.cfm

coupled stiffness. The variation in the bearing characteristics for static eccentricity and misalignment working conditions is then presented in a parametric study.

Acknowledgment

The authors wish to thank Centre National d'Etudes Spatiales and Snecma Moteurs for supporting this work.

Nomenclature

a = terms of the linear system (30)
C_0 = centered clearance
C_D = orifice discharge coefficient
C_{XX}, C_{XY}, C_{YX}, C_{YY} = damping coefficients
e_X, e_Y = eccentricities
f = friction factor
D = diameter
D_h = hydraulic diameter
E_g = groove depth
H = film thickness
H_g = groove height
h = roughness height
K_{XX}, K_{XY}, K_{YX}, K_{YY} = stiffness coefficients
k = iteration level in (33)
L_f = thin film axial length
L_g = groove axial length
$\dot{M}$ = mass flow rate
M_{XX}, M_{XY}, M_{YX}, M_{YY} = added-mass coefficients
P = pressure
P_s = supply pressure
P_r = restrictor pressure
R = journal (rotor) radius
S^τ, S^{U_g} = source terms
t = time
U = circumferential velocity
V = resultant velocity
W = axial velocity
$x=R\theta$ = circumferential coordinate,
z = axial coordinates
ϑ_g = groove volume
Ω = journal rotation speed
ι = tangential-against-rotation angle
μ = dynamic viscosity
ρ = density
τ = shear stress
ω = perturbation frequency
ξ = pressure drop coefficient

Subscripts

o = orifice
n, s = upper and lower boundary of the imaginary recess
S, R = stator, rotor
z, x, θ = coordinate directions
g = groove
∂g = groove boundary
∂r = boundary of the imaginary recess
S, P, N = circumferential location of the restrictors

Superscripts

(0), (1) = zeroth and first order
$\cdot$, $\cdot\cdot$ = time derivatives

References

[1] Hagg, A. C., 1947, "The Influence of Oil-Film Journal Bearings on the Stability of Rotating Machines," J. Appl. Mech., **68**, A-211-20; 14, **69**, A-77-8.
[2] Frêne, J., Nicolas, D., Degueurce, B., Berthe, D., and Godet, M., 1990, *Lubrification Hydrodynamique. Paliers et Butées*, Editions Eyrolles, Paris.
[3] Childs, D. W., 1993, *Turbomachinery Rotordynamics. Phenomena, Modeling and Analysis*, Wiley–Interscience, New York.
[4] Von Pragenau, G. L., 1992, "From Labyrinth Seals to Damping Seals/Bearings," *4th International Symposium on Transport Phenomena and Dynamics of Rotating Machinery*, ISCROMAC-4, pp. 277–285.
[5] Massey, I., 1985, "Subsynchronous Vibration Problems in High Speed Multistage Centrifugal Pumps," *Proceedings of the 14th Turbomachinery Symposium*, Texas A&M University, pp. 11–16.
[6] Kim, C. H. and Lee, Y. B., 1994, "Test Results for Rotordynamic Coefficients of Anti-Swirl Self-Injection Seals," ASME J. Tribol., **116**, pp. 508–513.
[7] Kanki, H. and Kawakami, T., 1987, "Experimental Study on the Dynamic Characteristics of Screw Grooved Seals," *Rotating Machinery Volume 1*, ASME DE-Vol. 2, pp. 273–278.
[8] Arauz, G. L. and San Andrés, L., 1996, "Experimental Study on the Effects of a Circumferential Feeding Groove on the Dynamic Force Response of a Sealed Squeeze Film Damper," ASME J. Tribol., **118**, pp. 900–905.
[9] Franchek, N. and Childs, D., 1994, "Experimental Test Results for Four High-Speed, High Pressure, Orifice-Compensated Hybrid Bearings," ASME J. Tribol., **116**(2), pp. 285–290.
[10] San Andrés, L. and Childs, D., 1997, "Angled Injection-Hydrostatic Bearings, Analysis and Comparison to Test Results," ASME J. Tribol., **119**(1), pp. 179–187.
[11] Fayolle, P. G., Phillips, S. G., and Childs, D. W., 1997, "Experimental Rotordynamic Coefficient Results for a 0.100-mm Clearance Tangential-Against-Rotation Injection Lomakin Bearing," Technical Report No. TAMU 0710, Texas A&M University, College Station, TX.
[12] Soulas, T., 2001, "A Bulk-Flow Model of Angled Injection Lomakin Bearings," M.S. thesis, Texas A&M University, College Station, TX.
[13] San Andrés, L., Soulas, T., Challier, F., and Fayolle, P., 2002, "A Bulk-Flow Model for Angled Injection Lomakin Bearings," Paper No. 275, in Proceedings of the ASME TURBO EXPO 2002, June.
[14] San Andrés, L., 1991, "Analysis of Variable Fluid Properties, Turbulent Annular Seals," ASME J. Tribol., **113**, pp. 694–702.
[15] Hélène, M., Arghir, M., and Frêne, J., 2002, "Numerical Three-Dimensional Pressure Patterns in a Recess of a Turbulent and Compressible Hybrid Journal Bearing," ASME J. Tribol. **125**, pp. 301–308.
[16] San Andrés, L., 1990, "Turbulent Hybrid Bearings With Fluid Inertia Effects," ASME J. Tribol., **112**(3), pp. 699–707.
[17] Launder, B. E. and Leschziner, M., 1978, "Flow in Finite-Width, Thrust Bearings Including Inertial Effects," ASME J. Lubr. Technol., **100**, pp. 330–338.
[18] Arghir, M. and Frêne, J., 2001, "A Triangle Based Finite Volume Method for the Integration of Lubrication's Incompressible Bulk Flow Equations," ASME J. Tribol., **123**(1), pp. 118–124.

Downloaded 02 Jun 2010 to 171.66.16.98. Redistribution subject to ASME license or copyright; see http://www.asme.org/terms/Terms_Use.cfm

Influence of Fluid Dynamics on Heat Transfer in a Preswirl Rotating-Disk System

Gary D. Lock

Michael Wilson

J. Michael Owen

Department of Mechanical Engineering,
University of Bath,
Bath BA2 7AY, UK

Modern gas turbines are cooled using air diverted from the compressor. In a "direct-transfer" preswirl system, this cooling air flows axially across the wheel space from stationary preswirl nozzles to receiver holes located in the rotating turbine disk. The distribution of the local Nusselt number Nu on the rotating disk is governed by three nondimensional fluid-dynamic parameters: preswirl ratio β_p*, rotational Reynolds number* Re_ϕ*, and turbulent flow parameter* λ_T*. This paper describes heat transfer measurements obtained from a scaled model of a gas turbine rotor-stator cavity, where the flow structure is representative of that found in the engine. The experiments reveal that Nu on the rotating disk is axisymmetric except in the region of the receiver holes, where significant two-dimensional variations have been measured. At the higher coolant flow rates studied, there is a peak in heat transfer at the radius of the preswirl nozzles associated with the impinging jets from the preswirl nozzles. At lower coolant flow rates, the heat transfer is dominated by viscous effects. The Nusselt number is observed to increase as either* Re_ϕ *or* λ_T *increases.* [DOI: 10.1115/1.1924721]

1 Introduction

The specific work of gas turbines increases with higher gas temperature, and typical modern engines experience turbine entry temperatures (TET) of up to 1800 K. At these elevated temperatures, the turbine components (disks, nozzle guide vanes, and rotor blades) require cooling for safe operation and acceptable lifetime. Increasing the mass flow rate of coolant allows an increase in the TET, which is the main objective of using cooling flow. However, effective turbine cooling incurs a thermodynamic cost: first, the compressed air is diverted from the main flow and not used in combustion; second, there are coolant pressure losses in the feed, delivery, and blade passages; and third, the viscous mixing of coolant with the mainstream after ejection will reduce the aerodynamic efficiency of the turbine. The engine designer has the task of creating a coolant system that optimizes the specific fuel consumption, using a compromise between increased TET and this reduced turbine efficiency.

Preswirl nozzles are often used in gas turbines to deliver the cooling air to the turbine blades, as illustrated in Fig. 1. The stationary nozzles swirl the cooling air in the direction of rotation of the turbine disk, thereby reducing the temperature of the air relative to the blades. The designer needs to know the effect of the preswirl ratio β_p, the coolant flow rate, and the rotational speed Ω on the pressure drop and temperature difference between the preswirl nozzles and the receiver holes in the disk. It is also important to know the effect of these parameters on the distribution of Nusselt number Nu over the surface of the rotating disk.

Designers can obtain some information using turbine-based rigs running close to engine-operating conditions. However, deeper insight can be gained from fundamental research which measures, computes and explains the flow and heat transfer in generic, fully-instrumented rigs operating under more benign conditions. Computational codes, validated on these detailed measurements, can then be used to conduct calculations extrapolated to engine conditions.

Owen and Rogers [1], Karabay et al. [2], and Pilbrow et al. [3] presented experimental and computational results for flow and heat transfer in a "cover-plate" (rotating cavity) preswirl system, showing that the structure of these flows is governed principally by the values of β_p and the turbulent-flow parameter, $\lambda_T = C_w\,\mathrm{Re}_\phi^{-0.8}$. (The turbulent flow parameter, which combines the effects of the nondimensional preswirl flow rate C_w and the rotational Reynolds number Re_ϕ for the disk, is related to the entrainment of fluid into the boundary layer on a rotating disk; for turbulent flow, $\lambda_T \approx 0.22$ for the entrainment due to an unconfined disk [3].) The heat transfer is governed by the above two parameters as well as by the rotational Reynolds number Re_ϕ and by the temperature distribution on the rotating disk.

This paper discusses the effects of β_p, λ_T, and Re_ϕ on the heat transfer between the air and the rotating disk in a generic rig. The experimental facility is a simplified model of a gas turbine rotor-stator system designed to accommodate pressure and temperature instrumentation in the test section and to provide optical access to the wheel-space.

Meierhofer and Franklin [4] were the first to experimentally confirm the significant reduction in relative total temperature using a preswirl system and quantified the effectiveness of such a system in terms of the ratio of delivery air velocity to disk speed. Extensive research is currently being conducted at the University of Karlsruhe: Dittmann et al. [5,6] have reported the discharge behavior and Geis et al. [7] have reported measurements of temperature reduction in preswirl systems. Chew et al. [8] presented a theoretical analysis to determine cooling air delivery temperatures, which was shown to correlate well with experimental measurements.

2 Experimental Apparatus

Experiments were conducted using a scaled model of a gas-turbine rotor-stator system. The geometry, which was based on information obtained for existing engine designs, is illustrated schematically in Fig. 2. The air entered the test section through the stator at low radius via preswirl nozzles and flowed radially out-

Contributed by the International Gas Turbine Institute (IGTI) of THE AMERICAN SOCIETY OF MECHANICAL ENGINEERS for publication in the ASME JOURNAL OF ENGINEERING FOR GAS TURBINES AND POWER. Paper presented at the International Gas Turbine and Aeroengine Congress and Exhibition, Vienna, Austria, June 13–17, 2004, Paper No. 2004-GT-53158. Manuscript received by IGTI, October 1, 2003; final revision, March 1, 2004. IGTI Review Chair: A. J. Strazisar.

Copyright © 2005 by ASME

Downloaded 02 Jun 2010 to 171.66.16.98. Redistribution subject to ASME license or copyright; see http://www.asme.org/terms/Terms_Use.cfm

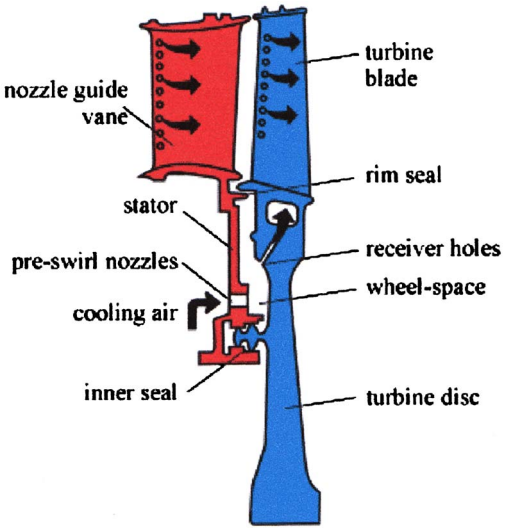

Fig. 1 Simplified diagram of typical pre-swirl cooling-air system for a gas turbine

ward between the rotating disk and the stator, exiting through receiver holes in the rotating disk representing the entrance to the blade-cooling passages in the engine.

The disk radius was $b=216$ mm, and the other principal dimensions are the inner-to-outer radius ratio $a/b=0.67$ and the gap ratio $s/b=0.051$. The stator was machined from aluminum and contained 24 circular preswirl nozzles angled at 20 deg to the tangential direction. The rotating disk was machined from transparent polycarbonate, with sectors sprayed with thermochromic liquid crystals (TLC) and black paint, and contained 60 axial receiver holes with a length-to-diameter ratio of 1.25. The nondimensional radius of the nozzles, $x_p=r_p/b=0.74$, was less than that of the receiver holes, $x_b=r_b/b=0.93$, and the area ratio of the receiver holes to that of the nozzles was 2.9.

A cross-sectional drawing of the working section is shown in Fig. 3, identifying the different materials used in the construction of the apparatus. A small flow of air was passed through an annular chamber to seal the periphery. All mass flow rates were measured using a standard orifice plate.

The disk could be rotated up to speeds of 5000 rpm, providing a maximum rotational Reynolds numbers Re_ϕ (based on disk radius) up to 1.2×10^6. This value is typically an order of magnitude less than those found in gas turbines. The mass flow rates were chosen to simulate engine-representative values of β_p and λ_T and, as discussed above, the flow structure within the rotating cavity depends principally on these two parameters and only weakly on

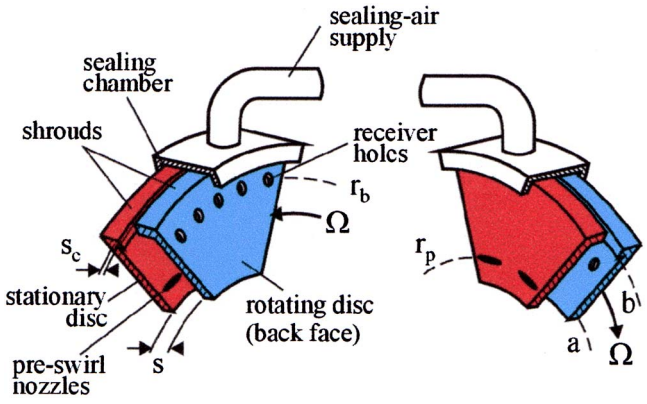

Fig. 2 Schematic diagram of test-section geometry

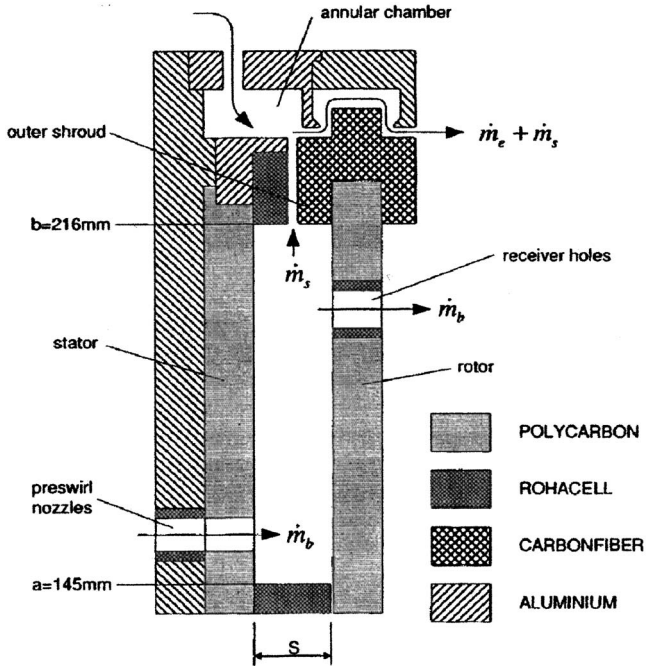

Fig. 3 Cross-sectional drawing of test rig

Re_ϕ. Hence the flow structure is considered to be representative of that found in cooling systems of engines. Experiments were conducted for around 20 test conditions covering the following parametric range: $0.78\times10^6<\mathrm{Re}_\phi<1.2\times10^6$; $0.125<\lambda_T<0.36$; $0.5<\beta_p<1.5$. The geometric properties and operating conditions are summarized in Table 1.

The number of preswirl nozzles N could be reduced from $N=24$ to 12 by blocking every other nozzle, and this allowed higher inlet swirl ratios to be tested for the preswirl flow rates available. The ratio of the area of the receiver holes to that of the nozzles was 2.9 for $N=24$ and 5.8 for $N=12$. The design of the rig did not allow independent testing of β_p and λ_T. The inlet swirl ratio β_p was calculated from

$$\beta_p=\frac{C}{N}\left(\frac{C_{W,p}}{\mathrm{Re}_\phi}\right)=\frac{C}{N}\lambda_T\,\mathrm{Re}_\phi^{-0.2}$$

where

$$C=\frac{4b^3\cos\theta}{\pi d^2 r_p}$$

for preswirl nozzles of diameter d and tangential angle θ.

The fluid dynamics of this facility has been investigated both experimentally and computationally by Yan et al. [9]. The effects of rotational speed, flow rate, preswirl ratio, and the number of preswirl nozzles on the flow field and on the total pressure losses in the system have been reported. These measurements and computations showed that there was a significant loss of total pressure

Table 1 Summary of geometry and operating conditions

Disk radius, b	216 mm
Inner radius, a	$a/b=0.67$
Gap, s	$s/b=0.051$
Preswirl radius	$r_p/b=0.74$
Receiver-hole radius	$r_b/b=0.93$
Re_ϕ	$0.78-1.2\times10^6$
λ_T	0.125–0.36
β_p	0.5–1.5

Downloaded 02 Jun 2010 to 171.66.16.98. Redistribution subject to ASME license or copyright; see http://www.asme.org/terms/Terms_Use.cfm

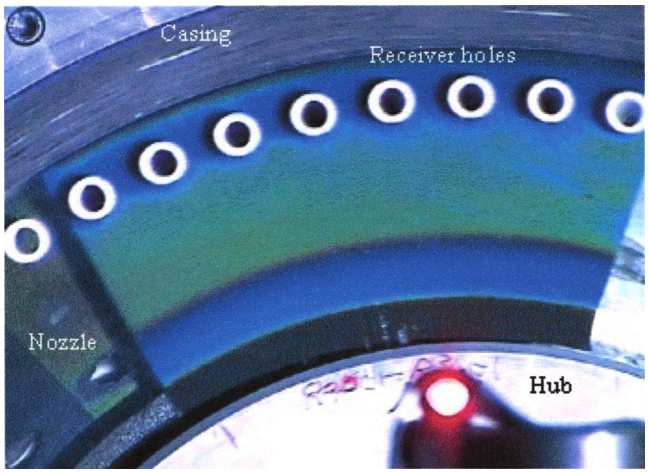

Fig. 4 Video image of TLC on rotating disk. Color photograph available in ASME Paper 2004-GT-53158.

between the outlet from the preswirl nozzles and the rotating core of fluid in the wheel space. This loss increased as the preswirl flow rate and inlet swirl ratio increased and as the number of nozzles decreased. The discharge coefficient of the receiver holes increased as the preswirl ratio at the receiver-hole radius approached unity. (Information concerning discharge coefficients is given in the Appendix.)

3 Heat Transfer Experiments

Local heat transfer coefficients on the rotating disk were determined from transient surface-temperature measurements using thermochromic liquid crystals (TLC), as described by Lock et al. [10]. These experiments were conducted under known thermal boundary conditions, using air that had been preheated to approximately 60°C using a mesh heater upstream of the preswirl nozzles. The measurements relied on the accurate measurement of the time taken for 30°C and 40°C narrow-band TLC on the rotor surface to reach a unique value of hue, which had been calibrated against temperature. The crystals were sprayed on the disk in sectors inside the wheel space, which could be viewed through the transparent polycarbonate by a digital video camera, running at 25 fps, under the illumination of a strobe light synchronized to the disk frequency. A thin layer of black paint was used to provide contrast to the color play of the TLC.

Figure 4, taken from Lock et al. [10], is a color image selected from a time sequence obtained by the digital camera during a typical experiment. This image shows the color play of the TLC as viewed through the transparent polycarbonate disk. Initially clear when below its activation temperature, the TLC changed color from red to green to blue as the disk was heated by the hot gas entering through the preswirl nozzles. The image appears "frozen" because the rotor was illuminated by the stroboscopic light synchronized with the disk rotating at 5000 rpm.

The hub and casing, at radii a and b, are marked in Fig. 4. The blade receiver holes, insulated using low-conductivity, white-colored rohacell foam, are also labeled. The narrow-band TLC and overcoat of black paint had been sprayed in a 48 deg sector on the disk covering eight of the 60 receiver holes. To the left of this painted sector the stator, coated with wideband TLC, two of the 24 preswirl nozzles are visible through the transparent (unpainted) polycarbonate at low radius. Some shadows appear around the receiver holes because of constraints with the lighting and viewing angles.

In Fig. 4 both the 30°C and 40°C narrow-band TLC have been activated into their visible range and display different colors at different locations on the rotating disk. Blue reveals higher temperature, indicating that there is a region of relatively high heat transfer around the receiver holes. The virtually identical TLC patterns around each of these holes indicate the periodicity of the flow structure. Note that the stator, as indicated by the change in color of the wideband TLC, has also been heated throughout this transient process.

Color images (typically 800×600 pixels), recorded at 25 fps by the digital camera, were subsequently converted to hue. It was then possible to obtain the hue history of each pixel in the image and, hence, the time taken for the surface to reach a prescribed value of hue.

The air total temperature was measured using fast-response thermocouple probes in the preswirl cavity. These probes and the TLC calibration are described by Lock et al. [10].

4 Data Analysis

The heat transfer coefficient h is defined as

$$q_w = h(T_{aw} - T_w) \tag{4.1}$$

where q_w is the surface heat flux from the air to the wall, T_w is the surface temperature of the wall, and T_{aw} is the adiabatic-wall temperature. T_{aw} depends on the total temperature of the air T_a and on the fluid dynamics.

In a typical transient test, an abrupt change in air temperature is generated and narrow-band TLC is used to determine the surface temperature T_w of the test piece. Knowing the time t at which the surface reaches T_w, h (assumed time-invariant) can be calculated from the solution of Fourier's one-dimensional conduction equation for the case of a semi-infinite plate.

In the tests reported here, the mesh heater created an effective step change in the air temperature, but at the test section an exponential-type of behavior (or so-called slow transient) was produced. Lock et al. [10] show that the adiabatic wall temperature T_{aw} could be fitted by an exponential series of m terms, such that

$$T_{aw}(t) = T_{a,0} + \sum_{j=1}^{m} T_{a,j}(1 - e^{-t/\tau_j}) + F \tag{4.2}$$

where $T_{a,0}$ is the air temperature at $t=0$, $T_{a,j}$ and τ_j are the constant amplitudes and time constants, respectively and F is a time-invariant parameter that depends on the fluid dynamics.

As $t\to\infty$,

$$T_{aw,\infty} = T_0 + \sum_{j=1}^{m} T_{a,j} \tag{4.3}$$

where T_0 is the initial temperature of the wall, such that

$$T_0 = T_{a,0} + F \tag{4.4}$$

Fourier's conduction equation for a semi-infinite slab has been solved by Gillespie et al. [11] for the case where there is a simple exponential increase in the air temperature, corresponding to the case where $m=1$ in Eq. (4.3). The solution is

$$\Theta = \frac{T_w - T_0}{T_{aw,\infty} - T_0} = g(\beta, \beta_\tau) \tag{4.5}$$

where

$$g(\beta,\beta_\tau) = 1 - \frac{1}{1+\beta_\tau^2} e^{\beta^2}\,\mathrm{erfc}(\beta) - e^{-t/\tau}\frac{\beta_\tau^2}{1+\beta_\tau^2} \times \left\{ 1 + \frac{1}{\beta_\tau}\left[\frac{1}{\pi}\sqrt{\frac{t}{\tau}} + \frac{2}{\pi}\sum_{n=1}^{\infty}\frac{1}{n} e^{-\pi^2/4}\sinh\left(n\sqrt{\frac{t}{\tau}}\right)\right]\right\} \tag{4.6}$$

Downloaded 02 Jun 2010 to 171.66.16.98. Redistribution subject to ASME license or copyright; see http://www.asme.org/terms/Terms_Use.cfm

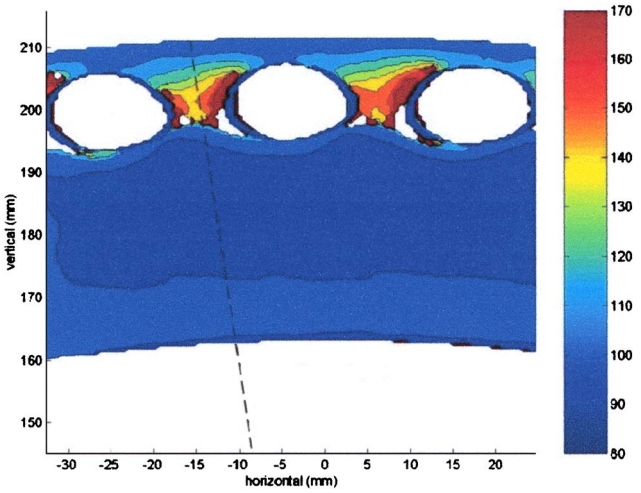

Fig. 5 Contour map of heat transfer coefficient (W/m²K) for viscous dominated flow: $Re_\phi \approx 0.8\times10^6$, $\lambda_T \approx 0.125$, $\beta_p \approx 0.5$. The disk is rotating counter-clockwise. Color contours available in ASME Paper 2004-GT-53158.

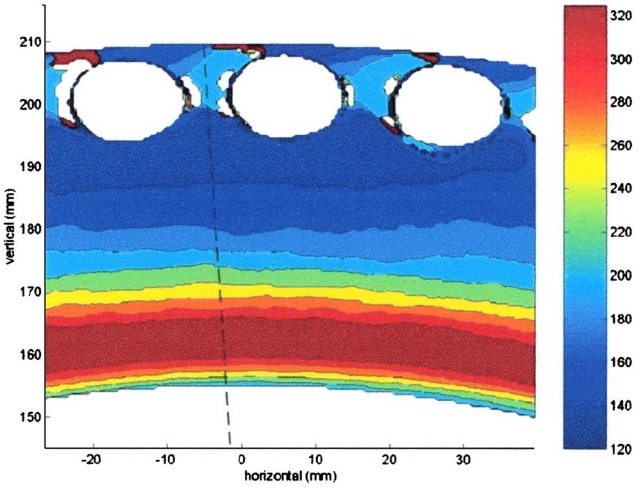

Fig. 6 Contour map of heat transfer coefficient (W/m²K) for inertially dominated flow: $\lambda_T \approx 0.36$, $\beta_p \approx 1.4$, $Re_\phi \approx 0.8\times10^6$. Counter-clockwise rotation. Color contours available in ASME Paper 2004-GT-53158.

$$\beta = \frac{h\sqrt{t}}{\sqrt{\rho c k}} \tag{4.7}$$

and

$$\beta_\tau = \frac{h\sqrt{\tau}}{\sqrt{\rho c k}} \tag{4.8}$$

For the case where $\tau=0$, Eq. (4.5) simplifies to

$$\Theta = f(\beta) \tag{4.9}$$

where, from Eq. (4.6),

$$f(\beta) = 1 - e^{\beta^2}\,\mathrm{erfc}(\beta) \tag{4.10}$$

which is the well-known solution of Fourier's equation for a step change in the air temperature.

The general solution for an exponential series, corresponding to Eq. (4.3), is given by Newton et al. [12] as

$$\Theta = \sum_{j=1}^{m} \frac{T_{a,j}}{T_{aw,\infty} - T_0} g(\beta, \beta_{\tau_j}) \tag{4.11}$$

For the special case where $m=1$, $T_{a,1}=T_{aw,\infty}-T_0$ and Eq. (4.11) reduces to (4.6).

5 Two-Dimensional Experimental Results

Figures 5 and 6 are typical contour maps of heat transfer coefficient on the rotating disk. The data were collected from experiments conducted at the same Re_ϕ, but different values of β_p and λ_T and the different flow structures have created markedly different heat transfer patterns. The data are based on the 40°C narrowband TLC.

The fluid dynamic conditions for Fig. 5 feature a relatively low value of λ_T, hence relatively weak impingement from the preswirl nozzles, and this "viscous" flow regime is dominated by the boundary layer on the rotating disk. The largest levels of h are measured near the receiver holes. These holes have created three-dimensional flow near the surface of the disk, which, in turn, leads to the two-dimensional distribution of h in their vicinity. Away from this region there is little radial or circumferential variation in h.

The fluid dynamic conditions for Fig. 6 feature a relatively high value of λ_T, hence relatively high-velocity jets exiting the preswirl nozzles, and this "inertial" flow regime is dominated by impingement on the rotating disk. There is a strong radial variation in h, with the highest levels located at the nozzle radius ($x=0.74$); there is also a smaller peak near the receiver holes. The h contours show little circumferential variation away from this vicinity.

6 Radial Variation of Nusselt Number

Lock et al. [10] presented two-dimensional distributions of local Nusselt number over the rotating disk surface for different test conditions. In all cases these exhibited nearly axisymmetric behavior, except in regions near and around the receiver holes. There was generally good repeatability for measurements obtained between different pairs of holes. This section will discuss how the governing fluid dynamic parameters, Re_ϕ, λ_T, and β_p, and the number of nozzles N effect the Nusselt number distribution.

Effect of λ_T and β_p at Constant Re_ϕ and $N=24$. Figures 7 and 8 illustrate, respectively, the effect of varying λ_T (and as a consequence, of varying β_p) on the measured radial variation of Nu for $Re_\phi=0.8\times10^6$ and 1.2×10^6. The measurements correspond to radial lines midway between the receiver holes (see the dotted line in Figs. 5 and 6).

At both Reynolds numbers the Nusselt number variation with x is characterized by viscous behavior at low values of $\lambda_T=0.12$

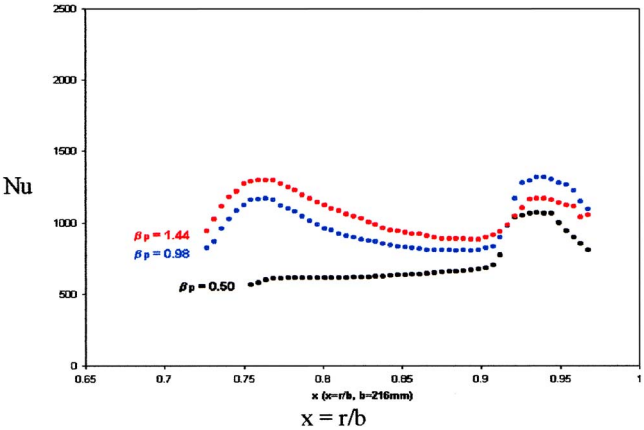

Fig. 7 Effect of λ_T and β_p on the radial distribution of Nu: $Re_\phi \approx 0.8\times10^6$

Downloaded 02 Jun 2010 to 171.66.16.98. Redistribution subject to ASME license or copyright; see http://www.asme.org/terms/Terms_Use.cfm

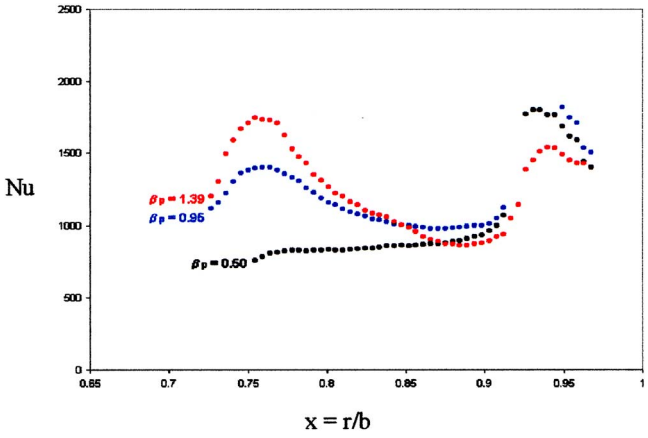

Fig. 8 Effect of λ_T and β_p on the radial distribution of Nu: $Re_\phi \approx 1.2 \times 10^6$

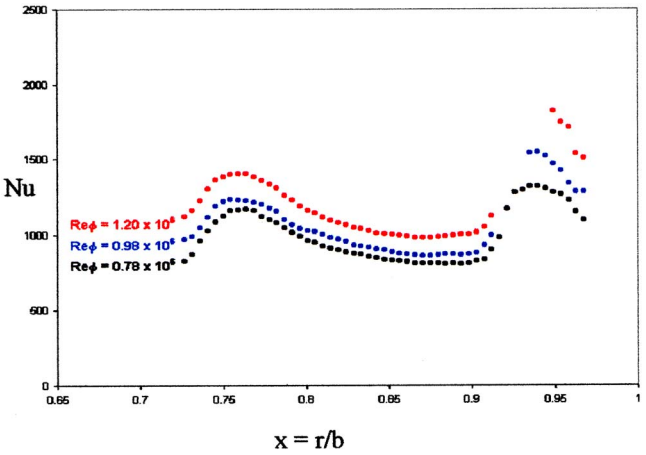

Fig. 10 Effect of Re_ϕ on the radial distribution of Nu: $\lambda_T \approx 0.24$, $\beta_p \approx 1.0$

(β_p=0.5), where the heat transfer is governed by the boundary layer flow on the rotating disk. Here Nu increases with radius for $x > x_p$. For $x > 0.9$ there is a local peak in Nu. In this region the disk boundary layer fluid enters the receiver holes and there is a strong flow axially toward the disk, causing an increase in heat transfer coefficient.

At higher values of λ_T=0.24 and 0.36 (and the corresponding higher values of $\beta_p \approx 1.0$ and 1.2), the Nusselt number variation with radius is characterized by an inertial regime. The combined effect of increasing λ_T and β_p is greatest opposite the preswirl nozzles (x_p=0.74), where the more powerful preswirl flow at large λ_T impinges onto the disk. The Nusselt number decreases for $x_p < x < x_b$. The three-dimensional motion of the flow creates an increase in heat transfer coefficient near the receiver holes in all cases. In this region and outward of the receiver holes, Nu is less sensitive to λ_T and β_p.

Effect of Re_ϕ at Constant λ_T, β_p, and N=24. Figures 9–11 illustrate the effect of Re_ϕ on the radial variation of Nusselt number at fixed values of λ_T=0.12, 0.24, and 0.36, approximately, for which β_p=0.5, 1.0, and 1.2, respectively. For each fixed value of λ_T (and hence β_p) the magnitude of Nu increases with increasing Re_ϕ at all radii, but there is little effect of Re_ϕ on the *shape* of the Nu distribution. For the case characterized by the viscous regime (Fig. 9, $\lambda_T \approx 0.12$), the highest level of Nu is near the receiver holes. This local peak in Nu near the receiver holes occurs for all cases, but the maximum Nu is observed opposite the preswirl nozzles for cases with large β_p.

Effect of N and β_p at Constant Re_ϕ and λ_T. Figure 12 illustrates Nu distributions with radius for two experiments at common Re_ϕ and λ_T (hence common mass flow rate), but with different numbers of nozzles (N=12 and N=24) and hence different β_p.

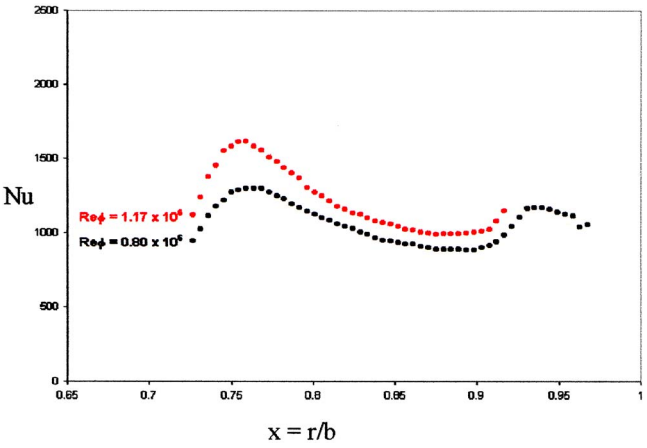

Fig. 11 Effect of Re_ϕ on radial distribution of Nu: $\lambda_T \approx 0.36$, $\beta_p \approx 1.2$

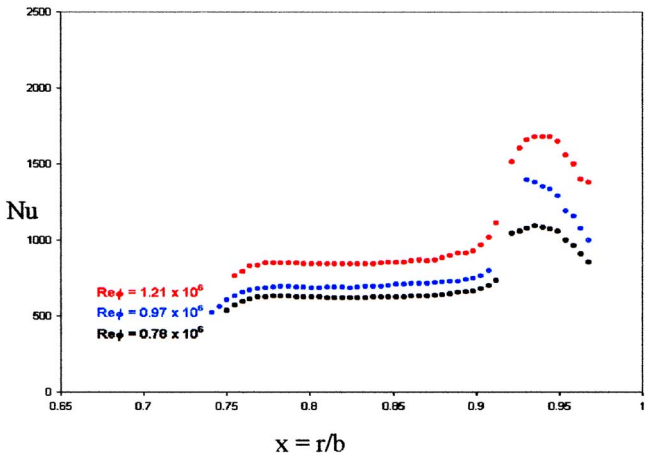

Fig. 9 Effect of Re_ϕ on the radial distribution of Nu: $\lambda_T \approx 0.125$, $\beta_p \approx 0.5$

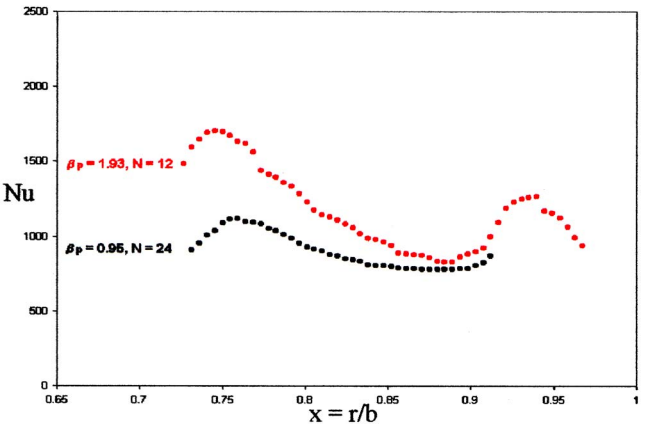

Fig. 12 Effect of β_p and N on radial distribution of Nu: $Re_\phi \approx 1.0 \times 10^6$, $\lambda_T \approx 0.24$

Downloaded 02 Jun 2010 to 171.66.16.98. Redistribution subject to ASME license or copyright; see http://www.asme.org/terms/Terms_Use.cfm

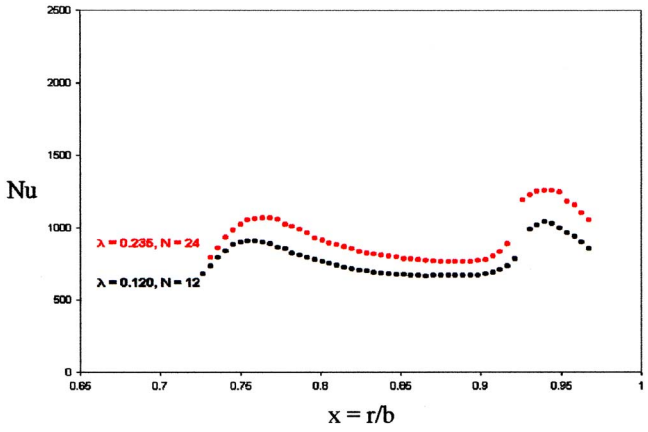

Fig. 13 Effect of λ_T and N on radial distribution of Nu: $Re_\phi \approx 0.8\times10^6$, $\beta_p \approx 1.0$

This figure clearly illustrates higher levels of Nu for the case $N=12$, which corresponds to greater nozzle jet velocities and impingement or inertial effects.

Effect of N and λ_T at Constant Re_ϕ and β_p. For a simple rotating-disk system, heat transfer on the disk is controlled by the development of the viscous boundary layer and this, in turn, is affected by the level of swirl outside the boundary layer $\beta_{p,m}$ [1]. Gord et al. [13] have shown that for constant β_p the level and distribution of $\beta_{p,m}$ is not sensitive to the number of nozzles N at the experimental conditions considered here. Figure 13 illustrates Nu distributions with radius for two experiments at common Re_ϕ and β_p, but with different numbers of nozzles ($N=12$ and $N=24$) and hence different λ_T. As the level of β_{pm} (which influences viscous effects) for these two cases is similar, these results suggest that increased inertial effects, for the higher mass flow rate at $N=24$, are mainly responsible for the increase in Nu. The uncertainty in the measurement of Nusselt number, based on the method described by Owen et al. [14], is estimated as ±5%.

7 Conclusions

An experimental study has been undertaken to investigate the influence of flow rate, swirl ratio, and rotational Reynolds number on the heat transfer in a rotor-stator system with preswirled air. Thermochromic liquid crystal (TLC), in conjunction with a stroboscopic light and digital video camera, has been used to obtain contour maps of Nusselt number Nu on the rotating disk in conditions featuring engine-representative flow structure.

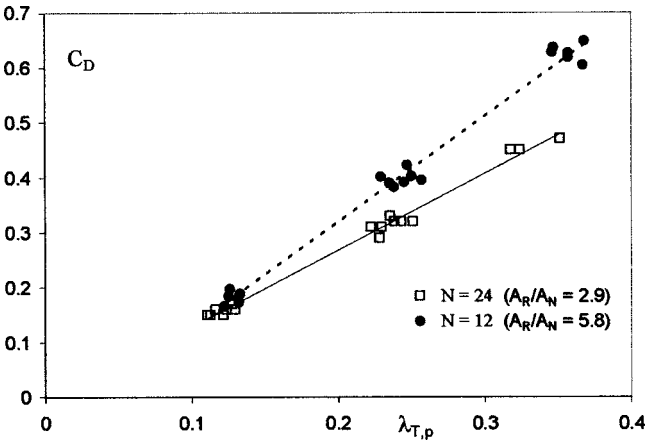

Fig. 14 Measured variation of C_D with $\lambda_{T,p}$ (corrected version of Fig. 8(*a*) of Yan et al. [9])

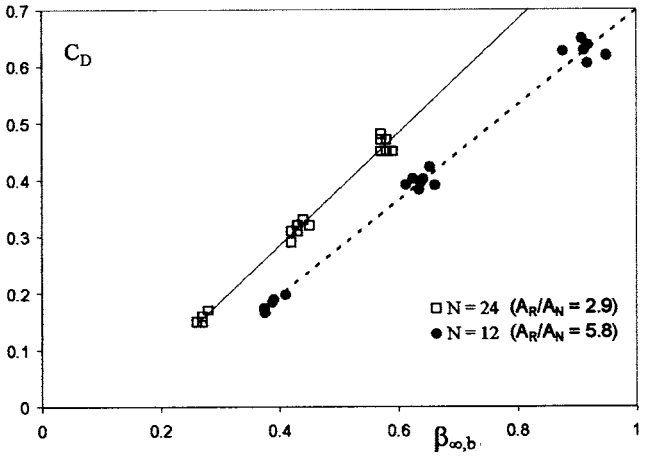

Fig. 15 Measured variation of C_D with $\beta_{\infty,b}$ (corrected version of Fig. 8(*b*) of Yan et al. [9])

Two heat transfer regimes were observed: a viscous regime at relatively low values of λ_T and an inertial regime at high values of λ_T. The viscous regime corresponds to axisymmetric boundary-layer flow over most of the rotating disk: for $x<x_b$, Nu increases as x increases. The inertial regime corresponds to impingement on the rotating disk around the preswirl nozzle radius, $x=x_p$. There is a peak in Nu near $x=x_p$ and, for $x_p<x<x_b$, Nu decreases as x increases; this behavior is also virtually axisymmetric.

Three-dimensional flow near the receiver holes on the disk creates nonaxisymmetric flow in this region, with large values of Nu between and around the holes. For both regimes, Nu increases as Re_ϕ, λ_T, and β_p increase.

Acknowledgment

This work was funded by Alstom Power Ltd. (now Siemens Industrial Turbines) and the UK Engineering and Physical Sciences Research Council. The authors are also grateful for the assistance of Dr. Y. Yan.

Nomenclature

a = inner radius of the disk
b = outer radius of the disk
c = specific heat of wall
c_p = specific heat at constant pressure of air
C_w = nondimensional mass flow rate ($=\dot{m}/\mu b$)
d = preswirl nozzle diameter
$f(\beta)$ = step-change solution of the Fourier equation
F = time-invariant adiabatic-wall parameter ($=T_{aw}-T_a$)
$g(\beta,\beta_\tau)$ = exponential solution of the Fourier equation
h = heat transfer coefficient [$=q_w/(T_{aw}-T_w)$]
k = thermal conductivity of wall
m = number of terms in exponential series
$\dot{m}$ = mass flow rate
Nu = Nusselt number [$=q_w r/k(T_{aw}-T_w)$]
q_w = heat flux from air to wall
r = radius from axis of rotation
Re_ϕ = rotational Reynolds number ($=\rho\Omega b^2/\mu$)
s = gap width
s_c = clearance spacing
t = time
T = temperature inside wall
T_a = total temperature of air
T_{aw} = adiabatic wall temperature
T_w = surface temperature of wall

Downloaded 02 Jun 2010 to 171.66.16.98. Redistribution subject to ASME license or copyright; see http://www.asme.org/terms/Terms_Use.cfm

x = nondimensional radius ($=r/b$)
β = parameter in step-change solution ($=h\sqrt{t/\rho ck}$)
β_p = preswirl ratio ($=V_{\phi,p}/\Omega r_p$)
β_τ = parameter in exponential solution ($=h\sqrt{\tau/\rho ck}$)
λ_T = turbulent flow parameter ($=C_{w,p}/\mathrm{Re}_\phi^{0.8}$)
ρ = density
θ = angle of preswirl nozzle to tangential
Θ = nondimensional temperature $[=(T_w-T_0)/(T_{aw,\infty}-T_0)]$
μ = dynamic viscosity
Ω = angular speed of rotating disk
τ = time constant

Subscripts

b = blade
e = exterior
j = jth term in series
m = outside the boundary layer
p = preswirl nozzle
o = value at $t=0$
s = seal
∞ = value as $t\rightarrow\infty$

Appendix: Corrected Measured Discharge Coefficients for the Paper by Yan et al. [9]

As explained by Yan et al. [9], corrections were made to the calculation of measured discharge coefficients C_D, compared to the conference paper version that appeared previously. The correct modified text was printed correctly in the journal version, however, the corresponding corrected figures were not. These corrected figures, which are consistent with the discussion in Yan et al. [9], are given in Figs. 14 and 15. In Ref. [10] the disk described in Figs. 7 and 8 should be described as rotating counterclockwise, not clockwise.

References

[1] Owen, J. M., and Rogers, R. H., 1989, *Flow and Heat Transfer in Rotating Disc Systems: Vol. 1, Rotor-Stator Systems*, Research Studies Press, Taunton, UK and Wiley, New York.
[2] Karabay, H., Wilson, M., and Owen, J. M., 2001, "Predictions of Effect of Swirl on Flow and Heat Transfer in a Rotating Cavity," Int. J. Heat Fluid Flow, **22**, pp. 143–155.
[3] Pilbrow, R., Karabay, H., Wilson, M., and Owen, J. M., 1999, "Heat Transfer in a "Cover-Plate" Pre-Swirl Rotating-Disc System," ASME J. Turbomach., **121**, pp. 249–256.
[4] Meierhofer, B., and Franklin, C. J., 1981, "An Investigation of a Pre-Swirled Cooling Airflow to a Turbine Disc by Measuring the Air Temperature in the Rotating Channels," ASME Paper No. 81-GT-132.
[5] Dittmann, M., Geis, T., Schramm, V., Kim, S., and Wittig, S., 2002, "Discharge Coefficients of a Pre-Swirl System in Secondary Air Systems," ASME J. Turbomach., **124**, pp. 119–124.
[6] Dittmann, M., Dullenkopf, K., and Wittig, S., 2003, "Direct Transfer Pre-Swirl System: One-Dimensional Modular Characterization of the Flow," ASME Paper No. GT-2003-38312.
[7] Geis, T., Dittmann, M., and Dullenkopf, K., 2003, "Cooling Air Temperature Reduction in a Direct Transfer Pre-Swirl System," ASME Paper No. GT-2003-38231.
[8] Chew, J. W., Hills, N., Kalatov, J. S., Scanlon, T., and Turner, A. B., 2003, "Measurement and Analysis of Flow in a Pre-Swirled Cooling Air Delivery System," ASME Paper No. GT-2003-38084.
[9] Yan, Y., Gord, M. F., Lock, G. D., Wilson, M., and Owen, J. M., 2003, "Fluid Dynamics of a Pre-Swirl Rotating-Disk System," ASME J. Turbomach., **125**, pp. 641–647.
[10] Lock, G. D., Yan, Y., Wilson, M., and Owen, J. M., 2003, "Heat Transfer Measurements Using Liquid Crystal in a Pre-Swirl Rotating-Disc System," ASME Paper 2003-GT-38123.
[11] Gillespie, D. R. H., Wang, Z., and Ireland, P. T., 1998, "Full Surface Local Heat Transfer Coefficient Measurements in a Model of an Integrally Cast Impingement Cooling Geometry," ASME J. Turbomach., **120**, pp. 92–99.
[12] Newton, P. J., Yan, Y., Stevens, N. E., Evatt, S. T., Lock, G. D., and Owen, J. M., 2003, "Transient Heat Transfer Measurements Using Thermochromic Liquid Crystal, Part 1: An Improved Technique," Int. J. Heat Fluid Flow, **24**, pp. 14–22.
[13] Gord, M. F., Wilson, M., and Owen, J. M., 2003, "Effects of Swirl and Flow Rate on the Flow and Heat Transfer in a Pre-Swirl Rotating-Disc System," IGTC2003 Tokyo TS-064.
[14] Owen, J. M., Newton, P. J., and Lock, G. D., 2003, "Transient Heat Transfer Measurements Using Thermochromic Liquid Crystal, Part 2: Experimental Uncertainties," Int. J. Heat Fluid Flow, **24**, pp. 23–28.

Downloaded 02 Jun 2010 to 171.66.16.98. Redistribution subject to ASME license or copyright; see http://www.asme.org/terms/Terms_Use.cfm

A Novel Cooling Method for Turbine Rotor-Stator Rim Cavities Affected by Mainstream Ingress

Y. Okita

M. Nishiura

S. Yamawaki

Y. Hironaka

Aero-Engine and Space Operations,
Ishikawajima-Harima Heavy Industries (IHI),
Tokyo, Japan

A combined experimental and numerical study of interaction between cooling flow and mainstream gas flow in a turbine rotor-stator rim cavity is reported. Particular emphasis is put on the flow phenomena in a rim cavity downstream of rotor blades. The experiments are conducted on a rig simulating an engine HP-turbine in which cooling effectiveness distributions as well as velocities, turbulence quantities, pressure, and temperature profiles are measured. Numerical calculation, especially at a full 3D, unsteady solution level, can lead to satisfactory predictions in fluid and mass transfer inside the cavity. Both experimental and numerical results indicate that large turbulence stresses near the rotor disk intensify turbulent diffusion across the cavity and consequently axial distribution of the cooling effectiveness inside the cavity becomes uniform. In order to obtain an adequate distribution of cooling effectiveness across the rim cavity and to suppress the turbulence level near the rotor surface for more efficient cooling, a novel cooling method is developed using numerical simulation. The disk-front and -rear cavities are then redesigned according to the new cooling strategy and integrated in the test rig. Experimental results verify a significant advance in cooling performance with the new method. [DOI: 10.1115/1.1925647]

Introduction

To avoid overheating of turbine disks, ingestion of mainstream hot gas into rim cavities must be controlled to a minimum. This can be realized by bypassing high pressure compressor air to the turbine where it is ejected into the mainstream through the rim seals. To minimize performance penalties, the sealing flows usually need to be kept as low as possible. This requires a better understanding of the interaction mechanism between mainstream and sealing flows, more accurate quantitative estimates of the amount of coolant needed, and progress toward improved seal configurations. For this reason, intensive researches have been carried out to tackle these issues in the last several decades.

Previous work on turbine rim sealing centered on the effects of disk pumping which tends to draw flow into the cavity (e.g. Bayley and Owen [1]), and the influence of circumferential pressure variations in the annulus flow which was first noted by Campbell [2] and later confirmed experimentally by other researchers. The combined effects of pressure asymmetries due to stationary vanes and rotating blades have been considered recently by Bohn et al. [3], Roy et al. [4], and Hills et al. [5]. Hills et al. measured pressures and seal effectiveness with both vanes and blades present. Based on their measurements and the result that an unsteady CFD gave considerably better agreement with ingestion data than steady models they concluded that the unsteadiness plays an important role in the ingestion process. It may be noted that most research so far has concentrated on the seal downstream of a row of stationary vanes. Investigations to clarify the flow mechanisms in seals downstream of a row of rotating blades are very few.

Apart from the effects of time-averaged and/or coherent blade-periodic nature of the flow field, turbulence in the rim seal region is another important factor associated with the hot gas ingestion process. Ko and Rhode [6] pointed out from their numerical results with two-scale eddy-viscosity model that the extremely high turbulent kinetic energy is generated in the rim cavity from the intense shear stress by the interaction between mainstream and coolant flow. Because of this strong generation of turbulent kinetic energy at the interface, highly turbulent eddies accelerate the exchange of heat from the hot mainstream to the rim cavity. They concluded that such turbulent heat diffusion ingress is as influential as the convection ingress.

Parallel to the efforts toward clarifying the physical mechanisms of ingress, various kinds of seal arrangements have been developed and investigated in order to reduce the amount of cooling air. Depending on the type and shape of rim seal the cooling effectiveness varies drastically. Different kinds of rim seals are in use in modern engines starting from relatively simple axial seals with and without seal lips ranging to complex overlapping radial seal arrangements. Bohn et al. [3] showed that cooling air savings of up to 30% are feasible by adjusting the shape of rim seals employed for a full stage. Even though there may be still room for improvement by optimizing the shape of these conventional seal arrangements, a new cooling measure is needed for more drastic coolant reduction.

In this paper, a combined experimental and numerical study of interaction between main gas path and rim cooling flow is reported. In the experiment, the turbulence quantities as well as the mean flow field are measured. Particular emphasis is put on the flow phenomena in a rim cavity downstream of rotor blades where the authors' group has previously shown the possibility of serious overheating due to mainstream ingress (Yamawaki et al. [7]). Another main contribution of the present work is to develop a novel cooling method for turbine rim cavities which enables a substantial reduction of cooling air. The effects of mainstream ingress will be described in the next section. An improvement of cooling effectiveness by the new cooling method is then reported and discussed in the followed section, with the main conclusions being summarized in the final section.

Contributed by the International Gas Turbine Institute (IGTI) of THE AMERICAN SOCIETY OF MECHANICAL ENGINEERS for publication in the ASME JOURNAL OF ENGINEERING FOR GAS TURBINES AND POWER. Paper presented at the International Gas Turbine and Aeroengine Congress and Exhibition, Vienna, Austria, June 13–17, 2004. Paper No. GT2004-53016. Manuscript received by IGTI, October 1, 2003; final revision, March 1, 2004. IGTI Review Chair: A. J. Strazisar.

Effects of Mainstream Ingress

Experimental Setup. The experiments are conducted in a turbine rig test facility at IHI. The configuration, shown in Fig. 1, is composed of a full-scale model of the 1.5 turbine stage in a mod-

 Copyright © 2005 by ASME

Downloaded 02 Jun 2010 to 171.66.16.98. Redistribution subject to ASME license or copyright; see http://www.asme.org/terms/Terms_Use.cfm

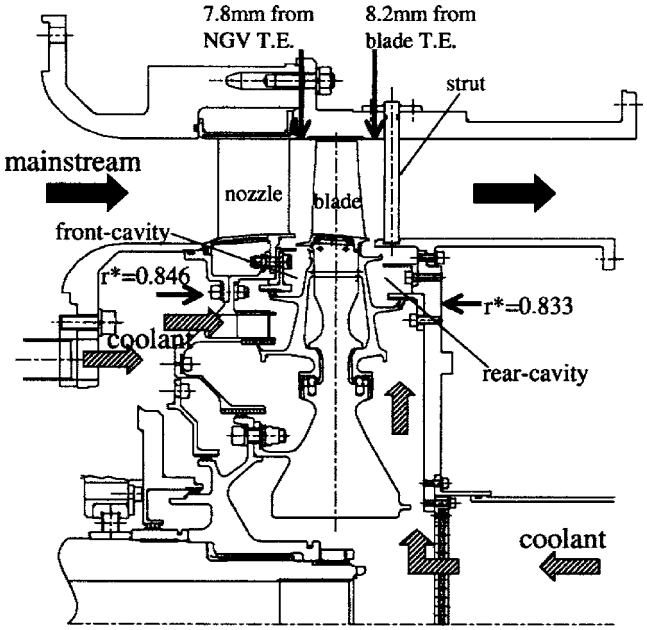

Fig. 1 Schematic of the turbine test

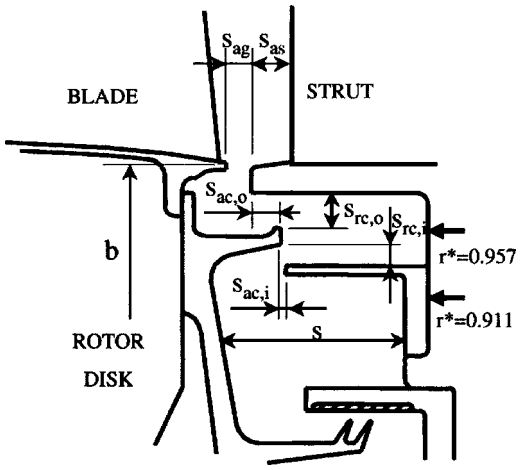

Fig. 2 Detail of the rear-cavity seal geometry

ern gas turbine engine. The stage has 31 nozzle guide vanes (NGV) and 66 rotating blades (RB). The present test is carried out using IHI standard reaction blading. Downstream of the blades, 36 struts are placed. The disk outer radius (b) is 0.272 m and the passage height to disk outer radius ratio is 0.26. The mainstream flowing through a calibrated orifice is supplied by a large compressor, IHI-NK64. The power introduced to the rotor is dissipated by a Nishishiba NEDE-233 eddy current brake dynamometer. In the entrance of the mainstream wire meshes are used to help obtain a symmetric inlet distribution. Measured total pressure variation (radial and circumferential) at 2 chord upstream of the NGVs is less than 0.2%. The cavity cooling flow provided by a separate source of air, a rotary blower TRE-150, is admitted to the rim cavities through labyrinth seals at $r^*=0.846$ (front) and at $r^*=0.833$ (rear). Cylindrical head bolts (ISO 4762) with projected area 78.5 mm^2 per bolt (front) and with 53.8 mm^2 (rear) exist in the both cavities. The numbers of the bolts are 56 and 30, respectively. A double lip on the stator combined with a single lip on the rotor, which is typically used inside a modern aeroengine, is first examined as the "base" seal arrangement both for the cavity downstream of the vanes (front-cavity) and the cavity downstream of the blades (rear-cavity). Figure 2 (only for the rear-cavity) and Table 1 give a detail of the geometric and the flow parameters investigated. There are some spanwise variations in the mainstream flow conditions. The values shown in Table 1 correspond to the streamline nearest to the hub endwall where the main interest of the present work exists. The test conditions are able to model the flow structures expected in modern gas turbine engines. The geometric parameters given in Table 1 are for the static condition. With structural analysis, the rotor disk is estimated to expand 0.34 mm radially at the running condition. The variation in axial clearance between rotor and stator during the experiment, monitored with a gap sensor, is less than 0.5 mm (±0.01 mm uncertainty). Thermal expansion of the stator components at the running condition is considered to be negligible.

The mainstream is instrumented with kiel rakes, wall static pressure tappings (1 mm bore), and thermocouples from which the stage performance can be obtained. The circumferential variation of the static pressure in the mainstream is determined using 6 tappings in the annulus hub and tip endwall drilled at 2 deg intervals and located 7.8 mm downstream of the vanes and 8.2 mm downstream of the blades. Pressures inside the rear-cavity are measured by 6 static pressure taps distributed at 2 deg intervals at $r^*=0.957$ on the stator surface. All pressures throughout the mainstream and the cavities as well as the orifice plates are measured with a Scanivalve DSA3016. Also stationary frame total temperature of cavity air are measured by the sheathed K-type thermocouples at $r^*=0.856$ and at 0.911 to evaluate the temperature rise due to the windage heating. The uncertainty of the orifice plate measurements is ±0.9%. The uncertainty of the thermocouples is determined as ±0.095%. The uncertainty in the measured static pressure estimated on the basis of the instrument and data acquisition uncertainties is ±0.13%.

The cooling effectiveness of the coolant in the rim cavity is measured using a CO_2 tracer technique. The CO_2 sampling probes (1 mm bore) are connected to a pneumatic multiplexer, with the output led to HORIBA VIA-510 CO_2 analyzers. The cavity coolant is seeded with CO_2 to approximately 9000 ppm using a static mixer installed in the coolant supply line. To measure the CO_2 concentration in the front-cavity, the sampling probes are installed at $r^*=0.929$ on the stator and near the rotor surface on two circumferential positions. For the rear-cavity, the probes are installed at $r^*=0.911$ (see Fig. 2), two angular positions and traversed axially. The uncertainty in the gas concentration measurements, estimated at ±1.8%, is mainly due to a drift of the gas analyzer, the averaging of the small fluctuations in concentration inside the cavity and a variation in CO_2 concentration at the static mixer exit.

The velocities and turbulence quantities measurements inside the rear-cavity have been performed using calibrated dual-sensor

Table 1 Geometric and flow parameters

	Front-cavity	Rear-cavity
G	0.06257	0.11997
$G_{ac,i}$	0.00186	0.00307
$G_{ac,o}$	0.00407	–0.01897[a]
$G_{rc,i}$	0.00760	0.01316
$G_{rc,o}$	0.01765	0.02204
S_{ad}/b	0.05896	0.05018
S_{ag}/b	0.00407	0.01593
S_{as}/b	0.01497	0.02572

π	1.64	α_1	72 deg
$Re_{m,1}$	1.59×10^6	α_2	24 deg
$Re_{m,2}$	3.02×10^5	C_w	3500–35000
M_1	0.881	Re_ϕ	2.5×10^6
M_2	0.370	λ_T	0.027–0.27

[a]The negative value means seal overlapping

Downloaded 02 Jun 2010 to 171.66.16.98. Redistribution subject to ASME license or copyright; see http://www.asme.org/terms/Terms_Use.cfm

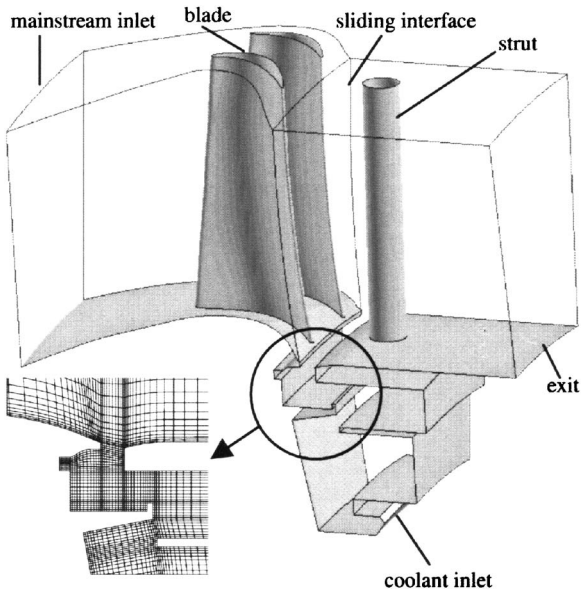

Fig. 3 Computational domain of the unsteady simulation and mesh in the interaction region

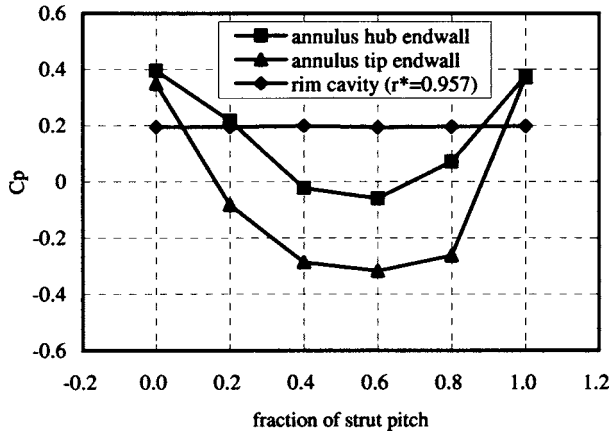

Fig. 4 Measured circumferential distribution of pressure downstream of the blade for C_w=3650

fiber-film probes, DANTEC 55R52, made of two 70 μm in diameter fiber wires, crossed at right angles. The probes at two circumferential positions are introduced through the stator at $r^*=0.911$ and can be axially moved using a traversing system. For all turbulence measurements, 2^{17}(=131072) samples are recorded with a data acquisition rate equal to 20 kHz. The uncertainty of measured velocities is ±4.2% (see Appendix for the details).

Numerical Modelling. The aim of numerical investigation is to give physical insight into the ingestion phenomenon especially for the rear-cavity where the main interest of the present work exists, though some limited computations are also carried out for the front-cavity.

The time-dependent 3D Reynolds-averaged compressible Navier–Stokes equations are solved using a pressure correction algorithm. The turbulent stresses and heat fluxes are modeled through the standard $k-\varepsilon$ model with the standard wall functions at the near-wall cells. The assumption of fully turbulent computation is considered reasonable since in the experiment the mainstream is made fully turbulent by a turbulence grid located well upstream of the test section and, based on the rotational Reynolds number inside the cavities under consideration, the laminar region, if any, should be confined only in a small area. To quantify ingestion, a species concentration equation is also solved. The model calculates the unsteady flow with the solution for rotating and stationary parts of the domains simultaneously via a sliding interface. The computational domain (Fig. 3) including the rear-cavity and the same section of the annulus consists of two rotor blades and a single strut, assuming 68 blades and 34 struts. The unsteady solution is obtained using implicit time stepping with a time step of 5.38×10^{-6} s, approximately 30 time steps per pass of a rotor blade by a strut. Several steady-state computations are also carried out for the model including the rear-cavity with upstream blades only (in rotating frame of reference) and for the model which consists of the cavity and downstream struts only (in stationary frame of reference).

Periodicity in the circumferential direction is assumed at the appropriate boundaries and the no-slip conditions are applied on solid surfaces. At the cooling flow inlet, the mass flux is set uniformly so as to give the required mass flow, swirl ratio is set to 0.2 to be consistent with the solution of a one-dimensional equation of angular momentum conservation within the upstream labyrinth seal, and the species concentration is set to unity. The turbulent kinetic energy is set with a turbulence intensity of 3% and the dissipation rate then obtained assuming turbulence Reynolds number R_T equal to 100. In the annulus, the mass flux, total temperature, flow angle, and a species concentration of zero are specified at the inlet. The values are derived from a through-flow analysis of the 1.5 turbine stage. The turbulence boundary conditions are the same as the cooling flow inlet. At the flow exit, static pressure is specified at the hub, the pressure distribution is obtained from the radial equilibrium conditions, and zero axial gradient is assumed for other variables.

The number of hexahedra control-volume cells is 343,000. A finer 980,000 mesh is also tested for grid sensitivity comparisons and it is confirmed that the axial distribution of cooling effectiveness at $r^*=0.911$ obtained with the two grids are practically identical. The mesh growth rate is kept under 1.2 throughout the model. The converged solutions have near-wall mesh y^+ values in the range $10<y^+<120$. A meridional section of the computational mesh in the interaction region is shown in Fig. 3.

Species concentration at $r^*=0.911$ on the rotor surface is monitored during the calculation to check the convergence of the unsteady solution. After a total calculation time of about 120 blade passing periods, the solution appears to be close to convergence to periodic behavior. Radial velocities in the cavity are of the order of 10 m/s at most. Such low velocities result in the slow convergence. The flow in the cavity takes 8×10^{-3} s, approximately 50 blade passing periods, to recirculate the whole cavity. The solution requires several times this amount of time to converge.

Results. The measured circumferential variation of static pressure downstream of the blades in the mainstream and in the rear-cavity at C_w=3650, are plotted as a pressure coefficient in Fig. 4. In the figure, where location is given as a fraction of strut pitch, 0 represents a leading edge position. The experimental data shows that the circumferential asymmetry is maximum at the annulus tip endwall, the highest pressure being near the strut leading edge. Clearly, the data suggests that this pressure variation is attributed to the downstream struts. Inside the cavity, there is no discernible circumferential pressure variation at the stator disk even near its rim.

Figure 5 shows the axial distribution of the measured tangential velocity in the rear-cavity at $r^*=0.911$ for C_w=3,600 and C_w=19,460. As expected from the theory of rotor-stator system with superposed coolant flow, the experiments show that the core rotation increases with decreasing values of the coolant flow rate. A comparison has been made with the LDA measurements of a rotor-stator cavity without mainstream flow by Gentilhomme et al. [8]. At high sealing flow (C_w=19,460), the tangential velocities in the present case are slightly above the data obtained in [8]. At low coolant flow rate, however, the velocities in the rear-cavity are

Downloaded 02 Jun 2010 to 171.66.16.98. Redistribution subject to ASME license or copyright; see http://www.asme.org/terms/Terms_Use.cfm

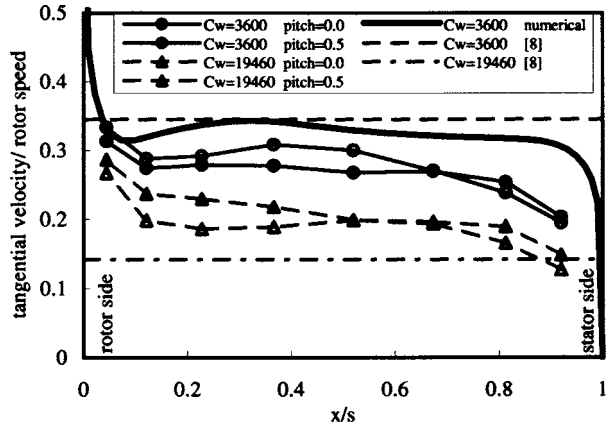

Fig. 5 Tangential velocity distributions in the rear-cavity at r^* =0.911 for C_w=3600 and C_w=19460

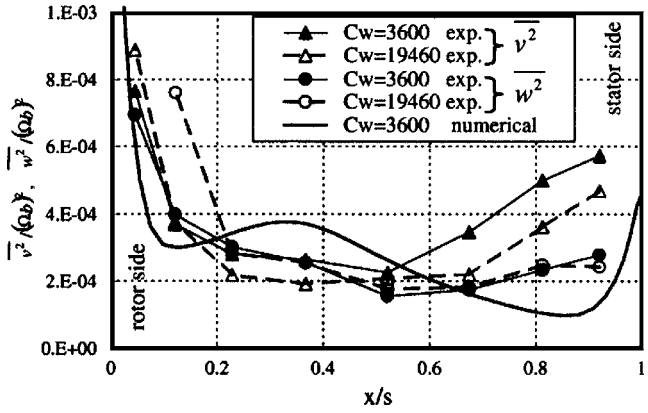

Fig. 7 Reynolds stress distributions in the rear-cavity at r^* =0.911 for C_w=3600 and C_w=19460

well below the reference data. This behavior is a direct consequence of annulus flow ingestion affecting the cavity flow at low values of cooling flow. Downstream of the present rotor blades, the annulus flow possesses a negative swirl velocity component and with part of this flow being ingested through the rim seal clearance the swirl of the rotating core is decreased. The results from the unsteady numerical solution for C_w=3600 are also presented in the figure. In this figure and all the followed figures which show the numerical results, the computational values are time-averaged over one blade passing period by a strut and also circumferentially averaged, if not mentioned otherwise. The numerical result suggests that a steep gradient of the velocity exists near the rotor surface, while it is not resolved by the hot-wire measurements. The computation slightly overestimates the level inside the inviscid core. The thickness of the stator boundary layer is predicted thinner than the measurements.

The radial velocity profile is shown in Fig. 6. The distributions at the stator side show only slight difference in the range of tested coolant conditions and between the two circumferential positions. Under the experimental coolant flow conditions the location of source region edge is deduced to vary from 0.44 to 0.87 (r_e^* $=1.79\lambda_T^{0.385}$ [9]). Then the measured location (r^*=0.911) is expected inside the rotating core in any case of the experiment, thus the radial velocity field is less affected by the coolant flow rate. On the other hand, there is a distinguishable difference in the values near the rotor surface. The effect of higher superposed coolant flow is to increase the radial outflow in the boundary layer

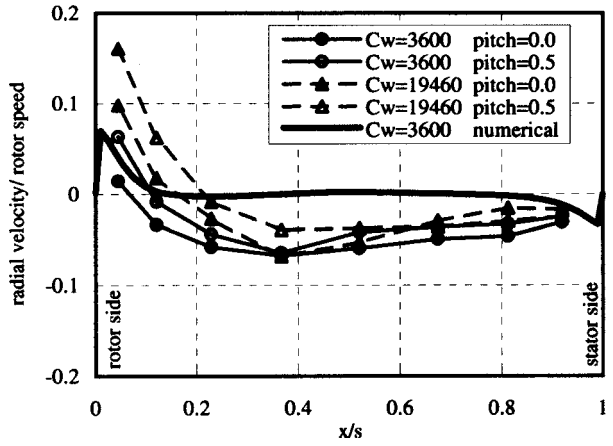

Fig. 6 Radial velocity distributions in the rear-cavity at r^* =0.911 for C_w=3600 and C_w=19460

on the rotating disk. At any coolant condition the magnitude of the outflow is consistently larger at the strut midpitch position than at the strut leading edge position, which implies the annulus pressure asymmetry due to the downstream struts aforementioned induces the circumferentially nonuniform ingestion and, as a consequence, affects the radial velocity field inside the cavity. The computation for C_w=3600 misses the small inflow inside the rotating core. A possible explanation is that the computations are somewhat sensitive to the small inconsistency that arise in the coolant inlet boundary (possibly, the velocity distribution) and the discrepancies are amplified at higher radii. The peak value at the rotor side seems at reasonable level and indicates the radial velocity gradient across the boundary layer is much less than in the tangential velocity distribution.

The Reynolds stress profiles of Fig. 7 aim to provide a better understanding of the flow behavior in the rear-cavity. The steep axial gradient of tangential velocity near the rotor surface causes a large local turbulence generation rate, which in turn, produces a large turbulence stress in the Ekman layer, and thus, a locally intensified turbulent diffusion and an enhanced mixing across the cavity. The figure shows that the tangential normal stress is dominant at the stator side. This anisotropy, however, diminishes as the distance to the wall increases, and in the central core of the flow, the turbulence is apparently quasi-isotropic. It should be also noted that the difference in $\overline{v^2}$ level between two cases is the damping of turbulence at the stator side, which is caused by the increase of throughflow. Computed values of the normal Reynolds stress for C_w=3600 is also shown in the figure. The turbulence model chosen in the calculation is an eddy viscosity model and therefore, the anisotropy of turbulence cannot be resolved. The computations provide the right behavior, with a maximum in the Ekman layer. Satisfactory levels are computed in the core region, though some over- and undershoots are observed. The computation makes it even clearer that the turbulence level inside the rotor surface Ekman layer is much higher than at the stator side. The resultant turbulence Reynolds number R_T, which is a direct measure of turbulent mass diffusion, is over 4×10^3 near the rotor surface in the computational result. This is considerably higher than the level in the mainstream where R_T is order of 500 except for the wake region.

It is worth mentioning briefly the effect of the unshielded bolt heads of the stator, because some of the large turbulent diffusion can be attributed to their presence. Some limited cases are measured without the bolts to investigate the effect. Figure 8 shows these results compared with the "base" configuration with the bolts. The data near the rotor is not available. The turbulent stresses, especially $\overline{v^2}$, near the stator appears to be affected by the inclusion of the bolt heads. As far as the present limited results concerned, however, there is no clear indication that the static

Downloaded 02 Jun 2010 to 171.66.16.98. Redistribution subject to ASME license or copyright; see http://www.asme.org/terms/Terms_Use.cfm

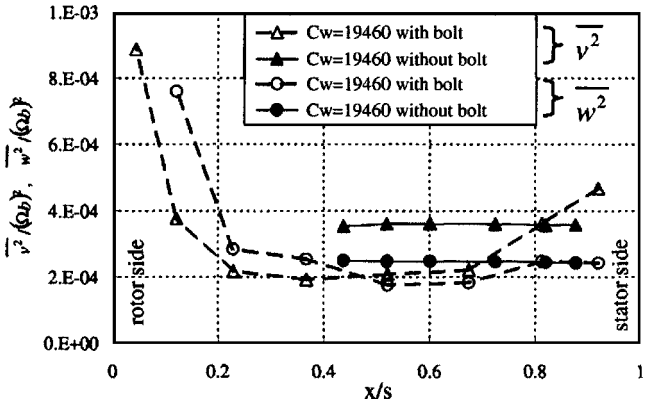

Fig. 8 Comparison of measured Reynolds stress distributions in the rear-cavity with and without the static bolt heads at $r^*=0.911$ for $C_w=19460$

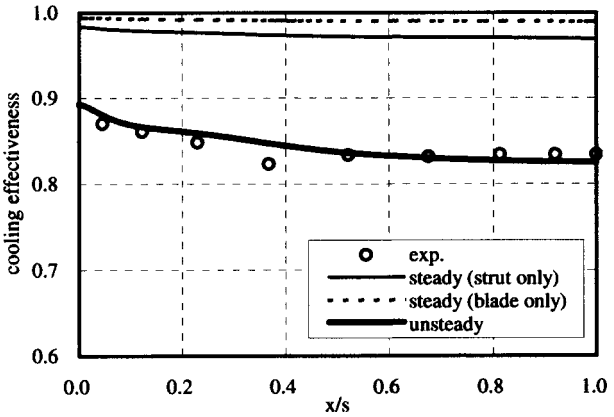

Fig. 10 Comparison of measured and calculated cooling effectiveness in the rear-cavity for $C_w=3600$ at $r^*=0.911$

bolts increase whole the turbulence level in the cavity. Arguably, more investigations are needed to clarify the effect of static (or rotating) bolt protrusions on the cavity flow field.

In Fig. 9, the measured axial distributions of cooling effectiveness at $r^*=0.911$ in the rear-cavity are shown for $C_w=3,650$ and 20,000. The distributions are relatively flat, which indicates the mixing between coolant and ingested mainstream are very much enhanced. This is mainly because the rotating core dominates almost whole the cavity within the tested conditions. The result with the minimum coolant flow case shows that the effects of ingestion are less over the rotor side than on the stator side. In all cases considered the cooling effectiveness is consistently lower at the circumferential position corresponding to the downstream strut leading edge than the strut midpitch position, though the differences are relatively small.

Figure 10 compares the measured and calculated cooling effectiveness for $C_w=3600$ in the rear-cavity. There are very significant differences between the simulation models. Any of the steady models which include only blades or struts clearly underpredict the level of ingestion. The agreement between the unsteady calculation and the measurements is striking. It is clear from comparisons of the different simulations that the combined effect of the asymmetries due to the rotor blades passing and struts downstream gives considerably more mainstream ingestion than either the rotor or stator acting alone.

Contours of cooling effectiveness from the unsteady solution for $C_w=3600$ in the seal gap in two different meridional planes at a time instant when the trailing edge of the blade locates at the same circumferential position as the strut leading edge are shown in Fig. 11. This is the time point identified from the unsteady calculation as the mainstream ingress being most intensified by the blade-strut interaction. It can be seen that the ingestion occurs mainly in the regions close to the stator driven by the pressure maxima from the strut leading edge. The complex flow field in this seal gap region is illustrated by the computed vector plots in the same planes at the same time point in Fig. 12. As can be seen from these plots, ingestion mainly occurs near the leading edge of the struts downstream, while the coolant flow leaves around midway between the struts. The decrease in cooling effectiveness in the rear-cavity in the unsteady solution would appear to be due to the increase in mixing between the coolant flow and the ingested mainstream due to the high frequency variation in radial velocity

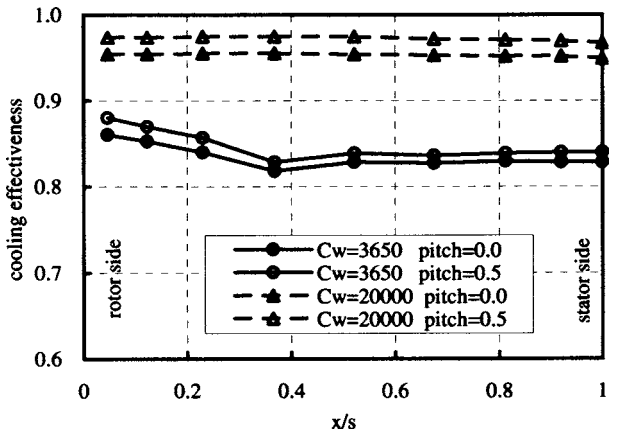

Fig. 9 Measured cooling effectiveness distributions in the rear-cavity at $r^*=0.911$ for $C_w=3650$ and $C_w=20000$

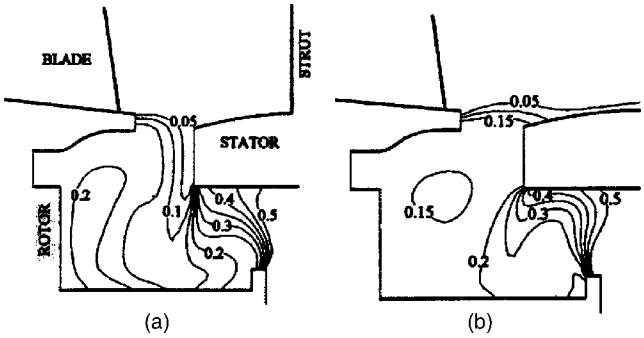

Fig. 11 Contours of calculated instantaneous cooling effectiveness in the seal region for $C_w=3600$ in two meridional planes (*a*) strut pitch=0; (*b*) strut pitch=0.5

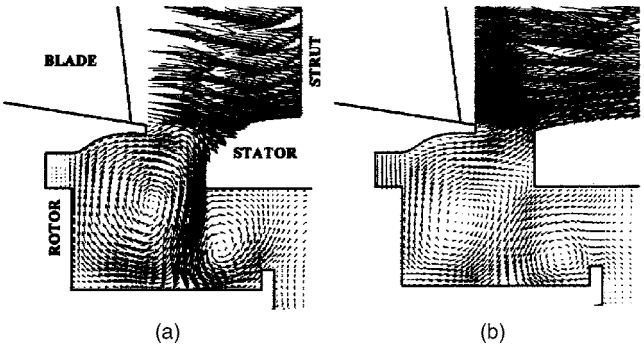

Fig. 12 Calculated instantaneous velocity vector plots in the seal region for $C_w=3600$ in two meridional planes (*a*) strut pitch=0; (*b*) strut pitch=0.5

Downloaded 02 Jun 2010 to 171.66.16.98. Redistribution subject to ASME license or copyright; see http://www.asme.org/terms/Terms_Use.cfm

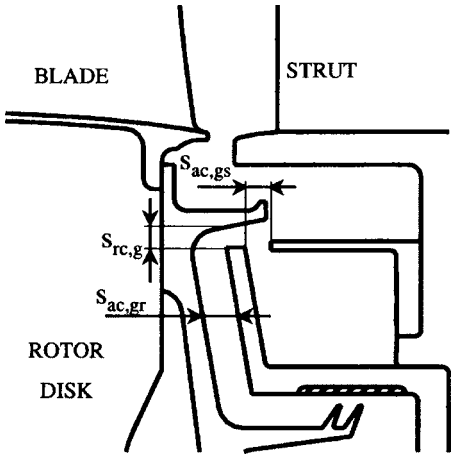

Fig. 13 Schematic of the new cooling method applied to the rear cavity

imposed by the rotor blades-struts interaction. The unsteady solution reveals that the level of unsteadiness in concentration and radial velocity is significant. Such an enhancement of mixing by the unsteady blade-strut interaction is very similar to the ingestion mechanism observed in the cavity downstream of the NGVs where it is reported that the unsteadiness by the vane-blade interaction plays an important role. Although not presented in this paper, it may be noted that inclusion of the further upstream NGVs into the current blade-strut unsteady model does not significantly change the magnitude nor distribution of the cooling effectiveness in the rear-cavity. This indicates that the influence of the upstream vane, in the present case, is minimal.

A Novel Cooling Method for Rotor-Stator Rim Cavities

Scope and Aim of the Proposed Method. In rim cavities of actual gas turbines, the rotor disk components are often working in much more mechanically critical conditions than the stator components. In such cases, the amount of coolant can be minimized if the rotor side is more effectively cooled than the stator side. However, for most gas turbine rim cavities, λ_T in order of 0.1 or less, and so there occurs usually an rotating core dominant flow, which enhances mixing in the cavity and then flatten the cooling effectiveness axial distribution as described in the previous section. Also the high turbulence across the rotor boundary layer is considered to be detrimental to effective cooling over the rotor disk. The observation has motivated the authors' group to investigate a novel cooling method which allows the cooling effectiveness to adequately vary within the cavity, suppress the diffusion due to the high turbulence near the rotor surface and consequently minimizes the amount of coolant.

In order to realize such a cooling concept, several configurations are devised and evaluated via numerical simulations. As a result of this numerical feasibility study, a new cooling method, shown in Fig. 13 and Table 2, is finally selected. The computed cooling effectiveness for "base" and "new" method are compared in the Fig. 14. Only the hardware difference from the "base" configuration is a divider plate which extends from the stationary labyrinth seal support. The function of the divider plate is to avoid

Table 2 Geometric parameters of the new cooling method

	Front-cavity	Rear-cavity
$S_{ac,gr}/b$	0.01506	0.02134
$S_{ac,gs}/b$	0.01444	0.01569
$S_{rc,g}/b$	0.02032	0.01323

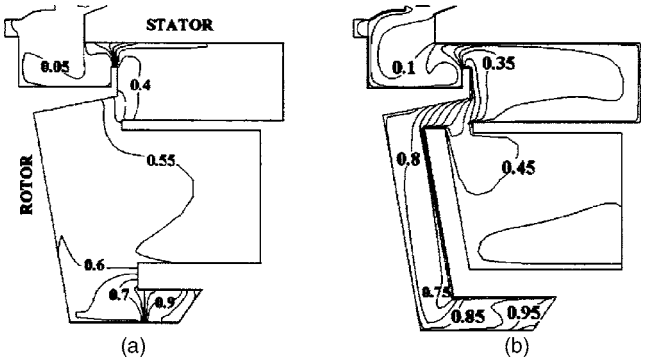

Fig. 14 Computed cooling effectiveness in the rear cavity with (*a*) base (*b*) new cooling method for C_w=1020

the cooling flow along the rotor surface being mixed with the rest part of the rim cavity and to achieve more viscous and less turbulent flow along the rotor surface. Then the coolant is able to keep high cooling effectiveness along the rotor surface without contaminated by the ingested mainstream. In compensation for the improvement along the rotor side, the simulation results indicate that the cooling effectiveness in the stator side has deteriorated to some degree. The method is applicable both in the disk front- and rear-cavity. This new method is selected not only from the predicted superior cooling performance but also from its structural simplicity bearing in mind the applicability to actual engines. Then the disk-front and -rear cavities of the present 1.5 turbine stage are redesigned according to the proposed new cooling method, integrated in the rig facility and tested to verify its performance.

Experimental Evaluation of the New Method. Figure 15 compares the measured variation of cooling effectiveness against the coolant flow parameter for the two cooling configurations in the rear-cavity. The values on the stator surface ("stator") and near-rotor surface ("rotor") are plotted for each configuration. Also a comparison is made with the minimum sealing flow estimated using the equation of Bohn et al. [10]. The improvements on the rotor side especially in the lower flow rate that result with the introduction of the new method are remarkable. It should be also noted that the predicted deterioration of cooling effectiveness on the stator side is not observed in the experiment.

Though the primary interest is in the rear-cavity flow phenomena, the disk front-cavity is also redesigned according to the proposed new cooling scheme and tested in the experiment in order to show the universal validity of the method. The measured cooling performance with the base and the new method applied in the

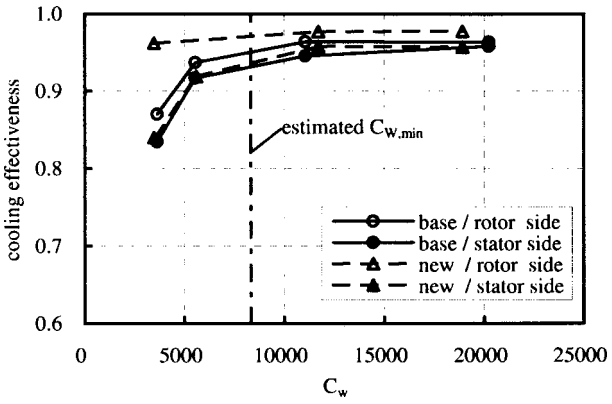

Fig. 15 Comparison of measured cooling effectiveness in the rear-cavity at r^*=0.911

Downloaded 02 Jun 2010 to 171.66.16.98. Redistribution subject to ASME license or copyright; see http://www.asme.org/terms/Terms_Use.cfm

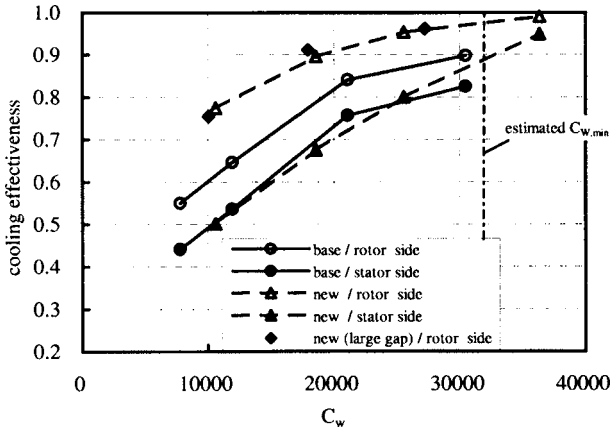

Fig. 16 Comparison of measured cooling effectiveness in the front-cavity at $r^+=0.929$

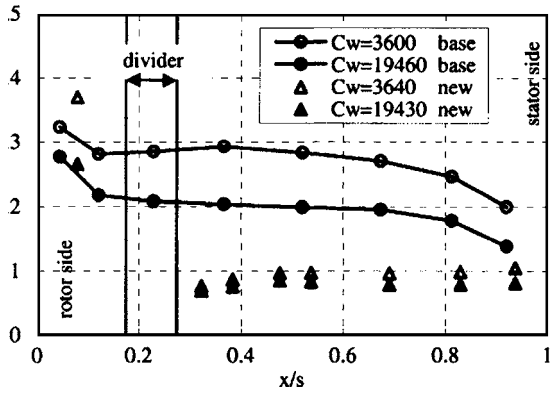

Fig. 18 Comparison of measured tangential velocity in the rear-cavity at $r^+=0.911$

front-cavity are compared in Fig. 16. The improvement with the new method is even clearer than in the rear-cavity. On the rotor side the advantage in applying the new method is more significant in the lower flow rate. Again, the cooling effectiveness on the stator side is not largely affected by the introduction of the divider plate.

For the front-cavity a case with wider axial clearance between the rotor and the divider plate is also tested in order to investigate the sensitivity of the axial clearance to cooling effectiveness. If any serious damage occurs in shafts and/or bearings in an actual engine, vanes and blades may be tangled with each other, but contact between rotor and stator disk should be avoided. Therefore, relatively wider clearances between rotor and stator disk components are often required in an actual engine design. The test result shows that even if the clearance is set at approximately the largest value of this engine size ($S_{ac,gr}/b=0.04358$), the cooling effectiveness along the rotor surface with the new method is almost never affected ("large gap" in Fig. 16). The sensitivity of the radial clearance in the new method is also investigated, but only with numerical simulation. Figure 17 shows a computed cooling effectiveness in the rear cavity with larger radial clearance for a low coolant flow rate case. Compared with Fig. 14(*b*), deterioration in cooling effectiveness is 3 pts, at most, along the rotor surface. Though the studies are very limited, it appears that the effect of radial clearance to the cooling performance is relatively small.

Figure 18 compares the axial distribution of the measured tangential velocity in the rear-cavity. In the new configuration, the effect of the divider plate is noticeable at the stator side where the core rotation speed is reduced and also is less affected by the coolant flow rate. At the rotor side the tangential velocity in the lower flow rate increases with the new configuration. This is due to the reduction of effective cavity gap width for the rotor by the introduction of the divider plate. It is widely recognized that the inertial effects due to the tangential velocity in the cavity is significant and increasing the tangential velocity of the cooling flow tends to reduce ingestion. The higher tangential velocity along the rotor surface with the new cooling method may contribute to some extent to the improved cooling effectiveness in the lower flow rate.

The radial velocity profile is compared in Fig. 19. Again the magnitude of the inflow inside the trapped cavity between the divider plate and the stator in the new configuration is very small and almost unrelated to the amount of coolant flow rate. On the rotor side the effect of higher superposed coolant flow is to slightly decrease the radial outflow with the new configuration. In such a narrow rotor-stator cavity as the one between the rotor and the divider plate it is reported that the increase in the purge flow rate lead to the decrease of the radial outflow along the rotor [11] and the present result agrees with that observation.

The Reynolds stress profiles of Fig. 20 most clearly indicate the effect of the proposed new method. A significant difference between the base and the new method is the damping of turbulence throughout the cavity, especially along the rotor surface. In the trapped cavity between the divider plate and the stator the magnitude of the velocity decreases as shown in Figs. 18 and 19, thus the reduced shear stress on the stator surface gives a lower turbulence generation rate. In the narrow gap between the rotor disk and the divider plate there is no inviscid core anymore. Instead

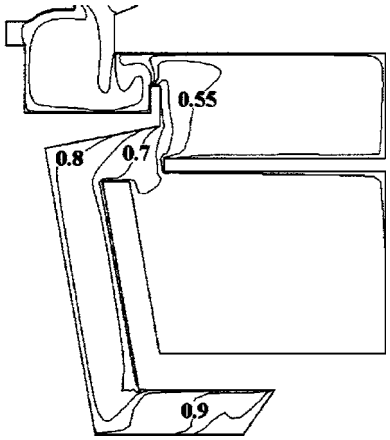

Fig. 17 Computed cooling effectiveness in the rear cavity with larger radial clearance ($s_{rc,g}/b=0.02$) for $C_w=1020$

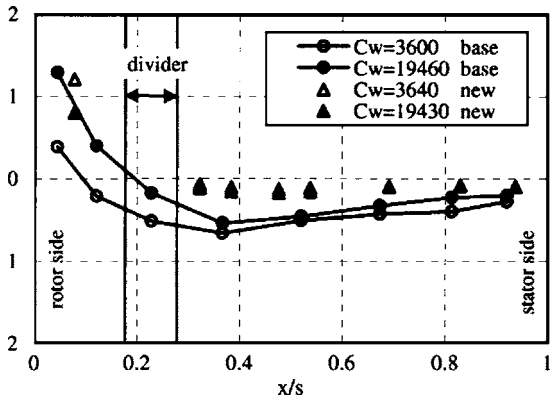

Fig. 19 Comparison of measured radial velocity in the rear-cavity at $r^+=0.911$

Downloaded 02 Jun 2010 to 171.66.16.98. Redistribution subject to ASME license or copyright; see http://www.asme.org/terms/Terms_Use.cfm

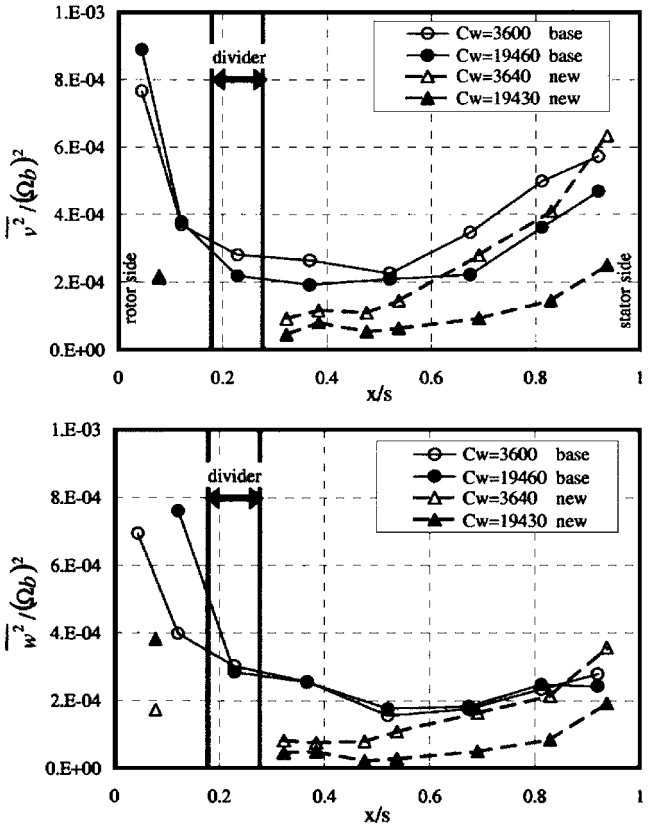

Fig. 20 Comparison of measured Reynolds stress in the rear-cavity at $r^*=0.911$ (upper: $\overline{v^2}$; lower: $\overline{w^2}$)

Couette-type flow is expected in which the viscous region fills the whole gap between the two surfaces, though the flow is still turbulent. In such a flow field, the viscous sublayer thickening occurs inside the boundary layer and consequently the turbulence is suppressed. The reduced turbulence level lead to the less turbulent diffusion, which in turn, avoids the excessive mixing occurred in the base seal configuration and improves the cooling effectiveness.

Conclusion

Mainstream gas ingestion through rim cavities of a full-scale model of a 1.5 turbine stage has been considered using the experimental and numerical approach. Particular emphasis is put on the flow phenomena in a rim cavity downstream of rotor blades. For the case considered reasonable agreement is found between numerical calculations and measurements when both the rotor blades and struts downstream are included in a full 3D, unsteady simulation. The numerical calculations provide strong support for the view that unsteadiness due to the rotor blade-struts interaction as well as circumferential pressure variations in the annulus flow lead to more ingestion. Detailed velocity and turbulence quantities measurements with aid of numerical results suggest that a steep axial gradient of tangential velocity near the rotor surface causes a large local turbulence generation rate, which in turn, produces a large turbulence stress in the Ekman layer, and thus, a locally intensified turbulent diffusion and an enhanced mixing across the cavity. Consequently the axial distributions of the cooling effectiveness inside the cavity are flattened.

The expectation that the amount of coolant required for a rim cavity will be greatly reduced if the cooling effectiveness can be adequately varied in the cavity and if the high turbulence generation rate along the rotor surface can be suppressed motivates the authors to investigate a novel cooling method to realize such a flow field. As a result of a numerical feasibility study, a new cooling method, in which a divider plate is attached to the seal support in order to avoid the cooling flow along the rotor surface being mixed with the rest part of the rim cavity, reduce turbulent diffusion across the boundary layer and thus to keep high cooling effectiveness along the rotor surface, is finally selected. Experimental results verify a significant advance in cooling performance with the new method both in disk-front and -rear rim cavities, especially for the rotor side.

Acknowledgment

The authors would like to express their thanks to the New Energy and Industrial Technology Development Organization (NEDO) and the Ministry of Economy, Trade and Industry (METI), who gave them the opportunity to conduct "Research and Development of Environmentally Compatible Propulsion System for Next-Generation Supersonic Transport (ESPR) project."

Nomenclature

A, B = constants in fiber probe uncertainty analysis ($A=1.396, B=0.895$)
b = outer radius of cavity (=0.272 m)
c = chord length of nozzle or blade
C_P = pressure coefficient=$(p-p_{\text{ave},m})/p_{\text{dynamic},m}$
C_w = coolant mass flow parameter=$\dot{m}_c/\mu b$
E = voltage output from fiber probe anemometer
E_{AD} = A/D board input of fiber probe anemometer
G = gap ratio=s/b
G_{ac} = clearance ratio=s_{ac}/b
G_{rc} = clearance ratio=s_{rc}/b
k = coverage factor in uncertainty analysis=2 or $\sqrt{3}$
M = mainstream Mach number
$\dot{m}$ = mass flow rate
N = number of samples in fiber probe data acquisition
n = resolution in bits of fiber probe anemometer
r = radius
r^* = radius ratio=r/b
P = pressure
Re_m = mainstream Reynolds number=$\rho U_m c/\mu$
Re_ϕ = rotational Reynolds number=$\rho\Omega b^2/\mu$
R_T = turbulence Reynolds number=$\rho k^2/\varepsilon\mu$
STDV = standard deviation of a normal distribution
s = axial width of cavity
s_{ac} = seal axial clearance (or overlap)
s_{ad} = axial distance between vane (or blade) trailing edge and blade (or strut) leading edge
s_{ag} = axial gap of shroud
s_{rc} = seal radial clearance
s_{as} = length of stator shroud
T = temperature
T_u = turbulence intensity
U = velocity
$\overline{v^2}, \overline{w^2}$ = tangential and radial components of normal Reynolds stress
x = axial coordinate
α = mainstream flow angle to axial direction
λ_T = turbulent flow parameter=$C_w\text{Re}_\phi^{-0.8}$
μ = viscosity
π = stage expansion ratio
θ = fiber probe position
ρ = density
Ω = rotational speed

Subscripts

0 = ambient or reference

Downloaded 02 Jun 2010 to 171.66.16.98. Redistribution subject to ASME license or copyright; see http://www.asme.org/terms/Terms_Use.cfm

Table 3 Error sources and uncertainties for velocity acquired with the fiber probes

Source of uncertainty	Input variants Δx_i	Output variants $\Delta y_i/U$	Uncertainty $\Delta y_i/(kU)$
Calibrator	ΔU_{cal}	$2\cdot\mathrm{STDV}(\Delta U_{\mathrm{cal}})$	0.02
Linearization	ΔU_{lin}	$2\cdot\mathrm{STDV}(\Delta U_{\mathrm{fit}})$	0.005
A/D resolution	E_{AD}, n	$1/U\cdot E_{\mathrm{AD}}/2^n\cdot\partial U/\partial E$	0.0011
Probe positioning	θ	$1-\cos(\theta($	≈ 0
Temperature variations[a]	ΔT	$1/U\cdot\Delta T/(T_w-T_0)\cdot(A/B\cdot U^{-0.5}+1)$	≈ 0
Temperature variations[b]	ΔT	$\Delta T/273$	0.0026
Ambient pressure	ΔP	$\Delta P/(P_0+\Delta P)$	≈ 0
Humidity	ΔP_{wv}	$1/U\cdot\partial U/\partial P_{\mathrm{wv}}\cdot\Delta P_{\mathrm{wv}}$	≈ 0
Time averaging	$T_u, \sqrt{N}$	$T_u/\sqrt{N}$	≈ 0
Expanded uncertainty: $2\sqrt{\Sigma[\Delta y_i/(kU)]^2}=0.042$			

[a]Uncertainty due to change in sensor overtemperature
[b]Uncertainty due to change in air density with temperature

1 = downstream of vane
2 = downstream of blade
c = coolant
e = edge of source region
i = inner seal
m = mainstream
o = outer seal
r = rotor
s = stator
w = sensor surface of fiber probe
wv = water vapor condition

Appendix A: Uncertainty of the Fiber Probe Measurements

The uncertainties in the measured velocities are summarized in Table 3. It appears that the major contributions come from the calibrator and the linearization (curve fitting). Variations in temperature during the measurement may also play a role.

References

[1] Bayley, F. J., and Owen, J. M., 1970, "The Fluid Dynamics of a Shrouded Disk System with a Radial Outflow of Coolant," ASME J. Eng. Power, **92**, pp. 335–341.

[2] Campbell, D. A., 1978, "Gas Turbine Disc Sealing System Design," Proc. AGARD Conf. on Seal Technology in Gas Turbine Engines, AGARD-CP-237.

[3] Bohn, D., Rudzinsky, B., Surken, N., and Gartner, W., 2000, "Experimental and Numerical Investigation of the Influence of Rotor Blades on Hot Gas Ingestion into the Upstream Cavity of an Axial Turbine Stage," ASME Paper No. 2000-GT-284.

[4] Roy, R. P., Xu, G., Feng, J., and Kang, S., 2001, "Pressure Field and Main Stream Gas Ingestion in a Rotor Stator Disc Cavity," ASME Paper No. 2001-GT-564.

[5] Hills, N. J., Chew, J. W., and Turner, A. B., 2002, "Computational and Mathematical Modeling of Turbine Rim Seal Ingestion," ASME J. Turbomach., **124**, pp. 306–315.

[6] Ko, S. H., and Rhode, D. L., 1999, "Disk Temperature Details of Rim Seal Turbulent Heat Diffusion and Disk Frictional Heating," AIAA J., **15**, pp. 280–287.

[7] Yamawaki, S., Okita, Y., Kodama, H., Yoshida, T., Nozaki, O., and Yamane, T., 1999, "CFD Contribution to Development of HYPR Engine," AIAA paper 99-0886.

[8] Gentilhomme, O., Hills, N. J., Turner, A. B., and Chew, J. W., 2002, "Measurement and Analysis of Ingestion Through a Turbine Rim Seal," ASME Paper No. GT-2002-30481.

[9] Owen, J. M., and Rogers, R. H., 1989, *Flow and Heat Transfer in Rotating Disc System: Vol. 1, Rotor-Stator Systems*, John Wiley, New York.

[10] Bohn, D., and Wolff, M., 2003, "Improved Formulation to Determine Minimum Sealing Flow-$C_{W,\mathrm{min}}$-for Different Sealing Configurations," ASME Paper No. GT2003-38465.

[11] Daily, J. W., Ernst, W. D., and Asbedian, V. V., 1964, "Enclosed Rotating Discs with Superposed Throughflow; Mean Steady and Periodic Unsteady Characteristics of Induced Flow," Report No. 64, Hydrodynamic Laboratory, MIT.

Downloaded 02 Jun 2010 to 171.66.16.98. Redistribution subject to ASME license or copyright; see http://www.asme.org/terms/Terms_Use.cfm

Mechanical Properties of Overaluminized MCrAlY Coatings at Room Temperature

Yoshiyasu Itoh
Senior Manager

Masahiro Saitoh

Power and Industrial Systems R&D Center,
Toshiba Corporation,
2-4, Suehiro-cho, Tsurumi-ku,
230-0045 Yokohama, Japan

The objective of this study is to compare the mechanical properties of overaluminized MCrAlY coatings sprayed by a vacuum plasma spraying process for the protection against high-temperature corrosion and oxidation in the field of gas turbine components. Recently, the overaluminized MCrAlY coatings are used for improving further the high-temperature oxidation resistance. However, the mechanical properties of aluminized MCrAlY coatings, which have an important effect on coating lives, have not been clarified. Five kind of freestanding MCrAlY specimens (CoCrAlY, CoNiCrAlY, CoNiCrAlY +Ta, NiCrAlY, NiCoCrAlY) were machined from the thick vacuum plasma sprayed (VPS) coatings. And, the heat-treated MCrAlY specimens (1393 K, 2 h, argon cooled and 1116 K, 24 h, argon cooled) and the overaluminized specimens (Al-Cr-Al_2O_3-NH_4Cl pack, 1173–1273 K, 10 h) after the heat-treatment were used. The experimental results suggested that the volume fraction of precipitated aluminum compounds in the VPS MCrAlY coatings and the residual stress induced by the overaluminizing treatment had important effects on the mechanical properties. The Vickers hardness and Young's modulus of the overaluminized MCrAlY coatings showed higher values in comparison with the VPS MCrAlY coatings. There was a tendency that the bend strength of overaluminized VPS MCrAlY coatings decreased by the aluminizing treatment and also with increasing volume fraction of precipitated aluminum compounds in the VPS MCrAlY coatings. It was also confirmed that the bend strength of aluminized layers themselves was reduced with increasing volume fraction of precipitated aluminum compounds in the VPS MCrAlY coatings. These tendencies were caused by the enrichment of brittle precipitates, such as NiAl and/or CoAl intermetallic compounds. [DOI: 10.1115/1.1688766]

Introduction

Coatings are used for many engineering applications in order to improve the surface properties of components to protect them against environmental degradation, [1,2]. Diffusion coating processes have been applied for many years to improve the environmental resistance by enriching the surface of nickel-based superalloys with chromium, aluminum, or silicon element. In recent years, a vacuumed plasma spray (VPS) process has been established in the field of gas turbines and is used for hot parts, turbine blades and duct segments, etc., which are exposed to oxidation and corrosive atmosphere at high-temperature. Overlay coatings based on MCrAlY alloy systems (M is Ni, Co or both elements) are commonly used as oxidation and corrosion resistance. As operating temperatures of gas turbines are increased, the excellent performance of diffusion coatings applied on top of MCrAlY overlay coatings has been realized, [3,4]. The overaluminized MCrAlY coatings have been used to improve the high-temperature oxidation resistance. The overaluminizing is also effective in improving the oxidation resistance of the MCrAlY bond coat of thermal barrier coatings, [5–7]. The aluminizing behaviors of the VPS MCrAlY coatings, such as CoCrAlY, CoNiCrAlY, CoNiCrAlY+Ta, NiCrAlY, and NiCoCrAlY, were made clear from the viewpoint of reaction diffusion, [8]. Hitherto, the performance evaluation of coatings has been conducted using a burner rig for relative comparison. The mechanical properties of coating layers, such as aluminized layers, have not been fully characterized and the lack of information becomes difficult to make up the adequate modeling of the behaviors of coating-substrate composite systems. It is very important that a matching design of coating-substrate composite systems, which is based on the analysis and database of coating materials, is inevitable to maintain the coating reliability.

A number of studies on the mechanical properties of coated superalloys at high temperature have been performed, [9,10]. Studies on the mechanical properties of the MCrAlY coatings are even rare. Not many data have been reported on the mechanical properties of the overaluminized MCrAlY coatings and the aluminized layers themselves, primarily because of the experimental difficulties in determining their mechanical properties. As a matter of course, basic properties such as mechanical properties and residual stress characteristics of brittle aluminized layer of MCrAlY coatings, which have an important effect on coating lives, have not always been clarified.

In the present paper, five kinds of vacuum plasma sprayed MCrAlY coatings, such as CoCrAlY, CoNiCrAlY, CoNiCrAlY +Ta, NiCrAlY, and NiCoCrAlY were selected for the comparison of characteristics of overaluminized layers. The Vickers hardness, Young's modulus, Poisson's ratio, and four-point bend strength of the overaluminized MCrAlY coatings were measured at room temperature in comparison with the freestanding MCrAlY coatings. Also, the residual stress characteristics are measured by X-ray diffraction. Furthermore, the bend strength of aluminized layers themselves was estimated after due consideration of the residual stresses at the aluminized layer.

Experimental Procedure

This investigation used an IN738LC as a coating substrate, which was a typical nickel-based superally for gas turbine blades. The chemical composition is given in Table 1. Also, the normal heat-treatment condition for IN738LC is shown in Table 1. Five kinds of commercial spraying powders, such as CoCrAlY, CoNiCrAlY, CoNiCrAlY+Ta, NiCrAlY, and NiCoCrAlY, were se-

Contributed by the Manufacturing Materials and Metallurgy Committee of THE AMERICAN SOCIETY OF MECHANICAL ENGINEERS for publication in the ASME JOURNAL OF ENGINEERING FOR GAS TURBINES AND POWER. Manuscript received by the MM&M Committee October 2000; final revision received December 2002. Committee Chief: J. Conner.

Copyright © 2005 by ASME

Downloaded 02 Jun 2010 to 171.66.16.98. Redistribution subject to ASME license or copyright; see http://www.asme.org/terms/Terms_Use.cfm

Table 1 Chemical composition and mechanical properties of IN738LC

Material	Chemical composition (mass %)								
	Ni	Cr	W	Mo	Co	Al	Ti	Nb	Ta
IN738LC	Bal.	15.8	2.46	1.78	8.11	3.45	3.60	0.92	1.92

Tensile test at room temperature

0.2% proof stress	Tensile strength	Elongation	Hardness (HRC)
936 MPa	1149 MPa	7%	41.5

Heat treatment; 1393 K×2 h Ar cooled
1116 K×24 h Ar cooled

lected from the viewpoint of practical use. The CoCrAlY is used for corrosion protective coating powder at medium temperature (1000–1200 K). The NiCrAlY is used for oxidation protective coating powder at high temperature (≥1200 K) and as the bond coat layer of thermal barrier coatings. The CoNiCrAlY, CoNiCrAlY+Ta, and NiCoCrAlY are advanced coating powders that have the superior properties against the more severe environment conditions. These spraying powders are produced by argon gas atomization. The chemical composition and mesh size of these powders are given in Table 2.

The VPS coatings were carried out with A-2000V VPS system (Plasma Technik) under the following conditions; preheating temperature 843 K during transferred arc treatment, voltage 64 V, current 685 A, spraying distance 270 mm, argon gas atmosphere 6 kPa. The process temperature was controlled less than 843 K. Single face of all IN738LC substrates, which were 60×60 ×5 mm^t, was sprayed MCrAlY coatings with 2 mm in thickness after the pretreatment of blasting and transferred arcing. It was confirmed that the microstructure and Vickers hardness was almost same between thick coating samples and 0.25 mm thick coatings used in gas turbine. The four-point bend test specimens (50×5×1.5 mm^t) were machined out of the thicker coatings without any metallurgical influence from substrates using diamond cutter. After heat treatment (1393 K, 2 h, argon gas cooled and 1116 K, 24 h, argon gas cooled), specimens were subjected to an aluminizing treatment at 1173, 1223, and 1273 K for 10 h in a pack-cementation retort purged with pure argon gas, respectively. The heating rate was 380 K/h, and the cooling rate was 160 K/h until 900 K and furnace cooled after that. The pack mixture composition is an Al+Cr alloy powder (20 mass %) as the aluminum source, NH_4Cl (0.5 mass %) as the activator, and alumina powder (79.5 mass %) as the inert filler. In the same manner, single face of IN738LC substrate, which were 15×15×1.5 mm^t was sprayed MCrAlY coatings with 0.3 mm in thickness and was overaluminized for measuring the residual stress characteristics.

After the overaluminizing treatment, the cross-section of test specimens was observed and the thickness of overaluminized layer was measured using an optical microscope. Namely, intermetallic compounds precipitated in the VPS MCrAlY coatings and the aluminizing layer were observed by scanning electron microscopy (SEM) and electron probe micro analyzer (EPMA).

Table 2 Chemical composition of spraying powders used

Materials	Chemical composition (mass %)					
	Co	Ni	Cr	Al	Y	Ta
CoCrAlY −400 mesh	Bal.	<0.10	28.9	6.15	0.28	—
CoNiCrAlY −400 mesh	Bal.	32.08	21.22	8.33	0.39	—
CoNiCrAlY+Ta −400 mesh	Bal.	9.7	24.6	7.0	0.48	5.5
NiCrAlY −400 mesh	—	Bal.	31.45	11.55	0.825	—
NiCoCrAlY −325 mesh	23.23	Bal.	16.94	12.47	0.49	—

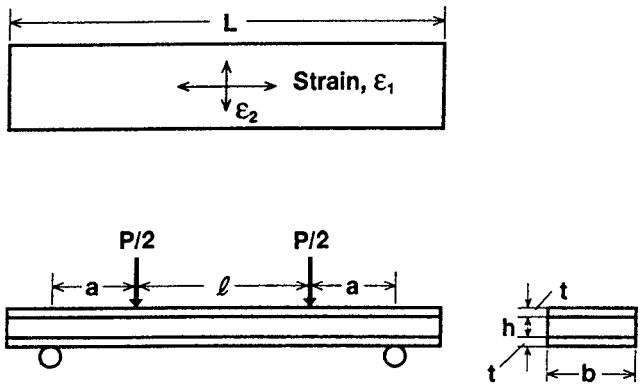

Fig. 1 Four-point bend test specimen for aluminized VPS MCrAlY coatings

The mechanical properties, such as Young's modulus, Poisson's ratio and bend strength are measured by four-point bend test specimens using strain gage under the condition of cross-head speed 0.1 mm/min. Figure 1 shows schematically the four-point bend test. The specimen is supported by two rollers 40 mm apart and loaded by second set of rollers 20 mm apart. The overaluminized layers of specimens were approximately 30–120 μm in thickness. Young's modulus of aluminized layer, Ec, can be calculated from the load, P versus strain, ε_1 curve by the equation described below, which is derived from three-layered beam theory.

$$Ec=[3(P/\varepsilon_1)a(h+2t)-bh^3Es]/b/[(h+2t)^3-h^3] \quad (1)$$

Poisson's ratio of aluminized layer, νc can be calculated from the measured strain, ε_1 and ε_2.

$$\nu c=\varepsilon_1/\varepsilon_2 \quad (2)$$

where Es is the Young's modulus of substrate. In case of supposing that the effect of aluminized layer is taken no account. The apparent strength, σ_B can be calculated from the equation, assuming $Ec=Es$:

$$\sigma_B=[3P(L-1)]/[2b(h+2t)^2]. \quad (3)$$

The four-point bend strength of aluminized layer. σ_b can be calculated from the equation by taking account of three-layered beam theory:

$$\sigma_b=[3Pa(h+2t)]/b[(h+2t)^3+h^3(Es/Ec-1)]. \quad (4)$$

The residual stresses at the surface of overaluminized VPS MCrAlY coatings were determined by X-ray diffraction at room temperature. The measurement condition is shown in Table 3.

Table 3 Measurement condition of residual stress by X-ray diffraction

Used apparatus	JDX-3500 (JEOL)
Analysis method	Parallel-beam, $\sin^2\psi$
Characteristic X-ray	Cr-Kα
Tube voltage	30 kV
Tube current	300 mA
Irradiation area	15 mm×5 mm
Diffraction plane	Cubic, (200): NiAl,CoAl

Downloaded 02 Jun 2010 to 171.66.16.98. Redistribution subject to ASME license or copyright; see http://www.asme.org/terms/Terms_Use.cfm

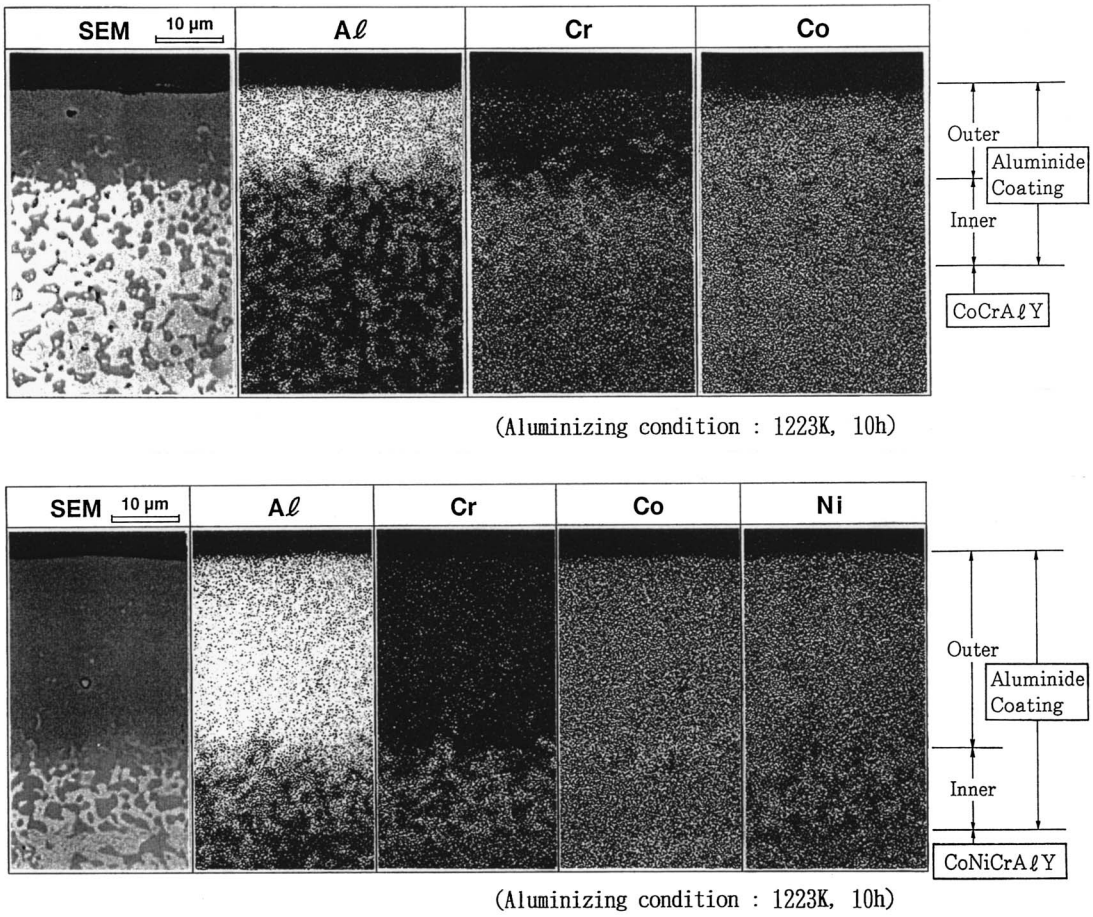

Fig. 2 SEM observation and EPMA analysis of aluminized VPS MCrAlY coatings; (*a*) aluminized layer of heat-treated VPS CoCrAlY coating, (*b*) aluminized layer of heat-treated VPS CoNiCrAlY coating

Microstructure of Overaluminized MCrAlY Coatings

Typical cross-section microstructures of the overaluminized layer formed at the surface of heat-treated VPS CoCrAlY coating after aluminizing treatment at 1223 K for 10 h is shown in Fig. 2(*a*). It had been clearly found that the microstructure of all MCrAlY coatings was composed of precipitated aluminum compound phase in the Ni and/or Co matrix. For example, the matrix of VPS CoCrAlY was identified by EPMA as α-CoCr solid solution phase whereas the precipitated phase consisted of β-CoAl. Similarly, the VPS NiCoCrAlY is composed of two phases, which are precipitated β-(Ni,Co)Al intermetallic compounds and α-NiCoCr solid solution matrix, [10]. Namely, the precipitated aluminum compound phase differs with MCrAlY coatings. And the percentage of precipitated Al intermetallic compounds could be easily determined by the composition of SEM photograph of MCrAlY coatings. Two reaction diffusion layers can be clearly observed using EPMA analysis, consisting of an aluminum rich outer layer and an inner diffusion layer. The pore size in heat-treated VPS CoCrAlY coating is very small and is not expected to affect the aluminizing quality. The aluminum rich outer layer mainly consisted of the CoAl precipitates phase, which can be observed on the cross-section view of the aluminized CoCrAlY, and is nearly 15 μm in thickness. Also, the inner diffusion layer is nearly 15 μm in thickness, consisting of an aluminum and chromium rich layer. There is a tendency that the CoAl precipitates like island decreases from the outer layer to the CoCrAlY. Namely, it is because the CoAl precipitates in the aluminized layer are formed by the inner diffusion of aluminum element, and chromium is enriched by exceeding its dissolution limit in the CoCrAlY coating, [8].

Next, microstructures of the overaluminized layer formed at the surface of heat-treated CoNiCrAlY after aluminizing treatment at 1223 K for 10 h is shown in Fig. 2(*b*). It is clearly found that the two reaction diffusion layers can be observed in the same manner as shown in Fig. 2(*a*). The thickness of the aluminum rich diffusion layer is nearly 30 μm. It was confirmed using X-ray diffraction that precipitated β-(Ni,Co)Al intermetallic compounds were mainly formed at the outer reaction diffusion layer. The inner diffusion layer is nearly 15 μm in thickness, consisting of an aluminum and chromium rich layers. In the inner layer, β-(Ni,Co)Al intermetallic compounds precipitates like islands are decreased toward the inside and become small islands gradually, [8].

Within this experiment, it seems that the pores have no noticeable effect on the aluminizing behaviors. There is no difference of the aluminizing behaviors among heat-treated MCrAlY coatings without the thickness of aluminized layer. It was confirmed using X-ray diffraction that precipitated β-(Ni,Co)Al intermetallic compounds were formed at the surface of CoNiCrAlY+Ta and NiCoCrAlY coatings and that precipitated β-NiAl intermetallic compounds were formed at the surface of NiCrAlY by the overaluminizing treatment. The thickness of aluminized layer for each MCrAlY coatings is different. The thickness of aluminized layers is defined as the sum of the thickness of the inner and outer

Downloaded 02 Jun 2010 to 171.66.16.98. Redistribution subject to ASME license or copyright; see http://www.asme.org/terms/Terms_Use.cfm

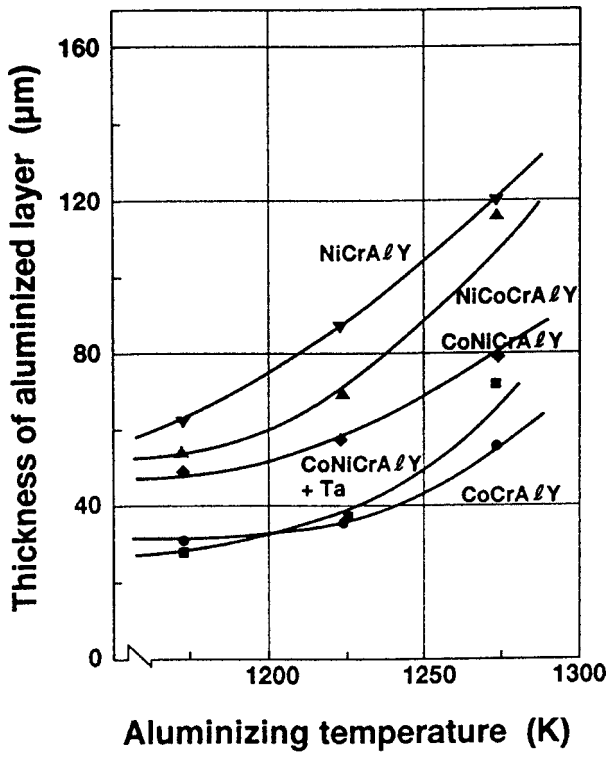

Fig. 3 Aluminized behaviors of various VPS MCrAlY coating

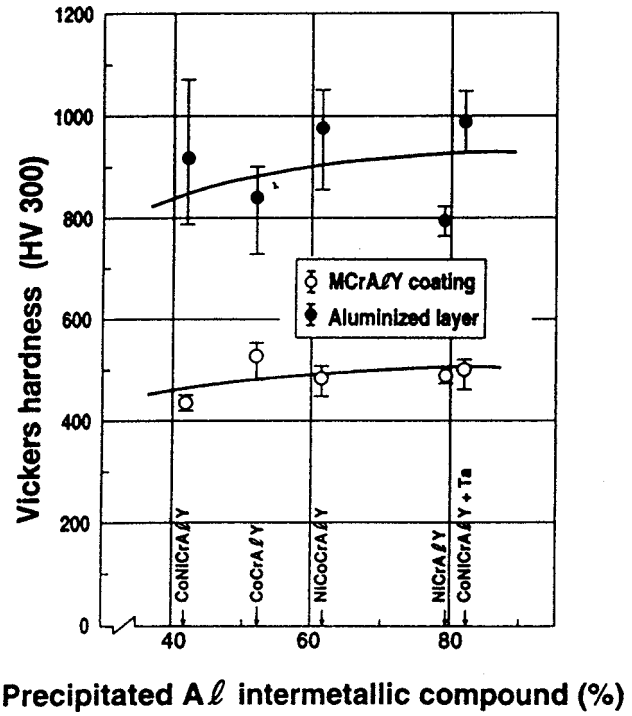

Fig. 4 Vickers hardness of aluminized VPS MCrAlY coatings in comparison with that of VPS MCrAlY coatings

diffusion layers in this study. The growth behaviors of aluminized layers formed at the surface of MCrAlY coatings are shown in Fig. 3 for a heating time of 10 h. There is a tendency for the aluminized thickness to increase with increasing aluminizing temperature. In this experiment, the mechanical properties are evaluated the MCrAlY coatings after aluminizing treatment at 1223 K for 10 h.

The Vickers hardness is important to conveniently evaluate the precipitates of intermetallic compounds. The measurement results of Vickers hardness for the MCrAlY coatings and their overaluminized layer are shown in Fig. 4. The horizontal axis shows volume fraction of precipitated Al intermetallic compounds measured from the SEM photomicrographs of the MCrAlY coatings. The Vickers hardness of MCrAlY coatings (400–500 HV) was inferior in comparison to the MCrAlY coatings subjected to the overaluminizing treatment (800–1000 HV). This is caused by the formation of hard precipitates, such as NiAl and/or CoAl intermetallic compounds. And it seems that the Vickers hardness difference between NiAl and CoAl is not remarkable. Therefore, there is a tendency for the Vickers hardness to increase slightly with increasing amount of precipitated Al intermetallic compounds.

Young's Modulus and Poisson's Ratio of Aluminized Layers

Freestanding VPS MCrAlY specimens and their overaluminized specimens were used for the measurement of Young's modulus and Poisson's ratio. In Fig. 5, the Young's modulus of overaluminized layers is shown in comparison with that of freestanding MCrAlY coatings. Namely, the measurement results of Young's modulus obtained by a strain gage method and Eq. (1) are shown in Fig. 5. A dashed line in Fig. 5 shows the experimental results of Ni-based MCrAlY coatings, and a solid line shows the experimental results of Co-based MCrAlY coatings. There is a tendency for the Young's modulus of Ni-based MCrAlY coatings to increase with increasing volume fraction of precipitated Al intermetallic compounds from nearly 140 to 170 GPa. These tendencies are due to the network formation of precipitated Al intermetallic compounds at higher volume fractions.

On the other hand, it seems that the Young's modulus of Co-based MCrAlY coatings is not affected by volume fraction of

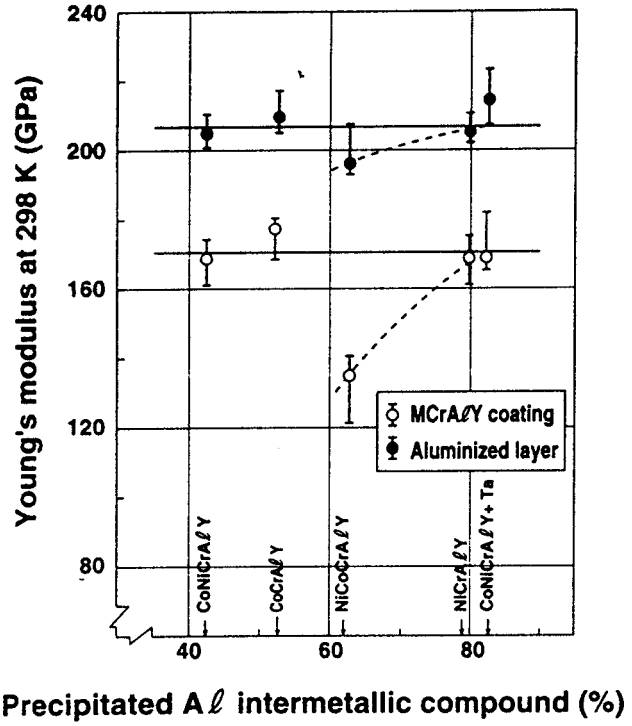

Fig. 5 Young's modulus of aluminized VPS MCrAlY coatings in comparison with that of VPS MCrAlY coatings

Downloaded 02 Jun 2010 to 171.66.16.98. Redistribution subject to ASME license or copyright; see http://www.asme.org/terms/Terms_Use.cfm

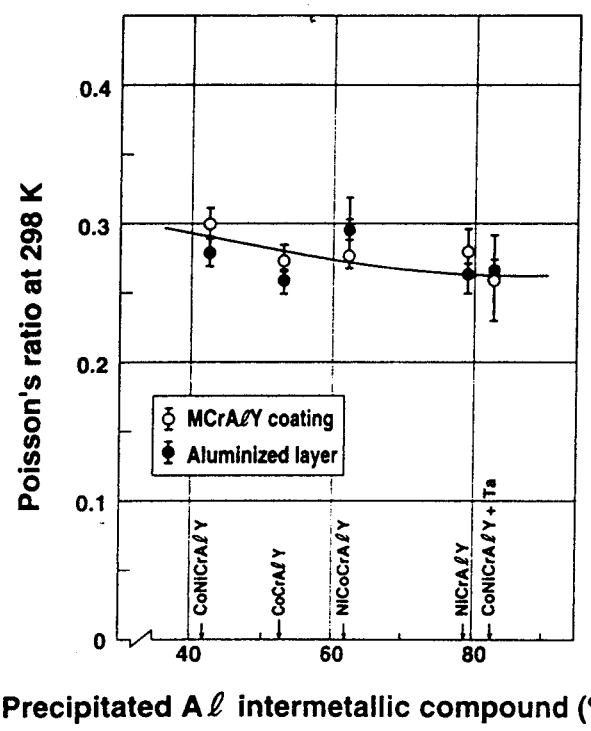

Fig. 6 Poisson's ratio of aluminized VPS MCrAlY coatings in comparison with that of VPS MCrAlY coatings

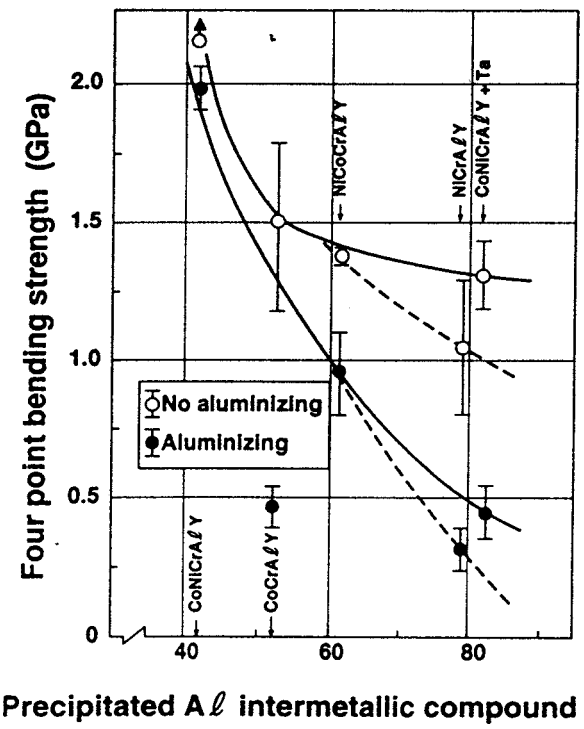

Fig. 7 Four-point bend strength of aluminized VPS MCrAlY coatings in comparison with that of VPS MCrAlY coatings

precipitated Al intermetallic compounds within this experiment. The Young's modulus of MCrAlY coatings is lower than a typical polycrystalline superalloy that shows nearly 200–220 GPa. There is a tendency for the Young's modulus of aluminized layers of Ni-based MCrAlY coatings to increasing volume fraction of precipitated Al intermetallic compounds from nearly 190–205 GPa. The Young's modulus of overaluminized layers of Co-based MCrAlY coatings shows nearly 210 GPa and is not affected by volume fraction of precipitated Al intermetallic compounds within this experiment.

The results of Poisson's ratio obtained by the strain gage method and Eq. (2) are shown in Fig. 6. The Poisson's ratio of overaluminized layer is shown in comparison with that of the freestanding MCrAlY coatings. There is a tendency for the Poisson's ratio of MCrAlY coatings and aluminized layers seems to decrease slightly with increasing volume fraction of the precipitated Al intermetallic compounds from nearly 0.3 to 0.25. However, the difference in Poisson's ratio between the MCrAlY coatings and their overaluminized layers is not clear within this experiment.

Four-Point Bend Strength of Overaluminized MCrAlY Coatings

Figure 7 shows the four-point bend strength of MCrAlY coatings and overaluminized MCrAlY coatings against volume fraction of precipitated Al compounds in each MCrAlY coatings. The four-point bend strength of the overaluminized MCrAlY coatings and the MCrAlY coatings is calculated by Eq. (3). Namely, an apparent strength in case of overaluminized MCrAlY coatings is calculated on the assumption that the elastic constants of aluminized layers are the same as the MCrAlY coatings. Only CoNiCrAlY bend specimens showed yield point (2.0 GPa) and maximum load point (2.5 GPa). And the specimens could not be separated by the four-point bend test. Other bend specimens failed in an apparently brittle manner, and the load-deflection relationships were straight lines until their failure. These brittle fractures are caused by the formation of many intermetallic compounds inside the MCrAlY coatings. High-temperature protective coatings very often consist of precipitated phases normally considered as brittle NiAl and/or CoAl intermetallic compounds. The volume fraction of such brittle phases embedded in a ductile matrix has to be considerable influence the mechanical properties. The ductile CoNiCrAlY bend specimens subjected to overaluminizing treatment failed in an apparently brittle manner. There is a tendency that the bend strength of MCrAlY coatings decreases with increasing volume fraction of precipitated Al compounds. It seems that this tendency is remarkable in case of the Ni-based MCrAlYs. Apparently the trend is similar to that for overaluminized MCrAlY coatings.

Figure 8 shows the modified four-point bend strength of overaluminized MCrAlY coatings against volume fraction of precipitated Al compounds. Namely, the four-point bend strength of aluminized layers was calculated from the Eq. (4) by taking account of three-layered beam theory. The Young's modulus and Poisson's ratio of overaluminized MCrAlY coatings shown in Fig. 5 and 6 are used for this calculation. In Fig. 8, the apparent strength of the overaluminized MCrAlY coatings in Fig. 7 is shown by comparison. It is clear that the modified four-point bend strength is slightly higher than the apparent strength of overaluminized MCrAlY coatings and the remarkable difference by using Eq. (4) can't be observed.

As mentioned above, the four-point bend strength of MCrAlY coatings is reduced by the overaluminizing treatment, and there is a tendency that the bending strength of overaluminized MCrAlY coatings decreases with increasing volume fraction of precipitated Al compounds. This tendency is caused by the enrichment of brittle precipitates, such as NiAl and/or CoAl intermetallic compounds at the surface layer of MCrAlY coatings. However, the reduction of the bend strength of CoCrAlY is irregular in comparison with any other MCrAlY coatings.

Estimated Strength of Aluminized Layers

It has shown that the presence of overaluminized layers has remarkable reduced the bend strength of MCrAlY coatings. This

Downloaded 02 Jun 2010 to 171.66.16.98. Redistribution subject to ASME license or copyright; see http://www.asme.org/terms/Terms_Use.cfm

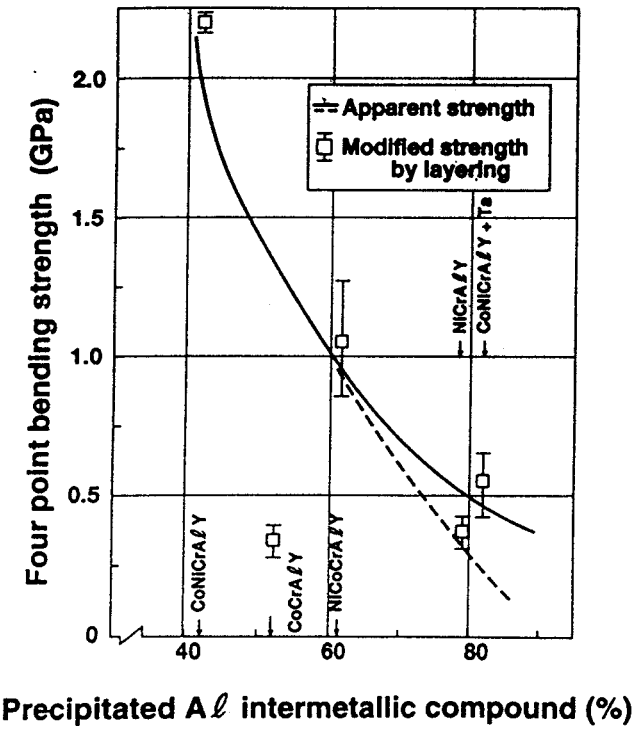

Fig. 8 Modified four-point bend strength of aluminized VPS MCrAlY coatings by taking account of three-layered effect

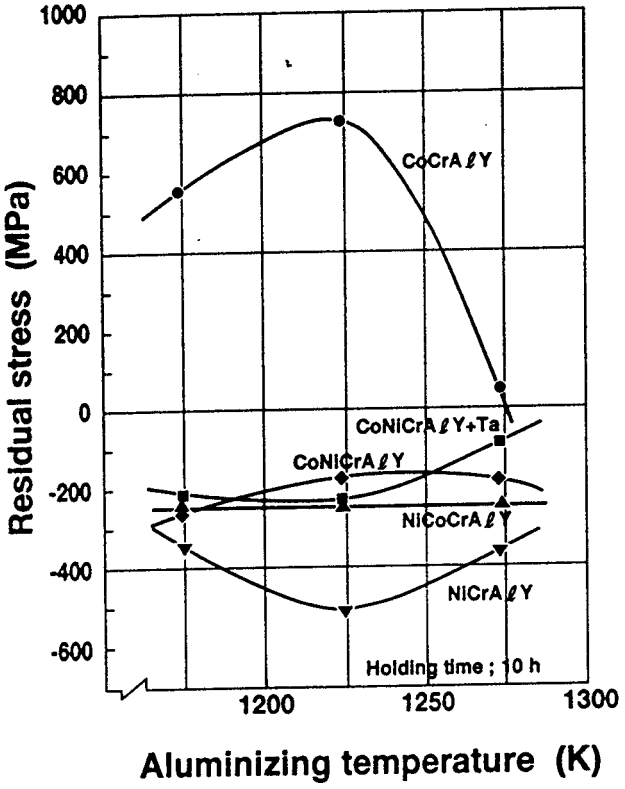

Fig. 9 Measurement results of residual stress for aluminized VPS MCrAlY coatings

phenomenon for the reduction of the strength of MCrAlY coatings is very important problem to safely design the coated components. The purpose of this section is to mainly investigate the strength of overaluminized layers themselves that are formed over the MCrAlY coatings.

The four-point bend strength shown in Fig. 8 neglects the fact that the aluminized layer is subjected to the residual stresses during the aluminizing process. The residual stresses will be introduced due to the mismatch in the thermal expansion coefficient of the overaluminized layer and the MCrAlY coating during the aluminizing treatment. The residual stresses at the aluminized layers are considered to be an important property, because they are believed to influence the strength and lifetime of the MCrAlY coatings. We used the measurement results of Young's modulus and Poisson's ratio of the aluminized layer in Figs. 5 and 6 for the residual stress measurement. The residual stresses at the aluminized surface layers measured by X-ray diffraction are shown in Fig. 9. The diffraction peak of precipitated CoAl intermetallic compounds is used to measure the residual stresses of the aluminized CoCrAlY coatings, and the diffraction peak of NiAl is used to measure the residual stresses of the other aluminized MCrAlY coatings. It is clear that the high tensile residual stresses are measured at the aluminized surface layer of CoCrAlY coating. On other hand, compressive residual stresses are measured at the aluminized surface layer of the other MCrAlY coatings. There is a tendency that the residual stresses induced by the mismatch of thermal expansion coefficient between the MCrAlY coating and aluminized layers increases with increasing aluminizing temperature. However, the aluminized layer becomes thicker with increasing the aluminizing temperature, and there is tendency that the residual stresses decrease with an increase in the thickness of aluminized layers. Because the constraint of substrate (MCrAlY coatings) reduces with increasing the thickness of aluminized layer. It is considered that the reduction of residual stresses the aluminizing temperature 1223 K is caused by the latter effect.

It is considered that the real strength of aluminized layer can be obtained by taking the residual stress effect from the modified four-point bend strength of the overaluminized MCrAlY coatings in Fig. 8. We have already measured the residual stresses of MCrAlY coatings with 0.3 mm in thickness sprayed on IN738LC substrate, [11]. The residual stress measured at the surface of NiCrAlY coating is −70 MPa, and the residual stresses at the surface of other MCrAlY coatings are 50–75 MPa. The residual stresses induced by aluminizing can be obtained by subtracting these residual stresses of MCrAlY coatings from the residual stresses of the aluminized MCrAlY coatings. The four-point bend strength of aluminized layers obtained by subtracting the residual stresses induced by the aluminizing from the modified four-point bend strength in Fig. 8 is shown in Fig. 10. The apparent strength of the overaluminized MCrAlY coatings in Fig. 7 is shown by comparison. The four-point bend strength of aluminized layers becomes slightly lower than the apparent strength of the overaluminized MCrAlY coatings. As a result, there is a tendency that the four-point bend strength of overaluminized layers of MCrAlY coatings decreased with increasing volume fraction of precipitated Al compounds.

Summary

In the present paper five kinds of vacuum plasma sprayed MCrAlY coatings, such as CoCrAlY, CoNiCrAlY. CoNiCrAlY + Ta, NiCrAlY, and NiCoCrAlY, were selected for an overaluminized treatment. Two reaction diffusion layers could be clearly observed at the overaluminized MCrAlY coatings, consisting of a thick aluminum rich outer layer and an inner diffusion layer. It was confirmed that CoAl intermetallic compounds were formed at the surface of CoCrAlY coating and (Ni, Co)Al intermetallic compounds were formed at the surface of CoNiCrAlY, CoNiCrAlY + Ta and NiCoCrAlY coatings and NiAl intermetallic compounds were formed at the surface of NiCrAlY coating by the aluminizing treatment.

The Vickers hardness of MCrAlY coatings subjected to the overaluminizing treatment (800–1000 HV) was higher in com-

Downloaded 02 Jun 2010 to 171.66.16.98. Redistribution subject to ASME license or copyright; see http://www.asme.org/terms/Terms_Use.cfm

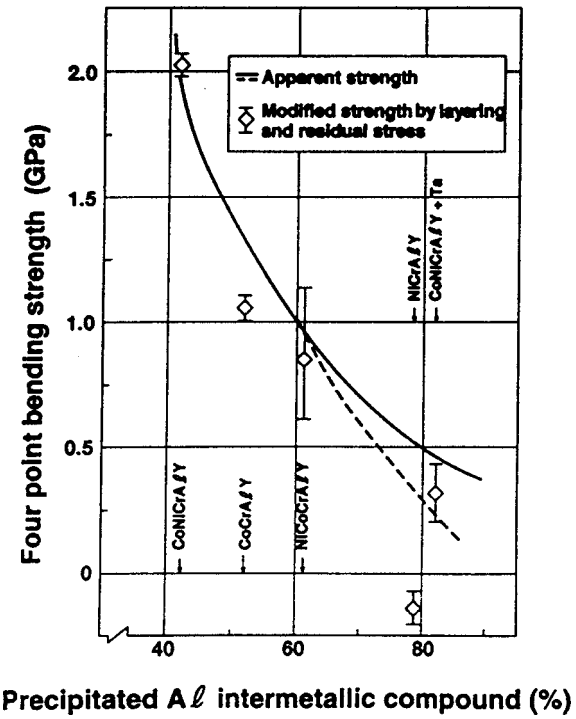

Fig. 10 Modified four-point bend strength of aluminized VPS MCrAlY coatins by taking account of three-layered effect and residual stress

parison to the MCrAlY coatings (400–500 HV). The Young's modulus of MCrAlY coatings (140–170 GPa) was lower than a typical polycrystalline that showed nearly 200–220 GPa. There was a tendency for the Young's modulus of aluminized layers of Ni-based MCrAlY coatings to increase with increasing volume fraction of precipitated Al intermetallic compounds from nearly 190 to 205 GPa. The Young's modulus of aluminized layer of Co-based MCrAlY coatings showed nearly 210 GPa and was not affected by volume fraction of precipitated Al intermetallic compounds within this experiment. There was a tendency for the Poisson's ratio of MCrAlY coatings and their aluminized layers to decrease slightly with increasing volume fraction of precipitated Al intermetallic compounds from about 0.3 to 0.25.

On the other hand, there was a tendency that the four-point bend strength of MCrAlY coatings decreased with increasing volume fraction of precipitated Al compounds and it was reduced by the overaluminizing treatment. High tensile residual stresses were measured by X-ray diffraction at the aluminized surface layer of the CoCrAlY coating and compressive residual stresses were measured at the aluminized surface layer of the other MCrAlY coatings. The strength of aluminized layers themselves was estimated by measuring the residual stress and the three-layered effect from the bend strength of overaluminized MCrAlY coatings. The bend strength of aluminized layers themselves became slightly lower than the apparent bend strength of the overaluminized MCrAlY coatings. There was a tendency that the four-point bend strength of overaluminized layers of MCrAlY coatings decreased with increasing volume fraction of precipitated Al compounds.

References

[1] Bettridge, D. F., and Ubank, R. G., 1986, "Quality Control of High-Temperature Protective Coatings," Mater. Sci. Technol., **2**, pp. 232–242.

[2] Mevrel, R., 1989, "State of the Art on High-Temperature Corrosion-Resistant Coatings," Mater. Sci. Eng., A, **A120**, pp. 12–24.

[3] Das, D. K., Singh, Y., and Joshi, S. V., 1998, "Evolution of Aluminide Coating Microstructure on Nickel-Base Cast Superalloy CM-247 in a Single-Step High-Activity Aluminizing Process," Metall. Mater. Trans. A, **29A**, pp. 2173–2188.

[4] Cheruvu, N. S., Chan, K. S., and Leverant, G. R., 2000, "Cyclic Oxidation Behavior of Aluminide, Platinum Modified Aluminide and MCrAlY Coatings on GTD-111," ASME J. Eng. Gas Turbines Power, **122**, pp. 50–54.

[5] Miller, A. M., 1987, "Current States of Thermal Barriar Coatimgs—An Overview," Surf. Coat. Technol., **30**, pp. 1–11.

[6] Wortman, D. J., Nagaraj, B. A., and Duderstadt, E. C., 1989, "Thermal Barriar Coatings for Gas Turbines Use," Mater. Sci. Eng., A, **A121**, pp. 433–440.

[7] Wu, B. C., Chao, C. H., and Chang, E., 1990, "Effect of Bond Coat Pre-Aluminizing Treatment on the Properties of ZrO2-8wt.%Y2O3/Co-29Cr-6Al-1Y Thermal Barriar Coatings," Mater. Sci. Eng., A, **A124**, pp. 215–221.

[8] Itoh, Y., Saitoh, M., and Ishiwata, Y., 2001, "Aluminizing Behaviors of Vacuum Plasma Sprayed MCrAlY Coatings," ASME J. Eng. Gas Turbines Power, **124**, pp. 270–275.

[9] Schnerder, K., and Grunling, H. W., 1983, "Mechanical Aspect of High Temperature Coatings," Thin Solid Films, **107**, pp. 395–416.

[10] Itoh, Y., 1999, "Reaction Diffusion Behaviors for Interface Between Ni-Based Super Alloys and Vacuum Plasma Sprayed MCrAlY Coatings," ASME J. Eng. Gas Turbines Power, **121**, pp. 476–483.

[11] Itoh, Y., Saitoh, M., and Miyazaki, M., 1994, "Influence of High-Temperature Protective Coatings on the Mechanical Properties of Nickel-Based Superalloys," J. Mater. Sci., **34**, pp. 3957–3966.

Downloaded 02 Jun 2010 to 171.66.16.98. Redistribution subject to ASME license or copyright; see http://www.asme.org/terms/Terms_Use.cfm

S. C. Forth
United Technologies Research Center,
NASA Langley Research Center,
MS 188E,
Two West Reid Street,
Hampton, VA 23682

B. S. Annigeri
United Technologies Research Center,
MS 129-73,
411 Silver Lane,
East Hartford, CT 06108

W. D. Keat
Mechanical Engineering Department,
Union College,
Steinmetz Hall,
Schenectady, NY 12308

Life Prediction for Complex Structures

The surface integral method, an indirect boundary element method that represents a crack as a distribution of force dipoles, has been developed to model three-dimensional nonplanar crack growth in complex structures. The finite body was effectively modeled by superposition of stress influence functions for a half-space. As a result of this strategy, only the fracture has to be discretized. Crack propagation was modeled using the maximum circumferential stress theory to predict crack direction and the Forman fatigue equation, modified with an equivalent stress intensity solution for mixed-mode, to predict extension. Comparisons with benchmark solutions and field data verified the computational methodology and defined the limits of its applicability. [DOI: 10.1115/1.1448330]

Introduction

Only recently have modern computational methods been applied to three-dimensional crack growth problems involving the kind of complex loading situations often encountered in the field, such as mixed-mode fatigue and spectrum loadings. For example, mixed-mode growth of surface cracks has been modeled by Cisilino et al. [1] using the dual boundary element method. A variational boundary integral method (Guanshui et al. [2]) as well as the surface integral method (Forth and Keat [3]) have been developed to simulate nonplanar growth of interior cracks. It was not until the two-dimensional models by Elber [4] and the three-dimensional planar models by Newman [5,6] that spectrum loading models have been developed with acceptable accuracy and efficiency. These models combine weight function methods (Newman and Raju [7]) and strip yield techniques (Dugdale [8] and Irwin [9]) to represent the load interactions (Newman, [10]) that occur during a spectrum load.

In this paper, the three-dimensional surface integral model of Forth and Keat [3,11] was extended to finite geometries by introducing a meshless representation of free surface effects. A spectrum loading model was also developed and added to the formulation. After verification of the static fracture model, the applicability of the growth model was investigated by comparing results to data from a mixed-mode fatigue experiment and a failed part which had been subject to a spectrum loading.

Surface Integral Model

The surface integral method is a numerical representation of a fracture by means of multipole or dislocation superposition. Multipoles, a system of force dipoles can be used to model a mixed-mode fracture by superposition (Love [12]). The tractions induced by a fracture can thus be represented by the integral equation

$$t_k = \int \int_A \Gamma_{kmn} n_m \delta_n dA \tag{1}$$

where t_k is the traction vector, A is the surface area of the nonplanar fracture, Γ_{kmn} is the stress influence function for a half-space, n_m is the normal to the fracture surface, and δ_n is the crack displacement vector where δ_1 is crack opening normal to the crack face, and δ_2 δ_3 are in-plane components of crack shear displacements.

The stress influence functions used in this formulation were derived by Keat et al. [13], starting from Rongved's [14] fundamental solution for point forces near a planar bimaterial interface. These functions can be decomposed into singular (Γ^S_{kmn}) and nonsingular (Γ^N_{kmn}) terms to facilitate the use of specialized integration procedures:

$$\Gamma_{kmn} = \Gamma^S_{kmn} + \Gamma^N_{kmn} \tag{2}$$

where Γ^S_{kmn} is the infinite region solution and the addition of Γ^N_{kmn} has the effect of zeroing out the tractions on a single planar free surface of specified position and orientation with respect to the fracture.

Traction boundary conditions were enforced at collocation points located at the element centroids of a piecewise planar representation of the fracture. In the vicinity of a collocation point, one can subtract off the integral equivalent of a rigid-body displacement to reduce the order of the singularity

$$t_k = \int \int_A \Gamma_{kmn} n_m \delta_n dA - \int \int_{A_\infty} \Gamma^S_{kmn} n_m \hat{\delta}_n dA \tag{3}$$

where A_∞ is a plane of infinite extent that is coplanar with the singular element containing the collocation point; $\hat{\delta}_n$ represents crack opening/shear at the collocation point.

Substituting Eq. (2) into Eq. (3), the singular element of area A_S can now be integrated in the Cauchy Principal-value sense by arranging terms as follows:

$$t_k = \int \int_{A-A_S} \Gamma^S_{kmn} n_m \delta_n dA + \int \int_{A_S} \Gamma^S_{kmn} n_m (\delta_n - \hat{\delta}_n) dA - \int \int_{A_\infty - A_S} \Gamma^S_{kmn} n_m \hat{\delta}_n dA + \int \int_A \Gamma^N_{kmn} n_m \delta_n dA \tag{4}$$

where specialized integration procedure have been developed for each of the integrals appearing in Eq. (4). Discretization of the fracture surface into triangular crack elements then leads to the following equivalent form of the traction equation:

Contributed by the International Gas Turbine Institute (IGTI) of THE AMERICAN SOCIETY OF MECHANICAL ENGINEERS for publication in the ASME JOURNAL OF ENGINEERING FOR GAS TURBINES AND POWER. Paper presented at the International Gas Turbine and Aeroengine Congress and Exhibition, Munich, Germany, May 8–11, 2000; Paper 00-GT-630. Manuscript received by IGTI November 1999; final revision received by ASME Headquarters February 2000. Associate Editor: D. Wisler.

 Copyright © 2005 by ASME

Downloaded 02 Jun 2010 to 171.66.16.98. Redistribution subject to ASME license or copyright; see http://www.asme.org/terms/Terms_Use.cfm

$$t_k = \sum_{\substack{i=1 \\ i \neq q}}^{Nele} \int\int_{A_i} \Gamma^S_{kmn} n^q_m h_n \hat{\delta}^i_n dA + \int\int_{A_q} \Gamma^S_{kmn} n^q_m (h_n - 1) \hat{\delta}^q_n dA + \oint_{A_q} \mathbf{N}^q \cdot \nabla \phi_{kn} \hat{\delta}^q_n dS + \sum_{i=1}^{Nele} \int\int_{A_i} \Gamma^N_{kmn} n^q_m h_n \hat{\delta}^i_n dA \quad (5)$$

where the superscript i indicates crack element correspondence, q identifies the singular crack element containing the collocation point, A_i is the surface area of the ith crack element, *Nele* is the number of elements in the crack mesh, $\mathbf{N}$ is the in-plane outward unit normal to the contour enclosing A_q, and it follows from Green's Lemma (Pearson, [15]) that $\Gamma^S_{kmn} n^q_m = \nabla \cdot \nabla \phi_{kn}$ where Γ^S_{kmn} and ϕ_{kn} are continuously differentiable along the closed contour. Note that the line integral is equivalent to the third term in Eq. (4) and was introduced to avoid having to discretize the area $A_\infty - A_S$ which is nonsingular and of infinite extent. The remaining area integrals were evaluated using Gauss quadrature.

Local interpolation functions for crack opening were selected based on proximity to the crack front. The interior elements were assumed to have constant crack-opening displacements such that $h_n = 1$, and a specialized interpolation function was developed for the tip elements using the plane strain elasticity solution. The latter states that the near-tip displacements vary as the square root of the perpendicular distance from the crack front. When using constant elements in the interior, tip elements should span at least 15 percent of the crack radius to maintain accuracy.

The computational approach taken to model a finite body was to approximate the stress influence for the finite body as

$$\Gamma_{kmn} = \Gamma^S_{kmn} + \sum_{j=1}^{Nif} \Gamma^{N_j}_{kmn} \quad (6)$$

in which *Nif* is the number of planar free surfaces being modeled and the subscript on N identifies the free surface. Each nonsingular stress influence function j exactly satisfies the boundary conditions on the planar free surface to which it corresponds, while adding small tractions to the other free surfaces. The error associated with these small tractions has been found to be tolerable for a fairly wide range of geometries. As a result, the fourth integral in Eq. (5) is redefined for finite bodies with more than one planar free surface to be

$$I_4 = \sum_{i=1}^{Nele} \sum_{j=1}^{Nif} \int\int_{A_i} \Gamma^{N_j}_{kmn} n^q_m h_n \hat{\delta}^i_n dA. \quad (7)$$

Finally, Eq. (5) can be rewritten using shorthand notation as

$$t_k = C_{kn} \hat{\delta}_n \quad (8)$$

where C_{kn} represents the coefficient matrix.

Fatigue Crack Growth

Three-dimensional fracture models, such as the surface integral method, can make use of two-dimensional growth laws by applying them locally along the crack front. To propagate the crack, both the direction and extension must be computed at each crack tip element. The maximum circumferential stress theory (Erdogan and Sih [16]) for direction, and the Forman fatigue equation (Forman and Mettu [17]) for extension, were applied here due to their wide industrial acceptance and ease of implementation.

Maximum Circumferential Stress Theory. Maximum circumferential stress theory determines the direction of crack propagation by maximizing the circumferential stress at the crack tip. When related to the stress intensity factor solution, it yields the following nonlinear equation that can be solved iteratively for θ:

$$K_I \sin\theta + K_{II}(3\cos\theta - 1) = 0 \quad (9)$$

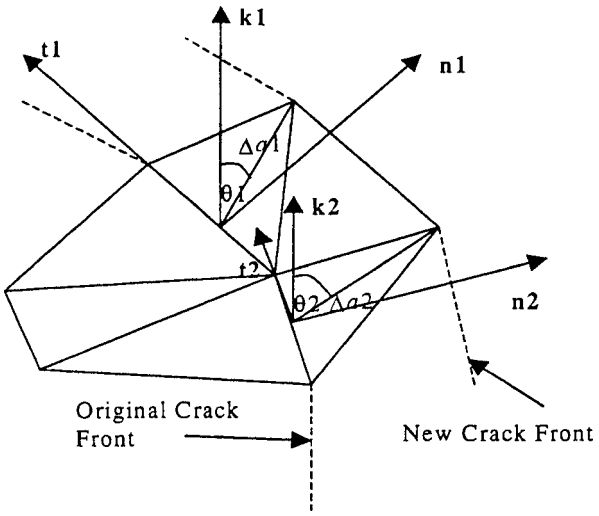

Fig. 1 Advancement of the fracture surface

where θ is the angle of growth direction expressed in the local normal-tangential coordinate system of the tip element as shown in Fig. 1.

Forman Fatigue Equation. The Forman fatigue equation was developed to curve fit a large material database that is available through the NASA Johnson Space Center. The Forman equation is defined as

$$\frac{da}{dN} = \frac{C(1-f)^n (\Delta K_{eq})^n \left(1 - \frac{\Delta K_{th}}{\Delta k_{eq}}\right)^p}{(1-R)^n \left(1 - \frac{\Delta K_{eq}}{(1-R)K_C}\right)^q} \quad (10)$$

where da/dN is the rate of crack extension based on crack length a and cycle count N; R is the stress ratio $\sigma_{min}/\sigma_{max}$; ΔK_{eq} is the equivalent stress intensity factor range which for mixed-mode is defined to be $\Delta K_{eq} = \sqrt{(\Delta K_I)^2 + (\Delta K_{II})^2 + (\Delta K_{III})^2}$ in accordance with the mixed-mode definition of strain energy release rate (Erdogan [18]); C, n, p, and q are empirically derived material constants; K_c is the fracture toughness; ΔK_{th} is the threshold stress intensity factor range, and f is the crack-opening function.

Spectrum Loading Model. Spectrum loadings are comprised of a series of load blocks, each of which are characterized by maximum and minimum loads repeated over time. These load blocks are typically arranged in a designated order to mimic a stress profile that a part undergoes in the field. The loads can be as simple as constant amplitude spectra or as complex as a wing transport spectrum (deJonge et al. [19]), a simplification of the stresses an aircraft wing experiences.

Given the applied loads, one can determine (e.g., using finite elements) the tractions applied locally to the crack for each load block. Equation (8) can then be solved for each block of the spectrum using the same coefficient matrix:

$$t^{(l)}_k = C_{kn} \hat{\delta}^{(l)}_n \quad \text{where} \quad l = 1, L_B \quad (11)$$

where L_b is the number of load blocks in the spectrum, and the superscript in parentheses indicates the load block. The stress intensity factors follow immediately upon substitution of the tip element displacements into the plane-strain definitions.

The calculation of the crack extension is performed locally at each crack-tip element i (see Fig. 1) by setting the cycle increment $\Delta N^{(l)}$ to that defined in the spectrum for the loading block l under consideration such that

Downloaded 02 Jun 2010 to 171.66.16.98. Redistribution subject to ASME license or copyright; see http://www.asme.org/terms/Terms_Use.cfm

$$\Delta a_i^{(l)} = \Delta N^{(l)} \frac{C(1-f)^n (\Delta K_{eq_i})^n \left(1 - \frac{\Delta K_{th}}{\Delta K_{eq_i}}\right)^p}{(1-R)^n \left(1 - \frac{\Delta K_{eq_i}}{(1-R)K_C}\right)^q}. \quad (12)$$

The contributions of each load block to the crack extensions are accumulated for each tip element i

$$\Delta a_i^{TOT} = \sum_{l=1}^{L} \Delta a_i^{(l)} \quad (13)$$

until either one pass through the spectrum has been completed (so that L is equal to the number of load blocks) or the sum of the load block contributions exceeds the maximum allowed growth increment (*maxstep*).

If the maximum value of Δa_i^{TOT} is less than *maxstep* after one pass through the spectrum then the ratio of *maxstep* to Δa_i^{TOT} is used to define a scaling factor such that

$$\text{scale} = \frac{maxstep}{\max_i(\Delta a_i^{TOT})} \quad (14)$$

where *maxstep* was set to 20 percent of the current crack radius. This scaling factor is applied to the spectrum to determine the cycle count, ΔN^{TOT}, required to propagate the tip element with the maximum computed extension a distance equal to *maxstep*.

$$\Delta N^{TOT} = \text{scale} * \left[\sum_{l=1}^{L} \Delta N^{(l)} \right] \quad (15)$$

This scaling factor is then applied to the local crack extensions, Δa_i^{TOT}, to advance the crack front as illustrated in Fig. 1.

However, if the sum of the load block contributions computed in Eq. (13) exceeds *maxstep* before completing one pass through the spectrum, then the growth increments at each tip element are redefined in terms of the load block contributions as follows:

$$\Delta a_i^{TOT} = \alpha \Delta a_i^{(1)} + \sum_{l=2}^{L-1} \Delta a_i^{(l)} + \beta \Delta a_i^{(L)} \quad (16)$$

where α and β denote fractional parts of the first and last load blocks spanning the growth increment. β is evaluated at the tip element with the largest value of Δa_i^{TOT} by setting Δa_i^{TOT} equal to *maxstep* in Eq. (16) and rearranging to obtain

$$\beta = \left(maxstep - \left(\alpha \Delta a_i^{(1)} + \sum_{i=1}^{L-1} \Delta a_i^{(l)} \right) \right) \Big/ \Delta a_i^{(L)} \quad (17)$$

in which $\alpha = 1$ for the initial growth increment, and for subsequent growth increments is set equal to $1-\beta^*$, where β^* corresponds to β from the previous growth increment. The cycle count for the growth increment is computed using the same values of α and β:

$$\Delta N^{TOT} = \alpha \Delta N^{(1)} + \sum_{l=2}^{L-1} \Delta N^{(l)} + \beta \Delta N^{(L)}. \quad (18)$$

Results

Benchmark Solutions. The modeling strategy for finite structures, represented in Eqs. (6) and (7), was tested by comparing results for a center cracked plate under tension with the analytical solution by Tada [20]. The 240 elements used in the model were all located on the crack surface since free surface effects were accounted for through the deployment of multiple sets of the stress influence functions for a half-space. Results are shown in Fig. 2 for a plate width to thickness ratio of 8:1. Accuracy eventually degrades for high aspect ratio through cracks but can be improved by application of corrective tractions as described in Keat et al. [21].

Implementation of the half-space solution in the nonplanar model of Keat and Forth [22] was verified in part by examining the asymptotic behavior of the curved surface crack geometries depicted in Figs. 3 and 4. Both cracks were produced by wrapping a semi-circular crack front of radius a around a cylinder of radius r. Corresponding stress intensity factors, nondimensionalized such that $K_i = F_i \sigma \sqrt{\pi a}$, are plotted in Figs. 5 and 6 against radius of curvature. As expected, K_{II} and K_{III} tend towards zero as the crack flattens, and the value of K_I drops quickly as the crack curves parallel to the applied loading.

Comparison to Test. Comparison of the crack growth model to experimental data was performed for a variety of angled surface cracks in 7075-T73 aluminum as reported in Forth et al. [23].

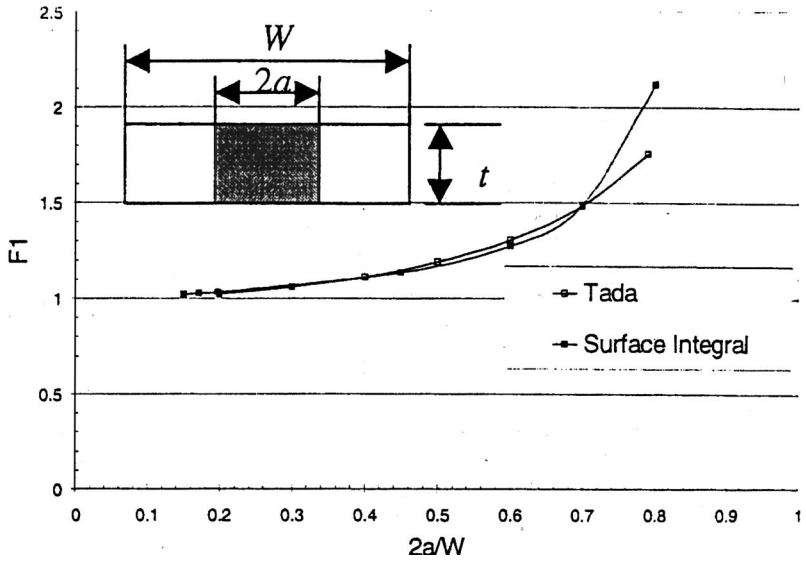

Fig. 2 Mode I stress intensity factor versus crack length for a through crack in a thick plate ($W/t = 8.0$)

Downloaded 02 Jun 2010 to 171.66.16.98. Redistribution subject to ASME license or copyright; see http://www.asme.org/terms/Terms_Use.cfm

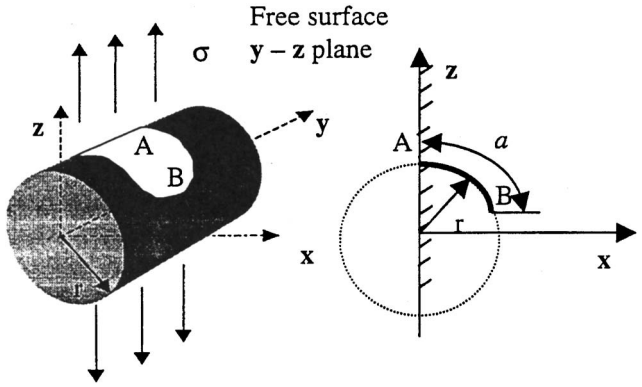

Fig. 3 Curved surface crack (geometry I)

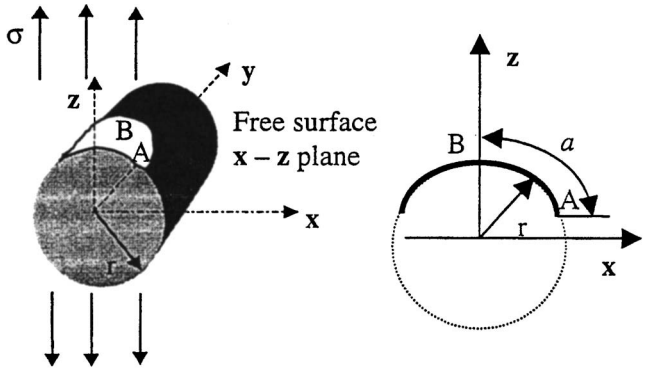

Fig. 4 Curved surface crack (geometry II)

Application of a constant amplitude tension loading produced repeatable nonplanar fracture surfaces against which to compare the computational results. The initial semi-circular flaw was meshed using 300 elements while use of Eq. (6) to approximate the stress influence function eliminated the need to discretize the four free surfaces forming the cross section of the specimen. Results from Forth et al. [23] for an initial flaw 60 deg off-axis to the applied load are presented in Fig. 7. Excellent correlation to the data was achieved using the maximum circumferential stress theory and the Forman equation with the mixed-mode definition of ΔK_{eq}. Results indicated that failure to include K_{II} and K_{III} in the definition ΔK_{eq} will, at least in this case, lead to predictions that are highly nonconservative.

The spectrum loading model was evaluated on a part for which field data was available. A 260-element model of the initial flaw was placed near the observed crack initiation site of the full-scale test and propagated under a spectrum loading similar to that experienced by the actual part. The crack growth simulation was allowed to continue until ΔK_{eq} exceeded the fracture toughness of the material. The results are shown in Fig. 8 where fairly close agreement between the computational and experimental results can be observed. Here again, the free surfaces forming the cross-section of the crack plane were modeled as piecewise planar using Eq. (6). The normal tractions acting on the crack surface and driving the crack growth were obtained from a finite element model of the uncracked part. One may note in the mesh plot of Fig. 8 that the value of *maxstep* was often less than the recommended value of 20 percent of the current crack radius, as *maxstep* was internally scaled back if spurious oscillations, indicative of a numerical instability, were detected along the crack front.

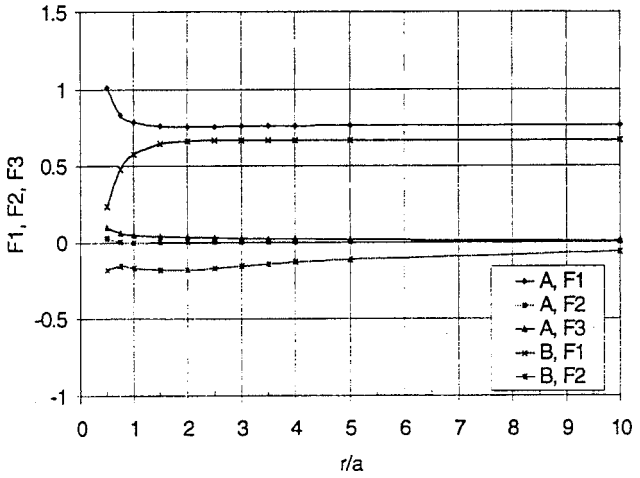

Fig. 5 Effect of changes in curvature on stress intensity factors for geometry I

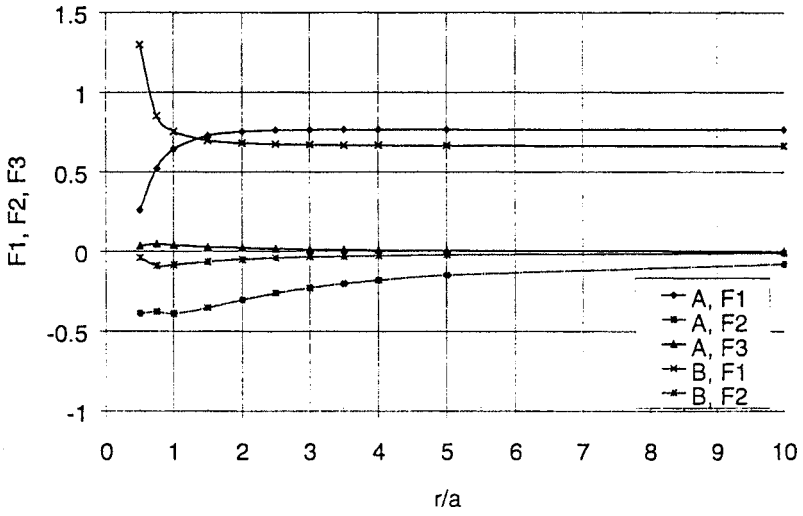

Fig. 6 Effect of changes in curvature on stress intensity factors for geometry II

Downloaded 02 Jun 2010 to 171.66.16.98. Redistribution subject to ASME license or copyright; see http://www.asme.org/terms/Terms_Use.cfm

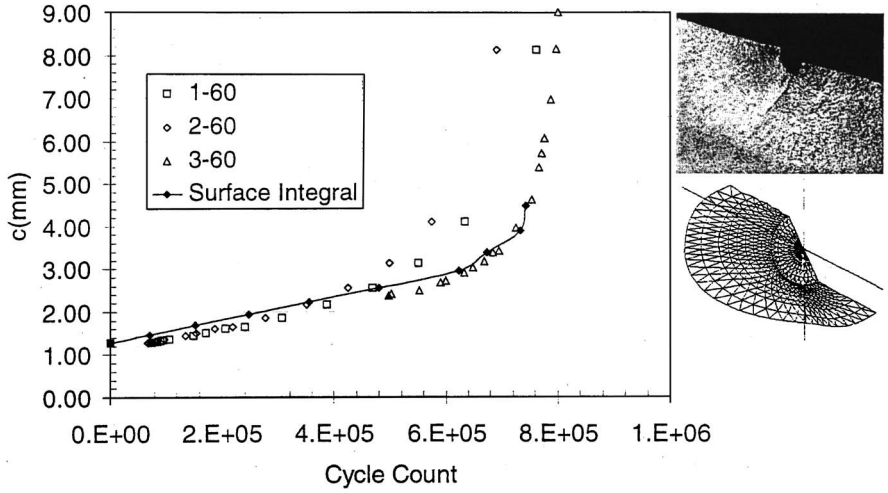

Fig. 7 Comparison of surface integral model results to experimental data for 60 deg angled surface crack subject to cyclic tension loading. Graph (above) shows number of cycles plotted against crack half-length, *c*, at the free surface where *c* is measured perpendicular to the direction of the load. Photograph (above right) of precrack with growth rings is consistent with resulting crack mesh (below right).

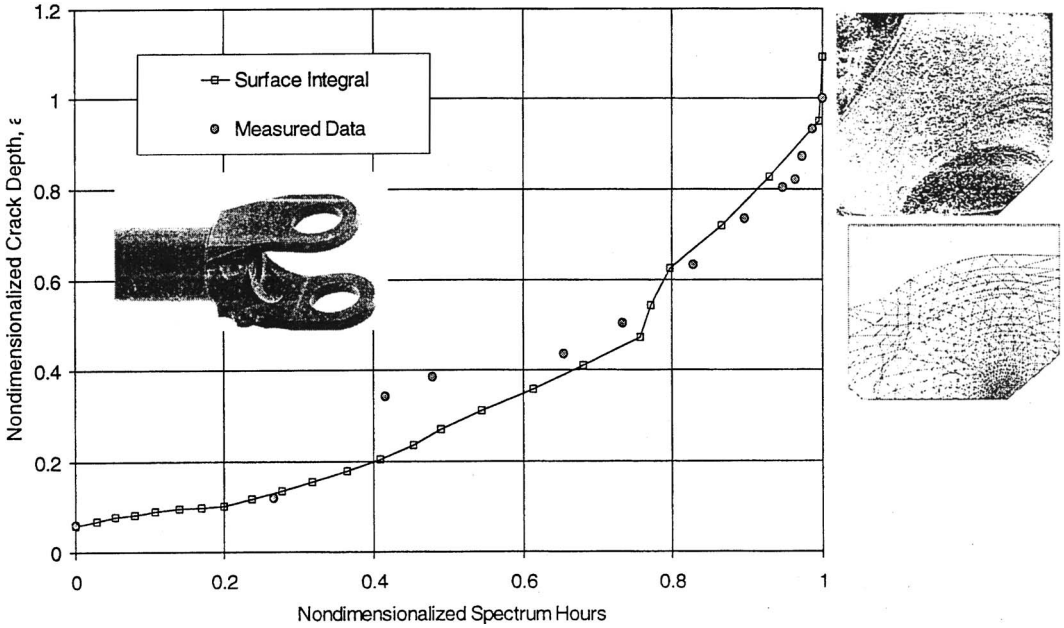

Fig. 8 Comparison of surface integral model results to field data for a part undergoing spectrum loading. Graph above shows number of spectrum hours versus crack depth. Photograph (above right) of growth rings corresponds to cross section indicated on part insert. Succession of crack fronts predicted by the model is also shown (below right).

Summary

The surface integral method was further advanced to model a three-dimensional nonplanar fracture in a finite domain. This was accomplished using a half-space superposition technique that proved to be an accurate representation for several problems. Comparison of the fatigue crack growth data to the predictions agrees well, as illustrated in Figs. 7 and 8. The predicted crack paths are representative of the actual data. Discrepancies in Fig. 8 could be attributed to a redistribution of load in the actual part as the crack propagated which was not accounted for in the computational model. Also, load interactions characterized by crack retardation after an overload or crack acceleration after an underload have not been directly accounted for. However, even with these shortcomings, it is shown in Fig. 8 that the final fatigue life of the prediction is very close to the actual data. The accuracy of this prediction can be attributed to explicitly modeling the spectrum load and stress gradient across the cross section as closely as possible to that of the part.

References

[1] Cisilino, A. P., and Aliabadi, M. H., 1997, "Three-Dimensional BEM Analysis for Fatigue Crack Growth in Welded Components," Int. J. Pressure Vessels Piping **70**, pp. 135–144.
[2] Guanshui, X., Argon, A. S., Ortiz, M., and Bower, A., 1995, "Development of a Variational Boundary Integral Method for Analysis of Fully Three-Dimensional Crack Advance Problems," Comp. Mech., **2**, pp. 2874–2889.
[3] Forth, S. C., and Keat, W. D., 1997, "Nonplanar Crack Growth Using the

Downloaded 02 Jun 2010 to 171.66.16.98. Redistribution subject to ASME license or copyright; see http://www.asme.org/terms/Terms_Use.cfm

Surface Integral Method,'' ASME J. Eng. Gas Turbines Power, **119**, pp. 964–968.
[4] Elber, W., 1971, ''The Significance of Fatigue Crack Closure,'' *Damage tolerance of aircraft structures*, ASTM-STP-486, ASTM, Philadelphia, pp. 230–242.
[5] Newman, J. C., Jr., 1982, ''Prediction of Fatigue Crack Growth Under Variable-Amplitude and Spectrum Loading Using a Closure Model,'' *Design of Fatigue and Fracture Resistant Structures*, ASTM-STP-761, ASTM, Philadelphia.
[6] Newman, J. C., Jr., 1984.
[7] Newman, J. C., Jr., and Raju, I. S., 1984, ''Prediction of Fatigue Crack Growth Patterns and Lives in Three-Dimensional Cracked Bodies,'' NASA TM-85787.
[8] Dugdale, D. S., 1960, ''Yielding of Steel Sheets Containing Slits,'' J. Mech. Phys. Solids, **8**, No. 2, pp. 100–104.
[9] Irwin, G. R., 1960, ''Plastic Zone Near a Crack and Fracture Toughness,'' *Proceedings of the 7th Sagamore Conference*.
[10] Newman, J. C., Jr., 1981, ''A Crack Closure Model for Predicting Fatigue Crack Growth Under Aircraft Spectrum Loading,'' *Methods and Models for Predicting Fatigue Crack Growth Under Random Loading*, ASTM-STP-748, ASTM, Philadelphia, pp. 53–84.
[11] Forth, S. C., and Keat, W. D., 1996, ''Three-Dimensional Nonplanar Fracture Model Using the Surface Integral Method,'' Int. J. Fract., **77**, No. 3, pp. 243–262.
[12] Love, A. E. H., 1944, *A Treatise on Mathematical Theory of Elasticity*, Dover, New York.
[13] Keat, W. D., Erguven, M. E., and Dwyer, J. F., 1997, ''Modeling of Three-Dimensional Mixed-Mode Fractures Near Planar Bimaterial Interfaces Using Surface Integrals,'' Int. J. Numer. Methods Eng., **39**, pp. 3679–3703.
[14] Rongved, 1955, ''Force at a Point in the Interior of a Semi-Infinite Solid,'' *Proc. 2nd Midwestern Conf. On Solid Mech.*, pp. 1–13.
[15] Pearson, C. E., 1983, *Handbook of Applied Mathematics*, Van Nostrand Reinhold, New York.
[16] Erdogan, F., and Sih, G. H., 1963, ''On the Crack Extension in Plates Under Plane Loading and Transverse Shear,'' ASME J. Basic Eng., **85**, pp. 519–527.
[17] Forman, R. G., and Mettu, S. R., 1992, ''Behavior of Surface and Corner Cracks Subjected to Tensile and Bending Loads in Ti-6Al-4V Alloy,'' ASTM-STP-1131, ASTM, Philadelphia, pp. 519–546.
[18] Erdogan, F., 1983, ''Stress Intensity Factors,'' ASME J. Appl. Mech., **50**, pp. 992–1002.
[19] deJonge, J. B., Schutz, D., Lowak, H., and Schijve, J., 1973, ''A Standardized Load Sequence for Flight Simulation Tests on Transport Aircraft Wing Structures (TWIST),'' National Lucht-en Ruimtevaartlaboratium, NLR-TR 73029U.
[20] Tada, H., 1971, ''A Note on the Finite Width Corrections to the Stress Intensity Factor,'' Eng. Fract. Mech., **3**, No. 3, pp. 345–347.
[21] Keat, W. D., et al., 1996.
[22] Keat and Forth, 1997.
[23] Forth, S. C., Favrow, L. H., and Keat, W. D., 1999, ''Mixed-Mode Crack Growth: An Experimental and Computational Study,'' *Fatigue '99 Conf. Proc.*, Vol. 4, pp. 2533–2538.

Downloaded 02 Jun 2010 to 171.66.16.98. Redistribution subject to ASME license or copyright; see http://www.asme.org/terms/Terms_Use.cfm

Application of Computational Fluid Dynamics Analysis for Rotating Machinery—Part II: Labyrinth Seal Analysis

Toshio Hirano

Zenglin Guo

R. Gordon Kirk

Mechanical Engineering Department,
Rotor Dynamics Laboratory,
Virginia Polytechnic Institute and State University,
Blacksburg, Virginia 24061

Labyrinth seals are used in various kinds of turbo machines to reduce internal leakage flow. The working fluid, or the gas passing through the rotor shaft labyrinth seals, often generates driving force components that may increase the unstable vibration of the rotor. It is important to know the accurate rotordynamic force components for predicting the instability of the rotor-bearing-seal system. The major goals of this research were to calculate the rotordynamic force of a labyrinth seals utilizing a commercial CFD program and to further compare those results to an existing bulk flow computer program currently used by major US machinery manufacturers. The labyrinth seals of a steam turbine and a compressor eye seal are taken as objects of analysis. For each case, a 3D model with eccentric rotor was solved to obtain the rotordynamic force components. The leakage flow and rotor dynamics force predicted by CFX TASCFlow are compared with the results of the existing bulk flow analysis program DYNLAB. The results show that the bulk flow program gives a pessimistic prediction of the destabilizing forces for the conditions under investigation. Further research work will be required to fully understand the complex leakage flows in turbo machinery. [DOI: 10.1115/1.1808426]

Introduction

In the 1980s the analytical methods employing bulk flow models were developed to estimate the instability of rotor systems. They are still used in the rotating machinery industries and have helped engineers to design stable rotating machinery. The bulk flow models are so simplified that the program applying them can be run on a personal computer with standard memory. However, they require the empirical correction to have the analysis predictions match the experimental results [1–6].

Recently the progress of computer technologies makes it possible to utilize a CFD program for predicting the rotordynamic force of rotating machinery seals. With this progress, the personal computer can have enough speed and the required memory capacity for a 3D analysis of the labyrinth seal. Rhode [7,8], Ishii, [9] and Kwanka [10] calculated the rotordynamic force of gas labyrinth seals using the CFD programs they developed. Moore [11] used SCISEAL, a CFD code specially developed for the analysis of the seals, and compared the results with experiment results and the bulk flow programs.

Currently, the CFD analysis for fluid-film bearings and labyrinth seals has been carried out at the Virginia Tech Rotor Dynamics Laboratory. A commercial CFD program, CFX-TASCflow, is mainly used for the analysis. In the previous paper [12], the application of CFD in the calculation of hydrodynamic and hydrostatic bearings is presented. The results of the CFD analysis are compared to various standard lubrication theory numerical calculation programs. The results show reasonable agreement, but leave room for future work to refine the methods of computation.

Another major goal of this research is to calculate the rotordynamic force of gas labyrinth seals, from which the dynamic stiffness and damping can be solved. Labyrinth seals are used in various kinds of turbo machines to reduce internal leakage flow. In this paper the labyrinth seals of a steam turbine and a compressor eye seal are taken as objects of analysis. For each case a 3D model with eccentric rotor is solved to obtain the rotordynamic force. The leakage flow and rotordynamic force from CFX-TASCflow are compared with the results by an existing bulk flow analysis computer program [4–6].

The simulation presented in this paper was conducted by using the CFX-TASCflow 2.11.1 [13]. For grid generation a self-developed code were employed. It can generate a 3D mesh for TASCflow from geometrical data such as the diameter, the clearance, the pitch, etc. On the hardware side, one Intel 2×Pentium III 800 MHz CPU computer with 512 MB RAM, and three Intel Pentium 4 1.7 GHz CPU computers with 2 GB RAM, all operating on the Windows NT 4.0/2000 systems, were utilized, respectively. The typical simulation times ranged from a few minutes to several hours depending on the complexity of the models and the parameters used for the solver. More details of the required time of computation with the CFD analysis will be given in the following discussion of results.

Compressor Eye Seal

Dimensions and Conditions. Figures 1 and 2 show the labyrinth seal model for calculation. It is called a straight seal and consists of a rotor with flat surface and a stator with teeth. Table 1 and Fig. 3 show the dimensions and conditions used for calculation.

This calculation assumes the fluid to be an ideal gas and the entire flow to be turbulent. The k-ε model is used for turbulence. The scalable log law wall function is applied to wall boundary conditions. The swirl at the inlet is zero.

Mesh Density Study. The mesh density study is performed to investigate the effect of mesh density and to know how fine of a mesh is necessary for this calculation. The flow domain is divided into different regions as shown in Fig. 4. There are 3 regions (1–3) in a_chamber and 1 region (4) between the tip of tooth and rotor. In Fig. 4, n1, n2, and n3 are the number of elements of the

Contributed by the International Gas Turbine Institute (IGTI) of THE AMERICAN SOCIETY OF MECHANICAL ENGINEERS for publication in the ASME JOURNAL OF ENGINEERING FOR GAS TURBINES AND POWER. Paper presented at the International Gas Turbine and Aeroengine Congress and Exhibition, Atlanta, GA, June 16–19, 2003, Paper No. 2003-GT-38984. Manuscript received by IGTI, October 2002, final revision, March 2003. Associate Editor: H. R. Simmons.

 Copyright © 2005 by ASME

Downloaded 02 Jun 2010 to 171.66.16.98. Redistribution subject to ASME license or copyright; see http://www.asme.org/terms/Terms_Use.cfm

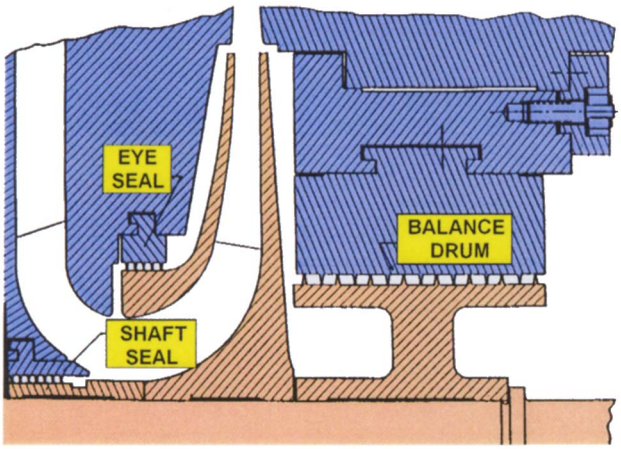

Fig. 1 Typical compressor labyrinth configuration

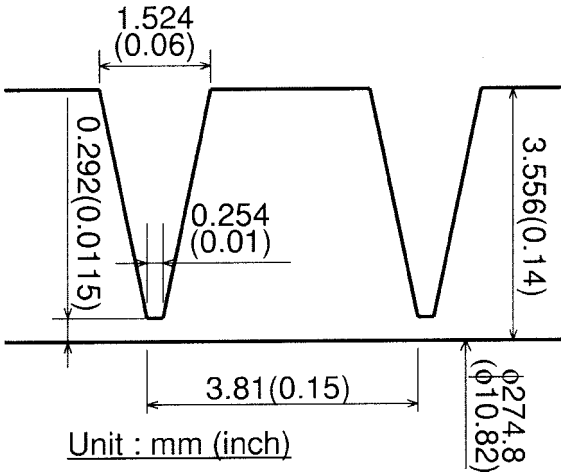

Fig. 3 Dimensions of compressor eye seal

region (1), (2), and (3), respectively, in radial direction. And n4 and n5 are the number of elements of regions (1), (2), (3) and (4) in the axial direction. The number of elements in the circumferential direction is n6.

First, n1, n2, n3, n4, n5, and n6 are set to 10, 10, 10, 20, 10, and 36, respectively, for the original mesh (CASE 0). Figure 5 shows the mesh of CASE 0 in the meridional plane. More nodes are placed near the walls because the change of the flow may be large. The nodes are distributed so that the ratio of the length of each element and the adjacent one is the same. The ratio is 1.1. A 3D mesh is built for the analysis with eccentric rotor. The eccentricity of the rotor is 29.2 μm (1.15 mils), which equals 10% of the tip clearance. Computation time for this model is 4 h with the Pentium®4 1.7 GHz processor.

Then, each parameter (n1–n6) is increased independently and the leakage flow and the seal force of each case are compared.

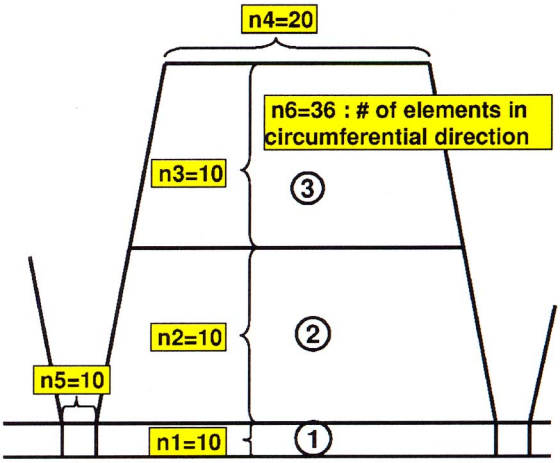

Fig. 4 Regions

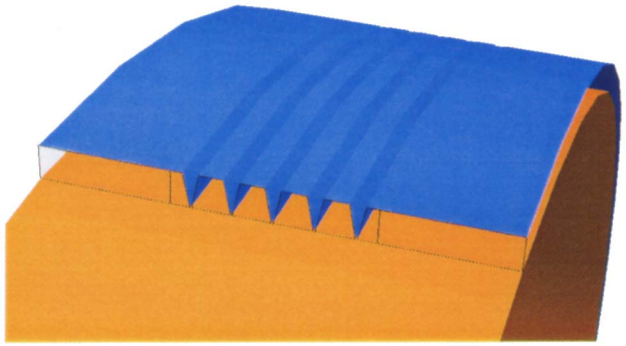

Fig. 2 Analysis model for compressor eye seal

Table 1 Dimensions and conditions

Rotor diameter	274.8 mm (10.82 in.)
Clearance at teeth	0.292 mm (0.0115 in.)
No. of teeth	5
Rotation speed	1162 rad/s (11,097 rpm)
Inlet pressure	3.447 MPa (500 psi)
Outlet pressure	1.724 MPa (250 psi)
Inlet temperature	366.7 K (660 R)
Inlet swirl	0
Flow	Compressible Turbulent k-ε Scalable Log law wall function
Fluid	Air (Ideal gas)

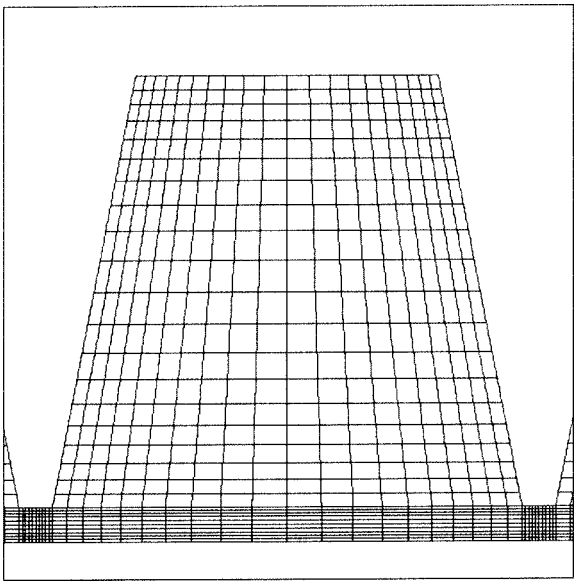

Fig. 5 Mesh of CASE 0

Downloaded 02 Jun 2010 to 171.66.16.98. Redistribution subject to ASME license or copyright; see http://www.asme.org/terms/Terms_Use.cfm

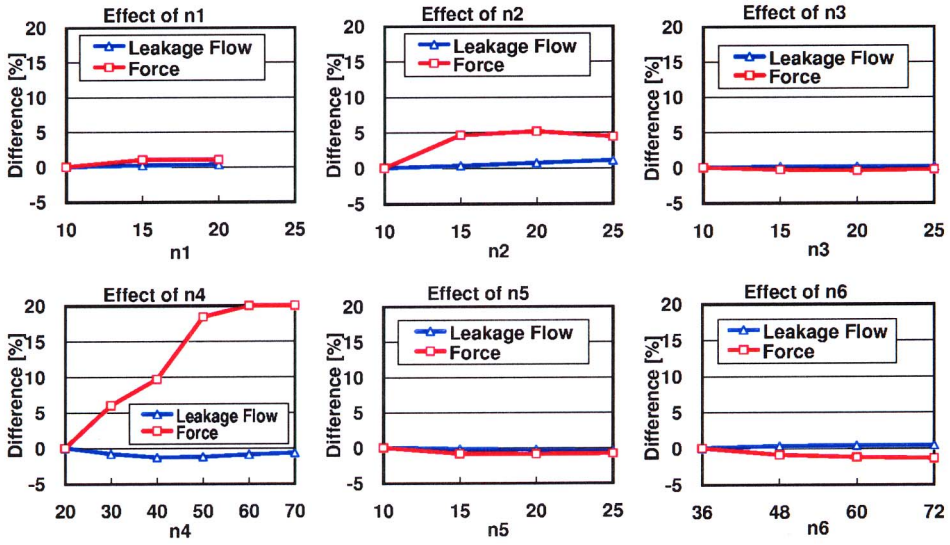

Fig. 6 Result of mesh density study

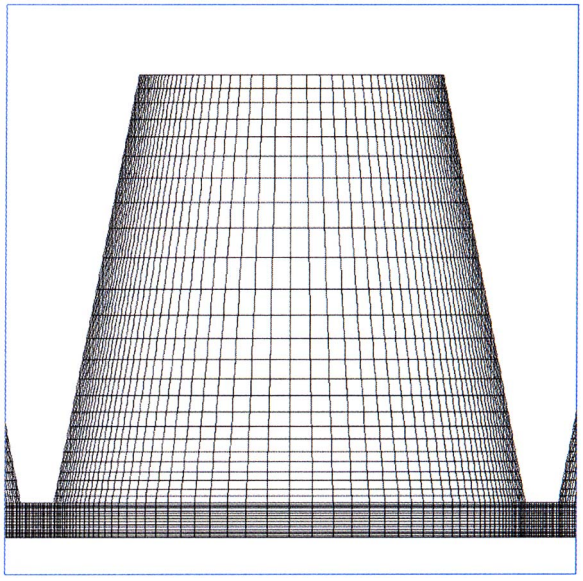

Fig. 7 Mesh after adjustment

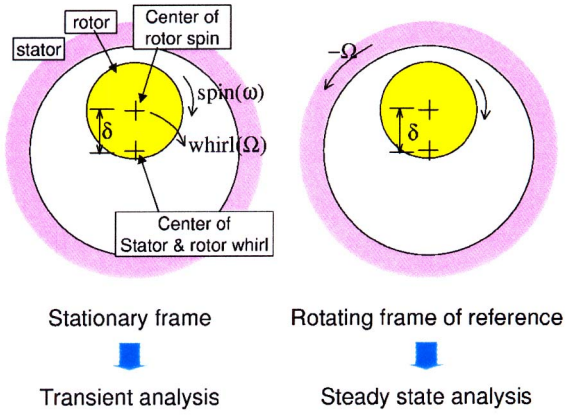

Fig. 8 Axial view of rotor and stator

Figure 6 shows the results of mesh density study. The calculation with n1=25 does not converge. In this case, n4 has the largest effect, n1, n2, n5, and n6 have some, and n3 has little.

For more accurate calculation, n1, n2, n3, n4, n5, and n6 are set to 15, 15, 10, 50, 10, and 48, respectively. The total number of

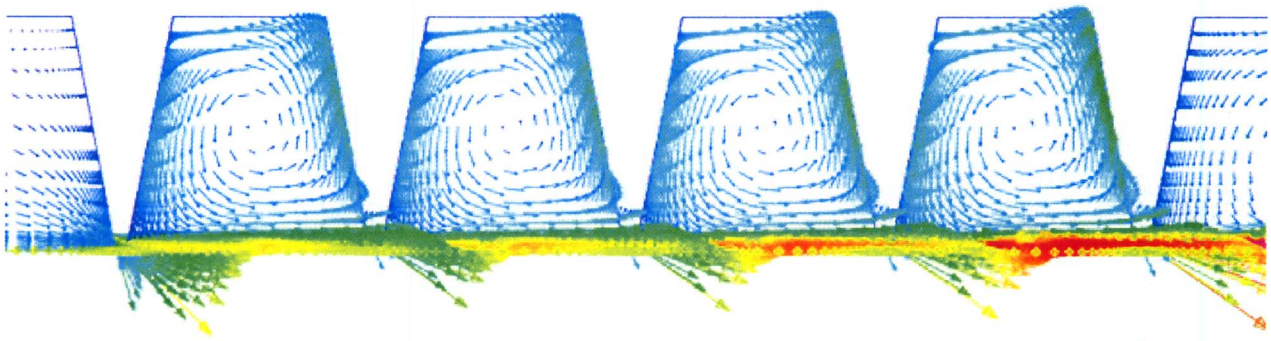

Fig. 9 Vector plot

Downloaded 02 Jun 2010 to 171.66.16.98. Redistribution subject to ASME license or copyright; see http://www.asme.org/terms/Terms_Use.cfm

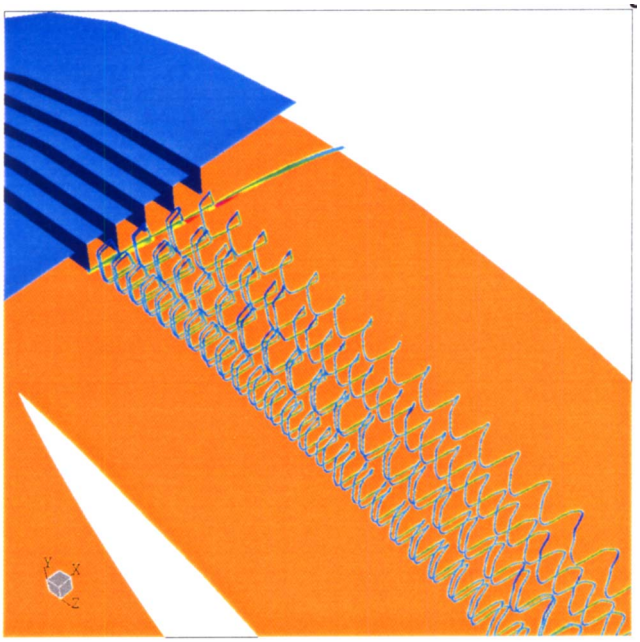

Fig. 10 Streak line

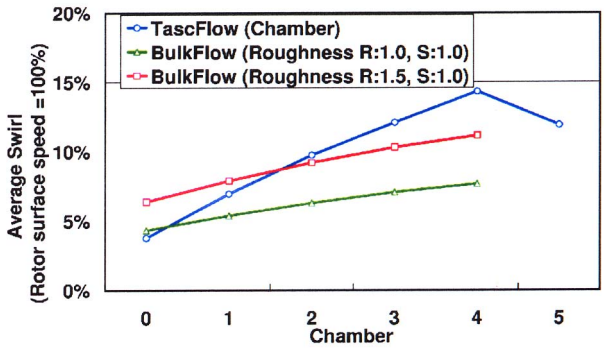

Fig. 11 Average swirl

nodes is 761,852. Figure 7 shows the mesh after adjustment. It takes 3 h 30 min for the calculation of this model, with the initial value interpolated from the result of CASE 0.

To obtain the dynamic coefficients, the calculation with a whirling rotor is necessary. Figure 8 shows the axial view of the rotor

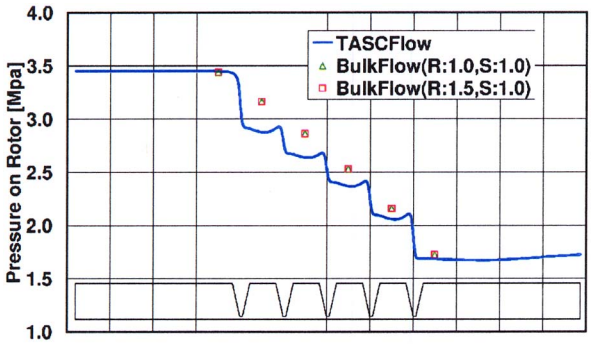

Fig. 12 Pressure distribution

Table 2 Leakage

	Leakage flow (kg/s)	Difference
CFD (TASCflow)	1.08	0
Bulk flow (DYNLAB) −R:1.0, S:1.0	1.28	18.5%
Bulk flow (DYNLAB) −R:1.5, S:1.0	1.28	18.5%

and stator. Here, it is assumed that the rotor is whirling around the center of the seal and that the speed of spinning and whirling are ω and Ω, respectively.

If they are observed from a stationary frame of reference, the geometry of the rotor seems to be moving, so the moving grid and transient analysis are necessary. But observed from the frame of reference rotating with Ω, the rotor always stays at the same place. In this case the analysis becomes steady state.

After solutions with various whirl speeds (Ω) are obtained, the seal force of each case is calculated by integrating the pressure on the rotor. Assuming the effect of inertia is negligible, the dynamic coefficients are derived from the following equations:

$$F_r/\delta = -K - \Omega c$$
$$F_t/\delta = k - \Omega C \tag{1}$$

where K is direct stiffness, k is cross-coupled stiffness, C is direct damping coefficient, c is cross-coupled damping coefficient, F_r is seal force in radial direction, F_t is seal force in tangential direction, and δ is eccentricity.

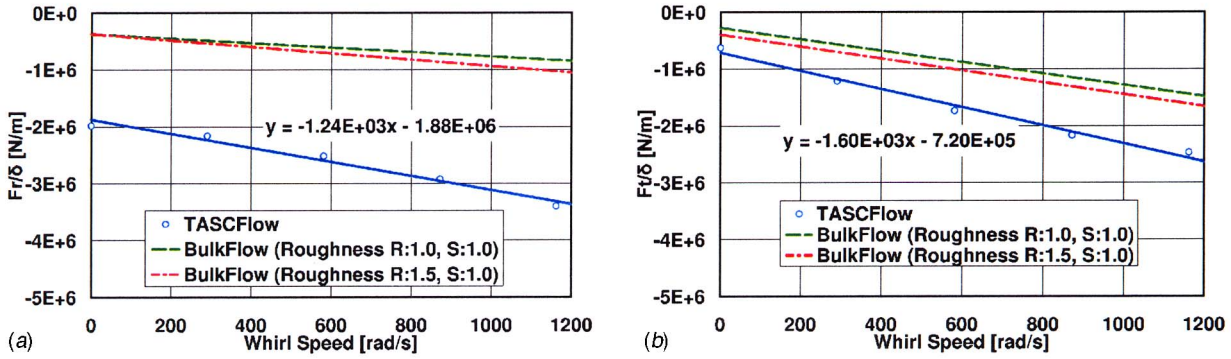

Fig. 13 Seal force versus whirl speed: (*a*) radial direction; (*b*) tangential direction

Downloaded 02 Jun 2010 to 171.66.16.98. Redistribution subject to ASME license or copyright; see http://www.asme.org/terms/Terms_Use.cfm

Table 3 Dynamic characteristics

	K (N/m)	k (N/m)	C (Ns/m)	c (Ns/m)
CFD (TASCflow)	1.88 $\times 10^6$	-7.20×10^5	1.60 $\times 10^3$	1.24 $\times 10^3$
Bulk flow (DYNLAB) R:1.0, S:1.0	3.76 $\times 10^5$	-2.82×10^5	1.00 $\times 10^3$	3.97 $\times 10^2$
Bulk flow (DYNLAB) R:1.5, S:1.0	3.75 $\times 10^5$	-4.00×10^5	1.05 $\times 10^3$	5.67 $\times 10^2$

Results. Figure 9 shows the calculated velocity vectors. The pattern of vectors at each chamber is similar. There is a high-speed jet at the tip of each tooth and a large vortex inside each chamber. Figure 10 shows the streak lines that start from the gap between the first tooth and rotor. The vortex becomes the spiral

Fig. 14 Analysis model

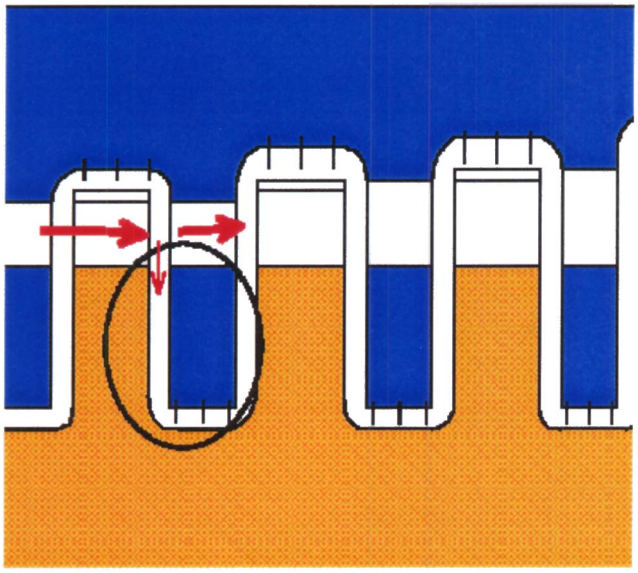

Fig. 15 Cross-section of steam turbine

Table 4 Dimensions and conditions

Rotor diameter	700 mm (27.6 in.)
Clearance at teeth	0.6/0.7/0.8 mm (0.0236/0.0276/0.0315 in.)
No. of teeth	20
Rotation speed	3600 rpm
Inlet pressure	18 MPa (2611 psi)
Outlet pressure	15 MPa (2176 psi)
Inlet temperature	500°C (932°F)
Fluid	Steam

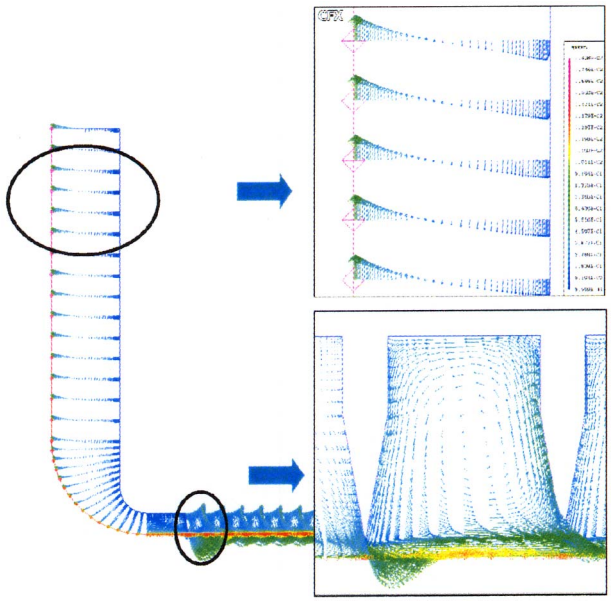

Fig. 16 Velocity vector

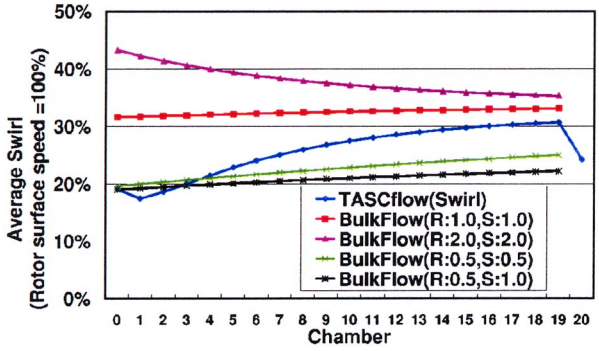

Fig. 17 Average swirl

Table 5 Dynamic characteristics

	K (N/m)	k (N/m)	C (Ns/m)	c (Ns/m)
CFD (TASCflow)	5.29 $\times 10^6$	-4.86×10^6	1.50 $\times 10^4$	3.06 $\times 10^3$
Bulk flow (DYNLAB) R:1.0, S:1.0	-1.52×10^7	4.49 $\times 10^6$	2.41 $\times 10^4$	2.36 $\times 10^4$
Bulk flow (DYNLAB) R:2.0, S:2.0	-1.45×10^7	8.81 $\times 10^6$	2.96 $\times 10^4$	2.38 $\times 10^4$
Bulk flow (DYNLAB) R:0.5, S:0.5	-1.50×10^7	1.59 $\times 10^6$	2.02 $\times 10^4$	2.12 $\times 10^4$
Bulk flow (DYNLAB) R:0.5, S:1.0	-1.46×10^7	2.07 $\times 10^6$	2.12 $\times 10^4$	1.58 $\times 10^4$

Downloaded 02 Jun 2010 to 171.66.16.98. Redistribution subject to ASME license or copyright; see http://www.asme.org/terms/Terms_Use.cfm

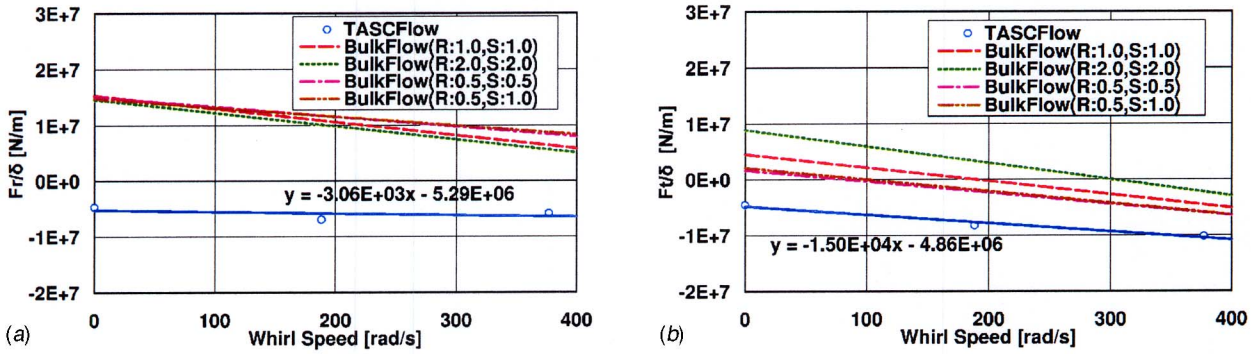

Fig. 18 Seal force versus whirl speed: (*a*) radial direction; (*b*) tangential direction

flow because of rotation of the rotor. Figure 11 shows the average swirl (the flow in the circumferential direction) at each chamber by TASCFlow and an existing bulk flow PC analysis program [4]. In this figure the bulk flow program has two kinds of results with different rotor surface roughness. In all three results the swirl increases as the flow goes downstream. The increment of the swirl by TASCFlow is larger than that by bulk flow program. Figure 12 shows the pressure distribution. The pressure drop mainly occurs at the tips of teeth and the pressure inside each chamber is almost equal.

Table 2 shows the calculated leakage flow. The leakage flow by TASCflow shows reasonably good agreement with the result by the bulk flow analysis program [4].

Figures 13(*a*) and 13(*b*) show the relation between the seal force and whirl speed. The seal force in the tangential direction by TASCFlow is close to those by the bulk flow program (DYNLAB), though there is some difference for the results in the radial direction. The predicted seal forces by TASCFlow are smaller than those by DYNLAB. It means that TASCFlow gives more stabilizing results. The inertia coefficients in both directions are negligible because each plot is almost a straight line. The dynamic coefficients derived from the intercept and slope of the graph are shown in Table 3.

Labyrinth Seal for Steam Turbine

Analysis Model. Figure 14 shows the labyrinth seal model for this calculation. This model is for the labyrinth seal between stages of a steam turbine as shown in Fig. 15. This model includes the upstream section before the seal section. Table 4 shows the dimensions and conditions used for calculation. They are similar to the condition of the labyrinth seal between the first and second stage of the high pressure section of a large scale steam turbine.

Result. Figure 16 shows the calculated velocity vectors. The flow pattern at the seal section is similar to that of the compressor eye seal. There is reverse flow near the rotor surface at the upstream section. It is because the tangential velocity is large and the centrifugal force is also large.

Figure 17 shows the average swirl in each chamber. This graph includes a result by TASCFlow and four results by the bulk flow program [4] with various surface roughness. In the graph R means the relative roughness of rotor and S means relative roughness of stator. On the whole the results of TASCFlow and the bulk flow program do not agree very well. It may be because the reverse flow in the upstream section is not considered in the bulk flow program.

Table 5 shows the dynamic characteristics. Figure 18 shows the relation between the seal force and whirl speed. The difference of result between of TASCFlow and the bulk flow program in this case is larger than that in the compressor eye seal case. This may be also due to the reverse flow in the upstream section. The advantage of using CFD programs, such as TASCFlow, is that they can properly and more accurately deal with the various kinds of seal geometry found in real machinery.

Conclusions

It has been demonstrated that the general CFD code, CFX-TASCflow, can be used to simulate the flow of labyrinth seals and predict the rotor dynamics force.

The labyrinth seals of a steam turbine and a compressor eye seal were taken as objects of analysis. For each case, a 3D model with eccentric rotor was solved to obtain the rotordynamic force components. The leakage flow and rotor dynamics force predicted by CFX TASCFlow were compared with the results the existing bulk flow analysis program DYNLAB. The results show that the bulk flow program gives a pessimistic prediction of the destabilizing forces for the conditions under investigation. The obvious advantage of the bulk flow analysis is the 0.1 s run time per case, compared to 4–19 h for TASCflow. Further research work will be required to fully understand the complex leakage flows in turbo machinery.

Acknowledgment

The authors express their gratitude to the Virginia Tech Rotor Dynamics Lab Industry Affiliates Group and Toshiba Corporation, for their support to this research work.

References

[1] Iwatsubo, T., 1980, "Evaluation of Instability Forces of Labyrinth Seals in Turbines or Compressors," Proc. Rotordynamic Instability Problems in High Performance Turbomachinery, NASA CP-2133, Texas A&M University, pp. 139–167.
[2] Scharrer, J. K., 1987, "Theory Versus Experiment for the Rotordynamic Coefficients of Labyrinth Gas Seals: Part I—A Two Control Volume Model," Proc. ASME 11th Biennial Conference on Mechanical Vibration and Noise, Rotating Machinery Dynamics Volume Two, pp. 411–426.
[3] Childs, D. W., and Scharrer, J. K., 1987, "Theory Versus Experiment for the Rotordynamic Coefficients of Labyrinth Gas Seals: Part II—A Comparison to Experiment," Proc. ASME 11th Biennial Conference on Mechanical Vibration and Noise, Rotating Machinery Dynamics Volume Two, pp. 427–434.
[4] Kirk, R. G., 1988, "Evaluation of Aerodynamic Instability Mechanisms for Centrifugal Compressors—Part II: Advanced Analysis," ASME J. Vib., Acoust., Stress, Reliab. Des., **110**, No. 2, pp. 207–212.
[5] Kirk, R. G., 1990, "A Method for Calculating Labyrinth Seal Inlet Swirl Velocity," ASME J. Vibr. Acoust., **112**, No. 3, pp. 380–383.
[6] Kirk, R. G., Raju, K. V. S., and Ramesh, K., 1999, "PC-Based Analysis of

Downloaded 02 Jun 2010 to 171.66.16.98. Redistribution subject to ASME license or copyright; see http://www.asme.org/terms/Terms_Use.cfm

Turbomachinery Vibration,'' Shock Vib. Dig., **31**, No. 6, pp. 449–454.
[7] Rhode, D. L., Hensel, S. J., and Guidry, M. J., 1992, ''Labyrinth Seal Rotordynamic Forces Using a Three-Dimensional Navier-Stokes Code,'' ASME J. Turbomach., **114**, pp. 683–689.
[8] Rhode, D. L., Hensel, S. J., and Guidry, M. J., 1993, ''Three-Dimensional Computations of Rotordynamic Force Distribution I a Labyrinth Seal,'' STLE Tribol. Trans., **36**, No. 3, pp. 461–469.
[9] Ishii, E., Kato, C., Kikuchi, K., and Ueyama, Y., 1997, ''Prediction of Rotordynamic Forces in a Labyrinth Seal Based on Three-Dimensional Turbulent Flow Computation,'' JSME Int. J., Ser. C, **40**, No. 4, pp. 743–748.
[10] Kwanka, K., Sobotzik, J., and Nordman, R., 2000, ''Dynamic Coefficients of Labyrinth Gas Seals a Comparison of Experimental Results and Numerical Calculations,'' ASME International Gas Turbine and Aeroengine, Congress & Exhibition, 2000-GT-403.
[11] Moore, J. J., 2001, ''Three-Dimensional CFD Rotordynamic Analysis of Gas Labyrinth Seals,'' Proc. DETC'01, VIB-21394.
[12] Guo, Z., Hirano, T., and Kirk, R. G., 2003, ''Application of CFD Analysis for Rotating Machinery, Part 1: Hydrodynamic, Hydrostatic Bearings and Squeeze Film Damper,'' ASME J. Eng. Gas Turbines Power, **127**, pp. 445–451.
[13] AEA Technology, 2001, CFX-TASCflow 2.11.1 Documentation.

Downloaded 02 Jun 2010 to 171.66.16.98. Redistribution subject to ASME license or copyright; see http://www.asme.org/terms/Terms_Use.cfm

Masayoshi Shimo
e-mail: shimo@ecn.purdue.edu

James V. Canino

Stephen D. Heister

School of Aeronautics and Astronautics,
Purdue University,
1282 Grissom Hall West,
Lafayette, IN 47907-1282

Modeling Oil Flows on Seal Runners and Engine Sump Walls

Oil flow behavior within a lubrication system utilized in a turbofan engine has been studied using a two-dimensional model for a seal runner and a sump wall. A two-dimensional, axisymmetric boundary layer method is utilized to derive a model for the film on the seal runner. An integral method analysis of boundary layer equations are utilized to derive a model for the film behavior on the outer wall of the sump neglecting variations in the axial direction. Parametric studies for oil flow at the seal runner and one the sump wall have been generated for a wide range of oil film properties and ambient conditions. [DOI: 10.1115/1.1924431]

Introduction

Although the oil system of a modern gas turbine engine is quite varied in design, most units display similar characteristics. In a great majority of cases, a pump furnishes oil to the several parts of the engine to be lubricated and cooled, after which, a scavenging system returns the oil to the tank for reuse. To prevent oil leakage into the internal air system, a positive air flow must be maintained into the chamber through the chamber seals. Significant forces are induced on the fluid due to windage, gravity and viscous stresses against both moving and stationary parts. These processes give rise to extremely complex two phase air/oil flow, however, the understanding of the physical phenomena associated with the lubrication system is quite important in the design of engine oil systems and there are numerous problems that could arise if insufficient or oversupply of oil is provided to the lubricating parts. The efficient collection of oil is required to prevent leakage. Leakage past seals can lead to oil vapors in the cabin and can adversely effect oil consumption and seal life.

The Seal Runner and Sump. Figure 1 shows the cross-sectional view of a sump used in a typical gas turbine. Oil is sprayed onto bearings and seal runners for lubrication and cooling—the present study focuses on flow of oil in the seal runner and the subsequent flow induced on the outer sump wall. A simplified schematic diagram is shown in Fig. 2 which depicts the sump wall enclosing the seal runner and center shaft. The oil film leaving the seal runner is flung to the sump wall where it is collected for reuse. The oil droplets and the oil film on the sump wall interact with the core air flow which causes oil migration along the wall. The collected oil is generally scavenged from the system at the bottom of the sump via a gravity drain.

Previous Experimental and Modeling Work. The authors were unable to find any publications dealing specifically with the seal runner analysis. The physical situation is similar to the flow outside of rotating shaft and there are a few publications dealing with such problems. Hansen et al. [1] used an incompressible, viscous free-surface flow analysis of a film on a rotating cylinder using an integral-equation formulation applied to the Stokes approximation of the Navier–Stokes equations. Their results of free-surface profiles and free-surface velocity distributions had excellent agreement with the results of thin-film theory and a high degree of symmetry about a horizontal axis was observed. In their studies they also considered the vertical gravity field, however, the results are limited to very low rotational shaft speeds consistent with a Stokes-flow approximation.

For the sump wall analysis, there are several relevant contributions, mainly emphasizing the air/flow in the bearing chamber. Wittig et al. [2,3] carried out experiments to obtain film thickness, heat transfer measurements and some data on droplet size distributions around an annulus. Glahn and Wittig [4] carried out further measurements of film velocity profiles and the former reported oil droplet velocity measurements at rig speeds up to 16 000 rpm. Chew [5] utilized a simple geometry to study the distribution of oil in chamber through a study of a rimming flow. The model of the film flow was established utilizing an integral approach with gravity and wall shear stress. Chew considered a partially filled chamber which is rotated with a certain angular velocity and a stationary chamber with the input of a swirling mass flow into the film. In this study, the core gas flow was assumed to be too small to affect the calculations. Comparisons with experiments were also carried out, but good agreements with measurements of heat transfer and film thickness could not be obtained. However, this was attributed to the simplified modeling of the bearing lubrication system especially regarding to its modeling of the scavenge.

Modeling the flow of a liquid film has been considered in many studies but few linked to a situation with high shear applied to its surface. Johnson [6] has carried out work on the distribution of film thickness on the inside of a horizontally rotating cylinder where it was found that a number of solutions could be obtained depending on whether the film partially or wholly covered the surface. Stanton et al. [7] utilized a similar approach to that of Chew in order to produce a general model of the film flow across arbitrary surfaces that included gravity, shear forces and pressure effects on the film. In addition, source terms were introduced for the inclusion of mass and momentum resulting from droplet impact on the film. Farrall et al. [8] derived a model for the film accounting for the effects of shear and gravity in a 1D annulus. They considered the steady state mean film thickness of a film flowing down an inclined plane with and without a counter current air flow to include shear force by the air flow. To our knowledge, the present work emphasizing wall film flows with windage, gravity, and mass addition effects provides a unique approach to bearing chamber analysis.

Model Development

The current investigation is directed toward a two-dimensional axisymmetric model for film on the sump and seal runner surfaces assuming no circumferential variations in the case of the seal runner and no axial variations in the case of the outer sump wall. For both analyses we begin with the boundary layer equations in orthogonal curvilinear coordinates to estimate oil film thicknesses, axial and circumferential velocities on the surface.

Seal Runner Analysis. The schematic diagram of seal runner is

Contributed by the Structures & Dynamics Division of THE AMERICAN SOCIETY OF MECHANICAL ENGINEERS for publication in the ASME JOURNAL OF ENGINEERING FOR GAS TURBINES AND POWER. Manuscript received by the S&D Division September 3, 2003; final revision received December 13, 2004. Associate Editor: N. Arakere.

Copyright © 2005 by ASME

Downloaded 02 Jun 2010 to 171.66.16.98. Redistribution subject to ASME license or copyright; see http://www.asme.org/terms/Terms_Use.cfm

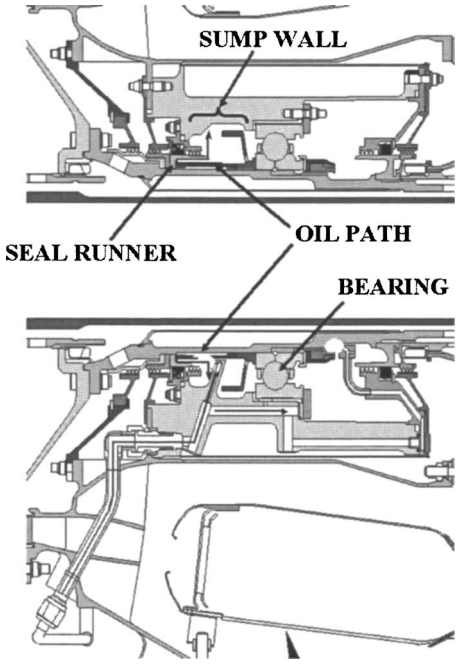

Fig. 1 The cross-sectional view of a gas turbine center sump top and bottom

shown in Fig. 3 where an orthogonal curvilinear coordinate system is applied. While the resultant flow can be very complicated, we chose to look at a force parallel to the oil film rather than to look at a force which can separate the oil film from shaft since its thickness is very small compared with the rotating shaft radius. This vertical force to the film can be neglected even if the separation of oil film takes place due to our assumption that it does not significantly affect velocities and oil film thicknesses at the lip of seal runner. The approach illustrated herein is also applicable to roller bearing cavities, although the momentum of the oil leaving the bearing would need to reflect the epicyclic speed of rotation as

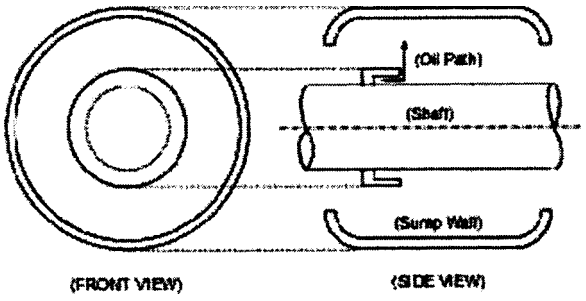

Fig. 2 Front and side view of sump wall

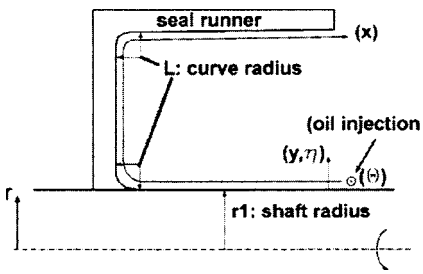

Fig. 3 2D axisymmetric boundary layer model elements of the seal runner

well as the obvious geometric differences from seal runners.

For this analysis the oil film thickness, h, the velocity along the seal runner, u, and the circumferential velocity, w, are computed using steady boundary layer equations. It is further assumed that the initial oil film thickness is uniformly distributed in the circumferential direction at the location of oil injector due to the axisymmetric nature of the model. Under the above-mentioned stated assumptions, the steady state boundary layer equations for incompressible flows past bodies of revolution in orthogonal curvilinear coordinates can be written as

$$\frac{\partial ru}{\partial x} + \frac{\partial rv}{\partial y} = 0 \tag{1}$$

$$\frac{\partial ru^2}{\partial x} + \frac{\partial ruv}{\partial y} = w^2 \frac{dr}{dx} + rv\frac{\partial^2 u}{\partial y^2} \tag{2}$$

$$\frac{\partial r^2 uw}{\partial x} + \frac{\partial r^2 uw}{\partial y} = r^2 \nu \frac{\partial^2 w}{\partial y^2} \tag{3}$$

In order to compose a closed system, boundary conditions at the wall and film interface must be specified. Hence the zero shear and the no-slip conditions are applied for the free surface and for the wall side of the film, respectively.

With respect to solving a system of the boundary layer equations, the Keller box method was employed for numerical discretization and Newton's method was used for integrating the set of descretized equations [9].

Sump Wall Analysis. As with the seal runner analysis, the boundary layer equations in orthogonal curvilinear coordinate were utilized to analyze the flow field on the sump wall. In addition, a parabolic velocity profile assumption was introduced to develop an integral method analysis and reduce computational work load. Time accurate treatments were also required on the ground that the flow on the periphery of the sump is inherently unsteady due to the competition between gravity, windage, and mass/momentum flux effects from the seal runner. As a result, the model equations appropriate for the sump wall analysis can be written as follows considering gravity, windage, gravity drain, and additional mass/momentum flux effects.

$$\frac{\partial h}{\partial t} + \frac{1}{r}\frac{\partial h\bar{w}}{\partial \theta} = -\frac{\dot{m}_D}{\rho A_D} + \frac{\dot{m}_s}{\rho A_{CV}} \tag{4}$$

$$\frac{\partial rh\bar{u}}{\partial t} + \frac{\partial h\overline{uw}}{\partial \theta} = -r\nu \left.\frac{\partial u}{\partial y}\right|_0 - r(g\sin\beta\sin\theta)h - \frac{\dot{m}_D r}{\rho A_D}u + \frac{\dot{m}_S r}{\rho A_{CV}}u_S \tag{5}$$

$$\frac{\partial rh\bar{w}}{\partial t} + \frac{\partial h\overline{w^2}}{\partial \theta} = -r\nu \left.\frac{\partial w}{\partial y}\right|_0 - (g\cos\theta)hr - \frac{\dot{m}_D r}{\rho A_D}w + \frac{\dot{m}_S r}{\rho A_{CV}}w_S + r\frac{\tau_w}{\rho} \tag{6}$$

Here, $\dot{m}_D$ and $\dot{m}_S$ represent mass flows to the drain and from the seal runner, respectively, and τ_w is the windage shear stress. The θ direction is measured counterclockwise from the 3:00 clock position, the angle β is the local wall slope as measured from horizontal, and $\overline{(\ )}$ indicates an averaged parameter based on the parabolic velocity profile assumptions. Letting η be the dimensionless film thickness, the parabolic velocity profiles in Eq. (7) and below, associated averaged velocity components and wall gradients become

$$u = \dot{u}_e[1-(1-\eta)^2] \tag{7}$$

$$\bar{u} = \frac{1}{h}\int_0^h u dy = \frac{2}{3}u_e \tag{8}$$

Downloaded 02 Jun 2010 to 171.66.16.98. Redistribution subject to ASME license or copyright; see http://www.asme.org/terms/Terms_Use.cfm

$$\overline{u^2} = \frac{1}{h}\int_0^h u^2 dy = \frac{6}{5}\bar{u}^2 \tag{9}$$

$$\left.\frac{\partial u}{\partial y}\right|_{\eta=0} = 3\frac{\bar{u}}{h} \tag{10}$$

$$w = w_e[1-(1-\eta)^2] \tag{11}$$

$$\bar{w} = \frac{1}{h}\int_0^h w dy = \frac{2}{3}w_e \tag{12}$$

$$\overline{w^2} = \frac{1}{h}\int_0^h w^2 dy = \frac{6}{5}\bar{w}^2 \tag{13}$$

$$\left.\frac{\partial w}{\partial y}\right|_{\eta=0} = 3\frac{\bar{w}}{h} \tag{14}$$

$$\overline{uw} = \frac{1}{h}\int_0^h uw dy = \frac{6}{5}\bar{u}\cdot\bar{w} \tag{15}$$

Mass/momentum influx to the film were provided via a droplet impact model due to Weinstock [10] and the drain flow is assumed to be equivalent to the inlet flow from the seal runner in the present calculations, i.e. steady-state volume of oil in the sump is assumed to have been achieved.

The Harten–Yee Total Variation Diminishing (TVD) discretization scheme with the Lower-Upper Symmetric Gauss–Seidel method for time integration was used to numerically solve the set of equations [9]. Grid function convergence studies were conducted on both the seal runner and wall film codes to verify accuracy and consistency of implementation.

Undoubtedly the oil film behavior in a sump wall cavity is three-dimensional, however, the above two-dimensional model was selected as a first attempt to model the physical processes that are most critical to sump performance. A second reason for selecting a two-dimensional model was the need for short run times in order to investigate multiple design geometries.

Determination of the Windage Effect. The shear stress due to the airflow is an important force acting on the liquid film. However, often complex numerical modeling is required to obtain this force. In this section, a simple parametric model will be developed to compute τ_w [11]. The high shaft speeds generate turbulent airflows with Reynolds numbers based on the gap between the shaft and the outer wall typically in the 10^6 range. Given that the airflow is turbulent, an algebraic model for the turbulent windage needed to be determined. The CFD package Fluent was utilized for the windage modeling [12]. A simple two-dimensional annular geometry with end walls was selected since the geometry lends itself to easy analysis for parametric studies. In order to further simplify the analysis, the oil droplets affect on the windage solution was neglected. An incompressible turbulent two-dimensional swirling flow simulation of the steady state flow field using the Reynolds Stress Model was conducted for various shaft speeds, oil film velocities, sump geometries, and air properties. Since the oil droplets were neglected no oil film was present on the outer sump wall for the fluent calculations. Since the oil film is thin, furthermore, the thickness of the oil film was neglected and an angular velocity was specified on the outer sump wall to simulate the effect of an oil film with a uniform angular velocity.

During initial investigations of the behavior of the oil film, the Couette solution was utilized to determine the shear stress acting on the film. Figure 4, however, shows that the swirl velocity is significantly different between the Couette flow solution and the turbulent solution at the symmetry plane of the annular gap. The large change in the turbulent velocity near the sump wall, results

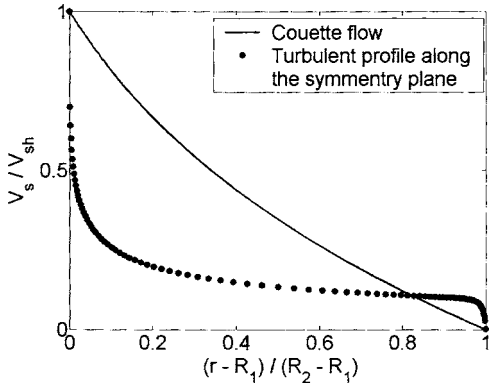

Fig. 4 Comparison of the swirl velocity for the Couette flow solution and the current turbulent solution

in a shear stress acting on the film which is approximately 80 times larger than if the Couette solution is employed. Of course, using the shear stress from the turbulent profile had a significant impact on subsequent results.

Figure 5 shows the variation of the shear stress along the outer sump wall as a function of the axial coordinate with the shaft speed, air density, and air viscosity as parameters. Due to the axial symmetry of the annular geometry only half of the physical geometry was used in the computation. Therefore, in Fig. 5 the end wall of the annulus is at an axial coordinate of zero and the symmetry plane is at an axial coordinate of 0.5. Furthermore, the variable Re^* is the Reynolds number divided by the baseline Reynolds number of 1.4×10^6 used for the parametric analysis. The variable in parentheses next to the Re^* value in the legend is the variable which was changed to produce that Re^* value. As Fig. 5 shows, scaling the shear stress by the shaft velocity to the 1.7 power, the air density to the 0.75 power and the air viscosity to the 0.25 power resulted in the smallest percent difference between different Re^* values. This simplification provides a general result for τ_w valid for a range of flow conditions and geometries.

Since the sump wall analysis is a quasi-one dimensional, a single average value of the shear stress is needed for the sump wall analysis. The average shear stress was determined using Eq. (16),

$$\overline{\tau_w} = \frac{1}{L}\int_0^L \tau_w \tag{16}$$

The variation of the average shear stress with gap ratio, GR, and outer sump wall velocity are shown in Fig. 6. Again, the oil film is neglected and the outer sump wall is given a velocity (V_{sw}) to simulate the presence of an oil film. In Fig. 6, the outer sump wall velocity, V_{sw}, is expressed as a percent of the shaft velocity. The effect of decreasing the gap ratio is to increase the value of

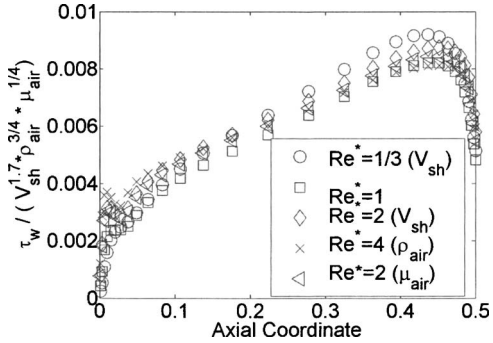

Fig. 5 Variation of the shear stress along the sump wall

Downloaded 02 Jun 2010 to 171.66.16.98. Redistribution subject to ASME license or copyright; see http://www.asme.org/terms/Terms_Use.cfm

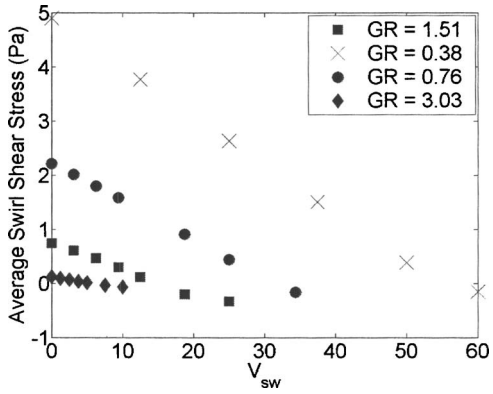

Fig. 6 Effect of the sump wall velocity on the shear stress

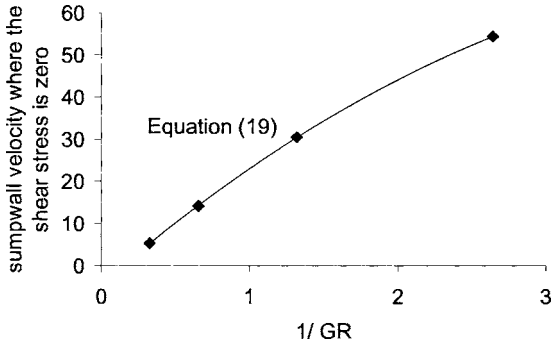

Fig. 8 Velocity of the oil film where the shear stress is zero as a function of the inverse of gap ratio

V_{sw} where the shear stress is zero and to increase the shear stress for all V_{sw}. In order to collapse the positive shear stress values shown in Fig. 6 to one universal curve, the y axis was scaled by the radius ratio, R_2/R_1, and the x-axis was shifted such that the average shear stress was zero at the same outer sump wall velocity for all radius ratios. The result of scaling the x and y axes are shown in Fig. 7. The data in Fig. 7 was fit with a quadratic to give a general result for τ_w.

$$\overline{\tau_w}\left(\frac{R_2}{R_1}\right)\left(\frac{1}{\mu_{air}}\right)^{0.25}\left(\frac{1}{\rho_{air}}\right)^{0.75}\left(\frac{1}{V_{sh}}\right)^{1.7} = -1.372\times10^{-6}(V_{sw}^{*})^2 - 9.528\times10^{-4}V_{sw}^{*} + 0.0302 \quad (17)$$

where,

$$V_{sw}^{*} = V_{sw} + (30.553 - V_{sw}|_{\overline{\tau_s}=0}) \quad (18)$$

and μ_{air}, ρ_{air}, V_{sh}, and $\overline{\tau_w}$ are in units of kg/(m s), kg/m^3, m/s, and Pa, respectively.

In order to use Eqs. (17) and (18) the velocity of the oil film where the shear stress is zero, $V_{sw}|_{\overline{\tau_s}=0}$, must be known. Figure 8 shows the velocity of the oil film where the shear stress is zero as a function of the inverse of the gap ratio. A quadratic was fit between these four points to determine Eq. (19) for $V_{sw}|_{\overline{\tau_s}=0}$.

$$V_{sw}|_{\overline{\tau_s}=0} = -3.1421\left(\frac{1}{GR}\right)^2 + 30.609\left(\frac{1}{GR}\right) - 4.5016 \quad (19)$$

where, GR is the gap ratio. The curve fits presented in Eqs. (17)–(19) are for preliminary design purposes only. Moreover, the accuracy of this algebraic model is on the order of ±20%.

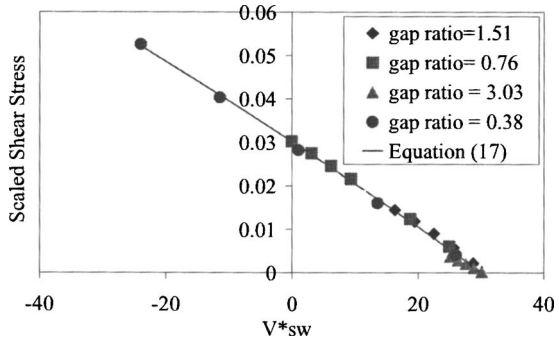

Fig. 7 Scaled shear stress as a function of the shifted sump wall velocity

Results

Seal Runner Analysis: Baseline Case. A 0.061 m (6.1 cm) shaft radius was selected for the study of seal runner analysis. The seal runner length was selected to be 0.021 m (2.1 cm) and total x-direction length from the injector point to the end of seal runner was 0.050 m (5.0 cm). The diameter of injector is about 2 mm which is just drilled straight through with no taper or anything fancy. The shaft speed is substantial (95.8 m/s) for an assumed 15 000 rpm condition. Therefore, it seems that oil film thickness builds up very quickly before advancing further toward the x-direction. According to this consideration, it is assumed that 2 mm oil film thickness is distributed along the θ-direction initially and its initial velocity can be computed from a steady-state mass flow balance. This value was used as an initial tangential edge-velocity, $u_e|_{x=0}$. In addition, gravity and gas phase effects were neglected (Table 1).

Baseline case results are shown in Fig. 9 below. The velocities shown are averaged parameters which can be calculated by the following equation:

Table 1 Baseline geometry and flow conditions

Property	Value
Oil temperature (°C)	85
Oil density (kg/m^3)	955.71
Oil viscosity (Pa s)	0.0066
Initial total mass flow rate (kg/s)	0.0211
Initial oil film thickness (m)	0.0002
Shaft rotational rate (rpm)	15000

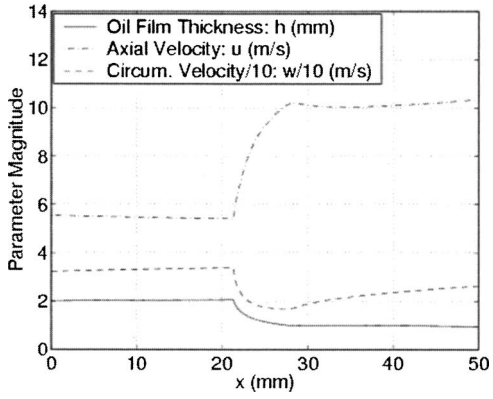

Fig. 9 Oil film thickness, and axial and circumferential velocity distributions for baseline case

Downloaded 02 Jun 2010 to 171.66.16.98. Redistribution subject to ASME license or copyright; see http://www.asme.org/terms/Terms_Use.cfm

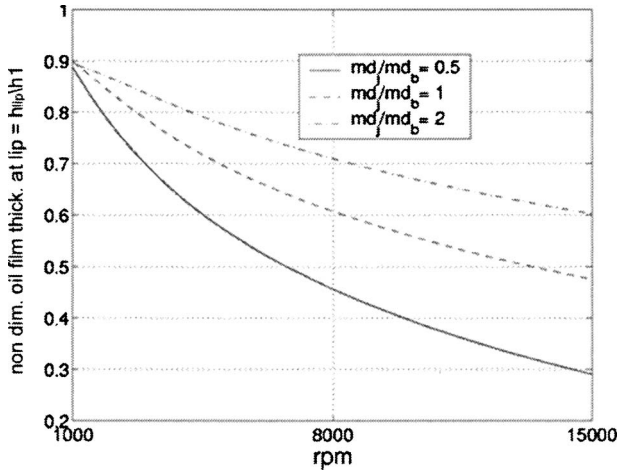

Fig. 10 Nondimensionalized oil film thickness at the end of the seal runner versus shaft rotational rate in three different mass flow rates [h_1 (initial film thickness) =2 mm, md_b (baseline mass flow)=0.021 kg/s]

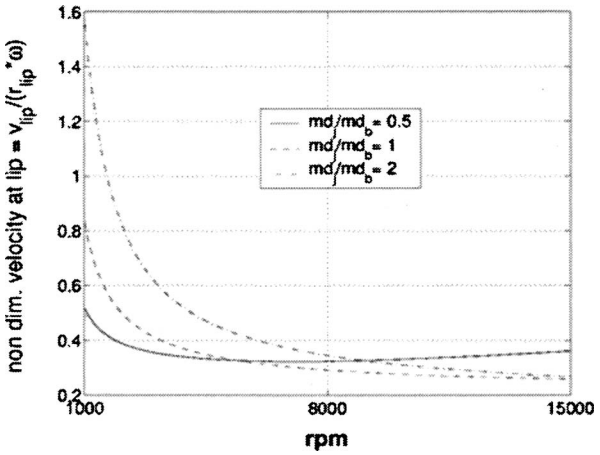

Fig. 11 Nondimensionalized velocity at the end of the seal runner versus shaft rotational rate in three different mass flow rates [r_{lip} (radius of seal runner at lip)=68.2 mm, md_b =0.021 kg/s]

$$(\text{Averaged Parameter}) = \frac{1}{h}\int_0^h f dy \tag{20}$$

Here, f is an arbitrary velocity. The results show each parameter as a function of distance along the seal runner. The film thickness increases on the shaft and the tangential velocity decreases due to the shear stress against the wall. After the oil film turns the first corner, the film thickness is dramatically decreased due to the centrifugal force provoked by rotation. This region also shows strong acceleration in the tangential direction (x) as shown in Fig. 3. The averaged circumferential velocity, w, is dramatically reduced at the first corner of the seal runner according to Fig. 9. The main reason seems to be the oil film thickness being dramatically decreased at the first corner due to the sudden increase of centrifugal force.

After passing the second corner of the seal runner, the axial velocity, u, slightly decreases due to friction and increases again as shown in Fig. 9. This phenomenon is attributed to a change of velocity profile [9]. Before passing the second corner of the seal runner, the velocity profiles in the tangential direction show higher velocities near the wall due to the sudden acceleration by centrifugal forces. However, after passing the second corner of the seal runner, its velocity profiles gradually return to parabolic shapes due to viscous effects.

Seal Runner Analysis: Parametric Sensitivity Study. Parametric sensitivity studies were conducted to assess the effects of oil mass flow and temperature and shaft size on the oil film exit conditions (film thickness and exit velocity). These studies were conducted over a range of shaft speeds from 1000 to 15000 rpm. Figures 10 and 11 depict the sensitivity of oil film parameters at the exit of the seal runner to changes in the mass flow rate, for mass flow as high/low as twice/half the baseline rate. Film thickness at the seal runner exit increases with oil flow as shown in Fig. 10. However, the velocity at the end of the seal runner decreases with increasing mass flow rate as shown in Fig. 11. The main reason is that although the film gets less shear stress as its height increases, the initial film thickness is fixed (2 mm) so that initial film tangential velocity increases with mass flow, which results in the increase of shear force. At high shaft speeds, the film exits the seal runner at 30%–40% of the rotational speed.

The sensitivity of oil film parameters to variations in shaft radius are shown in Figs. 12 and 13. In the range between 6000 rpm and 15,000 rpm film thickness at the exit lip scales as the inverse of the shaft radius as one might expect due to the higher rotational speeds with larger shaft radii. In the region below 6000 rpm there are some interesting crossovers in the curves attributed to the influence of the axial shear stress. At the low shaft speeds, the axial stress is significant; this stress scales with film thickness

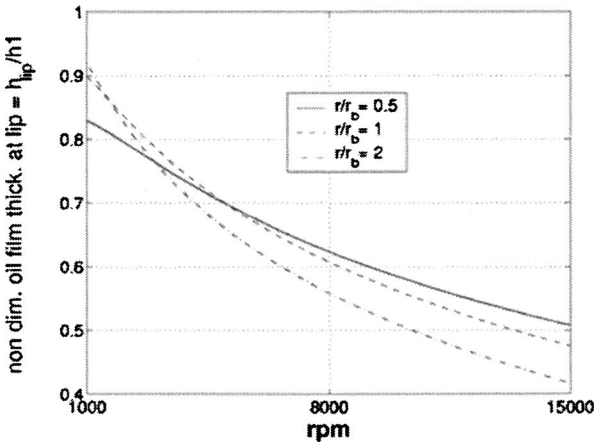

Fig. 12 Nondimensionalized oil film thickness at the end of the seal runner versus shaft rotational rate in three different shaft radii [h_1=2 mm, r_b (baseline shaft radius)=60.6 mm]

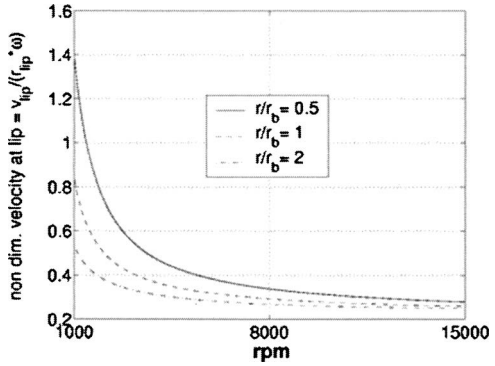

Fig. 13 Nondimensionalized velocity at the end of the seal runner versus shaft rotational rate in three different shaft radii (r_{lip}=r+7.7 mm, r_b=60.6 mm)

Downloaded 02 Jun 2010 to 171.66.16.98. Redistribution subject to ASME license or copyright; see http://www.asme.org/terms/Terms_Use.cfm

Table 2 Various oil properties used in the baseline case

Property	Value
Oil temperature (°C)	85
Oil density (kg/m^3)	955.71
Ini. oil film thickness along the sump wall (m)	0.002
Ini. oil circum. vel. along the sump wall (m/s)	18.56
Ini. oil axial vel. along the sump wall (m/s)	0
Ini. total mass flow rate (kg/s)	0.0211
Droplet mass flow rate per unit area (kg/(s m^2))	0.87
Droplet mass momen. per unit area (kg/(s^2 m))	16.15

which is inversely proportional to shaft radius. For this reason, it is possible to have thicker films exiting larger diameter shafts as indicated in the figure.

Sump Wall Analysis: Baseline Case. The required input parameters in the baseline case are shaft rotational speed, initial oil film thickness on the sump wall, initial circumferential velocity on the sump wall, oil properties, and droplet mass/momentum flux computed with a oil droplet tracking package developed by Weinstock [10]. Oil properties were obtained assuming Mobil Jet Oil II [9]. Table 2 highlights the assumed oil properties for the baseline case.

An initial uniform film thickness of 2 mm was selected for the computation. Although the model assumes that the amount of mass addition by oil droplets from the seal runner is equal to the amount of mass subtraction via the drain, the oil film may dry out if its initial thickness is too thin to compute. The oil temperature was selected as 85 °C based on a typical temperature within the sump. The initial oil circumferential velocity was selected as 18.56 m/s based on the oil droplets averaged circumferential velocity at the wall from the droplet tracking work of Weinstock [10]. In addition to oil property selection, a baseline wall design must be selected. In this baseline case, Table 3 provides a summary of the sump wall/center shaft geometry and speed.

Unsteady results were obtained for all simulations due to the imbalance between gravitational, windage, and shear forces with time. Figures 14 and 15 show 2 s histories of oil film thickness, h, and circumferential velocity, w, along the θ direction. One can note that the initial assumed velocity is rapidly "forgotten" and the velocity rapidly enters a bounded limit cycle within about 1 s. Figures 16 and 17 show distributions of oil film thickness during this limit cycle behavior. In Fig. 16, the oil film thickness is amplified 15 times to enhance clarity. A "wave" of larger film height oscillates about the outer wall in a quasiperiodic fashion. This behavior is attributed to a competition between the gravitational, fluid momentum, and windage forces. Thickening of the film reduces overall viscous forces but also increases body forces while thinning of the film has the opposite effect. The gravitational body force acts to slow down the liquid on the rising side, -90 deg $< \theta <$ 90 deg, indicated by the general increase in film thickness in these regions in Fig. 17. Conversely the surface shear and gravitational forces act to a general thinning of the film between 90 deg $< \theta <$ 270 deg. A minimum in the film thickness is observed to occur near the bottom of the sump, θ=270 deg. Note that this behavior is counterintuitive if one is accounting for only gravity as one would expect the maximum thickness at the bottom, θ=270 deg.

Figure 18 shows acceleration histories for each source term at θ=0 deg. Note that all source terms contribute unsteadiness due to

Table 3 Sump wall/center shaft properties used in the baseline case

Property	Value
Center shaft radius (m)	0.0672
Sump wall radius (m)	0.0961
Center shaft rotation rate (rpm)	15000

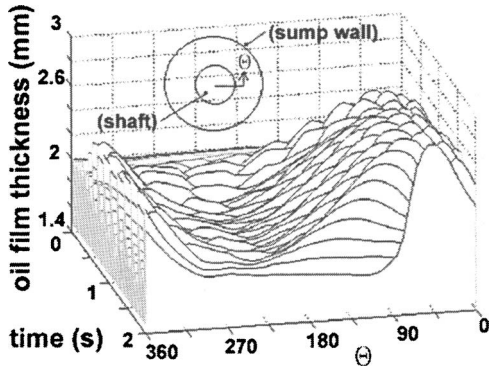

Fig. 14 Film thickness propagation along θ direction until 2 s

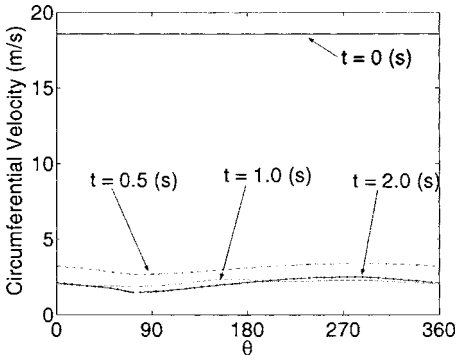

Fig. 15 Film velocity propagation along θ direction until 2 s

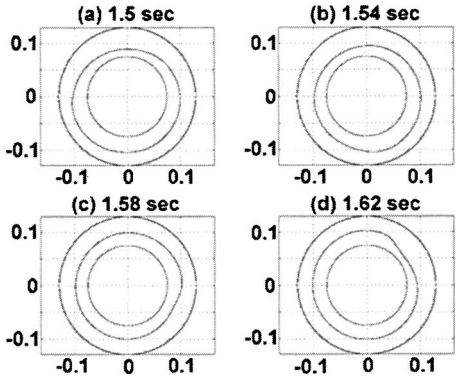

Fig. 16 Plots of oil film thickness distributions with the sump

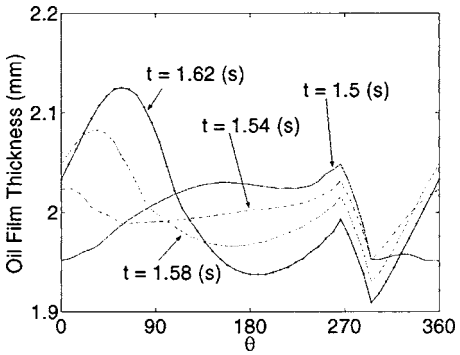

Fig. 17 Expanded plots of oil film thickness distributions along the θ-direction

Downloaded 02 Jun 2010 to 171.66.16.98. Redistribution subject to ASME license or copyright; see http://www.asme.org/terms/Terms_Use.cfm

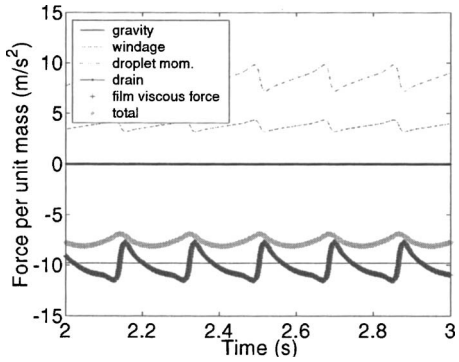

Fig. 18 Histories of each source term at θ=0 deg

the dependence on film thickness (gravity appears as a constant acceleration, but the force itself will change with h). The main reason for the oscillation is that viscous force is out of phase with gravity and windage. When the film thickness increases, the viscous force decreases and windage and gravity forces increase. When the film thickness decreases, the opposite effects occur. Hence, the physical phenomenon creates a quasiperiodic oscillation state.

Sump Wall Analysis: Parametric Sensitivity Studies. Figure 19 depicts the sensitivity of the time averaged oil film thickness and circumferential velocity to changes in initial film thickness. Note that their general trends are similar to the baseline case in that the maximum time-averaged thickness exists near θ=70 deg and the minimum value is near θ=300 deg while their circumferential velocities take opposite trends. In this case, the main sensitivity to the oil film property variations occurs through its effect on the viscous force of oil film. Large initial film thicknesses reduce viscous effects, which increases the circumferential velocity at the equilibrium and transports a comparatively large amount of oil film along the annulus. In addition, time to reach the equilibrium becomes longer in case of large initial oil film thickness. The time-averaged oil film thickness becomes essentially constant for the h=10 mm case in Fig. 19. This behavior is attributed to the initial velocity as for this very thick film, the asymptotic behavior is correlated with the initial velocity chosen as viscous stresses are relatively minor here. However, this film thickness is considerably greater than what one would typically expect in an engine sump.

Figure 20 depicts the sensitivity of averaged film height and velocity to changes in the oil film temperature. Increasing oil temperature has a large effect on oil viscosity so that oil film is transported around the wall much more readily at higher temperatures as shown in Fig. 20, where the time-averaged thickness is much more flat in case of 149°C compared with the 85°C case. This is also reflected by the higher circumferential velocity at the equilibrium in case of higher oil temperature. Basically, it is easier to circulate oil along the sump at high temperature. If the oil temperature is decreased below 85°C, its viscosity increases so that oil film might not be circulated and portions of the wall dry out.

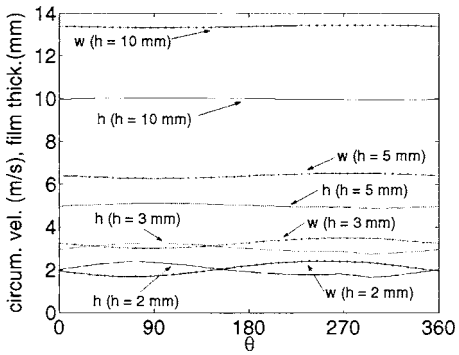

Fig. 19 Time-averaged oil film thicknesses and circumferential velocities in various initial film thicknesses

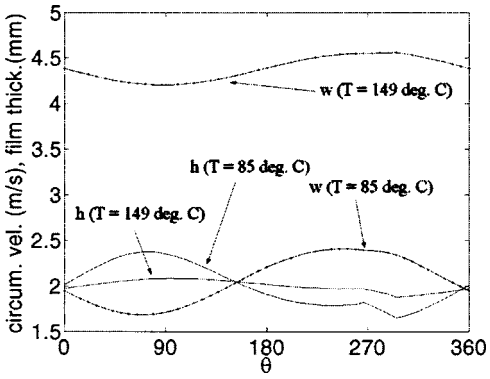

Fig. 20 Time-averaged oil film thicknesses and circumferential velocities in various oil temperatures

The parametric studies show that sumps can exhibit a full range of behaviors depending on the design conditions and fluid properties. Cases with film height and velocity being nearly constant can easily be obtained if the outer wall is close to the shaft or the oil is at high temperature. In other cases, gravity, windage, and shear can all play significant roles leading to unsteady behavior. If the windage forces are small or the sump outer wall is far from the shaft, then the wall can effectively dry out over a significant portion of the perimeter.

Summary and Conclusions

Thin film boundary layer models have been developed for oil flow on a seal runner and the sump wall in a gas turbine engine lubrication system. The seal runner analysis provides a complete boundary layer solution, while the sump wall analysis uses an integral treatment of the boundary layer terms including windage, gravitational effects, mass and momentum addition from impact of oil droplets and the sump drain. Using parametric CFD solutions generalized expressions have been developed for windage stresses on the wall film for a range of operating conditions and geometries. Parametric studies have been conducted using both seal runner and wall film models to identify the sensitivity of film characteristics to engine speed, oil flowrate, and sump geometry.

For conditions relevant to medium and large gas turbine engines, the flows exit the seal runner with a velocity between 25%–40% of the tangential velocity at the seal runner lip. Film thicknesses at the seal runner exit are typically in the 1–2 mm range. The oil film on the sump outer wall is generally unsteady with the competition of gravity, windage, and droplet momentum forces. At conditions relevant to medium/large gas turbines, the films have average velocities of the order of a few m/s. A quasiperiodic behavior is shown to exist with a frequency near 5 Hz for the cases investigated. Increasing oil temperature tends to increase wall velocities due to reduction in viscosity.

Acknowledgment

The authors gratefully acknowledge the support of Rolls-Royce Allison under the technical guidance of Mr. John H. Munson.

Nomenclature

A = surface area
GR = gap ratio $(R_2-R_1)/R_1$
Re^* = Reynolds number scaled by the baseline Reynolds number

Downloaded 02 Jun 2010 to 171.66.16.98. Redistribution subject to ASME license or copyright; see http://www.asme.org/terms/Terms_Use.cfm

V_{sw} = oil film velocity as a percent of the shaft velocity
V_s = swirl velocity of the air in the sump
V_{sw}^* = shifted oil film velocity as a percent of the shaft velocity
g = gravity acceleration
h = oil film thickness
$\dot{m}$ or md = mass flow rate
r = radial coordinate direction
t = time
u = axial velocity component
v = velocity component normal to wall
w = circumferential velocity component
w_0 = shaft rotational speed at surface
x,y = orthogonal curvilinear coordinate directions
η = nondimensionalized oil film thickness
μ = dynamic viscosity
ν = kinematic viscosity
ω = angular velocity
ρ = density
τ_ω = shear stress acting on film
β = slope angle on surface of wall
θ = angle toward circumferential direction
$\overline{(\,)}$ = averaged parameter based on the parabolic velocity profile
R_1 = shaft radius
R_2 = radius to the outer sump wall
x = distance along the seal runner

Subscripts

CV = control volume
D = drain
e = film edge
i,j = mesh index
S = seal runner
air = reference to the property evaluated for air
sh = shaft
b = baseline
lip = value at the edge of the seal runner lip

References

[1] Hansen, E., and Kelmanson, M., 1994, "Steady, Viscous, Free-Surface Flow on a Rotating Cylinder," J. Fluid Mech., **272**, pp. 91–107.
[2] Wittig, S., Himmelsbach, J., Noll, B., Feld, H. J., Samenfink, W., Halupovich, Y., Naton, B., and Rom, J., 1992, "Motion and Evaporation of Shear-Driven Liquid Films in Turbulent Gases," J. Eng. Gas Turbines Power, **114**, pp. 395–400.
[3] Wittig, S., and Schulz, A., 1992, "A Survey on Efforts in Heat and Mass Transfer Analysis in Aero Engine Secondary Air/Oil Systems," International Symposium on Heat Transfer in Turbomachinery, Athens, Greece.
[4] Glahn, A., Kurreck, M., Willmann, M., and Wittig, S., 1995, "Feasibility Study on Oil Droplet Flow Investigations Inside Aero Engine Bearing Chambers-PDPA Techniques in Combination with Numerical Approaches," ASME paper No. 95-GT-100.
[5] Chew, J. W., 1996, "Analysis of the Oil Film on the Inside Surface of an Aero-Engine Chamber Housing," ASME paper No. 96-GT-300.
[6] Jonson, R. E., 1988, "Steady-State Coating Flows Inside a Rotating Horizontal Cylinder," J. Fluid Mech., **190**, pp. 321–342.
[7] Stanton, D. W., and Rutland, C. J., 1998, "Multi-Dimensional Modeling of Thin Liquid Films and Spray-Wall Interactions Resulting From Impinging Sprays," Int. J. Heat Mass Transfer, **41**, pp. 3037–3054.
[8] Farrall, M. B., Hibberd, S., and Simmons, K., 2000, "Computational Modeling of Two-Phase Air/Oil Flow Within an Aero-Engine Bearing Chamber," FEDSM 2000-11081, in Proceedings of ASME 2000 Fluids Engineering Division Summer Meeting, Boston, Massachusetts.
[9] Shimo, M., 2001, "Modeling of Film Behavior on a Seal Runner and a Sump Wall," Master thesis, Purdue University, West Lafayette.
[10] Weinstock, V. D., 2001, "Modeling of Drop Trajectories and Drop/Wall Interactions in Gas Turbine Engine Sumps," Master thesis, Purdue University, West Lafayette.
[11] Canino, J., 2002, "Characterization of the Turbulent Windage in an Annulus and its Incorporation into Two Sump Design Codes," Master thesis, Purdue University, West Lafayette.
[12] Fluent Inc., V5.5 Users Guide.

Downloaded 02 Jun 2010 to 171.66.16.98. Redistribution subject to ASME license or copyright; see http://www.asme.org/terms/Terms_Use.cfm

J. A. Kenyon
Air Force Research Laboratory,
Propulsion Directorate,
Wright-Patterson AFB, OH 45433
e-mail: james.kenyon@wpafb.af.mil

J. H. Griffin
Department of Mechanical Engineering,
Carnegie Mellon University,
Pittsburgh, PA 15213
e-mail: jg9h@Andrew.cmu.edu

N. E. Kim
Hood Technologies,
Hood River, OR 97031
e-mail: nek@hoodtach.com

Sensitivity of Tuned Bladed Disk Response to Frequency Veering

A continuous method is presented for representing the mode interaction that occurs in frequency veering in terms of the nominal sector modes of a cyclic symmetric bladed disk model constrained at a reference interblade phase angle. Using this method, the effect of frequency veering on the mode shapes can be considered in the context of the generalized forces exciting the system and the modal response of the bladed disk. It is shown that in a blade-dominated family of modes, the transfer of modal energy to the disk in the veering results in a lower generalized force exciting the mode as well as reduced response amplitude in the blade. For the disk-dominated modes, the sharing of modal energy with the blades can lead to the disk being excited by aerodynamic loading. These effects can have important implications for predicting and interpreting forced response in bladed disks. Numerical examples are provided to illustrate these concepts.
[DOI: 10.1115/1.1924486]

Introduction

Frequency veering, sometimes called curve veering, refers to a phenomenon in which the loci of the eigenvalues of a system converge and then veer apart without crossing when the eigenvalues are plotted as a function of some characteristic parameter. This type of veering behavior has been observed in a wide range of applications, from molecular physics [1] to rotor dynamics [2,3] to a number of applications in vibrations [4–6]. In vibrations, the eigenvalues are generally related to the natural frequencies of a structure, and frequency veering is associated with an interaction or coupling between two or more system vibration modes. An early paper on frequency veering suggests that the phenomenon is the result of approximation error due to discrete modeling techniques [7]. It has since been shown that frequency veering is indeed a physical phenomenon that occurs in structural dynamic systems. For example, Perkins and Mote [5] demonstrate veering behavior in the natural frequencies of a number of systems, including a circular string, a coupled oscillator, cables, and rectangular membranes. Balmés [6] describes how varying a stiffness element in a lumped parameter system with three degrees of freedom results in a frequency veering and shows that the mode shapes of the two modes that interact are exchanged through the veering. In other words, the mode shape associated with the first natural frequency becomes the mode shape for the second natural frequency, and vice versa. This exchange of mode shapes is a key aspect of frequency veering, and has been observed not only in simple models such as the lumped parameter system in [6], but also in more complex systems such as rotor-bearing systems [3] and turbine engine fan blades [8].

In turbine engine bladed disks, the frequency veering phenomenon has been observed in conjunction with rotor speed [8,9] as well as interblade phase angle or nodal diameter [10,11]. Modern bladed disks are particularly susceptible to frequency veering as a result of low aspect ratio blading. Low aspect ratio blades tend to compress more vibration modes into a smaller frequency space, leading to increased opportunities for mode interaction and, consequently, more numerous frequency veerings. Frequency veering associated with rotor speed involves interaction between blade modes that occurs due to changes in centrifugal loading of the blades as the rotor speed changes. Certain blade mode shapes are more sensitive to centrigual loading than others. For example, bending mode shapes tend to experience significant stiffening due to radial loading under rotating conditions, while torsional mode shapes, which have a node line oriented in the radial direction, do not experience as much stiffening. As a result, if a bending mode has a frequency that is slightly less than the frequency of a torsion mode at rest, the effect of rotor speed will be to increase the stiffness and thus the frequency of the bending mode until it approaches the frequency of the torsion mode, leading to the mode interaction and frequency veering. This type of frequency veering has been shown to make modal identification and forced response interpretation difficult for bladed disks [12]. However, analytical methods have been developed that have been largely successful in modeling this behavior [13,14].

Frequency veering in bladed disks that occurs in conjunction with interblade phase angle or nodal diameter often involves interaction between blade-dominated and disk-dominated families of modes. To observe this behavior, the dynamics of the tuned system are often characterized by plotting the natural frequencies of the system as a function of the number of nodal diameters in the mode shapes, for example, see Fig. 3 of [10].[1] Blade and disk-dominated families of modes are easily distinguishable in this format. The strain energy in the modes of a blade-dominated family tends to be concentrated in the blades, so that the number of nodal diameters in each mode has only a small effect on natural frequency. Consequently, the frequency locus appears nearly horizontal when plotted as a function of nodal diameter. In contrast, disk-dominated families of modes appear diagonal in the plot. Most of the strain energy in these modes resides in the disk, so that a higher number of nodal diameters means increased stiffness and thus a higher frequency for each mode. When the frequency loci of the blade-dominated and disk-dominated families of modes converge, the mode families interact, and frequency veering occurs.

Frequency veering due to interblade phase angle is an important consideration for determining the vibration response of turbomachinery bladed disks. It has been shown that when frequency veering is present in a rotationally periodic structure such as bladed disks, the system is sensitive to perturbations in the system prop-

Contributed by the International Gas Turbine Institute (IGTI) of THE AMERICAN SOCIETY OF MECHANICAL ENGINEERS for publication in the ASME JOURNAL OF ENGINEERING FOR GAS TURBINES AND POWER. Paper presented at the International Gas Turbine and Aeroengine Congress and Exhibition, Vienna, Austria, June 13–17, 2004. Paper No. GT2004-53280. Manuscript received by IGTI, October 1, 2003; final revision, March 1, 2004. IGTI Review Chair: A. J. Strazisar.

[1] In the gas turbine industry the term "nodal diameter" is commonly used to indicate the phase angle of the cyclic symmetric constraint applied in a single sector finite element analysis used to calculate the natural frequencies and mode shapes of the bladed disk. It is understood that the actual number of nodal diameters is often larger than this because of nodal diameters within the sector model, e.g., torsion modes have at least one nodal diameter per blade.

Copyright © 2005 by ASME

Downloaded 02 Jun 2010 to 171.66.16.98. Redistribution subject to ASME license or copyright; see http://www.asme.org/terms/Terms_Use.cfm

erties, i.e., mistuning. In particular, mistuning can lead to mode localization in a bladed disk, especially when frequency veering exists in the tuned system dynamics. Mode localization refers to the concentration of modal energy into a small region of the structure, such as a single blade or small group of blades [15,16]. It has been identified as one of the major factors resulting in extremely high vibration response and high cycle fatigue in mistuned turbine engine bladed disks [11,17]. A number of researchers have assessed the impact of frequency veering on the sensitivity of bladed disks to mistuning, for example [11,18]. Recently, Kenyon et al. [19] developed expressions that allowed a detailed analysis of the impact of frequency veering on the response of mistuned bladed disks. They pointed out that the amplitude magnification factor, or the ratio of the maximum mistuned response to the tuned response, depends greatly on the tuned mode chosen as a reference. This is an important conclusion since the amplitude magnification factor is often used to measure the severity of mistuning effects in bladed disks. In a study on the effects of multistage coupling on bladed disk dynamics, Bladh et al. [20] observed that shifts in the frequency veering characteristics of the tuned system due to boundary conditions led to significant changes in the tuned forced response amplitudes and mistuned amplitude magnification factors. Thus it is clear that the tuned system dynamics in a frequency veering can have an important effect on mistuned response. In addition, it is likely that the coupling of the disk response to the blade response in frequency veering regions can have some bearing on disk vibration.

This paper explores the sensitivity of the tuned mode shapes to frequency veering in bladed disks with blade and disk families of modes that interact. The impact of the tuned mode sensitivity on the forced vibration response of bladed disks will be discussed, both in terms of the generalized forces exciting the modes and the modal response amplitudes of the system. In particular, it will be shown that the response of the blades of the tuned system may actually be reduced in the veering region. This can have important implications for mistuning analyses that use amplitude magnification as a metric to measure the effects of mistuning on bladed disk response. It will also be shown that although the response of the blades may be reduced, energy is transferred into the disk or hub, which can lead to large stresses in that part of the system. The vibration in the hub region can be critical to structures such as seals and flanges that are directly impacted by the response of the disk or hub. Numerical examples will be provided to illustrate these concepts.

Theory

Mode Interaction Model. In a tuned bladed disk, the primary concern with frequency veering is how the tuned mode shapes change as result of the interaction between blade and disk modes. This can be observed by considering how the sector mode shapes of a cyclic symmetric bladed disk model change due to cyclic symmetry constraints. The sector modes are determined from the unperturbed eigenvalue problem

$$\mathbf{K}^{\circ}\mathbf{\Phi}^{\circ} = \mathbf{M}^{\circ}\mathbf{\Phi}^{\circ}\mathbf{\Omega}^{\circ 2} \tag{1}$$

where $\mathbf{K}$ and $\mathbf{M}$ are the stiffness and mass matrices of a single sector, $\mathbf{\Phi}$ is a matrix whose columns represent the sector mode shapes, $\mathbf{\Omega}^2$ is a diagonal matrix whose elements are the squares of the natural frequencies of the system, and the "°" denotes the unperturbed system. Here, the unperturbed system is the sector with zero interblade phase angle (i.e., the zero nodal diameter sector modes), and the perturbation in the system consists of the change in the sector stiffness as a result of cyclic symmetry constraints when the number of nodal diameters increases. The unperturbed modes are mass-normalized.

$$\mathbf{\Phi}^{\circ H}\mathbf{M}^{\circ}\mathbf{\Phi}^{\circ} = \mathbf{I} \tag{2}$$

$$\mathbf{\Phi}^{\circ H}\mathbf{K}^{\circ}\mathbf{\Phi}^{\circ} = \mathbf{\Omega}^{\circ 2} \tag{3}$$

The "H" superscript denotes the Hermitian operator, which becomes the transpose if the sector modes are real.

A simplified model of the cyclic symmetry constraint is used to investigate the general behavior of the system in the veering region. It is assumed that the effect of increasing interblade phase angle on the stiffness of the sector can be captured by

$$\mathbf{K} = \mathbf{K}^{\circ} + s^2\Delta\mathbf{K} \tag{4}$$

where $s^2 = \sin^2(\sigma_n/2)$, the interblade phase angle $\sigma_n = 2\pi n/N$, n is the number of nodal diameters in the system mode shape, and N is the number of blades on the rotor. The stiffness perturbation $\Delta\mathbf{K}$ represents a unit change in the sector stiffness matrix resulting from a unit change in interblade phase angle. In this approach, the scalar s^2 can be allowed to vary continuously to observe how the mode interaction in a frequency veering behaves away from the discrete interblade phase angles that arise from standard cyclic symmetry techniques. Conceptually, this approach is similar to that used by Bladh et al. [11]. The expression in Eq. (4) is exact for some simple lumped parameter (i.e., mass-spring) models of bladed disks. For more realistic cycle symmetry finite element models of bladed disks, this expression approximates the dynamic effects of strain stiffening in the disk or hub as the number of nodal diameters increases and can be considered only locally over a limited range of interblade phase angles.

The natural frequencies and sector mode shapes are now determined for the perturbed system that has nonzero interblade phase angle,

$$(\mathbf{K}^{\circ} + s^2\Delta\mathbf{K})\mathbf{\Phi}(s) = \mathbf{M}^{\circ}\mathbf{\Phi}(s)\mathbf{\Omega}^2(s) \tag{5}$$

where the mode shapes and frequencies are expressed as functions of s. Following the approach used in [14], the sector frequencies and modes at any interblade phase angle can be approximated in terms of the unperturbed modes and frequencies,

$$\mathbf{\Phi}(s) = \mathbf{\Phi}^{\circ}\mathbf{C}(s) \tag{6}$$

where $\mathbf{C} = [c_{ij}]$ and each c_{ij} indicates the contribution of the ith unperturbed mode to the fth perturbed mode. Using Eq. (6), Eq. (5) can be rewritten,

$$(\mathbf{K}^{\circ} + s^2\Delta\mathbf{K})\mathbf{\Phi}^{\circ}\mathbf{C}(s) = \mathbf{M}^{\circ}\mathbf{\Phi}^{\circ}\mathbf{C}(s)\mathbf{\Omega}^2(s) \tag{7}$$

Projecting Eq. (7) onto the unperturbed modes and taking advantage of Eqs. (2) and (3) yield a simplified eigenvalue problem for the mode participation and natural frequencies of the perturbed system with nonzero interblade phase angle

$$(\mathbf{\Omega}^{\circ 2} + s^2\Delta\hat{\mathbf{K}})\mathbf{C}(s) = \mathbf{C}(s)\mathbf{\Omega}^2(s) \tag{8}$$

where

$$\Delta\hat{\mathbf{K}} = \mathbf{\Phi}^{\circ H}\Delta\mathbf{K}\mathbf{\Phi}^{\circ} \tag{9}$$

is the stiffness perturbation projected onto the unperturbed mode shapes.

For the case of two families of modes interacting through a frequency veering, the interaction may be modeled using a 2×2 system with the form

$$\mathbf{C} = \begin{bmatrix} c_{11} & c_{12} \\ c_{12} & c_{22} \end{bmatrix} \tag{10}$$

$$\Delta\hat{\mathbf{K}} = \begin{bmatrix} k_{11} & k_{12} \\ k_{12} & k_{22} \end{bmatrix} \tag{11}$$

The eigenvalue problem is written

$$\mathbf{A}(s)\mathbf{C}(s) = \mathbf{C}(s)\mathbf{\Omega}^2(s) \tag{12}$$

where

Downloaded 02 Jun 2010 to 171.66.16.98. Redistribution subject to ASME license or copyright; see http://www.asme.org/terms/Terms_Use.cfm

$$\mathbf{A}(s) = \begin{bmatrix} \omega^{\circ 2}_1 + s^2 k_{11} & s^2 k_{12} \\ s^2 k_{12} & \omega^{\circ 2}_2 + s^2 k_{22} \end{bmatrix} \tag{13}$$

and ω°_1 and ω°_2 are the frequencies of the unperturbed modes.

For convenience in solving the eigenvalue problem, the matrix **A** is rewritten

$$\mathbf{A} = \begin{bmatrix} a & d \\ d & b \end{bmatrix} \tag{14}$$

where

$$a = \omega^{\circ 2}_1 + s^2 k_{11} \tag{15}$$

$$b = \omega^{\circ 2}_2 + s^2 k_{22} \tag{16}$$

$$d = s^2 k_{12} \tag{17}$$

Thus, the natural frequencies can be expressed as a function of the interblade phase angle variable s by

$$\omega^2(s) = \frac{(a+b) \pm \sqrt{(a-b)^2 + 4d^2}}{2} \tag{18}$$

Similarly, the eigenvectors describing the participation of the unperturbed modes in the system through the frequency veering comprise the columns of **C**, so that

$$\mathbf{C} = \begin{bmatrix} b - \omega_1^2 & -d \\ -d & a - \omega_2^2 \end{bmatrix} \tag{19}$$

The first column of **C** describes the participation of the two unperturbed modes in the first perturbed mode, while the second column of **C** describes the participation of the two unperturbed modes in the second perturbed mode. Examining Eqs. (15)–(19), if $\Delta\mathbf{K}$ is known explicitly, then the k_{ij} can be calculated and the frequencies and mode shapes of the system can be determined directly. However, if $\Delta\mathbf{K}$ is not known, then the k_{ij} may be determined numerically using a procedure similar to that described in Ref. [14].

In realistic bladed disk models, the stiffness change in the bladed disk may not be proportional to s^2 over all possible interblade phase angles. In this case, the stiffness perturbation due to the interblade phase angle may be approximated as proportional to s^2 locally. A reference interblade phase angle is chosen, which results in selection of s at a reference value, s_0. This interblade phase angle would be selected at a nodal diameter near the frequency veering. The unperturbed stiffness matrix is taken as the stiffness matrix at the reference interblade angle, so that

$$\mathbf{K}^{\circ} = \mathbf{K}(s_0) \tag{20}$$

In a similar fashion, the unperturbed natural frequencies and modes are computed at the reference interblade phase angle.

$$\mathbf{\Phi}^{\circ} = \mathbf{\Phi}(s_0) \tag{21}$$

$$\mathbf{\Omega}^{\circ} = \mathbf{\Omega}(s_0) \tag{22}$$

This situation can be accommodated readily within the current theory by substituting $(s^2 - s_0{}^2)$ for s^2 and allowing this parameter to assume negative values. This does not pose a problem algebraically since s always appears as squared in the formulation.

Mode Shapes, Generalized Force, and Forced Response. With the mode interaction model in place, the effect of frequency veering on the tuned mode shapes can be considered in the context of how the mode shapes impact the generalized forces exciting the system and the modal response of the bladed disk. In general, the unperturbed modes outside of the frequency veering are disk-dominated and blade-dominated, respectively, so that

$$\vec{\phi}^{\circ}_1 \rightarrow \vec{\phi}^{\circ}_D \tag{23}$$

$$\vec{\phi}^{\circ}_2 \rightarrow \vec{\phi}^{\circ}_B \tag{24}$$

where the D and B subscripts denote the "disk" and "blade" modes, respectively. For a harmonic excitation **f**, the generalized forces exciting these modes can be written

$$F^{\circ}_D = \vec{\phi}^{\circ H}_D \mathbf{f} \tag{25}$$

$$F^{\circ}_B = \vec{\phi}^{\circ H}_B \mathbf{f} \tag{26}$$

Typically in a bladed disk, the unsteady forcing that contributes to high cycle fatigue is a result of aerodynamic pressure loads on the blade surfaces. Consequently, $F^{\circ}_D \ll F^{\circ}_B$. The generalized forces exciting the perturbed modes can now be written in terms of the unperturbed generalized forces. With Eqs. (19), (25), and (26), the generalized forces in the two perturbed modes are

$$F_1 = c_{11} F^{\circ}_D + c_{21} F^{\circ}_B \tag{27}$$

$$F_2 = c_{12} F^{\circ}_D + c_{22} F^{\circ}_B \tag{28}$$

The resonant response of the bladed disk in each mode can be expressed in terms of the continuous mode interaction solution. The resonant response is written in dimensional form

$$\mathbf{x}_j = F_j \vec{\phi}_j / b_j \omega_j \tag{29}$$

where b_j is the (dimensional) damping in the jth mode, ω_j is the natural frequency of the jth mode, and $j \in \{1,2\}$. For modes in a frequency veering that have closely spaced frequencies, the frequencies and damping may be assumed to be nearly equal, so that $b_1\omega_1 \approx b_2\omega_2 = \gamma$. Expressing the resonant response in terms of the unperturbed modes using Eqs. (19), (23), and (24), the resonant response in each of the two modes is

$$\mathbf{x}_1 = F_1 (c_{11} \vec{\phi}^{\circ}_D + c_{21} \vec{\phi}^{\circ}_B)/\gamma \tag{30}$$

$$\mathbf{x}_2 = F_2 (c_{12} \vec{\phi}^{\circ}_D + c_{22} \vec{\phi}^{\circ}_B)/\gamma \tag{31}$$

Considering the behavior of the c_{ij} in Eq. (19), the expressions for the generalized forces in Eqs. (28) and (29) and for the resonant response in Eqs. (30) and (31) can be used to examine how the disk and blade motion changes in the frequency veering. The first mode is disk-dominated in the unperturbed system and has a small generalized force since c_{21} is small. Thus, both the blade and disk motion are small. As the interblade phase angle increases, the generalized force increases. In addition, the blade modal response grows, so that the blade motion in this mode increases monotonically and becomes large. The disk motion grows initially as the interblade phase angle increases, and then declines as the mode becomes blade-dominated, i.e., c_{11} becomes small. The second mode is blade-dominated in the unperturbed system (large c_{22}), so that both the generalized force and the blade modal response are large. Thus the blade amplitude is large; however, the disk motion is small. As the interblade phase angle grows, the blade participation c_{22} declines, so that the generalized force and blade modal response decrease and become small. The disk motion initially grows as the disk participation c_{12} increases, but then declines as the generalized force becomes small.

Overall, the blade motion is significant in one or both modes over the entire range of interblade phase angles. However, the blade amplitude reaches a local minimum near the frequency veering where the mode shapes are being exchanged. The disk motion reaches a local maximum in both modes near the frequency veering, but is small elsewhere. These trends will be demonstrated quantitatively for the blade motion in the first example using a lumped parameter bladed disk model and qualitatively for the disk motion using a finite element model in the second example. The implications of these trends for bladed disk forced response will be discussed.

Downloaded 02 Jun 2010 to 171.66.16.98. Redistribution subject to ASME license or copyright; see http://www.asme.org/terms/Terms_Use.cfm

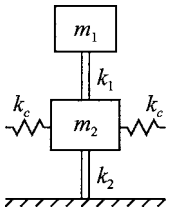

Fig. 1 Lumped parameter model of bladed disk dynamics

Example-Lumped Parameter Model

System Definition and Analysis. The first example consists of a lumped parameter model of bladed disk dynamics with two degrees of freedom per sector and 16 blades or sectors, Fig. 1. Because of its simplicity this example allows for a detailed analysis of the effects of frequency veering on bladed disk response. The lumped parameters of the system can be thought of as modal parameters for the component substructures of a sector of the bladed disk; the mass m_1 and stiffness k_1 represent the modal mass and stiffness for a blade mode, while m_2 and k_2 represent the modal mass and stiffness for a disk mode. The stiffness k_c represents the stiffness of the disk in the circumferential direction projected into the disk modal domain. The values for these parameters are listed in Table 1. It should be noted that these values are not intended to represent any specific bladed disk, but are chosen simply to demonstrate the appropriate physics associated with the frequency veering. Therefore, no dimensions or units are connected with these values except to note that they are consistent.

The natural frequencies of the lumped parameter system are shown as a function of nodal diameter by the discrete dots in Fig. 2. A frequency veering is evident near two nodal diameters. As a reference, the natural frequencies of the blade and disk substructures are also shown. It is clear from the figure that the frequencies of the bladed disk system are closely approximated by the frequencies of the component substructures away from the veering, but near the veering, the frequency loci veer away from each other and the substructure frequencies, indicative of the coupling between the disk and blade modes in this region.

With the lumped parameter model, the stiffness perturbation matrix $\Delta\mathbf{K}$ due to cyclic symmetry constraints can be determined explicitly, so that the natural frequencies and mode projections, Eqs. (18) and (19), can be calculated directly. The lumped parameter model can be replaced by an equivalent sector model with cycle symmetry constraints. The natural frequencies and modes of the constrained sector are determined and then projected around the disk to obtain the system modes in a manner similar to that used in cyclic symmetric finite element models [21]. Applying the cyclic symmetry approach, the disk modal stiffness and sector coupling stiffness are replaced by a single equivalent stiffness k_e that accounts for the cyclic symmetry constraints. Thus, the sector stiffness matrix is written

$$\mathbf{K}_{\text{sector}} = \begin{bmatrix} k_1 & -k_1 \\ -k_1 & k_1 + k_e \end{bmatrix} \tag{32}$$

where

$$k_e = k_2 + 4k_c s^2 \tag{33}$$

and s^2 is defined as before. Using Eqs. (32) and (33), the sector stiffness matrix can be written in the form $\mathbf{K} = \mathbf{K}^\circ + s^2\Delta\mathbf{K}$, where

$$\mathbf{K}^\circ = \begin{bmatrix} k_1 & -k_1 \\ -k_1 & k_1 + k_2 \end{bmatrix} \tag{34}$$

$$\Delta\mathbf{K} = \begin{bmatrix} 0 & 0 \\ 0 & 4k_c \end{bmatrix} \tag{35}$$

Projecting $\Delta\mathbf{K}$ onto the tuned modes, Eq. (9), the k_{ij} of Eq. (11) are determined and used to calculate the sector natural frequencies and modes as continuous functions of s^2 from Eqs. (18) and (19).

Table 1 Properties of the lumped parameter model

Parameter	Value
m_1	15
m_2	250
k_1	23,000
k_2	10,000
k_c	600,000

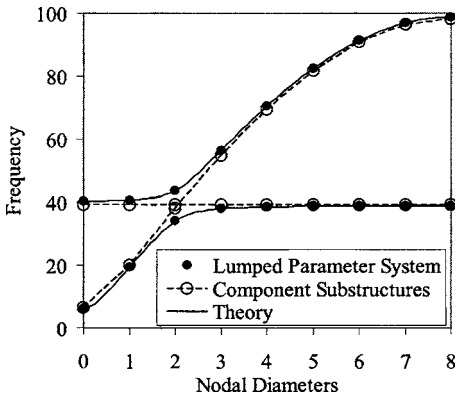

Fig. 2 Natural frequencies of the lumped parameter system

The mode interaction model was used to calculate the natural frequencies and mode projections onto the unperturbed modes as continuous functions of interblade phase angle for the lumped parameter model of Fig. 1. The frequency loci predicted by the model are displayed in Fig. 2 as smooth curves that fit exactly through the natural frequencies of the bladed disk model at the integer nodal diameters. The amplitude of the projections of the modes onto the unperturbed modes at zero nodal diameters are shown in Fig. 3. The top part of the figure shows the projections of the modes onto the blade-dominated unperturbed mode. The individual circles provide a numerical benchmark and are the projections of the modes for the lumped parameter system. The solid curves give the projections calculated from the continuous mode interaction model, Eq. (19). Good agreement is observed between the continuous model and the benchmark. It can be seen that the blade-dominated mode at zero nodal diameters loses its blade characteristics through the veering as the projection is reduced. On the other hand, the disk-dominated mode gains more blade participation through the veering, becoming blade-dominated at high nodal diameters.

The bottom part of Fig. 3 shows a similar projection of the mode shapes onto the disk-dominated unperturbed modes. Again, good agreement is seen between the continuous model and the numerical benchmark. The disk-dominated mode at zero nodal diameters is seen to lose much of its disk participation, while the original blade-dominated mode becomes disk-dominated after the veering. It is interesting to note that the interblade phase angle in Fig. 3 where the disk and blade participation in the sector modes is equal does not correspond exactly with the nodal diameter where the veering occurs, Fig. 2. This likely occurs because of mode normalization effects when the perturbed mode shapes are projected onto the unperturbed modes. Thus, the effects of the frequency veering on the bladed disk forced response are expected to be most pronounced near the veering since the mode normalization is not critical in forced response applications.

Forced Response Considerations. With the mode interaction model in place, the effects of the frequency veering on the resonant forced response can be considered. A pressure load on the "blade" of the lumped parameter system is modeled by the forcing

Downloaded 02 Jun 2010 to 171.66.16.98. Redistribution subject to ASME license or copyright; see http://www.asme.org/terms/Terms_Use.cfm

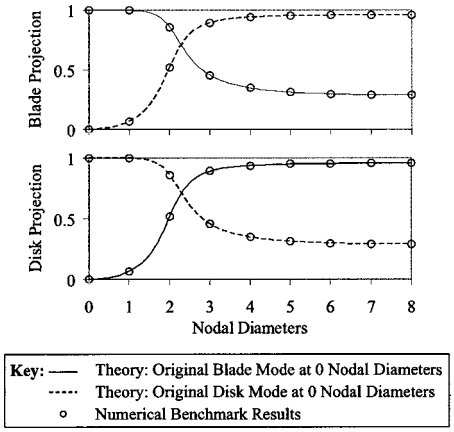

Fig. 3 Mode shape exchange in frequency veering

vector, $\mathbf{f}=\{1\ 0\}^T$. Therefore, the force on the disk is zero, and the calculations for the generalized forces due to a blade load, Eqs. (25) and (26), are simplified, $F_j=\Phi_{1j}$. The generalized forces in the two sector modes are shown as functions of nodal diameter in Fig. 4. The key for Fig. 4 is the same as in the previous figure. It is clear from the figure that as the blade-dominated mode passes through the veering, the blade contribution is decreased and thus the generalized force is decreased as the disk becomes the dominant component in the mode. The generalized force in the disk-dominated mode exhibits a corresponding increase as the blade motion becomes the dominant attribute of that mode. Two important features should be noted. First, the generalized force is the same in both modes at the frequency veering very near two nodal diameters, reference Fig. 2. This means that both modes are excited near the veering, and both modes will exhibit a significant forced response. Second, the maximum generalized force exciting either mode is minimized at the frequency veering, as shown by the dip in the envelope of the two curves at two nodal diameters. Since both modes share vibration energy with the disk at this interblade phase angle, the blade modal amplitude is reduced and the resulting generalized forces that can excite either of these modes are subsequently reduced.

Frequency veering has a similar, though possibly more pronounced, impact on the blade response amplitude. The modal response is defined here as the product of the generalized force and the mode shape, comprising essentially the parameters of the forced response that are not dependent directly on frequency or damping. The modal response amplitude of the blade is shown for the two modes in Fig. 5. Both of the curves are shown as solid lines in the figure, though in this context it is clear that one blade amplitude locus is for the original blade-dominated mode from the unperturbed system and the other blade amplitude corresponds to the original disk-dominated mode. The results from the lumped parameter system are again shown at discrete nodal diameters. The key feature in Fig. 5 is the sharp minimum that occurs in the upper envelope of the blade modal response at two nodal diameters. This minimum implies that the blade amplitude is reduced at two nodal diameters due to the frequency veering and mode interaction, so that the maximum tuned forced response to a second engine order excitation would be significantly lower than the response to other engine orders. This local minimum in blade response is consistent with the observation made in the development of the resonant response expressions in the previous section. The steep slope near the veering implies that the system may be sensitive to perturbations that shift the location of the minimum with respect to the integer nodal diameter.

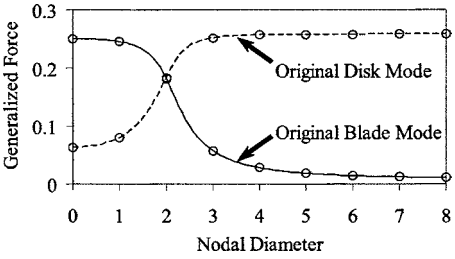

Fig. 4 Effects of frequency veering on generalized forces

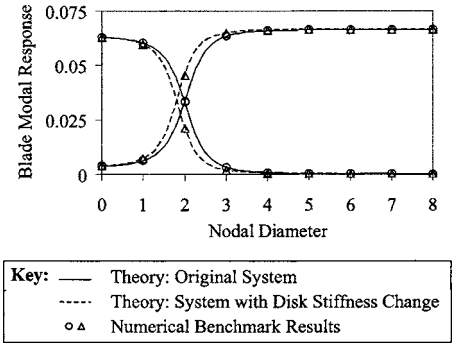

Fig. 5 Effect of frequency veering on blade modal response, baseline, and perturbed system with disk stiffness change

To illustrate the sensitivity of the blade modal response near the frequency veering, the lumped parameter model is subjected to a 20% increase in the disk stiffness k_2 and k_c. This change in the disk stiffness is roughly equivalent to a 10% change in the disk frequencies and may represent uncertainty in approximating the boundary conditions on a bladed disk, for example [20]. The mode interaction is again modeled using the continuous formulation to see how the frequency veering shifts in relation to the integer nodal diameter. From this analysis, the blade modal response is obtained for the system with the increased disk stiffness and is shown in Fig. 5 as a dashed line. The blade modal response at the integer nodal diameters is again shown for reference. The figure shows that the frequency veering and the minimum blade response is shifted to the left of the second nodal diameter. As a consequence, the modal response at the integer nodal diameter is farther from the minimum, and is thus greater than the modal response in the original system. In this example, the modal response at two nodal diameters is 35% higher than in the original system.

To see the effects of shifting the frequency veering on the forced response more explicitly, forced response simulations for the lumped parameter bladed disk were performed with both the original disk stiffness and the 20% increase in disk stiffness. The system was excited by a second engine order traveling wave excitation with a sector force distribution $\mathbf{f}=\{1\ 0\}^T$. The engine order traveling wave excitation represents the excitation that a rotor experiences as it rotates through stationary disturbances in the flow field, for instance the wakes from upstream stators. This type of excitation is further described in Refs. [17,19]. The frequency resolution for the numerical simulation was chosen so that the error in the amplitude was less than 0.05%, and a modal damping ratio $\zeta=0.005$ was assumed.

The results from the forced response simulations are shown in Fig. 6. Both frequency response functions have been normalized by the maximum value of the response in the baseline system with the original disk stiffness. Thus the results are analogous to the amplitude magnification factor used in mistuning analysis. It can be seen in the figure that the system with the increased stiffness in the disk exhibits a higher forced response amplitude; the ratio of the maximum response in this system to the response in the baseline system is 1.29, indicative of the sensitivity of the response near the frequency veering to perturbations in the tuned system

Downloaded 02 Jun 2010 to 171.66.16.98. Redistribution subject to ASME license or copyright; see http://www.asme.org/terms/Terms_Use.cfm

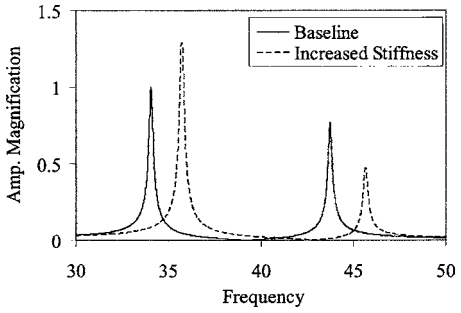

Fig. 6 Increase in forced response amplitude due to a perturbation in tuned system properties

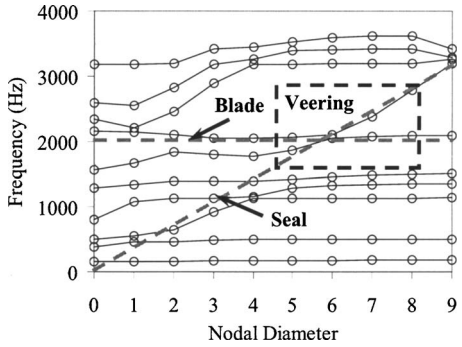

Fig. 8 Bladed disk natural frequencies with veering between blade and seal modes

properties. It should be noted that perturbations in the system properties may lead to decreases in response amplitude as well as increases as shown here near a frequency veering. The key issue is that perturbations or uncertainties in tuned system properties can have a significant impact on tuned resonant response amplitudes, depending on the proximity of the veering to possible engine order excitations.

The sensitivity of the tuned blade response in a bladed disk with frequency veering to perturbations in the system properties has important implications for mistuning analyses involving the amplitude magnification factor. Since the tuned forced response amplitude comprises the denominator of the mistuned amplitude magnification factor, the sensitivity of the tuned response to perturbations may well be reflected in the sensitivity of the mistuned amplitude magnification factor to mistuning. Moreover, the local minimum in blade response amplitude associated with frequency veering can contribute to high amplitude magnification factors in mistuned bladed disks Thus, extremely large amplitude magnification factors predicted for a system with frequency veering may not necessarily indicate excessive displacement amplitudes and high stresses. From this discussion, it is clear that understanding how the tuned bladed disk responds near frequency veering regions is an important aspect of predicting mistuned bladed disk forced response.

Example-Finite Element Model

The second example consists of a finite element model of an integrally bladed disk with 18 blades as shown in Fig. 7. The low aspect ratio blades of the rotor are represented by flat plates; however, the dynamic response of the blades is relevant to modern gas turbines for the first several blade modes. A knife-edge seal with simplified geometry is shown at the hub on the aft side of the bladed disk. Such seals are commonly used in turbomachinery rotors at the interface with adjacent stators. The natural frequencies of the tuned bladed disk are shown versus nodal diameters in Fig. 8. The dynamic behavior of the bladed disk as displayed in the figure is representative of modern turbomachinery applications, for example [11]. The nominal material properties of the bladed disk are those for steel, though the stiffness of the blade and seal substructures has been tuned to provide mode interaction and frequency veering in a region of the nodal diameter map, Fig. 8, where the structural dynamics are relatively easily understood with the concepts presented here. In other words, the response of the system near the veering is not further complicated by interaction with other families of modes. The frequencies of the blade and seal modes are emphasized by dashed lines in the figure for clarity, and the veering region of interest is indicated by a box. The blade mode in the frequency veering represents a typical second torsion blade mode, while the seal mode is a first bending mode in the seal substructure cantilevered to the disk. It should be noted that a detailed mathematical analysis of the frequency veering will not be provided for this example as for the previous lumped parameter system. Instead, this example is intended to provide a straightforward application of the concepts developed here to a more realistic bladed disk model and to demonstrate the potential effects of frequency veering on disk/seal vibration response.

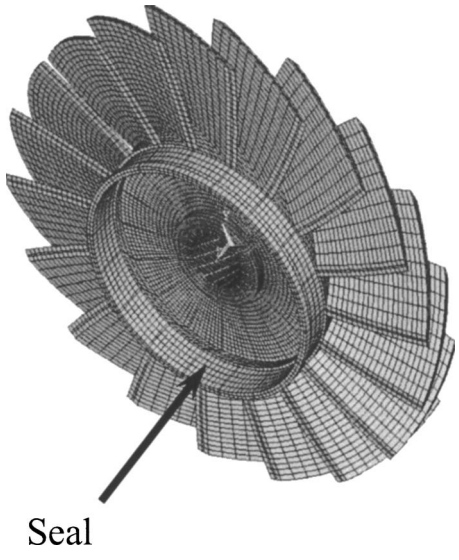

Fig. 7 Finite element model of a fan rotor with a knife-edge seal

A detailed view of the frequency veering is shown in the middle portion of Fig. 9. In addition to the natural frequencies from the finite element analysis, a local fit of natural frequencies predicted using the continuous method is displayed. The finite element model frequencies are the discrete points in the figure, while the continuous curves represent the local fit of the theoretical model. For the prediction, the reference interblade phase angle parameter s_0 was selected to correspond to five nodal diameters, and the continuous model was fit over nodal diameters five through seven. It is clear from the figure that the theoretical model approximates the behavior of the frequencies reasonably well in the veering, though the accuracy of the fit starts to break down farther away from the reference s_0 at five nodal diameters. As a second check of the theoretical model, the projections of the mode shapes onto the seal-dominated reference mode at five nodal diameters are shown in Fig. 10. The theory captures the trends in the exchange of modal characteristics in the veering. Some error is present in the mode shape projections, especially at seven nodal diameters, which is well away from the reference. Similar agreement was observed for projections onto the unperturbed blade mode. From these results, it is clear that the theoretical model captures the relevant physical characteristics of the frequency veering over a range of interblade phase angles.

Downloaded 02 Jun 2010 to 171.66.16.98. Redistribution subject to ASME license or copyright; see http://www.asme.org/terms/Terms_Use.cfm

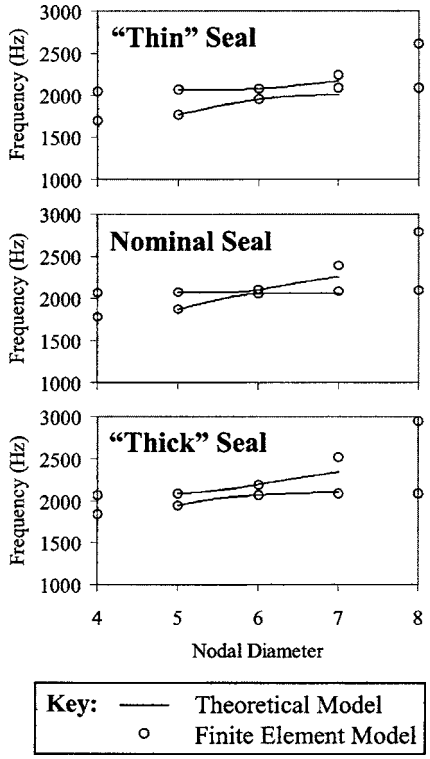

Fig. 9 Changes in veering behavior due to changes in seal stiffness–thickness

The finite element example can be used to illustrate the importance of the veering proximity to possible sources of excitation. As shown by the continuous model approximation in the middle of Fig. 9, the frequency veering occurs very close to six nodal diameters. Thus, it is expected that the mode interaction and, therefore, the effects of the frequency veering on the forced response of the system described by the middle of Fig. 9 will be significant. This result is also consistent with Yang and Griffin [13], as well as Marugabandhu and Griffin [14], who observed that the separation between the frequencies of the modes in the veering is one of the key parameters governing the interaction between the modes.

In this example, the primary concern is the vibration response of the knife-edge seal to unsteady aerodynamic loads on the blades. To simulate the aerodynamic loading, a forced response simulation was performed with the finite element model by applying a harmonic point load to the leading edge tip of each blade phased to simulate an engine order traveling wave excitation that a rotor might experience during operation. The forced response simulation was performed for a sixth engine order excitation, corresponding to the six nodal diameter modes where the frequency veering takes place, and the maximum principal stress in the seal

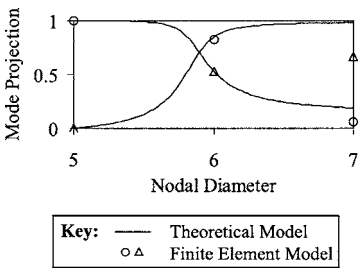

Fig. 10 Projection of finite element model modes onto seal mode at 5 nodal diameters

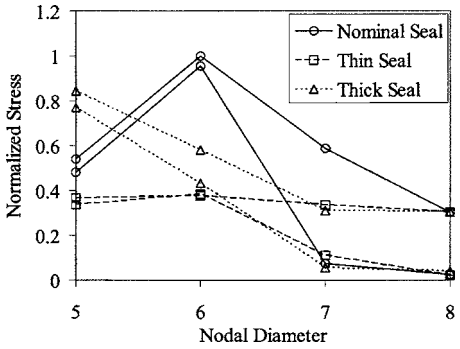

Fig. 11 Effect of frequency veering proximity on seal stress

substructure during resonance was determined. For the first bending seal mode, the maximum principal stress occurred at the seal outer diameter near the intersection of the seal with the disk. In addition, forced response simulations were repeated for several other engine orders or nodal diameters near the frequency veering to demonstrate that the seal is not as strongly excited by the aerodynamic blade loading away from the frequency veering.

The results from this analysis are shown by the circles labeled "Nominal Seal" in Fig. 11. The stresses are normalized by the maximum principal stress at six nodal diameters, and the points are connected by solid lines to help in visualizing the trend in the stresses around the frequency veering. Two sets of data are shown because two families of modes are interacting in the veering. It is clear from Fig. 11 that the stresses caused by an engine order excitation reach a local maximum near the frequency veering at six nodal diameters. This result is consistent with the theoretical observation of a local maximum in disk response from the expressions for forced response derived in the previous section. The seal stresses near the frequency veering at six nodal diameters are much higher than the stresses caused by engine order excitations away from the frequency veering. For this system, the highest stress at either of the adjacent nodal diameters is approximately 40% lower than the stress at six nodal diameters, where the frequency veering leads to high seal response from aerodynamic loading.

The local maximum in the seal response suggests a design approach to avoid high seal vibration due to aerodynamic loading of the rotor blades. If the seal frequencies can be tuned to move the frequency veering away from a number of nodal diameters corresponding to an engine order excitation, then high seal vibration response may be avoided. For instance, the seal may be made thinner so that the substructure is less stiff and the seal frequencies are generally lower. This would effectively shift the frequency veering to the right. This approach was emulated with the finite element model by reducing the elastic modulus of the seal material by approximately 12% to simulate the reduction in the stiffness of the thinner seal.

The natural frequencies in the veering region of the bladed disk with reduced seal stiffness are shown in the top part of Fig. 9. The local fit of the frequencies from the theory clearly indicates that the frequency veering is shifted to the right of six nodal diameters. Forced response simulations were performed in a fashion similar to those for the nominal seal. The principal stresses in the seal from the simulations were normalized by the maximum stress at six nodal diameters for the nominal seal so that a direct assessment could be made with regard to how the stresses changed due to shifting the frequency veering. The results are shown in Fig. 11 and labeled "Thin Seal." The stresses are greatly reduced in comparison to the nominal seal; the highest stresses still occur at six nodal diameters, but are approximately 60% lower than in the nominal seal.

It should be noted that some caution must be exercised with this approach, as some design changes may not entirely mitigate the

Downloaded 02 Jun 2010 to 171.66.16.98. Redistribution subject to ASME license or copyright; see http://www.asme.org/terms/Terms_Use.cfm

potential for high stresses in the seal. To illustrate this point, a second design change is considered in which the thickness of the seal is increased, thereby increasing the stiffness and the frequencies of the seal. This design change was emulated with the finite element model by increasing the modulus of the seal material by 12% to simulate the increased stiffness. The natural frequencies of the system with the thicker seal are shown in the bottom part of Fig. 9. The local continuous fit of the predicted frequencies from the theory indicates that the frequency veering is shifted to the left of six nodal diameters, and actually approaches five nodal diameters. The forced response simulations were repeated, with the results given in Fig. 11 and labeled "Thick Seal." Indeed, the seal stresses are reduced at six nodal diameters by roughly 40%. However, the maximum stress would occur in the seal for this bladed disk due to an excitation in the fifth nodal diameter. Here the stress exceeds 80% of the maximum stress in the nominal system. Thus, if there is a potential for an additional fifth engine order excitation, or if a later design change results in a different number of stator vanes upstream of the rotor that yields a fifth engine order excitation, the resulting stresses in the seal may still be unacceptably large. Finally, it should be noted that the changes in the forced response that occur due to a shift in the seal frequencies and the frequency veering could also be replicated by manufacturing variations. Thus, seals that are designed for low stress could inadvertently exhibit much larger stress because of variations in the seal thickness that result from manufacturing.

Conclusions

Frequency veering commonly occurs in modern turbomachinery rotors due to interaction between blade-dominated families of modes and disk-dominated families of modes. A method has been presented for representing this mode interaction in terms of the nominal cyclic symmetry modes of a bladed disk sector model with constraints applied at the sector boundaries corresponding to a reference interblade phase angle. The method approximates the cyclic symmetry constraints as a perturbation to the sector stiffness matrix that varies proportionally to a parameter s^2, such that $s^2=\sin^2(\sigma_n/2)$ and σ_n is the interblade phase angle of the cyclic symmetry constraint. The advantage of this approach is that it provides a continuous representation of the mode interaction through the frequency veering rather than only at discrete integer nodal diameters. The continuous representation allows for the effects of the proximity of the frequency veering to integer nodal diameters where potential excitations can occur to be observed and more fully understood. For simple lumped parameter models of bladed disk dynamics, the method is exact over the entire range of interblade phase angles or nodal diameters that the bladed disk modes may exhibit. In more realistic finite element models, the method can be used to approximate the system dynamics locally in the frequency veering region of interest.

Using the mode interaction model derived here as a basis, the effect of frequency veering on the sector mode shapes can be considered in the context of how the mode shapes impact the generalized forces exciting the system and the modal response of the bladed disk. It was shown that the forced blade vibration is significant in one or both modes over the entire range of interblade phase angles. However, the blade amplitude reaches a local minimum near the frequency veering where the mode shapes are being exchanged. This local minimum in blade amplitude can occur abruptly, depending on the characteristics of the frequency veering, which can have important implications for mistuning analyses using blade amplitude magnification factor as a metric for determining the severity of mistuning effects. On the other hand, the disk vibration response is relatively small over most interblade phase angles, but reaches a local maximum in both modes near the frequency veering. Thus in the frequency veering, the disk can be excited by aerodynamic forcing on the blades.

These concepts were applied to two examples consisting of cyclic symmetry bladed disk models to demonstrate the effects of frequency veering on tuned bladed disk response. The first example used a lumped parameter system with two degrees of freedom per sector. The lumped parameter model demonstrated a sharp reduction in the blade vibration amplitude in the frequency veering, and the sensitivity of the response to perturbations in the tuned system properties was illustrated. The second example consisted of a finite element model of a bladed disk representative of modern turbomachinery applications. The frequency veering represented an interaction between a blade-dominated family of modes and a family of modes characterized by vibration of a knife-edge seal on the disk. This example demonstrated a local maximum in the seal vibration response when the frequency veering occurred at an integer number of nodal diameters corresponding to an engine order aerodynamic excitation. A design change was suggested in which the frequency veering is moved away from the integer nodal diameter by changing the thickness of the seal. The viability of this design approach for reducing seal vibration amplitudes was demonstrated.

References

[1] Ramaswamy, R., and Marcus, R. A., 1981, "Perturbative Examination of Avoided Crossings," Journal of Chemistry and Physics, 74, pp. 1379–1384.

[2] Crandall, S. H., and Yeh, N. A., 1989, "Automatic Generation of Component Modes for Rotordynamic Substructures," ASME J. Vib., Acoust., Stress, Reliab. Des., **111**, p. 6–10.

[3] Jei, Y.-G., and Lee, C.-W., 1992, "Does Curve Veering Occur in the Eigenvalue Problem of Rotors?" ASME J. Vibr. Acoust., **114**, pp. 32–36.

[4] Kuttler, J. R., and Sigillito, V. G., 1981, "On Curve Veering," J. Sound Vib., **75** (4), pp. 585–588.

[5] Perkins, N. C., and Mote, C. D., 1986, "Comments on Curve Veering in Eigenvalue Problems," J. Sound Vib., **106** (3), pp. 451–463.

[6] Balmés, E., 1993, "High Modal Density, Curve Veering, Localization: A Different Perspective on the Structural Response," J. Sound Vib., **161**, (2), pp. 358–363.

[7] Leissa, A. W., 1974, "On a Curve Veering Aberration," Z. Angew. Math. Phys., **25**, pp. 99–111.

[8] Kenyon, J. A., 1999, "Investigation of Curve Veering Using Computational and Experimental Techniques," Proceedings of the 40th AIAA/ASME/ASCE/AHS/ASC Structures, Structural Dynamics, and Materials Conference, AIAA, St. Louis, Missouri, pp. 1550–1558.

[9] Afolabi, D., and Mehmed. O., 1994, "On Curve Veering and Flutter of Rotating Blades," ASME J. Eng. Gas Turbines Power, **116**, pp. 702–708.

[10] Castanier, M. P., Óttarsson, G., and Pierre, C., 1997, "A Reduced-Order Modeling Technique for Mistuned Bladed Disks," ASME J. Vibr. Acoust., **119**, pp. 439–447.

[11] Bladh, R., Pierre, C., Castanier, M. P., and Kruse, M. J., 2002, "Dynamic Response Predictions for a Mistuned Industrial Turbomachinery Rotor Using Reduced-Order Modeling," ASME J. Eng. Gas Turbines Power, **124**, pp. 311–324.

[12] Kenyon, J. A., Cross, C. J., and Minkiewicz, G. R., 2000, "Mechanical Coupling Effects on Turbomachine Mistuned Response," J. Propul. Power, **16** (6), pp. 1149–1154.

[13] Yang, M.-T., and Griffin, J. H., 1997, "A Normalized Modal Eigenvalue Approach for Resolving Modal Interaction," ASME J. Eng. Gas Turbines Power, **119**, pp. 647–650.

[14] Marugabandhu, P., and Griffin, J. H., 2003, "A Reduced-Order Model for Evaluating the Effect of Rotational Speed on the Natural Frequencies and Mode Shapes of Blades," ASME J. Eng. Gas Turbines Power, **125**, pp. 772–776.

[15] Pierre, C., 1988, "Mode Localization and Eigenvalue Loci Veering Phenomena in Disordered Structures," J. Sound Vib., **126** (3), pp. 485–502.

[16] Triantafyllou, M. S., and Triantafyllou, G. S., 1991, "Frequency Coalescence and Mode Localization Phenomena: A Geometric Theory," J. Sound Vib., **150** (3), pp. 485–500.

[17] Kenyon, J. A., Griffin, J. H., and Feiner, D. M., 2003, "Maximum Bladed Disk Forced Response from Distortion of a Structural Mode," ASME J. Turbomach., **125**, pp. 352–363.

[18] Yang, M.-T., and Griffin, J. H., 2001, "A Reduced-Order Model of Mistuning Using a Subset of Nominal System Modes," ASME J. Turbomach., **123**, pp. 893–900.

[19] Kenyon, J. A., Griffin, J. H., and Kim, N. E., 2004, "Frequency Veering Effects on Mistuned Bladed Disk Forced Response," J. Propul. Power, **20**(5), pp. 863–870.

[20] Bladh. R., Castanier, M. P., and Pierre, C., 2003, "Effects of Multistage Coupling and Disk Flexibility on Mistuned Bladed Disk Dynamics," ASME J. Eng. Gas Turbines Power, **125**, pp. 121–130.

[21] Thomas, D. L., 1979, "Dynamics of Rotationally Periodic Structures," Int. J. Numer. Methods Eng., **14**, pp. 81–102.

Downloaded 02 Jun 2010 to 171.66.16.98. Redistribution subject to ASME license or copyright; see http://www.asme.org/terms/Terms_Use.cfm

Rotordynamic Coefficients for a Tooth-on-Stator Labyrinth Seal at 70 Bar Supply Pressures: Measurements Versus Theory and Comparisons to a Hole-Pattern Stator Seal

Arthur Picardo
Test Engineer
Flowserve Corp.,
Vernon, CA 90058

Dara W. Childs
Leland T. Jordan Professor of Mechanical Engineering
Turbomachinery Laboratory,
Texas A&M University,
College Station, TX 77843
e-mail: dchilds@mengr.tamu.edu

Rotor dynamic and leakage coefficients are presented for a labyrinth seal that was tested at a supply pressure of 70 bar-a and speeds up to 20,200 rpm. Tests were conducted at clearances of 0.1 mm and 0.2 mm, pressure ratios of 0.10, 0.31, and 0.52, and three preswirls ratios. Comparisons are made between test data and predictions from one-control-volume and two-control-volume bulk-flow models. Generally, theoretical predictions agree poorly with the test results, with the one-control volume model giving better predictions. The one-control-volume model provides a conservative prediction for effective damping; i.e., this parameter is underestimated. Both models under predict leakage rates. Comparisons are also made between rotordynamic coefficients of labyrinth and hole-pattern seals. [DOI: 10.1115/1.1924634]

Introduction

In this paper, labyrinth seals refer to seals with smooth rotors and the labyrinth teeth on the stator. The seal reaction-force components are modeled by

$$\{F_s\} = -\begin{Bmatrix} F_{sx} \\ F_{sy} \end{Bmatrix} = \begin{bmatrix} K_{xx} & K_{xy} \\ K_{yx} & K_{yy} \end{bmatrix} \begin{Bmatrix} X \\ Y \end{Bmatrix} + \begin{bmatrix} C_{xx} & C_{xy} \\ C_{yx} & C_{yy} \end{bmatrix} \begin{Bmatrix} \dot{X} \\ \dot{Y} \end{Bmatrix} \quad (1)$$

For small motion about a centered position, this model becomes

$$-\begin{Bmatrix} F_{sx} \\ F_{sy} \end{Bmatrix} = \begin{bmatrix} K & k \\ -k & K \end{bmatrix} \begin{Bmatrix} X \\ Y \end{Bmatrix} + \begin{bmatrix} C & c \\ -c & C \end{bmatrix} \begin{Bmatrix} \dot{X} \\ \dot{Y} \end{Bmatrix} \quad (2)$$

The diagonal terms (K, C) are the direct stiffness and damping coefficients, and the off-diagonal terms (k, c) are the cross-coupled stiffness and damping coefficients.

For many years, labyrinth seals have been identified as primary causes of rotordynamic instability in steam turbines and high-pressure injection compressors. Tests conducted by Wachter and Benckert in the late 1970s showed destabilizing cross-coupled stiffness coefficients that were strongly tied to preswirl of the gas entering the seal. As reviewed below, tests by various investigators have been reported in the intervening years.

"Bulk-flow" models were developed starting with Iwatsubo in 1980 [1] to predict seal rotor dynamic coefficients. Test results at low speeds and low pressures have tended to agree reasonably well with this type of model; however, tests at higher speeds and higher pressures have not. Today, there is a general move towards CFD predictions of these coefficients. However, no sufficiently credible public-domain data exist to anchor these efforts. The present test results were developed to eliminate that deficit and to evaluate the accuracy of presently employed bulk-flow models in predicting rotor dynamic coefficients.

Benckert and Wachter [2] tested seals at an inlet pressure of 1.42 bar-a. Higher-pressure (up to 18.3 bar-a) labyrinth seal tests were reported by Childs and Scharrer [3,4] and Pelletti [5]. Their test results correlate well with Scharrer's two-control volume model at low speeds, low supply pressures and larger clearances. They correlate poorly at higher pressures and speeds and tighter clearances, particularly in regard to the dependence of the cross-coupled stiffness coefficient on the inlet circumferential velocity. However, the preswirl measurements by Childs and Scharrer and Pelletti are questionable, since they were not measured directly, but inferred from the angle of the inlet guide vanes. Wyssmann et al. [6] and Wagner [7] have tested labyrinth seals at inlet pressures of 140 and 70 bar-a, respectively, however they present very limited information about the rotordynamic coefficients.

The following questions exist with respect to of labyrinth seals:

(1) Are the rotordynamic coefficients of Eq. (2) frequency dependent? Test results show strong frequency dependency in hole-pattern (Weatherwax and Childs [8]) and honeycomb seals (Dawson et al. [9]). Prior tests by Childs and Scharrer and Pelletti were performed over a very small frequency range that was inadequate to answer this question.
(2) For small eccentricities, is the model of Eq. (2) correct? Specifically, does $Kxx=Kyy=K?$ $Cxx=Cyy=C?$ $Kxy=Kyx=k?$ and $Cxy=Cyx=c?$
(3) What is the influence of preswirl on cross-coupled stiffness and direct damping? The present test rig uses a Pitot-tube measurement to accurately measure preswirl.
(4) How does clearance effect rotordynamic coefficients and stability? Several early instabilities in compressors were thought to result from reductions in clearances; however, no data are available to assess this view.
(5) How do the measured coefficients compare with predictions from the bulk-flow models?

Contributed by the International Gas Turbine Institute (IGTI) of THE AMERICAN SOCIETY OF MECHANICAL ENGINEERS for publication in the ASME JOURNAL OF ENGINEERING FOR GAS TURBINES AND POWER. Paper presented at the International Gas Turbine and Aeroengine Congress and Exhibition, Vienna, Austria, June 13–17, 2004. Paper No. GT2004-53327. Manuscript received by IGTI, October 1, 2003; final revision, March 1, 2004. IGTI Review Chair: A. J. Strazisar.

Copyright © 2005 by ASME

Downloaded 02 Jun 2010 to 171.66.16.98. Redistribution subject to ASME license or copyright; see http://www.asme.org/terms/Terms_Use.cfm

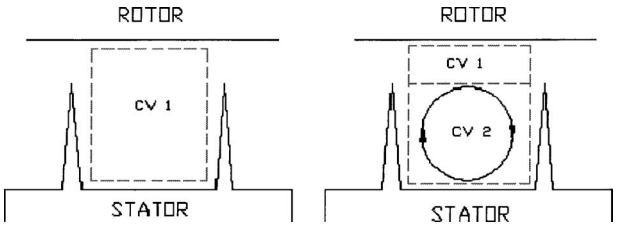

Fig. 1 Schematic of one-control-volume and two-control-volume models

(6) How do the leakage and rotordynamic coefficients of a labyrinth seal compare with results for a hole-pattern seal?

Bulk-Flow Models for Labyrinth Seals. As noted above, bulk-flow models are used for predicting the pressure and circumferential-velocity distribution and the rotordynamic coefficients. Iwatsubo [1] presented a one-control-volume model to predict the labyrinth seal coefficients. Childs and Scharrer [10] modified Iwatsubo's theory to include the angular area derivatives in the continuity and circumferential momentum equations. Wyssmann et al. [6] proposed a "box-in-a-box" two-control volume model to predict the coefficients. Scharrer [11] modified this two-control volume model to include the recirculation velocity in a labyrinth cavity. Figure 1 illustrates Childs and Scharrer's one-control-volume (1CVM) and Scharrer's two-control-volume models (2CVM).

Description of the Test Rig. The test rig was originally designed to test high-speed hydrostatic bearings (HBR). Childs and Hale [12] provide a complete description of the original HBR. Dawson et al. provide the details of the modifications done to the HBR for testing annular gas seals at low pressures. Subsequent modifications were done to the exhaust air piping to regulate the backpressure to obtain pressure ratios from 0.1 to 0.6, Weatherwax and Childs [7].

As shown in Fig. 2, the test rotor is supported on two hydrostatic bearings. High-pressure air enters the stator from the center plane, flows through a preswirl ring and then through the two seals into a backpressure annulus and then across two backpressure labyrinth seals. (Swirl brakes are installed upstream of these backpressure seals to minimize their contribution to the cross-coupled stiffness coefficients.) The stator is connected axially by three "pitch stabilizer" rod assemblies that enforce parallel motion between the rotor and stator. The backpressure is regulated using a control valve to vent air from the backpressure annulus to obtain the desired pressure ratio. The stator housing is excited with a pseudorandom waveform (frequency range of 20–230 Hz), using two orthogonally positioned hydraulic shakers. Marquette et al. [13] discuss the test procedure and method for data acquisition. Childs and Hale [12] discuss the method used to obtain the impedances from the raw test data. Parameters measured during a test include: the relative displacements between the stator and the rotor, the force exerted by the shakers, and the stator acceleration.

This basic design has worked very well in testing smooth, honeycomb stator, and hole-pattern stator seals. However, with labyrinth seals, the stator (rather than the rotor) becomes unstable as preswirl increases. Other researchers have reported similar difficulties, and the pitch stabilizers had previously been stiffened to eliminate this type of problem. However, they were clearly inadequate to cope with the present stator instability. The problem was eliminated by introducing stiffness asymmetry in the support planes. As shown in Fig. 3, four opposed radial stiffeners with a total stiffness of 17.52 MN/m were added to the horizontal plane through the stator.

Fluid preswirl is measured using a Pitot tube and a static pressure orifice connected to a differential pressure transmitter, as shown in Fig. 4. This pressure is then used to calculate the inlet circumferential velocity of the fluid. Details of the preswirl and leakage measurement are given by Picardo [14]. The preswirl ratio is defined as the ratio of the circumferential velocity of the

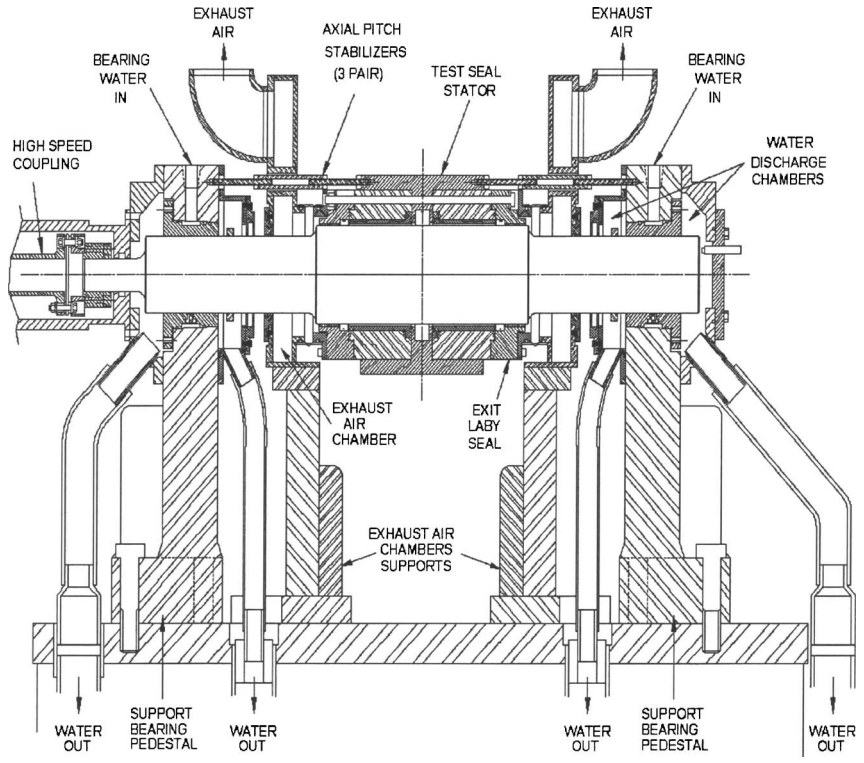

Fig. 2 Cross-sectional view of the test rig

Downloaded 02 Jun 2010 to 171.66.16.98. Redistribution subject to ASME license or copyright; see http://www.asme.org/terms/Terms_Use.cfm

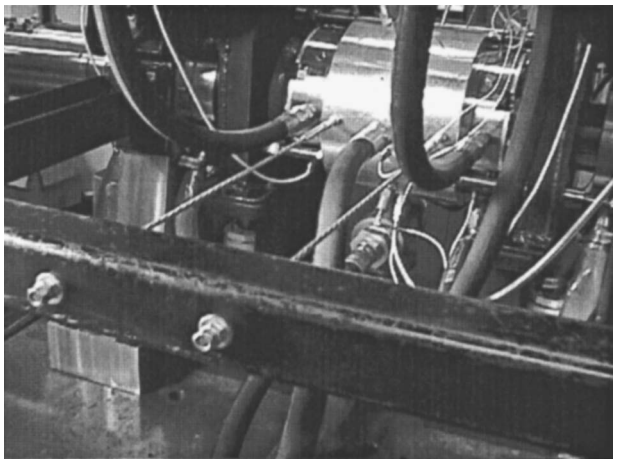

Fig. 3 Stator support asymmetry

fluid to rotor surface velocity, given by Eq. (3). Fig. 4 also shows the details of the three preswirl rings used to obtain the different preswirl ratios. The pivot tube has a diameter of 1.5 mm and is located 2.5 mm away from the preswirl ring as shown in Fig. 4. It is defined as

$$\text{preswirl ratio, PS} = \frac{V_t \cdot 60}{\pi \cdot D_r \cdot N} \tag{3}$$

where, V_t is the tangential (circumferential) velocity of the fluid and D_r is the diameter of the rotor, and N is rotor rpm.

Parameter Identification Model. As noted above, the stator is excited by hydraulic shakers in two orthogonal planes. The equation of motion for the stator is

$$\begin{Bmatrix} F_{xx} - m_s A_{xx} \\ F_{xy} - m_s A_{xy} \end{Bmatrix} = -\{F_s\} \tag{4}$$

where, F_s is the seal reaction force given by Eq. (1). Restating Eq. (4) in the frequency domain gives

$$\begin{Bmatrix} F_{xx} - m_s A_{xx} \\ F_{xy} - m_s A_{xy} \end{Bmatrix} = \begin{bmatrix} H_{xx} & H_{xy} \\ H_{yx} & H_{yy} \end{bmatrix} \begin{Bmatrix} D_{xx} \\ D_{xy} \end{Bmatrix} \tag{5}$$

where, F_{ij} are the measured excitation forces, A_{ij} are the measured acceleration vectors of the stator, and m_s is the stator mass. The impedances H_{ij} are defined in terms of the rotor dynamic coefficients by

$$H_{ij} = K_{ij} + j(\omega \cdot C_{ij}), \tag{6}$$

and ω is the excitation frequency.

Equations (5) and (6) define the seal dynamic stiffness coefficients in the frequency domain. To provide enough equations to solve for the four unknown impedances in Eq. (5), alternate shakes are conducted on the stator in orthogonal directions (X and Y), yielding four equations and four unknowns, given by Eq. (7).

Table 1 Test conditions

Inlet pressure P_i (bar)	Preswirl ratio	Pressure ratio PR$=P_e/P_i$	Speed N (rpm)	Clearance C_r (mm)
70 and 52	High (1.0)	0.15	10,200	0.10, 0.20
			15,200	0.10, 0.20
			20,200	0.10, 0.20
	Medium (0.5)	0.35	10,200	0.10, 0.20
			15,200	0.10, 0.20
			20,200	0.10, 0.20
	None (0)	0.50	10,200	0.10, 0.20
			15,200	0.10, 0.20
			20,200	0.10, 0.20

$$\begin{bmatrix} F_{xx} - m_s A_{xx} & F_{yx} - m_s A_{yx} \\ F_{xy} - m_s A_{xy} & F_{yy} - m_s A_{yy} \end{bmatrix} = \begin{bmatrix} H_{xx} & H_{xy} \\ H_{yx} & H_{yy} \end{bmatrix} \begin{bmatrix} D_{xx} & D_{yx} \\ D_{xy} & D_{yy} \end{bmatrix} \tag{7}$$

The data obtained from the seal tests directly provides all of the above variables except the impedances (H_{ij}'s). Frequency-dependent impedances are obtained from Eq. (7). Once the impedances are determined, Eq. (6) is used to solve for the rotordynamic stiffness and damping coefficients via

$$K_{xx} = \text{Re}(H_{xx}) \tag{8}$$

$$C_{xx} = \frac{\text{Im}(H_{xx})}{\omega} \tag{9}$$

$$K_{xy} = \text{Re}(H_{xy}) \tag{10}$$

$$C_{xy} = \frac{\text{Im}(H_{xy})}{\omega} \tag{11}$$

Test Conditions and Seal Geometry. Table 1 summarizes the test conditions, and Table 2 gives the important seal dimensions.

Uncertainty of Test Data. Test data uncertainty results from individual uncertainties inherent with each instrument and the uncertainty of the Fast Fourier Transform (FFT) performed on the measured data to determine the impedances. Kurtin et al. [15] performed an uncertainty analysis of the instrumentation for this test rig. The uncertainties for the static parameters are shown in Table 3.

The uncertainty in the preswirl ratio arises primarily from measurement uncertainties in differential pressure with a reduced dependence on the inlet temperature and pressure and the running speed. Taking all of these factors into consideration, the calculated uncertainty for the 0.1 mm clearance at zero, medium, and high preswirl values is on the order of 100%, 10%, and 2.5%. For the 0.2 mm clearance cases, clearance at zero, medium, and high preswirl values is on the order of 100%, 2.6%, and 0.7%. The high relative uncertainties at zero preswirl arise because the measured preswirl is very small—on the same order as the uncertainty.

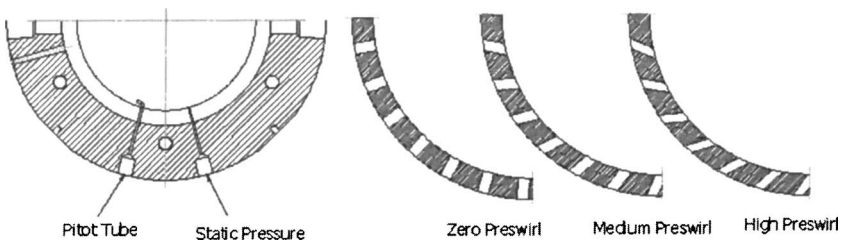

Fig. 4 Pivot tube location and preswirl rings

Downloaded 02 Jun 2010 to 171.66.16.98. Redistribution subject to ASME license or copyright; see http://www.asme.org/terms/Terms_Use.cfm

Table 2 Seal dimensions

Seal diameter	114.70 mm
No. of teeth	20
Length/diameter (L/D)	0.75
Tooth cavity width	4.3 mm
Tooth height	4.3 mm
Tooth thickness	0.254 mm

Table 3 Static uncertainty

Parameter	Uncertainty
Shaft speed (N)	10 rpm
Pressure (P)	3.747 kPa
Flow rate ($\dot{O}$)	0.177 l/min
Eccentricity ratio (ε)	0.05

These uncertainty values correspond to 1 sigma limits. The percentage uncertainties are higher at tight clearances because the leakage gas velocity leaving the preswirl rings is lower.

The dynamic tests are obviously aimed at measuring the rotor dynamic coefficients of the labyrinth seals. However, the measurement procedure will also measure stiffness and damping arising from the exit seals, hose connections, etc. To account for these additional elements, "baseline" tests are conducted with the test labyrinth seals removed. These tests are conducted at reduced supply pressures to match the "real test" backpressures experienced by the backpressure seals.

To estimate the variability of the dynamic data, ten consecutive tests are conducted at 15,200 rpm. During these tests, operating pressures are maintained as close to constant as possible. Each dynamic test consists of 32 separate shake tests, which are averaged over the frequency domain using power-spectral-density analysis. Thus, the uncertainties are obtained for an average of 320 shakes. The data from these tests are reduced, and the standard deviation of the impedances and rotor dynamic coefficients are obtained for discrete frequencies. The standard deviation obtained from these tests for both the baseline and test seals define the error bars. The overall test uncertainty is calculated as the square root of the sum of the squares of baseline uncertainty and seal test uncertainty. The average uncertainty for the frequency range is displayed on the plots for the impedances.

Results

Test results will be reviewed in terms of the questions posed at the outset of this paper.

Are the rotordynamic coefficients frequency dependent? A typical plot of the impedances versus excitation frequency is shown in Fig. 5. Note that the direct and cross-coupled damping terms [defined from Eqs. (8) and (10) as the slopes of $\mathrm{Im}(H_{xx})$, $\mathrm{Im}(H_{yy})$, and $\mathrm{Im}(H_{xy})$, $\mathrm{Im}(H_{yx})$, respectively] are *frequency independent*. The cross-coupled stiffness [$\mathrm{Re}(H_{xy})$, $\mathrm{Re}(H_{yx})$ in Eq. (9)] shows frequency independency out to a frequency of 150 Hz. However, the direct stiffness [$\mathrm{Re}(H_{xx})$ and $\mathrm{Re}(H_{yy})$ in Eq. (7)] seems to be frequency dependent. Figure 5 also shows the magnitude of the uncertainties for the tests.

Small errors in the stator mass are responsible for the apparent frequency dependency of the direct-stiffness coefficient. Equation (3) shows that the stator mass is an important parameter in identifying the test impedances. The stator mass used in the calculations is obtained by weighing the stator assembly with all the accessories such as hoses and pitch stabilizers. This mass is 43.97

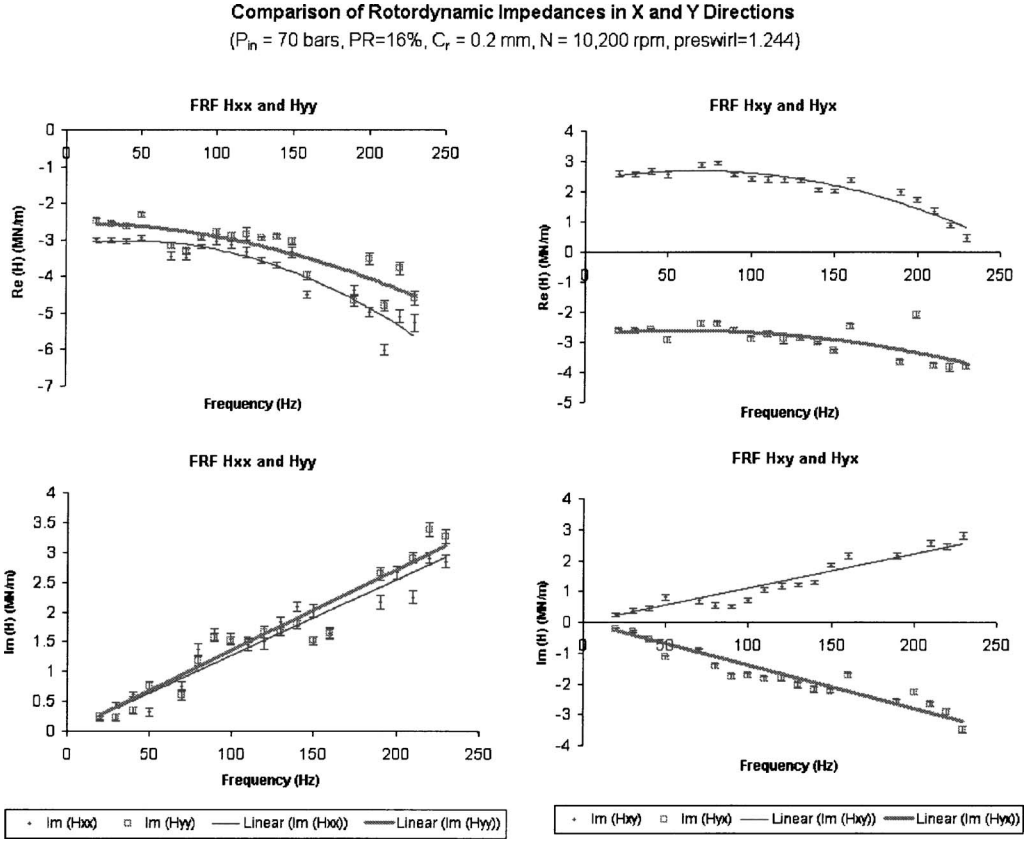

Fig. 5 Impedance plots at 10,200 rmp, high preswirl, 16% PR and C_r=0.2 mm

Downloaded 02 Jun 2010 to 171.66.16.98. Redistribution subject to ASME license or copyright; see http://www.asme.org/terms/Terms_Use.cfm

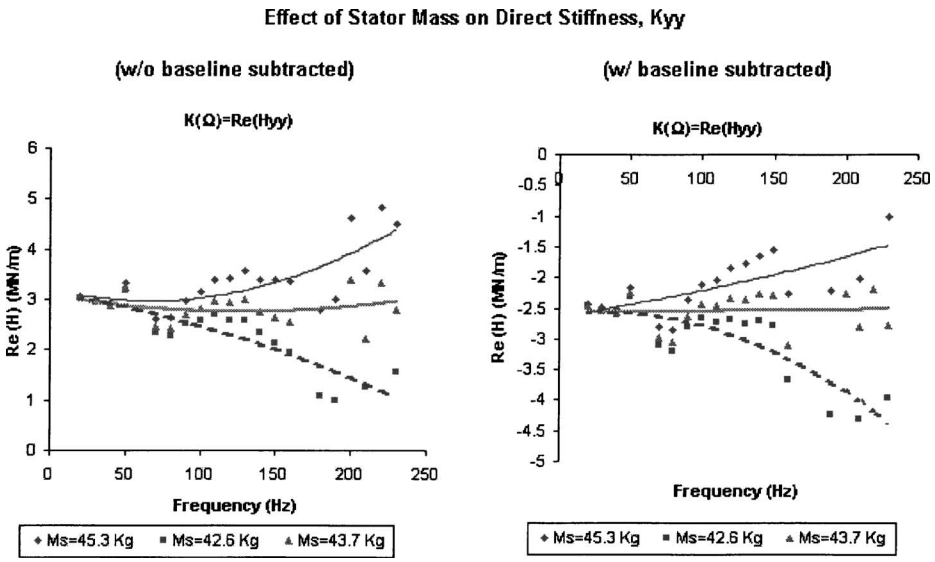

Fig. 6 Effect of change in stator mass on direct stiffness

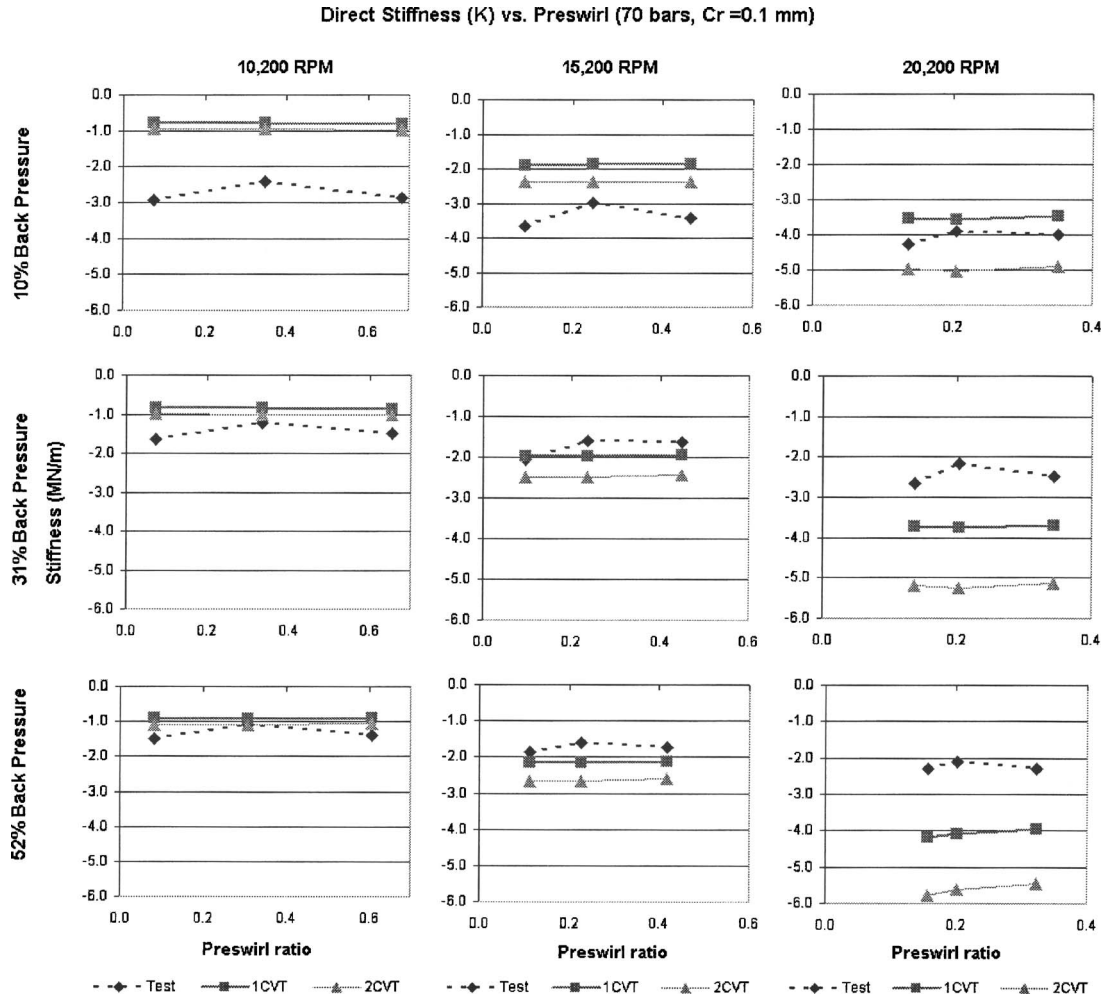

Fig. 7 Predictions versus measured direct stiffness for C_r=0.1 mm

Downloaded 02 Jun 2010 to 171.66.16.98. Redistribution subject to ASME license or copyright; see http://www.asme.org/terms/Terms_Use.cfm

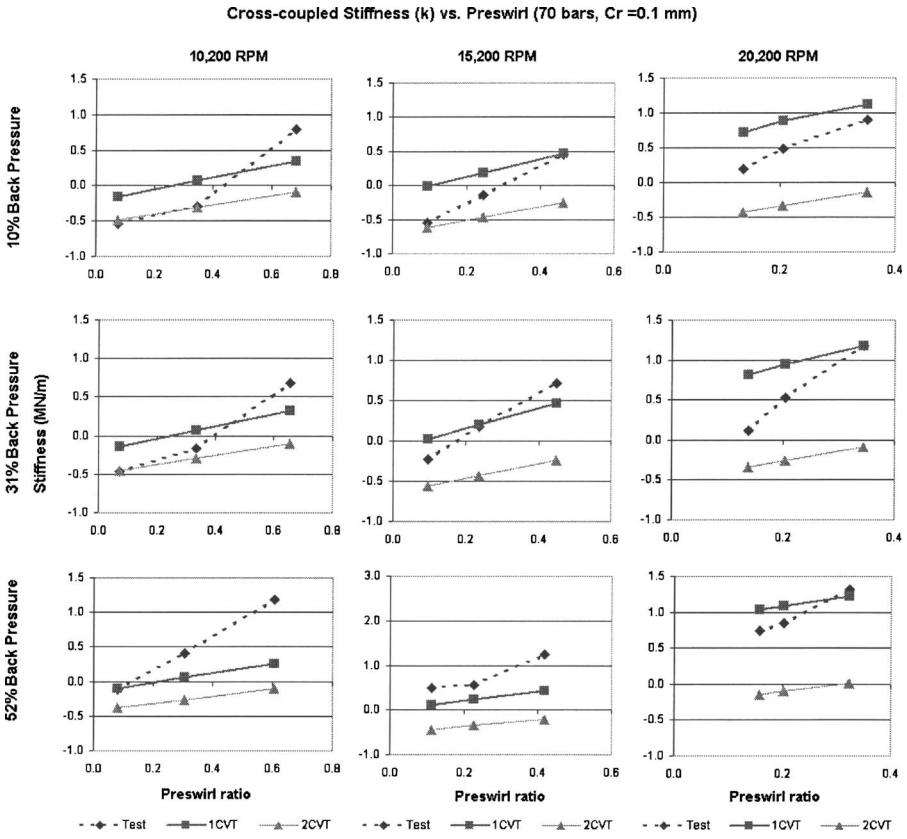

Fig. 8 Predictions versus measured cross-coupled stiffness for C_r=0.1 mm

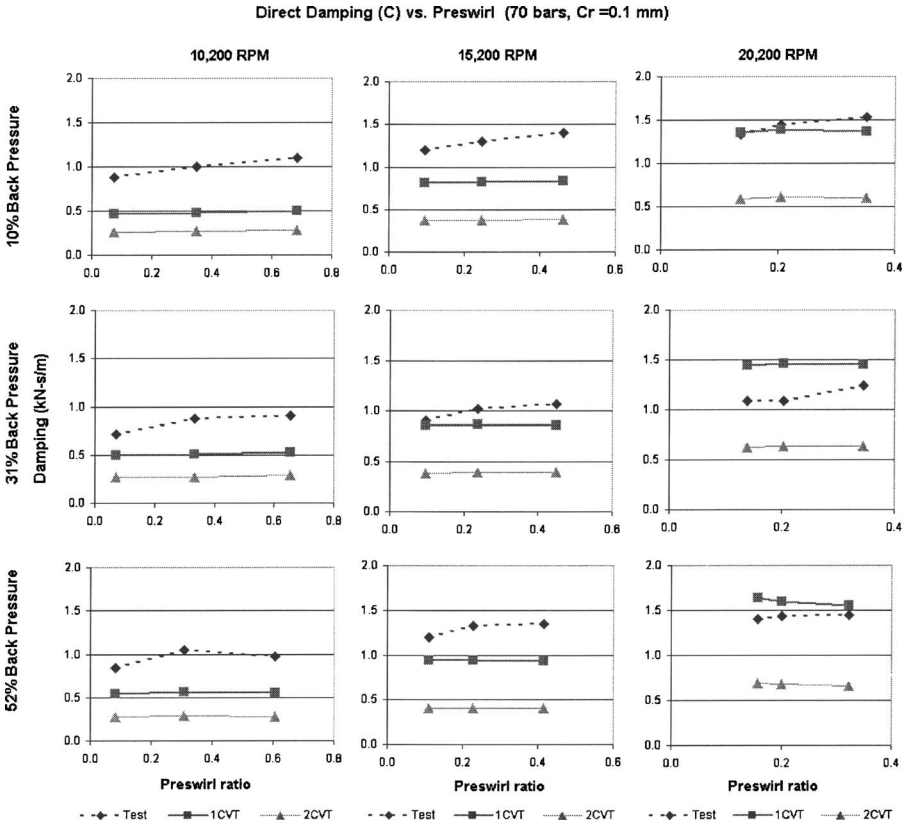

Fig. 9 Predictions versus measured direct damping for C_r=0.1 mm

Downloaded 02 Jun 2010 to 171.66.16.98. Redistribution subject to ASME license or copyright; see http://www.asme.org/terms/Terms_Use.cfm

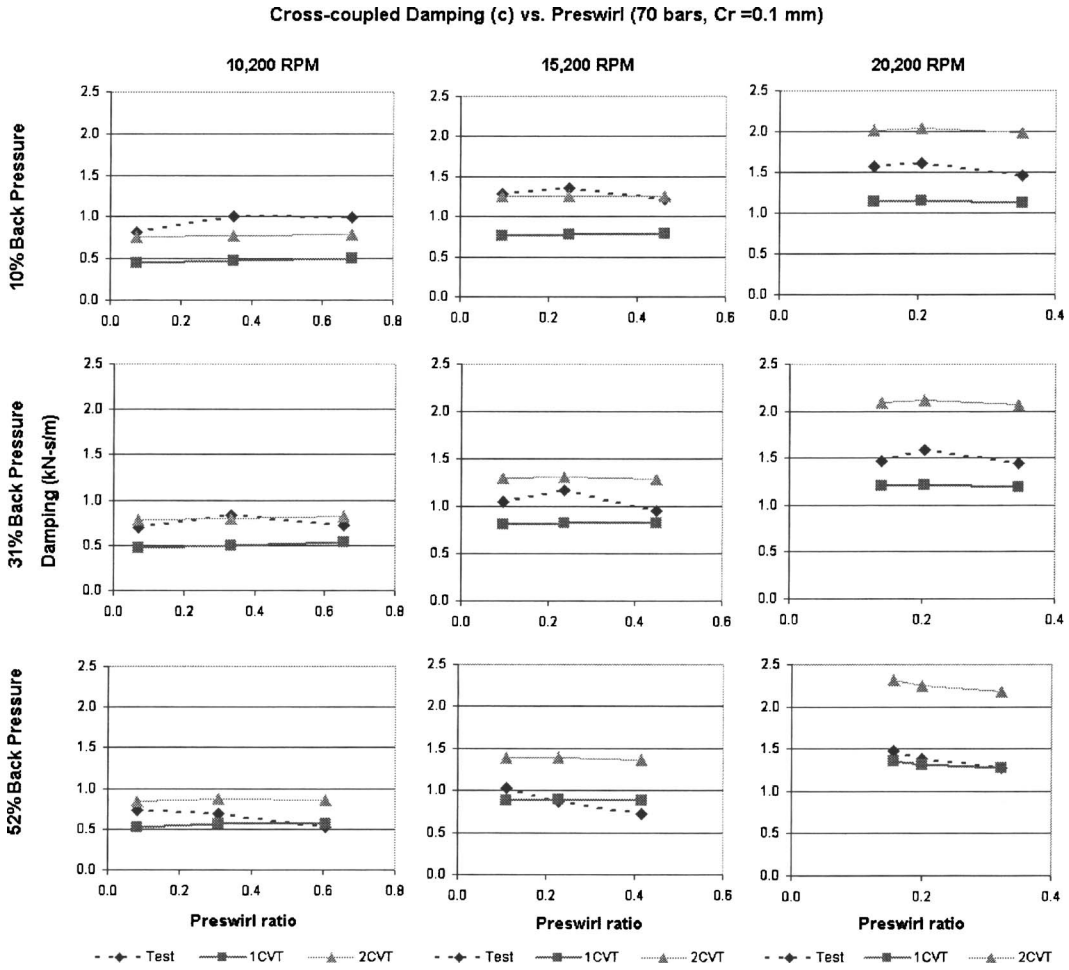

Fig. 10 Predictions versus measured cross-coupled damping for C_r=0.1 mm

kg. Fig. 6 shows the variation of the real part of the direct impedance, H_{yy} at three different stator masses, 45.3, 42.6, and 43.7 kg. Note that the direct stiffness shown in Fig. 5 is obtained at the following conditions: 10,200 rpm, preswirl ratio=1.244, C_r =0.2 mm, and P_i=70 bar-a, PR=16%. Thus a stator mass (m_s) can be chosen such that the direct stiffness is frequency independent (see Fig. 6).

From the trend lines fitted to the real part of H_{yy} for different stator masses, direct stiffness is frequency independent for a stator mass of 43.7 kg. The average stator mass of 43.18 kg from all the tests conducted was used for reducing the data and calculating the impedances. Similar computation for the baseline yielded a stator mass of 42.5 kg. Figure 6 also shows the effect of stator mass on direct stiffness when the baseline results are subtracted. In the balance of this paper, cited values for direct stiffness coefficients are the zero-frequency intercept of H_{xx} and H_{yy}. Although not shown here, changing the stator mass has negligible influence on the remaining coefficients.

A reasonable explanation for this change in the stator mass is that at higher backpressures the exhaust hoses are filled with higher pressure air and are stiffer, resulting in a higher resistance to motion, and causing more mass to be excited. Also, note that the labyrinth seal direct stiffness coefficients are quite small and would have a minimal influence on the rotordynamic characteristics of a compressor or steam turbine rotor.

In the centered position does $K_{xx}=K_{yy}=K$? $C_{xx}=C_{yy}=C$? $K_{xy}=K_{yx}=k$? and $C_{xy}=C_{yx}=c$? Figure 5 shows that $K_{xx}\approx K_{yy}=K$ and $C_{xx}\approx C_{yy}=C$. Figure 5 also shows that the cross-coupled stiffness terms are equal in magnitude with opposite sign up to a frequency of 150 Hz. Although, the cross-coupled stiffness coefficients are of opposite signs, for excitation frequencies beyond 150 Hz, notice that the magnitudes are different ($|H_{xy}|\neq|H_{yx}|$). This behavior is not seen for the data obtained with medium preswirl test configuration. At present, the authors have no explanation for this result. The cross-coupled damping coefficients are equal in magnitude with opposite sign.

How do the measured coefficients compare with predictions from the bulk-flow model predictions? Data are presented for a seal clearance (C_r) of 0.1 mm. Results obtained at C_r=0.2 mm are similar to the coefficients obtained at C_r=0.1 mm. Details of the impedances and the magnitude of the uncertainty can be obtained from Picardo [14]. Comparisons are made with theoretical predictions obtained from Childs and Scharrer's one-control volume model (1CVM) and Scharrer's two-control-volume model (2CVM).

Figures 7 and 8 compare the predicted and measured direct stiffness coefficients obtained at C_r=0.1 mm. The test data are shown in dotted line, 1CVM predictions are shown in thick continuous line and 2CVM predictions are shown in thin solid line. The columns represent the speeds, and the rows represent the pressure ratio (PR=P_e/P_i). The flow is choked at a backpressure of 10% and unchoked for the other pressure ratios (31% and 52%). Code predictions only provide reasonable predictions at 10,200 rpm with 31% and 52% PR. The 1CVM predictions are closer to test data. However, both models overpredict the stiffness coefficients by a factor of 2–2.5 at 52% PR and 20,200 rpm. Both models correctly predict direct stiffness coefficients that are inde-

Downloaded 02 Jun 2010 to 171.66.16.98. Redistribution subject to ASME license or copyright; see http://www.asme.org/terms/Terms_Use.cfm

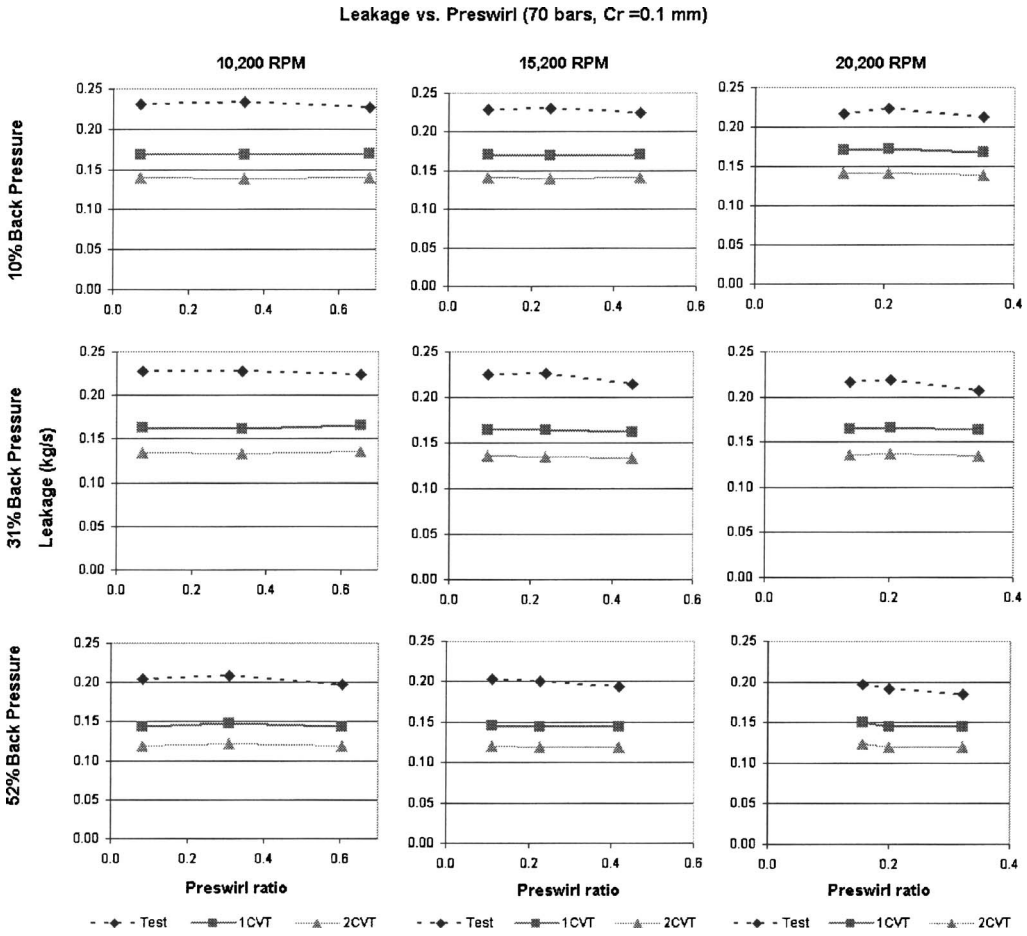

Fig. 11 Predictions versus measured seal leakage for C_r=0.1 mm

pendent of preswirl.

Figure 8 presents measured and predicted values of k versus preswirl for Cr=0.1 mm. Note that measured k values increase more rapidly with increasing preswirl than the 1CV model predictions. The 1CVM under predicts the negative cross-coupled stiffness coefficients at the low preswirl condition with PR of 10% and 31% at 10,200 rpm. The 2CV model incorrectly predicts negative cross-coupled stiffness coefficients at the medium and high preswirl condtitions tested. Results from the 1CV model, although displaying considerable variation, show better agreement in terms of predicting the trend.

Figure 9 compares predictions with measured direct damping coefficients (C) for Cr=0.1 mm. Both models correctly predict an increase in damping with increase in speed (increase in rotor speed reduces the preswirl ratio from Eq. (3)), for a given PR. However, both models greatly under-predict damping at 10,200 and 15,200 rpm. At 20,200 rpm the 1CV model overpredicts damping for 31% and 52% PR. Again, the 1CV model performs better than the 2CV model. At 10% PR or highest DP, the 1CV model under predicts damping by a factor of about 2 at 10,200 and 15,200 rpm. Similar trends are seen for a seal clearance of 0.2 mm from Picardo [14]. However, the direct damping coefficients for Cr=0.2 mm increase more sharply with increase in preswirl than for Cr=0.1 mm.

Cross-coupled damping coefficients of seals are not considered important in rotordynamic analysis. However, they add to the direct stiffness coefficients to get the effective stiffness. Figures 10 and 11 compare predictions and measured cross-coupled damping values for C_r=0.1 mm. The 2CV model performs better than the 1CV model at 10,200 rpm and at 15,200 rpm at pressure ratios of 10% and 31%.

Figure 11 shows that the seal leakage remains fairly constant with increase in preswirl. The 1CV model is more accurate than the 2CV model. However, the 1CV model underpredicts the observed leakage by a factor of about 1.3.

Effective damping, given by Eq. (12) provides a good basis for comparing the stabilizing characteristics of seal configurations. Figure 12 compares predictions and measurements of effective damping for Cr=0.1 mm. At 10% PR and 31% PR and 10,200 and 15,200 rpm predictions are lower than measured values. The predictions from the 1CV model match with the measured effective damping values at 52% PR at all speeds. This is not surprising since the 1CV model had under predicted both the cross-coupled stiffness and the direct damping coefficients. However, the predictions at Cr=0.1 mm do not agree as well with measurements as the predictions for Cr=0.2 mm.

$$C_{\text{eff}} = C - \frac{k}{\Omega} \tag{12}$$

Figure 13 compares the effective damping obtained at C_r =0.2 mm and C_r=0.1 mm. Effective damping at the two clearances is about equal.

Comparison Between Hole-pattern and Labyrinth Seal Coefficients. Nondimensional and normalized coefficients for the labyrinth seal are compared with hole-pattern seal coefficients measured by Wade and Childs [16]. They measured the rotordynamic coefficients for a hole-pattern seal with a cell diameter of 3.18 mm (1/8 in.), a hole-depth of 3.3 mm (130 mils), and a cell to area ratio of 68.4%. The stiffness coefficients are nondimen-

Downloaded 02 Jun 2010 to 171.66.16.98. Redistribution subject to ASME license or copyright; see http://www.asme.org/terms/Terms_Use.cfm

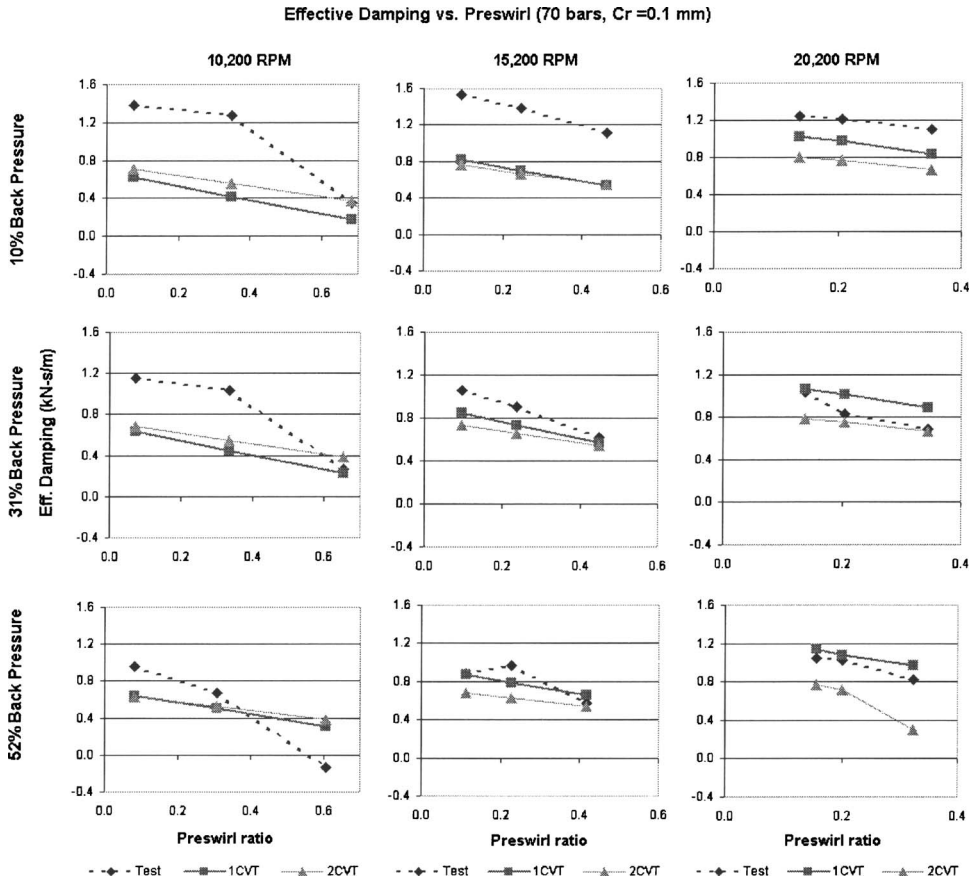

Fig. 12 Predictions versus measured effective damping for C_r=0.1 mm

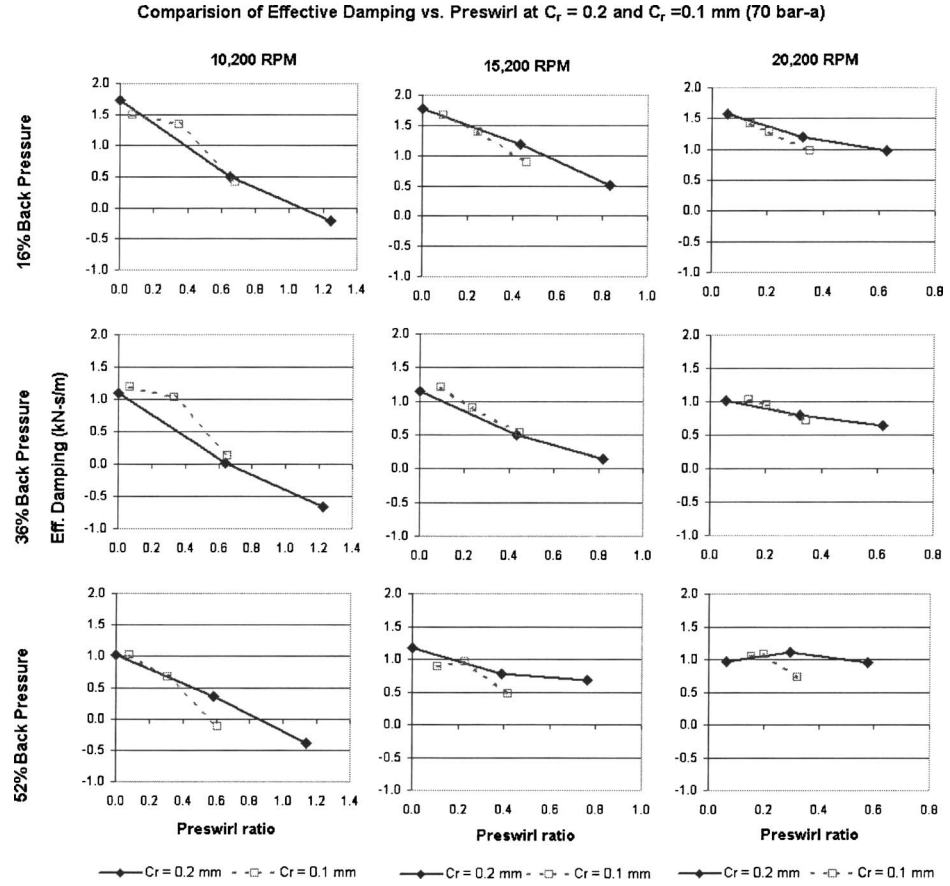

Fig. 13 Comparison of effective damping between C_r=0.2 and C_r=0.1 mm

Downloaded 02 Jun 2010 to 171.66.16.98. Redistribution subject to ASME license or copyright; see http://www.asme.org/terms/Terms_Use.cfm

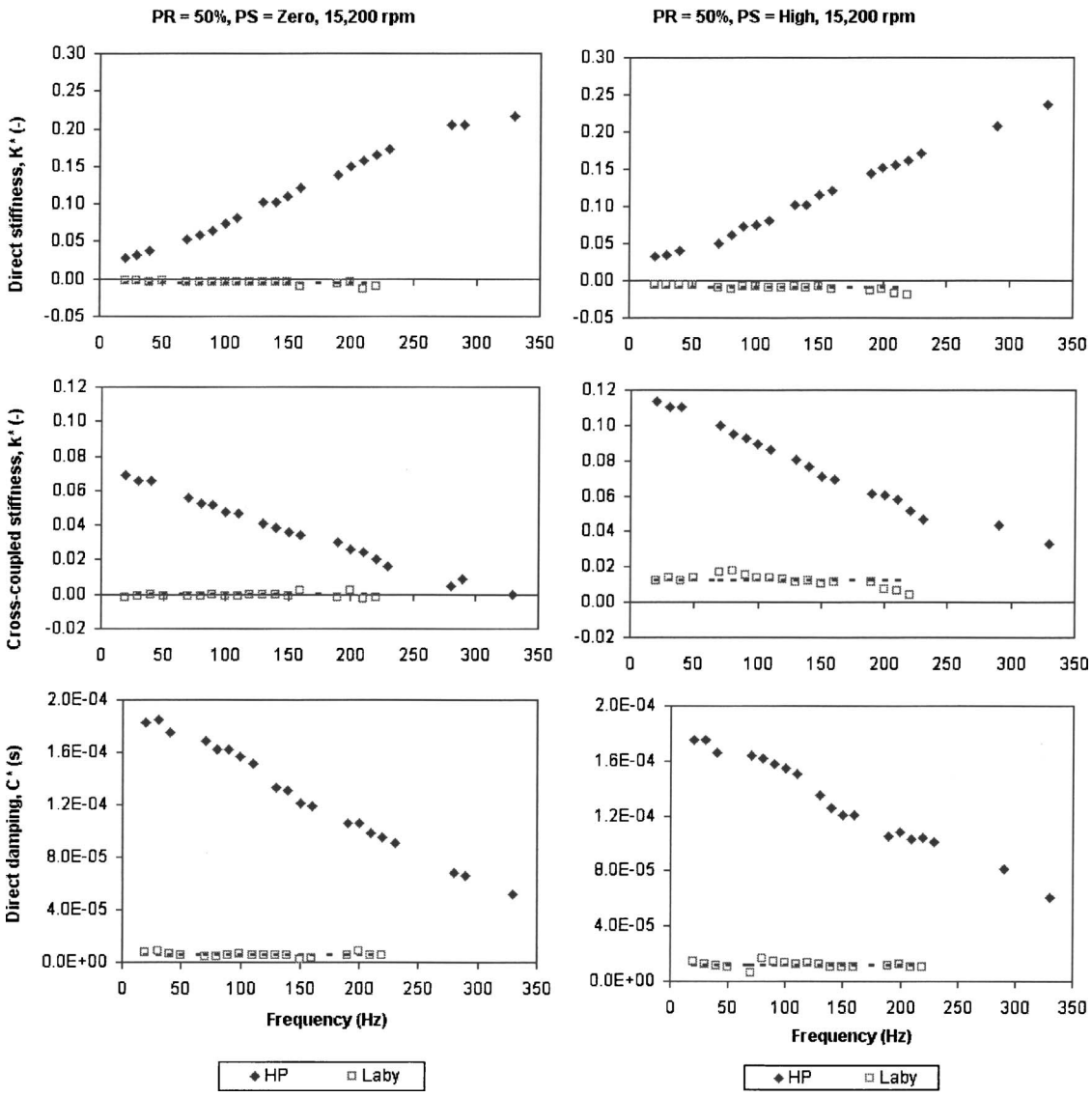

Fig. 14 Nondimensional and normalized coefficients, hole-pattern versus labyrinth seal

sionalized using Eq. (13). The normalized damping coefficients (dimension of seconds) are obtained from the same equation by replacing K with C.

$$K^* = \frac{K}{\left[\frac{L \cdot D \cdot \Delta P}{C_r}\right]} \tag{13}$$

Since most industrial applications for these seals are at a pressure ratio of 50% and a speed of about 15,200, comparison between the two seal types (Figs. 14 and 15) is done at 15,200 rpm and 50% PR (52% PR for the labyrinth seal and 48% PR for the hole-pattern seal). The first column denotes the zero preswirl data and the second column denotes high preswirl (ratio=1.2) data.

Figure 14 shows the comparison between the nondimensional (ND) hole-pattern (identified as HP) and labyrinth seal (identified as Laby) coefficients obtained at C_r=0.2 mm. The first, second, and third rows show the ND direct stiffness (K^*), ND cross-coupled stiffness (k^*), and normalized direct damping (C^*) coefficients, respectively.

In contrast to the labyrinth seals, the stiffness and damping coefficients for hole-pattern seals are frequency dependent. Both the direct stiffness and cross-coupled stiffness coefficients for the hole-pattern seal are much larger than the coefficients for labyrinth seals. The ND damping coefficients for hole-pattern seals keep decreasing with increase in frequency. The direct damping coefficient for labyrinth seals is lower by a factor of about 30 when compared to the damping coefficient for hole pattern seals, at a frequency range 70–100 Hz.

Figure 15 compares the effective stiffness and damping coefficients of hole-pattern and labyrinth seals at Cr=0.2 mm. The effective stiffness, effective cross-coupled stiffness, and effective damping coefficients given by Eqs. (14), (15), and (12), respectively, are presented.

$$K_{\text{eff}} = K + c \cdot \Omega \tag{14}$$

Downloaded 02 Jun 2010 to 171.66.16.98. Redistribution subject to ASME license or copyright; see http://www.asme.org/terms/Terms_Use.cfm

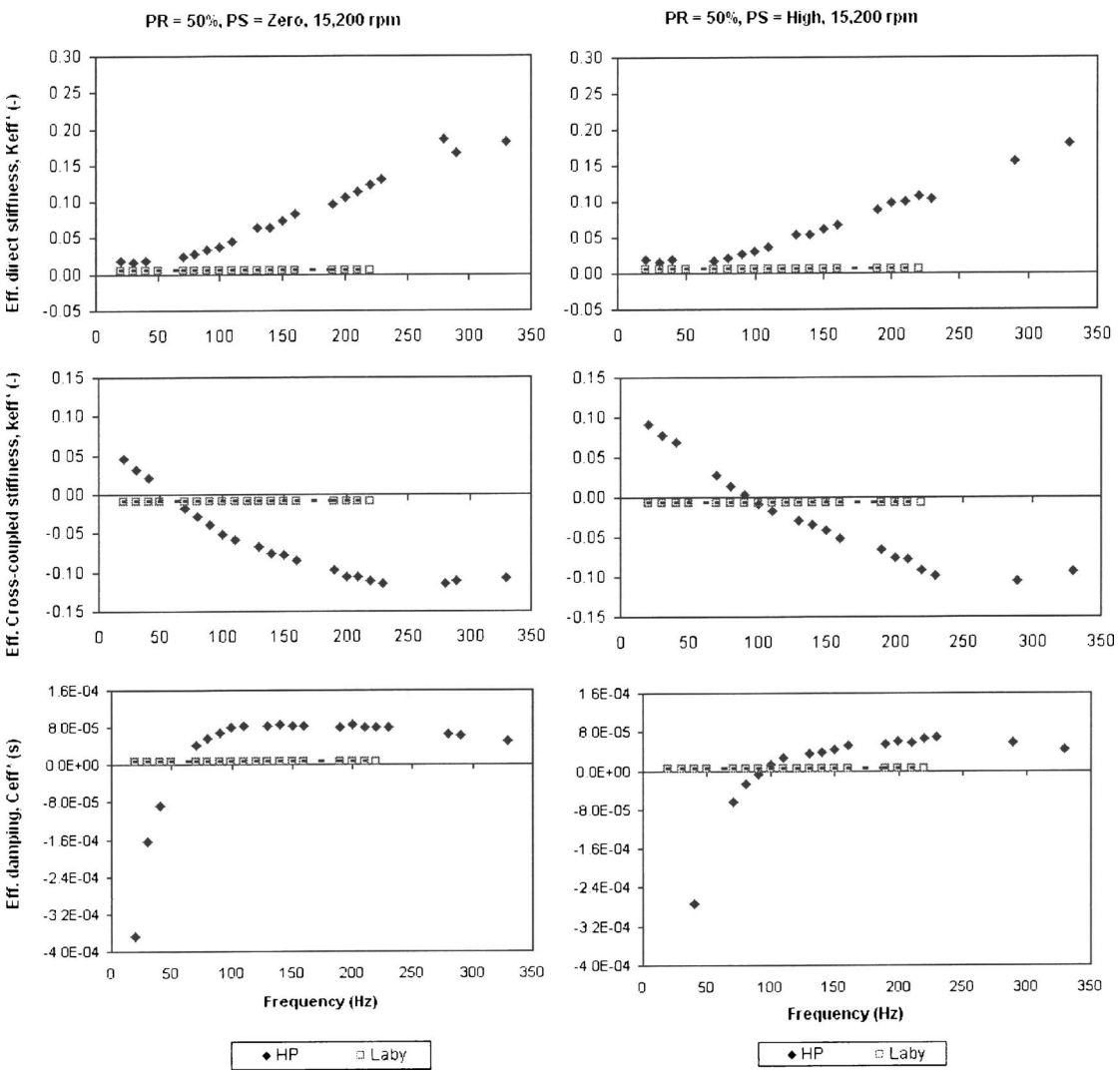

Fig. 15 Nondimensional and normalized effective stiffness and damping coefficients, hole-pattern versus labyrinth seal

$$k_{\text{eff}} = k - C \cdot \Omega \tag{15}$$

where Ω is the running speed for labyrinth seals and is the excitation frequency (w) for hole-pattern seals.

From Fig. 15, the effective stiffness (K_{eff^*}) for the labyrinth seals is positive but close to zero at both preswirl ratios, whereas K_{eff^*} for hole-pattern seals is also positive but increases with increasing frequency. (Negative values of K_{eff^*} were measured at low frequencies for a hole-pattern seal with a hole-depth of 3.175 mm. Extrapolating the data for this deeper-hole seal resulted in negative values at zero-frequency. Negative direct "static" stiffnesses can cause serious problem.)

The effective cross-coupled stiffness (k_{eff^*}) for the hole-pattern seals is positive up to a frequency of 60 Hz for zero preswirl and up to 100 Hz for high preswirl. For labyrinth seals, k_{eff^*} is close to zero. For hole-pattern seals, the effective damping (C_{eff^*}) is negative up to a frequency of 60 Hz at zero preswirl and up to 100 Hz at high preswirl.

From a stability viewpoint, a seal configuration's effectiveness-depends on the location of a rotor's first natural frequency. For the present test results, a natural frequency below 60 Hz (no preswirl implying a swirl brake) or 110 Hz (high preswirl, no swirl brake) would be stabilized by a labyrinth seal and destabilized by a hole-pattern seal. If the natural frequency is above these values, hole-pattern seals would perform much better. Very low natural frequencies can arise in compressors that use squeeze-film dampers and softly mounted rotors.

Fig. 16 compares the normalized effective damping of the hole-pattern and honeycomb seals at C_r=0.1 mm. The frequency at which either the effective damping changes from negative to positive or the effective cross-coupled stiffness changes from positive to negative is termed as the "crossover" frequency. The "crossover" frequency for the hole-pattern seal is the same ($\approx$60 Hz) for both the clearances with zero fluid preswirl. However, comparing Figs. 15 and 16, with high fluid preswirl the cross over frequency changes to about 70 Hz in the case of C_r =0.1 mm, compared to 110 Hz at C_r=0.2 mm. Hence, for high fluid preswirl, with tighter clearances the hole-pattern seals become more effective than the labyrinth seals at a lower running speed.

Figure 17 compares the seal leakage versus the seal differential pressure, between ladyrinth and hole-pattern at 15,200 rpm and zero preswirl. Data for the other speeds and preswirls are similar. The hole-pattern seal leaks slightly more than the labyrinth seal at

Downloaded 02 Jun 2010 to 171.66.16.98. Redistribution subject to ASME license or copyright; see http://www.asme.org/terms/Terms_Use.cfm

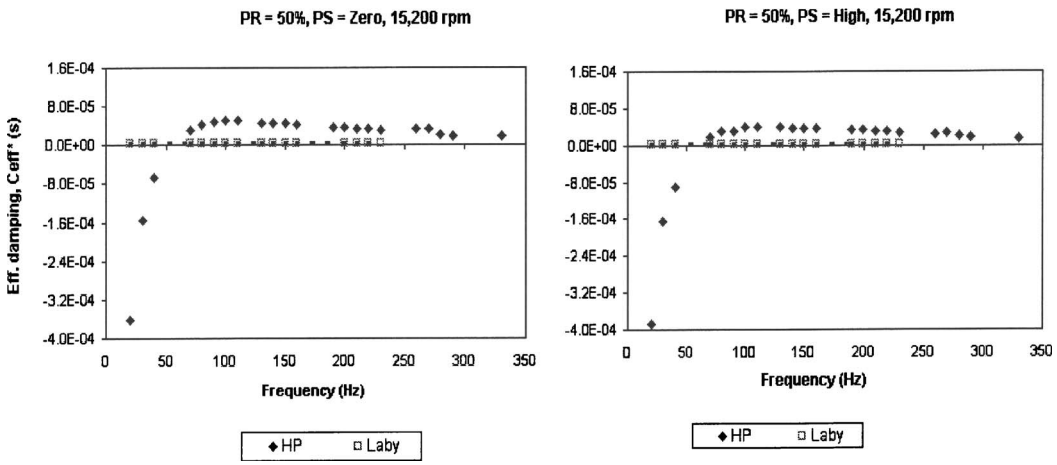

Fig. 16 Normalized effective damping coefficients, hole-pattern versus labyrinth seal, C_r=0.1 mm

C_r=0.2 mm. However, at the reduced clearance (C_r=0.1 mm) the hole-pattern seal leaks slightly less than the labyrinth seal.

Conclusions and Discussion

(1) The rotor dynamic coefficients for labyrinth seals are frequency independent up to a frequency of 150 Hz.
(2) Cross-coupled stiffness coefficients are equal in magnitude with opposite signs ($K_{xy}=-K_{yx}$).
(3) Bulk-flow models under predict the effect of preswirl on the rotor dynamic coefficients especially the cross-coupled stiffness and direct damping coefficients. Predictions from the bulk-flow models at zero preswirl are acceptable. The bulk-flow models also under predict seal leakage. Bulk-flow models for labyrinths incorporate empirical leakage models that can be adjusted to improve leakage predictions; however, these adjustments do not markedly change the rotordynamic predictions.
(4) Decreasing the labyrinth seal clearance (from 0.2 mm to 0.1 mm) does not have much effect on effective damping and stability.

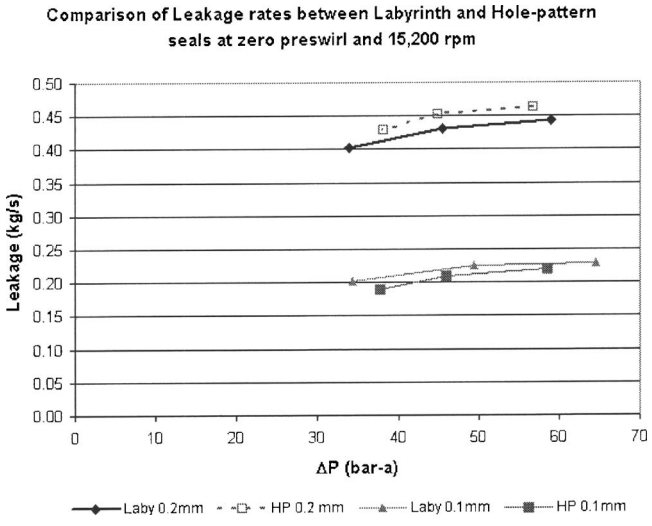

Fig. 17 Comparison of leakage, labyrinth versus hole-pattern seals

(5) Labyrinth seal rotordynamic coefficients magnitudes are much smaller than hole-pattern seal coefficients.
(6) Softly supported compressors, incorporating squeeze-film dampers, can have very low natural frequencies. Hole-pattern seals are destabilizing below a "crossover" frequency that can be reduced via swirl brakes. If the "crossover" frequency is below the natural frequency, a hole-pattern seal will enhance stability. If it is above, it will degrade stability. Labyrinth seals may be a better choice for these compressors, and a retrofit from labyrinth to hole-pattern seals should be approached carefully.
(7) Labyrinth seals leak about 5% less than hole-pattern seals at the larger clearance. Seal leakage is halved with a 50% reduction in clearance for the labyrinth seals.

The poor comparisons between measurements and predictions from bulk-flow codes argue strongly for ending the use of bulk-flow models in favor of CFD calculations. The experimental results presented here should be useful for anchoring CFD predictions. Neither of the bulk-flow models used here captures the flow physics adequately for the comparatively simple "see-through" labyrinths tested. More complicated interlocking labyrinths are even less likely to be modeled adequately by bulk-flow models. Longer balance-piston and division-wall seals that have a major impact on rotordynamics are likely candidates for CFD calculations. The failure of bulk-flow models for labyrinth seals stands in contrast to their successful application to hole-pattern stator seals 16.

Acknowledgment

The work reported here was supported in part by the Turbomachinery Research Consortium.

Nomenclature

A_{ij} = stator acceleration (L/T2)
C_r = radial clearance (L)
C = direct damping (FT/L)
c = cross-coupled damping (FT/L)
C_{ij} = damping coefficient (FT/L)
C_{eff} = effective damping (FT/L)
C^* = normalized direct damping (1/T)
D = seal diameter (L)
D_{ij} = relative displacement (L)
F_s = seal reaction forces (F)

Downloaded 02 Jun 2010 to 171.66.16.98. Redistribution subject to ASME license or copyright; see http://www.asme.org/terms/Terms_Use.cfm

F_{ij} = force (F)
H_{ij} = impedance (F/L)
j = $\sqrt{-1}$
K = direct stiffness (F/L)
K^{eff} = effective direct stiffness (F/L)
K^* = nondimensional direct stiffness
k = cross-coupled stiffness (F/L)
K_{ij} = stiffness coefficient (F/L)
m_s = stator mass (M)
N = rotor speed (1/T)
P_i = inlet pressure (F/L2)
P_e = exit pressure (F/L)]
PR = pressure ratio
PS = preswirl ratio
V_t = inlet circumferential velocity (L/T)
$\dot{X},\dot{Y}$ = velocities (L/T)
ΔP = differential pressure (F/L2)
ω = excitation frequency (1/T)
Ω,N = running speed (1/T)

Subscripts

ij = direction of force and response
eff = effective

References

[1] Iwatsubo, T., 1980, "Evaluation of Instability of Forces of Labyrinth Seals in Turbines or Compressors," Workshop on Rotordynamic Instability Problems in High-Performance Turbomachinery, Texas A&M University, NASA Conference Publication No. 2133, pp. 139–67.

[2] Benckert, H., Wachter, J., 1980, "Flow Induced Spring Constants of Labyrinth Seals," IMechE, Proceedings of the Second International Conference, Vibrations in Rotating Machinery, Cambridge, England, pp. 53–63.

[3] Childs, D., Scharrer, J., 1986, "Experimental Rotordynamic Coefficient Results for Teeth-on-Rotor and Teeth-on-Stator Labyrinth Gas Seals," J. Eng. Gas Turbines Power **108**, pp. 599–604.

[4] Childs, D., Scharrer, J., 1988, "Theory Versus Experiment for the Rotordynamic Coeffcient of Labyrinth Gas Seals: Part II—A Comparrison to Experiment," J. Vibr. Acoust. **110**, pp. 281–287.

[5] Pelletti, J., 1990, "A Comparison of Experimental Results and Theoretical Predictions for the Rotordynamic Coefficients of Short (L/D=1/6) Labyrinth Seals," M.S. thesis, Texas A&M University.

[6] Wyssmann, H., Pham, T., Jenny, R., June 1984, "Prediction of Stiffness and Damping Coefficients for Centrifugal Compressor Labyrinth Seals," ASME Paper No. 84-GT-86.

[7] Wagner, N. G., and Steff, K., 1996, "Dynamic Labyrinth Coefficients from a High-Pressure Full-Scale Test Rig Using Magnetic Bearings," *Proceedings of the Conference on Rotordynamic Instability Problems in High-Performance Turbomachinery*, NASA Conference Publication, No. 3344, pp. 95–111.

[8] Weatherwax, M., and Childs, D. W., 2002, "The Influence of Eccentricity on the Leakage and Rotordynamic Coefficients of a High-Pressure Honeycomb Annular Gas Seal, Measurements Versus Predictions," ASME Paper No. 2002-TRIB-207.

[9] Dawson, M. P., Childs, D., Holt, C., and Phillips, S., 2002, "Theory Versus Experiments for the Dynamic Impedances of Annular Gas Seals: Part 2—Smooth and Honeycomb Seals," ASME J. Eng. Gas Turbines Power, **24**, pp. 963–970.

[10] Childs, D., and Scharrer, J., 1986, "Iwatsubo-Based Solution for Labyrinth Seals: Comparison to Experimental Results," J. Eng. Gas Turbines Power, Transactions of the ASME, **108**, pp. 325–331.

[11] Scharrer, J., 1988, "Theory Versus Experiment for the Rotordynamic Coefficient of Labyrinth Gas Seals: Part I—A Two Control Volume Model," J. Vibr. Acoust., **110**, pp. 270–280.

[12] Childs, D., and Hale, K., 1994, "A Test Apparatus and Facility to Identify the Rotordynamic Coefficients of High-Speed Hydrostatic Bearings," ASME J. Tribol., **116**, pp. 337–334.

[13] Marquette, O. R., Childs, D. W., and San Andres, L., 1997, "Eccentricity Effects on the Rotordynamic Coefficients of Plain Annular Seals: Theory Versus Experiment," Trans. ASME, **119**, pp. 443–448.

[14] Picardo, A. M., 2003, "High Pressure Testing of Labyrinth Seals," M.S. thesis, Mechanical Engineering department, Texas A&M University, College Station, TX.

[15] Kurtin, K. A., Childs, D. W., San Andres, L. A., and Hale, R. K., 1993, "Experimental Versus Theoretical Characteristics of a High-Speed Hybrid (Combination Hydrostatic and Hydrodynamic) Bearing," ASME J. Tribol., **115**, pp. 160–169.

[16] Wade, J. L., and Childs, D. W., 2003, "Rotor Dynamic Coefficient and Leakage Characteristics for a Hole-Pattern-Stator Annular Gas Seal Versus Predictions," 2003 STLE/ASME International Joint Tribology Conference (to be published).

Downloaded 02 Jun 2010 to 171.66.16.98. Redistribution subject to ASME license or copyright; see http://www.asme.org/terms/Terms_Use.cfm

Characterization of Turbine Blade Friction Dampers

K.-H. Koh

J. H. Griffin

S. Filippi[1]

A. Akay

Department of Mechanical Engineering,
Carnegie Mellon University,
Pittsburgh, PA 15213

This paper discusses an approach for characterizing the dynamic behavior of a friction damper. To accomplish this, the deflection of the damper is measured as a function of an applied force for a range of amplitudes, normal loads, and excitation frequencies. The resulting hysteresis curves are used to generate curves of nonlinear stiffness and damping as a function of the amplitude of motion. A method of presenting this information in a dimensionless format is demonstrated. This format allows direct comparisons of the nonlinear stiffness and damping of actual dampers with that often used in analytical models to compute the dynamic response of frictionally damped turbine blades. It is shown that for the case of a damper with a spherical head significant differences exist between the actual behavior of the damper and that often assumed in simple analytical models. In addition, Mindlin's analysis of a sphere on a half space is used to estimate the damper's stiffness as well as its theoretical hysteresis curves. The hysteresis curves are then used to determine dimensionless stiffness and damping curves. The results compare favorably with those found experimentally. [DOI: 10.1115/1.1926312]

1 Introduction

Friction dampers are used in gas turbine engines to increase energy dissipation and reduce vibratory response. Dampers are pieces of metal that fit between the blades and that are held in place by centrifugal force. They dissipate energy when sliding occurs across the friction interface. In addition, the damper acts like a weak nonlinear spring that affects the frequency of peak, vibratory response. Thus, friction dampers control the amplitude and, less strongly, the frequency of the peak response.

Two recent review papers on the general topic of friction damping are by Feeny et al. [1] and by Gaul and Nitsche [2]. Predicting and optimizing the performance of turbine blade friction dampers is an active area of research in its own right. For example, consider the review paper by Griffin [3], the papers by Yang and Menq [4–7], Sanliturk et al. [8], Petrov and Ewins [9,10], Szwedowicz et al. [11], Cha and Sinha [12,13], Csaba [14], and Sextro et al. [15]. Computer codes that developed from these research efforts are widely used by the gas turbine industry to predict and optimize damper performance. Nearly all of the codes use spring elements that can slip as their basic friction element [16]. For example, a friction damper that connects adjoining blade platforms may be modeled by a spring connection (or a series of spring connections in parallel) that slips if the magnitude of its force equals a certain limiting value, μN. Analyzing the effect of the friction force becomes more complex when the damper and blade's contact surfaces are inclined so that the normal load varies dynamically during a cycle [17,18] or if the relative motion across the contacting surfaces follows a two-dimensional path [19,20].

A significant effort has been made by engine manufacturers to assess how well the resulting computer codes predict damper behavior. Recently, the US Air Force Office of Scientific Research, the US Navy, and the Sandia National Laboratories sponsored two workshops on contact mechanics and friction damping [21]. It was attended by representatives from General Electric, Pratt and Whitney, Rolls Royce, and Siemens Westinghouse as well as representatives from academia and U.S. government. The general opinion expressed by the industrial representatives at the workshop was that the codes used by industry have to be calibrated with test data before they can be used to reliably predict the performance of a particular blade/damper design under engine conditions. Specifically, the consensus view was that the damper stiffness used in the computer code that correlates with the test data is usually significantly less than that calculated from a finite element model of the damper. The purpose of the research reported in this paper is to measure the properties of a real, but simple, damper and to assess why it might be difficult to characterize its behavior with a simple spring element.

In order to perform this assessment, a prototype damper with a spherical head was manufactured and tested under various conditions. The data from the resulting friction force-displacement hysteresis curves were processed to determine the damper's effective nonlinear damping and stiffness as a function of the amplitude of the motion across the friction interface. The results were then compared with that of the simple spring damper model and were seen to exhibit significant differences.

The contact problem of a sphere on a half space subjected to periodically applied shear loads was analyzed by Mindlin [22,23] and by Deresiewicz [24]. Experimental studies that support the theory have been reported by Mindlin [25], Johnson [26], and Goodman and Brown [27]. The hysteresis curves of damper with a spherical head in contact with a flat plate can be predicted analytically using Mindlin's analysis. The resulting curves can then be processed in the same manner as the experimental data to predict the damper's effective nonlinear damping and stiffness. It will be shown that Mindlin's solution accurately captures the experimental behavior of the damper over a range of testing conditions.

The organization of this paper is as follows. First, the analytical properties of the spring damper element are reviewed. They will be used as the benchmark in this study. Of specific interest is the manner in which the dimensionless, nonlinear stiffness, and damping curves are used to characterize its behavior. Section 3 will describe how the hysteresis curves of the test dampers are measured and then processed to get dimensionless, nonlinear stiffness and damping curves that can be compared with those of the spring damper. In Sec. 4, Mindlin's solution will be used to generate theoretical values of nonlinear stiffness and damping that are then compared with the experimental results. Implications of the results are discussed in Sec. 5. Concluding remarks are provided in the last section.

[1]On leave from Politecnico di Torino, Turin, Italy.

Contributed by the International Gas Turbine Institute (IGTI) of THE AMERICAN SOCIETY OF MECHANICAL ENGINEERS for publication in the ASME JOURNAL OF ENGINEERING FOR GAS TURBINES AND POWER. Paper presented at the International Gas Turbine and Aeroengine Congress and Exhibition, Vienna, Austria, June 13–17, 2004. Paper No. GT2004-53278. Manuscript received by IGTI, October 1, 2003; final revision, March 1, 2004. IGTI Review Chair: A. J. Strazisar.

 Copyright © 2005 by ASME

Downloaded 02 Jun 2010 to 171.66.16.98. Redistribution subject to ASME license or copyright; see http://www.asme.org/terms/Terms_Use.cfm

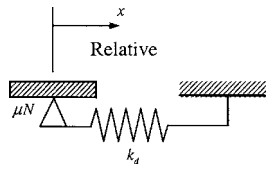

Fig. 1 Spring damper element

2 Spring Damper Model: Benchmark

To understand how friction dampers work, consider the case of a single degree of freedom oscillator constrained by the spring friction damper shown in Fig. 1. For a spring damper the energy dissipated during one cycle of motion is the area enclosed by the bilinear hysteresis curve shown in Fig. 2. It is considered a "macroslip" element since it does not dissipate any energy unless there is gross slip across the interface. It is characterized by its stiffness, k_d, and the slip load, N.

If the nonlinear friction force from the spring damper that resists the motion is f_N, the equation of motion is

$$m\ddot{x} + c\dot{x} + kx = f_0 \cos \omega t - f_N(t) \tag{1}$$

The nonlinear friction force may be approximated by a spring and viscous damper acting in parallel, i.e.,

$$f_N(t) \approx k_e x + c_e \dot{x} \tag{2}$$

The effective stiffness and damping are found using the Harmonic Balance (HB) method. Some examples of the application of HB method can be found in [16,28–30]. In the HB method it is assumed that the displacement is sinusoidal and that the nonlinear force has the same period as the motion. The force is expanded in a Fourier series and truncated after its fundamental terms since the mass spring system is an oscillator that filters out the higher frequency components. The fundamental terms in the Fourier series can be expressed so that one is in-phase with the motion and one is out-of-phase. The in-phase term effectively represents a spring force and the out-of-phase term an equivalent damping force. Since the Fourier coefficients depend on the amplitude of the motion, the effective stiffness and damping are nonlinear functions of the amplitude. The amplitude of the motion can be normalized by dividing by the distance required to cause slip, i.e., $\tilde{A} = A/(\mu N/k_d)$. Then the nondimensionalized effective stiffness and damping of the spring friction element are given by the equations [31]:

$$\tilde{k}_e(\tilde{A}) = \frac{k_e(A)}{k_d} = \frac{1}{\pi}\left[\cos^{-1}\left(1 - \frac{2}{\tilde{A}}\right) - 0.5 \sin\left\{2 \cos^{-1}\left(1 - \frac{2}{\tilde{A}}\right)\right\}\right] \tag{3}$$

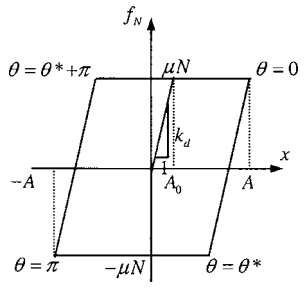

Fig. 2 Hysteresis from spring damper element

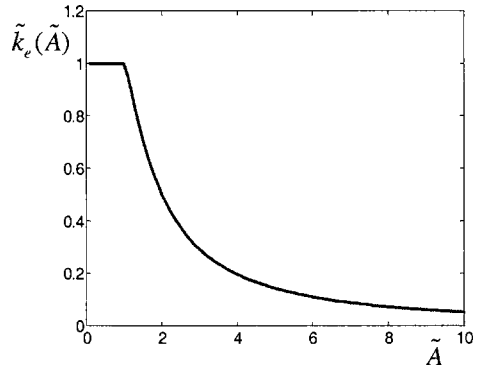

Fig. 3 Nondimensional effective stiffness

$$\tilde{c}_e(\tilde{A}) = \frac{c_e(A)}{k_d/\pi\omega} = \frac{4}{\tilde{A}}\left(1 - \frac{1}{\tilde{A}}\right) \tag{4}$$

where the arc cosine is defined to lie between 0 and π. The dimensionless stiffness and damping of a spring friction element are plotted as a function of amplitude in Figs. 3 and 4. They completely characterize the dynamic behavior of the spring damper and determine the response of the single degree of freedom system. Note, that for $\tilde{A} < 1$, the damper does not slip. Consequently, the damper's effective stiffness remains equal to its elastic value and its effective damping is zero, i.e., the spring element exhibits only macroslip behavior.

3 Experiment

3.1 Experimental Setup. Two different experiments are used to measure the behavior of the dampers. One is a quasi-static test conducted at 0.1 Hertz. The second is a dynamic test conducted at 50 Hertz. They are described in the following sub-sections.

3.1.1 Quasi-Static Test. The quasi-static test were done using the MTS testing machine shown in Fig. 5. The specimens have two parts. A fork type specimen with two prongs is mounted in the upper part of the MTS and damper type specimen, Fig. 6, in the lower part. The friction damper specimen is inserted between the prongs which are then compressed with a clamp. The prongs of fork are thin plates that are meant to represent the blade's platform. Strain gages are attached to the flat faces of the damper specimen. They are used to monitor the normal load on the friction interface during the tests. An extensometer is used to measure the relative displacement. A special fixture was designed so that the extensometer measures the relative displacement directly across the friction interface. This eliminates errors caused by the rotational deflection of the fork and improves the repeatability of the measurement. The load cell in the MTS machine is used to

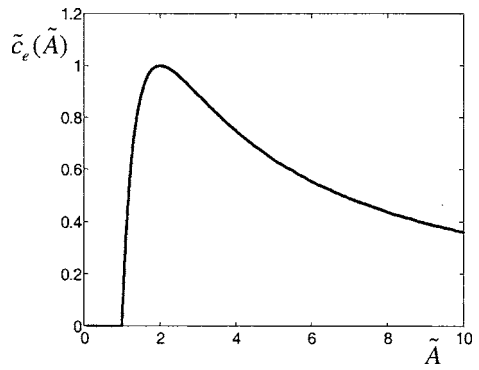

Fig. 4 Nondimensionalized effective damping

Downloaded 02 Jun 2010 to 171.66.16.98. Redistribution subject to ASME license or copyright; see http://www.asme.org/terms/Terms_Use.cfm

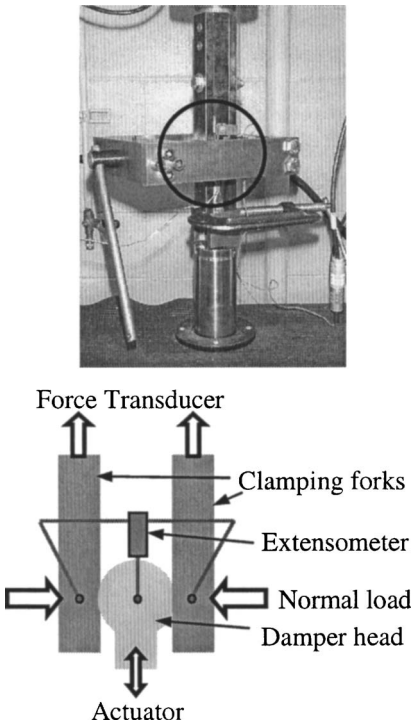

Fig. 5 Experimental setup for quasi-static test

measure the friction force.

In order to facilitate testing, the specimens were made larger than those commonly used in engines. If the dimensions of a damper are scaled by a factor S then the displacements are also scaled by S and are easier to measure. To compensate, the normal loads are scaled in proportion to the square of S in order to maintain realistic contact stresses. The specimens are made of Maraging steel. The advantages of Maraging steel are its fair machinability before heat treating and its high yield stress after. Once it is heat-treated, it has a yield stress of 2,068–2,758 MPa, comparable to that of the super Nickel alloys used in turbines. An advantage of using this high strength alloy is that the deformation in the contact region tends to stay elastic. The faces of the damper that come in contact with the prongs of the fork are spherical and have a radius of curvature of 127 mm.

3.1.2 Dynamic Test. The apparatus used in the dynamic test is shown in Fig. 7. Its complete description is given in [32]. In this experiment, the horizontal beam element is excited by a shaker at 50 Hertz. A friction damper is attached to the beam at its center. The damper consists of a hemispherical damper specimen in contact with a flat plate. Its radius of curvature is 12.7 mm, an order of magnitude smaller than those tested in the MTS machine. The normal load is applied using pulleys and a dead weight. The normal load was maintained at 69 N during the tests reported here. The damper shear force is measured by a load cell in series with the damper specimen. The relative motion across the friction interface is measured with a laser vibrometer.

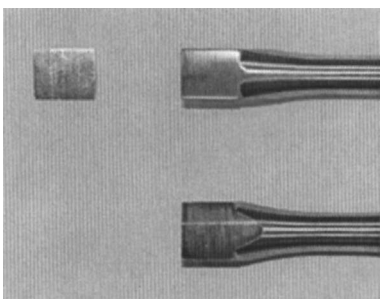

Fig. 6 Friction damper specimen for quasi-static test

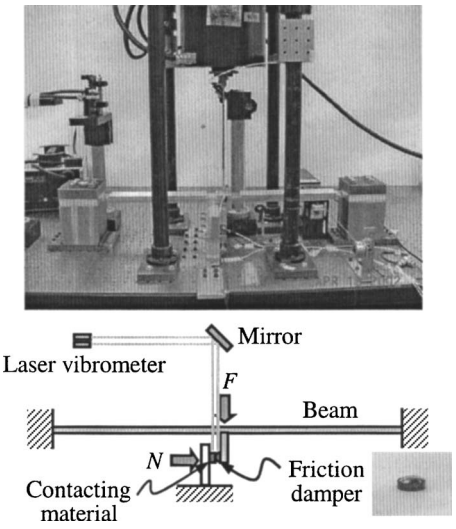

Fig. 7 Experimental setup for dynamic test

Hysteresis curves were generated under dynamic conditions using this apparatus. The tests provide an interesting contrast to the quasi-static experiment since the frequency is two orders of magnitude higher, the radius of curvature one order of magnitude lower, and the normal load two orders of magnitude lower than in the quasi-static tests.

3.2 Measurement. The tests were conducted for a range of amplitudes and at different normal loads.

Representative results for quasi-static test are shown in Fig. 8. The quasi-static tests were done for two different normal loads, 8.9 and 17.8 kN. Similar curves were generated using the dynamic test apparatus, Fig. 9.

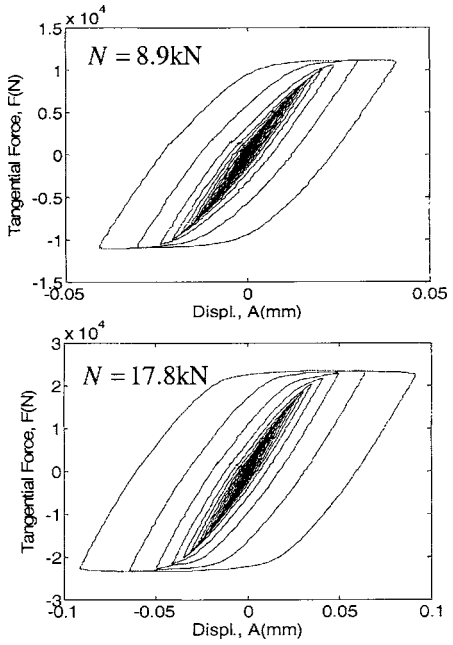

Fig. 8 Hysteresis curves from quasi-static tests

Downloaded 02 Jun 2010 to 171.66.16.98. Redistribution subject to ASME license or copyright; see http://www.asme.org/terms/Terms_Use.cfm

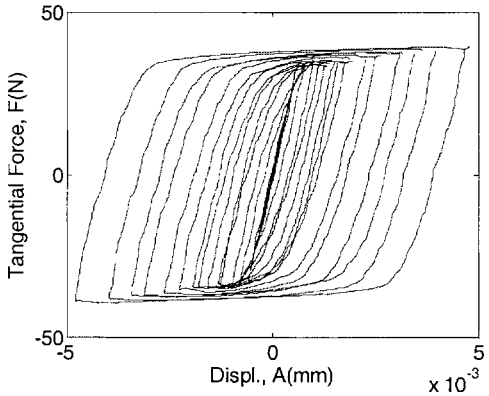

Fig. 9 Hysteresis curves from dynamic tests

3.3 Data Processing. The hysteresis curves from the tests were processed in a manner consistent with that used to determine the equivalent stiffness and damping of the spring damper. First, it was necessary to nondimensionalize the amplitude of motion. This requires knowing the damper's physical stiffness k_d and the force required for gross slip, μN. The stiffness was inferred from the hysteresis curves by averaging the slopes during the initial unloading and loading portions of the cycle $k_d \approx (k_1+k_2)/2$, Fig. 10. The gross slip load μN was also determined from the hysteresis curves by applying sufficiently large amplitude that the curves flattened out. Thus, the characteristic length $A_0=\mu N/k_d$ was determined from the experimental data. The dimensionless amplitude $\tilde{A}$ could then be calculated by dividing the physical amplitude by A_0.

The dimensionless effective stiffness and damping are given by:

$$\tilde{k}_e(\tilde{A}) = \frac{1}{\pi \tilde{A} \mu N} \int_0^{2\pi} f_N \cos\theta d\theta \tag{5}$$

$$\tilde{c}_e(\tilde{A}) = -\frac{1}{\tilde{A} \mu N} \int_0^{2\pi} f_N \sin\theta d\theta \tag{6}$$

These quantities were calculated using the force and displacement information from the hysteresis curves and integrating the data numerically in MATLAB. The integration was fairly accurate since a large number of data points, about 200, were measured each cycle.

3.4 Key Results. Figure 11 shows the nonlinear effective stiffness and damping plots produced by the quasi-static and dynamic tests. Observe that the quasi-static experiments with the two different normal loads 8.9 and 17.8 kN give almost identical curves. The normalized data points from the dynamic test also look quite similar. This is quite an interesting result since it tends to imply that a unique set of dimensionless stiffness and damping curves exist for a particular damper geometry even though the test conditions varied significantly from one test to the next.

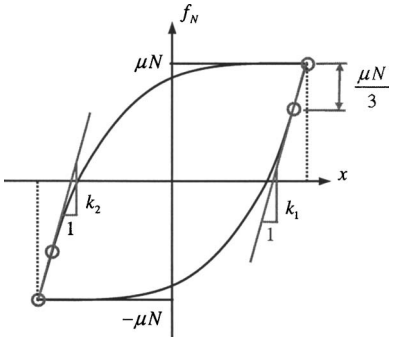

Fig. 10 Calculating damper stiffness from the hysteresis

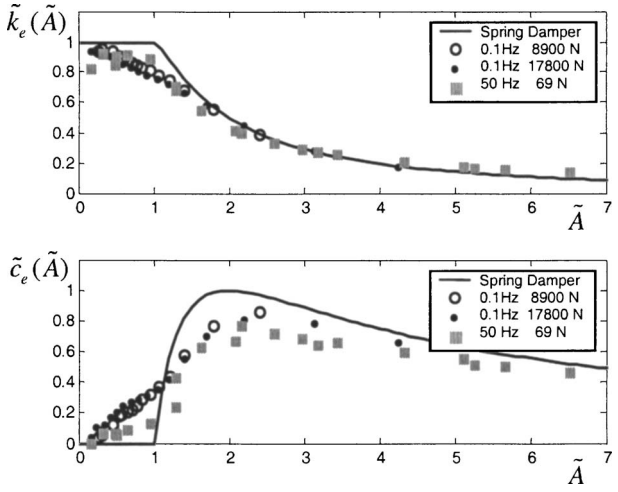

Fig. 11 Experimentally generated curves compared with benchmark

When our experimentally determined curves of effective stiffness are compared with those of the spring damper they agree reasonably well for large displacements, $\tilde{A}>3$. However, because of microslip the dimensionless effective stiffness of the experimental damper is smaller than that of the spring damper when the amplitude is small. More importantly, the experimental data has much more damping at low amplitudes than the spring model and somewhat less at high amplitudes.

The values of damper stiffness determined from the experiments are summarized in Table 1. Note that the stiffness of the quasi-static specimen increased with normal load

In the next section a classical elasticity solution will be investigated in order to assess the extent to which it captures the behavior seen in the tests.

4 An Analytical Model: Mindlin's Approximate Solution

In this section an approximate solution by Mindlin [25,33] is summarized for the elasticity problem of a tangential load applied to a sphere in contact with a half space. It will be used to calculate the damper's stiffness, k_d, the hysteresis curves, and the dimensionless effective stiffness and damping curves for a sphere on a half space.

An interesting aspect of three-dimensional contact problems in elasticity is that the relative displacement between the contacting bodies approaches a finite limit in the far field. For example, when a sphere contacts the flat surface shown in Fig. 12, this behavior limits the relative displacement between the bodies. Thus, when shear loads are applied the displacement of the center line has the behavior indicated by x in Fig. 13 provided there is no gross slip.

Table 1 Stiffness values from experiments

Dynamic condition (Hz)	Radius (m)	Normal load (N)	$\bar{k}_{exp}$(N/m)
Dynamic (50)	0.0127	69	$31.6\times10^{6^{+11.6\%}_{-7.9\%}}$
Quasi-static (0.1)	0.127	8900	$327\times10^{6^{+5.0\%}_{-8.2\%}}$
Quasi-static (0.1)	0.127	17800	$401\times10^{6^{+9.1\%}_{-4.7\%}}$

Downloaded 02 Jun 2010 to 171.66.16.98. Redistribution subject to ASME license or copyright; see http://www.asme.org/terms/Terms_Use.cfm

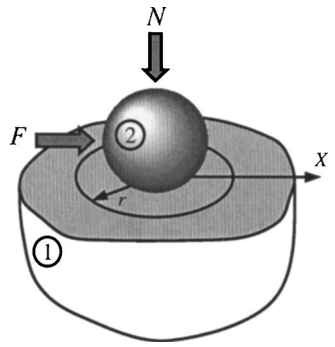

Fig. 12 Friction contact of sphere on a flat surface

Consequently, there is a unique stiffness k_∞ that characterizes the far field behavior. From Mindlin's theory the far field stiffness is:

$$k_d \approx k_\infty = \frac{F}{x_\infty} = \left(\frac{4Ga}{2-\nu}\right) = \left(\frac{4G}{2-\nu}\right) \cdot \left[\frac{3NR(1-\nu)}{4G}\right]^{1/3} \quad (7)$$

where G is the shear modulus, ν is Poisson's ratio, R is the radius of curvature, a is the contact radius, and N is the normal load.

Mindlin also gives analytical expressions that define the various parts of the hysteresis curves, Fig. 14(a).

Specifically, the relative motion is given by:

For the initial loading with zero initial displacement [OPQ in Fig. 14]

$$x = \frac{3}{2}A_0\left[1 - \left(1 - \frac{F}{\mu N}\right)^{2/3}\right] \quad (8)$$

for unloading [PRS in Fig. 14]

$$x = \frac{3}{2}A_0\left[2\left(1 - \frac{F^* - F}{2\mu N}\right)^{2/3} - \left(1 - \frac{F^*}{\mu N}\right)^{2/3} - 1\right] \quad (9)$$

and for cyclic reloading (STP in Fig. 14)

$$x = -\frac{3}{2}A_0\left[2\left(1 - \frac{F^* + F}{2\mu N}\right)^{2/3} - \left(1 - \frac{F^*}{\mu N}\right)^{2/3} - 1\right] \quad (10)$$

$$\text{where } A_0 = \frac{\mu N}{k_d} \quad (11)$$

These formulae were used to generate the hysteresis curves shown in Fig. 14(b). The curves were processed in the same manner as the experimental data to determine the dimensionless effective stiffness and damping curves for the Mindlin model. Comparisons between the experimental results and the result from Mindlin's analysis are shown in Fig. 15. In general, the agreement is quite good.

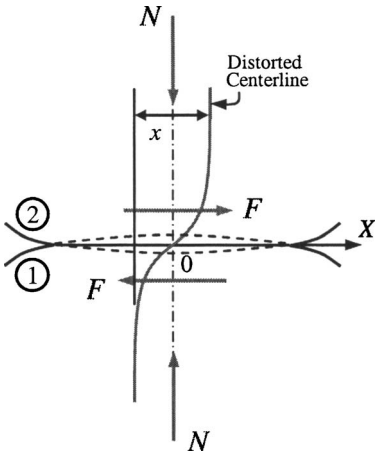

Fig. 13 Relative displacement between two bodies in contact ($F < \mu N$)

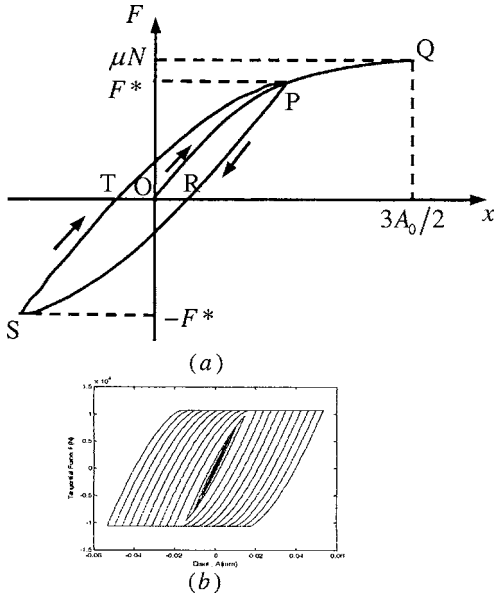

Fig. 14 Hysteresis from Mindlin analysis

Mindlin's estimate of the damper's physical stiffness (7) is a function of material properties, normal load, and radius. A comparison of the stiffnesses measured in the experiment and those calculated from (7) is shown in Table 2. It is clear that Mindlin's formula certainly captures the trend seen in the experiments. This is quite remarkable considering the wide difference in the test conditions in the quasi-static and dynamic tests.

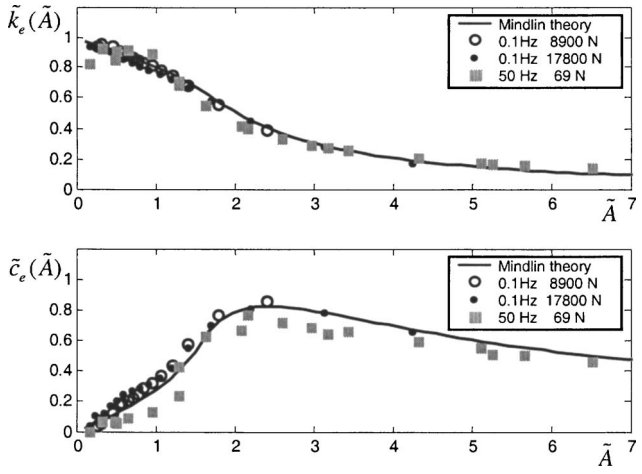

Fig. 15 Comparison between experiments and Mindlin analysis

Table 2 Stiffness comparison between experiments and Mindlin theory

Dynamic condition (Hz)	Radius (m)	Normal load (N)	$\bar{k}_{\text{exp}}$(N/m)	k_{Mindlin} (N/m)
Dynamic (50)	0.0127	69	$31.6\times10^{6+11.6\%}_{-7.9\%}$	31.7×10^6
Quasi-static (0.1)	0.127	8900	$327\times10^{6+5.0\%}_{-8.2\%}$	345×10^6
Quasi-static (0.1)	0.127	17800	$401\times10^{6+9.1\%}_{-4.7\%}$	435×10^6

Downloaded 02 Jun 2010 to 171.66.16.98. Redistribution subject to ASME license or copyright; see http://www.asme.org/terms/Terms_Use.cfm

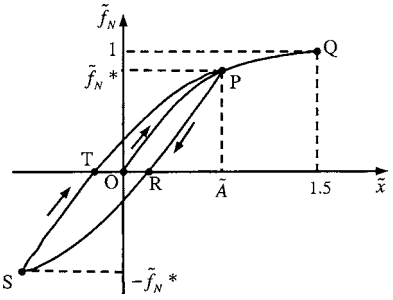

Fig. 16 Dimensionless hysteresis loop from Mindlin theory

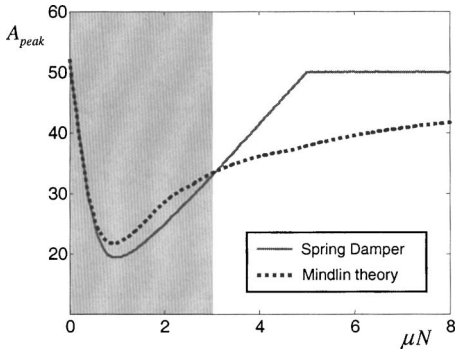

Fig. 17 Design range in damper optimization curve

5 Model Implications

Since the Mindlin analysis agreed well with the experimental data, it was used to examine other implications of the theory. First, rewrite (9)–(11) in dimensionless form where $\tilde{x} \equiv x/A_0$ and $\tilde{f}_N \equiv f_N/\mu N$. Then

$$\tilde{x} = \frac{3}{2}[1 - (1 - \tilde{f}_N)^{2/3}] \text{ for OPQ} \tag{12}$$

At the point P in Fig. 16, $\tilde{x}=\tilde{A}$ and $\tilde{f}_N=\tilde{f}_N^*$. Equation (12) implies

$$\tilde{f}_N^* = \tilde{f}_N^*(\tilde{A}) = 1 - \left(1 - \frac{2}{3}\tilde{A}\right)^{2/3} \tag{13}$$

and (10) and (11) imply

$$\tilde{x} = \frac{3}{2}\left[2\left(1 - \frac{\tilde{f}_N^* - \tilde{f}_N}{2}\right)^{2/3} - (1 - \tilde{f}_N^*)^{2/3} - 1\right] \text{ for PRS} \tag{14}$$

$$\tilde{x} = -\frac{3}{2}\left[2\left(1 - \frac{\tilde{f}_N^* - \tilde{f}_N}{2}\right)^{2/3} - (1 - \tilde{f}_N^*)^{2/3} - 1\right] \text{ for STP} \tag{15}$$

Inverting (14) and (15) to find explicit expressions for the cyclic force $\tilde{f}_N$ results in

$$\tilde{f}_N(\tilde{A},\theta) = \tilde{f}_N^* - 2\left\{1 - \left(\frac{1}{2}\right)^{3/2}\left[\frac{2}{3}\tilde{A}\cos\theta + (1 - \tilde{f}_N^*)^{2/3} + 1\right]^{3/2}\right\} \text{ for PRS} \tag{16}$$

$$\tilde{f}_N(\tilde{A},\theta) = -\tilde{f}_N^* + 2\left\{1 - \left(\frac{1}{2}\right)^{3/2}\left[\frac{2}{3}\tilde{A}\cos\theta + (1 - \tilde{f}_N^*)^{2/3} + 1\right]^{3/2}\right\} \text{ for STP} \tag{17}$$

where $\tilde{f}_N^*=\tilde{f}_N^*(\tilde{A})$ is given by (13). Now substitute (16) and (17) into (5) and (6). It is clear that

$$\tilde{k}_e(\tilde{A}) = \frac{\frac{1}{\pi}\int_0^{2\pi} \tilde{f}_N(\tilde{A},\theta)\cos\theta d\theta}{\tilde{A}} \tag{18}$$

$$\tilde{c}_e(\tilde{A}) = -\frac{\int_0^{2\pi} \tilde{f}_N(\tilde{A},\theta)\sin\theta d\theta}{\tilde{A}} \tag{19}$$

Since the θ dependence in (18) and (19) is integrated out, it is found that the dimensionless effective stiffness and damping are only functions of dimensionless amplitude $\tilde{A}$.

$$\tilde{k}_e(\tilde{A}) = \frac{F_C(\tilde{A})}{\tilde{A}} \tag{20}$$

$$\tilde{c}_e(\tilde{A}) = -\frac{\pi \cdot F_S(\tilde{A})}{\tilde{A}} \tag{21}$$

where

$$F_C(\tilde{A}) \equiv \frac{1}{\pi}\int_0^{2\pi} \tilde{f}_N(\tilde{A},\theta)\cos\theta d\theta \tag{22}$$

$$F_S(\tilde{A}) \equiv \frac{1}{\pi}\int_0^{2\pi} \tilde{f}_N(\tilde{A},\theta)\sin\theta d\theta \tag{23}$$

Consequently, it is clear that the dimensionless effective stiffness and damping predicted by Mindlin's theory are independent of size, material, normal load, and friction coefficient. Thus, according to Mindlin's theory, there are unique nonlinear, dimensionless stiffness and damping curves for a sphere on a half space.

Another result from Mindlin's theory is that you can determine how the stiffness and damping change for small motions. To first order, the dimensionless, nonlinear stiffness decreases by $\tilde{A}/6$ and the damping equals $2\tilde{A}/9$. In dimensional terms, for example, this means that for physical amplitudes A less than $\mu N/k_d$ the effective damping is approximately equal to

$$c_e(A) = \frac{2Ak_d^2}{9\omega\pi\mu N} \tag{24}$$

6 Concluding Remarks

While in general it is not possible to use nondimensionalization techniques for highly nonlinear systems, in the case of the spherical damper geometry considered in this paper it was found that the test data and the analytical solution indicate there is a unique set of dimensionless curves that characterize its performance. In addition, two additional parameters, k_d and μ, need to be known in order to complete the description of a specific damper. It was found that the stiffness of the spherical damper k_d could be reasonably well approximated by Mindlin's theory, Eq. (7). Since Mindlin's theory is based on an elasticity analysis that takes into account nonlinear contact this result suggests that the stiffness of dampers used by industry might be calculated from elasticity theory provided sufficient care is taken to model the effect of nonlinear contact and the resulting, very local stress concentrations.

The harmonic balance method was used to calculate the vibratory response of a frictionally damped, single degree of freedom oscillator in which the friction element was represented by a spring damper [16] and then by the Mindlin model. The results are shown in the damper optimization curves of Fig. 17. Damper op-

Downloaded 02 Jun 2010 to 171.66.16.98. Redistribution subject to ASME license or copyright; see http://www.asme.org/terms/Terms_Use.cfm

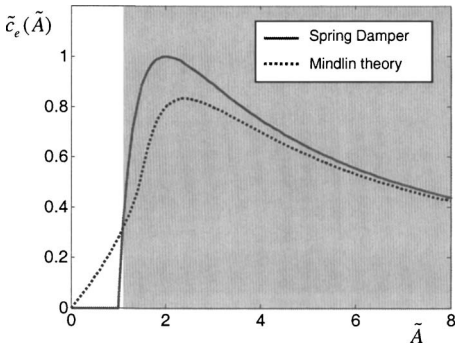

Fig. 18 Design range in effective damping curve

timization curves plot the maximum amplitude of response, A_{peak}, as a function of the normal load, N, applied to the friction joint [16]. In most applications, turbine blade dampers are designed to work in the white-colored range. In fact, this range corresponds to the white colored range in Fig. 18 where the dimensionless amplitude $\tilde{A}$ varies between 0 and 1.094. In this operating range, it is clear that the real damping was very different from that predicted by the spring model. The results imply that microslip effects may be very important over the part of the operating range typically used by friction damper designers. Based on these observations, it is believed that the problem that the friction damper designers have in calculating the correct damper stiffness is due in part to the fact that their models may not properly account for microslip. As a result, they are changing a parameter in their macroslip model, k_d, in order to try to match behavior that is dominated by microslip effects. This hypothesis that industrial dampers primarily work in the microslip regime is also supported by the fact that industrial dampers rarely show gross wear after use in the engine. However, whenever the test data were taken for $\tilde{A} > 2$, significant levels of wear were observed after only a few hundred cycles.

Lastly, an additional challenge remains in predicting the coefficient of friction, μ. During the experiments it was observed that μ changed with time as the surface finish of the contact surfaces degraded.[2] Consequently, it is an open issue what its value would be after the damper has operated for some time in the engine. In our tests μ increased by about a factor of two, when the motion across the friction interface became large after enough cycles. If the damper does, in fact, work in the microslip regime, then from (24) it is clear that an increase in μ would result in less damping and higher vibratory response. Consequently, it is important to insure that μ achieves a stable value representative of engine operating conditions in evaluating the damper's effectiveness during early testing.

Acknowledgment

This research was supported by NAVAIR, Contract No. N00421-01-1-0001 and by AFOSR, award number F49620-02-1-0168. The authors would like to acknowledge the stimulating discussions and suggestions provided by Dr. Daniel J. Segalman of Sandia National Laboratories.

References

[1] Feeny, B. F., Guran, A., Hinrichs, N., and Popp, K., 1998, "A Historical Review of Dry Friction and Stick–Slip Phenomena," Appl. Mech. Rev., **51**(5), pp. 321–341.
[2] Gaul, L., and Nitsche, R., 2001, "The Role of Friction in Mechanical Joints," Appl. Mech. Rev., **54**(2), pp. 93–106.
[3] Griffin, J. H., 1990, "A Review of Friction Damping of Turbine Blade Vibration," *International Journal of Turbo and Jet Engines*, 7, pp. 297–307.
[4] Yang, B. D., and Menq, C. H., 1997, "Modeling of Friction Contact and Its Application to the Design of Shroud Contact," ASME J. Eng. Gas Turbines Power, **119**(4), pp. 958–963.
[5] Yang, B. D., and Menq, C. H., 1998, "Characterization of Contact Kinematics and Application to the Design of Wedge Dampers in Turbomachinery Blading, Part I: Stick-slip Contact Kinematics," ASME J. Eng. Gas Turbines Power, **120**(2), pp. 410–417.
[6] Yang, B. D., and Menq, C. H., 1998, "Characterization of Contact Kinematics and Application to the Design of Wedge Dampers in Turbomachinery Blading, Part II: Prediction of Forced Response and Experimental Verification," ASME J. Eng. Gas Turbines Power, **120**(2), pp. 418–423.
[7] Yang, B. D., and Menq, C. H., 1998, "Characterization of 3D Contact Kinematics and Prediction of Resonant Response of Structures Having 3D Frictional Constraint," J. Sound Vib., **217**(5), pp. 909–925.
[8] Sanliturk, K. Y., Ewins, D. J., and Stanbridge, A. B., 2001, "Underplatform Dampers for Turbine Blades: Theoretical Modeling, Analysis and Comparison With Experimental Data," ASME J. Eng. Gas Turbines Power, **123**, pp. 919–929.
[9] Petrov, E. P., and Ewins, D. J., 2003, "Analytical Formulation of Friction Interface Elements for Analysis on Nonlinear Multi-Harmonic Vibrations of Bladed Discs," ASME J. Turbomach., **125**, pp. 364–371.
[10] Petrov, E. P., and Ewins, D. J., 2003, "Generic Friction Models for Time-domain Vibration Analysis of Bladed Discs," *Proceedings of ASME Turbo Expo 2003*, Atlanta, Georgia, GT-2003-38475.
[11] Szwedowicz, J., Kissel, M., Ravindra, B., and Kellerer, R., 2001, "Estimation of Contact Stiffness and its Role in the Design of a Friction Damper," *Proceedings of ASME Turbo Expo*, 2001-GT-0290.
[12] Cha, D., and Sinha, A., 1999, "Computation of the Optimal Normal Load of a Friction Damper Under Different Types of Excitation," *ASME International Gas Turbine Conference*, Indianapolis, IN, ASME 99-GT-413.
[13] Cha, D., and Sinha, A., 2000, "Statistics of Responses of a Mistuned and Frictionally Damped Bladed Disk Assembly Subjected to White Noise and Narrow Band Excitations," *ASME International Gas Turbine Conference*, Munich, Germany, ASME 2000-GT-542.
[14] Csaba, G., 1999, "Modeling of a Microslip Friction Damper Subjected to Translation and Rotation," *ASME International Gas Turbine Conference*, Indianapolis, IN, ASME 99-GT-149.
[15] Sextro, W., Popp, K., and Wolter, I., 1997, "Improved Reliability of Bladed Disks Due to Friction Dampers," *ASME International Gas Turbine Conference*, ASME 97-GT-189.
[16] Griffin, J. H., 1980, "Friction Damping of Resonant Stresses in Gas Turbine Engine Airfoils," ASME J. Eng. Power, **102**, pp. 329–333.
[17] Menq, C. H., Griffin, J. H., and Bielak, J., 1986, "The Influence of a Variable Normal Load on the Forced Vibration of a Frictionally Damped Structure," ASME J. Eng. Gas Turbines Power, **108**, pp. 300–305.
[18] Yang, B. D., Chu, M. L., and Menq, C. H., 1998, "Stick–slip–separation Analysis and Nonlinear Stiffness and Damping Characterization of Friction Contacts Having Variable Normal Load," J. Sound Vib., **210**(4), pp. 461–481.
[19] Menq, C. H., Chidamparam, P., and Griffin, J. H., 1991, "Friction Damping of Two-dimensional Motion and Its Application in Vibration Control," J. Sound Vib., **144**, pp. 427–447.
[20] Menq, C. H., and Yang, B. D., 1998, "Nonlinear Spring Resistance and Friction Damping of Frictional Constraint Having Two-Dimensional Motion," J. Sound Vib., **217**(1), pp. 127–143.
[21] Ewins, D. J., and Griffin, J. H., 2001, "Workshop on the Modeling, Analysis, and Measurement of Friction Constraints in Gas Turbine Components," *Final Report submitted to USAF, AFRL, AFOSR/NA*, Award Number F49620-01-1-0325.
[22] Mindlin, R. D., 1949, "Compliance of Elastic Bodies in Contact," ASME J. Appl. Mech., **16**, pp. 259–268.
[23] Mindlin, R. D., and Deresiewicz, H., 1953, "Elastic Spheres in Contact Under Varying Oblique Forces," ASME J. Appl. Mech., **20**, pp. 327–343.
[24] Deresiewicz, H., 1957, "Oblique Contact of Non-Spherical Bodies," ASME J. Appl. Mech., **24**, pp. 623.
[25] Mindlin, R. D., Mason, W. P., Osmer, T. F., and Deresiewicz, H., 1952, "Effects of an Oscillating Tangential Force on the Contact Surfaces of Elastic Spheres," *Proceedings of the First U.S. National Congress of Applied Mechanics*, pp. 203–208.
[26] Johnson, K. L., 1955, "Surface Interaction Between Elastically Loaded Bodies Under Tangential Forces," Proc. R. Soc. London, Ser. A, **A230**, pp. 531–549.
[27] Goodman, L. E., and Brown, C. B., 1962, "Energy Dissipation in Contact Friction: Constant Normal and Cyclic Tangential Loading," ASME J. Appl. Mech., **29**, pp. 17–22.
[28] Den Hartog, J. P., 1931, "Forced Vibrations With Combined Coulomb and Viscous Friction," Trans. ASME, **53**, pp. 107–115.
[29] Caughey, T. K., 1960, "Sinusoidal Excitation of a System With Bilinear Hysteresis," ASME J. Appl. Mech., **27**, pp. 640–643.
[30] Gaul, L., 1983, "Wave Transmission and Energy Dissipation at Structural and Machine Joints," ASME J. Vib., Acoust., Stress, Reliab. Des., **105**, pp. 489–496.
[31] Menq, C. H., and Griffin, J. H., 1985, "A Comparison of Transient and Steady State Finite Element Analyses of the Forced Response of a Frictionally Damped Beam," ASME J. Vib., Acoust., Stress, Reliab. Des., **107**, pp. 19–25.
[32] Filippi, S., Akay, A., and Gola, M. M., 2003, "Measurement of Tangential Contact Hysteresis During Microslip," ASME J. Tribol. (to be published).
[33] Wilner, K., and Gaul, L., 1995, "A Penalty Approach for Contact Description by FEM Based on Interface Physics," *Contact Mechanics II, Computational Mechanics Publications*, Southampton, pp. 257–264.

[2]Note that we had to periodically measure μ and take its change into account in developing the dimensionless damping and stiffness curves quoted in this paper.

Downloaded 02 Jun 2010 to 171.66.16.98. Redistribution subject to ASME license or copyright; see http://www.asme.org/terms/Terms_Use.cfm

Combined Fatigue Life Test and Extrapolation of Turbine Disk Mortise at Elevated Temperature

Rongqiao Wang
School of Jet Propulsion,
Beijing University of Aeronautics & Astronautics,
Beijing 100083, China

Chongdu Cho
Department of Mechanical Engineering,
Inha University,
Inchon 402-751, S. Korea

Jingxu Nie
School of Jet Propulsion,
Beijing University of Aeronautics & Astronautics,
Beijing 100083, China

To investigate the crack failure of a certain turbine disc mortise, a test system with a new low- and high-cycle noninterfering loading scheme was established to study the low- and high-cycle combined fatigue (L-HCCF) of fir-tree mortise at elevated temperature. Then, for 50 and 100 Hz *vibrations with constant stress amplitude superimposed on the same low cycle loading, respectively, the contrast L-HCCF life tests of light- and serious-corrosive disc mortises were carried out. Through real-time crack detection of the first teeth, the crack propagation rule of fir-tree mortise, a typical multiple load path structure, was obtained. Finally, a new method, two-frequency-ratio method, was presented to relate the load and life of laboratory test to the equivalent those of service in order to help the definition of the failure criteria for serious-corrosive discs in actual practice. The extrapolative results show that the life policies in use for light-corrosive turbine disc can not be applied to serious-corrosive disc directly because its reliable life is greatly less than an overhaul schedule, and it is urgent to establish criteria for withdrawal from service of the serious-corrosive discs to assure the structural integrity of this aeroengine.* [DOI: 10.1115/1.1926314]

Introduction

The turbine blades of an aero-engine are generally attached to the disc by means of a fir-tree design, a typical multiple load path structure (Fig. 1), to allow for different rates of expansion between the disc and the blade while still holding the blade firmly against centrifugal loads. During the operation of the aero-engine, this attachment always endures a low amplitude and high frequency vibration combined with a high level, low frequency stress. For mortise teeth of the disc, the variation of the centrifugal stress (stemmed from the centrifugal force of the blade) and the thermal stress corresponding to various flight phases (take-off, cruise, landing) is the main cause of low cycle fatigue (LCF), while vibrations due to resonances, rotating stalls and self-excitations of the blade are the source of the superimposed high cycle fatigue (HCF). Because of the interactive effects of LCF and HCF, i.e., the low and high cycle combined fatigue (L-HCCF) described here, the fatigue damage of the mortise teeth is largely increased [1–10]. These effects may be responsible for the unscheduled crack failures in service of the mortise on a certain aeroengine second turbine disc, especially the serious-corrosive mortise. Field experience and metallograph analysis show that the crack, usually started from the first tooth, is certainly caused by the L-HCCF. This failure seriously endangers the aircraft. Therefore, it is extremely urgent to study L-HCCF experimentally to explore the crack propagation rule of the fir-tree mortise, compare L-HCCF test life of light- and serious-corrosive mortises, and further provide evidence for establishing the failure criterion for serious-corrosive discs. Meanwhile, it is necessary to make extrapolation of the test results to the equivalent service lives in order to use the test data for flight criterion, but this extrapolation is difficult due mainly to the disagreement of the vibration load in test and in service. Consequently, a new extrapolation method, two-frequency-ratio method, should be presented to extrapolate the load and life of laboratory test to those of service. Corresponding to this extrapolative method, 50 and 100 Hz vibrations with constant stress amplitude superimposed on the same low cycle loading were utilized in the present test.

Contributed by the International Gas Turbine Institute (IGTI) of THE AMERICAN SOCIETY OF MECHANICAL ENGINEERS for publication in the ASME JOURNAL OF ENGINEERING FOR GAS TURBINES AND POWER. Paper presented at the International Gas Turbine and Aeroengine Congress and Exhibition, Vienna, Austria, June 13–17, 2004. Paper No. 2004-GT-53331. Manuscript received by the IGTI, October 1, 2003; final revision, March 1, 2004. IGTI Review Chair: A. J. Strazisar.

Experimental Method

Usually, the standard L-HCCF testing machine is mainly used to study the characteristic of material, and is suitable for standard specimen only, not for a large-scale component [1,4,6,7]. However, the actual crack growth and fracture failure of the mortise teeth are not only determined by the characteristic of the material, but are also affected by the structure, dimension, and the teeth space of the mortise. Consequently, a special experimental facility with a unique low- and high-cycle loading scheme is required to find the practical L-HCCF rule of the mortise teeth using a actual full scale disc. For this reason, we developed a new experimental system using a Ferris Wheel (a low cycle fatigue tester) to simulate the L-HCCF of the actual mortise teeth with low cycle radial pulse loading overlapping the high cycle winding loading at elevated temperature. This ingeniously achieved the combined loading in a simple mechanical way, high-frequency induction local heating (550°C constant temperature), control of high cycle vibration frequency and amplitude, and crack real-time monitoring. The main techniques of this test system are briefly introduced herein, and the details can be refered to [9].

New Test Loading Method. The loading scheme is the key technique of this experiment to achieve failure rendition of the mortise teeth in the laboratory. The diagrammatic sketch of the actual loading is shown in Fig. 1. Where, F is the low cycle loading due mainly to the centrifugal force of the blade, and M is the vibration bending moment.

To achieve a rational and noninterfering treatment of the low- and high-cycle loading, a new low and high cycle noninterference loading method is presented. The sketch is shown in Fig. 2.

Contrary to the direct exertion of loading on the bearing ear (see (8) in Fig. 2), the new loading method places the low cycle loading exerting point to the back of the mortise through the load-bearing bar (see (10) in Fig. 2), then transmits the loading using a pair of load-transmitting plate (see (5) in Fig. 2) to the bearing ear. Thus, the high cycle vibrating center point moves backward and

Copyright © 2005 by ASME

Downloaded 02 Jun 2010 to 171.66.16.98. Redistribution subject to ASME license or copyright; see http://www.asme.org/terms/Terms_Use.cfm

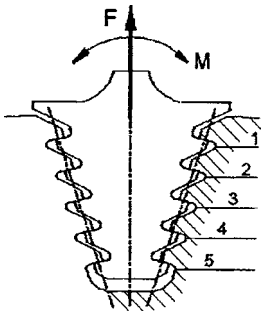

Fig. 1 A sketch of an attachment structure and loading

lengthen the arm of the high cycle vibration; meanwhile, when the blade vibrates around the center point, the vibrating force reaches the mortise teeth first, then the low cycle load exerting point. Therefore, the vibrating force can be transmitted to the mortise teeth with no loss. This is proven by the stress measurements: When the vibrating force is constant, the stress on the mortise teeth approximately keeps constant as the low cycle loading is changing from 40 to 70 kN; meanwhile, the stress on the teeth is well distributed.

Experimental Method. Based on the service loading of a certain aeroengine, a L-HCCF test load scheme was designed, as indicated in Fig. 3.

Experienced a period of 20 s, one major low cycle includes three loading blocks: Two short blocks and one long block, corresponding to climing, landing, and cruising in a typical flight of an aircraft, respectively. On the low cycle loading, overlapping is the high cycle vibration, which simulates the resonance of the blade during aircraft operation.

With the new loading method, a special L-HCCF test facility controlled by a computer was developed. The most important feature of this system is that it allows the low and high frequency loading to be applied independently and without interaction. The

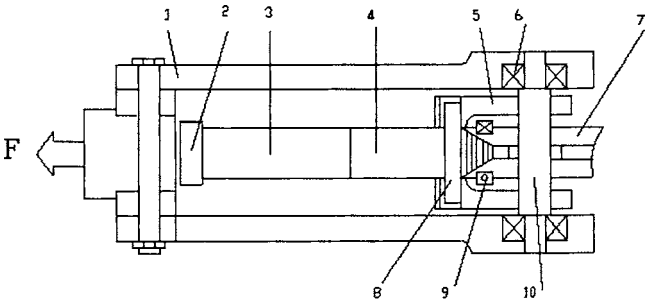

1 Drawplate 2 Vibrating point 3 Extending plate 4 Simulating blade
5 Load-transmission plate 6 Bearing 7 Actual turbine disk
8 Bearing ear 9 Heating ring 10 Load-bearing bar

Fig. 2 A sketch of the new loading method

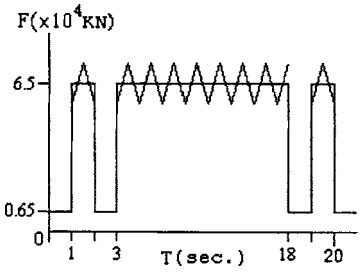

Fig. 3 A sketch of the test load spectrum(one load block)

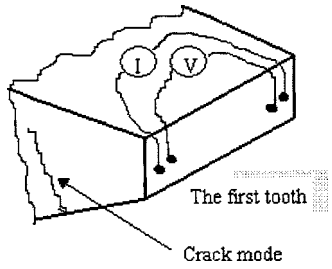

Fig. 4 Lead wires of crack monitoring

low cycle loading, with about 65 kN as its maximum value in this study (approximately the centrifugal force of the blade at the maximum working speed), is provided by the servo-hydraulic actuator. Since the frequencies associated with the high frequency cycles are relatively high, conventional servo-hydraulic systems did not appear to be suitable. Consequently, an electromagnetic vibrator was used to exert the sinusoidal vibration force on the extending part of the simulating blade, and then transmit to the mortise teeth by means of the method described previously. Meanwhile, the vibration amplitude can be adjusted, and vibration frequency can be changed from 0 to 650 Hz. Through measuring the vibration amplitude on the vibrating point (see (2) in Fig. 2) using a ZZF6-1 eddy current vibrating amplitude measure apparatus, the dynamic stress on the mortise teeth can be well controlled. That means the low- and high-cycle stress ratio on the mortise teeth can be varied for different experimental needs. Of course, the relationship between the dynamic stress on the first teeth and the vibrating amplitude on the vibrating point must be calibrated beforehand. Considering the extrapolation of the load and life from test to service flight, two vibration frequencies, 50 and 100 Hz, were used in this test. The initial amplitude of vibratory stress on the first teeth is kept 25% of that of the low cycle stress, which is over the threshold above which the vibrating loading becomes active for the fatigue damage of the mortises. Using high frequency induction local heating, the temperature of the experimental mortise can be controlled about $550\pm10^{\circ}C$. Confined by the condition of the elevated temperature and the monitoring space of mortise teeth, common method for crack propagation monitoring is difficult to use here. Therefore, we adopted the direct-current electrical potential technique, using the MDF-1 DC measurement system developed recently. Real-time monitoring of the crack propagation of the first teeth was then achieved, combining with the micrometer to monitor the radial displacement of the simulating blade so as to determine the failure of the second teeth. The arrangement of leads for crack monitoring are shown in Fig. 4. The number of the load blocks and the voltage ratio were automatically recorded by the computer system. Each test was terminated after the blade was pulling out of the test mortise.

Dynamic Demarcation. Using dynamic strainometer and 0.5×0.5 mm strain gauge, dynamic demarcation of stress on each tooth was accomplished. The demarcating results show that the low- and high-cycle load can be transmitted to mortise teeth without interaction, and the strain ratio of the first, second, third, and fourth tooth is about 1:0.3:0.2:0.15. Meanwhile, the relationship between the dynamic strain on the first tooth and the amplitudes for 50 and 100 Hz on the vibration point was obtained. Then, by controlling this amplitude, we can keep the stress transmitting to each tooth equal for two test vibration frequencies, and furthermore, the vibration stress range of the first tooth can be changed from 0% to 30% of the low cycle stress.

Crack Propagation Rule of Fir-Tree Mortise

The L-HCCF crack propagation of the first pair of teeth was monitored continuously throughout each test using the direct-current electrical potential technique. The results show that a

Downloaded 02 Jun 2010 to 171.66.16.98. Redistribution subject to ASME license or copyright; see http://www.asme.org/terms/Terms_Use.cfm

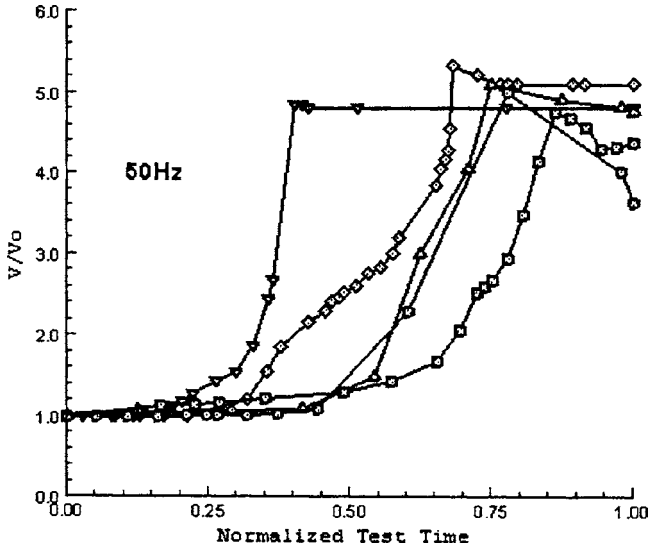

Fig. 5 Crack propagation monitoring results for 50 Hz

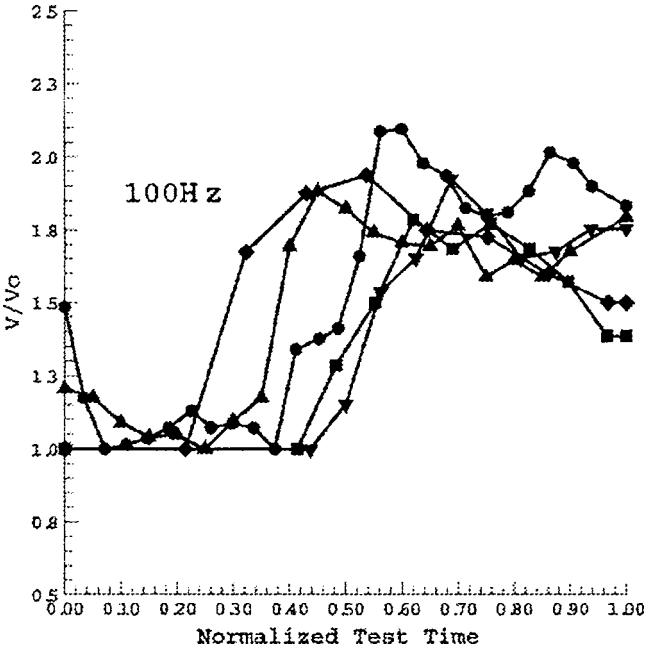

Fig. 6 Crack propagation monitoring results for 100 Hz

crack is always originated from the root of the first tooth, and then the second tooth, and so on. The angle between the direction of crack propagation and the working surface of the mortise tooth is about 45 deg (see Fig. 4). The metallographic analyses of the fracture surface show that the combined fatigue is the main failure mechanism of the mortise. The fatigue area of the first teeth is larger than that of the second teeth, and the remaining three teeth have almost no fatigue area in their fracture surface. Furthermore, the location and direction of the test fatigue crack are identical to the service's failure. That means the main factors led to the service's failure of the mortise were successfully simulated in this test. This fact, on the other hand, can also prove that the service's failure is due to the L-HCCF at an elevated temperature.

The crack propagation monitoring results of ten test mortises, five for 50 Hz and five for 100 Hz, respectively, are shown in Figs. 5 and 6, where V/Vo is the relative potential associated with the crack size, and Vo the potential of the initial state with no crack.

In Figs. 5 and 6, the points from which the voltage value begins to move upward rapidly are considered as the crack formation points of the first teeth. The highest point represents the failure of the first tooth, and the end point represents the failure of the second tooth, which is also the final failure of the mortise. The reason is that the blade cannot be held in the mortise by the remaining three teeth and will be pulled out after the invalidation of the upper two teeth. Here the failure life of the mortise is defined as the total test time until the blade pulling out of the mortise, the extending life as the time from the crack formation point to the end of the test, and the residual life as the time from the failure of the first teeth to the end of the test.

Referring to Fig. 5, it is clear that the average crack formation, extending, and residual lives of the mortise are about 33.88%, 66.12%, and 30.2% of its total life, respectively, when the vibration frequency is 50 Hz. For 100 Hz, the corresponding values are 33.82%, 66.18%, and 42.7% (Fig. 6). Refered to the test results in Table 1, we can find that even though the relative residual life is different, the absolute residual life of 50 and 100 Hz is quite approximative.

The reason is that the high-frequency stress, about 25% of the low cycle centrifugal stress on the first teeth initially, is bigger than the threshold value above which the high cycle fatigue becomes active and has great influence on the crack formation, growth and failure of the first teeth; when the first teeth are failure, the influence of the high cycle stress on the failure of the other teeth is very small because its value is only about 7.5% of the corresponding low cycle stress and can not reach the threshold value [1, 7, 9, 10]. The failure of the remaining teeth is mainly due to the low cycle load, which is equal on the conditions of 50 and 100 Hz. Therefore, the absolute residual lives of mortises with different high frequencies are close to equal.

Summarily, the crack propagation rule of the fir-tree mortise, a typical multiple path load structure, is similar for 50 and 100 Hz vibration frequencies, and can be concluded as (1) the crack formation life is obviously smaller than the crack propagation life of the mortise; (2) the vibration load has great influence on the failure of the first tooth, but has little contribution to the failure of the other teeth; (3) the remaining three pairs of mortise teeth almost have no life when the second pair of teeth is failure. This rule provides experimental evidence for the failure criterion of this disc practice.

L-HCCF Life Test of Disc Mortise

The test mortises were first classified into two groups, light-corrosive mortises and serious-corrosive mortises in accordance with the military specification, i.e., by the degree of intercrystalline corrosion before the test. Using the method described above, a contrast test of light- and serious-corrosive disc mortises under two vibrational frequencies, 50 and 100 Hz, was carried out. 25 mortises on 12 discs were divided into 4 groups, 7 light-corrosive mortises for 50 Hz, 7 light-corrosive mortises for 100 Hz, 6 serious-corrosive mortises for 50 Hz, and 5 serious-corrosive mortises for 100 Hz. The material of the disc is GH36, an iron-base superalloy, and its chemical composition and mechanical properties at 550°C can be referred to [10].

Practical experience shows that the fatigue life of disc mortise, at an elevated temperature, is subjected to the log-normal distribution. Therefore, the test data were analyzed using the theory of log-normal distribution, with the final results shown in Table 1. Meanwhile, using the least-square method, the comparison p(survival rate or reliability)$\sim N_B$(load blocks) curves for the failure lives of the test mortises are given as an example in Fig. 7 for light-corrosive mortises and Fig. 8 for serious-corrosive mortises, respectively, where p is defined by [11]

Downloaded 02 Jun 2010 to 171.66.16.98. Redistribution subject to ASME license or copyright; see http://www.asme.org/terms/Terms_Use.cfm

Table 1 Contrast test statistical life results of light- and serious-corrosive mortises (unit: load block)

	Light-corrosive disc 50 Hz			Light-corrosive disc 100 Hz			Serious-corrosive disc 50 Hz			Serious-corrosive disc 100 Hz		
Survival rate (%)	Total life	Extending Life	Residual life	Total life	Extending Life	Residual life	Total life	Extending Life	Residual life	Total life	Extending Life	Residual life
50	1022	676	282	582	390	250	671	443	202	392	259	162
90	605	402	141	301	208	123	204	135	61	147	97	61
95	521	347	116	249	174	101	146	96	44	111	73	46
99	394	263	80	176	125	69	77	51	23	66	43	27
99.9	288	193	53	118	86	45	38	25	12	37	24	15

$$p = 1 - \frac{i}{n+1}$$

where n is the number of test mortises per group, and i the order number when arranging the test mortises of each group in the order of short life span.

Table 1 and Figs. 7 and 8 show that compared with a light-corrosive mortise, the failure life of a serious-corrosive one is obviously decreased, and displays a rapid downtrend at a high survival rate. Figures 7 and 8 also show that the dispersion of the failure lives of serious-corrosive mortises is larger than that of light-corrosive mortises.

With the above test results, the two-frequency-ratio extrapolation method should be presented next, and then the necessary extrapolation of test results to service times of interest will be undertaken in virtue of this method.

Two-Frequency-Ratio Extrapolation Method

Considering the actual loading condition of the mortise, it is rational to suppose that the damage of the mortise tooth owing to the vibration loading of blade is a function of vibration stress amplitude (or amplitude ratio, that is, the ratio of high cycle stress amplitude to low cycle stress amplitude) and vibration frequency (or frequency ratio, i.e., the ratio of high cycle frequency to low cycle frequency) approximately. When the vibration stress amplitude keeps constant and its value exceeds the onset threshold of high cycle damage, the fatigue damage due to blade vibration depends only upon the vibration frequency. With this assumption, a frequency ratio (or a high cycle frequency) can be obtained from the above test results and the statistical service failure data using a certain method. Then kept the other conditions in the above test unchangeable, the test with this frequency ratio can produce the damage equivalent to that induced by the service loading. The two-frequency-ratio method addressed as follows can be used for this extrapolation.

The damage produced by the low- or high-cycle loading in L-HCCF can not be considered as the damage done by a single factor, i.e., the low- or high-cycle loading itself. There exists some coupling effect or interaction between the low cycle and high cycle fatigue, which is the most significant characteristic of L-HCCF. Then the coupling low cycle damage unit, $1/A$, and as such the coupling high cycle damage unit, $1/B$, are introduced in this paper to express the damage induced by one low cycle loading block and one high cycle loading in L-HCCF, respectively. Here $1/A$ and $1/B$ are considered as the function of combined form of low cycle and high cycle loadings, the properties of the material tested, etc., and independent of the frequency ratio n. Therefore, with the same combined form of the two loading components, and given that two combined low cycle lives, $(N_{CL})_{n1}$ and $(N_{CL})_{n2}$, corresponding to two different frequency ratios, n_1 and n_2, respectively, we can establish the equations as follows

$$1/A + n_1/B = 1/(N_{CL})_{n1} \tag{1}$$

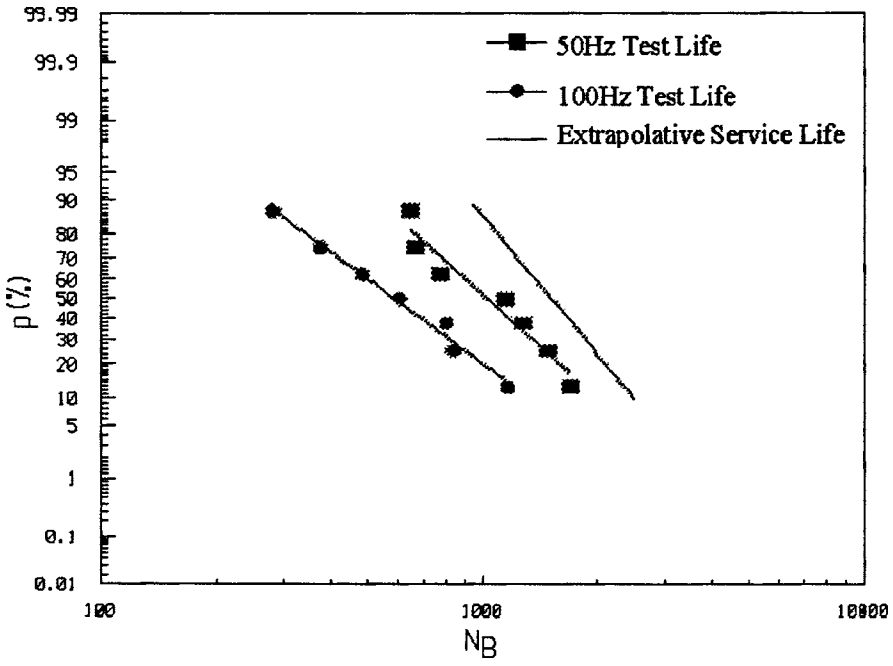

Fig. 7 Failure life curves for light-corrosive mortises

Downloaded 02 Jun 2010 to 171.66.16.98. Redistribution subject to ASME license or copyright; see http://www.asme.org/terms/Terms_Use.cfm

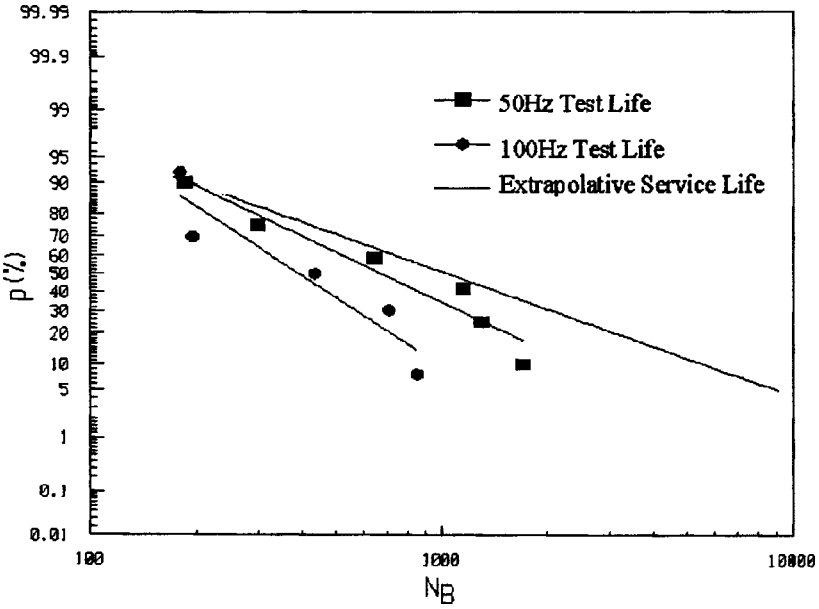

Fig. 8 Failure life curves for serious-corrosive mortises

$$1/A + n_2/B = 1/(N_{CL})_{n2}$$

then $1/A$ and $1/B$ can be derived as

$$\begin{cases} \dfrac{1}{A} = \dfrac{1}{(N_{CL})_{n1}} - \dfrac{n_1}{n_1 - n_2}\left[\dfrac{1}{(N_{CL})_{n1}} - \dfrac{1}{(N_{CL})_{n2}}\right] \\ \dfrac{1}{B} = \dfrac{1}{n_1 - n_2}\left[\dfrac{1}{(N_{CL})_{n1}} - \dfrac{1}{(N_{CL})_{n2}}\right] \end{cases} \tag{2}$$

Furthermore, under the same combined form of low and high cycle loadings, the combined fatigue life with any frequency ratio n can be obtained as

$$(N_{CL})_n = 1/(1/A + n/B) \tag{3}$$

and as such if combined fatigue life $(N_{CL})_n$ is determined, the frequency ratio n can be calculated as

$$n = B[1/(N_{CL})_n - 1/A] \tag{4}$$

This is the basic principle of the two-frequency-ratio extrapolation method for L-HCCF, which was confirmed by a series of fatigue tests and fully described in [9].

Extrapolation of Test Load and Life to Service

According to the service data of flight experience, the median failure life of light-corrosive mortise on an actual turbine disc can be statistically deduced to be about 742 h. The time of a typical flight pattern is about 30 min., which means that one loading block in the present test is comparable to half an hour in service. So the median failure life of a service mortise is equivalent to 1484 test loading blocks.

Corresponding to the same failure mode as service, the test median failure life of light-corrosive mortise is 1022 loading blocks for the vibration frequency of 50 Hz, and 582 blocks for 100 Hz (Table 1). It is clear in Fig. 3 that the hold time of the low cycle loading for one block is 17 s, and consequently the number of high cycles sustained during this time are 850 for 50 Hz, and 1700 for 100 Hz, which are also the frequency ratios for the two different test loadings. Then from Eq. (2), we can get that $A=4173$ and $B=1.151\times10^6$. Referring to Eq. (4) and considering the service combined low cycle $(N_{CL})_n=1484$, we can find that $n=496$, which can be considered as the test frequency ratio equivalent to the actual loading strength in service.

Based on the curves of $p\sim N_B$ for two test vibration frequencies, the A and B corresponding to a certain survival rate can be calculated by Eq. (2). Furthermore, considering $n=496$, the corresponding service life can be thus derived by Eq. (3). Following this procedure, a series of service lives for different survival rates can be deduced. Then the $p\sim N_B$ curve for service life can be fitted as

$$u_p = C + Dl_gN_B$$

where C and D are fitting constants; u_p is a function of survival rate p, and can be obtained from standard table of normal distribution, for example, $u_p=-3.09$ when $p=99.9\%$, $u_p=-2.326$ when $p=99\%$ and so on. The curves of extrapolative service failure lives for light- and serious-corrosive mortises are illustrated in Figs. 7 and 8, respectively. The other curves of extrapolative crack extending lives and residual lives in service can be referred to [9].

Table 2 Service lives of light- and serious-corrosive mortises (unit: load block; hour in parentheses)

Survival rate (%)	Light-corrosive Mortises			Serious-corrosive Mortises			Serious-corrosive/Light-corrosive×100%		
	Total life	Extending life	Residual life	Total life	Extending life	Residual life	Total life	Extending life	Residual life
99.9	459(229.5)	224(112)	35(17.5)	8(4)	5(2.5)	3(1.5)	1.74	2.23	8.6
99	616(308)	322(161)	59(29.5)	27(13.5)	18(9)	9(4.5)	4.4	5.6	15.3
95	800(400)	446(223)	95(47.5)	78(39)	51(25.5)	24(12)	9.8	11.4	25.3
90	920(460)	530(265)	122(61)	137(68.5)	91(45.5)	39(19.5)	14.9	17.2	32

Downloaded 02 Jun 2010 to 171.66.16.98. Redistribution subject to ASME license or copyright; see http://www.asme.org/terms/Terms_Use.cfm

Finally, with four different survival rates, the comparison of the service failure lives was undertaken, and the detail results are listed in Table 2.

Conclusions

1. A test system with a new low- and high-cycle noninterfering loading scheme was established to study the L-HCCF of a fir-tree mortise on a full-scale turbine disc.

2. The tests reappeared the service's failure of the disc mortise, that is to say, the main factors led to the service's failure of the mortise were successfully simulated by the tests all the time. The fact, on the other hand, also proved that the service's failure is due to the L-HCCF at an elevated temperature.

3. The unique crack propagation rule of the fir-tree mortise, a multiple path load structure, was obtained. This rule provides an experimental evidence for the failure criterion of this disc in use.

4. Compared with the light-corrosive disc, the failure life of serious-corrosive disc is dropped obviously, especially on a high survival rate. This can be confirmed from Table 1.

5. Two-frequency-ratio method was presented to extrapolate the loading and life of test to those of service rationally. For example, as seen in Table 2, with 99% survival rate, the extrapolative service extending life of light-corrosive mortise is 322 blocks, that is, the number of typical flight pattern is 322, approximately equivalent to 161 flight hours. That means the light-corrosive disc with cracks on the first teeth can be safely used for an overhaul schedule, which is identical to the failure criteria in practice.

6. The extrapolative results show that the life policies in use for light-corrosive turbine disc cannot be applied to the serious-corrosive disc directly because its reliable life is greatly less than an overhaul schedule, and it is urgent to establish a new criteria for withdrawal from service of the serious-corrosive disc to assure the structural integrity of this aeroengine. Using the failure life as an example, with a 99% survival rate, the failure life of the light-corrosive disc is 616 blocks, equivalent to 308 flight hours. On the other hand, the failure life of the serious-corrosive disc is only about 27 blocks, i.e., 13 flight hours, which are seriously less than an overhaul schedule.

References

[1] Powell, B. E. et al., 1982, "The Influence of Minor Cycle on Low Cycle Fatigue Crack Propagation," Int. J. Fatigue, **4**, pp. 4–14.

[2] Makhutov, A. Romanov, and Gadenin, M., 1979, "High-Temperature Low-Cycle Fatigue Resistance under Superimposed Stresses at Two Frequencies," Fatigue Fract. Eng. Mater. Struct., **1**, pp. 281–285.

[3] Guedou, Y., and Rongvaux, J. M., 1988, "Effect of Superimposed Stresses at High Frequency on Cycle Fatigue," ASTM Spec. Tech. Publ., **942**, pp. 939–960.

[4] Powell, B. E., 1995, "Fatigue Crack Growth Behavior of Two Contrasting Titanium Alloys," Int. J. Fatigue, **17**, pp. 221.

[5] Powell, B. E., and Duggan, T. V., 1986, "Predicting the Onset of High Cycle Fatigue Damage: an Engineering Application for Long Crack Fatigue Threshold Data," Int. J. Fatigue, **8**, pp. 187.

[6] Powell, B. E., and Duggan, T. V., 1987, "Crack Growth in Ti-6Al-4V under the Conjoint Action of High and Low Cycle Fatigue," Int. J. Fatigue, **9**, pp. 195–202.

[7] Ouyang, J., Wang, Z., Song, D., and Yan, M., 1988, "Influence of High Frequency Vibrations on the Low Cycle Fatigue Behavior of a Superalloy at Elevated Temperature," ASTM Spec. Tech. Publ., **942**, pp. 961–971.

[8] Perovich, W. Bessler, and Ziegler, W., 1986, "Ineracive Effects of High and Low Frequency Loading on the Faigue Crack Growth of Inconel 718," ASTM Spec. Tech. Publ., ASTM STP **905**, pp. 169–184.

[9] Wang, Rongqiao, 1996, "Research on Combined Fatigue of Turbine Disc Fir-Tree Mortises at Elevated Temperature," Ph.D. thesis, Beijing Univ. of Aero. & Astro., Beijing (in Chinese).

[10] Wang, Rongqiao, and Nie, Jingxu, 1997, "A New Experimental Method to Study Combined Fatigue of Actual Turbine Disk Mortise Teeth at Elevated Temperature," ASME J. Eng. Gas Turbines Power, **119**, pp. 969–972.

[11] Gao, Z. T., 1986, *Statistics for fatigue application*, National Defence industry Press, Beijing (in Chinese).

Downloaded 02 Jun 2010 to 171.66.16.98. Redistribution subject to ASME license or copyright; see http://www.asme.org/terms/Terms_Use.cfm

Methods for Specific Emission Evaluation in Spark Ignition Engines Based on Calculation Procedures of Air-Fuel Ratio: Development, Assessment, and Critical Comparison

Stefano d'Ambrosio

Ezio Spessa
e-mail: ezio.spessa@polito.it

Alberto Vassallo

Dipartimento di Energetica
IC Engines Advanced Laboratory,
Politecnico di Torino,
Corso Duca degli Abruzzi, 24,
Torino 10129, Italy

New computational procedures are proposed for evaluating the exhaust brake specific mass emissions of each pollutant species in internal combustion (IC) engines. The procedures start from the chemical reaction of fuel with combustion air and, based on the measured exhaust raw emissions THC, CH_4, NO_x, CO, O_2, CO_2, calculate the volume fractions of the compounds in the exhaust gases, including those that are not usually measured, such as water, nitrogen and hydrogen. The molecular mass of the exhaust gases is then evaluated and the brake specific emissions can be obtained if the exhaust flow rate and the engine power output are measured. The algorithm can also be applied to the evaluation of air-fuel ratio from measured raw volume emissions of IC engines. The new procedures take the effects of various fuel and combustion air compositions into account, with particular reference to different natural gas blends as well as to the presence of water vapor, CO_2, Ar and He in the combustion air. In the paper, the algorithms are applied to the evaluation of air-fuel ratio and brake specific mass emissions in an automotive bi-fuel Spark Ignition (SI) engine with multipoint sequential port-fuel injection. The experimental tests were carried out in a wide range of steady-state operating conditions under both gasoline and compressed natural gas operations. The specific emissions calculated from the new procedures are compared to those evaluated by applying Society of Automotive Engineers (SAE) and International Standards Organization (ISO) recommended practices and the air-fuel ratio results are compared to those obtained either from directly measured air and fuel mass flow rates or from Universal Exhaust Gas Oxygen (UEGO) sensor data. The sensitivity of the procedure results to the main engine working parameters, the influence of environmental conditions (in particular the effect of air humidity on NO_x formation) and the experimental uncertainties are also determined.
[DOI: 10.1115/1.1852566]

Introduction

Specific emissions are much more significant than molar concentrations for evaluating pollutants emitted by internal combustion (IC) engines. Volume fractions of exhaust species are uniquely measured using a standard automotive raw exhaust gas analyzer, whereas a variety of methods can be applied to determine specific emissions. Results on specific emissions are usually reported without any reference to the procedures and related assumptions used for their evaluation. In addition, most of the methods used for specific emission evaluation are addressed to gasoline engine only [1] or to engines running on a limited selection of different fuels [2]. Compressed natural gas (CNG) has recently gained an increasing interest among the alternative fuels and is considered a key strategy to reduce IC engine environmental impact. However, CNG composition is highly variable and strongly dependent on the supply source. Hence, in order to accurately evaluate mass emissions from CNG engines, specific emission evaluation methods are required capable of taking fuel flexible composition into account.

The present paper develops, validates and applies new procedures for the evaluation of the mass specific emissions in IC engines running on fuel blends with variable composition, on the basis of the measurement of the raw exhaust emission concentrations. The proposed methods stem from procedures similar to those used in Refs. [3–7] for mixture air-fuel ratio calculation only. Such procedures are here reorganized, refined and extended so as to develop new different mass emission calculation methods. In addition, the new methods support fuel flexible composition, with specific reference to various natural gas blends, and can also be applied when the raw emissions of some pollutants are measured on dry basis and those of the others are measured on wet basis. These methods can also be used to evaluate mixture air-fuel ratio.

Mass Emission Evaluation Procedures

In order to determine the exhaust emissions on a mass basis, three major parameters are required, that is, the volume fraction of the pollutants, the molecular mass of the exhaust gases, and the associated flow term

Contributed by the Internal Combustion Engine Division of THE AMERICAN SOCIETY OF MECHANICAL ENGINEERS for publication in the ASME JOURNAL OF ENGINEERING FOR GAS TURBINES AND POWER. Manuscript received by the ICE Division, October 24, 2003; final revision received June 1, 2004. Associate Editor: D. Assanis.

Copyright © 2005 by ASME

Downloaded 02 Jun 2010 to 171.66.16.98. Redistribution subject to ASME license or copyright; see http://www.asme.org/terms/Terms_Use.cfm

$$\dot{m}_X = \dot{m}_{\text{exh}} \cdot \frac{M_X}{M_{\text{exh}}} \cdot [X]_{\text{wet}} \tag{1}$$

The brake specific mass emissions are hence evaluated as

$$\{X\}_{\text{bs}} = \frac{\dot{m}_{\text{exh}} \cdot \frac{M_X}{M_{\text{exh}}} \cdot [X]_{\text{wet}}}{W} \tag{2}$$

The volume fractions of the exhaust species are measured using a standard automotive raw exhaust gas analyzer, the power output W of the engine is measured by means of the dynamometric brake, whereas a variety of methods can be applied to determine the exhaust gas flow rate and the molecular weight of the exhaust gases.

Exhaust Gas Flow Rate Evaluation

If the direct measurements of both wet air and fuel flow rates are available, the exhaust gas flow rate can be evaluated as

$$\dot{m}_{\text{exh}} = \dot{m}_{\text{air,wet}} + \dot{m}_{\text{fuel}} \tag{3}$$

If only one of the two flow rates is measured, the following expressions apply:

$$\dot{m}_{\text{exh}} = \dot{m}_{\text{air,wet}} \left(1 + \frac{1}{\alpha \cdot (1 + H_{\text{abs}} \cdot 10^{-3})} \right) \tag{4a}$$

$$\dot{m}_{\text{exh}} = \dot{m}_{\text{fuel}} [1 + \alpha \cdot (1 + H_{\text{abs}} \cdot 10^{-3})] \tag{4b}$$

where α can be either measured by means of a Universal Exhaust Gas Oxygen (UEGO) sensor or calculated from the composition of the exhaust gases according to Eq. (28); H_{abs} can be measured by means of a hygrometer.

Exhaust Gas Molecular Weight Evaluation

If the number of moles of the chemical species at the engine outlet are known, the exhaust gas average molecular weight can be evaluated as

$$M_{\text{exh}} = \frac{\Sigma_j (n_j \cdot M_j)}{\Sigma_j n_j} \tag{5}$$

The number of moles n_j of each emission at the engine outlet can be evaluated by means of either the authors' procedures (described in Section "Evaluation of the Mole Number of the Combustion Products at the Engine Outlet") or a simplified model such as that described in Ref. [8].

As an alternative, M_{exh} can be evaluated according to the practices recommended in Society of Automotive Engineers (SAE) J1088 [1] and International Standards Organization (ISO) 8178 [2].

Measurement of Volume Fractions of Exhaust Species

The volume fractions of the exhaust species can be measured either on dry basis or on wet basis. Since the pollutant concentrations on a wet basis are required in Eqs. (1) and (2), when the measurements are taken on a dry basis a conversion factor CF must be applied so that

$$[X]_{\text{wet}} = CF \cdot [X]_{\text{dry}} \tag{6}$$

Such a conversion factor can be evaluated by means of either the authors' procedures described in Section "CF Calculation" or according to the practices recommended in SAE J1088 and ISO 8178.

Evaluation of the Mole Number of the Combustion Products at the Engine Outlet

The following combustion reaction is considered:

$$\begin{aligned} &C_xH_yO_z + EH_2 + FO_2 + GN_2 + LCO_2 + PH_2O + QCO + RHe \\ &\quad + SAr + n(O_2 + AN_2 + BCO_2 + CH_{\text{abs}}H_2O + DAr) \\ &\quad \rightarrow aCO_2 + bCO + cH_2 + dH_2O + eO_2 + fN_2 + gNO + g'NO_2 \\ &\quad + hCH_4 + h'C_{x'}H_{y'}O_{z'} + iAr + qHe \end{aligned}$$

In order to take different blends of natural gas into account, the generic fuel is represented not only by the hydrocarbon with average composition $C_xH_yO_z$ but also by an additional mixture of other chemical species, such as hydrogen, oxygen, nitrogen, carbon dioxide, water, carbon monoxide, helium and argon. If the volume fractions of each chemical species in the fuel are known, the coefficients x, y, z, E, F, G, L, P, Q, R and S can be determined as follows:

$$x = \frac{\Sigma_{u=1}^{\eta} \Sigma_{v=1}^{\mu} \Sigma_{w=1}^{\nu} (u \cdot [C_uH_vO_w])}{\Sigma_{u=1}^{\eta} \Sigma_{v=1}^{\mu} \Sigma_{w=1}^{\nu} ([C_uH_vO_w])}$$

$$y = \frac{\Sigma_{u=1}^{\eta} \Sigma_{v=1}^{\mu} \Sigma_{w=1}^{\nu} (v \cdot [C_uH_vO_w])}{\Sigma_{u=1}^{\eta} \Sigma_{v=1}^{\mu} \Sigma_{w=1}^{\nu} ([C_uH_vO_w])}$$

$$z = \frac{\Sigma_{u=1}^{\eta} \Sigma_{v=1}^{\mu} \Sigma_{w=1}^{\nu} (w \cdot [C_uH_vO_w])}{\Sigma_{u=1}^{\eta} \Sigma_{v=1}^{\mu} \Sigma_{w=1}^{\nu} ([C_uH_vO_w])}$$

$$E = \frac{[H_2]}{\Sigma_{u=1}^{\eta} \Sigma_{v=1}^{\mu} \Sigma_{w=1}^{\nu} ([C_uH_vO_w])}$$

$$F = \frac{[O_2]}{\Sigma_{u=1}^{\eta} \Sigma_{v=1}^{\mu} \Sigma_{w=1}^{\nu} ([C_uH_vO_w])}$$

$$S = \frac{[Ar]}{\Sigma_{u=1}^{\eta} \Sigma_{v=1}^{\mu} \Sigma_{w=1}^{\nu} ([C_uH_vO_w])}$$

As far as the combustion air is concerned, the presence of water vapor, carbon dioxide, and argon is also considered. The coefficients A, B, and D must be determined according to the considered composition of the combustion air

$$A = \frac{[N_2]_{\text{amb}}}{[O_2]_{\text{amb}}}$$

$$B = \frac{[CO_2]_{\text{amb}}}{[O_2]_{\text{amb}}}$$

$$D = \frac{[Ar]_{\text{amb}}}{[O_{2\text{amb}}}$$

If a measurement of the water in the combustion air is available as absolute humidity H_{abs} (g/kg dry air) the coefficient C is expressed by

$$C = \frac{M_{\text{air,dry}} / M_{H_2O}}{[O_2]_{\text{amb}}} \cdot 10^{-3},$$

where

$$M_{\text{air,dry}} = \frac{1 \cdot (2M_O) + A(2M_O) + B(M_C + 2M_O) + D(2M_{Ar})}{1 + A + B + D}$$

The variable n represents the number of moles of oxygen in the combustion air that react with a single mole of average hydrocarbon $C_xH_yO_z$.

As far as the combustion products are concerned, it is assumed that the measurement of the exhaust concentrations of CO_2, CO, O_2, NO, NO_2, CH_4, and $C_{x'}H_{y'}O_{z'}$ are available and that the average composition $C_{x'}H_{y'}O_{z'}$ of unburned nonmethane hydrocarbons has been evaluated by means of exhaust gas chromatography. If CH_4 measurement is not available, it is sufficient setting $[CH_4] = 0$ in Eqs. (13*a*,*b*) and (14*a*,*b*) and leaving the remaining

Downloaded 02 Jun 2010 to 171.66.16.98. Redistribution subject to ASME license or copyright; see http://www.asme.org/terms/Terms_Use.cfm

equations unchanged. The concentrations of CO_2, CO, and O_2, are usually measured on a dry basis (i.e., extracting the water vapor from the exhaust gas before the analysis, usually by means of a cooler), therefore

$$a=[CO_2]_{dry}\cdot n_{tot,dry}\cdot CF_{cooler} \tag{7}$$

$$b=[CO]_{dry}\cdot n_{tot,dry}\cdot CF_{cooler} \tag{8}$$

$$e=[O_2]_{dry}\cdot n_{tot,dry}\cdot CF_{cooler} \tag{9}$$

where

$$n_{tot,dry}=a+b+c+e+f+g+g'+h+h'+i+q \tag{10}$$

$$CF_{cooler}=\frac{n_{tot,dry}+n_{H_2O,cooler}}{n_{tot,dry}}=\frac{1}{1-[H_2O,cooler]}$$

$[H_2O,cooler]$ indicates the residual fraction of water vapor that can still be present in the sample after it exits the cooler outlet. Hence, the coefficient CF_{cooler} can be calculated as

$$[H_2O,cooler]=\frac{n_{H_2O,cooler}}{n_{tot,dry}+n_{H_2O,cooler}}=\frac{p_{vap}(T_{cooler})}{p_{baro}}$$

The concentrations of NO, NO_2, CH_4 and $C_{x'}H_{y'}O_{z'}$ can be measured either on a dry or on a wet basis, therefore

$$g=[NO]_{dry}\cdot n_{tot,dry}\cdot CF_{cooler} \quad \text{dry basis} \tag{11a}$$

$$g=[NO]_{wet}\cdot (n_{tot,dry}+d) \quad \text{wet basis} \tag{11b}$$

$$g'=[NO_2]_{dry}\cdot n_{tot,dry}\cdot CF_{cooler} \quad \text{dry basis} \tag{12a}$$

$$g'=[NO_2]_{wet}\cdot (n_{tot,dry}+d) \quad \text{wet basis} \tag{12b}$$

$$h=[CH_4]_{dry}\cdot n_{tot,dry}\cdot CF_{cooler} \quad \text{dry basis} \tag{13a}$$

$$h=[CH_4]_{wet}\cdot (n_{tot,dry}+d) \quad \text{wet basis} \tag{13b}$$

$$h'=\frac{([THC]_{dry}-[CH_4]_{dry})\cdot n_{tot,dry}\cdot CF_{cooler}}{x'} \quad \text{dry basis} \tag{14a}$$

$$h'=\frac{([THC]_{wet}-[CH_4]_{wet})\cdot (n_{tot,dry}+d)}{x'} \quad \text{wet basis} \tag{14b}$$

CH_4 and THC volume fractions are measured as C_1 equivalent.

Hence, the variables of the problem are: n, $n_{tot,dry}$, a, b, c, d, e, f, g, g', h, h', i, q, so that six further independent equations must be considered in addition to Eqs. (7)–(14*a*,*b*).

By introducing Eqs. (7), (8), (13*a*,*b*) and (14*a*,*b*) into the carbon balance equation, the following Eqs. (15*a*) and (15*b*) can be used to express $n_{tot,dry}$ when the unburned hydrocarbons are measured on a dry or wet basis, respectively,

$$n_{tot,dry}=\frac{x+L+Q+n\cdot B}{([CO_2]_{dry}+[CO]_{dry}+[THC]_{dry})\cdot CF_{cooler}} \tag{15a}$$

$$n_{tot,dry}=\frac{x+L+Q+n\cdot B-[THC]_{wet}\cdot d}{([CO_2]_{dry}+[CO]_{dry})\cdot CF_{cooler}+[THC]_{wet}} \tag{15b}$$

Finally, the helium, argon, oxygen, nitrogen, and hydrogen balances are imposed and the following expressions are obtained:

$$q=R \tag{16}$$

$$i=S+nD \tag{17}$$

$$n=\frac{2a+b+d+2e+g+2g'+h'z'-z-2F-2L-P-Q}{2+2B+CH_{abs}} \tag{18}$$

$$f=G+nA-\frac{g}{2}-\frac{g'}{2} \tag{19}$$

$$c=\frac{y-4h-h'y'}{2}+E+P+nCH_{abs}-d \tag{20}$$

Full Mass Balance Method. By combining Eqs. (10), (16), (17), (18), (19), and (20) and by rearranging terms, the following expression for the number d of water moles in the exhaust gases can be found:

$$d=\frac{1}{\left(1-\frac{2+2B+CH_{abs}}{A+D}\right)}\cdot\left[\frac{2+2B+CH_{abs}}{A+D}\left(n_{tot,dry}-a-b-\frac{y-4h-h'y'}{2}-E-P-nCH_{abs}-e-G-\frac{g}{2}-\frac{g'}{2}-h-h'-S-R\right)-2a-b-2e-g-2g'-h'z'+z+2F+2L+P+Q\right] \tag{21}$$

The moles of the combustion products can be evaluated by numerically solving the set of Eqs. (7)–(9), (11)–(21). The equation sets are circular because

- d in Eq. (21) also depends on n, which, in turn, depends on d; and
- when CH_4, THC, or NO or NO_2 are measured on a wet basis, one must consider that $n_{tot,dry}$, g, g', h and h' are also functions of d.

This could be avoided by an algebraic simplification process that leads to closed form equations for d and n. Since such equations are very long and intricate, the authors believe that it is more convenient to numerically solve one of the two equation sets reported above by means of a fixed point iteration similar to that suggested in Ref. [4].

Water-Gas Reaction Method. In the engine cylinder CO_2 and H_2O may dissociate during the combustion process of a rich mixture due to the high temperature values, creating amounts of H_2 and CO that depend on temperature and pressure values. These four species reach an equilibrium described by the equilibrium constant K for the so-called water-gas reaction. Such an equilibrium depends on the combustion process. As the combustion products leave the cylinder, the proportion of CO_2, H_2O, H_2 and CO are frozen at the equilibrium concentrations

$$CO_2+H_2\leftrightarrow CO+H_2O$$

and the equilibrium is described by the constant K

$$K=\frac{[CO]\cdot[H_2O]}{[CO_2\cdot[H_2]}=\frac{b\cdot d}{a\cdot c} \tag{22}$$

The value of K depends on the combustion temperature and values between 3.5 and 3.8 are indicated in the literature as producing good matches between the theory and the experimental measurements in engine exhaust upstream from the catalyst [5,6]. More specifically, in Ref. [5] it is observed that, since the catalyst itself causes the combustion to continue at lower temperatures, the values of K measured downstream from catalyst show larger variations depending on catalyst efficiency. Nevertheless, a conventional value of K between 3.5 and 3.8 can still be retained as the mass emissions are virtually unaffected by the extremely low H_2 concentrations downstream from the catalyst [5].

As far as the calculation of the moles of the combustion products at the engine outlet is concerned, Eq. (20) can be combined with Eq. (22) leading to

Downloaded 02 Jun 2010 to 171.66.16.98. Redistribution subject to ASME license or copyright; see http://www.asme.org/terms/Terms_Use.cfm

$$d=\frac{(y-4h-h'y'+2E+2P+2nCH_{\text{abs}})}{2\left(1+\frac{b}{aK}\right)} \tag{23}$$

The equation set (7)–(9), (11)–(20), (23) can be numerically solved and the moles of the combustion products can be evaluated.

As can be easily inferred, the equations obtained with the water-gas reaction method are circular. As far as the possibility of rearranging the proposed expressions so as to obtain closed form equations is concerned, similar considerations to those reported in Section "Full Mass Balance Method" hold.

No Oxygen Measurement Method. In some lower-cost exhaust-gas analyzer systems the measurement of oxygen concentration in exhaust gases is not available, so Eq. (9) cannot be used. In this case, in order to evaluate the moles of the combustion products, it is possible to combine the methods described in Section "Full Mass Balance Method" and Section "Water-Gas Reaction Method." By combining Eqs. (10), (16)–(20) together with Eq. (23), the following expression for the number e of oxygen moles in the exhaust gases can be found:

$$e=\frac{1}{\left(1+2\frac{A+D}{2+2B+\text{CH}_{\text{abs}}}\right)}\cdot\left[n_{\text{tot,dry}}-a-b-\frac{y-4h-h'y'}{2}-E\right.$$
$$-P-n\text{CH}_{\text{abs}}+d\frac{A+D}{2+2B+\text{CH}_{\text{abs}}}(2a+b+d+g+2g'+h'z'$$
$$\left.-z-2F-2L-P-Q)-G-\frac{g}{2}-\frac{g'}{2}-h-h'-S-R\right] \tag{24}$$

Hence, the moles of the combustion products can be evaluated by numerically solving the set of Eqs. (7), (8), (11)–(20), (24).

The equations obtained with the no oxygen measurement method are also circular and similar considerations to those previously reported in Section "Full Mass Balance Method" and Section "Water-Gas Reaction Method" hold. It is worthwhile pointing out that this procedure can be used also if the measurement of oxygen in exhaust gases is available. In this case, the concentration of oxygen calculated by the method can be used to estimate the experimental uncertainty by comparing it to the measured one.

CF Calculation. With reference to the pollutant species that are measured on a dry basis, the conversion factor CF introduced in Section "Measurement of Volume Fractions of Exhaust Species" can be now evaluated as follows:

$$CF=\frac{[X]_{\text{wet}}}{[X]_{\text{dry}}}=\frac{\frac{n_X}{n_{\text{tot,dry}}+d}}{\frac{n_X}{n_{\text{tot,dry}}+n_{\text{H}_2\text{O,cooler}}}}=\frac{n_{\text{tot,dry}}+n_{\text{H}_2\text{O,cooler}}}{n_{\text{tot,dry}}}$$
$$\cdot\frac{n_{\text{tot,dry}}}{n_{\text{tot,dry}}+d}=CF_{\text{cooler}}\frac{n_{\text{tot,dry}}}{n_{\text{tot,dry}}+d} \tag{25}$$

Final Remarks. The methods proposed in Section "Full Mass Balance Method" and in Sections "Water-Gas Reaction Method," "No Oxygen Measurement Method" are based on procedures similar to those presented in Refs. [3,4] and in [5–7], respectively. In Refs. [3–7] such procedures were developed for the mixture air/fuel ratio calculations only. In the present paper these procedures were reorganized and extended to obtain different mass emission calculation methods. Furthermore, two additional features were included: fuels with complex composition, such as various natural gas blends, were taken into account and both cases of pollutant emission measurements taken on either dry or wet basis were considered.

Mixture Air-Fuel Ratio Calculation

The procedures described in Sections "Full Mass Balance Method," "Water-Gas Reaction Method," "No Oxygen Measurement Method" can also be applied to the calculation of mixture relative air-fuel ratio λ

$$\lambda=\left(\frac{\dot{m}_{\text{air,dry}}}{\dot{m}_{\text{fuel}}}\right)\Big/\left(\frac{\dot{m}_{\text{air,dry}}}{\dot{m}_{\text{fuel}}}\right)_{\text{st}}=\left(\frac{n_{\text{air}}\cdot M_{\text{air,dry}}}{n_{\text{fuel}}\cdot M_{\text{fuel}}}\right)\Big/\left[\left(\frac{n_{\text{air}}}{n_{\text{fuel}}}\right)_{st}\frac{M_{\text{air,dry}}}{M_{\text{fuel}}}\right]$$
$$=\left(\frac{n_{\text{air}}}{n_{\text{fuel}}}\right)\Big/\left(\frac{n_{\text{air}}}{n_{\text{fuel}}}\right)_{\text{st}}$$

In the combustion reaction considered in Section "Evaluation of the Mole Number of the Combustion Products at the Engine Outlet," $n_{\text{air}}=n$ and $n_{\text{fuel}}=1$, therefore

$$\lambda=\frac{n}{n_{\text{st}}}$$

where n_{st} is the value of n for a stoichiometric complete combustion reaction between fuel and dry air

$$n_{\text{st}}=x+\frac{y}{4}-\frac{z}{2}+\frac{E}{2}-F+\frac{Q}{2}$$

Hence, the relative air-fuel ratio of the mixture can be calculated as

$$\lambda=\frac{n}{x+\frac{y}{4}-\frac{z}{2}+\frac{E}{2}-F+\frac{Q}{2}} \tag{26}$$

The mixture air-fuel ratio α is

$$\alpha=\frac{\dot{m}_{\text{air,dry}}}{\dot{m}_{\text{fuel}}}=\lambda\,\alpha_{\text{st}}$$

where α_{st} is the value of α for a stoichiometric complete combustion reaction between fuel and dry air

$$\alpha_{\text{st}}=\frac{n_{\text{st}}\cdot M_{\text{air,dry}}(1+A+B+D)}{M_{\text{fuel}}(1+E+G+L+P+Q+R+S)}. \tag{27}$$

Hence, the above expressions lead to

$$\alpha=\frac{n\cdot M_{\text{air,dry}}(1+A+B+D)}{M_{\text{fuel}}(1+E+G+L+P+Q+R+S)} \tag{28}$$

where

$$M_{\text{fuel}}=\frac{1}{1+E+G+L+P+Q+R+S}\cdot[1\cdot(\text{x}M_{\text{C}}+\text{y}M_{\text{H}}+\text{z}M_{\text{O}})$$
$$+\text{E}(2M_{\text{H}})+\text{F}(2M_{\text{O}})+\text{G}(2M_{\text{N}})+\text{L}(M_{\text{C}}+2M_{O})$$
$$+\text{P}(2M_{\text{H}}+M_{\text{O}})+\text{Q}(M_{\text{C}}+M_{\text{O}})+\text{R}(M_{\text{He}})+\text{S}(M_{\text{Ar}})]$$

The value of n can be calculated from any of the methods described in Section "Evaluation of the Mole Number of the Combustion Products at the Engine Outlet."

In addition, the air-fuel ratio can be either derived from UEGO sensor output ("UEGO" method) or calculated from direct measurements of air and fuel flow rates ("Air & Fuel" method). In this latter case the following expression is applied:

$$\alpha=\left(\frac{1}{1+H_{\text{abs}}\cdot 10^{-3}}\right)\frac{\dot{m}_{\text{air,wet}}}{\dot{m}_{\text{fuel}}} \tag{29}$$

Effect of Mixture Humidity on NO Formation

A reduction in NO formation is caused by an increase in mixture humidity due mainly to the drop in the maximum flame temperature. It was found [9] that each 1% (by weight) of water vapor

Downloaded 02 Jun 2010 to 171.66.16.98. Redistribution subject to ASME license or copyright; see http://www.asme.org/terms/Terms_Use.cfm

Table 1 Main engine specifications

Bore	84 mm
Stroke	90 mm
Compression ratio	10.35
Connecting rod length	145.4 mm
Cylinder number	4
Displacement	1995 cm^3

Table 2 λ uncertainties for gasoline operations

Gasoline	λ≈0.8	λ≈1.0	λ≈1.4
UEGO	<0.5%	<1%	<3%
W-G reaction	<1%	<0.5%	<1%
Mass balance	<6%	<6%	<6%
No oxygen	<2%	<2.5%	<2.5%
Air & Fuel	<3.5%	<3.5%	<3.5%

reduced a hydrogen-air and ethylene-air flame temperature by approximately 20°C. This lowered the initial rate of nitric oxide production by about 25%.

In order to take the moisture effect on NO formation into account, the SAE J1088 and ISO 8178 recommended practices suggest using a dimensionless correction factor KH

$$[\mathrm{NO}]_{\mathrm{corr}} = [\mathrm{NO}] \cdot KH \tag{30}$$

For SAE J1088 [1]

$$KH = \frac{1}{1 - 0.0047 \cdot (\mathrm{H}_{\mathrm{abs}} - 75)} \tag{31}$$

where H_{abs} is measured in grain/lb.

According to ISO 8178 for Spark Ignition (SI) engines [2]

$$KH = 0.6272 + 44.030 \cdot 10^{-3} \cdot H_{\mathrm{abs}} - 0.862 \cdot 10^{-3} \cdot H_{\mathrm{abs}}^2 \tag{32}$$

Based on Eqs. (31), (32) KH is equal to unity (i.e., no correction is applied) when $H_{\mathrm{abs}} = 10.71$ g/kg (75 grain/lb).

As reported in Ref. [9], the dependence of NO formation on air humidity is roughly linear at constant engine operating conditions. Therefore, another correction formula is here proposed by the authors

$$[\mathrm{NO}]_{\mathrm{corr}} = [\mathrm{NO}] + KH' \cdot (H_{\mathrm{abs}} - 10.71) \tag{33}$$

KH' values are indicated in Section "Results and Discussions."

Test Engine and Experimental System

The engine is a multivalve FIAT-Lancia 16 V VIS (variable intake system). Main engine specifications are provided in Table 1 [10]. The engine head present a pent-roof combustion chamber, four valves per cylinder, one centrally located spark plug and tumble inducing inlet ports with variable runner configuration, which are of particular interest for a CNG fueled engine, due to the lack of data for this engine type. The engine is also equipped with a three-way catalyst and a lambda-oxygen sensor for pollutant emission reduction.

Originally, the engine was provided with a multipoint "Bosch Motronic M1.7" electronic module controlling the injection duration and the spark timing for operation with gasoline. In order to allow the engine to run on natural gas, this module was replaced by a "Magneti Marelli IAW" Electronic Control Module (ECM) designed for obtaining a multipoint sequential injection in the engine running on CNG. The "IAW" Law ECM is also used for engine operation with gasoline and it was necessary to determine the engine maps for both CNG and gasoline working conditions.

High pressure CNG is supplied through a stainless steel distribution pipe from storage cylinders to a double-stage Tartarini regulator for pressure reduction to 9 bar. Further details on the natural gas conversion of the gasoline engine as well as on the CNG fuel plant design and installation are reported in Ref. [10].

The engine was operated on a test bench which had been previously installed and instrumented in an engine hall for typical dynamometer experiments. The engine is equipped with a "Degussa—Hartmann & Braun" hot-film air-mass sensor in the intake system, with two "MicroMotion" Coriolis mass flow meters (one for gasoline and the other for CNG), with two air-fuel ratio "NGK" UEGO sensors (one for rich mixtures and the other for lean ones) in the exhaust system, with a pressure sensor in the injection rail and with thermocouples for measuring the temperatures of the intake flow, of the fuel and of the exhaust gases. A water-cooled piezoelectric transducer was installed on the engine cylinder head for taking the pressure time history of the gases in the combustion chamber. The engine speed was measured by a crank-shaft driven encoder which simultaneously generated the time base for the acquisition system [10].

For the present investigation, the test facility was also equipped with an upgraded "Fisher-Rosemount" exhaust-gas analyzer [11]. This is a multipurpose analyzer which can measure the pollutant emission levels in the exhaust from gasoline and diesel engines, including Exhaust Gas Recirculation (EGR), as well as from engines fueled by alternative fuels such as liquefied petroleum gas (LPG) and CNG. The Fisher–Rosemount gas analyzer is essentially made up of the following modules: two heated flame ionization detectors for the analysis of unburned hydrocarbons (HC), one for the analysis of total HC (THC) and the other with a "cutter" for measuring the concentration of methane HC, so that it is possible to have the concentration of nonmethane HC separately; one chemiluminescence detector (CLD) for the analysis of NO_x; two nondispersive infrared analyzers for measuring the concentrations of CO and CO_2, and an additional detector for CO_2 concentration analysis in the EGR; one paramagnetic oxygen detector. The exhaust-gas analyzer is equipped with both cold and heated lines for HC concentration measurements and includes the possibility of incorporating a heated CLD module for NO_x analysis. All the measuring instruments were connected to a PC based National Instrument data acquisition system, allowing simultaneous measurement of the major engine operating quantities. These included: torque, crankshaft angular speed, flow rates, pressures, temperatures and the exhaust gas composition. A high frequency acquisition card enabled measurements of the in-cylinder pressure time history to be recorded over the whole engine cycle.

Experimental Uncertainty

Based on the accuracy of instrumentation, and on the average deviations of repeated measurement sets, the following maximum uncertainties can be ascribed: 0.6% of the measured gasoline flow rates, 1.5% of CNG flow rates and 3% of air flow rates. This latter can be further reduced by a specific calibration of the air mass flow rate sensor. The raw exhaust gas analyzers have a relative accuracy of 1% of the full-scale range used, whereas span gases are provided with 2% accuracy of nominal concentration. If measurement ranges and optimum span gas concentrations are properly set, the accuracy on λ values reported in Tables 2 and 3 is obtained for gasoline and CNG operations, respectively. For a comparison, accuracies on λ values for UEGO and Air & Fuel methods are reported.

Table 3 λ uncertainties for CNG operations

CNG	λ≈0.8	λ≈1.0	λ≈1.4
UEGO	<0.5%	<1%	<3%
W-G reaction	<1%	<0.5%	<1%
Mass balance	<6%	<6%	<6%
No oxygen	<2%	<2.5%	<3%
Air & Fuel	<3.5%	<3.5%	<3.5%

Downloaded 02 Jun 2010 to 171.66.16.98. Redistribution subject to ASME license or copyright; see http://www.asme.org/terms/Terms_Use.cfm

Table 4 Specific emission uncertainties for gasoline and CNG operations

	Gasoline			CNG		
	W-G reaction	Mass balance	No oxygen	W-G reaction	Mass balance	No oxygen
THC	<4%	<5%	<4%	<4%	<5%	<5%
NO_x	<5%	<6%	<5%	<5%	<6%	<5%
CO	<3%	<5%	<4%	<3%	<5%	<4%
CO_2	<1%	<5%	<2%	<1%	<6%	<3%
M_{exh}	<0.5%	<1%	<0.5%	<0.5%	<1.5%	<0.5%

Finally, Table 4 shows the uncertainties on pollutant specific emissions and on exhaust average molecular mass, calculated according to the authors' procedures described in Section "Evaluation of the Mole Number of the Combustion Products at the Engine Outlet."

Results and Discussions

The methods proposed by the authors for specific emission evaluation were extensively tested in a wide range of engine operating conditions (N=2000–6000 rpm, bmep=200–790 kPa, λ=0.80–1.45) for both gasoline and CNG fueling. The results were also compared to those obtained applying SAE J1088 and ISO 8178 recommended practices.

The experimental data were taken with the engine test facilities described in Section "Test Engine and Experimental System." In the present paper, all the raw pollutant emission measurements were taken on a dry basis upstream from the catalytic converter.

A standard gasoline and two different blends of CNG were used in the present work. Based on the results of gas chromatographic analyses, the composition of the standard unleaded gasoline is specified in Table 5, whereas the composition of the two blends of CNG is reported in Table 6. As far as the ambient air composition is concerned, based on the standard air data reported in Table 7, the following values for the coefficient A, B, C, D are used in the present paper: $A=3.72745$, $B=0.04439$, $C=0.00767$, $D=0.00143$.

The methods for evaluating the exhaust mass flow rates are compared in Fig. 1 for various engine operating conditions, for $\lambda=1$ and SA set to metal base transistor (MBT) Timing. Figures 1(*a*) and 1(*c*) refer to gasoline operations, whereas Figs. 1(*b*) and 1(*d*) refer to CNG operations. The following methods were applied:

- *UEGO*: Eq. (4*b*) is used, where α is calculated from UEGO sensor output and $\dot{m}_{fuel}$ is measured by the Coriolis sensor;
- *W-G reaction*: Eq. (4*b*) is used, where α is calculated according to the procedure in Section "Water-Gas Reaction Method" and using Eq. (28), whereas $\dot{m}_{fuel}$ is measured by the Coriolis sensor;
- *Mass balance*: Eq. (4*b*) is used, where α is calculated according to the procedure in Section "Full Mass Balance Method" and using Eq. (28), whereas $\dot{m}_{fuel}$ is measured by the Coriolis sensor;
- *No oxygen*: Eq. (4*b*) is used, where α is calculated according to the procedure in Section "No Oxygen Measurement Method" and using Eq. (28), whereas $\dot{m}_{fuel}$ is measured by the Coriolis sensor;
- *Air & Fuel*: Eq. (3) is used, where $\dot{m}_{air,wet}$ and $\dot{m}_{fuel}$ are the mass flow rates that were measured by hot film and by Coriolis sensors, respectively.

The abscissa axes in Fig. 1 report the mass flow rates obtained with the UEGO method, which is the most widely adopted procedure and has a very high accuracy under stoichiometric conditions. The empty square, the star, the cross and the empty diamond symbols refer to the exhaust mass flow rates obtained with W-G reaction, mass balance, No oxygen, and Air & Fuel methods, re-

Table 5 Unleaded gasoline composition

α_{st}	14.61
H_i [MJ/kg]	44
x	8.26
y	15.5
z	0
y/x	1.88
n_{st}	12.14
M_{fuel}	114.83

Table 6 CNG composition

Species	CNG #1	CNG #2
Methane	90.80	88.30
Ethane	5.00	6.30
Propane	1.40	1.40
Iso-butane	0.20	0.20
Iso-pentane	0.05	0.05
Hexane and higher	0.05	0.05
Hydrogen	0.00	0.00
Free Oxygen	0.00	0.00
Nitrogen	1.15	2.35
Carbon dioxide	1.30	1.30
Water	0.00	0.00
Carbon monoxide	0.00	0.00
Helium	0.05	0.05
Argon	0.00	0.00
α_{st}	16.137	15.812
H_i [MJ/kg]	47.1	46.2
x	1.091	1.105
y	4.182	4.211
z	0.000	0.00
y/x	3.833	3.810
E	0.000	0.00
F	0.000	0.00
G	0.012	0.024
L	0.013	0.014
P	0.000	0.000
Q	0.000	0.000
R	0.001	0.001
S	0.000	0.000
n_{st}	2.137	2.158
M_{fuel}	17.778	18.104

Table 7 Principle air constituents of dry air

Species	ppm by volume	Molar fraction	Molar ratio
Oxygen	209 500	0.2095	1
Nitrogen	780 900	0.7809	3.727
Argon	9300	0.0093	0.044
Carbon Dioxide	300	0.0003	0.001
Air	1 000 000	1	4.773

Downloaded 02 Jun 2010 to 171.66.16.98. Redistribution subject to ASME license or copyright; see http://www.asme.org/terms/Terms_Use.cfm

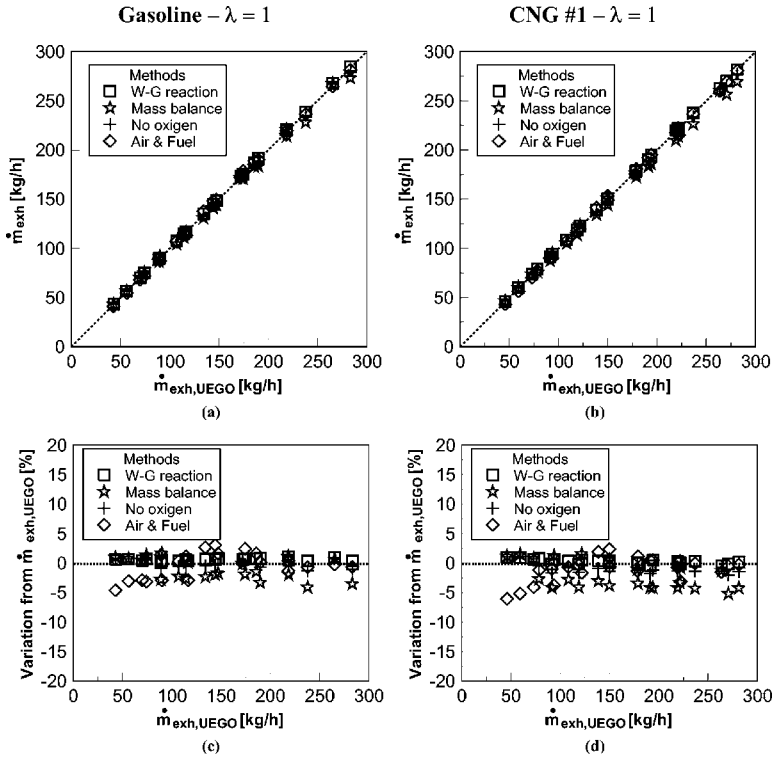

Fig. 1 Exhaust mass flow rates and variations from $\dot{m}_{exh,UEGO}$ for gasoline and CNG operations

spectively. The bisector (dotted line) is also reported for comparison. A good agreement is exhibited by all the methods for all of the considered operating conditions under both gasoline and CNG fueling.

Figures 1(*c*) and 1(*d*) highlight the percentage variation of each method from the UEGO procedure. W-G reaction and No oxygen showed the best accordance with UEGO, the highest differences being always lower than 1% and 2%, respectively, of nominal value for both fuels. Larger differences (up to approximately 5%) can be found with Air & Fuel, mainly at low flow rates. Such a large difference can be reduced by a proper calibration of the air mass flow rate sensor.

Figures 2(*a*) and 2(*b*) compare the λ values calculated with the abovementioned methods for a λ sweep taken at fixed throttle position and engine speed under MBT timing operating conditions. In particular, the experimental tests were performed at $N = 2600$ rpm and the test point at $\lambda = 1$ was obtained at bmep = 790 kPa. The abscissa axes report the λ values obtained with the W-G reaction procedure, i.e., by applying the method described in Section "Water-Gas Reaction Method" and Eq. (26). This was selected as reference method because it evidences a really low experimental uncertainty under all tested λ values and, in addition, for stoichiometric condition it gives λ values which are virtually equal to those obtained with UEGO. The different symbols in Fig. 2 indicate the different methods used for λ evaluation

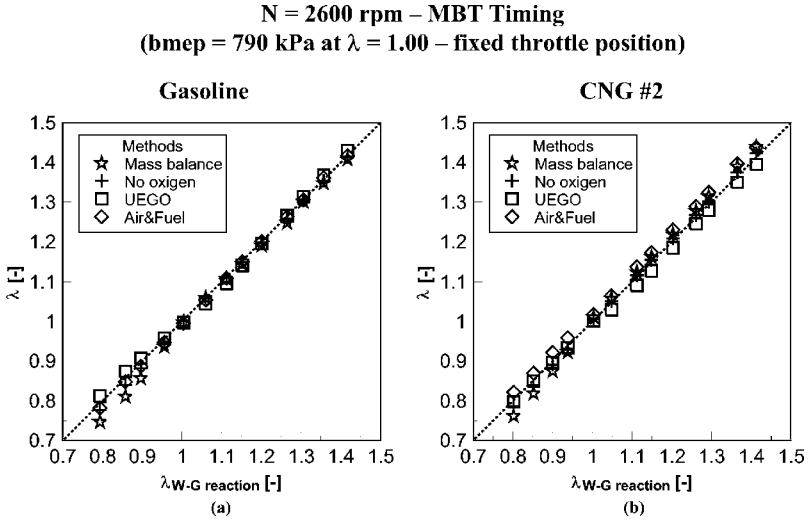

Fig. 2 Estimated λ for gasoline (*a*) and CNG (*b*) operations

Downloaded 02 Jun 2010 to 171.66.16.98. Redistribution subject to ASME license or copyright; see http://www.asme.org/terms/Terms_Use.cfm

Table 8(*a*) Gasoline operations—brake power output, flow rates, air humidity, and acquired emissions

Run	W [kW]	$m_{air,wet}$ [kg/h]	m_{fuel} [kg/h]	H_{abs} [g/kg]	THC [ppmC1]	NO_x [ppm]	CO [ppm]	CO_2 [ppm]	O_2 [ppm]
				Gasoline—$N=2600$ rpm—MBT timing (bmep=790 kPa at $\lambda=1.00$—fixed throttle position)					
#1	34.7	130.3	11.27	11.9	3300	370	75 400	104 500	2600
#2	34.9	129.7	10.35	11.1	2870	845	51 500	119 500	2660
#3	34.8	129.2	9.85	11.3	2580	1350	37 400	128 000	2820
#4	34.2	128.8	9.21	11.4	2260	2305	18 000	138 500	3740
#5	33.3	129.1	8.78	11.6	1990	2980	7200	142 000	6970
#6	32.4	129.4	8.31	11.5	1640	3645	1480	140 500	14 200
#7	31.6	130.7	7.97	11.8	1570	4015	760	134 000	23 300
#8	30.5	131.3	7.73	11.5	1510	3580	770	129 500	30 300
#9	29.3	132.2	7.45	11.7	1550	3025	760	123 500	38 500
#10	27.6	132.8	7.11	11.6	1670	2260	740	117 000	48 200
#11	26.8	133.2	6.91	11.1	1750	1705	730	113 000	53 900
#12	25.6	134.2	6.67	11.7	1990	1285	730	108 000	60 600
#13	24.7	134.6	6.43	10.9	2300	1200	690	103 000	67 800

Table 8(*b*) Molar fractions for Gasoline operations—W-G reaction

Run	λ	CO_2	CO $\times 10$	H_2	H_2O	O_2 $\times 10$	N_2	NO_x $\times 100$	THC $\times 100$	CF
#1	*0.794*	0.088	0.638	0.026	0.133	0.022	0.674	0.030	0.280	0.866
#2	*0.858*	0.101	0.435	0.016	0.135	0.022	0.690	0.070	0.242	0.863
#3	*0.897*	0.108	0.317	0.011	0.136	0.023	0.697	0.112	0.219	0.862
#4	*0.956*	0.118	0.154	0.005	0.137	0.032	0.708	0.194	0.193	0.862
#5	*1.004*	0.122	0.062	0.002	0.135	0.060	0.714	0.252	0.171	0.863
#6	*1.060*	0.121	0.012	0.000	0.131	0.123	0.719	0.309	0.142	0.867
#7	*1.112*	0.116	0.006	0.000	0.127	0.203	0.721	0.342	0.136	0.871
#8	*1.152*	0.113	0.006	0.000	0.123	0.265	0.723	0.306	0.132	0.875
#9	*1.201*	0.108	0.006	0.000	0.119	0.337	0.724	0.258	0.136	0.879
#10	*1.265*	0.103	0.006	0.000	0.114	0.424	0.726	0.195	0.146	0.885
#11	*1.306*	0.100	0.006	0.000	0.110	0.478	0.728	0.149	0.155	0.888
#12	*1.357*	0.096	0.006	0.000	0.107	0.539	0.729	0.111	0.177	0.891
#13	*1.417*	0.092	0.006	0.000	0.102	0.606	0.731	0.106	0.206	0.896

Table 8(*c*) Molar fractions for gasoline operations—Mass balance

Run	λ	CO_2	CO $\times 10$	H_2	H_2O	O_2 $\times 10$	N_2	NO_x $\times 100$	THC $\times 100$	CF
#1	*0.747*	0.092	0.666	0.050	0.115	0.023	0.662	0.031	0.292	0.884
#2	*0.811*	0.105	0.453	0.038	0.118	0.023	0.678	0.073	0.252	0.880
#3	*0.857*	0.112	0.327	0.028	0.123	0.024	0.689	0.116	0.226	0.876
#4	*0.937*	0.120	0.156	0.013	0.131	0.032	0.704	0.197	0.196	0.868
#5	*0.998*	0.123	0.062	0.004	0.134	0.060	0.713	0.253	0.172	0.865
#6	*1.060*	0.121	0.012	0.000	0.131	0.123	0.719	0.309	0.142	0.867
#7	*1.108*	0.117	0.006	0.002	0.126	0.203	0.720	0.343	0.137	0.873
#8	*1.145*	0.113	0.006	0.003	0.121	0.266	0.721	0.307	0.133	0.877
#9	*1.191*	0.109	0.006	0.004	0.116	0.340	0.723	0.260	0.136	0.882
#10	*1.248*	0.104	0.006	0.005	0.110	0.428	0.724	0.197	0.148	0.889
#11	*1.302*	0.100	0.006	0.002	0.109	0.479	0.728	0.150	0.156	0.889
#12	*1.348*	0.096	0.006	0.003	0.105	0.542	0.728	0.112	0.178	0.893
#13	*1.408*	0.092	0.006	0.003	0.100	0.609	0.730	0.107	0.207	0.898

Table 8(*d*) Molar fractions for gasoline operations—No oxygen

Run	λ	CO_2	CO $\times 10$	H_2	H_2O	O_2 $\times 10$	N_2	NO_x $\times 100$	THC $\times 100$	CF
#1	*0.777*	0.090	0.652	0.027	0.135	0.000	0.675	0.031	0.286	0.864
#2	*0.840*	0.103	0.444	0.016	0.138	0.000	0.690	0.072	0.247	0.861
#3	*0.882*	0.110	0.322	0.011	0.138	0.000	0.698	0.115	0.223	0.860
#4	*0.949*	0.119	0.155	0.005	0.138	0.018	0.708	0.196	0.195	0.861
#5	*1.002*	0.123	0.062	0.002	0.136	0.057	0.715	0.253	0.172	0.863
#6	*1.060*	0.122	0.013	0.000	0.132	0.123	0.719	0.310	0.143	0.867
#7	*1.111*	0.117	0.007	0.000	0.128	0.201	0.721	0.343	0.137	0.871
#8	*1.149*	0.113	0.007	0.000	0.124	0.261	0.723	0.307	0.133	0.875
#9	*1.198*	0.109	0.007	0.000	0.120	0.333	0.725	0.260	0.136	0.879
#10	*1.258*	0.104	0.007	0.000	0.115	0.417	0.727	0.196	0.148	0.884
#11	*1.304*	0.100	0.007	0.000	0.111	0.476	0.729	0.150	0.156	0.888
#12	*1.353*	0.096	0.006	0.000	0.108	0.536	0.729	0.112	0.178	0.891
#13	*1.413*	0.092	0.006	0.000	0.103	0.603	0.732	0.107	0.207	0.896

Downloaded 02 Jun 2010 to 171.66.16.98. Redistribution subject to ASME license or copyright; see http://www.asme.org/terms/Terms_Use.cfm

Table 9(*a*) CNG operations—brake power output, flow rates, air humidity and acquired emissions

	CNG #2—$N=2600$ rpm—MBT timing (bmep=790 kPa at $\lambda=1.00$—fixed throttle position)								
Run	W [kW]	$m_{air,wet}$ [kg/h]	m_{fuel} [kg/h]	H_{abs} [g/kg]	THC [ppmC1]	NO_x [ppm]	CO [ppm]	CO_2 [ppm]	O_2 [ppm]
#1	31.7	134.3	9.96	12.5	3040	250	58 100	80 000	4410
#2	32.4	134.2	9.42	11.6	2530	520	44 100	89 000	4210
#3	32.9	134.8	8.92	12.8	2070	990	30 400	97 900	3880
#4	33.1	135.0	8.59	12.8	1790	1680	19 700	104 500	3740
#5	32.0	136.0	8.15	12.6	1430	3150	4530	113 000	5490
#6	31.8	136.7	7.83	12.4	1230	4080	930	111 500	11 800
#7	30.2	138.4	7.43	11.7	1100	4160	415	105 000	23 450
#8	30.4	139.8	7.27	12.0	1110	3960	400	101 000	30 000
#9	29.4	140.7	6.98	12.2	1150	3000	400	96 000	39 500
#10	28.5	142.3	6.73	12.6	1270	2330	410	91 000	48 500
#11	27.7	142.8	6.57	12.2	1400	1965	420	88 500	52 500
#12	26.6	144.0	6.29	11.5	1510	1610	415	83 000	62 000
#13	25.7	144.3	6.12	12.0	1620	1420	415	80 000	67 900

Table 9(*b*) Molar fractions for CNG operations—W-G reaction

Run	λ	CO_2	CO $\times 10$	H_2	H_2O	O_2 $\times 10$	N_2	NO_x $\times 100$	THC $\times 100$	CF
#1	*0.802*	0.064	0.464	0.037	0.187	0.035	0.651	0.019	0.242	0.811
#2	*0.852*	0.071	0.352	0.026	0.190	0.034	0.664	0.041	0.202	0.808
#3	*0.900*	0.078	0.242	0.017	0.194	0.031	0.674	0.076	0.165	0.804
#4	*0.938*	0.084	0.158	0.010	0.195	0.030	0.681	0.129	0.143	0.803
#5	*1.003*	0.091	0.037	0.002	0.194	0.044	0.692	0.245	0.116	0.804
#6	*1.048*	0.091	0.008	0.000	0.190	0.096	0.696	0.318	0.100	0.809
#7	*1.112*	0.087	0.003	0.000	0.180	0.193	0.701	0.334	0.091	0.818
#8	*1.149*	0.084	0.003	0.000	0.176	0.248	0.702	0.321	0.092	0.823
#9	*1.203*	0.080	0.003	0.000	0.169	0.329	0.705	0.244	0.096	0.829
#10	*1.261*	0.077	0.003	0.000	0.163	0.407	0.708	0.189	0.107	0.836
#11	*1.293*	0.075	0.004	0.000	0.159	0.445	0.709	0.160	0.119	0.839
#12	*1.365*	0.071	0.004	0.000	0.151	0.532	0.713	0.135	0.129	0.848
#13	*1.413*	0.069	0.004	0.000	0.147	0.584	0.714	0.120	0.139	0.852

Table 9(*c*) Molar fractions for CNG operations—Mass balance

Run	λ	CO_2	CO $\times 10$	H_2	H_2O	O_2 $\times 10$	N_2	NO_x $\times 100$	THC $\times 100$	CF
#1	*0.762*	0.066	0.479	0.056	0.1745	0.036	0.640	0.019	0.250	0.824
#2	*0.819*	0.072	0.361	0.041	0.180	0.034	0.655	0.042	0.207	0.818
#3	*0.875*	0.079	0.246	0.027	0.187	0.031	0.668	0.077	0.168	0.811
#4	*0.923*	0.084	0.159	0.016	0.191	0.030	0.678	0.130	0.145	0.807
#5	*1.011*	0.090	0.036	0.000	0.196	0.044	0.694	0.243	0.115	0.802
#6	*1.058*	0.091	0.007	0.000	0.192	0.095	0.699	0.316	0.099	0.807
#7	*1.124*	0.086	0.003	0.000	0.184	0.191	0.704	0.331	0.090	0.815
#8	*1.162*	0.084	0.003	0.000	0.179	0.246	0.706	0.317	0.091	0.819
#9	*1.219*	0.080	0.003	0.000	0.173	0.325	0.709	0.241	0.095	0.826
#10	*1.278*	0.076	0.003	0.000	0.167	0.402	0.712	0.187	0.105	0.832
#11	*1.314*	0.074	0.003	0.000	0.165	0.439	0.714	0.158	0.117	0.835
#12	*1.390*	0.071	0.003	0.000	0.158	0.524	0.719	0.133	0.127	0.842
#13	*1.440*	0.068	0.003	0.000	0.154	0.575	0.720	0.117	0.137	0.846

Table 9(*d*) Molar fractions for CNG operations—No oxygen

Run	λ	CO_2	CO $\times 10$	H_2	H_2O	O_2 $\times 10$	N_2	NO_x $\times 100$	THC $\times 100$	CF
#1	*0.787*	0.065	0.471	0.038	0.190	0.004	0.650	0.020	0.246	0.824
#2	*0.840*	0.072	0.356	0.026	0.192	0.009	0.663	0.041	0.205	0.818
#3	*0.891*	0.079	0.245	0.017	0.195	0.014	0.673	0.077	0.167	0.811
#4	*0.932*	0.084	0.158	0.010	0.196	0.020	0.681	0.130	0.144	0.807
#5	*1.006*	0.091	0.037	0.002	0.194	0.050	0.692	0.244	0.115	0.802
#6	*1.052*	0.090	0.008	0.000	0.189	0.102	0.697	0.318	0.100	0.807
#7	*1.117*	0.086	0.003	0.000	0.180	0.200	0.701	0.333	0.091	0.815
#8	*1.154*	0.084	0.003	0.000	0.175	0.256	0.703	0.319	0.092	0.819
#9	*1.209*	0.080	0.003	0.000	0.169	0.336	0.705	0.243	0.095	0.826
#10	*1.268*	0.076	0.003	0.000	0.162	0.415	0.708	0.188	0.106	0.832
#11	*1.301*	0.074	0.004	0.000	0.158	0.454	0.709	0.159	0.118	0.835
#12	*1.374*	0.071	0.004	0.000	0.150	0.542	0.713	0.134	0.128	0.842
#13	*1.423*	0.068	0.004	0.000	0.146	0.594	0.715	0.119	0.138	0.846

Downloaded 02 Jun 2010 to 171.66.16.98. Redistribution subject to ASME license or copyright; see http://www.asme.org/terms/Terms_Use.cfm

- *Mass balance*: the procedure described in Section "Full Mass Balance Method" is applied and Eq. (26) is used for λ evaluation;
- *No oxygen*: the procedure described in Section "No Oxygen Measurement Method" is applied and Eq. (26) is used for λ evaluation;
- *UEGO*: λ is calculated from UEGO sensor output;
- *Air & Fuel*: λ is calculated from air and fuel flow rate direct measurements by applying Eqs. (27) and (29).

The bisector (dotted line) is also reported for comparison.

All the methods generally show a good agreement. However, Mass balance slightly underestimates the actual λ value in the rich field due to an over evaluation of the molecular hydrogen in the engine exhaust. Such an inaccuracy can be further reduced by a more accurate calibration of the CO_2 analyzer, i.e., by employing span gases in which $[CO_2]$ is determined with an accuracy higher than 1%. As far as the UEGO method is concerned, it is worthwhile pointing out that data with the same reference λ show a λ_{UEGO} about 2% richer for CNG in comparison to gasoline. This shift was also detected in Ref. [12] under stoichiometric operation only. It can be mainly ascribed to the different H/C molar ratio of CNG (H/C≈3.8) with respect to the gasoline (H/C=1.88) used for the factory calibration of UEGO sensors.

Tables 8 and 9 report the λ values, the number of moles of each pollutant at the engine exhaust, and the *CF* coefficients obtained with the Water-gas reaction [Tables 8(*b*) and 9(*b*)], Full mass balance [Tables 8(*c*) and 9(*c*)] and No oxygen measurement [Tables 8(*d*) and 9(*d*)] methods for the engine running on gasoline (Table 8) and CNG (Table 9). The corresponding experimental data are reported in Tables 8(*a*) and 9(*a*) and refer to the same engine runs of Fig. 2 (i.e., λ sweep at $N=2600$ rpm, fixed throttle position and MBT timing; the run at $\lambda=1$ was performed at bmep $=790$ kPa). Very slight differences can be found in the molar fractions of the combustion products calculated with the three methods.

Figures 3(*a*) and 3(*b*) compare the average exhaust molecular mass of gasoline (Fig. 3(*a*)) and CNG (Fig. 3(*b*)) calculated with the different methods indicated in the legend for the λ sweep of Fig. 2. The curve 'SAE J1088' (dash-dot line) is calculated with reference to procedure [1], which has been specifically developed for SI engines fueled by gasoline. The curve 'ISO 8178' (dotted line) is calculated with reference to procedure [2], which gives for each pollutant X a ratio M_X/M_{exh} constant for every λ, implicitly fixing $M_{exh}=28.98$ g/mol. The curve 'Simplified model' (solid line) derives from an abridged combustion equation ([8]) in which air humidity is not considered, air is made up only of N_2 and O_2, and the combustion products are composed by CO_2, H_2O, N_2 and O_2 in the lean region, and by CO_2, H_2O, N_2, CO and H_2 in the rich region. As far as the results obtained with the W-G reaction (empty squares), Mass balance (stars), and No oxygen (crosses) methods, a good agreement is shown in Figs. 3(*a*) and 3(*b*). In fact, small differences can be found in the molar fractions of the combustion products calculated with these three methods (Tables 8 and 9). For both gasoline (Fig. 3(*a*)) and CNG (Fig. 3(*b*)) operations in the rich side, M_{exh} decreases almost linearly when λ decreases. This M_{exh} trend can be explained considering that the richer the mixture is the higher is the influence of CO and H_2O which have lower molecular mass than CO_2. In the lean mixture field, M_{exh} is virtually constant for gasoline operations (Fig. 3(*a*)), whereas it slightly increases as λ increases for CNG operations (Fig. 3(*b*)). In fact, for gasoline fueling the stoichiometric combustion products have almost the same average molecular mass of the combustion air, whereas for CNG fueling the stoichiometric combustion products have a lower average molecular mass than air. The curves 'W-G reaction,' 'Mass balance,' and 'No oxygen' can be interpolated at least square fits and the following expression can be obtained for gasoline

$$\begin{cases} M_{exh}=32.62-59.87\cdot\dfrac{1}{\alpha} & \dfrac{1}{\alpha}\leqslant\dfrac{1}{\alpha_{st}}=0.0683 \\ M_{exh}=28.82-4.20\cdot\dfrac{1}{\alpha} & \dfrac{1}{\alpha}>\dfrac{1}{\alpha_{st}}=0.0683 \end{cases}$$

and for CNG

$$\begin{cases} M_{exh}=32.42-82.36\cdot\dfrac{1}{\alpha} & \dfrac{1}{\alpha}\leqslant\dfrac{1}{\alpha_{st}}=0.0617 \\ M_{exh}=28.45-18.51\cdot\dfrac{1}{\alpha} & \dfrac{1}{\alpha}>\dfrac{1}{\alpha_{st}}=0.0617 \end{cases}$$

As far as the SAE J1088 and ISO 8178 are concerned, Fig. 3(*a*) (gasoline operations) shows appreciable differences with respect to the procedures proposed by the authors. This can be ascribed to the fact that both the procedures neglect the contribution of low concentration species. In fact, the results obtained with the Simplified model almost overlap those of the SAE J1088 in the whole investigated λ range and those of the ISO 8178 in the lean region. Figure 3(*b*) indicates that the methods SAE J1088 and ISO 8178

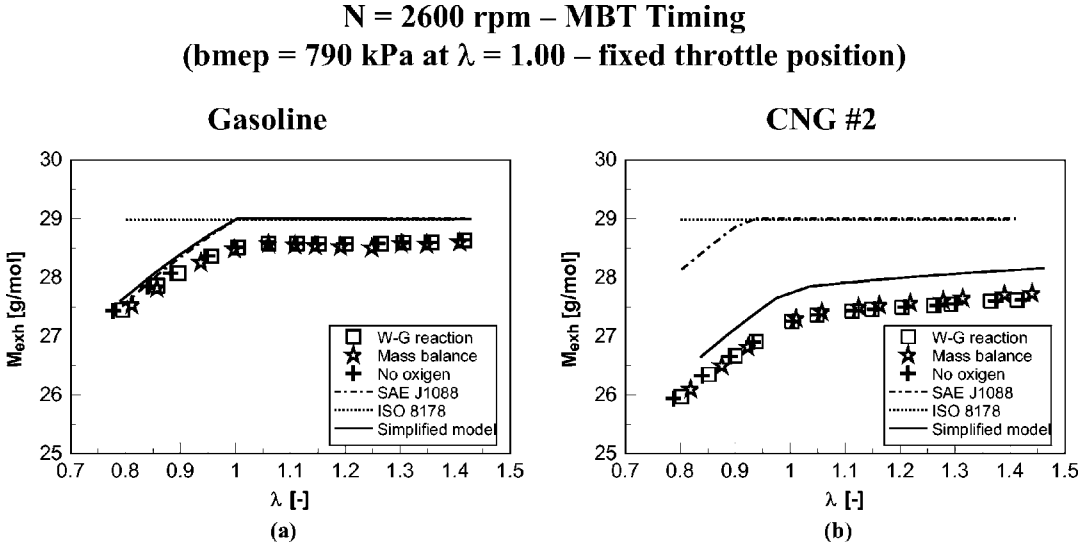

Fig. 3 Exhaust averaged molecular mass for gasoline (*a*) and CNG (*b*) operations

Downloaded 02 Jun 2010 to 171.66.16.98. Redistribution subject to ASME license or copyright; see http://www.asme.org/terms/Terms_Use.cfm

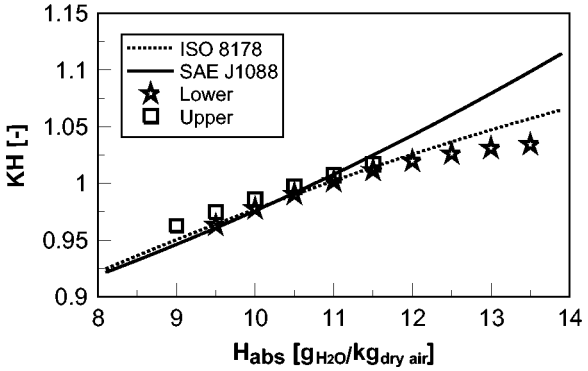

Fig. 4 KH correction factors

are less accurate than the others for CNG fueling. The M_{exh} distribution obtained with the Simplified model exhibits a similar trend to those obtained with the authors' methods, even though the 'Simplified model' curve is shifted towards higher M_{exh} values in the whole λ range. Such an offset is of the same magnitude of that shown in Fig. 3(*a*) for gasoline operations and is due to neglecting the contribution of low concentration species.

As far as the effect of mixture humidity on NO_x formation is concerned, in Fig. 4 the correction factors *KH* calculated according to Eqs. (31) and (32) are reported as 'SAE J1088' (solid line) and 'ISO 8178' (dotted line), respectively. In addition, engine-calibrated correction factors *KH* were also evaluated according to Eq. (30) for comparison. To that end, for steady-state operations the air humidity at the engine intake was slowly varied around the reference value $H_{abs}=10.71$ g/kg in the range 9–14 g/kg. The corresponding raw NO_x concentrations at the exhaust were recorded over a period of 180 s. Taking the time delay between the measure of air humidity and that of raw $[NO_x]$ into account, the values of the correction factor KH were determined for each H_{abs} according to Eq. (30), so that each $[NO_x]_{corr}$ approaches the raw $[NO_x]$ value measured when $H_{abs}=10.71$ g/kg. The *KH* values versus absolute air humidity were then interpolated at least square fits. This procedure was repeated for a wide range of steady-state engine operations in the range $N=2000-6000$ rpm, bmep=200–800 kPa, for both gasoline and CNG fueling. Figure 4 plots the curves 'Lower' (stars) and 'Upper' (empty squares) which refer to the minimum and maximum correction factor *KH* determined for all the tested working conditions. It can be inferred that correction factors (31) and (32) overestimate the effect of intake air humidity on NO_x formation, especially for higher values of H_{abs}. However, Eq. (32) appears to be more consistent with the experimental results determined on the test engine.

The engine-calibrated *KH* coefficients calculated according to the described procedure show a dependence not only on H_{abs}, but also on engine operating variables, such as *N* and bmep. However, a well defined trend of *KH* versus *N* and bmep could not be detected. Therefore, a different correction factor *KH'* is proposed by the authors. To that end, the same experimental data and the above described procedure were used to evaluate the alternative *KH'* correction term, according to Eq. (33). Such correction term was then correlated to bmep and *N* values of the considered tests, according to the following expression:

$$KH' = \delta_1 + \delta_2 \cdot N + \delta_3 \cdot \text{bmep} + \delta_4 \cdot N \cdot \text{bmep} \tag{34}$$

In this equation, when *KH'*, bmep and *N* are expressed in $(g/kg)^{-1}$, kPa and rpm, respectively, the values of the constants δ are $\delta_1=15.99E-6$, $\delta_2=0.0136E-6$, $\delta_3=0.0080E-6$ and $\delta_4=-6E-12$.

Figures 5(*a*) and 5(*b*) show the results obtained by applying Eq. (34) to two different engine runs at the indicated operating conditions. In the upper part of Figs. 5(*a*) and 5(*b*) the air humidity is reported as a thin solid line. In the lower part of Figs. 5(*a*) and 5(*b*), the thick solid line represents raw $[NO_x]$, the dotted line represents $[NO_x]_{corr}$ according to ISO 8178, the dash-dot line represents $[NO_x]_{corr}$ according to SAE J1088, and the starred line refers to $[NO_x]_{corr}$ according to Eq. (34). Response times for hygrometer and CLD analyzer were 3 and 1 s, respectively, whereas during the tests of Fig. 5 the transient time of air humidity was in the range of 130–180 s, i.e., significantly higher than response times of instrumentation. Air humidity and raw $[NO_x]$ were sampled at a frequency of 1 Hz. The proposed correction factor *KH'* appears to be more suitable to the test engine for all the considered operating conditions. Besides, Eq. (33) has the following advantage with respect to Eq. (30), i.e., the corrected value of the raw mean concentration is equal to the average of corrected sampled values

$$(\langle [\text{NO}] \rangle)_{corr} = \langle [\text{NO}]_{corr} \rangle$$

As a consequence, any uncertainty of the estimated time delay between the measure of air humidity and the measure of NO concentration in the CLD analyzer does not affect calculation.

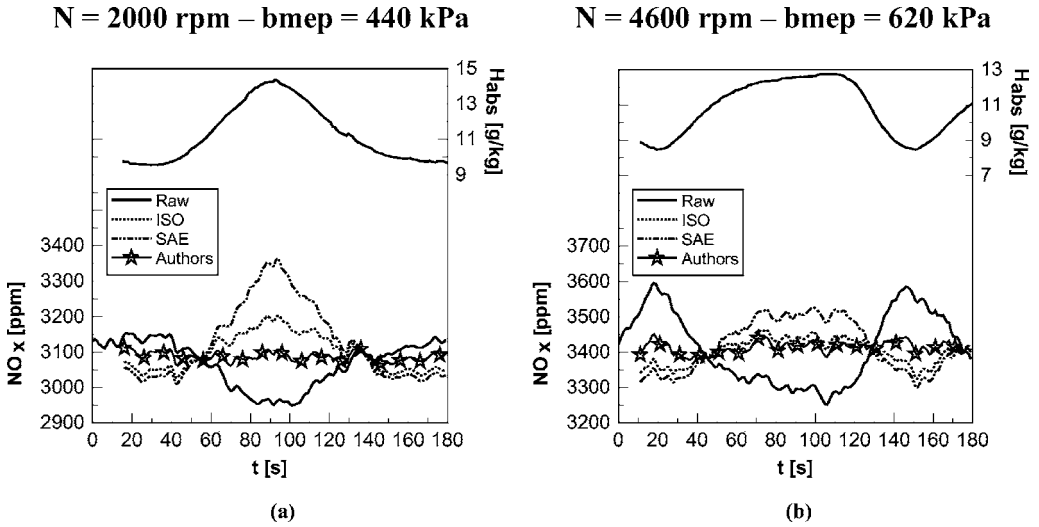

Fig. 5 Comparison among different NO_x emission corrections

Downloaded 02 Jun 2010 to 171.66.16.98. Redistribution subject to ASME license or copyright; see http://www.asme.org/terms/Terms_Use.cfm

Figure 6 reports the trends of brake specific emissions of all the pollutants for a λ sweep at $N=2600$ rpm and bmep=790 kPa under both gasoline (Figs. 6(*a*), 6(*c*), 6(*e*), and 6(*g*)) and CNG (Figs. 6(*b*), 6(*d*), 6(*f*), and 6(*h*)) operations. The different symbols used in the plot refer to the different methods used for the mass emission evaluation. More specifically

- *SAE A&F* (empty triangle): SAE J1088—Air and Fuel method [1] is applied;
- *SAE F* (reversed empty triangle): SAE J1088—Fuel method [1] is applied;
- *ISO 8178—I* (solid triangle): ISO 8178-I [2] is applied;
- *ISO 8178—II* (reversed solid triangle): ISO 8178-II [2] is applied;
- *W-G reaction* (empty square): the water-gas reaction method proposed in Section ''Water-Gas Reaction Method'' of the present paper is applied;
- *Mass balance* (empty star): the full mass balance method proposed in Section ''Full Mass Balance Method'' of the present paper is applied.
- *No oxygen* (cross): the no oxygen measurement method proposed in Section ''No Oxygen Measurement Method'' of the present paper is applied.

The specific emissions of the following pollutants are reported: THC (Figs. 6(*a*) and 6(*b*)), NO_x (Figs. 6(*c*) and 6(*d*)) and CO (Figs. 6(*e*) and 6(*f*)). CO_2 specific emissions (Figs. 6(*g*) and 6(*h*)) are also included because CO_2 is the most important greenhouse gas, even though it is not considered a pollutant.

As far as gasoline operations are concerned, a good agreement is generally found for all the considered methods. However, in the rich field the ISO 8178-I and ISO 8178-II methods underestimate specific emissions because of the overestimation of the average exhaust molecular mass highlighted in Fig. 3(*a*).

For CNG operations, Figs. 6(*b*), 6(*d*), 6(*f*), and 6(*h*) indicate that the level of each exhaust specific emission can be highly affected by the method used for the calculation when the SAE or ISO procedures are applied, whereas no differences are perceptible between the results when the three methods proposed by the authors are used. Figures 6(*b*), 6(*d*), 6(*f*), and 6(*h*) also evidence remarkable differences in the specific emission levels obtained from the SAE and ISO methods with respect to those calculated with the procedures proposed by the authors for all the investigated working conditions. This confirms that SAE J1088 and ISO 8178 procedures are not satisfactory when CNG fueling is considered. Therefore, in order to make a meaningful comparison between the specific emissions of engines running on alternative fuel blends (such as CNG) and those of engines running on conventional fuels, appropriate calculation methods, as those proposed by the authors, should be applied.

Conclusions

In the present paper an algorithm is developed so as to evaluate the mass emissions from internal combustion engines under steady-state operating conditions. Three procedures were developed: the Full mass balance method, the Water-gas reaction method and the No oxygen measurement method. The authors' procedures represent an extension and refinement of the methods proposed in Refs. [3–7] for air-fuel ratio calculation purposes only. Furthermore, two additional novelties were included in the authors' methods: the procedures were extended to fuels with complex composition in order to allow mass emission evaluation in engine running on alternative fuels, such as various CNG blends; the procedures can also be applied when raw pollutant emission measurements were acquired on either dry or wet basis. The authors' methods were extensively tested based on experimental measurements taken in a multivalve four-stroke automotive engine running on both gasoline and CNG under carefully controlled steady-state operating conditions.

In order to validate the authors' methods, the procedures were first applied to the evaluation of the air-fuel ratio. The λ results calculated from authors' procedures were compared to the experimental λ values obtained from directly measured air and fuel mass flow rates, as well as from more conventional UEGO sensor data. The comparison showed a generally good agreement between all the methods in the whole investigated range, even though the Mass balance method slightly underestimates λ for rich mixtures due mainly to the inaccuracy in H_2 volume fraction evaluation. Such an uncertainty can be further reduced by a more accurate calibration of the CO_2 analyzer, i.e., employing span gases in which $[CO_2]$ is determined with an accuracy higher than 1%. It is also worthwhile pointing out that if the same reference λ is considered for both gasoline and CNG operations, the UEGO sensor gives λ values that are usually 2% lower for CNG with respect to gasoline. This can be mainly ascribed to the different H/C molar ratio of CNG with respect to that of the gasoline used for the factory calibration of UEGO sensors.

The authors' procedures were then applied to brake specific mass emission calculation and the results were compared to those obtained according to SAE J1088 and ISO 8178 recommended practices for off-road steady-state IC engines.

As far as gasoline fueling is concerned, the specific emissions obtained with authors' procedures were shown to be comparable to those calculated according to SAE J1088 specifications in the whole considered operating range. However, slight differences were found with respect to ISO 8178 practices in the rich field. These differences can be ascribed to the fact that ISO 8178 procedure assumes a constant value of the average exhaust molecular mass for any λ value.

As far as CNG fueling is concerned, the authors' procedures revealed to be far more accurate than both SAE and ISO practices. This indicates that appropriate calculation methods, as those proposed by the authors, should be applied in order to compare the specific emissions from engines running on alternative fuel blends (such as CNG) to those of engines running on conventional fuels.

An insight into the effects of mixture humidity on NO formation was also given. More specifically, the correction factors suggested by SAE and ISO procedures were specifically calibrated for the test engine and a different correction formula was also proposed.

Acknowledgment

This research was financially supported by Centro Ricerche Fiat (CRF) and by Ministero dell'Università e della Ricerca (MIUR) under the Cofin'00 Program ''Thermo-Fluid Dynamic Processes and Techniques for Pollutant Emission Reduction in IC Engines.''

Nomenclature

a = moles of CO_2, per mole $C_xH_yO_z$, in the exhaust gas
A = moles of N_2 in the combustion air, per mole O_2 in the combustion air
b = moles of CO, per mole $C_xH_yO_z$, in the exhaust gas
B = moles of CO_2 in the combustion air, per mole O_2 in the combustion air
bmep = brake mean effective pressure
c = moles of H_2, per mole $C_xH_yO_z$, in the exhaust gas
C = $M_{air,dry}/M_{H_2O}/[O_2]_{amb}\cdot 10^{-3}$
CF = dry-wet correction factor
CLD = Chemi-Luminescence Detector
CNG = Compressed Natural Gas
d = moles of H_2O, per mole $C_xH_yO_z$, in the exhaust gas
D = moles of Ar in the combustion air, per mole O_2 in the combustion air

Downloaded 02 Jun 2010 to 171.66.16.98. Redistribution subject to ASME license or copyright; see http://www.asme.org/terms/Terms_Use.cfm

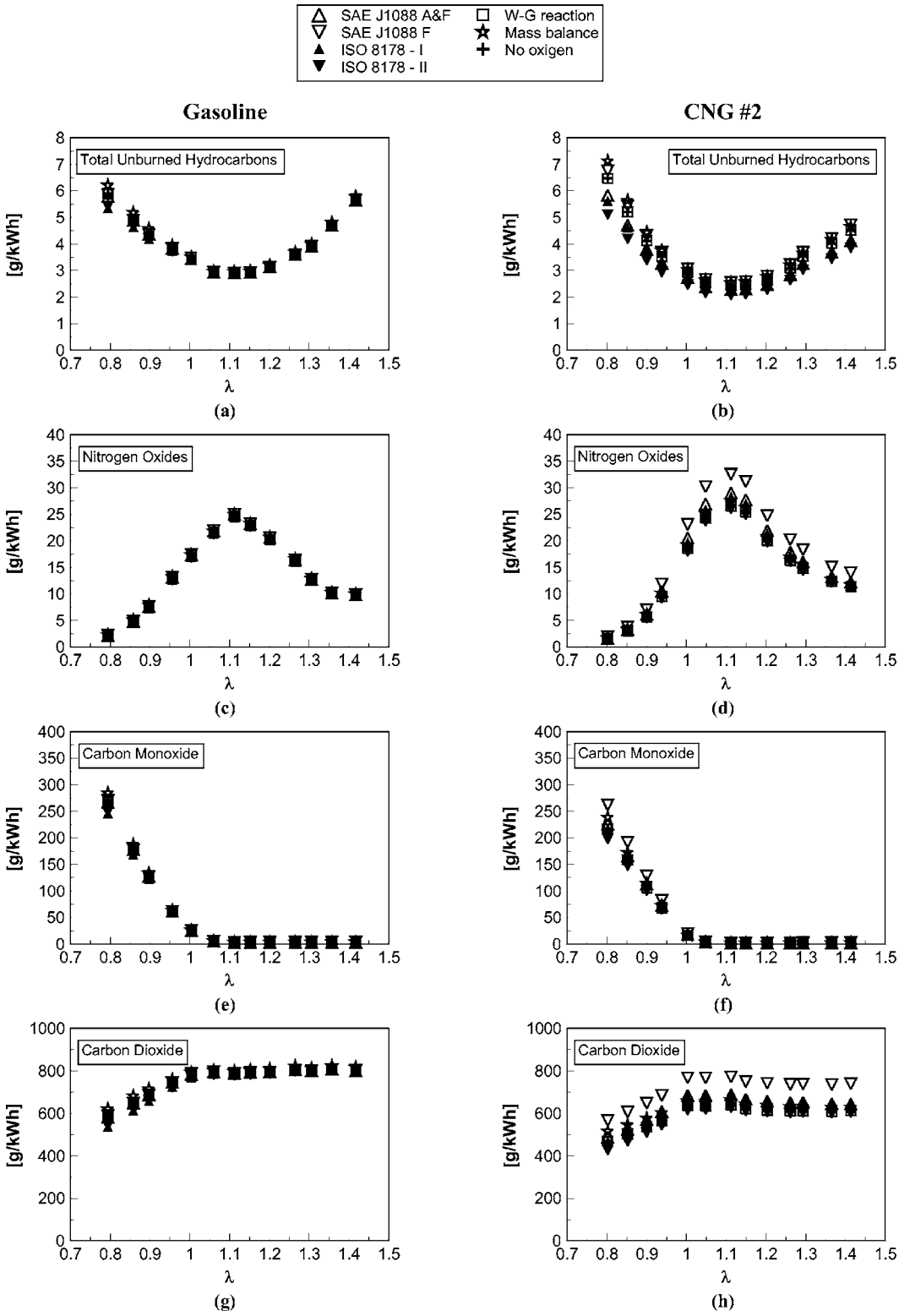

Fig. 6 Brake specific emissions for gasoline and CNG operations

Downloaded 02 Jun 2010 to 171.66.16.98. Redistribution subject to ASME license or copyright; see http://www.asme.org/terms/Terms_Use.cfm

e = moles of O_2, per mole $C_xH_yO_z$, in the exhaust gas
E = moles of H_2, per mole $C_xH_yO_z$, in the fuel
ECM = Electronic Control Module
EGR = Exhaust Gas Recirculation
f = moles of N_2, per mole $C_xH_yO_z$, in the exhaust gas
F = moles of O_2, per mole $C_xH_yO_z$, in the fuel
g = moles of NO, per mole $C_xH_yO_z$, in the exhaust gas
G = moles of N_2, per mole $C_xH_yO_z$, in the fuel
g = moles of NO_2, per mole $C_xH_yO_z$, in the exhaust gas
h = moles of CH_4, per mole $C_xH_yO_z$, in the exhaust gas
h' = moles of $C_{x'}H_{y'}O_{z'}$, per mole $C_xH_yO_z$, in the exhaust gas
H_{abs} = air absolute humidity, grams of water/kilograms of dry air
HC = Unburned Hydrocarbons
i = moles of Ar, per mole $C_xH_yO_z$, in the exhaust gas
IC = Internal Combustion
ISO = International Standards Organization
K = equilibrium constant for water-gas reaction
KH, KH' = correction factors for mixture humidity effects on NO formation
L = moles of CO_2, per mole $C_xH_yO_z$, in the fuel
$\dot{m}$ = flow rate
M = molecular weight
n = moles of O_2, per mole $C_xH_yO_z$, in the combustion air
n_j = number of moles of the species j
N = crankshaft rotational speed
p = pressure
P = moles of H_2O, per mole $C_xH_yO_z$, in the fuel
q = moles of He, per mole $C_xH_yO_z$, in the exhaust gas
Q = moles of CO, per mole $C_xH_yO_z$, in the fuel
R = moles of He, per mole $C_xH_yO_z$, in the fuel
S = moles of Ar, per mole $C_xH_yO_z$, in the fuel
SAE = Society of Automotive Engineers
SI = Spark Ignition
T = temperature
THC = total unburned hydrocarbon
u, v, w = number of C, H, O atoms in fuel hydrocarbons compounds, respectively
W = brake power output
x = number of C atoms in the hydrocarbon average molecular formula of fuel
X = any of the pollutant species
x' = number of C atoms in the average molecular formula of exhaust unburned hydrocarbon
y = number of H atoms in the hydrocarbon average molecular formula of fuel
y' = number of H atoms in the average molecular formula of exhaust unburned hydrocarbon
z = number of O atoms in the hydrocarbon average molecular formula of fuel
z' = number of O atoms in the average molecular formula of exhaust unburned hydrocarbon

Greek Symbols

α = air-fuel ratio
δ_1, δ_2, δ_3, δ_4 = coefficients for KH' evaluation
λ = relative air-fuel ratio
η, μ, ν = maximum number of C, H, O atoms in fuel hydrocarbon compounds, respectively

Subscripts

air = air
amb = ambient air
baro = barometric
cooler = cooler outlet
corr = corrected emissions
dry = dry basis
exh = exhaust gas
fuel = fuel
j = species j
st = stoichiometric
wet = wet basis

Notation

$[\ ]$ = volume fraction, concentration
$\{\}_{bs}$ = brake specific mass emission
$\langle\ \rangle$ = arithmetic average over the sampled records

References

[1] "Test Procedure for the Measurement of Exhaust Emissions From Small Utility Engines," SAE J1088, SAE Recommended Practice, 1983.
[2] "Reciprocating Internal Combustion Engines—Exhaust Emission Measurement," ISO 8178, 1996.
[3] Simons, W., 1985, "Berechnungen zur Bestimmung der Luftzahl bei Ottomotoren," MTZ Motortechnische Zeitschrift, **46**(7/8), pp. 257–259.
[4] Silvis, M. W., 1997, "An Algorithm for Calculating the Air/Fuel Ratio From Exhaust Emissions," SAE Paper No. 970514.
[5] Fukui, T., Tamura, Y., Omori, S., and Saitoh, S., 1989, "Accuracy of A/F Calculation From Exhaust Gas Composition of SI Engines," SAE Paper No. 891971.
[6] Brettschneider, J., 1997, "Extension of the Equation for Calculation of the Air-Fuel Equivalence Ratio," SAE Paper No. 972989.
[7] Spindt, R. S., 1965, "Air Fuel Ratios From Exhaust Gas Analysis," SAE Paper No. 650507.
[8] Heywood, J. B., 1988, *Internal Combustion Engine Fundamentals*, McGraw–Hill, New York.
[9] Patterson, D. J., and Henein, N. A., 1972, *Emissions from Combustion Engines and Their Control* (Ann Arbor Science, Ann Arbor, MI).
[10] Catania, A. E., Misul, D., Spessa, E., and Martorana, G., 2001, "Conversion of a Multivalve Gasoline Engine to Run on CNG," SAE 2000 Transactions, Journal of Engines, **109**, pp. 809–817.
[11] Catania, A. E., d'Ambrosio, S., Mittica, A., and Spessa, E., 2002, "Experimental Investigation of Fuel Consumption and Exhaust Emissions of a 16V Pent-Roof Engine Fueled by Gasoline and CNG," SAE 2001 Transactions, Journal of Engines, **110**, pp. 1213–1233.
[12] Jääskeläinen, H. E., and Wallace, J. S., 1993, "Performance and Emissions of a Natural Gas-Fueled 16 Valve DOHC Four-Cylinder Engine," SAE Paper No. 930380.

Downloaded 02 Jun 2010 to 171.66.16.98. Redistribution subject to ASME license or copyright; see http://www.asme.org/terms/Terms_Use.cfm

Multidimensional Predictions of In-Cylinder Turbulent Flows: Contribution to the Assessment of k-ε Turbulence Model Variants for Bowl-in-Piston Engines

Mirko Baratta

Andrea E. Catania

Ezio Spessa
e-mail: ezio.spessa@polito.it

Dipartimento di Energetica, LAQ Motoria Combustione Interna,[1]
Politecnico di Torino,
Corso Duca degli Abruzzi, 24,
Torino 10129, Italy

Rui L. Liu
Tianjin College of Transportation Engineering,
1 Dongjuzi, Hedong District,
Tianjin 300161, People's Republic of China

Multidimensional computational fluid dynamics (CFD) codes with reliable turbulence models are useful investigation and design tools for internal combustion engines, in-cylinder flow phenomena being critical to the combustion process and related emission sources. Although a variety of turbulence models has long been proposed, the assessment of even the most widely used k-ε model is still lacking, especially for bowl-in-piston engines. This paper provides a survey of k-ε turbulence model variants and their numerical implementation for in-cylinder flow analysis. Mean motion and turbulence quantities were simulated in the axisymmetric combustion chamber of a motored model engine featuring one centrally located valve and each of a flat-piston and cylindrical bowl-in-piston arrangements. A noncommercial CFD code developed by the authors was applied for calculation, using a finite-volume conservative implicit method and applying various order-of-accuracy numerical schemes. Simulation results are presented at the engine speed of 200 rpm throughout the whole engine cycle. These were obtained using three k-ε turbulence model versions, standard, renormalization group (RNG) and two scale, each of which focuses on one main engine flow feature, i.e., compressibility, anisotropy, and high unsteadiness, respectively. Modified boundary conditions with respect to conventional logarithmic wall functions were applied. Effects of equation-differencing scheme and computational-grid spacing on flow predictions were tested. The numerical results were compared to those of laser Doppler velocimetry measurements and the influence of the k-ε model variants on the flow-field features was examined during the induction stroke and around compression top dead center. For the flat-piston case, a comparison between the homemade and commercial STAR-CD® code results was also made.
[DOI: 10.1115/1.1852567]

1 Introduction

The in-cylinder flow field is one of the most important factors controlling the engine combustion process: it influences fuel evaporation and mixing processes as well as flame propagation and spray dynamics [1,2]. Therefore, it is very important for internal combustion engine (ICE) designers to have effective means of in-cylinder flow evaluation and improvement by engine characteristic and/or dimension modifications. To that end, computational fluid dynamics (CFD) codes with reliable turbulence models are powerful investigation and design tools, allowing design time and cost reduction, as the need of prototypes also diminishes. A variety of turbulence models has long been developed and applied to flows of practical interest. However, in-cylinder engine flows are much more complex than those used for turbulence model calibration: e.g., curvature, compression, moving walls and high flow unsteadiness can strongly influence the turbulence properties. Hence, the choice or development of an adequate turbulence model for simulating such complex flows still poses a challenge. In fact, the numerous turbulence models available in the literature differ from each other for the underlying concepts, complexity, accuracy in capturing flow characteristics. However, none of them can be considered of general application, so as to yield a satisfactory accuracy over a wide range of flow conditions.

The turbulence models that have mainly been applied for ICE flow analysis belong to the groups of eddy viscosity models (EVMs) [3–14] and Reynolds stress models (RSMs) [15–17]. Nevertheless, a third quite widely used turbulence modeling approach, that is, large eddy simulation (LES), requiring subgrid scale modeling (SSM), has recently been applied for turbulence prediction in engine combustion-chamber flows [18].

Linear EVMs, which are based on the Boussinesq stress-strain relationship, offer a good compromise between accuracy and computational cost. These models are found to work quite well in thin shear flows, but they are indicated to have several limitations in complex flows, such as those occurring in ICE combustion chambers, with particular reference to anisotropy, flow curvature, and unsteadiness effects, as was more recently pointed out in Ref. [17]. However, the relative importance of such and other effects on engine turbulent-flow prediction still needs assessment, mainly for bowl-in-piston engines. Especially, the wall function approach for treatment of wall boundary conditions in the high-Re version of EVM has been criticized, because of the strong departure of the actual velocity profile close to an engine wall from the "equilibrium" logarithmic profile [17]. Hence, in Ref. [17] the proper method of in-cylinder turbulence prediction seems to be the use of second-moment closure models (that is, RSM) with a low-Re approach for wall boundary conditions.

Among the Reynolds-averaged Navier-Stokes closure models, RSM can be considered as the most complete but they are the

[1]IC Engines Advanced Laboratory.

Contributed by the Internal Combustion Engine Division of THE AMERICAN SOCIETY OF MECHANICAL ENGINEERS for publication in the ASME JOURNAL OF ENGINEERING FOR GAS TURBINES AND POWER. Manuscript received by the ICE Division October 24, 2003; final revision received by the ASME Headquarters June 1, 2004. Associate Editor: D. Assanis.

Copyright © 2005 by ASME

Downloaded 02 Jun 2010 to 171.66.16.98. Redistribution subject to ASME license or copyright; see http://www.asme.org/terms/Terms_Use.cfm

most expensive ones. These models are indicated to be capable of naturally taking anisotropy, flow curvature, and unsteadiness into account, because the transport equation of each turbulent stress component is solved. RSM closure assumptions concern third-moment quantities and thus are less critical than EVM closure assumptions. Nevertheless, as is stated in Refs. [14,19], anisotropic dissipation, stress diffusion, and pressure-strain correlation term modeling can limit the accuracy of RSM, in their low-Re version. Furthermore, one should consider that the low-Re approach needs such a large number of grid points near the wall, because of the presence of exponential functions, that it can become unacceptable in three dimensions. A recent study in which the high-Re version of the Speziale, Sarkar, and Gatski (SSG) Reynolds stress model [15] is applied to in-cylinder flow numerical analysis can be found in Ref. [16].

The high computational cost required by RSM led to the development of nonlinear EVMs, which claim to reach the RSM accuracy with a much lower computational effort. Nonlinear EVMs are expected to take anisotropy and curvature effects into account [9].

EVMs are the most commonly used turbulence models for ICE flow simulation. The different versions proposed in the last two decades start from the basic k-ε model of Launder and Spalding [3] and introduce some modifications in order to include the distinct effects of compression [4–7], turbulence decay [10], anisotropy and flow curvature [8,11–13] on in-cylinder flow features. There is another feature that is relevant to engine flow application, that is, the high unsteadiness of the flow. The multiple time-scale modeling [20,21] seems to be a suitable approach to take such a feature into account in an explicit way.

With the present work, the authors intend to give a contribution to the assessment of three different versions of the k-ε turbulence model, namely, Reynolds, renormalization group (RNG) and two-scale models, by applying them to the flow field simulation within the chamber of a motored model engine in both cases of flat-piston and bowl-in-piston arrangements for which experimental data are available [22]. Actually, the Reynolds model is one of the first models that attempt to take compression effect into account, without changing Launder and Spalding's original coefficients. In what follows, this model will be referred to as "Standard." RNG model is used instead of nonlinear models, because it has underlying concepts similar to them, but is very simple at the same time. Two-scale models stem from multiple time-scale approach, focusing on flow unsteadiness. All of the considered k-ε turbulence model variants will be detailed in Sec. 3.

As is suggested in Ref. [23], the best way for carrying out multidimensional engine flow predictions is to simulate the whole engine cycle starting from the top dead center and analyzing induction, compression, and expansion strokes, so that at the beginning of compression nonarbitrary initial conditions for turbulence, length, and time scales are available. However, many authors (e.g., [14,17,24]) in their assessments start from specific crank angles during the compression stroke using initial conditions that are based on experimental data. In the authors' opinion, this is a rather inadequate approach because it is almost impossible to obtain time-scale values from experiments, whereas such values play a very important role because they determine the relative influence of the production terms in the ε equation and these terms are multiplied by ε/k, that is, the inverse of the time scale itself [23].

The authors followed the procedure suggested in Ref. [23] by simulating induction, compression as well as expansion strokes. They also examined the influence of different discretization schemes for spatial and time derivatives as well as of the grid spacing on the computational results, in order to choose the best numerical configuration and use it in the turbulence model assessment.

2 Prediction Method

2.1 Basic Equations. The flow is represented by the density-weighted ensemble-averaged differential conservation equations of mass, momentum, and stagnation enthalpy, in addition to the transport equations for the turbulence energy k and its dissipation rate ε. The Reynolds stresses arising from the averaging process are modeled by the linear Boussinesq approximation, that is, in Cartesian tensor notation

$$-\overline{\rho u_i u_j} = 2\mu_T\left(S_{ij} - \frac{1}{3}S_{\ell\ell}\delta_{ij}\right) - \frac{2}{3}\rho k\delta_{ij} \tag{1}$$

where

$$S_{ij} = \frac{1}{2}\left(\frac{\partial U_i}{\partial x_j} + \frac{\partial U_j}{\partial x_i}\right) \tag{2}$$

The model conservation equations are as follows:

$$\frac{\partial \rho}{\partial t} + \frac{\partial}{\partial x_j}(\rho U_j) = 0 \tag{3}$$

$$\frac{\partial(\rho U_i)}{\partial t} + \frac{\partial}{\partial x_j}(\rho U_j U_i) = -\frac{\partial p}{\partial x_i} + \frac{\partial}{\partial x_j}[2(\mu+\mu_T)S_{ij}] - \frac{2}{3}\frac{\partial}{\partial x_i}[(\mu + \mu_T)D + \rho k] \tag{4}$$

$$\frac{\partial(\rho h)}{\partial t} + \frac{\partial}{\partial x_j}(\rho U_j h) = \frac{\partial p}{\partial t} + \frac{\partial}{\partial x_j}\left[\left(\mu + \frac{\mu_T}{\sigma_h}\right)\frac{\partial h}{\partial x_j}\right] \tag{5}$$

Consistent with the approach of two-equation turbulence models, the turbulent viscosity in the above equations is given by

$$\mu_T = C_\mu \rho \frac{k^2}{\varepsilon} \tag{6}$$

in which the empirical constant C_μ is usually taken to be 0.09. The transport equation for k, which has the same form for all the considered models except the two-scale model (with reference to Sec. 3, "Turbulence Models"), is

$$\frac{\partial(\rho k)}{\partial t} + \frac{\partial}{\partial x_j}(\rho U_j k) = \frac{\partial}{\partial x_j}\left[\left(\mu + \frac{\mu_T}{\sigma_k}\right)\frac{\partial k}{\partial x_j}\right] + 2\mu_T S_{ij}S_{ij} - \frac{2}{3}(\mu_T D^2 + \rho k D) - \rho\varepsilon \tag{7}$$

The Standard and RNG versions of the ε transport equation can take the same expression, as follows:

$$\frac{\partial(\rho\varepsilon)}{\partial t} + \frac{\partial}{\partial x_j}(\rho U_j \varepsilon) = \frac{\partial}{\partial x_j}\left[\left(\mu + \frac{\mu_T}{\sigma_\varepsilon}\right)\frac{\partial \varepsilon}{\partial x_j}\right] + C_1\frac{\varepsilon}{k}\left[2\mu_T S_{ij}S_{ij} - \frac{2}{3}(\mu_T D^2 + \rho k D)\right] - C_2\rho\frac{\varepsilon^2}{k} + C_3\rho\varepsilon D - C_4 R \tag{8}$$

where the coefficients C_1, C_2, C_3, C_4 are available according to the model versions. The two-scale model equations will be discussed later. By indicating the generic dependent variable with φ, one can put the model equations in the general form

$$\frac{\partial(\rho\varphi)}{\partial t} + \frac{\partial}{\partial x_j}\left(\rho U_j \varphi - \Gamma\frac{\partial \varphi}{\partial x_j}\right) = S_\varphi \tag{9}$$

Obviously, $\varphi \equiv 1$ in the continuity equation, $\varphi \equiv U_i\,(i=1,2,3)$ in the momentum equation, $\varphi \equiv h$ in the energy equation, and so on. Equation (9) is useful to derive the discretized algebraic equations in a way that is suitable for all the conservation laws describing the fluid motion.

2.2 Discretization Procedure. In the finite volume approach, the starting point is the integral counterpart of Eq. (9):

Downloaded 02 Jun 2010 to 171.66.16.98. Redistribution subject to ASME license or copyright; see http://www.asme.org/terms/Terms_Use.cfm

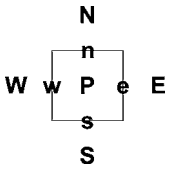

Fig. 1 Cell points used for discretization

$$\frac{\partial}{\partial t}\int_V \rho\varphi dV + \int_\Omega (\rho \mathbf{U}\varphi - \Gamma\nabla\varphi)\cdot \mathbf{n} d\Omega = \int_V S_\varphi dV \qquad (10)$$

Equation (10) is an integral conservation law and is applied to a single control volume arising from the discretization of the physical domain into a computational mesh (Fig. 1). For a piston-driven mesh, integrating Eq. (10) over each of the moving elemental control volumes and applying the midpoint rule to approximate surface and volume integrals, one obtains

$$\frac{\rho_P^{n+1}\varphi_P^{n+1}\Delta V^{n+1} - \rho_P^n\varphi_P^n\Delta V^n}{\Delta t} + J_e^{n+1} - J_w^{n+1} + J_s^{n+1} - J_n^{n+1} = S_{\varphi P}^{n+1}\Delta V^{n+1} \qquad (11)$$

where

$$\begin{aligned} F_e &= \rho_e v_e \Omega_e \\ F_w &= \rho_w v_w \Omega_w \\ F_s &= \rho_s u_s \Omega_s \\ F_n &= \rho_n u_n \Omega_n \\ J_e &= F_e\varphi_e - \Gamma_e\left(\frac{\partial\varphi}{\partial x}\right)_e \Omega_e \\ J_w &= F_w\varphi_w - \Gamma_w\left(\frac{\partial\varphi}{\partial x}\right)_w \Omega_w \\ J_s &= F_s\varphi_s - \Gamma_s\left(\frac{\partial\varphi}{\partial y}\right)_s \Omega_s \\ J_n &= F_n\varphi_n - \Gamma_n\left(\frac{\partial\varphi}{\partial y}\right)_n \Omega_n \end{aligned} \qquad (12)$$

In Eqs. (11) and (12) the subscripts e, w, s, n stand for the control volume faces and P, E, W, S, N are the grid nodes (Fig. 1), whereas the superscripts n and $n+1$ refer to the time steps: the "n" superscript concerns the old instant of time at which the variables are known, "$n+1$" refers to the new instant and designates unknown variables. The J fluxes and source terms in Eq. (11) are considered at time "$n+1$," which corresponds to the application of an implicit backward-time discretization scheme. The authors also implemented a trapezoidal second-order accurate time scheme, by evaluating the J's and source terms at the time step $n+1/2$. By applying both backward and trapezoidal time schemes, with the same spatial discretization scheme, it was ascertained that the results were virtually the same, but the trapezoidal scheme requires larger computational effort. Therefore, the backward time scheme was chosen. The superscript $n+1$ will be omitted in the following equations.

As far as the spatial discretization scheme is concerned, a useful way to represent various schemes in a general form is indicated in Ref. [25]. It was shown that Eq. (11), when combined with the product of φ_P and the discrete analogue to the continuity Eq. (3), can be converted into the following nonlinear algebraic equation:

$$a_P\varphi_P + a_E\varphi_E + a_W\varphi_W + a_S\varphi_S + a_N\varphi_N = b \qquad (13)$$

Table 1 Coefficients of Eq. (13)

$$\begin{aligned} a_E &= -\frac{\Gamma_e}{\Delta x_e}\Omega_e A(|P_e|) - \max(-F_e, 0) \\ a_W &= -\frac{\Gamma_w}{\Delta x_w}\Omega_w A(|P_w|) - \max(F_w, 0) \\ a_S &= -\frac{\Gamma_s}{\Delta y_s}\Omega_s A(|P_s|) - \max(-F_s, 0) \\ a_N &= -\frac{\Gamma_n}{\Delta y_n}\Omega_n A(|P_n|) - \max(F_n, 0) \\ a_P &= -a_E - a_W - a_S - a_N + \frac{\Delta V^n \rho_P^n}{\Delta t} \\ b &= S_{\varphi,P}\Delta V + \frac{\Delta V^n \rho_P^n \varphi_P^n}{\Delta t} \end{aligned}$$

whose a and b coefficients are reported in Table 1. In particular, different discretization schemes result from the following functions of the Peclet number $A(|P|)$:

$A(|P|) = 1 \Rightarrow$ first order hybrid upwind scheme
$A(|P|) = 1 - 0.5|P| \Rightarrow$ central difference scheme
$A(|P|) = \max[0, (1 - 0.1|P|)^5] \Rightarrow$ "power law" scheme

A staggered grid was chosen for calculations, that is, a grid in which the unknown scalar and velocity-component variables are located at different mesh points so as to give rise to the three typical control volumes shown in Fig. 2.

2.3 Solution Algorithm. The SIMPLER algorithm [25] for decoupling velocities and pressure was modified to take the flow compressibility into account [26]. At each time step, the discretized equations are iteratively solved, because of their nonlinear character. During each iteration, equations like Eq. (13) are turned sequentially into one of the following forms:

$$a_P\varphi_P + a_W\varphi_W + a_E\varphi_E = b - a_S\varphi_S - a_N\varphi_N$$

$$a_P\varphi_P + a_S\varphi_S + a_N\varphi_N = b - a_W\varphi_W - a_E\varphi_E$$

and then solved by means of the well known tri diagonal matrix algorithm. The continuity equation is replaced by a pressure equation, which is linearized first and then solved through the Gauss–Seidel algorithm (the related iterative solution procedure is called "internal iteration") requiring only a "virtually complete" convergence. In fact, after having spent a certain amount of effort on calculating the equation coefficients, one must extract a fairly good solution of the pressure equation, but should refrain from

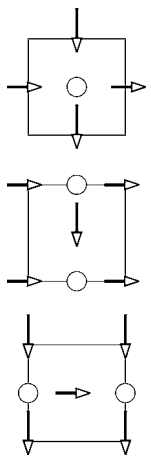

Fig. 2 Staggered grid control volumes

Downloaded 02 Jun 2010 to 171.66.16.98. Redistribution subject to ASME license or copyright; see http://www.asme.org/terms/Terms_Use.cfm

doing an excessive amount of work with coefficient values that are known to be only tentative. The overall convergence is obtained after iterating the solution of the whole discretized equation set (''external iteration''), so that the intermediate pressure values yielded by the internal iteration procedure take a gradually diminishing approximation level. The external iterations are stopped when the residual of each conservation equation is lower than a given tolerance.

3 Turbulence Models

3.1 Standard Model. As previously stated, the Reynolds model is referred to as standard k-ε model. In Ref. [5], it was considered that compressibility can be important for engine application and a suitable extension of Launder and Spalding's k-ε model was derived. The model was tuned so as to obtain the correct behavior in the limiting case of the rapid compression of a spherical eddy, and the following values for the model constants were obtained: $C_1=1.44$; $C_2=1.92$; $C_3=-0.373$; $C_4=0$; $\sigma_k=1.0$; $\sigma_\varepsilon=1.22$.

3.2 RNG Model. The RNG-based k-ε model is set within the same framework as the other two-equation models but uses renormalization group methods [8] which led to some remarkable results in the description of phase transitions in statistical physics. The model is said to provide improved predictions of near-wall and high streamline curvature flows in Ref. [13]. The underlying concept is the same as that for nonlinear k-ε models, i.e., the use of the tensor $\eta_{ij}=S_{ij}k/\varepsilon$ as an indicator of the anisotropy level, and hence its application in a proper modification of the turbulence model to take anisotropy effects into account. In nonlinear models, the Boussinesq relationship is replaced by an expansion of the stress tensor in powers of η_{ij}

$$\tau_{ij}-\frac{2}{3}\rho k\delta_{ij}=2C_\mu\rho k\eta_{ij}+O(\eta_{ij}^2)+\ \ldots \tag{14}$$

When the flow is highly anisotropic, i.e., the magnitude of η_{ij} is large, all the terms of Eq. (14) should be retained. Although the basic idea of the RNG k-ε model is the same as that of nonlinear models, the followed procedure is quite different from these. In the RNG approach, the Navier–Stokes equations are averaged over an infinitesimal band of small scales in order to remove these from consideration. It is assumed that the fluctuating velocity is governed by the Navier–Stokes equations driven by a random force, which is chosen in such a way that the global properties of the resulting flow field are the same as those in the flow driven by the mean strain S_{ij}. This averaging procedure is iterated until the corrections add up to yield stabilized finite changes. At this stage, a new term appears in the ε equation, namely R, which is handled by an infinite series expansion in powers of η_{ij} so that, after making some considerations, one can obtain [12]

$$R=\rho C_\mu\frac{\eta^3(1-\eta/\eta_0)}{1+\beta\eta^3}\frac{\varepsilon^2}{k} \tag{15}$$

where $\eta=\|\eta_{ij}\|$.

The RNG approach looks very attractive for anisotropic flows, because it does not change the Boussinesq stress-strain relationship with a more expensive one. It only requires the calculation of R, which is not too onerous as η was already needed in the production term of the k equation.

In this work, a slight modification of the coefficients was made, in order to improve the model predictions for engine flow application, which are quite different from those addressed by the original RNG approach [26]. The standard values reported in Refs. [11,12] are: $C_1=1.42$; $C_2=1.68$; $C_3=0$; $C_4=1.0$; $\sigma_k=1.39$; $\sigma_\varepsilon=1.39$; $\beta=0.012$; $\eta_0=4.38$. The authors found that these values led to a sensible underestimation of the turbulence kinetic energy with respect to the experimental evidence and to the simulations reported in Ref. [23]. A slight modification of the constant C_2 allowed the model to improve the predictions during induction, without sensibly modifying the results throughout the compression and expansion strokes. The changes of C_3, σ_k, and σ_ε were made for comparability reasons with the compressibility effect and diffusion modeling of the other turbulence models under consideration. Nevertheless, these changes did not significantly affect the results. Thus, the following constant values were used: $C_1=1.42$; $C_2=1.75$; $C_3=-0.373$; $C_4=1.0$; $\sigma_k=1.0$; $\sigma_\varepsilon=1.22$; $\beta=0.012$; $\eta_0=4.38$.

3.3 Two Scale Model. Both Standard and RNG models have a shortcoming, from a theoretical point of view [24], that is, when the flow is highly unsteady, so that mean flow and turbulence rapidly change, it is difficult to believe that the turbulence energy production is in equilibrium with the dissipation production. For example, if the turbulence energy production suddenly switches off, there is no constraint for ε to decrease immediately, since the molecular dissipation does not fall to zero. Nevertheless, these k-ε model versions immediately set the ε production to zero, as it is proportional to the production term in the turbulence energy equation.

A two-scale type k-ε model was first proposed in Ref. [20], for a better simulation of flows in which there are rapid changes of both mean flow and turbulence. Its basic idea is to split the turbulence energy spectrum into two parts which have different interactions with the mean flow. If one takes as κ_1 the wave number above which no significant mean-strain turbulence production occurs, while κ_2 is the largest wave number at which viscous dissipation of turbulence energy is unimportant, one can split the spectrum at κ_1 and define the resulting parts as follows:

- $\kappa<\kappa_1$: production region (in which the turbulence receives energy from the mean flow)$\Rightarrow$variables k_p and ε_p;
- $\kappa_1<\kappa<\kappa_2$: transfer region (in which energy is transferred to smallest eddies)$\Rightarrow$variables k_t and ε_t.

The transfer region has no links with the mean motion: the production term for k_t is ε_p, i.e., the feeding rate that comes from the production region. At wave numbers greater than κ_2 we assume that there is only molecular dissipation, i.e., the ''transfer region dissipation rate'' is actually the rate at which energy is converted into heat by viscosity effects. It seems reasonable to neglect the turbulence energy amount related to wave numbers above κ_2, so that one can write

$$k=k_p+k_t \tag{16}$$

The main consequence of this split-spectrum approach is that ε_t (and hence molecular dissipation) has no production terms deriving from those of k_p, so that it falls to zero more slowly than the dissipation rate ε of single-scale models. On the other hand, there is an additional computational cost because of two new differential equations which have to be solved. The model equations are

$$P_k=2\mu_T S_{ij}S_{ij}-\frac{2}{3}(\mu_T D^2+\rho kD) \tag{17}$$

$$\frac{\partial(\rho k_p)}{\partial t}+\frac{\partial}{\partial x_j}(\rho U_j k_p)=\frac{\partial}{\partial x_j}\left(\frac{\mu_T}{\sigma_{kp}}\frac{\partial k_p}{\partial x_j}\right)+P_k-\rho\varepsilon_p \tag{18}$$

$$\frac{\partial(\rho\varepsilon_p)}{\partial t}+\frac{\partial}{\partial x_j}(\rho U_j\varepsilon_p)=\frac{\partial}{\partial x_j}\left(\frac{\mu_T}{\sigma_{\varepsilon p}}\frac{\partial\varepsilon_p}{\partial x_j}\right)+C_{p1}P_k\frac{P_k}{\rho k_p}+C_{p2}P_k\frac{\varepsilon_p}{k_p}-C_{p3}\rho\varepsilon_p\frac{\varepsilon_p}{k_p} \tag{19}$$

$$\frac{\partial(\rho k_t)}{\partial t}+\frac{\partial}{\partial x_j}(\rho U_j k_t)=\frac{\partial}{\partial x_j}\left(\frac{\mu_T}{\sigma_{kt}}\frac{\partial k_t}{\partial x_j}\right)+\rho\varepsilon_p-\rho\varepsilon_t \tag{20}$$

Downloaded 02 Jun 2010 to 171.66.16.98. Redistribution subject to ASME license or copyright; see http://www.asme.org/terms/Terms_Use.cfm

$$\frac{\partial(\rho\varepsilon_t)}{\partial t}+\frac{\partial}{\partial x_j}(\rho U_j\varepsilon_t)=\frac{\partial}{\partial x_j}\left(\frac{\mu_T}{\sigma_{\varepsilon t}}\frac{\partial\varepsilon_t}{\partial x_j}\right)+C_{t1}\rho\varepsilon_p\frac{\varepsilon_p}{k_t}+C_{t2}\rho\varepsilon_p\frac{\varepsilon_t}{k_t}$$
$$-C_{t3}\rho\varepsilon_t\frac{\varepsilon_t}{k_t} \tag{21}$$

$$\mu_T=\rho C_\mu\frac{k^2}{\varepsilon_p} \tag{22}$$

The coefficients suggested in Ref. [21] are: $C_{p1}=0.21$; $C_{p2}=1.24$; $C_{p3}=1.84$; $C_{t1}=0.29$; $C_{t2}=1.28$; $C_{t3}=1.66$; $\sigma_{kp}=\sigma_{kt}=0.75$; $\sigma_{\varepsilon p}=\sigma_{\varepsilon t}=1.15$. The splitting of the production terms in Eqs. (19) and (21) into two parts allows the wave number κ_1 to be shifted according to the flow conditions [21]. In the present study, the model constants were tuned in relation to the specific case of ICE application. In fact, like the RNG model, the two-scale model with the standard coefficients also gives rise to an underprediction of turbulence throughout the induction stroke. This was removed by means of a slight decrease of C_{p1}, C_{p2}, C_{t1} and C_{t2}, and a limited increase of C_{p3} and C_{t3}. The following constant values were thus employed: $C_{p1}=0.20$; $C_{p2}=1.21$; $C_{p3}=1.90$; $C_{t1}=0.28$; $C_{t2}=1.25$; $C_{t3}=1.72$; $\sigma_{kp}=\sigma_{kt}=0.75$; $\sigma_{\varepsilon p}=\sigma_{\varepsilon t}=1.15$.

3.4 Boundary Conditions. The used boundary conditions for the difference equations are obtained by a modified procedure with respect to the simple application of the well known logarithmic wall functions. The particular feature of such a modified approach is that the most limiting hypothesis underlying the wall functions (i.e., local equilibrium between production and dissipation of turbulence in the logarithmic region) was given a virtually negligible weight. Under the hypothesis of local equilibrium one has [27]

$$\sqrt{\frac{\tau_w}{\rho}}=v^*=C_\mu^{1/4}\sqrt{k} \tag{23}$$

$$\varepsilon=\frac{C_\mu^{3/4}k^{3/2}}{\chi y} \tag{24}$$

$$\frac{U}{v^*}=1/\chi\log(Ey^+) \tag{25}$$

where $E=9.793$ and $\chi=0.419$ are the so-called wall logarithmic law and von Karman constants, respectively; $y^+=v^*y\rho/\mu$. In order to limit the effects of such hypothesis, the velocity and turbulence energy at the grid point nearest to the wall were computed by combining their conservation equations with Eqs. (23) and (25), as follows. With reference to the velocity component parallel to the wall, from Eq. (25), multiplying and dividing by v^*, one has [19]

$$\tau_w=\frac{\chi\rho C_\mu^{1/4}\sqrt{k}U}{\log(Ey^+)}=t_\mu U \tag{26}$$

Hence, the shear stress due to the wall can be incorporated into the momentum equation, in which it replaces the viscous part of the stress tensor opposing the flow motion at the wall ($t_\mu>0$)

$$a_Pu_P+a_Eu_E+a_Wu_W+a_Su_S+a_Nu_N=b-t_\mu\Omega_{\text{wall}}u_P \tag{27}$$

The magnitude of the wall resistance depends on the turbulence level, as is physically consistent, because t_μ is a function of the turbulence kinetic energy.

The boundary condition for the turbulence energy equation can be set by introducing a production term of the form

$$P_k=\tau_{ij}\frac{\partial U_i}{\partial x_j}\approx\tau_w\frac{\partial U}{\partial y} \tag{28}$$

under the hypothesis that the flow close to the wall is parallel to this.

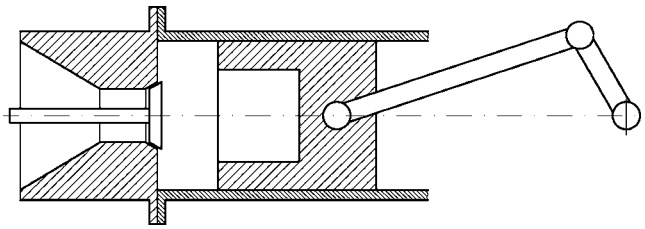

Fig. 3 Model engine. Cylinder bore: 75.4 mm; stroke: 94 mm; bumping clearance: 0.6 mm (bowl in piston), 16.49 mm (flat piston); bowl diameter: 23.5 mm; bowl depth: 41 mm; compression ratio: 6.7; valve diameter: 34 mm; maximum valve lift: 8 mm; valve seat angle: 60 deg.

By combining Eqs. (23) and (28), where $\partial U/\partial y\approx U/y$ is used for discretization, one obtains

$$P_k=\rho C_\mu^{1/2}k\frac{U}{y} \tag{29}$$

The conservation laws take the main physical phenomena into account, so that the effect of the local equilibrium hypothesis underlying the wall functions is sensibly mitigated. Only the dissipation rate at the node closest to the wall is derived directly from Eq. (24).

4 Model Engine

The model engine with its central valve and bowl-in-piston arrangement is schematically shown in Fig. 3. In Ref. [22], a detailed experimental analysis of the flow in such an engine is reported. It was carried out by means of laser Doppler velocimetry under motored conditions. The results in Ref. [22] were used for the present assessment of k-ε turbulence model variants.

5 Preliminary Evaluations

As a preliminary step, tests were carried out on the solution sensitivity to the mesh density and computational-time step size as well as to the equation differencing schemes for time and space derivatives. As is stated in Sec. 2.2, there is no significant difference in results if second-order trapezoidal or first-order backward implicit temporal schemes are used. Thus the backward fully implicit scheme was chosen for time derivatives as it required less computational time. With reference to the spatial derivative discretization, three different schemes were examined: central difference, hybrid upwind (first- and second-order accurate) and power law schemes.

The central difference scheme was ascertained to lead to numerical instability at high Peclet numbers (that is, when convection becomes more important than diffusion), hence the final choice had to be made between the hybrid upwind and power law schemes. Both schemes are numerically stable, but power law requires slightly higher computational efforts because of the complex function $A(P)$ which is used to provide a good numerical accuracy. As is shown in Ref. [25], for given values of the dependent variables at the nodes E and W (Fig. 1), the power law provides almost the same value at the node P as the exact solution of one-dimensional convection-diffusion problem where the diffusion coefficient is taken to be constant. The same order of accuracy and almost the same calculation times as the power law scheme were obtained applying a second-order hybrid upwind scheme. However, as such a scheme might give rise to instabilities, the hybrid power law was used for computations.

With respect to the influence of the mesh size and time step on results, rather coarse meshes were used by many authors in the past [23,24] and such meshes were accepted as adequate for turbulence-model comparisons. The tests made in the present work showed that finer meshes than those were required for ob-

Downloaded 02 Jun 2010 to 171.66.16.98. Redistribution subject to ASME license or copyright; see http://www.asme.org/terms/Terms_Use.cfm

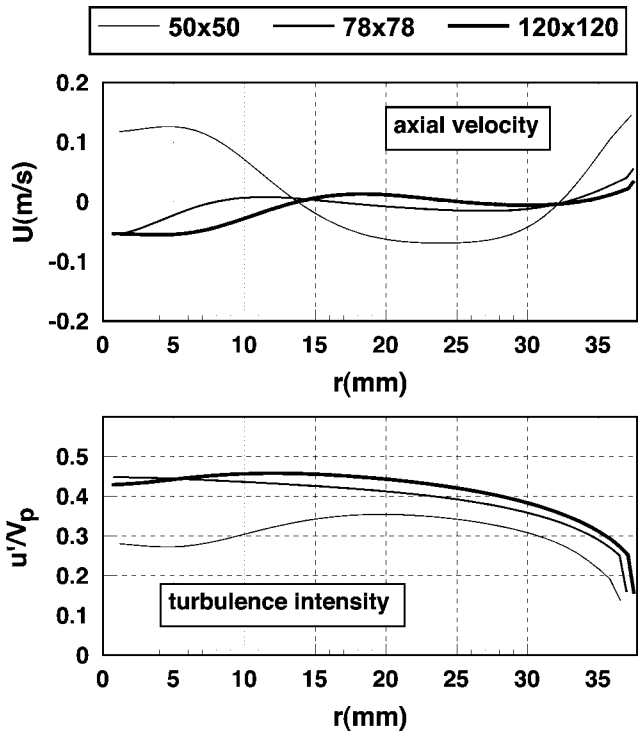

Fig. 4 Numerical accuracy test (TDC, $z=5$ mm)

taining a numerical solution which was not affected by the grid size (''converged'' solution). An example of the mesh effect is given by Fig. 4, in which predictions for the radial distributions of the axial velocity and normalized turbulence intensity at top dead center (TDC) in the flat-piston case are reported for 50×50, 78×78 and 120×120 grid points. The respective time steps corresponded to 0.08, 0.04 and 0.02 crank-angle degrees. Because there is still a sensible difference between the 78×78 and 120×120 grid results, 78×78 could not be taken as a grid providing converged solution. A 95×95 grid was verified to be a good compromise between computational time effort and numerical accuracy requirements, and therefore it was selected for investigation. It is worth pointing out that, in this grid sensitivity test, specific attention was paid to the difference in results between a certain grid and a finer one rather than to the correspondence degree of numerical results to the experimental ones.

6 Flow Evolution

An overall insight into the in-cylinder flow evolution, as is represented by the results obtained with the RNG model, is provided by Figs. 5, 6 (flat-piston arrangement) and by Figs. 7, 8 (bowl-in-piston engine). At the indicated crank angles, these figures report the velocity field and the isolines of the following adimensional turbulence quantities:

$$\text{turbulence intensity: } TI = \sqrt{\frac{2}{3}k} \Big/ V_p$$

$$\text{length scale: } \ell^* = \frac{C_\mu^{3/4} k^{3/2}}{\varepsilon B}$$

$$\text{time scale: } \tau^* = \frac{k}{\varepsilon T_{\text{cycle}}}$$

In the above expressions, V_p is the mean piston speed, B is the cylinder bore and T_{cycle} is the cycle period. It is important to point out that, for the turbulence model variants tested, differences in results can be expected everywhere throughout the engine cycle. This is due to the fact that such models were set up to account each for a certain number of flow features, such as compressibility, anisotropy, flow curvature, unsteadiness and so on, whereas all of these aspects can be met, singularly or all together, during the engine cycle. For example, if turbulence models which are focused only on compressibility effects are tested, their comparative assessment for engine flow application should be made during the compression and expansion strokes.

Details of the engine and valve design are given in Fig. 3. In order to simplify the management of the moving mesh, in the computational code the valve is represented by a ring-like opening, with variable dimensions, in the head surface. The experimental mass flow rate and velocity direction [28,29] were used to assign the velocity vectors at inlet. This choice determines some differences between computational results and the actual flow during induction, but only in a narrow zone around the valve. During compression and expansion the influence of the particular valve modeling and lift is negligible [23,30].

The pressure at the inlet is taken to be the external pressure, because the pressure losses in the very short intake manifold are virtually negligible at the considered low engine speed. The in-cylinder pressure during the intake process has a mean value equal to 0.98 bar.

6.1 Flat Piston. During the induction stroke the intake jet splits at the valve exit (Fig. 5) producing vortices in the upper region of the combustion chamber. The in-cylinder turbulence is mainly determined by the characteristics of the turbulence generated in the shear layers of the inlet jet. In the jet, ℓ^* is controlled by the valve opening and τ^* is very small, indicating a great tendency towards turbulence variation, while outside the jet ℓ^* is driven by the combustion chamber geometry and τ^* increases sensibly along the flow paths. This is consistent with the fact that the jet is the source of turbulence [23]. At the end of the induction stroke, the intake generated large structures change their relative size, the external vortex becoming dominant. The largest values of turbulence intensity occur in the main vortex central region and in the tiny top-side vortex core. The length scale is now strongly controlled by the chamber shape, according to Ref. [23].

During the compression stroke, the intake generated vortices weaken and break up, and turbulence decays towards a pancake geometry controlled structure. As a consequence, ℓ^* and τ^* both increase, but in the last part of compression ℓ^* decreases, as the effect of the reduced available volume overwhelms that of the decay process (Fig. 6(*a*)). After TDC, the flux rapidly becomes nearly one dimensional and turbulence intensity continues to decrease (Fig. 6(*b*)). The rate of change becomes higher than that in the compression stroke, because of the bulk expansion effect. The volume variation and turbulence decay have a combined effect that makes ℓ^* rapidly increase.

6.2 Bowl in Piston. On the induction stroke a new vortex can be seen, compared to the flat piston case (Fig. 7(*b*)). This is due to the bowl effect that encapsulates the flow, making it separate from the intake jet. The new vortex is confined within the bowl at the end of the induction stroke and determines a different distribution of turbulence energy: the main vortex has a smaller size than that in the previous case and does not show a turbulence level peak. The length scale ℓ^* undergoes the effects of the different piston geometry but presents almost the same values. The turbulence parameter which is most influenced by the bowl is the time scale τ^*. In fact, as the time scale is small where turbulence is produced and grows along the stream paths, it is clear that the greatest values of τ^* occur within the bowl vortex, because this location is reached at the end of the longest paths (Figs. 5(*b*), 7(*b*)).

During the compression stroke, the flow structure behavior becomes more and more different from that in the flat-piston case: a more rapid decay of the intake generated structure was observed, along with a new turbulence generation mechanism, that is a

Downloaded 02 Jun 2010 to 171.66.16.98. Redistribution subject to ASME license or copyright; see http://www.asme.org/terms/Terms_Use.cfm

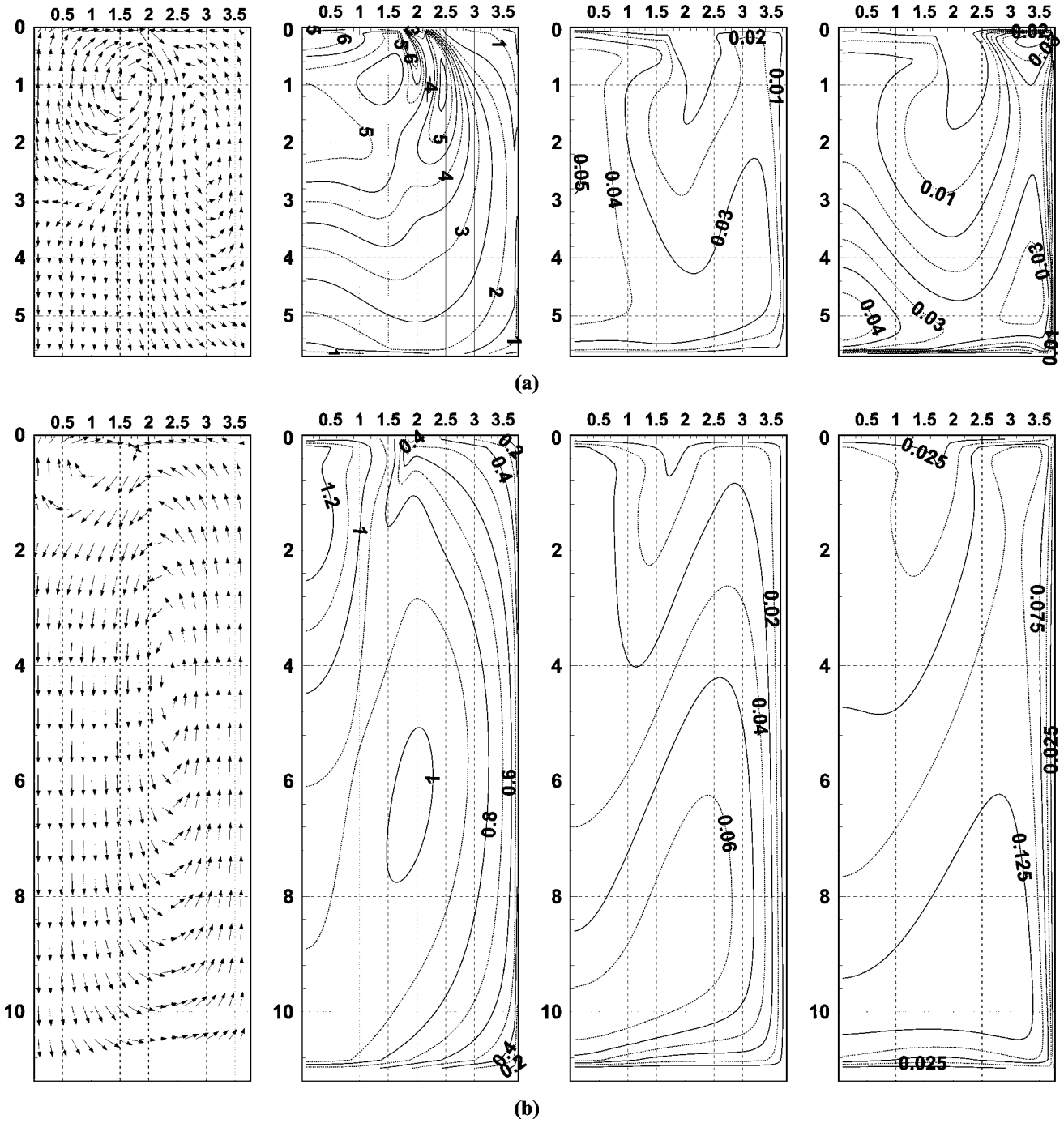

Fig. 5 Flow evolution for flat-piston arrangement—θ=72 deg (a), θ=180 deg (b), from left to right: velocity, *TI*, ℓ^*, τ^* fields

strong squish effect due to the presence of the bowl. The squish effect on mean flow and turbulence quantities at compression TDC can be observed in Fig. 8(*a*). Figure 9 shows the direct squish (θ=324 deg) on the left side and the reverse squish (θ =390 deg) on the right side.

The squish vortex arises in the upper cylinder region and is confined to the top right portion of the bowl volume at TDC. It gives a significant contribution to the turbulence production, as can be deduced from the comparison between Figs. 6(*a*) and 8(*a*) (θ=360 deg). At the end of compression, for the bowl-in-piston arrangement $TI>0.4$ almost everywhere, whereas for the flat piston $TI>0.4$ in more than half of the clearance volume. In the bowl-in-piston case, this production of turbulence determines a different behavior of ℓ^* and τ^*, depending on the location of the flow particles at bottom dead center (BDC), as can be inferred from Figs. 7(*b*) and 8(*a*): the fluid particles which were in the bowl vortex at BDC, and had relatively weak turbulence, undergo an increase of their *TI* values and a corresponding decrease of ℓ^* and τ^*. The opposite occurs for the flow outside the bowl with higher turbulence at the end of induction. During the expansion stroke (Fig. 8(*b*)) a reverse squish appears, indicating that the flux cannot become one dimensional, at least at the early expansion stage. As in the flat piston case, during the expansion stroke, ℓ^* and τ^* increase, whereas *TI* decreases.

7 Model Assessment

The prediction outcome of the three considered turbulence model variants was compared with the experimental results of

Downloaded 02 Jun 2010 to 171.66.16.98. Redistribution subject to ASME license or copyright; see http://www.asme.org/terms/Terms_Use.cfm

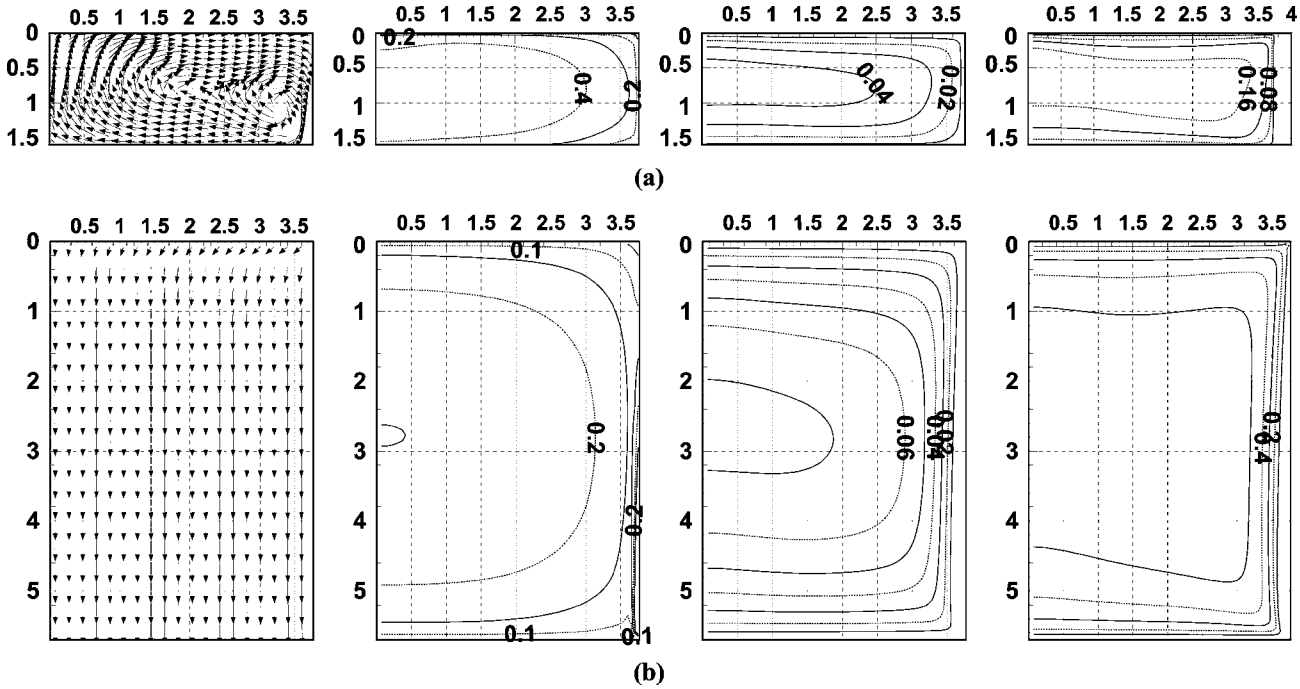

Fig. 6 Flow evolution for flat-piston arrangement—θ=360 deg (a), θ=432 deg (b), from left to right: velocity, *TI*, ℓ^*, τ^* fields

Ref. [22] in order to assess the capabilities of them. Reynolds averaging, i.e., ensemble averaging, was applied in Ref. [22] to extract the mean motion from the measured instantaneous velocities, so that the resultant turbulent fluctuations include the so-called cycle-to-cycle mean flow variations. This is consistent with the averaging procedure followed to derive the RANS equations.

7.1 Bowl in Piston. Radial profiles of axial mean velocity and turbulence intensity at different axial locations are shown in Fig. 10, for the bowl-in-piston arrangement, at the crank angles θ=36, 324, and 360 deg.

During the induction stroke, a fairly good agreement with experimental results can be seen for all the models, although none of them gives close correspondence in values for intermediate radial coordinates (Fig. 10(*a*)). On the whole, RNG model gives a better agreement with experiments than the other models for the turbulence intensity. In particular, the difference between numerical and experimental data between $r=10$ and $r=15$ mm is the lowest. During the compression stroke, it can be seen that all the models overpredict the squish intensity close to the cylinder axis (Figs. 10(*b*) and 10(*c*)): the only case of underprediction takes place for the two-scale k-ε model at θ=360 deg and axial location $z=35$ mm (Fig. 10(*c*)). In every case, this model usually predicts lower velocities and higher turbulence intensities near the axis than the other models. The standard k-ε model generally shows a rather worse agreement with experimental data than the other models, while the two-scale model shows a little less accurate overall reproduction of the curve trends (Figs. 10(*b*) and 10(*c*)).

With reference to the influence of the model constants on computational results, an increase in C_1 (in C_{p1}, C_{p2}, C_{t1}, C_{t2}, for the two-scale model) determines a decrease in the turbulence intensity and a growth in the velocity magnitudes, the opposite occurs for an increase in C_2 (in C_{p3} and C_{t3}, for the two-scale model). However, the trends shown by the curves are not influenced by these values, provided that small modifications from the standard settings are made. The numerical results obtained with the original and with slightly modified constant values present differences that are smaller than those yielded by the different models. The only case in which the effect of the constant modification on the results is quite important refers to the RNG model when the intake stroke is simulated. This is shown in Fig. 10(*a*), where the modified value of C_2 allows the RNG model to yield the better result. These findings also hold for the flat-piston configuration.

7.2 Flat Piston. Radial profiles of axial mean velocity and turbulence intensity are shown in Fig. 11, for crank angles of 324 and 360 deg and different axial locations.

The three models give quite different results from each other, with respect to the case where the squish effect due to the piston shape was fairly well reproduced by all the models. For the flat-piston configuration, RNG and two-scale models show a general better agreement with the experimental mean velocity trends as well as with both experimental trends and values of the turbulence intensity, than the standard model. However, for the highest radial coordinates, at θ=360 deg, all the models predict an opposite flow direction to that of experimental data, as was also shown in Ref. [30]. In this referenced work, the discrepancy was ascribed to the longer persistence in predictions of the intake generated main vortex throughout the compression stroke, with respect to the experiments. However, it should be pointed out that the main induced vortex predicted in Ref. [30] was clockwise, whereas an anticlockwise dominant vortex was predicted by the authors at the end of induction. Furthermore, in the present study, the residual clockwise vortex in the upper chamber region at the end of induction has not the same size for all the models, the standard model giving the highest size and RNG the smallest size (Fig. 5(*b*)). Besides, the calculations gave a larger and even dominant induction-generated clockwise vortex in the valve wake when coarser meshes were adopted. In spite of this, the results obtained for large radial abscissa at θ=360 deg (Fig. 11(*b*)) showed almost the same velocity pattern as that in Fig. 6(*a*), for all the turbulence models and for different mesh sizes. Hence, in the authors' opinion, it is most likely that some discrepancies are present in the experimental data, due to the very small mean velocities occurring in a highly fluctuating motion.

The numerical simulation of the flat-piston configuration was also carried out using the commercial computational fluid dynamics (CFD) code STAR-CD®. In particular, Fig. 12 shows the comparison between the results obtained with the homemade numeri-

Downloaded 02 Jun 2010 to 171.66.16.98. Redistribution subject to ASME license or copyright; see http://www.asme.org/terms/Terms_Use.cfm

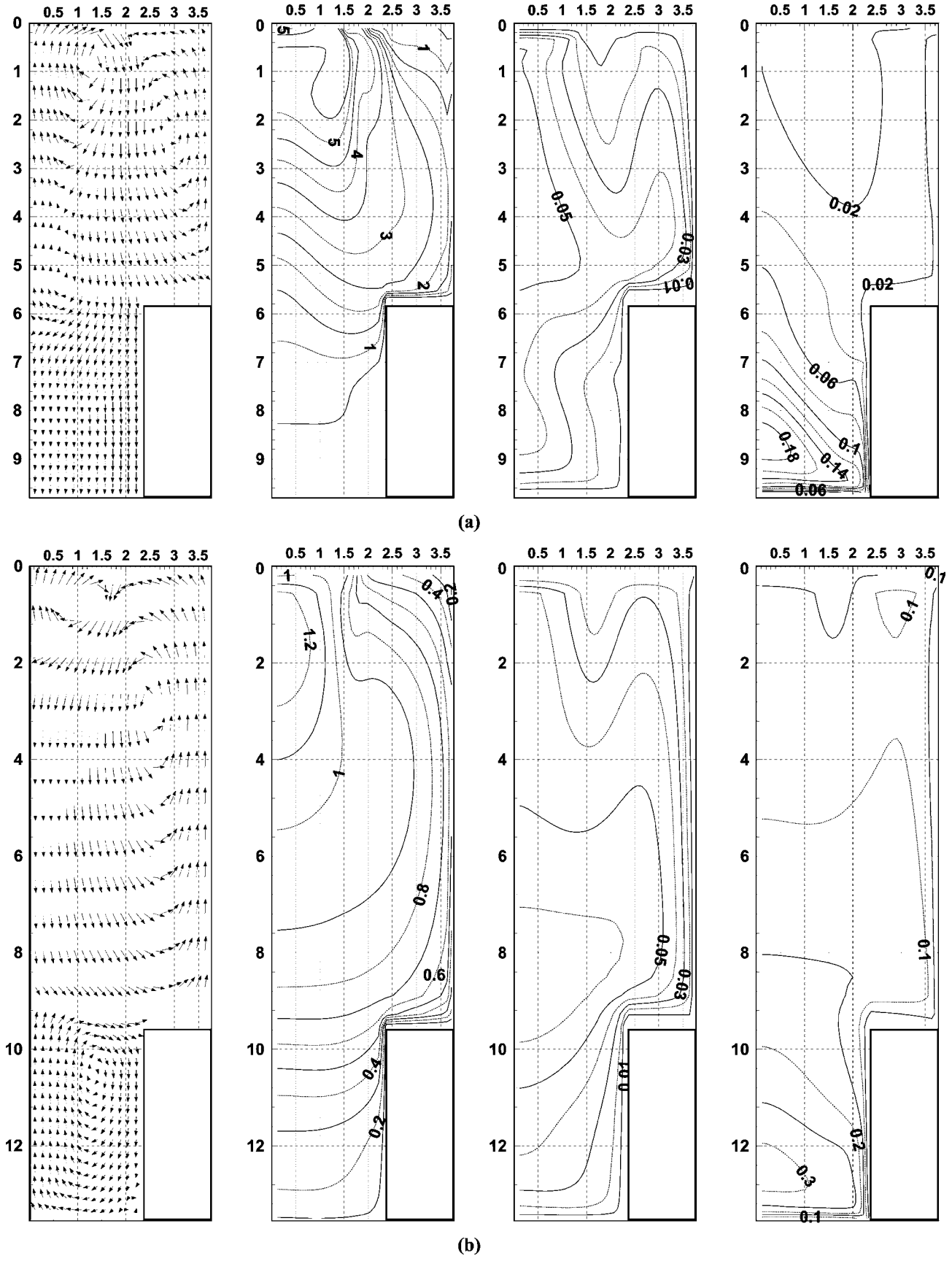

Fig. 7 Flow evolution for bowl-in-piston arrangement—θ=90 deg (a), θ=180 deg (b), from left to right: velocity, *TI*, ℓ^*, τ^* fields

Downloaded 02 Jun 2010 to 171.66.16.98. Redistribution subject to ASME license or copyright; see http://www.asme.org/terms/Terms_Use.cfm

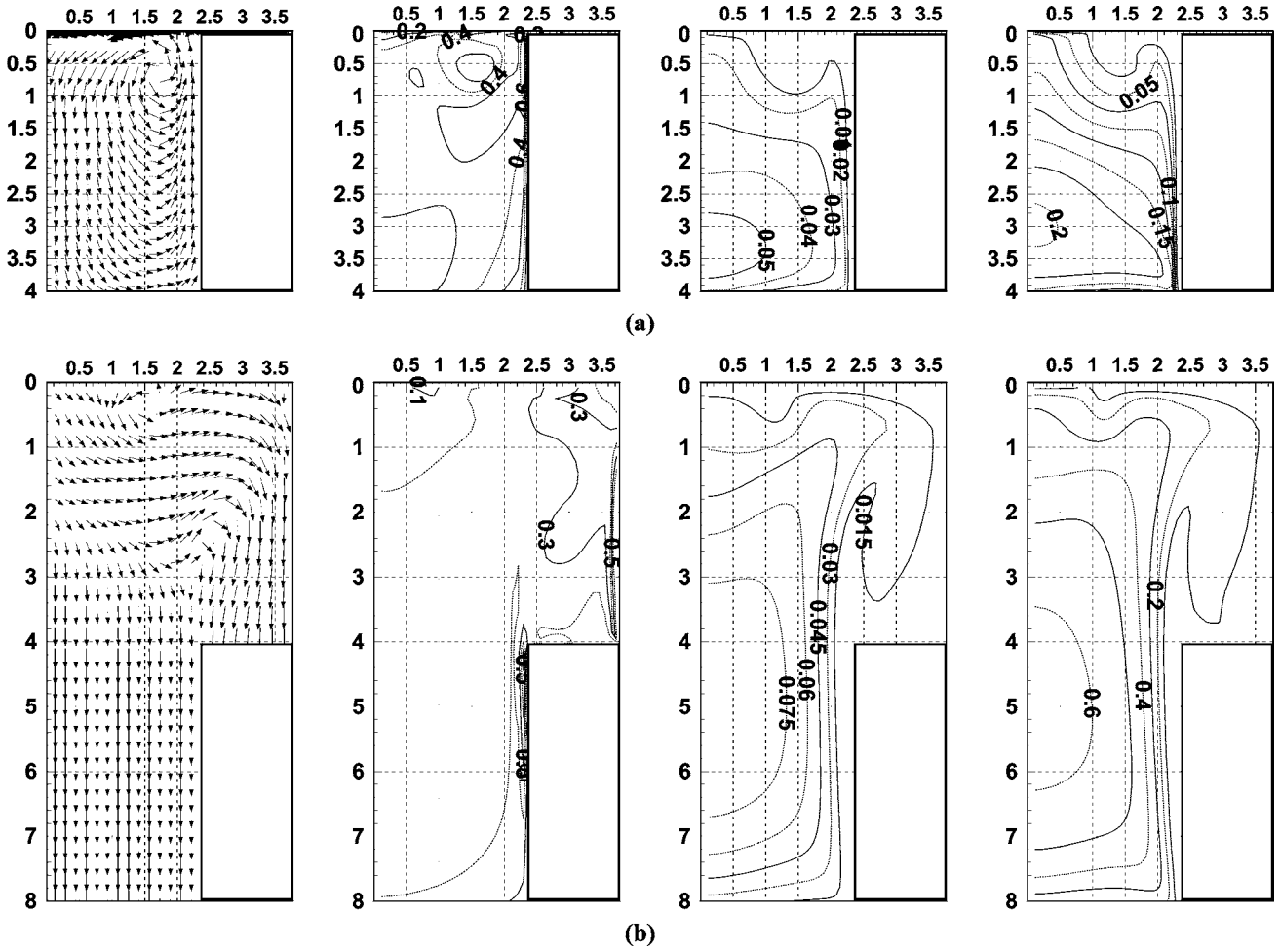

Fig. 8 Flow evolution for bowl-in-piston arrangement—θ=360 deg (a), θ=432 deg (b), from left to right: velocity, *TI*, ℓ^*, τ^* fields

cal code and with STAR-CD® for the flat-piston arrangement at θ=360 deg. As can be inferred from the figure, the flow direction given by the codes in the higher-radius region is the same, but STAR-CD® provides higher axial-velocity values there. The considered turbulence model was the standard k-ε in both codes, but the boundary condition was applied in a different manner. More specifically, in STAR-CD® the following boundary condition for the production term of the turbulence kinetic energy was used, instead of Eq. (29)

$$P_k = \rho C_\mu^{1/2} k \frac{U}{y \log(Ey^+)} \tag{30}$$

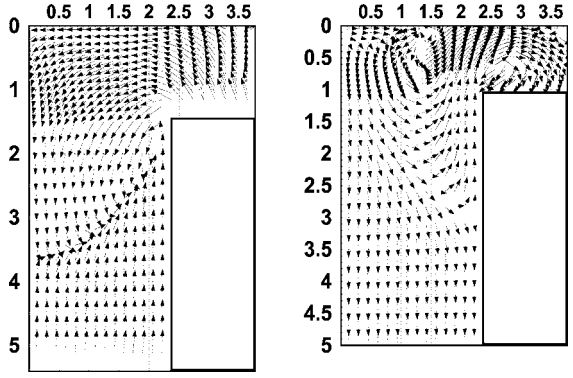

Fig. 9 Squish shape at θ=324 deg and θ=390 deg

8 Conclusions

Three different versions of the k-ε turbulence model, i.e., standard, RNG and two-scale models, were surveyed underlining their varieties, either present or purposely introduced in them, to take account of flow features that are relevant to engine application, such as compressibility, anisotropy, and unsteadiness. Furthermore, modified boundary conditions with respect to the conventional logarithmic-law wall-function method were proposed and applied. The turbulence models, with the revised wall-function approach, were assessed by their implementation, in a newly developed multidimentional CFD code, for the analysis of mean flow and turbulence quantities within the axisymmetric combustion chamber of a motored model engine featuring one centrally located valve and each of a flat-piston and cylindrical bowl-in-piston arrangements. Simulation results were obtained throughout the whole engine cycle and compared to those of laser Doppler velocimetry measurements available at an engine speed of 200 rpm for both piston arrangements. The influence of the k-ε model variants on the flow-field features was examined during the induction stroke and around compression TDC.

The RNG and two-scale models required a minor adjustment of their constants so as to improve their performance with particular reference to the induction stroke. It was verified that this adjust-

Downloaded 02 Jun 2010 to 171.66.16.98. Redistribution subject to ASME license or copyright; see http://www.asme.org/terms/Terms_Use.cfm

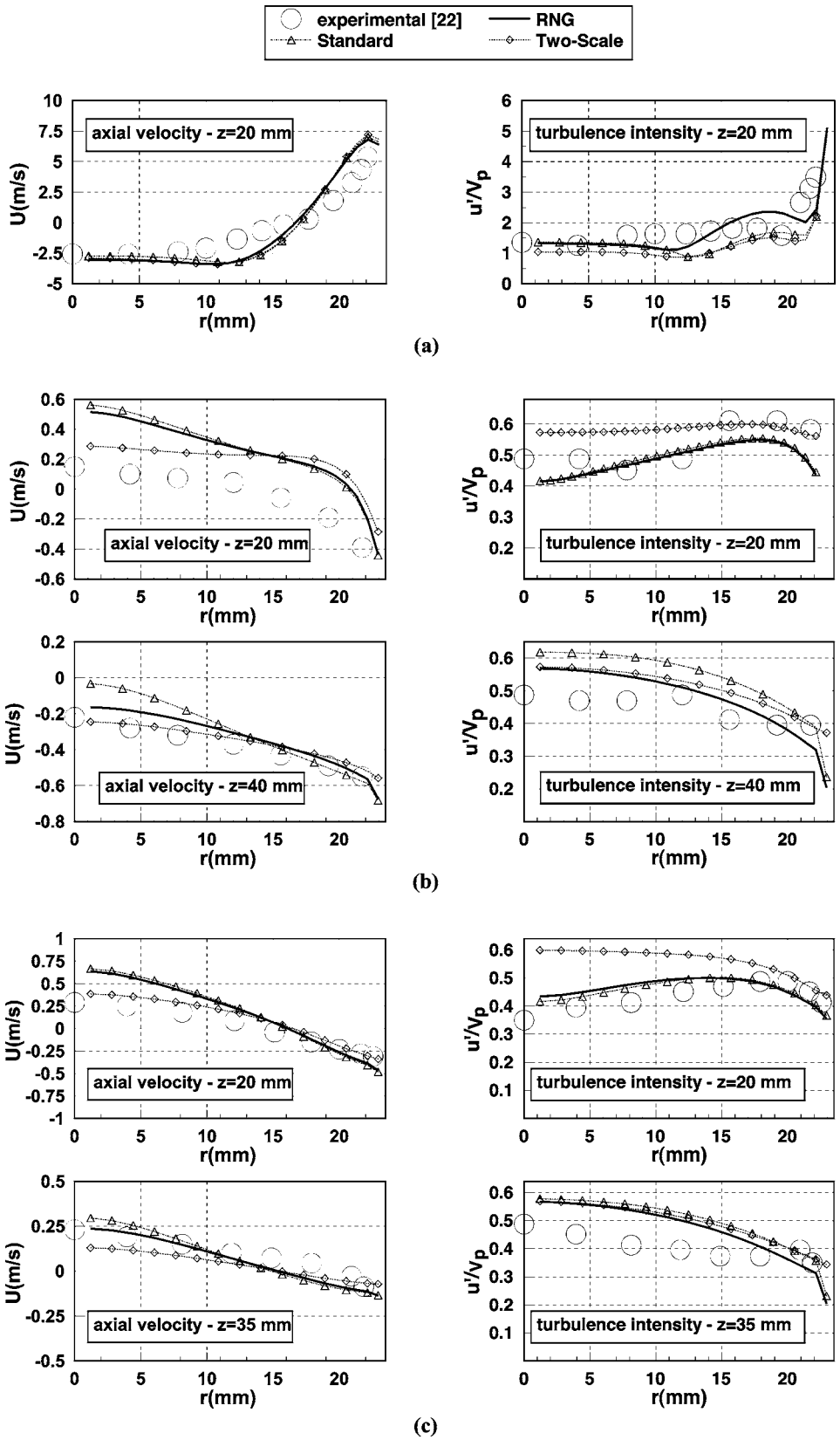

Fig. 10 Radial profiles of axial mean velocity and turbulence intensity—bowl-in-piston arrangement: (a) θ=36 deg, (b) θ=324 deg, (c) θ=360 deg

Downloaded 02 Jun 2010 to 171.66.16.98. Redistribution subject to ASME license or copyright; see http://www.asme.org/terms/Terms_Use.cfm

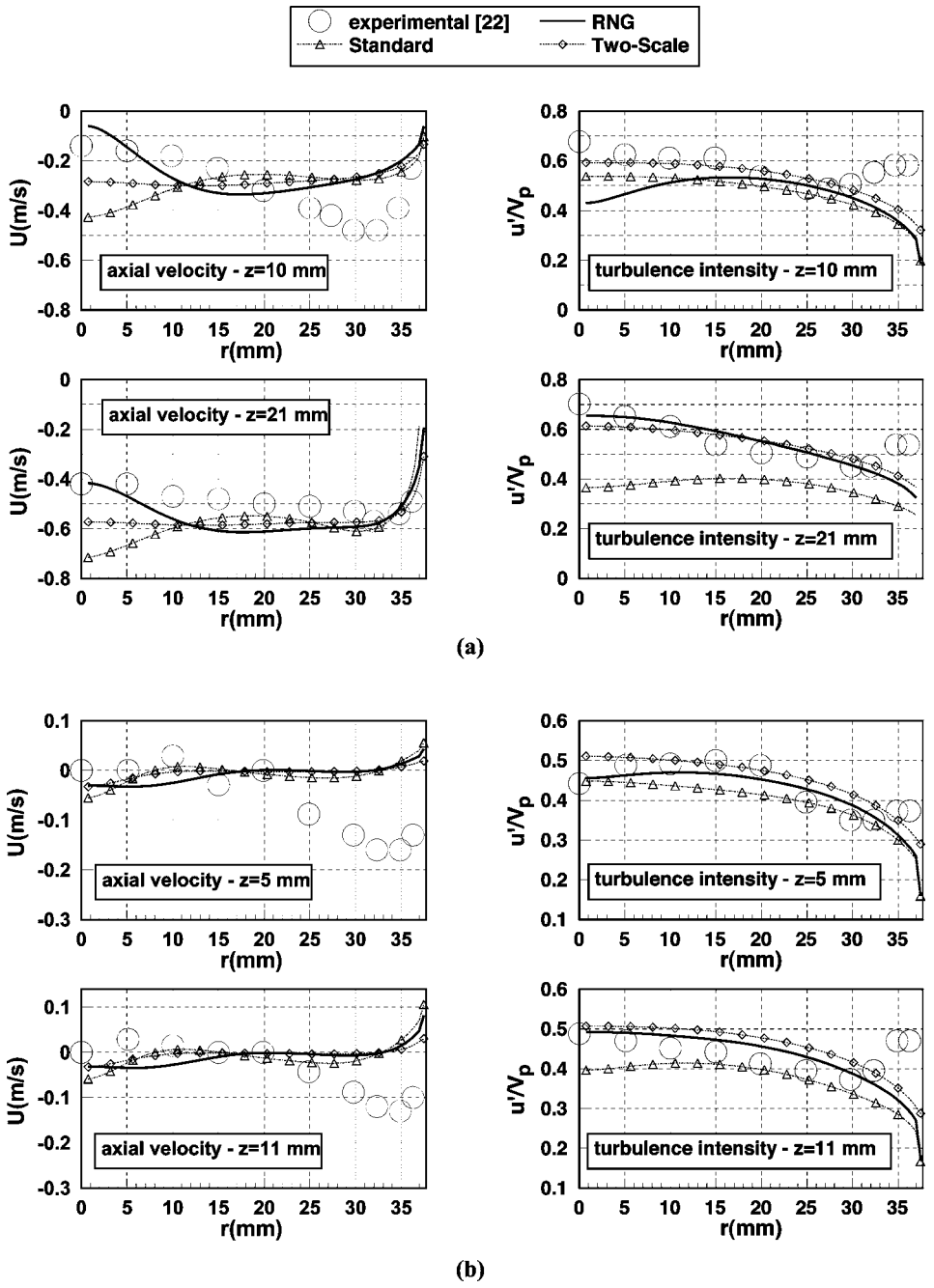

Fig. 11 Radial profiles of axial mean velocity and turbulence intensity—flat-piston arrangement: (a) θ=324 deg, (b) θ=360 deg

ment is not prejudicial to the evaluation of the relative merits of the models, as can be inferred by the fact that it does not determine significant differences during the compression and expansion strokes.

Two types of comparison were made: one between the flow features for the two engine-piston configurations and the other among the turbulence models for both of them. With reference to the first comparison, the most important aspect concerns the bowl effects on the in-cylinder flow and turbulence through the engine cycle, especially during the last stage of compression and the early expansion stroke, because of the presence of the squish motion, which is qualitatively well predicted by all the models.

As far as the comparison among the three variants of the k-ε turbulence model is concerned, in the authors' opinion, all of them can present advantages in some respects and drawbacks in others. At least for the present application, the RNG model was shown to give, on the average, a better agreement with experimental results than the other models in most of the mean-flow and turbulence property distributions, although it produced slightly worse results at a few of the axial locations examined, but in a narrow range of radial coordinates. Such findings refer particularly to the bowl-in-piston engine, most likely because the RNG model endeavors to take account of flow anisotropy, which is significant in squish-type flows, even in an axisymmetric engine configuration. With flat piston, both RNG and two-scale models gave quite good results. However, the use of a split-spectrum approach in the two-scale model led to a sensible increase of computational time, due to the increased number of equations to be solved and of iterations to be made per each time step, in addition to the lower time-step size which had to be chosen for achieving convergence. Since the

Downloaded 02 Jun 2010 to 171.66.16.98. Redistribution subject to ASME license or copyright; see http://www.asme.org/terms/Terms_Use.cfm

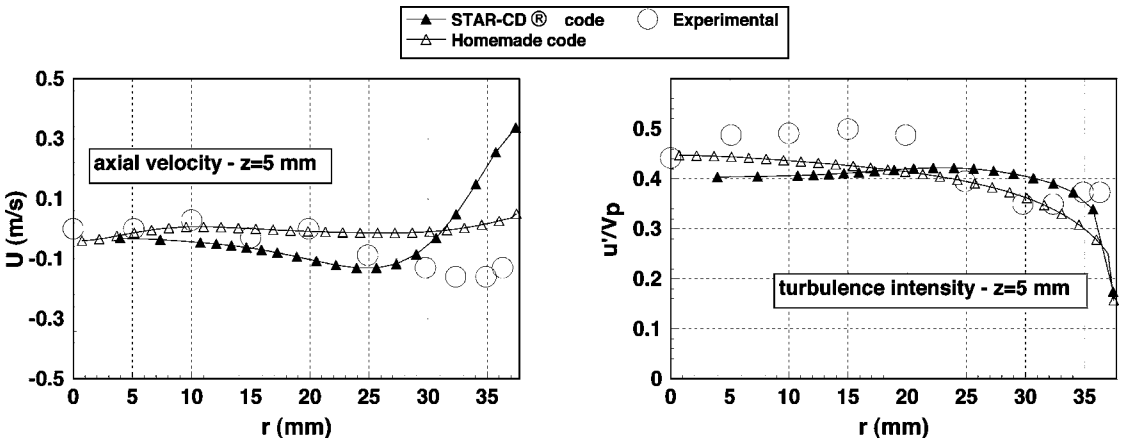

Fig. 12 Comparison between homemade and STAR-CD® code results

increased computational effort is not associated with an appreciably improved accuracy in results, the two-scale model seems to be less recommendable for engine flow application than the other two models.

For the flat-piston case, the homemade code results were compared to those of the commercial STAR-CD® code. A generally reasonable agreement was found between them, the discrepancies being mainly ascribable to the different wall boundary conditions.

Acknowledgment

Financial support to this research was provided by Centro Ricerche Fiat (CRF) and by Ministero dell'Università e della Ricerca (MIUR) under the Cofin'00 Program "Thermo-Fluid Dynamic Processes and Techniques for Pollutant Emission Reduction in IC Engines."

Nomenclature

C_1, C_2, C_3, C_4 = empirical constants for ε equation
C_{p1}, C_{p2}, C_{p3} = empirical constants for ε_p equation
C_{t1}, C_{t2}, C_{t3} = empirical constants for ε_t equation
C_μ = empirical constant for μ_T
$D=S_{\ell\ell}$ = velocity divergence
F = convective flux
h = stagnation enthalpy
k = turbulence kinetic energy
k_p = production-region turbulence kinetic energy
k_t = transfer-region turbulence kinetic energy
ℓ^* = adimensional turbulence length scale
$\mathbf{n}$ = versor normal to surface Ω
$P=F\Delta x/(\Gamma\Omega)$ = control volume Peclet number
P_k = turbulence kinetic energy production term
p = pressure
r = radial distance from cylinder axis
R = anisotropy function in the RNG k-ε model
S_{ij} = strain tensor
S_φ = source term for φ
t_μ = wall shear stress coefficient
U, U_i = absolute axial (mean) velocity, absolute (mean) velocity in the i direction
u_i = turbulent velocity fluctuation in the i direction
u', TI = turbulence intensity, adimensional turbulence intensity
u_n, u_s, v_e, v_w = relative mean velocities at control volume faces
V = volume
V_p = mean piston speed
v^* = wall friction velocity
y = distance from wall
z = axial distance from cylinder head
β, η_0 = constants in the RNG k-ε model
Γ = effective diffusivity
Δt = time step size
ΔV = mesh control volume
Δx, Δy = grid sizes
δ_{ij} = Kronecker delta
ε = turbulence energy dissipation rate
ε_p = production-region turbulence energy dissipation rate
ε_t = transfer-region turbulence energy dissipation rate
$\eta_{ij}=S_{ij}k/\varepsilon$ = dimensionless strain tensor
θ = crank angle
μ, μ_T = molecular viscosity, turbulent (eddy) viscosity
ρ = density
σ_h, σ_k, σ_ε, σ_{kp}, σ_{kt}, $\sigma_{\varepsilon p}$, $\sigma_{\varepsilon t}$ = Prandtl numbers
τ^* = adimensional turbulence time scale
$\tau_{ij}=-\rho\overline{u_iu_j}$ = Reynolds stress tensor
τ_w = wall shear stress
φ = general dependent variable
Ω, Ω_{wall} = surface of V, control-volume surface at wall

References

[1] Gosman, A. D., and Watkins, A. P., 1977, "A Computer Prediction Method for Turbulent Flow and Heat Transfer in Piston-Cylinder Assemblies," *Proc. of Symposium on Turbulent Shear Flows*, Pennsylvania State University, **5**, pp. 23–30.
[2] El Thary, S. H., and Haworth, D. C., 1992, "Directions in Turbulence Modeling for In-Cylinder Flows in Reciprocating Engines," J. Propul. Power, **8**(5), pp. 1040–1048.
[3] Launder, B. E., and Spalding, D. B., 1972, *Lectures in Mathematical Models of Turbulence*, Academic, Press London.
[4] Watkins, A. P., 1977, "Flow and Heat Transfer in Piston-Cylinder Assemblies," Ph.D. thesis, University of London.
[5] Reynolds, W. C., 1980, "Modeling of Fluid Motions in Engines—An Introductory Overview," *Combustion Modeling in Reciprocating Engines*, Plenum, New York, pp. 41–65.
[6] Morel, T., and Mansour, N. N., 1982, "Modeling of Turbulence in Internal Combustion Engines," SAE Paper No. 820040.
[7] El Tahry, S. H., 1983, "k-ε Equation for Compressible Reciprocating Engine Flows," AIAA J. Energy, **7**, pp. 345–353.
[8] Yakhot, V., and Orszag, S. A., 1986, "Renormalization Group Analysis of Turbulence," J. Sci. Comput., **1**, pp. 3–18.
[9] Speziale, C. G., 1987, "On Non-Linear k-ℓ and k-ε Models of Turbulence," J. Fluid Mech., **178**, pp. 459–475.

Downloaded 02 Jun 2010 to 171.66.16.98. Redistribution subject to ASME license or copyright; see http://www.asme.org/terms/Terms_Use.cfm

[10] Kido, H., Nakashima, K., Tajima, H., and Kitagawa, T., 1989, ''A Modification of the *k*-ε Turbulence Model for In-Cylinder Gas Flow,'' JSME Int. J., **32**(1), pp. 85–90.
[11] Yakhot, V., and Orszag, S. A., 1992, ''Development of Turbulence Models for Shear Flows by a Double Expansion Technique,'' Phys. Fluids A, **4**(7), pp. 1510–1520.
[12] Yakhot, V., and Smith, L. M., 1992, ''The Renormalization Group, the ε-Expansion and Derivation of Turbulence Models,'' J. Sci. Comput., **7**, pp. 35–61.
[13] Jones, R. M., Harvey III, A. D., and Acharya, S., 2001, ''Two Equation Turbulence Modeling for Impeller Stirred Tanks,'' ASME J. Fluids Eng., **123**, pp. 640–648.
[14] Bianchi, G. M., Cantore, G., Parmeggiani, P., and Michelassi, V., 2002, ''On Application of Nonlinear k-ε Models for Internal Combustion Engine Flows,'' ASME J. Eng. Gas Turbines Power, **124**, pp. 668–677.
[15] Speziale, C. G., Sarkar, S., and Gatski, T. B., 1991, ''Modeling the Pressure-Strain Correlation of Turbulence: An Invariant Dynamical Systems Approach,'' J. Fluid Mech., **227**, pp. 245–272.
[16] Yang, S. L., Peschke, B. D., and Hanjalic, K., 2000, ''Second-Moment Closure Model for IC Engine Flow Simulation Using Kiva Code,'' ASME J. Eng. Gas Turbines Power, **122**, pp. 355–363.
[17] Jakirlic, S., Tropea, C., Hadzic, I., Pascal, H., and Hanjalic, K., 2002, ''Computational Study of Joint Effects of Shear, Compression and Swirl on Flow and Turbulence in a Valveless Piston-Cylinder Assembly,'' SAE 2001 Trans., Journal of Engines, pp. 1402–1439.
[18] Celik, I., Yavuz, I., Smirnov, A., Smith, J., Amin, E., and Gel, A., 2000, ''Prediction of In-Cylinder Turbulence for IC Engines,'' Combust. Sci. Technol., **153**, pp. 339–368.
[19] Jones, W. P., 1997, ''Turbulence Modeling,'' *Lecture Series 1997-03*, Von Karman Institute for Fluid Dynamics.
[20] Hanjalic, K., Launder, B. E., and Schiestel, R., 1980, ''Multiple Time-Scale Concepts in Turbulent Transport Modeling,'' *Turbulent Shear Flows*, Springer, New York, pp. 36–49.
[21] Kim, S. W., 1991, ''Calculation of Divergent Channel Flows With a Multiple Time Scale Turbulence Model,'' AIAA J., **29**(4), pp. 547–554.
[22] Arcoumanis, C., Bicen, A. F., and Whitelaw, J. H., 1982, ''Squish and Swirl-Squish Interaction in Motored Model Engines,'' *Flows in Internal Combustion Engines*, T. Uzkan, ed., ASME Book H00245, ASME, New York, pp. 45–52.
[23] Ahmadi-Befrui, B., and Gosman, A. D., 1989, ''Assessment of Variants of the k-ε Turbulence Model for Engine Flow Applications,'' Int. J. Numer. Methods Fluids, **9**, pp. 1073–1086.
[24] Moriyoshi, Y., 1994, ''Experimental Evaluation of Calculation Models Used in In-Cylinder Flow Field Computations,'' *Proc. Int. Symp. COMODIA 94*, pp. 553–558.
[25] Patankar, S. V., 1980, *Numerical Heat Transfer and Fluid Flow*, McGraw–Hill, New York.
[26] Baratta, M., 2004, ''Multidimensional CFD Methods, Turbulence Models and Their Application to the Analysis of Charge Motion in an IC Engine Cylinder'' (in Italian), Ph.D. thesis, Politecnico di Torino.
[27] Bejan, A., 1995, *Convection Heat Transfer*, Wiley, New York.
[28] Bicen, A. F., Vafidis, C., and Whitelaw, J. H., 1984, ''Steady and Unsteady Air Flow Through an Intake Valve of a Reciprocating Engine,'' *Flows in Internal Combustion Engines-II*, ASME FED, **20**, pp. 47–55.
[29] Maier, A., Sheldrake, T. H., and Wilcock, D., 2000, ''Geometric Parameters Influencing Flow in Axisymmetric IC Engine Inlet Port Assembly: Part I-Valve Flow Characteristics,'' J. Fluids Eng., **122**, pp. 650–657.
[30] Ahmadi-Befrui, B., Gosman, A. D., and Watkins, A. P., 1984, ''Prediction of In-Cylinder Flow and Turbulence With Three Versions of *k*-ε Turbulence Model and Comparison With Data,'' *Flows in Internal Combustion Engines-II*, ASME FED Vol. 20, pp. 27–38.

Downloaded 02 Jun 2010 to 171.66.16.98. Redistribution subject to ASME license or copyright; see http://www.asme.org/terms/Terms_Use.cfm

Eberhard von Berg

Wilfried Edelbauer

Advanced Simulation Technologies,
AVL List GmbH,
Hans-List Platz-1,
A-8020 Graz, Austria

Ales Alajbegovic[1]
AVL Powertrain Engineering, Inc.,
47519 Halyard Drive,
Plymouth, MI 48170-2438

Reinhard Tatschl
Advanced Simulation Technologies,
AVL List GmbH,
Hans-List Platz-1,
A-8020 Graz, Austria

Martin Volmajer

Breda Kegl

Faculty of Mechanical Engineering,
University of Maribor, Slovenia

Lionel C. Ganippa[2]
Department of Thermo and Fluid Dynamics,
Chalmers University of Technology,
Gothenburg, Sweden

Coupled Simulations of Nozzle Flow, Primary Fuel Jet Breakup, and Spray Formation

Presented are two approaches for coupled simulations of the injector flow with spray formation. In the first approach the two-fluid model is used within the injector for the cavitating flow. A primary breakup model is then applied at the nozzle orifice where it is coupled with the standard discrete droplet model. In the second approach the Eulerian multi-fluid model is applied for both the nozzle and spray regions. The developed primary breakup model, used in both approaches, is based on locally resolved properties of the cavitating nozzle flow across the orifice cross section. The model provides the initial droplet size and velocity distribution for the droplet parcels released from the surface of a coherent liquid core. The major feature of the predictions obtained with the model is a remarkable asymmetry of the spray. This asymmetry is in agreement with the recent observations at Chalmers University where they performed experiments using a transparent model scaled-up injector. The described model has been implemented into AVL FIRE computational fluid dynamics code which was used to obtain all the presented results. [DOI: 10.1115/1.1914803]

Introduction

Reliable breakup models for diesel jets are an important prerequisite for the simulation of mixture formation in internal combustion (IC) engines. The initial stage of droplet formation in the injector proximity is not fully understood yet. Different ideas on the breakup mechanism are under consideration. For example, breakup can be caused by cavitation and turbulence effects within the nozzle or by aerodynamic breakup from self-exciting interaction between the liquid surface and the flow field outside the nozzle.

Several new models for primary breakup of fuel jets have been developed recently by the same authors [1,2]. The objective of the primary breakup models is to provide the initial size and velocity distribution of the spray droplets. This in turn links spray and mixture formation together with the injection parameters and locally resolved cavitating nozzle flow features. This is important for the optimization of the injectors as well as better understanding and consequent improvement of the overall mixture formation process.

Cavitating nozzle flow, spray formation, and spray propagation fall into the category of multi-phase flow phenomena. As such, two basic models can be used in their description. These are the Lagrangian discrete droplet model [3] and the Eulerian multi-fluid model [4]. In the simulations two approaches are used:

- Standard approach for the simulation of injector flow and spray is to perform two separate calculations. Eulerian two-fluid model can be used inside the injector and the discrete droplet model (DDM) outside of the injector in the spray region. Flow data in the nozzle orifice are transferred to the DDM model as initial conditions. In addition, a primary breakup model is applied within the DDM. Arcumanis and Gavaises [5] in a similar study did calculate flow within the nozzle, but did not explicitly calculate cavitation field as is done here.
- An alternative approach is to use only the Eulerian multi-fluid model in a single calculation covering both injector and spray regions. In this way, flow information is automatically transferred between the two regions. At the same time, this approach also allows more straightforward handling of the calculation.

A problem for all the primary breakup models is the validation procedure. Processes under consideration occur on a very small spatial scale. They are obscured within the injector and also by the formation of a dense spray cloud near the nozzle hole. As a result, it is very difficult to perform measurements of the diesel injection process and detailed experimental data are scarce [6]. Recently, experiments using the high-energy x rays were performed for the

[1]Current address: General Dynamics, Ann Arbor, MI 48105.
[2]Current address: Department of Applied Physics, University of Nijmegen, Netherlands.

Contributed by the Internal Combustion Engine Division of THE AMERICAN SOCIETY OF MECHANICAL ENGINEERS for publication in the ASME JOURNAL OF ENGINEERING FOR GAS TURBINES AND POWER. Manuscript received by the ICE Division June 13, 2003; final revision received April 16, 2004. Associate Editor: D. Assanis.

Copyright © 2005 by ASME

Downloaded 02 Jun 2010 to 171.66.16.98. Redistribution subject to ASME license or copyright; see http://www.asme.org/terms/Terms_Use.cfm

first time providing details of the spray structure downstream from the diesel injector [7,8]. Experiments of similar relevance were done revealing the cavitation and flow structure within the real size diesel injectors [9]. Recent experiments performed at Chalmers University for an enlarged model injector [10] provide good optical insight to the phenomena, cavitation, as well as spray cone formation. Since the scope here is the study of the flow both inside and outside the injector, these data are used for the validation of the primary breakup models and different numerical methods. Similar results have been obtained recently by Blessing et al. [11] using transparent real size diesel nozzles under typical IC engine operation conditions.

Previous Work

Cavitating nozzle flows have been simulated using several modeling approaches in the past. In part, the homogeneous flow model was applied [12–14] together with a separate transport equation for the vapor volume fraction describing the evolution of the cavitation region. The volume-of-fluid (VOF) method has been also used in the simulation of cavitating flows [15]. The proper application of the VOF method requires the resolution of all involved length and time scales. This results in very large computational effort. Therefore, this method is still limited to basic studies and can serve to improve fundamental understanding of the cavitation. When cavitation level is low and the resulting bubbles are smaller than the cells in the computational grid, it is possible to use the Euler-Lagrangian approach. In this approach each cavitation produced bubble is tracked in the Lagrangian frame [16,17]. Bubble diameter is modeled using the Rayleigh-Plesset equation. Here we use an extension of the previous efforts using the two-fluid model [18–20]. The two-fluid model allows a more detailed description of the flow compared to the homogeneous model, while at the same time it is less computationally intensive than the VOF approach. Thus, it is a suitable tool for engineering calculations applicable to processes covering a larger range of length scales.

Primary fuel jet breakup due to nozzle flow turbulence and aerodynamic forces has been studied first by Huh and Gosman [21] and later by Bianchi and Pelloni [22]. They calculated mean droplet size and production rate from estimated average turbulence properties of the nozzle flow. We extended this idea by using local nozzle flow properties as well as additional turbulent kinetic energy (TKE) sources from cavitation bubble collapses to calculate local distribution of breakup rates in the orifice cross section [1]. The model assumes homogeneous initial droplet sizes approximately equal to the nozzle diameter. The two-dimensional resolution is achieved by random sampling of the flow conditions in the orifice obtained from a three-dimensional (3D) calculation of the cavitating flow inside the injector. An even more recent addition to the model was to use the release of droplets from a coherent liquid core region and introduction of additional couplings between bubble dynamics and turbulence model [2].

Model Description

General Features of the Multi-Fluid Model. In the multi-fluid model bubbles, drops and bulk liquid or vapor phases are treated as interpenetrating continua. The basic mathematical formalism is obtained through ensemble averaging [23–25]. With respect to this, the two-fluid model corresponds to the Reynolds-averaged Navier-Stokes (RANS) model in the simulation of single-phase flows. For each of the phases a separate set of conservation equations is solved. The model equations of the multi-fluid approach are given in Table 1. The comparison with the single-phase RANS equations reveals essentially the same basic form of the equations with the addition of volume fraction, α_k, and the interfacial exchange terms. These terms are the sums on the right-hand sides of the equations given in Table 1. The details of the numerical implementation of the two-fluid model are presented by Basara et al. [26]. The interfacial exchange terms take into account the effects exerted between the phases at the interfaces. Due to the fact that the two-fluid model equations are obtained through ensemble averaging, the local morphology of the interface is lost. As a result, the interfacial exchange terms need to be modeled. Thus, they differ for cavitation and spray regions.

Table 1 Conservation equations for phase k with $k=1,\ldots,n$

Mass conservation equation:

$$\frac{\partial \alpha_k \rho_k}{\partial t} + \nabla \cdot \alpha_k \rho_k \mathbf{v}_k = \sum_{l=1, l\neq k}^{n} \Gamma_{kl} \tag{1}$$

Compatibility condition:

$$\sum_{k=1}^{n} \alpha_k = 1 \tag{2}$$

Momentum conservation equation:

$$\frac{\partial \alpha_k \rho_k \mathbf{v}_k}{\partial t} + \nabla \cdot \alpha_k \rho_k \mathbf{v}_k \mathbf{v}_k = -\alpha_k \nabla p + \nabla \cdot \alpha_k (\boldsymbol{\tau}_k + \mathbf{T}_k^t) + \alpha_k \rho_k \mathbf{g} + \sum_{l=1, l\neq k}^{n} \mathbf{M}_{kl} + \mathbf{v}_k \sum_{l=1, l\neq k}^{n} \Gamma_{kl} \tag{3}$$

Enthalpy equation:

$$\frac{\partial \alpha_k \rho_k h_k}{\partial t} + \nabla \cdot \alpha_k \rho_k \mathbf{v}_k h_k = \nabla \cdot \alpha_k (\mathbf{q}_k + \mathbf{q}_k^t) + \alpha_k \rho_k q_k''' + \alpha_k \boldsymbol{\tau}_k : \nabla \mathbf{v}_k + \alpha_k \frac{dp}{dt} + \sum_{l=1, l\neq k}^{n} \mathrm{H}_{kl} + h_k \sum_{l=1, l\neq k}^{n} \Gamma_{kl} \tag{4}$$

Turbulence kinetic energy equation:

$$\frac{\partial \alpha_k \rho_k k_k}{\partial t} + \nabla \cdot \alpha_k \rho_k \mathbf{v}_k k_k = \nabla \cdot \alpha_k \left(\mu_k + \frac{\mu_k^t}{\sigma_k} \right) \nabla k_k + \alpha_k P_k + \alpha_k P_{B,k} - \alpha_k \rho_k \varepsilon_k + \sum_{l=1, l\neq k}^{n} \mathrm{K}_{kl} + k_k \sum_{l=1, l\neq k}^{n} \Gamma_{kl} \tag{5}$$

Turbulence energy dissipation equation:

$$\frac{\partial \alpha_k \rho_k \varepsilon_k}{\partial t} + \nabla \cdot \alpha_k \rho_k \mathbf{v}_k \varepsilon_k = \nabla \cdot \alpha_k \left(\mu_k + \frac{\mu_k^t}{\sigma_\varepsilon} \right) \nabla \varepsilon_k + \sum_{l=1, l\neq k}^{n} D_{TED,kl} + \varepsilon_k \sum_{l=1, l\neq k}^{n} \Gamma_{kl} + \alpha_k C_1 P_k \frac{\varepsilon_k}{k_k} - \alpha_k C_2 \rho_k \frac{\varepsilon_k^2}{k_k} + \alpha_k C_3 \max(P_{B,k}, 0) \frac{\varepsilon_k}{k_k} - \alpha_k C_4 \rho_k \varepsilon_k \nabla \cdot \mathbf{v}_k \tag{6}$$

Two-Stage Approach. In this approach the calculation procedure is split into the following steps:

- calculation of cavitating nozzle flow with the two-fluid model
- calculation of the initial droplet distribution from a primary breakup model
- calculation of spray propagation with the Lagrangian discrete droplet model

The results from the nozzle flow calculations used by the breakup model are the local distributions of flow field variables in the

Downloaded 02 Jun 2010 to 171.66.16.98. Redistribution subject to ASME license or copyright; see http://www.asme.org/terms/Terms_Use.cfm

Table 2 Interfacial exchange models for cavitating nozzle flow (*n*=2)

Interfacial mass exchange

$$\Gamma_{12} = \frac{N'''}{C_R}\frac{\partial m_{\text{bub}}}{\partial t} = \rho_1 \frac{N'''}{C_R} 4\pi R_{\text{bub}}^2 \frac{\partial R_{\text{bub}}}{\partial t} \tag{7}$$

Simplified Rayleigh equation

$$\frac{dR_{\text{bub}}}{dt} = \text{sgn}(\Delta p)\sqrt{\frac{2\Delta p}{3\rho_2}} \quad \text{with}$$

$$\Delta p = p_{\text{sat}} - p + p_E \quad \text{and} \quad p_E = C_E \frac{2}{3}\rho_2 k_2 \tag{8}$$

Bubble radius

$$R_{\text{bub}} = \sqrt[3]{\frac{3\alpha_1}{4\pi N'''}} \quad \text{with} \quad N''' = N'''(\alpha) \tag{9}$$

Drag force

$$\mathbf{M}_{D,12} = c_D \frac{3\alpha_1\rho_2}{8R_{\text{bub}}}|\mathbf{v}_2 - \mathbf{v}_1|(\mathbf{v}_2 - \mathbf{v}_1) \tag{10}$$

Turbulent dispersion force

$$\mathbf{M}_{T,12} = C_{T,12}\rho_2 k_2 \nabla \alpha_1 \tag{11}$$

nozzle orifice. This introduces effects of nozzle flow turbulence and partial vapor formation into the breakup model.

Cavitation Model. In the two-stage approach, cavitation is treated using the two-fluid model with a continuous liquid and a dispersed vapor phase. Interfacial momentum exchange inludes drag as well as turbulent dispersion force. Drag is based on a single bubble drag formulation averaged over the ensemble. Turbulent dispersion relates bubble diffusion to the continuous phase turbulence kinetic energy and dispersed phase volume fraction gradient. Mass interfacial exchange is calculated from the rate of change of total vapor bubble mass due to evaporation or condensation. Bubble number density N''' is modeled using a simple correlation describing decay of number density with increasing volume fraction due to bubble coalescence or film formation. The cavitation model is based on the linearized Rayleigh-Plesset equation [18]. This process is driven by the pressure difference between the hydrodynamic and vapor pressures. An additional correction term for turbulent pressure fluctuations p_E is taken into account. The factor C_R in the mass interfacial exchange term allows the delay for the onset of re-condensation (or bubble collapse) of the generated vapor. It is set equal to 1 for evaporation and greater than 1 for condensation. This parameter reflects the fact that subcooled vapor may exist for some time in a nonequilibrium state. It is presently used as a tuning parameter and needs additional modeling in future work. The summary of the equations used is given in Table 2.

Figure 1 shows a representative picture of flow properties in the nozzle orifice cross section calculated from the two-fluid model. Large differences across the cross section can be observed in volume fraction and velocity distributions. These are expected to affect the breakup behavior and spray penetration either via the primary breakup model or via the locally changing boundary conditions for the DDM.

Primary Breakup Model. Nozzle flow data calculated with the two-fluid model are introduced into the breakup model on a polar auxiliary grid in the orifice cross section, which allows determining the desired resolution. On this auxiliary grid the breakup model of Bianchi and Pelloni [22] is applied locally. The model assumes that the turbulent fluctuations within the jet generate initial perturbations on the jet surface. These grow under the action of aerodynamic pressure forces until they detach as atomized droplets.

Using the local flow field data on the auxiliary grid the turbulent length scale is used to determine the atomization length scale

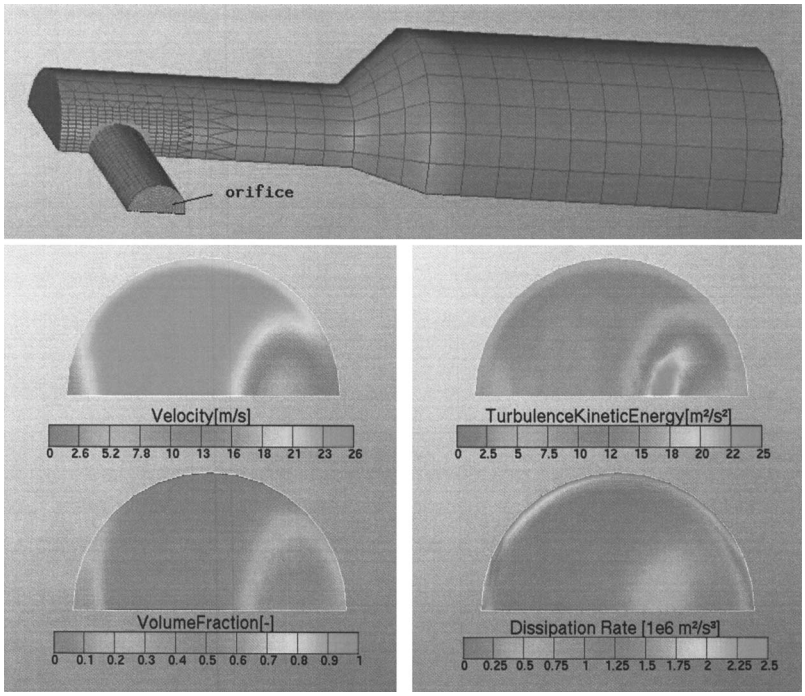

Fig. 1 Asymmetric distribution of flow properties in the nozzle orifice. Liquid phase velocity, vapor volume fraction, liquid phase turbulence kinetic energy (TKE), and turbulence energy dissipation (TED) for Chalmers case 4.

Downloaded 02 Jun 2010 to 171.66.16.98. Redistribution subject to ASME license or copyright; see http://www.asme.org/terms/Terms_Use.cfm

Table 3 Breakup model

Length scale	$L_A = C_2 C_\mu \frac{k^{1.5}}{\varepsilon}$	(11′)	Drop size: $R_{\text{drop}} = L_A/2$	(12)
Time scales	Turbulent: $\tau_T = C_\mu \frac{k}{\varepsilon}$	(13)	Aerodynamic: $\tau_W = L_W \left[\frac{\rho_g \rho_2 \nu_2^2}{(\rho_2 + \rho_g)^2} - \frac{\sigma}{(\rho_2 + \rho_g) L_W} \right]^{-0.5}$ with $L_W = 2 C_2 L_T$	(14)
Mixed time scale	$\tau_A = C_1 \tau_T + C_4 \tau_W$			(15)
Detachment velocity	Turbulent: $\nu_{\text{drop}} = \frac{L_A}{\tau_T} = \frac{C_2}{C_1} k^{0.5}$	(16)	Aerodynamic: $\nu_{\text{drop}} = \frac{L_A}{\tau_W} \sim u_{\text{inj}}$	(17)
Breakup rate	$\frac{dR_{\text{core}}}{dt} = \frac{L_A}{\tau_A}$	(18)	Erosion rate: $\frac{dR_{\text{core}}}{dz} = -\frac{1}{v_2} \overline{\left(\frac{L_A}{\tau_A} \right)}$	(19)

and also the droplet size. For the breakup time scale a hybrid value calculated from a weighted mean of turbulent and aerodynamic time scales is used. The aerodynamic time scale is calculated assuming breakup due to Kelvin-Helmholtz instability at the liquid interface. From the atomization length and time scales the local breakup rate is calculated according to the set of equations in Table 3. Droplet size depends on the local values of turbulent kinetic energy and turbulent energy dissipation. The initial droplet velocity is estimated from the ratio of the characteristic atomization length scale and the breakup time scale. Droplet detachment velocity in the limit of pure turbulent or pure aerodynamic conditions is also given in Table 3.

In order to determine the release positions of droplets approximate shape of the coherent liquid core is calculated using a 1D mass balance for slices of the liquid jet perpendicular to the direction of injection. For simplification, an averaging of the breakup rates is done along the perimeter of ring sections on the auxiliary grid. Using the average breakup rate the radial erosion of the liquid jet is determined and from it the coherent core length is calculated. To introduce the 2D structure of the flow the orifice data is projected to the core surface and the breakup model is applied locally at the corresponding surface elements. The cell

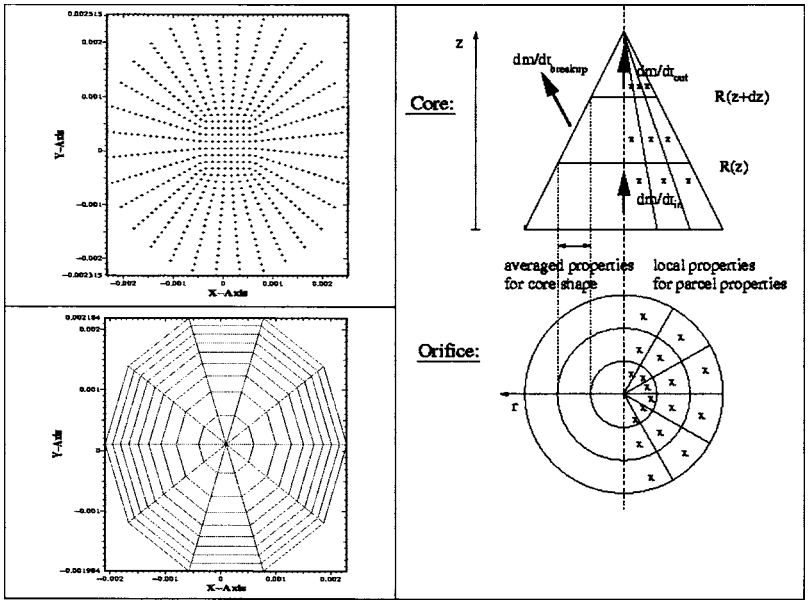

Fig. 2 Nozzle flow calculation grid and auxiliary grid as well as sketch of projection method to determine parcel release positions

Downloaded 02 Jun 2010 to 171.66.16.98. Redistribution subject to ASME license or copyright; see http://www.asme.org/terms/Terms_Use.cfm

Table 4 Numbering of phases used in coupled calculations

Phase number	1	$2,\ldots,(n-2)$	$n-1$	n
Component	gas	droplets	continuous liquid	vapor

centers of the auxiliary grid projected onto the core surface define the release positions for the initial droplet parcels. Figure 2 shows the transition from the nozzle flow grid to the auxiliary grid and a sketch of the projection procedure from orifice to the core surface elements. The nozzle flow is typically resolved in the orifice cross section by 500 to 1000 cells, while the polar auxiliary grid uses typically about 100 cells. This reduces calculation time for the primary breakup model. In addition, the auxiliary polar grid has been calculated with all cell faces having equal area. Thus, a homogeneous resolution is guaranteed by equal weighting of the flow conditions in the subsequent calculation of the DDM parcels from the primary breakup model. In the presented calculations the resolution is fixed within a single calculation. As the flow changes, the flow field conditions are mapped back to the detachment positions and re-enter the aerodynamic part of the breakup model.

Finally, the model delivers the initial droplet size and velocity distributions at the liquid core surface as well as the initial spray angle needed for the initialization of the representative droplet parcels within the discrete droplet model.

Liquid Core Turbulence and Bubble Dynamics Models. Vapor formation from upstream cavitation in the injection nozzle affects the flow and turbulence fields. The disturbances from collapsing vapor bubbles increase the turbulence level in the liquid and modify turbulent length and time scales, which are decisive for the breakup model. Similarly as in Ref. [1] these effects are treated as the source terms in the 1D k-ε turbulence model coupled with the Rayleigh-Plesset equation governing bubble dynamics. Additional coupling terms are a mass transfer term, which may damp or enforce bubble dynamics and a pressure correction p_E accounting for turbulent pressure fluctuations. The physical idea behind this term is that local turbulent fluctuations may cause an additional pressure drop below mean flow pressure, which enhances cavitation. Details of the model are given in Ref. [2].

Spray Propagation Model. Spray propagation is calculated using the classical Lagrangian parcel method. However, the parcels are no longer released in the orifice cross section, but on the liquid core surface. Thus, the initial size of the parcel droplets is not chosen equal to the nozzle diameter as it is usually done within the so-called blob-injection method. Moreover, the parcels start already with smaller diameters as determined from the primary breakup model described above. Since the work focuses on understanding of the primary breakup close to the nozzle orifice, no secondary breakup mechanism has been activated. It is expected that under the given low pressure and low velocity conditions secondary breakup might become relevant further downstream, if at all. The collision model has been also deactivated. Turbulent dispersion and drag model as well as evaporation have been activated. But, due to cold conditions practically no evaporation occurs.

Coupled Approach. An alternative to the two-stage approach is a more comprehensive calculation method for coupled injector flow and spray. In this approach both regions are treated with the multi-fluid model where different interfacial exchange terms are applied in the spray and cavitation regions.

The spray region is represented by multiple liquid phases: a bulk liquid phase representing the liquid jet leaving the injection hole and disintegrating into a number of separate dispersed droplet phases. Furthermore, there is a gas phase for the ambient medium as well as a vapor phase, which covers the vapor entering the spray region from the nozzle and also the fuel vapor produced in the spray region from the droplet evaporation. The assignment of phase numbers and phase content is given in Table 4. Test cases with up to seven phases will be shown below.

At the present state the drag force between gas or vapor and droplet phases takes into account effects of the bubble Reynolds number and volume fraction as well as deformation of the droplets. Other momentum exchange terms implemented cover Saffman force, which is due to shearing action of the gas flow on the droplets, and Magnus force from rotational motion of the droplets. This is modeled by averaging the single drop lift force to obtain the overall lift force on droplets in the two-fluid frame (see Ref. [27]). Turbulent dispersion force is modeled using the same approach as in the cavitation model with a constant turbulent dispersion coefficient C_T.

Table 5 Interfacial exchange models for the spray region

Mass exchange

Generation of droplet phases from the liquid phase:

$$\Gamma_{n-1,k} = \frac{3\dot{M}_{n-1}\alpha_{n-1}}{(n-3)R_{n-1}} \quad \text{with} \quad k = 2,\ldots,n-2 \tag{20}$$

Losses of bulk liquid phase with volume fraction α_{n-1}:

$$\sum_{k=2}^{n-2} \Gamma_{k,n-1} = -\frac{3\dot{M}_{n-1}\alpha_{n-1}}{R_{n-1}} \tag{21}$$

Drag force

$$\mathbf{M}_{D,1k} = C_D \frac{3\alpha_k \rho_1}{8R_k} |\mathbf{v}_k - \mathbf{v}_1|(\mathbf{v}_k - \mathbf{v}_1) = -\mathbf{M}_{D,k1} \tag{22}$$

$$C_D = \frac{24}{\mathrm{Re}_k}\left[(\alpha_1 + \alpha_n)^{-2.65} + \frac{\mathrm{Re}_k^{0.66}}{6}(\alpha_1 + \alpha_n)^{-1.78}\right] + C_{D,\mathrm{def}} \tag{23}$$

Turbulence dispersion force

$$\mathbf{M}_{T,1k} = C_{T,1k}\rho_1 k_1 \nabla \alpha_k = -M_{T,k1} \quad \text{with} \quad C_{T,k} \approx 0.1\text{–}1 \tag{24}$$

Downloaded 02 Jun 2010 to 171.66.16.98. Redistribution subject to ASME license or copyright; see http://www.asme.org/terms/Terms_Use.cfm

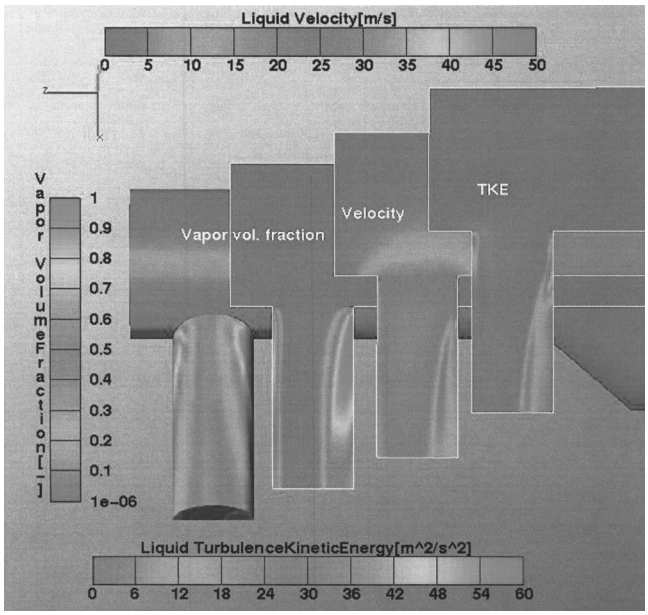

Fig. 3 Basic features of cavitating nozzle flow simulation for conditions taken from Chalmers case 4

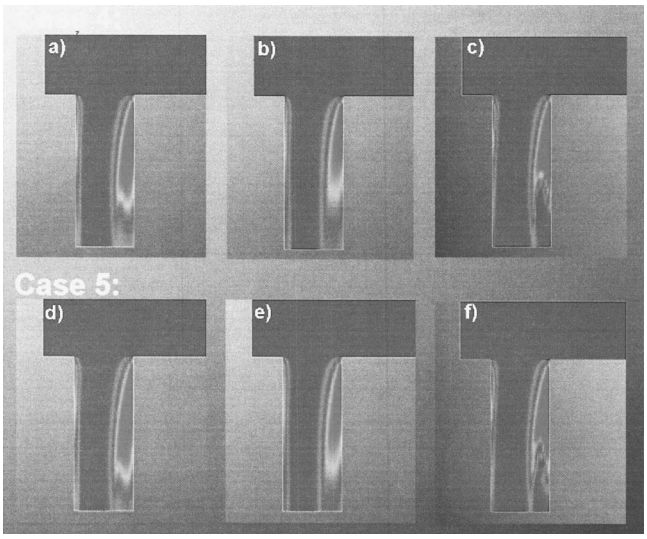

Fig. 5 Sensitivity of cavitation mass exchange model with respect to condensation reduction and turbulent pressure correction. Upper row: injection pressure 0.185 MPa, lower row: injection pressure 0.2 MPa. (*a*) and (*d*): reference case; (*b*) and (*e*): increased condensation reduction parameter; (*c*) and (*f*): activation of turbulent pressure correction (with C_E=1).

Primary breakup is treated as a special source term in the spray region, which causes mass transfer from the bulk liquid phase to the droplet phases. Currently, the breakup rate is kept constant or parametrically coupled with the injection velocity. The calculation of the breakup rate based on the Bianchi and Pelloni model is planned in the future. Nevertheless, the model already allows improved understanding of the basic features of the breakup and spray formation processes as will be shown in the results section.

The additional interfacial exchange terms in the spray region are summarized in Table 5.

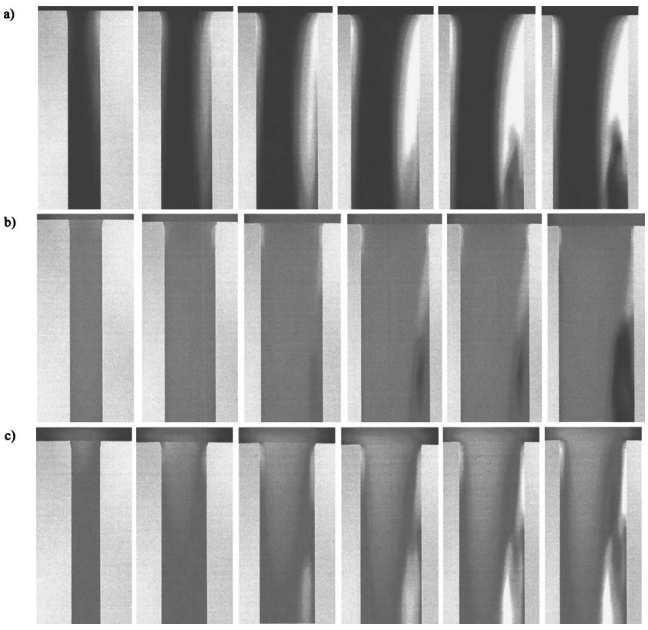

Fig. 4 Spatial structure of cavitating nozzle flow inside the injection hole. (*a*) vapor volume fraction (white: vapor; black: liquid), (*b*) liquid velocity (light colored: high; dark: low values), (*c*) liquid turbulent kinetic energy (light colored: high; dark: low values).

Preliminary Model Results

Results From the Two-Stage Approach

Basic Results of Cavitating Nozzle Flow. The calculations described below have been performed for the Chalmers model nozzle shown in Fig. 1. This nozzle has a single injection hole with about 5 mm diameter and 13 mm length. It is operated with water at pressure differences between 0.1 and 0.2 MPa. The injection hole is connected to the feed tube under an angle of 90 deg. The grid covers about 6 cm of the feed tube length and has about 10,000 cells. Near the entry into the injection hole multiple mesh refinements have been performed. Further, the connection to the feed tube is done via the arbitrary interface.

Basic features of the cavitating nozzle flow are shown in Fig. 3. It is clearly shown that cavitation occurs at the entrance region of the injection hole. A larger cavitation region is established on the right-hand side where the pressure drop from flow deflection and the acceleration are most pronounced. Vapor content is reduced again towards the orifice due to the pressure recovery that causes condensation. Liquid phase velocity distribution shows acceleration inside the nozzle and also vortex formation inside the water-vapor mixture region close to the orifice. In principle, flow recirculation at the nozzle outlet is possible. However, this may cause problems with the determination of the true boundary conditions for the spray region. Liquid turbulent kinetic energy also increases in shear layers at the boundary of the two vapor rich regions.

Figure 4 shows some results on the three-dimensional structure of the cavitating nozzle flow along the different cuts through the injection hole in the y direction. The cavitation region appears as a tube shaped structure on the right-hand side of the injection nozzle. Due to symmetry reasons there are two of these tubes. The more complicated fissured shape of the vapor region compared to Fig. 3 is due to the pressure correction, p_E, accounting for the pressure fluctuations causing enhanced vapor production in regions with high turbulence kinetic energy.

Figure 5 shows a sensitivity study for two of the model parameters at different injection pressure values (Chalmers cases 4 and 5, see Table 6). As compared with the reference cases given in pictures (*a*) and (*d*), pictures (*b*) and (*e*) show the effects of an increased condensation reduction parameter C_R. This finally yields an increase of the vapor volume fraction in the orifice. The right-

Downloaded 02 Jun 2010 to 171.66.16.98. Redistribution subject to ASME license or copyright; see http://www.asme.org/terms/Terms_Use.cfm

Table 6 Experimental conditions and inlet boundary conditions

Case	Δp (MPa)	Re	Cavitation number	Calculated outlet velocity (m/s)	Calculated inlet velocity (m/s)
1	0.100	55,860	1.00	14.1	0.88
2	0.120	61,250	1.20	15.5	0.97
3	0.150	68,600	1.50	17.3	1.08
4	0.185	75,460	1.85	19.2	1.20
5	0.210	78,890	2.10	20.5	1.28

hand side column shows turbulence effects on the cavitation structure by the turbulent pressure correction term, p_E. If the different inlet pressures in the upper and lower row are compared, an increased extent of the cavitation region is observed for all cases as expected.

Basic Results of Primary Breakup and Spray Calculation. Typical shape of the spray, droplet size distributions, and velocity field produced by applying the primary breakup model are shown in Figs. 6 and 7. The parameters of the breakup model have been matched to fit the experimental data of the Chalmers case 5. The selected values for the model parameters were $C_1=24$, $C_2=4$, $C_\mu=0.09$, and $C_4=0.01$. This means that turbulent effects are dominant under the given low velocity conditions. Figure 6 shows the spray front view, which is in the direction of the feed pipe, from which cavitation region appears symmetric. In this direction the spray shape is also symmetric. However, in the perpendicular direction there is a pronounced asymmetry of the spray. There is a much greater spray angle on the side with stronger cavitation. Furthermore, the biggest drops as well as the droplets with highest velocities are found on the side with less cavitation.

Results From the Coupled Approach. For the purpose of basic testing, the coupled model has been applied to a simplified single-hole Diesel injection nozzle with a flow direction of the Diesel equal to the direction of injection. No flow asymmetry is expected and a sector of the nozzle with a cake-shaped cross section has been used. Calculation domain has about 1200 cells in the nozzle region and about 800 cells in the spray region below. Test calculations have been performed with seven phases. Four droplet size classes with droplet diameters of 10, 25, 50, and 80 μm were used in the spray region as well as gas, vapor, and continuous liquid. Current selection of the number of spray phases is somewhat arbitrary. Their number is sufficient for basic testing, but appears to be insufficient if a detailed resolution of the spray is desired. However, no systematic parametric study on the number of phases has been performed yet.

Figure 8 shows volume fraction distributions for the phases in case of 50-MPa injection pressure into a gaseous atmosphere at 2 MPa. The nozzle diameter is 0.2 mm. Figures 8(*a*) and 8(*b*) show the continuous liquid phase with decay of volume fraction near the wall inside the nozzle due to cavitation and decay outside the

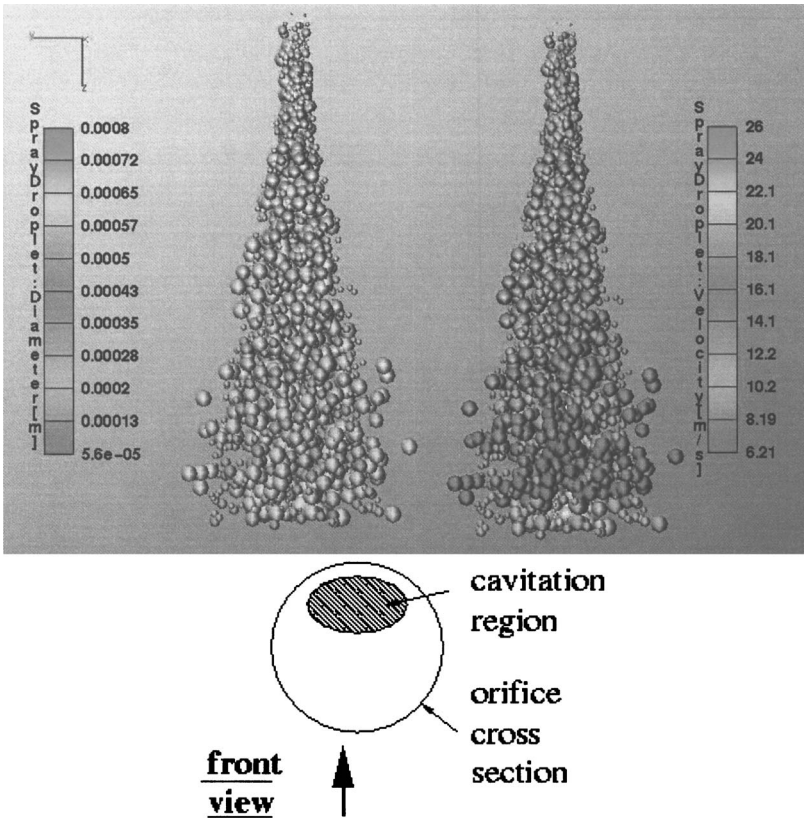

Fig. 6 Spray shape, droplet sizes, and velocities for Chalmers case 5 (front view)

Downloaded 02 Jun 2010 to 171.66.16.98. Redistribution subject to ASME license or copyright; see http://www.asme.org/terms/Terms_Use.cfm

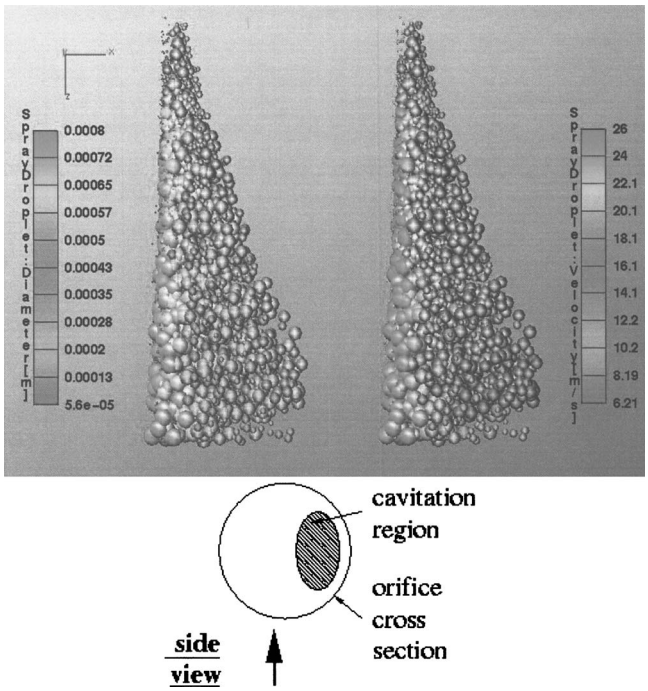

Fig. 7 Spray shape, droplet sizes, and velocities for Chalmers case 5 (side view)

nozzle due to the primary breakup. Currently, a simplified model with locally homogeneous breakup rate and equal mass distribution into the different droplet classes is used. Figure 8(*c*) shows the resulting spray formation with larger droplets penetrating somewhat deeper than the smaller ones. For comparison with the experimental data the total volume fraction of all spray droplet phases has to be used which is also depicted in Fig. 8(*c*).

Model Validation Against the Experimental Data

The cavitation structure and its influence on the spray pattern has been investigated at Chalmers University in a transparent nozzle having a hole perpendicular to the nozzle axis using a high-speed camera and stroboscopic visualization. These experiments have been done using a scaled-up injector model with approximately 5-mm injection nozzle diameter operated with water at Reynolds numbers between 55,000 and 80,000. The experimental conditions as well as the inlet boundary conditions used in the calculations are given in Table 6. The definition of the cavitation number used in the table is $C_N=(p_{\text{injection}}-p_{\text{back}})/(p_{\text{back}}-p_{\text{vapor}})$. The experimental findings are summarized in Fig. 9.

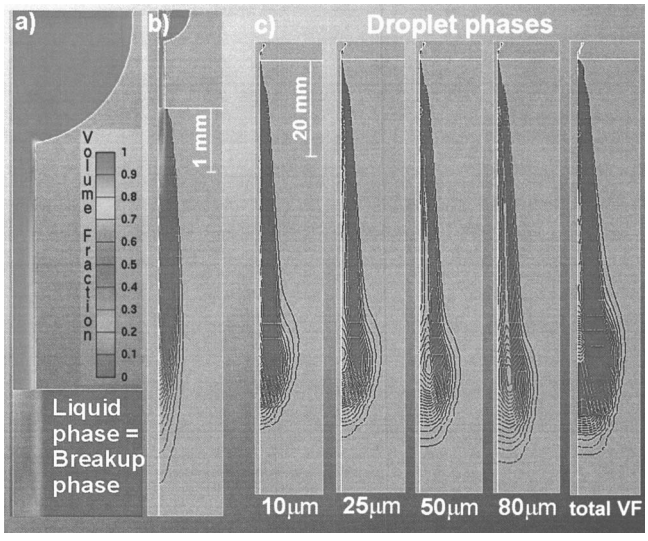

Fig. 8 Phase volume fractions in nozzle and spray region for Diesel injection. (*a*) continuous liquid phase with cavitation near the wall, (*b*) breakup of continuous liquid phase, (*c*) dispersed droplet phases and total spray droplet volume fraction.

Results From the Two-Stage Approach. When the numerical results are compared to the experimental data it has to be considered that the photographs taken from the experimental setup show the cavitation through the entire nozzle cross section. In contrast, the results of the numerical analysis always cover only a certain layer. To obtain comparable figures, the results at different cuts have to be superimposed. This is shown in Fig. 10 where surface values as well as several cuts for the vapor volume fraction are depicted together with the reconstruction of the superimposed view. However, in all the comparisons only single cuts have been used. Thus, the total vapor volume fraction from the calculation is expected to be somewhat larger.

Cavitation as well as the primary breakup models have been optimized for case 5, which shows the most pronounced asymmetric effects. The following experimental pressure variations have been calculated with unchanged parameter settings. The results of these calculations for the spray are shown in Fig. 11. These results clearly agree with the experimental trend of the increasing asymmetry for the spray angle with the increasing injection pressure.

The calculated results for cavitation and spray together with the corresponding experimental cases are shown in Figs. 12–16. For cavitation as well as for spray formation the results show same trends as the experimental observations. Cavitation amount increases with the increasing injection pressure. The shape of the cavitation region is asymmetric with more vapor generated at the right-hand side of the nozzle. In good agreement with the experiment is also the appearance of vapor phase at the outlet in cases 4 and 5.

More detailed observations of the cavitation phenomena show that the cavitation regions in numerical analyses of cases 1 and 2 are larger than in the experiments, while in cases 3, 4, and 5, with higher inlet pressures there seems to be more vapor generated in the experiments. This is also the case if various cuts are superimposed over each other. It has to be noted that there are also temporal fluctuations in the experimental data that can be observed in the collected movies. Here is shown only the qualitative comparison between the calculated results and single snapshots from the experiments. The agreement between the calculations and measurements is consistent for other snapshots and therefore the presented is an adequate comparison with the experimental data.

The spray pictures taken from the calculations close to the nozzle orifice always show a thinned region below the nozzle. This is due to the liquid core calculated within the primary breakup model. In this region there are no droplets yet. This is indicated by a triangle in the pictures. With respect to the spray formation there is also basic agreement with the trend of increased asymmetric spray angle with increasing amount of cavitation. Spray angles seem to be somewhat underestimated for all cases. Nevertheless, the overall agreement confirms the need to use local information from the nozzle flow for better understanding and predictive simulation of primary breakup and initial spray formation. The justification for applying the model also to diesel nozzle conditions is given by recent experimental work of Blessing et al. [11]. They show the characteristic asymmetry and deviation of spray axis towards the region of most pronounced cavitation also for real size diesel sprays generated from transparent multi-hole nozzles under typical operating conditions. The experiment confirms the importance of the turbulence driven breakup mechanism for the real size diesel injectors.

Downloaded 02 Jun 2010 to 171.66.16.98. Redistribution subject to ASME license or copyright; see http://www.asme.org/terms/Terms_Use.cfm

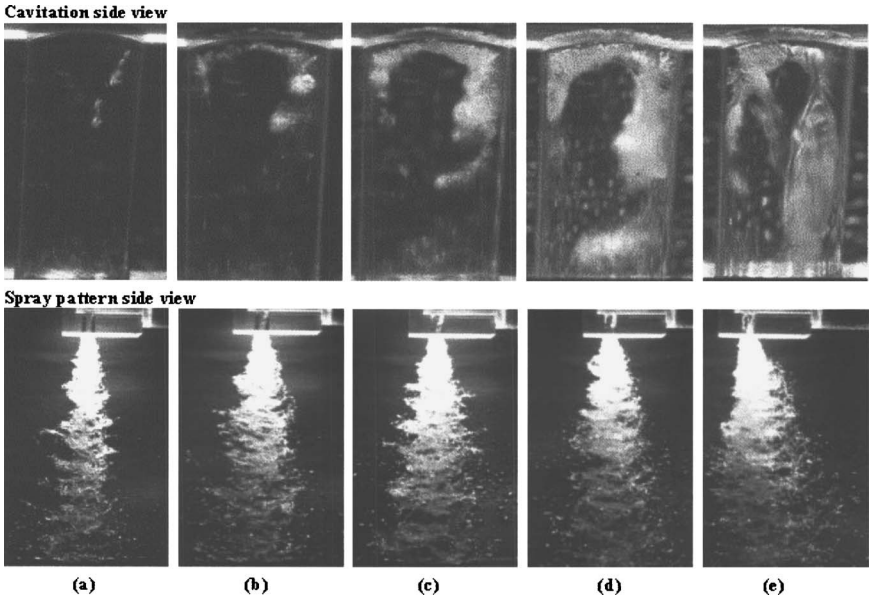

Fig. 9 The dispersion of the spray under different cavitating conditions. The bright regions show the location of vapor. Shown are snapshots from cases 1 to 5, denoted here by letters (*a*)–(*e*) in the upper row the enlarged view of the cavitating flow inside the nozzle hole is shown (diameter 5 mm). The second row shows the injector flow and spray together.

Results From the Coupled Approach. The coupled simulation method has also been applied to the Chalmers experiments. For these calculations the spray region upstream the nozzle orifice has been discretized with about 5000 additional cells. The calculations have been performed with five phases. These are the continuous liquid and vapor phases inside both the nozzle and spray regions, as well as two additional droplet phases and a continuous gas phase within the spray region. Mass transfer in the spray region is due to the primary breakup with locally homogeneous rate. Interfacial momentum exchange includes drag and turbulent dispersion. According to the large droplet sizes the latter is of minor importance.

The coupled method of calculating nozzle flow and spray formation based on the Eulerian multi-fluid approach has been used in this paper for the first time. The intention is to show both the capability and the potential of this new approach, which yields a closer and more complete coupling between the flow regimes. For this purpose the simple assumptions of constant breakup rate and use of only two size classes for the dispersed droplet phases have been applied. Results for the phase volume fraction distribution are given in Fig. 17 for the Chalmers case 4. On the left-hand side the continuous liquid phase distribution is depicted near the nozzle orifice. As in the calculations for the flow shown above, an asymmetric distribution of the cavitation region is visible inside the nozzle. After departure from the nozzle the continuous liquid phase rapidly decays into the two droplet phases shown beside. There is a slight deflection of the whole liquid jet detectable from the continuous liquid phase picture. The droplet phase volume fractions again show the asymmetric spray shape, as observed in the experiments. For better comparison with the experimental data all the liquid phase volume fractions are added up and depicted together with a contour of the experimental snapshots from case 4. This picture confirms the basic agreement with the most relevant experimental features.

It is remarkable that even without a detailed breakup model the asymmetric spray shape is predicted. This asymmetry follows from the general asymmetry of the nozzle flow, although not to

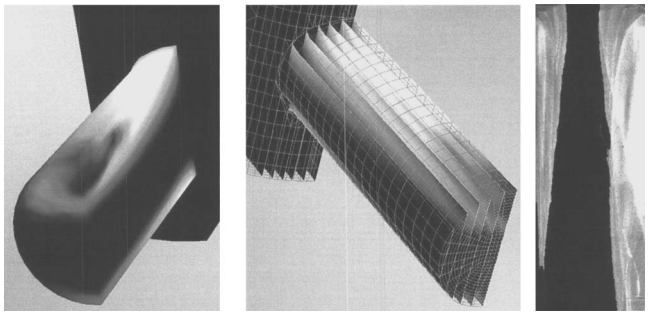

Fig. 10 Distribution of vapor volume fraction inside the injection hole (white: pure vapor; black: pure liquid)

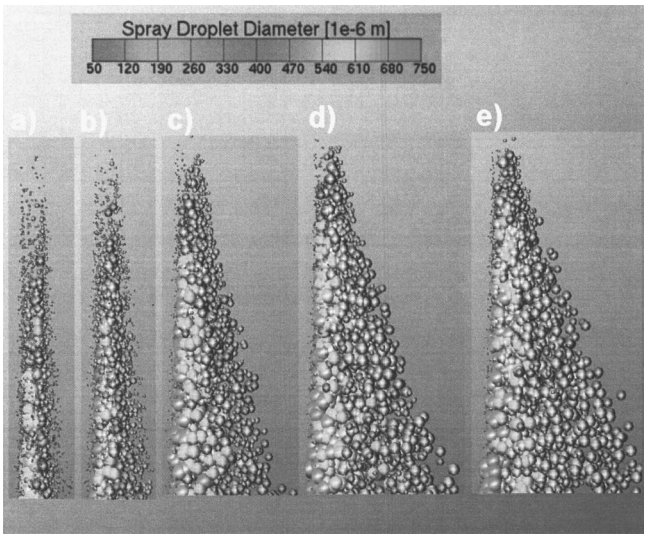

Fig. 11 Spray shape calculated for Chalmers experiments with increasing pressure. Pictures (*a*)–(*e*) corresponding to experimental cases 1–5

Downloaded 02 Jun 2010 to 171.66.16.98. Redistribution subject to ASME license or copyright; see http://www.asme.org/terms/Terms_Use.cfm

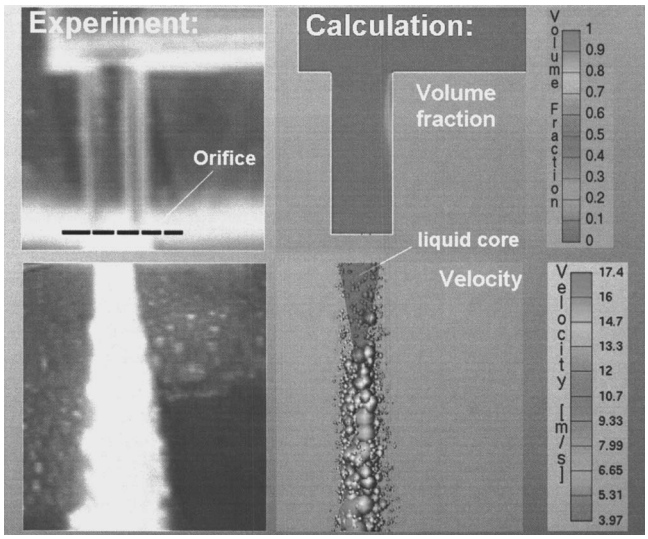

Fig. 12 Nozzle flow and spray for case 1 at Δp=0.1 MPa

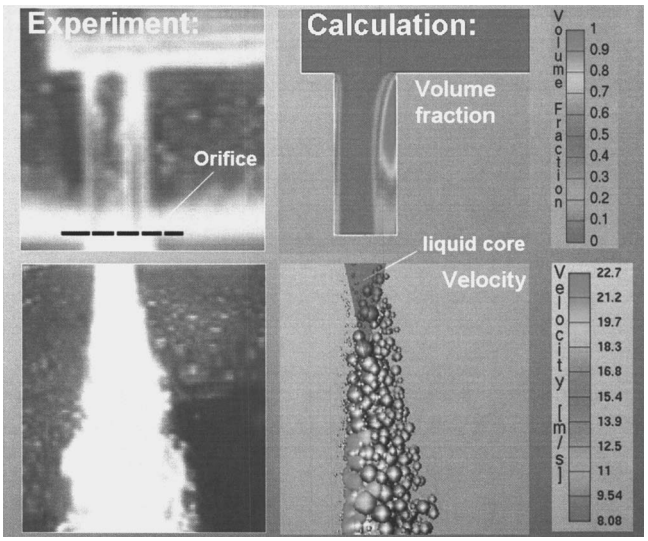

Fig. 14 Nozzle flow and spray for case 3 at Δp=0.15 MPa

full extent. This can be explained by the partly rotational flow around and towards the vapor region contracting further towards the orifice, which is shown in Fig. 18. A smaller amount of continuous liquid trapped between the vapor tube and nozzle wall achieves perceptible radial and circumferential velocity components, which are also convected into the spray region and transferred to the generated spray droplets. In addition, better mixing and more complete momentum transfer in the already premixed regions downstream the cavitation zone may contribute to the stronger widening of the spray on this side. Additional effects are expected from the asymmetries introduced by the application of the more elaborate primary breakup model described above. It can be concluded that both effects—nozzle flow structure and primary breakup model—are needed to explain the experimental findings. Thus, the presented model proves to be a valuable tool for the basic understanding of the spray propagation and mixture formation related to the cavitating nozzle flows.

At the present development status of the two models, both approaches show the same basic features. The coupled model has been applied using the simplified primary breakup model and thus underestimates the quantitative extension of the spray contour. However, the curvature of the spray contour is predicted in a more realistic way. It appears that the coupled approach is superior to the two-stage method when detailed resolution of the flow features is desired. On the other hand, the two-stage approach is more flexible and needs less computational time. In this case, the nozzle flow data from a single injector flow calculation can be easily applied to various spray calculations in different combustion chambers.

Summary

A new simulation methodology for the spray formation based on detailed analysis of cavitating nozzle flow and application of an advanced primary breakup model has been developed. The described model has been implemented into the AVL FIRE computational fluid dynamics (CFD) code which was also used in all the calculations. Two approaches are presented and validated using experimental data obtained at Chalmers University. The multifluid simulation approach yields detailed information on flow structure inside the injection hole. This is linked to spray formation using a primary breakup model applied on a local subgrid in the nozzle orifice. The model yields the release of droplet parcels from the liquid core. The initial size and velocity distributions as

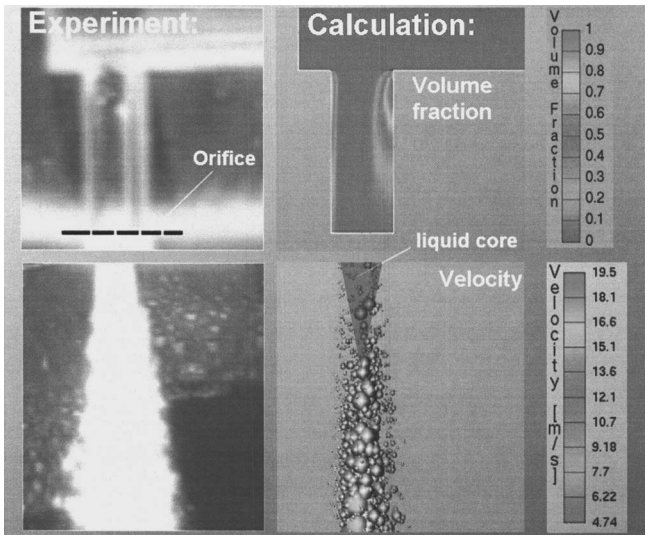

Fig. 13 Nozzle flow and spray for case 2 at Δp=0.12 MPa

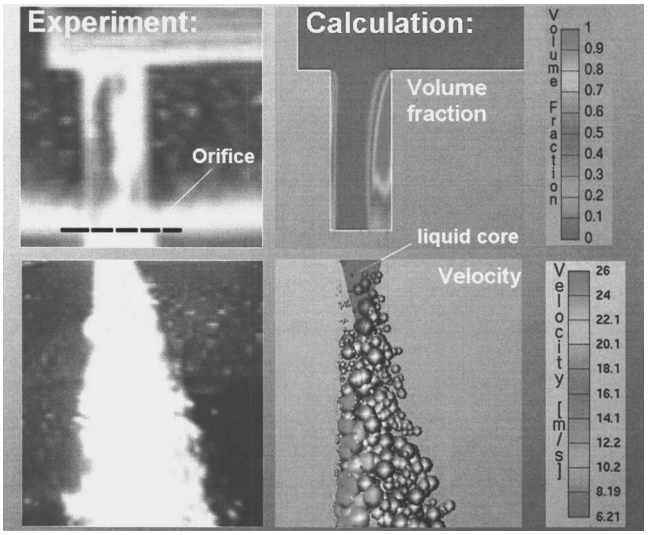

Fig. 15 Nozzle flow and spray for case 4 at Δp=0.185 MPa

Downloaded 02 Jun 2010 to 171.66.16.98. Redistribution subject to ASME license or copyright; see http://www.asme.org/terms/Terms_Use.cfm

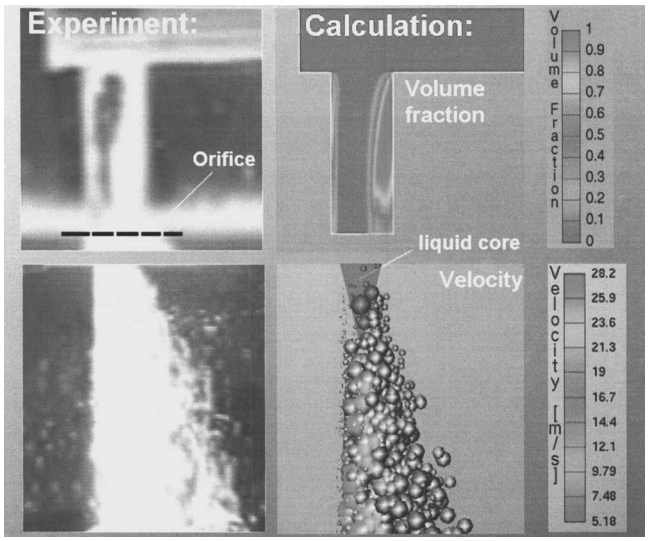

Fig. 16 Nozzle flow and spray for case 5 at Δp=0.21 MPa

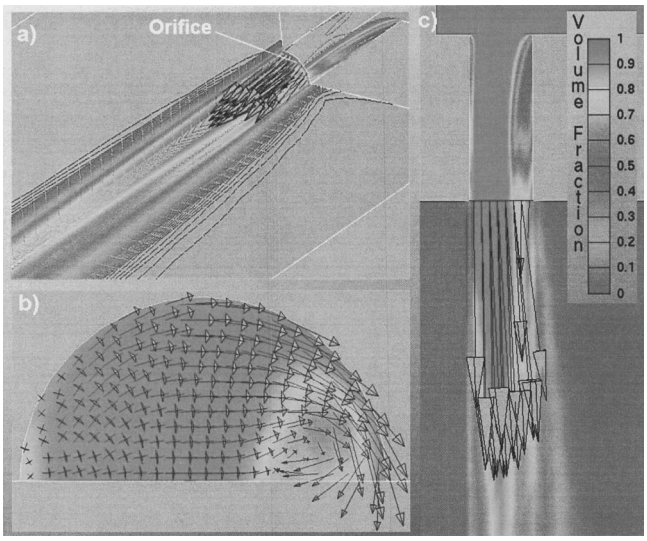

Fig. 18 Total liquid volume fraction and continuous liquid phase velocity vectors in the orifice plane: (*a*) side view; (*b*) cut through orifice plane; (*c*) cut through symmetry plane of the injection hole

well as the initial breakup angle is calculated from the turbulent kinetic energy and turbulent energy dissipation in the nozzle orifice. This methodology is applied in two separate calculations using the Lagrangian DDM for the spray simulation. A more comprehensive simulation method based on the multi-fluid fully coupled approach is also presented with promising results.

The most characteristic feature of the models is the prediction of the asymmetric cavitation region and spray shape. This is in agreement with the experimental data from Chalmers University. Inhomogeneous distribution of droplet properties within the spray cone is predicted as well. The comparison between the calculations and the experimental data show that the characteristic features observed in the experiments are predicted by the simulations. Furthermore, it has been demonstrated that basic understanding and evaluation of the decisive processes governing spray formation is improved using three-dimensional multi-phase flow analysis. Thus, the model can explain spray behavior in the nozzle proximity in more detail than the previous models and will support better understanding and optimization of mixture formation.

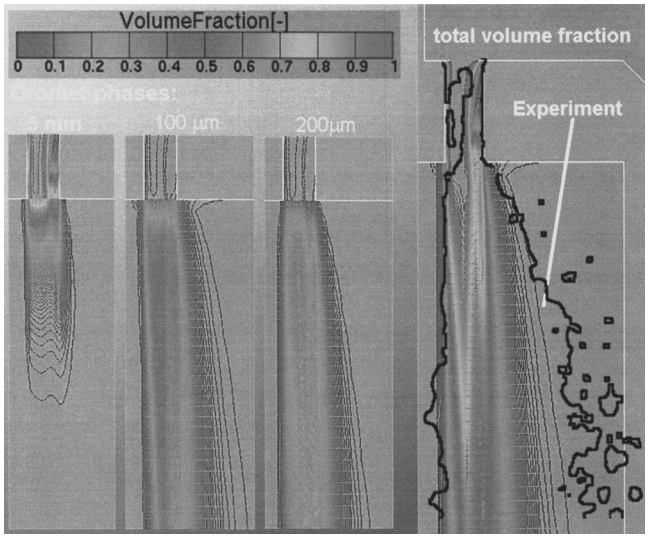

Fig. 17 Phase volume fraction distributions from coupled calculation with the multi-fluid model for Chalmers case 4

Acknowledgment

This study is partly based on European projects supporting development of multi-phase spray modeling as well as simulation of primary fuel jet breakup. The authors would like to acknowledge this support.

Nomenclature

C_E = Egler pressure coefficient
C_D = drag coefficient
C_N = cavitation number
C_R = condensation reduction factor
C = model parameter with various subscripts
D = turbulence dissipation interfacial exchange
$\mathbf{g}$ = gravitational acceleration
h = enthalpy
H = enthalpy source
k = turbulence kinetic energy
K = turbulence kinetic energy interfacial exchange
L = length scale
m = bubble mass
$\dot{M}$ = breakup rate
$\mathbf{M}$ = momentum interfacial exchange
n = number of phases
N''' = number density
p = pressure
P = turbulence production
R = bubble radius
Re = Reynolds number
$\mathbf{v}$ = velocity
t = time
$\mathbf{T}$ = Reynolds stresses
α_k = volume fraction
Γ = mass exchange
ε = turbulence energy dissipation
μ = dynamic viscosity
ρ = density
$\sigma_{k,\varepsilon}$ = turbulent Prandtl number
$\tau_{A,W,T}$ = time scales
$\boldsymbol{\tau}_k$ = shear stress

Downloaded 02 Jun 2010 to 171.66.16.98. Redistribution subject to ASME license or copyright; see http://www.asme.org/terms/Terms_Use.cfm

Subscripts

1 = vapor or gas
2 = continuous liquid
A = atomization
bub = bubble
E = Egler pressure
g = ambient gas
k = phase index
sat = saturation
T = turbulence
W = aerodynamic

References

[1] Tatschl, R., v. Künsberg Sarre, C., Alajbegovic. A., and Winklhofer, E., 2000, "Diesel Spray Break-Up Modelling Including Multidimensional Cavitation Nozzle Flow Effects," *16th ILASS-Europe Conf.*, Darmstadt, Germany.

[2] v. Berg, E., Alajbegovic, A., Greif, D., Poredos, A., Tatschl, R., and Ganippa, L. C., 2002, "Primary Break-Up Model for Diesel Jets Based on Locally Resolved Flow Field in the Injection Hole," *18th ILASS-Europe Conf.*, Zaragoza, Spain.

[3] Dukowicz, J. K., 1980, "A Particle-Fluid Numerical Model for Liquid Sprays," J. Comput. Phys., **35**, pp. 229–253.

[4] Durst, F., Milojevic, D., and Schönung, B., 1984, "Eulerian and Lagrangian Predictions of Particulate Two-Phase Flows: A Numerical Study," Appl. Math. Model., **4**, pp. 101–115.

[5] Arcoumanis, C., and Gavaises, M., 1998, "Linking Nozzle Flow with Spray Characteristics in a Diesel Fuel Injection System," Atomization Sprays, **8**, pp. 307–347.

[6] Badock, C., 1999, "Analysis of Cavitation Effects on Primary Fuel Jet Break-up Under Diesel Injection Conditions," Ph.D. thesis (in German), TU Darmstadt, Darmstadt, Germany.

[7] MacPhee, A. G., Tate, M. W., Powell, C. F., Yue, Y., Renzi, M. J., Ercan, A., Narayanan, S., Fontes, E., Walther, J., Schaller, J., Gruner, S. M., and Wang, J., 2002, "X-ray Imaging of Shock Waves Generated by High-Pressure Fuel Sprays," Science, **295**, pp. 1261–1263.

[8] Yue, Y., Powell, C. F., Poola, R., Wang, J., and Schaller, J., 2001, "Quantitative measurements of Diesel Fuel Spray Characteristics in the Near-Nozzle Region Using X-Ray Absorption," Atomization Sprays, **11**(4), pp. 471–490.

[9] Roth, H., Gavaises, M., and Arcoumanis, C., 2002, "Cavitation Initiation, Its Development and Link with Flow Turbulence in Diesel Injector Nozzles," SAE paper no. 2002-01-0214.

[10] Ganippa, L. C., Bark, G., Andersson, S., Chomiak, J., 2001, "The Structure of Cavitation and its Effect on the Spray Pattern in a Single-Hole Diesel Nozzle," SAE paper no. 2001-01-2008.

[11] Blessing, M., König, G., Krüger, C., Michels, U., and Schwarz., V., 2003, "Analysis of Flow and Cavitation Phenomena in Diesel Injection Nozzles and its Effects on Spray and Mixture Formation," SAE paper no. 2003-01-1358.

[12] Chen, Y., and Heister, S. D., 1995, "Modelling Hydrodynamic Non-Eqilibrium in Bubbly and Cavitating Flows," ASME J. Fluids Eng., **118**, pp. 172–178.

[13] Schmidt, D. P., Rutland, C. J., and Corradini, M., (1999), "A Fully Compressible Two-Dimensional Model of High Speed Cavitating Nozzle," Atomization Sprays, **9**(3), pp. 255–276.

[14] Yuan, W., and Schnerr, G. H., 2001, "Cavitation in Injection Nozzles—Effect of Injection Pressure Fluctuations," *Proc. of 4th Int. Symposium on Cavitation CAV2001*, Pasadena, CA.

[15] Marcer, R., and LeGouez, J. M., 2001, "Simulation of Unsteady Cavitating Flows in Diesel Injector with an Improved VOF-Method," *17th ILASS-Europe Conf.*, Zurich, Switzerland.

[16] Kameda, M., and Matsumoto, Y., 1996, "Shock Waves in a Liquid Containing Small Gas Bubbles," Phys. Fluids, **8**, pp. 322–335.

[17] Shimada, M., Nozaki, S., Kobayashi, T., and Matsumoto, Y., 1998, "Numerical Study of the Clud Cavitation in a Fuel Injection Pump," SAE paper no. 981023.

[18] Grogger, H., and Alajbegovic, A., 1998, "Calculation of the Cavitating Flow in Venturi Geometries using Two-Fluid Model," *1998 ASME Fluids Engineering Division Summer Meeting*, Washington, D.C., USA

[19] Alajbegovic, A., Grogger, H., and Philipp, H., 1999, "Calculation of the Transient Cavitation in Nozzle Using the Two-Fluid Model," *12th ILASS Conf.*, Indianapolis, IN, USA.

[20] Alajbegovic, A., Meister, G., Greif, D., and Basara, B., 2002, "Three Phase Cavitating Flows in High-Pressure Swirl Injectors," Exp. Therm. Fluid Sci., **26**(6-7), pp. 677–681.

[21] Huh, K. Y., and Gosman, A. D., 1991, "Phenomenological Model of Diesel Spray Atomisation," *Proceedings of the International Conference on Multiphase Flows*, Tsukuba, Japan.

[22] Bianchi, G., Pelloni, P., 1999, "Modelling the Diesel Fuel Spray Break-Up by Using a Hybrid Model," SAE paper no. 1999-01-0226.

[23] Ishii, M., 1975, *Thermo-Fluid Dynamics Theory of Two-Phase Flow*, Eyrolles, Paris.

[24] Drew, D. A., and Passman, S. L., 1998, *Theory of Multicomponent Fluids*, Springer, NY.

[25] Alajbegovic, A., Lahey, R. T., Jr., and Drew, D. A., 1999, "An Analysis of Phase Distribution and Turbulence in Dispersed Particle/Liquid Flows," Chem. Eng. Commun., **174**, pp. 85–133.

[26] Basara, B., Alajbegovic, A., and Beader, D., 2004, "Simulation of Single- and Two-Phase Flows on Sliding Unstructured Meshes Using Finite Volume Method," Int. J. Numer. Methods Fluids, **45**, pp. 1137–1159, (in press).

[27] v. Berg, E., Alajbegovic, A., Tatschl, R., Krüger, C., and Michels, U., 2001, "Multiphase Modelling of Diesel Sprays with the Eulerian/Eulerian Approach," *17th ILASS-Europe Conf.*, Zurich, Switzerland.

Downloaded 02 Jun 2010 to 171.66.16.98. Redistribution subject to ASME license or copyright; see http://www.asme.org/terms/Terms_Use.cfm

Feasibility Study of an On-Board Natural Gas to Dimethyl Ether Reactor for Dimethyl Ether Preinjection and Enhanced Ignition

David Horstman
Duane Abata
Jason Keith
Leroy Oberto

Michigan Technological University,
Houghton, MI 49931

Dual fuel (CI) engines provide an excellent means of maintaining high thermal efficiency and power while reducing emissions. This is particularly true in situations where the main CI fuel does not exhibit good autoignition characteristics, such as diesel engines operating on natural gas usually in stationary applications such as a pipeline installation. This paper explores the feasibility of chemically synthesizing DME from natural gas "on-board" and using it as an ignition source for a dual fuel engine. Conversion from diesel to dual fuel operation merits substantial benefits in PM emission reduction. Assuming a 5% pilot amount, a "once through" process has been modeled and a first law analysis (using practical isentropic efficiencies) demonstrates that this combined system can be operated with a reduction of between 5%–10% of the equivalent diesel efficiency. Significant quantities (~30 vol %) *of hydrogen are introduced to the natural gas as a byproduct of the DME synthesis process. The corresponding increase in combustion efficiency must be validated by experiments to determine DME and* H_2 *requirements for successful pilot ignition of the natural gas/*H_2 *mixture.* [DOI: 10.1115/1.1924433]

Introduction

Natural gas has been used as a fuel in stationary spark ignited (SI) engines for many years. This is because of its extensive geographic availability, reliability, and extremely low emissions. However, SI engines suffer from 15%–25% lower thermal efficiency than compression ignition (CI) engines due to throttling losses and the presence of a knock limit (low compression ratios) [4]. Figure 1 shows a comparison between a line of diesel engines and their equivalent natural gas (SI) engine for a power range from 200 to 1900 bkW (brake kilowatt). Not only is the approximately 20% decrease in thermal efficiency apparent, but perhaps just as importantly, nearly 30% less power is available in the comparable diesel construction. This ultimately translates into an increased cost per kW for the natural gas (SI) engine compared to the diesel.

Unfortunately, natural gas will not ignite in today's CI engines without assistance. This is because of the low cetane number ($CN < 2$) and high autoignition temperature (~650°C) of natural gas. Several ways to enhance the ignition of natural gas in a CI engine have been developed, including pilot diesel injection, fuel blends, glow plugs, stratified designs, and others [1–7]. Diesel pilot injection appears to be the most promising and practical; as this concept is currently being offered by several engine companies as either a dual fuel engine, or as a conversion to a current diesel engine. These are comprised of both high pressure gas injected engines, and low pressure injection (HCCI) engines. HCCI engines are similar to SI engines in that the air and primary fuel are mixed prior to introduction into the cylinder. However, dual fuel operation allows a pilot injection strategy to satisfactorily ignite the homogeneous mixture at multiple points within the cylinder for more stable and controlled combustion.

Contributed by the Internal Combustion Engine Division of The American Society of Mechanical Engineers for publication in the ASME Journal of Engineering for Gas Turbines and Power. Manuscript received by the ICE Division, January 20, 2003; final revision received September 23, 2004. Associate Editor: D. Assanis.

It has been found that preinjecting a small amount of diesel fuel (~1%–8% of thermal input) will produce adequate engine operation and minimal emissions. However, because two fuels must now be supplied, problems arise pertaining to the storage and availability of more than one fuel, especially in remote areas of the world. Therefore, the purpose of this work is to show the feasibility of manufacturing the ignition improving fuel directly "on-board" the engine.

Processes for producing synthetic fuels from natural gas have been around since the early 1900s. The most famous of these is the Fischer–Tropsch process whereby chains of hydrocarbons are indirectly synthesized to formulate fuels with properties similar to diesel fuel (termed: Fischer–Tropsch diesel). However, emission concerns have prompted research into other fuels that produce less exhaust pollutants than diesel. Dimethyl ether (formula: CH_3OCH_3), referred to as DME, is a simple oxygenate that has a cetane number and autoignition temperature similar to diesel fuel (see Table 1).

Investigations on the use of DME as a substitute to diesel fuel in CI engines have been carried out by Sorenson et al. at the Technical University of Denmark [8]. Thermal efficiency equivalent to that of using diesel fuel has been achieved, but with much lower NO_x emissions (~75%), and extremely low smoke.

DME has many favorable properties relative to diesel, greatest of which are its soot and sulfur free combustion. The sulfur is not present in DME due to its chemical processing, and the soot free combustion is attributed to its high oxygen content (~35%). In addition, DME can be manufactured from natural gas in a similar, but simpler, process than the Fischer Tropsch process. However, because the manufacture of DME from natural gas is less than 100% efficient, the use of DME as the primary fuel would not be practical because of the large equipment requirements and energy losses that will be mentioned in the proceeding sections.

Copyright © 2005 by ASME

Downloaded 02 Jun 2010 to 171.66.16.98. Redistribution subject to ASME license or copyright; see http://www.asme.org/terms/Terms_Use.cfm

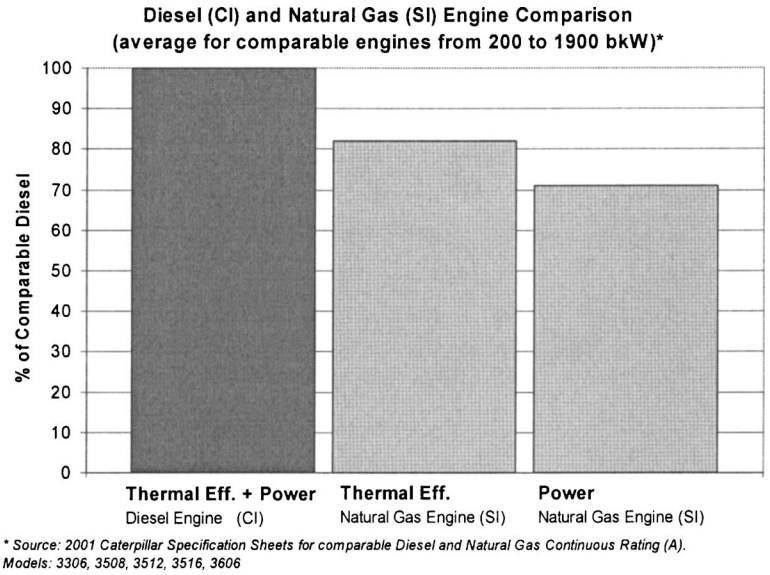

Fig. 1 Comparable diesel (CI) and natural gas (SI) engines

DME Manufacture (Background)

DME can be synthesized from natural gas by two different routes: indirect synthesis and direct synthesis. Indirect synthesis refers to natural gas first being converted to a mixture of CO, H_2, and CO_2 (called synthesis gas). The synthesis gas is then compressed, cooled, and passed over a suitable catalyst to form DME. Direct synthesis is defined as directly converting methane to DME while bypassing the synthesis gas step. However, this technology is limited by the low yields of desired products and it is yet unclear whether direct natural gas conversion technologies are competitive with the established indirect process [9]. Therefore the indirect synthesis route has been chosen to produce DME, both because of this reason, and because it is a well-proven technology.

The basic stages of indirect DME synthesis are listed in Fig. 2 and a more detailed explanation will follow.

Synthesis Gas Manufacture. Natural gas is approximately 90% methane (CH_4) with the remaining 10% comprising mostly of higher alkanes. Synthesis gas can be made from natural gas via four different routes. These are:

(1) Steam reforming [10,18]

$$CH_4 + H_2O \rightarrow CO + 3H_2 \quad \Delta H^o_{rxn} = +206 \text{ kJ/mol}$$

(2) Carbon dioxide reforming [10,11]

$$CH_4 + CO_2 \rightarrow 2CO + 2H_2 \quad \Delta H^o_{rxn} = +247 \text{ kJ/mol}$$

(3) Partial oxidation [12,13]

$$CH_4 + \tfrac{1}{2}O_2 \rightarrow CO + 2H_2 \quad \Delta H^o_{rxn} = -36 \text{ kJ/mol}$$

(4) Autothermal reforming (any combination of the above technologies) [14–16]

The water gas shift reaction (WGS) also occurs in the steam reformer:

$$\text{(WGS)}\ H_2O + CO \Leftrightarrow H_2 + CO_2 \quad \Delta H^o_{rxn} = -41 \text{ kJ/mol}$$

Compounds available for the manufacture of synthesis gas "on-board" engines are: natural gas, air (O_2,N_2), water (H_2O), and CO_2.

H_2O can be obtained easily either from a nearby water supply, condensed from the air (humidity), recycled from the methanol dehydration reaction during DME synthesis (explained later), or separated from the engines exhaust via condensation. The CO_2 can be found in the engine exhaust. However, it exists only in small quantities ($<$10% by vol) in the exhaust and separation could be relatively energy intensive and impractical.

Reactor design for a partial oxidation reaction (3) requires an oxygen separation unit in order to avoid the introduction of a large quantity of inerts (N_2) into the process (i.e., air is 21% O_2 and 79% N_2). This involves a large capital cost as well as additional safety concerns with the handling of pure oxygen [17].

Steam reforming, on the other hand, has been traditionally used

Table 1 Natural gas, DME, and deisel properties

	Natural Gas	DME	Diesel Fuel	Fischer-Tropsch Diesel
Cetane Number	< 2	> 55	40-55	> 74
Autoignition Temperature (°C)	650	235	250	250
Lower Heating Value (kJ/g)	48	29	43	43

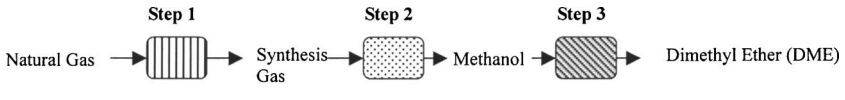

Step 1: Synthesis Gas manufacture from Natural Gas

Step 2: Methanol Synthesis from Synthesis Gas

Step 3: Methanol Dehydration to DME

Fig. 2 Indirect DME synthesis from natural gas

Downloaded 02 Jun 2010 to 171.66.16.98. Redistribution subject to ASME license or copyright; see http://www.asme.org/terms/Terms_Use.cfm

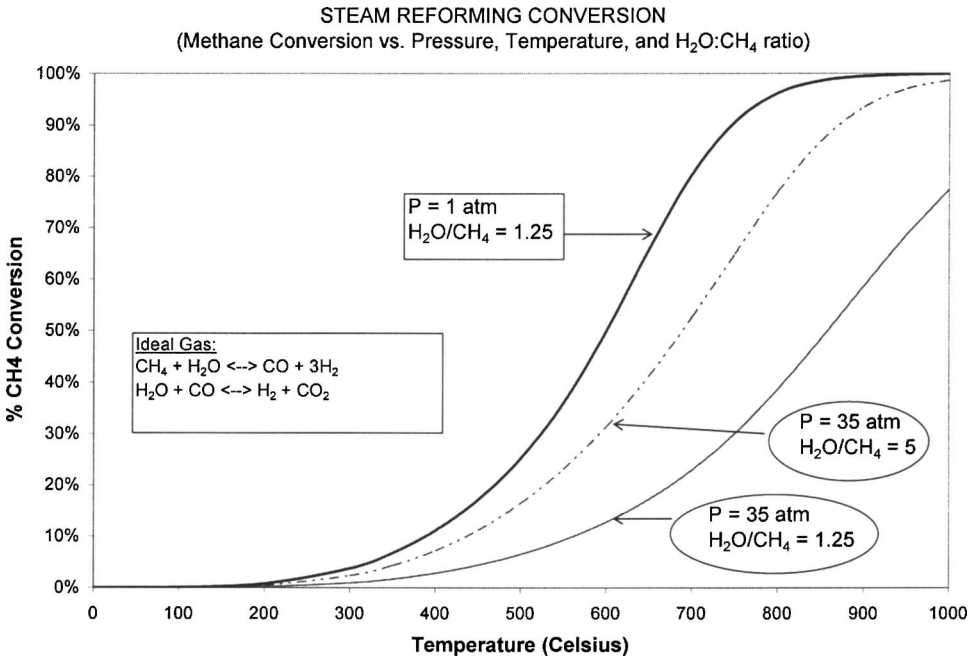

Fig. 3 Methane equilibrium conversion to synthesis gas via steam reforming (CH_4 to CO $+CO_2$)

in industry for the manufacture of synthesis gas (which is the building block of almost all industrial organic chemicals). It is the simplest of the 4 technologies mentioned above. A drawback of steam reforming is the high temperature required for reasonable conversion. Figure 3 shows the stoichiometric equilibrium conversion for the steam reforming reaction as a function of temperature, pressure, and the ratio of water to methane entering the reactor. Because moles are being produced in the reaction, conversion is greatest at low pressures. However, due to economics of the process, industry has typically reformed with nickel on magnesium oxide support at temperatures and pressures around 800°C and 35 atm, respectively [18].

A major issue of caution in catalytic reactions is preventing catalyst poisoning, which render it inactive. In steam reforming, this can be caused by both sulfur in concentrations greater than 10 parts per billion, and by carbon formation. The first obstacle is avoided by passing the natural gas through activated carbon to desulfurize it. Carbon formation can be suppressed, or at least minimized, by increasing the water to carbon ratio (WCR). The WCR is the molar proportion of inlet water to the carbon in the natural gas [18]. Overall stoichiometry of methane and water to DME is maximized at a WCR=1. However, thermodynamic equilibrium calculations demonstrate that at a temperature greater than 700°C, no solid carbon will be formed at WCR greater than or equal to 1.25. These are the constraints used for the proceeding modeling demonstration.

Another drawback of industrial steam reforming is that excess H_2 is produced which must be purged from the system, thus representing an energy loss to the process [19]. However, on-board generation offers the advantage that all purge gases from the reactor can be fed into the intake of the engine, which allows the available energy [in terms of Lower Heating Value (LHV)] of the purge gas to be recovered by combustion in the engine. Although cetane values for hydrogen have not been well defined, its wide flammability limits (5%–75% volume in air), large energy content (LHV=120 kJ/g), and zero emissions offer significant advantages for engine operation [20,21].

Upon leaving the steam reformer, the products must be cooled to condense any remaining water, and compressed (unless it has been compressed prior to the steam reformer) to the pressure of the methanol synthesis reactor.

Methanol Synthesis. The methanol for the reaction is produced in a separate reactor directly from synthesis gas by a combination of the methanol synthesis reaction (5) and the water–gas shift reaction.

$$(5)\ CO + 2H_2 \Leftrightarrow CH_3OH \quad \Delta H^{o}_{rxn} = -91\ \text{kJ/mol}$$

Thermodynamic equilibrium favors methanol conversion at low temperatures and high pressures (shown in Fig. 4).

A popular metal used for catalysis of the methanol synthesis is copper. Copper/zinc oxide on alumina support is active at temperatures above 200°C and has been used extensively by industry [17,22–24].

Finally, the methanol can be easily dehydrated into DME.

DME Synthesis. DME has predominantly been produced through a simple dehydration reaction (6) of methanol.

$$(6)\ 2CH_3OH \rightarrow CH_3OCH_3 + H_2O \quad \Delta H^{o}_{rxn} = -24\ \text{kJ/mol}$$

This is done at low temperatures (~250°C) and high pressures (~20 atm) over a gamma-alumina catalyst [25] (although pressure does not affect conversion). The equilibrium conversion for the methanol dehydration to DME reaction as a function of temperature is shown in Fig. 5. The dehydration of methanol to DME achieves high conversions (~90%) throughout a relatively large range of temperatures and pressures.

Several reports have suggested that the methanol synthesis reaction and the methanol dehydration reaction be carried out in the same reactor [10,26]. If this is done, the water formed from the methanol dehydration reaction can be converted to CO_2 and H_2 (which are feedstock for the methanol synthesis reaction) through the water-gas shift reaction, and therefore methanol conversion will increase. However, this complicates downstream separation and has not been used for the current analysis, but may be worth-

Downloaded 02 Jun 2010 to 171.66.16.98. Redistribution subject to ASME license or copyright; see http://www.asme.org/terms/Terms_Use.cfm

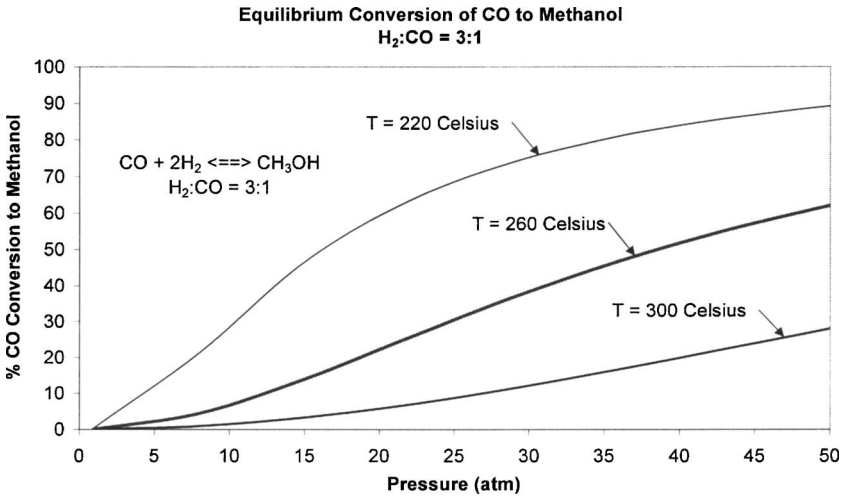

Fig. 4 Equilibrium conversion of (H_2:CO=3:1) synthesis gas to methanol

while to consider.

Once the reaction scheme has been determined, temperatures, pressures, and WCR are the major variables present in designing a suitable process and will directly affect:

(1) Conversion;
(2) Heat transfer duty;
(3) Heat exchanger size (proportional to cost);
(4) Compressor duty;
(5) Separation duty;
(6) Ignition quality and heating value of the "off gases" (directed to the engine);
(7) Safety;
(8) Reliability ("robustness of design");
(9) Overall cost.

A commercial process design simulator (HYSIS) has been used to determine a possible scenario, keeping the above factors in mind, for DME synthesis for use as a pilot fuel in a CI engine.

Process Model

The model is based on assuming both chemical and phase equilibrium is achieved throughout the process. Three reactors are using reactions (1), (5), and (6), respectively, in each reactor coupled with the water gas shift reaction. It has been established in literature that chemical equilibrium conversions can be achieved in each reactor, if properly designed. All the reactors are assumed to be isothermal. In the steam reformer, thermodynamic equilibrium predicts carbon formation at WCR's <1.25 at the reformer temperatures considered. Therefore, the WCR has been chosen to be 1.25. Incidentally, higher WCR's equate to much larger by-product production and further energy input to heat, cool, and compress this gas which will ultimately be purged to the engine, thus lowering the system efficiency. Finally, there are 3 separators, through which it is assumed that phase equilibrium is achieved. The process diagram is shown in Fig. 6.

Considering equilibrium conversions as well as the corresponding limits of catalyst activity, the process parameters were chosen. A multistage compressor with an inter-stage heat exchanger will be required for the pressure ratios involved (*compression work and heat removal duty will remain the same as presented in Table 2*). Incidentally, the isentropic compressor efficiency is assumed to be 80%.

In order to determine the amount of DME required, a mean value of specific fuel consumption (sfc) for diesel engines in the power range (200–1900 bkW) of about 200 g diesel equivalent/bkW h has been used. This gives a total chemical energy input to the engine of 8560 kJ_{fuel}/bkW h. 5% of this energy input is taken

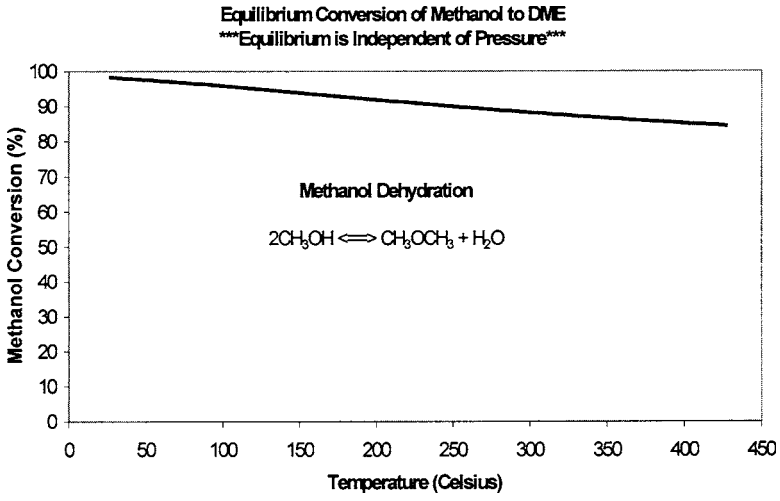

Fig. 5 Equilibrium conversion of methanol to DME

Downloaded 02 Jun 2010 to 171.66.16.98. Redistribution subject to ASME license or copyright; see http://www.asme.org/terms/Terms_Use.cfm

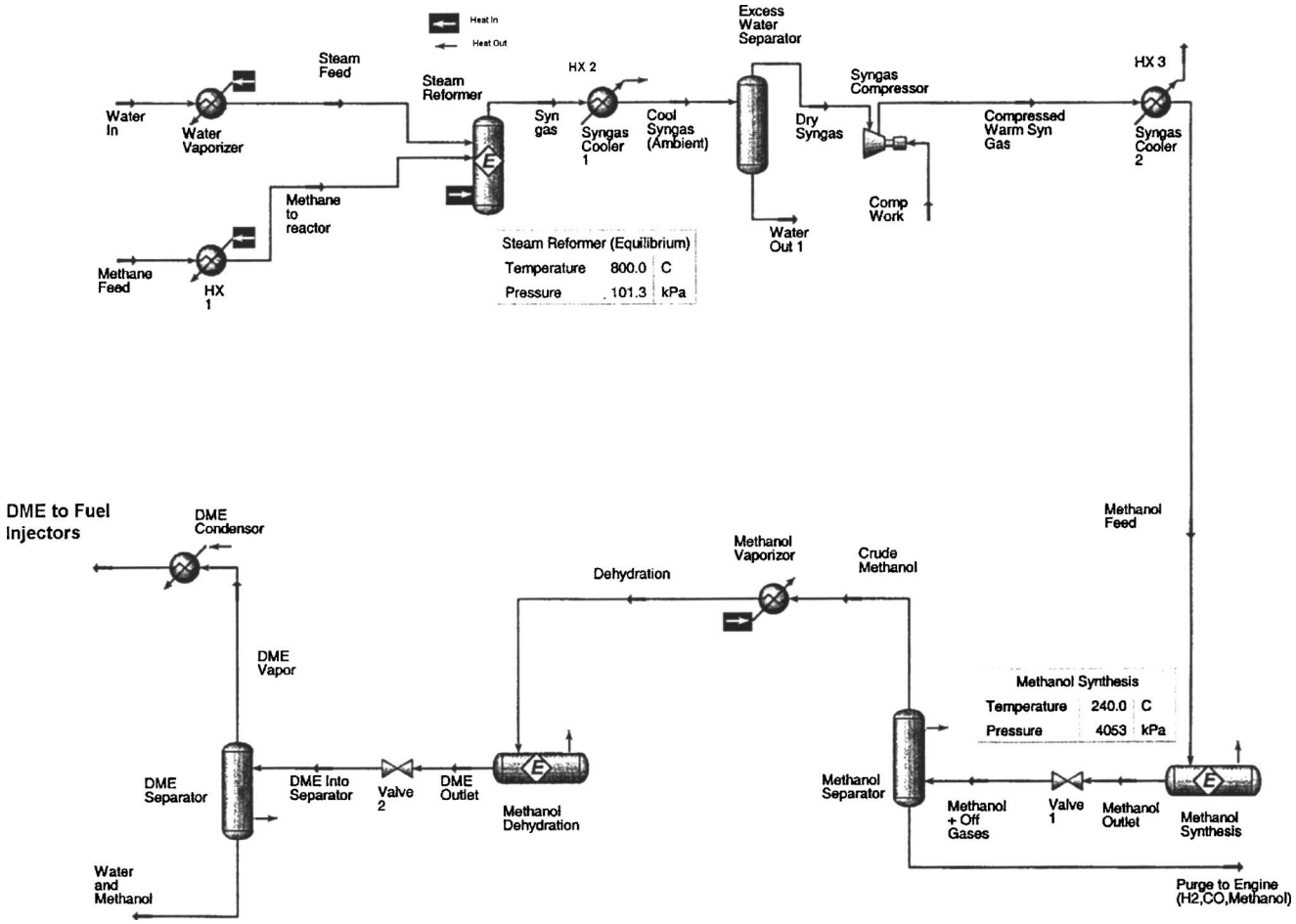

Fig. 6 Process diagram of DME synthesis from methane

as the amount of DME necessary for pilot injection, or about 15 g_{DME}/bkW h. This represents a rather conservative estimate for 3 reasons:

(1) SFC generally decreases as engine size (output) increases. (*SFC for a* 40 MW *engine might be some 15% lower than for a* 1 MW *engine.*)
(2) Diesel pilot is used in as little as 1% of total energy charge into the engine; this is 5 times less than specified here.
(3) DME is believed to have better ignition characteristics than

Table 2 Process conditions and energy demand

5% of Total Charge = 32.06 mol_{DME}/hr (1.5 kg_{DME}/hr)		Engine Brake Power = 100 kW sfc ($g_{diesel,eqv.}$/kW-hr) = 200, $\eta_{thermal}$ = 42%				
Process Equipment	Pressure (atm)	Heating (kW)	Cooling (kW)	Tin (Celsius)	Tout (Celsius)	ΔT
HX 1	1	1.9	*	35	800	**765**
Water Evaporator	1	4.0	*	35	800	**765**
HX 2	1	*	4.4	800	35	**-765**
HX 3	40	*	3.0	751	240	**-511**
Steam Reformer	1	9.5	*	800	800	**0**
Methanol Reactor	40	*	2.4	240	240	**0**
DME Reactor	40	*	0.2	240	240	**0**
Methanol Separator	20	*	2.0	238	20	**-218**
Methanol Evaporator	20	1.2	*	20	240	**220**
DME Separator	8	*	0.8	230	50	**-180**
DME Condenser	8	*	0.2	50	20	**-30**
Total Heat Transfer (kW)		**16.6**	**12.9**	$Q_{net\ in}$ (kW)		3.75
Compression (η_s=80%) (kW)		**4.1**				
Total Energy In (kW)		**7.8**				

Downloaded 02 Jun 2010 to 171.66.16.98. Redistribution subject to ASME license or copyright; see http://www.asme.org/terms/Terms_Use.cfm

Table 3 Energy balance of process

		Energy In		Energy Out				
		Water	CH_4	Purge	DME	Water and Methanol'	TOTAL OUT	Total Δ =out-in
		(kW)		(kW)				
Temperature	(C)	35	35	20	20	50	*	*
Molar Heat Capacity	(J/mol-C)	72.77	36.45	29.80	110.60	97.88	*	*
Total HEAT FLOW	(kW)	-15.70	-3.30	-5.81	-1.99	-3.37	-11.17	7.83
Energy Inputs	(kW)	7.83		0				-7.83
Total Energy Balance								**0.00**

diesel and perhaps pilot injection of DME will require less than 1% of the inlet charge energy.

Tables 2–5 present a first law analysis of the process. The process pressures and temperatures and energy demands are presented in Table 2 for the corresponding process equipment from Fig. 6.

The total heating load to the process is 16.6 kW, 90% of which goes into the steam reformer (including reactant heating). The total cooling load is 12.9 kW, 30% of which is used to cool the synthesis gas prior to compression to methanol synthesis pressure. Therefore, nearly two thirds of the heat transfer duty in the process is only for synthesis gas preparation. An energy balance as well as the specific heat capacity of each process stream is presented in Table 3 for the sake of completeness. Table 4 shows the mass balance for the process. Notice that the DME accounts for only 25% of the total mass moving through the system. Over 60% of the mass is purged back to the engine as CO, CO_2, and H_2. This is significant and may change the combustion characteristics of the natural gas/purge gas mixture.

Finally, Table 5 shows the respective heating values of each process stream. Notice that there is a net increase in the fuels' lower heating value (LHV) of 6.3 kW. The LHV of H_2 in the purge stream (23.8 kW) returned to the engine for combustion accounts for 10% of the total engine fuel energy input! This is expected to greatly enhance combustion [21]. Experiments are necessary to determine the effects and requirements of DME pilot injection and corresponding amount of H_2 in the combustion charge. Perhaps much smaller amounts of DME (and the corresponding H_2) can be used for successful engine combustion.

The DME is 5% of the energy value of the inlet charge, as defined above, and the remainder of the fuel is methane (natural gas).

DME Purity. The DME stream to be used for pilot injection is 96% pure DME with the remaining impurities being (wt. %): 2.9% CO_2, 0.5% H_2O, and 0.5% Methanol (Table 4). Constraints of DME purity for adequate combustion have also been defined previously [8]. This is illustrated in Fig. 7 for DME containing only H_2O and methanol. The effect of CO_2 had not been included in the analysis. However, because "the addition of water" reduces the area of good ignition [8], CO_2 is assumed to act in the same regard. Perhaps with a reduced effect because of the relatively smaller specific heat of CO_2 compared to water (about $\frac{1}{2}$ that of H_2O). Therefore, the DME produced by the above process lies in the range of "good" ignition characteristics defined in Fig. 7.

Thermal Efficiency Considerations. In order to quantify the effect of the DME synthesis process on the overall thermal efficiency of the engine, several assumptions are made:

(1) The increase in LHV (6.3 kW) is fully utilized by the engine;

Table 4 Mass balance of process

		Mass In		Mass Out			
	MW (g/mol)	Water	CH_4	Purge	DME	Water and Methanol	TOTAL OUT
		gram/hr		gram/hr			
Methane	16.041	0.0	2553.3	85.9	0.0	0.0	85.9
H_2O	18.016	3584.3	0.0	0.0	8.1	638.5	646.6
CO_2	44.01	0.0	0.0	1776.6	45.1	0.0	1821.7
CO	28.01	0.0	0.0	1058.2	0.0	0.0	1058.2
H_2	2.016	0.0	0.0	712.6	0.2	0.0	712.8
Methanol	32.041	0.0	0.0	59.0	7.7	264.5	331.3
DME	46.069	0.0	0.0	0.0	1477.0	3.2	1480.2
Total Stream Balance	(g/hr)	3584.3	2553.3	3692.3	1538.0	906.3	6136.6
Total Mass Balance	(g/hr)	**6137.6**		**6136.6**			

Table 5 Lower heating value of process streams

		LHV IN		LHV OUT				Total Δ =out-in
	LHV	Water	CH_4	Purge	DME	Water and Methanol	TOTAL OUT	
	(kJ/g)	(kW)		(kW)				(kW)
Methane	50.0	0.0	35.5	1.2	0.0	0.0	1.2	-34.3
H_2O	0.0	0.0	0.0	0.0	0.0	0.0	0.0	0.0
CO_2	0.0	0.0	0.0	0.0	0.0	0.0	0.0	0.0
CO	10.1	0.0	0.0	3.0	0.0	0.0	3.0	3.0
H_2	120.0	0.0	0.0	23.8	0.0	0.0	23.8	23.8
Methanol	21.1	0.0	0.0	0.3	0.0	1.6	1.9	1.9
DME	28.9	0.0	0.0	0.0	11.9	0.0	11.9	11.9
LHV of each Stream	(kW)	0.0	35.5	28.3	11.9	1.6	41.7	6.3
Total LHV	(kW)	35.5		41.7				**6.3**

Downloaded 02 Jun 2010 to 171.66.16.98. Redistribution subject to ASME license or copyright; see http://www.asme.org/terms/Terms_Use.cfm

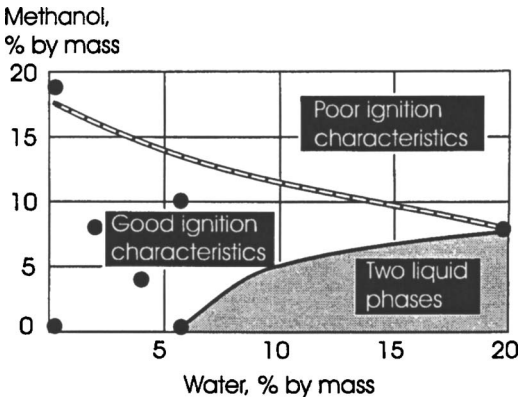

Fig. 7 Ignition limits in the engine for mixtures of DME, methanol, and water (Sorenson et al.) [8]

(2) Power required for cooling water or air fans for the heat exchangers is neglected;
(3) Efficiency for heating the process streams is 80% (by an external fuel source);
(4) Compressor efficiency is 80%.

With these assumptions in mind, a reduction in thermal efficiency can be determined for no heat integration (the cooling loads and heating loads do not interact), or for 100% heat integration (i.e., all 12.9 kW of cooling covers part of the 16.6 kW heating load). Although 100% heat integration would be impossible to achieve (considering the temperature differences in Table 2), it is useful to apply as a relative "best case" scenario.

It can be shown that the energy requirements for synthesizing 5% DME for pilot ignition of natural gas will reduce the overall thermal efficiency by anywhere between 5% and 10% (depending on the amount of heat integration).

Net Composition of Engine Fuel Charge for DME Synthesis Process. Figure 8 shows the DME synthesis process coupled with the engine. The composition of each stream is given in the diagram and the initial natural gas composition is defined to be that in the left-hand column of Table 6. It is readily apparent that the purge gas from the DME synthesis process is recycled to the natural gas and results in a significantly different net composition of the main fuel charge for the engine. Operation of a dual fuel engine can proceed either via high pressure gas injection or low pressure gas injection. For high pressure gas injection, the primary fuel is injected at extremely high pressure near the end of the compression stroke in which the pilot fuel ignites this "plume." Operation in this manner is truly CI (diffusion burn). On the other hand, low pressure gas injection operates on the HCCI principle in that a lean fuel/air mixture is fumigated into the intake manifold of the engine and ignition is controlled by the pilot fuel and the manner in which it is injected. Therefore, low pressure injection is a stratified combustion phenomenon and similar to SI combustion.

An investigation into the effects of changing the natural gas compositions on SI engine combustion has been previously carried out in Denmark by Søgard [27]. The compositions used are shown in the left two columns of Table 6. "RNG 2" is "steam reformed" natural gas; and it is basically natural gas with all the hydrocarbons ($>C_2$) converted to H_2 and CO_2. This has resulted in:

(1) Increasing the lean combustion limits;
(2) Up to 50% *lower* HC emissions;

Table 6 Composition of natural gas, reformed natural gas (RNG), and the net input to the engine for the present process

	Natural Gas	RNG 2	DME pilot process
	Composition (vol %)		
CH_4	87	70	55
C_2H_6	7	0	4
C_3H_8	3	0	2
C_4H_{10}	1	0	1
CO	0	0	3
H_2	0	23	28
CH_3OH	0	0	0
CH_3OCH_3	0	0	3
H_2O	0	1	0
CO_2	1	6	4
LHV_{total} (kJ/g)	47.7	42.1	42.5
Total Mass Flow for 100bkW, η=42% (g/s)	4.97	5.63	5.58

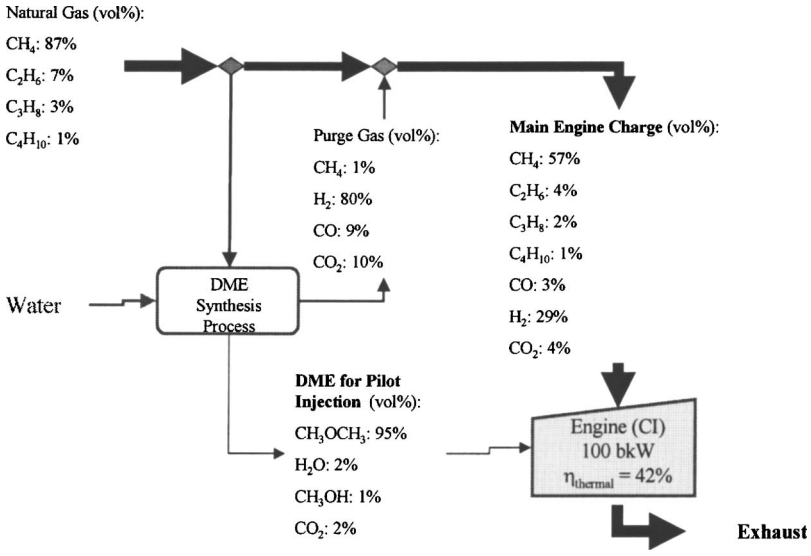

Fig. 8 DME synthesis for pilot injection of natural gas

Downloaded 02 Jun 2010 to 171.66.16.98. Redistribution subject to ASME license or copyright; see http://www.asme.org/terms/Terms_Use.cfm

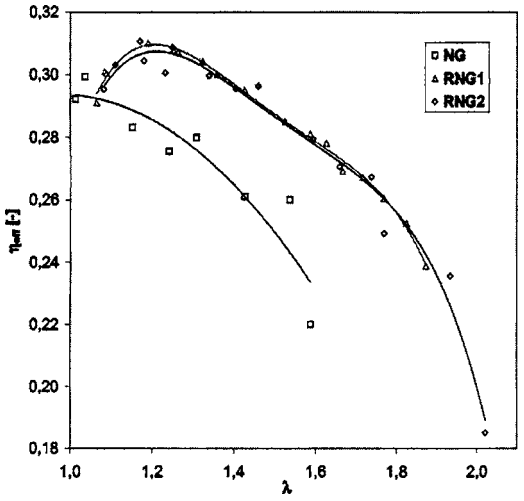

Fig. 9 Thermal efficiency versus excess air (Søgard [27])

(3) Up to 80% *lower* CO emissions;
(4) Up to 50% *higher* NO_x emissions;
(5) An increase in thermal efficiency of up to 25% (Fig. 9). (*Note: Table 6 gives the compositions of NG and RNG2 referred to in Fig. 9.*)

Figure 9 illustrates that the favorable effects of hydrogen addition are greatest at very lean mixtures, which is where HCCI engines operate in order to control NO_x emissions. Therefore, the benefits of hydrogen are suspected to be as great when used in a HCCI engine. The compositions of "RNG 2" and the net fuel for the combined DME synthesis process are presented in Table 6 for comparison. The DME process results in a DME content of 3 vol % (for pilot injection), and a H_2 content of 28 vol %. This is slightly higher than the H_2 content of the "RNG 2" (23 vol %). However, the DME process has traces of the higher hydrocarbons (undesirable for SI combustion due to their knock tendency [27]), whereas "RNG 2" has none.

Therefore, although there are decreases in net engine thermal efficiency due to energy loss to the DME synthesis process, it is expected that this will be more than compensated by the enhanced combustion characteristics of the final mixture, not to mention the increase in efficiency compared to a standard SI natural gas engine (see Fig. 1). Additional benefits in terms of emission reductions are expected.

Conclusion

Natural gas as a fuel for stationary engines presents many advantages over conventional fuels, especially in locations where pipeline gas is cheap and readily available. However, its use in SI engines imposes efficiency and power limitations. Dual fuel engines have proven to overcome these limitations, however, the supply of diesel fuel for pilot injection and subsequent ignition of CH_4 can be a problem in remote locations. *Therefore the present study has determined the possibility, and associated losses, with manufacturing DME as a pilot fuel from the main fuel at the same site (i.e., "on-board") where the engine is operating.*

Compared to the diesel pilot equivalent engine, a 1%–5% pilot amount of DME manufactured on-board with *no heat integration* results in, *respectively*,

(a) 1%–10% loss in total thermal efficiency;
(b) 0.4%–4% loss in power (compressor duty);
(c) 1%–10% (LHV %) introduction of H_2 into the engine.

Therefore, for small pilot amounts of DME (<10% on an energy basis) this process looks appealing considering the advantages in emissions over a diesel engine while maintaining efficiency and power.

Needs for Further Study

The following list outlines a few challenges that will be associated with making this process into a practical device.

(1) Heat exchanger size and materials of construction;
(2) Process control and monitoring;
(3) Development of reliable DME injectors;
(4) Auxiliary equipment (water deionization, gas conditioning, compressor cost, etc.);
(5) Catalyst lifetime.

However, the process outlined above illustrates the feasibility of "on-board" manufacture of DME for pilot ignition of natural gas in a CI engine and thus calls for the need of further study.

Prior to the construction of a DME synthesis plant, combustion characteristics should be defined for DME pilot injection of natural gas in CI engines. This analysis should include effects of H_2 content of the fuel entering the combustion chamber as this is intimately related to the DME production characterized by the process presented in this paper.

Normally, an industrial process for DME production will be inherently more complicated than the "once through" scheme presented above. This is because complicated recycle loops and enhanced separation technologies make the large-scale process more economical. The relatively small quantities of pilot fuel required (perhaps less than 1% of the chemical energy going into the engine) will make inefficiencies and losses in the process insignificant compared to the total energy savings from more efficient engine operation. Finally, because the objective in the present case is "enhanced combustion" and not limited to production of a "pure" chemical end product, the integration of a DME synthesis process with a CI engine operating on natural gas appears to be a feasible option.

Future Work

Developments will proceed at Michigan Technological University for a small scale DME synthesis unit to supply a single cylinder CFR diesel engine with sufficient DME for pilot ignition of natural gas for HCCI combustion.

Acknowledgment

The authors would like to thank the U.S. Department of Energy and the U.S. Department of Education for financing this project through the Interdisciplinary Center for Advanced Propulsion at Michigan Technological University.

Nomenclature

CI = compression ignition
DME = dimethyl ether (CH_3-O-CH_3)
HCCI = Homogeneous charge compression ignition
LHV = Lower heating value
PM = Particulate matter
RNG = Reformed natural gas (CH_4, CO, H_2)
SFC = Specific fuel consumption
SI = Spark ignition
Syn-Gas = Synthesis gas
WCR = Water to carbon ratio
WGS = Water-gas shift

References

[1] Douville, B. and Ursu, B., 1998, "Performance and Emissions of a Two-Stroke Engine Fueled Using High-Pressure Direct Injection of Natural Gas," SAE paper 981160.
[2] Miyamoto, N., Ogawa, H., Nurun, N., Obata, K., and Arima, T., 1998, "Smokeless, Low NO_x High Thermal Efficiency, and Low Noise Diesel Com-

Downloaded 02 Jun 2010 to 171.66.16.98. Redistribution subject to ASME license or copyright; see http://www.asme.org/terms/Terms_Use.cfm

bustion with Oxygenating Agents as Main Fuel," SAE Paper No. 980506.
[3] Chen, Z. and Konno, M., 2000, "Experimental Study of CI Natural-Gas/DME Homogeneous Charge Engine," SAE paper 2000-01-0329.
[4] Richards, B. and Willi, M., 1995, "Design and Development of a Direct Injected, Glow Plug Ignition-Assisted, Natural Gas Engine," J. Eng. Gas Turbines Power, **117**, pp. 799–803.
[5] Higashino, A. and Iwamoto, H., 2000, "Compression Ignition Combustion in a Prechambered and Heat Insulated Engine Using a Homogeneous Natural Gas Mixture," SAE paper 2000-01-0330.
[6] Doughty, G., Bell, S., and Midkiff, K., 1992, "Natural Gas Fueling of a Caterpillar 3406 Diesel Engine," J. Eng. Gas Turbines Power, **114**, pp. 459–465.
[7] Blizzard, D. and Schaub, E., 1992, "Development of the Cooper-Bessemer CleanBurn Gas-Diesel (Dual-Fuel) Engine," J. Eng. Gas Turbines Power, **114**, pp. 480–487.
[8] Sorenson, S. and Mikkelsen, S., 1995, "Performance and Emissions of a 0.273 Liter Direct Injection Diesel Engine Fuelled with Neat Dimethyl Ether," SAE 950064.
[9] Han, S. and Chang, C., 1991, *Synthetic (Liquid) Fuels, Kirk Othmer Encyclopedia of Chemical Technology*, Vol. 12, Wiley, New York, pp. 155–203.
[10] Peng, X., 1999, "Single Step Syngas to Dimethyl Ether Processes for Optimal Productivity, Minimal Emissions, and Natural Gas Derived Syngas," Ind. Eng. Chem. Res., pp. 4381–4388.
[11] Rostrup-Nielsen, J. and Bak Hansen, J., 1993, "CO_2 Reforming of Methane over Transition Metals," J. Catal., pp. 38–49.
[12] Hickman, D. and Schmidt, L., 1993, "Production of Syngas by Direct Catalytic Oxidation of Methane," Science.
[13] Ashcroft, A. and Cheetham, A., 1990, "Selective Oxidation of Methane to Synthesis Gas Using Transition Metal Catalysts," Nature (London), **344**, pp. 319–321.
[14] Tjatjopoulos, J., 1998, "Feasibility Analysis of Ternary Feed Mixtures of Methane With Oxygen, Steam, and Carbon Dioxide for the Production of Methanol Synthesis Gas," Ind. Eng. Chem. Res., pp. 1410–1421.
[15] Hansen, J. and Joensen, F., 1995, "Large Scale Manufacture of Dimethyl Ether—A New Alternative Diesel Fuel From Natural Gas," SAE paper 950063.
[16] Ashcroft, T. and Cheetham, A., 1991, "Partial Oxidation of Methane to Synthesis Gas Using Carbon Dioxide," Nature (London), **352**, pp. 225–226.
[17] Lange, J. P., 2001, "Methanol Synthesis: A Short Review of Technological Improvements," Catal. Today, **64**, pp. 3–8.
[18] Rostrup-Nielsen, Jens, 1984, *Steam Reforming Catalysts*, Springer-Verlag, Berlin.
[19] Farina, J. and Supp, E., 1992, "Produce Syngas for Methanol," Hydrocarbon Process., **71**, pp. 77–79.
[20] Bechtold, R., 1997, *Alternative Fuels Guidebook*, Society of Automotive Engineers, Warrendale, PA.
[21] Toshio, S., 2001, "Combustion Characteristics of $H_2-CO-CO_2$ Mixture in an IC Engine," SAE paper 2001-01-252.
[22] Eluers, B., Hawkings, S., and Schultz, G., 1990, *Methanol, Ullmann's Encyclopedia of Industrial Chemistry*, 5th ed., Cambridge, New York, Vol. A-16, pp. 465–485.
[23] Ng, K., Chadwick, D., and Toseland, B., 1999, "Kinetics and Modeling of Dimethyl Ether Synthesis From Synthesis Gas," Chem. Eng. Sci., **54**, pp. 3587–3592.
[24] Skrzypek, J. and Lachowska, M., 1991, "Kinetics of Methanol Synthesis Over Commercial Copper/Zinc Oxide/Alumina Catalysts," Chem. Eng. Sci., **46**, pp. 2809–2813.
[25] Bercic, G. and Levec, J., 1993, "Catalytic Dehydration of Methanol to Dimethyl Ether. Kinetic Investigation and Reactor Simulation," Ind. Eng. Chem. Res., **32**, pp. 2478–2484.
[26] Hansen, J. and Joensen, F., 1991, *High Conversion of Synthesis Gas Into Oxygenates, in Natural Gas Conversion*, Elsevier Science, Amsterdam.
[27] Søgard, C., Schramm, J., and Jensen, T., 2000, "Reduction of UHC-emissions From Natural Gas Fired SI-Engine-Production and Application of Steam Reformed Natural Gas," SAE 2000-01-2823.

Downloaded 02 Jun 2010 to 171.66.16.98. Redistribution subject to ASME license or copyright; see http://www.asme.org/terms/Terms_Use.cfm

An Analysis of Turbocharged Diesel Engine Dynamic Response Improvement by Electric Assisting Systems

Tomaž Katrašnik
e-mail: tomaz.katrasnik@fs.uni-lj.si

Ferdinand Trenc

Department of Mechanical Engineering,
University of Ljubljana,
Aškerčeva 6,
SI-1000 Ljubljana, Slovenia

Vladimir Medica
Faculty of Engineering,
University of Rijeka,
Vukovarska 58,
51000 Rijeka, Croatia

Stojan Markič
Iskra Avtoelektrika d.d.-R&D,
SI-5290 Šempeter pri Gorici, Slovenia

It is well known that turbocharged diesel engines suffer from an inadequate response to sudden load increase, this being a consequence of the nature of the energy exchange between the engine and the turbocharger. The dynamic response of turbocharged diesel engines could be improved by electric assisting systems, either by direct energy supply with an integrated starter-generator-booster (ISG) mounted on the engine flywheel, or indirect energy supply with an electrically assisted turbocharger. A previously verified zero dimensional computer simulation method was used for the analysis of both types of electrical assistance. The credibility of the data presented is further assured by the experimentally determined characteristics of the electric motors used as input parameters of the simulation. The paper offers an analysis of the interaction between a turbocharged diesel engine operating under various load conditions and electric assisting systems, as well as the requirements for supporting electric motors suitable for the improvement of an engine's dynamic response. It is evident that an electrically assisted turbocharger outperforms an integrated starter-generator-booster for vehicle application, however ISG is the preferred solution when instant power increase is demanded.
[DOI: 10.1115/1.1924533]

Introduction

An increase in the brake mean effective pressure (bmep) of a diesel engine is generally the consequence of turbocharging and subsequent charge cooling of the working medium. During the sudden load increase phase, turbocharged diesel engines reach a stationary value of bmep with a delay due to low starting boost pressure. Advanced turbocharged diesel engines are usually equipped with a boost pressure controlled fuel limiting system, LDA (German abbreviation for "Ladedruckabhängiger Vollastanschlag"). The purpose of the LDA is to assure complete combustion during engine transient operating conditions, thereby reducing exhaust gas emissions, above all, of black soot. Thus the LDA is indispensable for meeting strict environmental regulations. Black soot emission essentially starts increasing before incomplete combustion occurs; the LDA therefore generally dictates the injection of lower maximum fuel quantity than that which could have burned completely. The dynamic response of turbocharged diesel engines equipped with an LDA is therefore slower than that of those without one due to lower specific enthalpy of the exhaust gases. Simultaneously meeting strict environmental regulations and improving the baseline engine dynamic response is enabled by the application of supporting electric systems.

The idea of the electrically assisted turbocharger has already been presented in Refs. [1–6], whereas the concept of an electric motor driven compressor followed by an ordinary turbocharger was introduced in Ref. [7]. Numerical simulations in the papers [1,2,7] based on the neural network MATLAB SIMULINK software presented in Ref. [1] and in paper [3] are limited to the presentation of one realistic engine loading case with corresponding electrical assistance. However, a deeper understanding of the interaction between the turbocharged engine and electric assisting systems was not possible due to the large time scale dependence of the interaction. Improvement of the dynamic response of a turbocharged diesel engine by electric assisting systems is influenced by the engine speed change, applied load and mostly by the duration of the transient operation when an electrically assisted turbocharger is considered.

In this work, simulations of a turbocharged diesel engine propelling a truck in different gears are presented. An evaluation of dynamic response improvement of the turbocharged diesel engine by electric assisting systems under various load conditions on different time scales was therefore possible. Two options are simulated and compared: the engine with an electrically assisted turbocharger and the engine with an integrated starter-generator-booster (ISG) mounted on the flywheel. A variety of electric assisting systems combined with the operation of the engine under various loading conditions reveal improvements in the dynamic response of the turbocharged diesel engine equipped with electric assisting systems, their interaction with the diesel engine, as well as demands on them. The paper is organized as follows: Computer simulation program and its validation is described first, technical features of the applied engine, its supporting components, and electric assisting systems are discussed next, in the Results section different cases of vehicle acceleration together with the parametric study of the influence of electric assisting systems parameters on the dynamic response improvement of a turbocharged engine were investigated.

Simulation Program

The simulation program is based on the zero-dimensional filling and emptying method. The differential equations for mass and energy conservation are solved in each integration time step throughout the entire engine cycle, bypassing the need to prepare engine subsystem maps in advance as they could be indirectly influenced by the electric assisting systems. The basis of the simulation method is presented in Ref. [8], whereas the extended code used here is described in detail in Ref. [4] and briefly in Refs. [5,6]. Special care was devoted to the accuracy of the turbocharger modeling, as it in turn, via boost pressure and the LDA,

Contributed by the Internal Combustion Engine Division of The American Society of Mechanical Engineers for publication in the ASME Journal of Engineering for Gas Turbines and Power. Manuscript received by the ICE Division, November 10, 2003; final revision received July 23, 2004. Associate Editor: D. Assanis.

 Copyright © 2005 by ASME

Downloaded 02 Jun 2010 to 171.66.16.98. Redistribution subject to ASME license or copyright; see http://www.asme.org/terms/Terms_Use.cfm

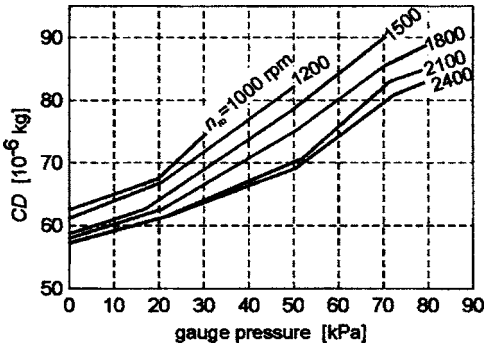

Fig. 1 LDA characteristics

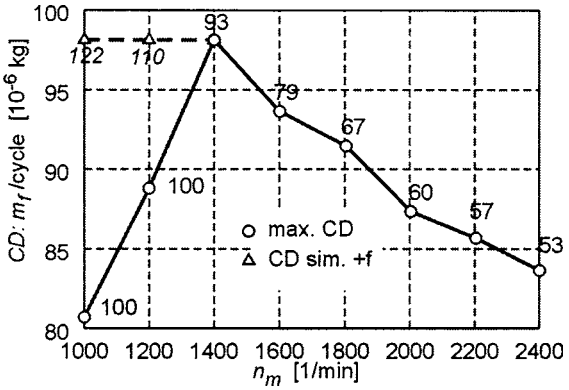

Fig. 2 Fuel injection pump characteristics

determines the quantity of fuel injected and therefore engine power in a transient operating regime. The accuracy and applicability of the zero-dimensional code was enhanced by the calibration of adjustable constants based on experimental data. Therefore, experimentally determined flow coefficients of inlet and exhaust valves, characteristic of the fuel delivery pump, the LDA, intercooler, and twin entry turbine, as well as combustion parameters based on the results of the analysis of measured $p-V$ diagrams were used in the simulation code. The experimentally determined characteristics of the twin entry turbocharger turbine were further processed with a turbine boundary condition computer program [9] enabling the consideration of various flow regimes on twin turbine inlets. As a result, a reliable and accurate simulation program compatible with the experimental results in stationary and transient engine operation was developed [4–6].

The validity of the presented data was additionally assured by the experimentally determined characteristics of the applied electric assisting systems as input parameters of the simulation. The vehicle dynamics simulation subroutine was developed according to Ref. [10]. The model of the vehicle dynamics includes features of the truck powertrain, truck geometry, and its weight as well as road characteristics.

Technical Features of the Engine, its Components, and Electric Assisting Systems

A 6.87 1 six cylinder turbocharged and aftercooled MAN D0826 LOH 15 diesel engine with a bore/stroke of 108/125 mm, compression ratio of 18:1, developing 820 Nm at 1500 rpm and 162 kW at 2400 rpm, equipped with a HOLSET H1E-8264BF/H16WA8 free floating (without any controlling devices) turbocharger ($J_{TC}=15.2\times10^{-5}$ kg m^2) and with a pneumatically controlled fuel limiting device (Fig. 1) was used in the investigations. This engine drives a MAN 8.225 LC 7490 kg gross weight truck equipped with a six gear S6-850 gearbox.

A simulated MAN engine (D0826 LOH 15) is equipped with a Bosch high-pressure fuel injection pump linked with a pneumatically controlled fuel limiting device, LDA. Figure 1 shows the influence of the gauge pressure (boost pressure-ambient pressure) on the cyclic fuel delivery (CD) for various engine speeds. The quantity of injected fuel decreases with increasing engine speed at constant gauge pressure. Figure 2 presents the maximum measured CD ("max. CD") as functions of the engine speed. The ratios (in percentages) of the LDA full fueling gauge pressure to stationary gauge pressure for the same quantity of injected fuel are plotted along the "max. CD" curve. It is obvious that at 1000 and 1200 rpm CD is limited by the LDA setting rather than by the characteristics of the fuel injection pump. This phenomenon is generally the consequence of free floating turbine flow characteristics, which in connection with the compressor produces low boost pressure at low engine speed, thus resulting in low CD at the set minimum air–fuel ratio. Above 1400 rpm the LDA no longer influences the stationary maximum CD. From 1400 to 2400 rpm CD decreases, maintaining almost constant maximum cylinder pressure.

Because the maximum CD is limited by the operation of the LDA below 1400 rpm the maximum CD would rise if boost pressure was increased, as in the case when using an electrically assisted turbocharger. For the simulation of the engine with an electrically assisted turbocharger, maximum CD below 1400 rpm was therefore set to a value equal to that at 1400 rpm. This is an acceptable value when peak cylinder pressure and thermal loadings are concerned. This modified CD was labeled with "CD sim.+f" in Fig. 2 and denoted by "maximum added CD."

Two electric motors mounted on the turbocharger shaft were used as an indirect energy supply with the aim of assuring faster boost pressure build up to enable the simultaneous injection of a larger amount of fuel. Both electric motors operate up to a maximum of 85 000 rpm, representing the equivalent to the maximum boost pressure still limiting full fuelling via an LDA [6]. A prototype asynchronous electric motor, labeled EM2, presented in detail in Refs. [4–6], which develops a maximum torque of 0.2 N m at 40 000 rpm, with mass moment of inertia 6×10^{-5} kg m^2 has been produced by ISKRA Avtoelektrika. Another high performance electric motor, denoted EMG, developing 0.57 N m at 20 000 rpm with 2.87×10^{-5} kg m^2 mass moment of inertia (produced by GfAS mbH [7]) was also used in the simulations for better comparisons. Thus, maximum torque to mass moment of inertia ratio (angular acceleration of free electric motor) is 3333 N m/kg m^2 (=rad/s^2) for EM2 and 19860 N m/kg m^2 (=rad/s^2) for EMG electric motor. Electric motors mounted on the turbocharger shaft improve turbocharger dynamics only if angular acceleration (α) of electrically assisted turbocharger is larger than that of the baseline turbocharger [1,4–6], thus

$$\frac{M_T+M_{EM}-M_C}{J_{TC}+J_{EM}}>\frac{M_T-M_C}{J_{TC}}. \quad (1)$$

An ISG produced and tested by ISKRA Avtoelektrika was used in the simulation as a direct energy supply source. Measured characteristics of the ISG operating in booster mode are presented in Fig. 3. The ISG partially compensates the difference between transient and stationary engine torque and therefore improves the dynamic behavior of the turbocharged engine.

Results

Improvement of the dynamic response of a vehicle by electric assisting systems presented above is investigated first. This analysis reveals the interaction between the diesel engine and electric assisting systems and forms a base for the parametric study of the influence of electric assisting systems parameters on the dynamic response improvement of a vehicle.

Downloaded 02 Jun 2010 to 171.66.16.98. Redistribution subject to ASME license or copyright; see http://www.asme.org/terms/Terms_Use.cfm

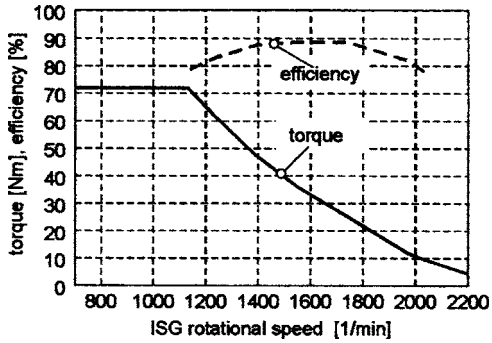

Fig. 3 ISG characteristic

Vehicle Acceleration

The results of four different loading cases of the engine propelling the vehicle presented above are analyzed in this chapter.

Vehicle acceleration in selected fixed gears is investigated, enabling the evaluation of improvements in vehicle dynamics by electric assisting systems under roadlike conditions. First, the fully loaded vehicle was running at a constant speed of 28 km/h (800 rpm) in fifth gear on a flat road; at time $t=0$ the fuel rack was pushed to its maximum. These results are discussed in detail and serve as the base for further brief explanations of other loading cases. Figure 4 presents vehicle speed (v) which corresponds to the engine speed for the selected gear, crankshaft power (P) =engine power+ISG power (when installed), air–fuel ratio (λ), relative cyclic fuel delivery (RCD), boost pressure (p_2), cyclic fuel delivery (CD), and angular acceleration of the turbocharger (α) for the described acceleration. RCD represents the ratio of instant injected fuel quantity to the maximum cyclic fuel delivery (Fig. 2 "max. CD"), and thus the ratio between instant and maximum stationary bmep, disregarding the influence of the medium exchange bmep. The maximum cyclic fuel delivery of the baseline engine was used as a reference value to form a realistic base for evaluating improvements. The use of an electrically assisted turbocharger could raise the RCD above 1 below 1400 rpm due to facts previously discussed.

Figure 5 represents trade-off between boost pressure and engine speed for different engine operating conditions: stationary and transient operation in different gears; since the behavior of the unit vehicle-turbocharged engine is significantly affected by the gear ratio. The data presented in this figure will be used (together with Figs. 4, 6, and 7) for better explanation of the following vehicle acceleration cases.

The acceleration of the baseline MAN engine represents the typical behavior of a turbocharged engine operating under transient conditions (Fig. 4). Only 87% of the maximum CD is injected immediately (Fig. 4-RCD) after the step change of driver command since boost pressure is well below its stationary value (Fig. 5) and therefore LDA restricts injected fuel quantity (Fig. 1). α and therefore p_2 increase due to the larger enthalpy of the exhaust gasses, enabling greater CD via the LDA. RCD decreases despite increasing CD, because at the same time the vehicle and, therefore the engine, is accelerating; "max. CD" increases up to 1400 rpm (Fig. 2). The lag of boost pressure behind the engine speed (Fig. 5) results in an increasing difference between instant and maximum stationary bmep (Fig. 4-RCD). After 7.9 s the engine reaches 1400 rpm and RCD starts to rise due to decreasing "max. CD" and due to the rising boost pressure. Maximum cyclic fuel delivery (RCD=1) is reached after 9.7 s. At this point the engine is running at 1570 rpm and boost pressure has just reached the value at which the LDA allows full fuelling at this engine speed. The phenomenon is clearly seen as the peak of CD in Fig. 4-CD, as well as the curve slope change in engine power (Fig. 4-P) and the air–fuel ratio (Fig. 4-λ). Angular acceleration of the turbocharger also decreases after 9.7 s (Fig. 4-α) since air–fuel ratio rises, resulting in lower exhaust gas temperature, therefore in lower enthalpy of exhaust gasses at the turbine entry and simultaneously in lower turbine torque output.

Turning on the ISG at the time of fuel rack change (increase) increases engine power with no delay (Fig. 4-P). The ISG adds power directly to the crankshaft and therefore does not directly affect turbocharger dynamics. Angular acceleration of the turbocharger and also the boost pressure of the engine with the ISG are only slightly higher than those of the baseline MAN engine due to a larger mass flow through the engine, as the consequence of higher vehicle (engine) speed. The lower value of RCD compared to that of the MAN engine up to 7 s is the consequence of still greater boost pressure delay versus engine speed resulting from the energy addition to the crankshaft and not to the turbocharger.

Angular acceleration of the electrically assisted turbocharger is larger than that of the baseline one, since Eq. (1) is fulfilled (Fig. 4-α); as the consequence boost pressure is higher, resulting in the injection of a larger fuel quantity and therefore in higher engine power. Larger α and faster boost pressure build up of the engine with the electrically assisted turbocharger is the consequence of additional electric motor (EM) torque and higher turbine torque due to higher CD and therefore a higher enthalpy of exhaust gasses (Eq. (1)). The engine with the EM2 reaches RCD=1 at 1270 rpm after 5.7 s, which is a substantially shorter time than that required by both previous engines. Angular acceleration of the turbocharger decreases after 6.7 s as the air–fuel ratio starts to rise, and then falls to zero at 7.8 s since the turbocharger has reached 85 000 rpm; no further turbocharger acceleration is needed since boost pressure has already exceeded full fuelling value [6]. The power of the engine with the ISG is larger than that of the engine with the EM2 up to 3.9 s because of the time required for the boost pressure to reach a value enabling the injection of additional fuel quantity equivalent to the power of the ISG. From Fig. 4-RCD it can be seen that the use of the EM2 enables the injection of added fuel quantity (RCD$>$1) only between 5.7 and 7 s, corresponding to engine speeds of 1300 to 1400 rpm. It is obvious that the EM2 is not powerful enough to make it possible to inject a significant amount of added fuel quantity in these operating conditions.

Angular acceleration of the turbocharger equipped with the EMG is much larger than that of the other turbochargers (Fig. 4-α) due to its supreme dynamic characteristics (Eq. (1)). As the consequence engine equipped with the EMG reaches RCD=1 after only 1.35 s at 900 rpm and enables the injection of added fuel up to 6.1 s, reaching 1400 rpm (Fig. 4-RCD). The power of the engine with the ISG is reached after only 0.9 s. The power of the engine with the EMG is essentially larger compared to that of the engines with the ISG and EM2 due to the significant amount of added injected fuel quantity resulting in the better acceleration of the vehicle (Fig. 4-P and v). Maximum added CD is injected from 3.6 to 6.1 s (Fig. 4-CD), indicating that an even more powerful electric motor would still have the potential to improve the acceleration of the vehicle at these loading conditions.

Conclusions already drawn for the difference between the engine with the ISG and the MAN engine are also valid for comparison between the engine with the ISG+EMG and the engine with the EMG.

The realistic judgment of electric assisting systems is reflected in variation of the vehicle velocity, as it is the only parameter perceptible to the driver. It is obvious that the engine equipped with ISG+EMG is the fastest during the whole acceleration period, as it unites the advantages of both direct and indirect energy supply systems. A maximum engine speed of 2400 rpm, corresponding to 85 km/h, is reached faster with the engine with the ISG and EM2 by 5.3%, with the EMG by 9.1% and with the ISG+EMG by 12.9% than with the baseline MAN engine, whereas 1600 rpm is correspondingly reached 8.8%, 11.3%, 19.7%, and 25.7% faster than with the MAN engine. The electric

Downloaded 02 Jun 2010 to 171.66.16.98. Redistribution subject to ASME license or copyright; see http://www.asme.org/terms/Terms_Use.cfm

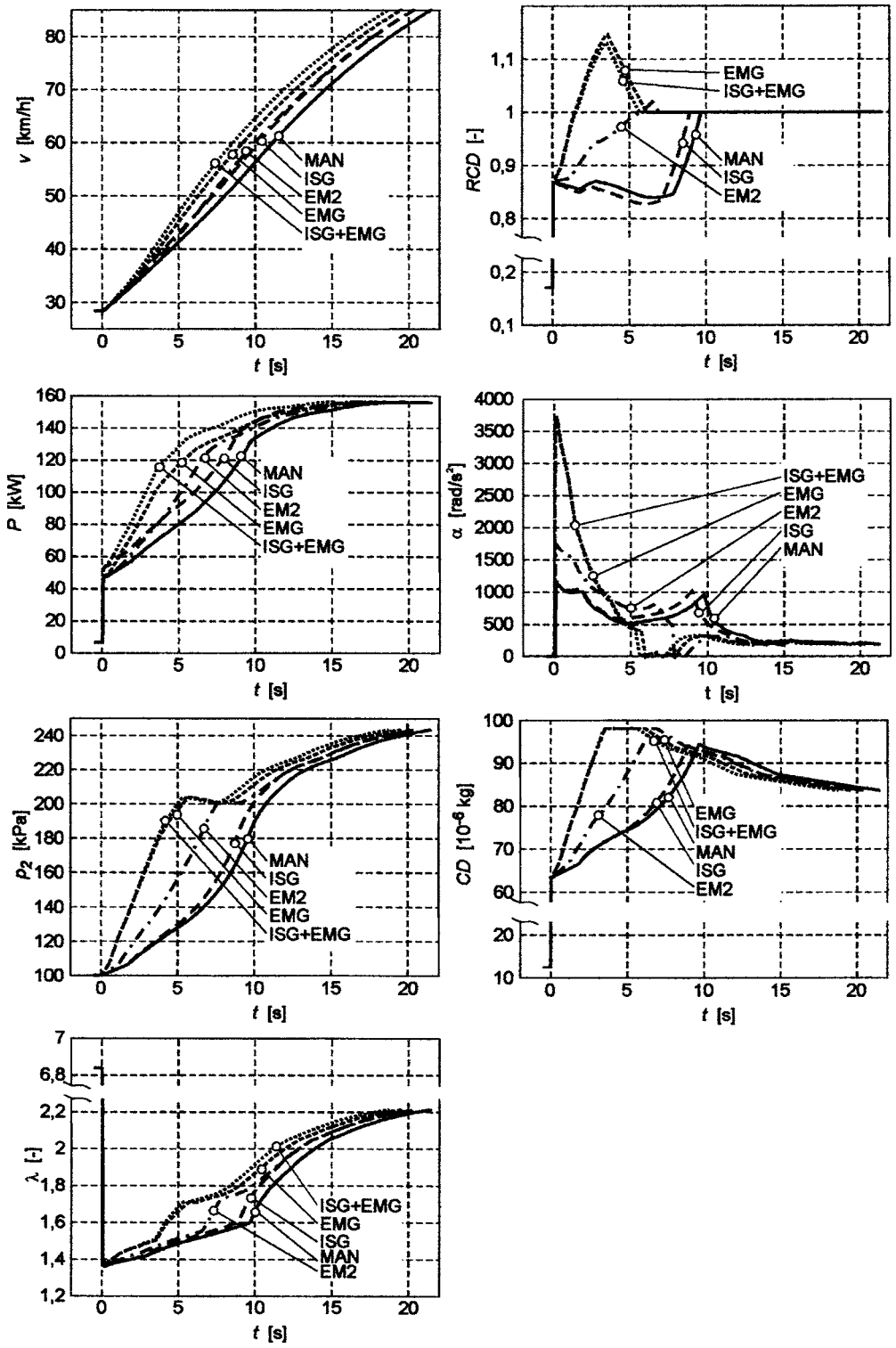

Fig. 4 Vehicle acceleration in fifth gear

assisting systems consumed (following the previously applied order of appearance) 106.4 kJ (0.7 Ah), 13.2 kJ (0.09 Ah), 16.7 kJ (0.11 Ah), and 106.6 kJ (0.7 Ah) of electric energy or electric charge at 42 V, respectively.

Figure 6 presents the vehicle acceleration in third gear, whereas all the other conditions are identical to those explained in Fig. 4. It is the representative case of fast engine acceleration. The RCD of the MAN engine again rises up to 87%, but then decreases faster until 1.8 s (1400 rpm) due to a still larger boost pressure lag behind engine speed compared to acceleration in fifth gear (Fig. 5). Maximum CD (RCD=1) is achieved after 3.7 s at 2100 rpm, which is a much higher value than 1570 rpm when accelerating in fifth gear. This is a consequence of the very short time required for the engine acceleration, provoking rapid increase of mass flow through the engine. Large boost pressure lag behind engine speed are the consequences of the turbocharger inertia and of the finite capacity of the inlet and exhaust manifolds. Ratio of the boost pressure versus turbine back pressure is therefore lower, resulting

Downloaded 02 Jun 2010 to 171.66.16.98. Redistribution subject to ASME license or copyright; see http://www.asme.org/terms/Terms_Use.cfm

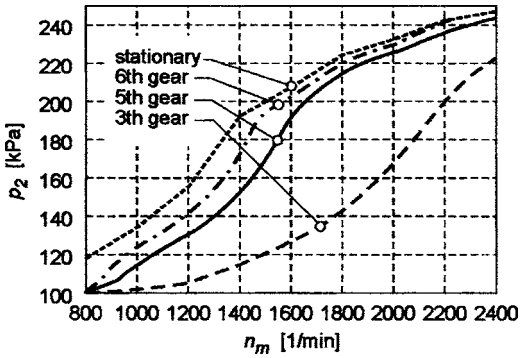

Fig. 5 Boost pressure vs engine speed for acceleration in different gears

in a larger difference in turbine and compressor torque and in faster turbocharger acceleration. Angular acceleration of the turbocharger of a baseline MAN engine rises from its initial value of 1250 rad/s^2 up to 3200 rad/s^2 at an engine speed of 2100 rpm

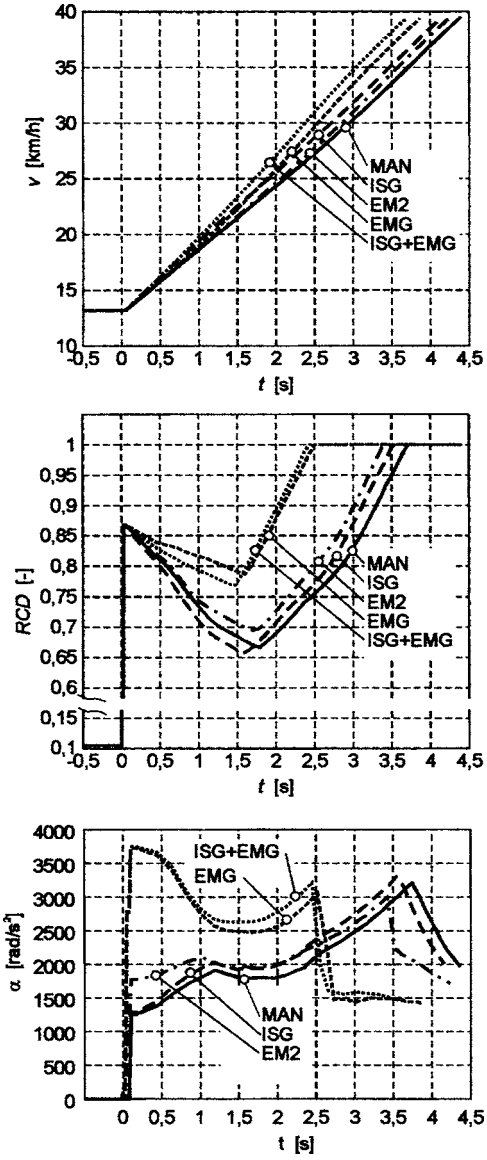

Fig. 6 Vehicle acceleration in third gear

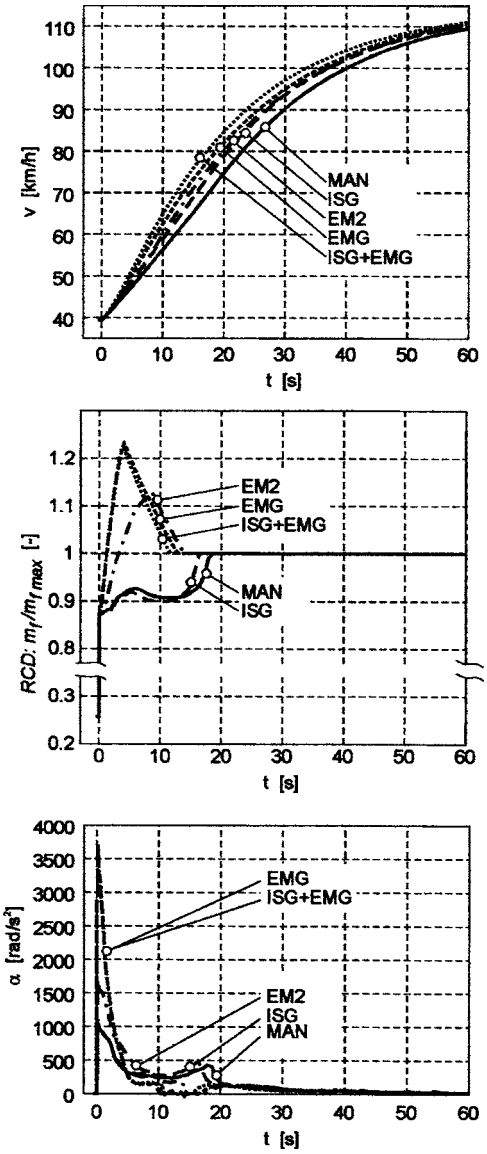

Fig. 7 Vehicle acceleration in sixth gear

(3.7 s). Figure 6-RCD indicates that the EM2 is unable to raise the boost pressure above a value allowing the injection of added fuel quantity. CD and also RCD of the engine with the EM2 is only slightly higher than that of the baseline MAN engine. The engine with the EM2 reaches RCD=1 as late as at 3.4 s at 2050 rpm. It is the consequence of turbocharger dynamics. The dynamics of the turbocharger with the EM2 is only slightly better (Eq. (1)) since maximum angular acceleration of the free EM2 (3333 rad/s^2) is only slightly larger than that of the baseline turbocharger (Fig. 6-α). When performing the same acceleration in second gear, the duration of which is shorter, the dynamics of the turbocharger with the EM2 and the baseline one are nearly the same, while at still faster acceleration in first gear the dynamics of the baseline turbocharger is better. Angular acceleration of the free EMG (19860 rad/s^2) is much higher than that of the baseline turbocharger, therefore EMG enables the injection of more fuel (Fig. 6-RCD) and consequently faster vehicle acceleration (Fig. 6-v). The example described reveals the need for an EM with relative high torque and much higher angular acceleration than that of the baseline turbocharger to efficiently improve engine dynamics.

It is characteristic of the case presented that an electrically assisted turbocharger improves engine dynamics mostly at high en-

Downloaded 02 Jun 2010 to 171.66.16.98. Redistribution subject to ASME license or copyright; see http://www.asme.org/terms/Terms_Use.cfm

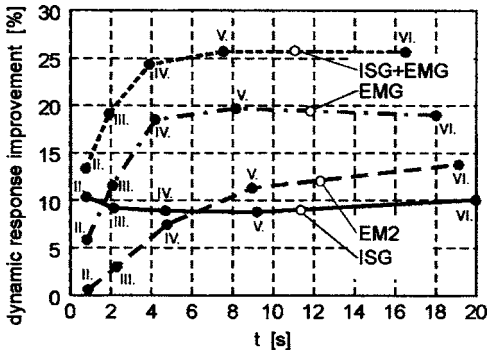

Fig. 8 Dynamic response improvement of the baseline TC diesel engine by electric assisting systems for accelerations in different gears (II–IV gear)

gine speeds, which is rather unusual. This phenomenon is evident from Fig. 6-RCD, since the largest difference in RCD (CD and engine power) and therefore vehicle acceleration between both engines with the EMG and other engines is observed at approximately 2.5 s, when the engine is running at 1800 rpm. Maximum engine speed corresponding to 39.5 km/h is reached with the engine with the ISG 6.2%, the EM2 3.3%, the EMG 12%, and the ISG+EMG 16.4% faster than with the MAN engine, whereas speed of 1600 rpm is reached 9.2%, 3%, 11.6%, and 19.2% faster than with the MAN engine. Appropriate electric energy consumption during the observed acceleration was 24 kJ (0.16 Ah), 4.7 kJ (0.031 Ah), 5.6 kJ (0.037 Ah), and 26.6 kJ (0.176 Ah) of electric energy or electric charge at 42 V, respectively.

Figure 7 presents vehicle acceleration in sixth gear, whereas all other conditions are identical to those explained in Fig. 4. It is an example of step change in fuelling accompanied by slow engine acceleration. The operating time of the electric assisting systems was limited to 30 s due to limited accumulator capacity and cooling ability regarding the ISG. The EM attached to the turbocharger shaft was able to reach maximum of 85 000 rpm and hence was switched off earlier. The MAN RCD curve (Fig. 7-RCD) does not fall below its initial value of 88% due to slow engine acceleration, which is a consequence of smaller boost pressure lag behind the engine speed (Fig. 5). Full fueling of the MAN engine is therefore reached already at 1460 rpm. The velocity difference of the vehicles equipped with engines with the EM2 and EMG is smaller than that presented in former cases because slower engine acceleration enables the injection of a significant added fuel quantity even with the use of the EM2 (Fig. 7-v and RCD). With the exception of the very beginning of the transient angular acceleration of the turbocharger is lower during slow engine acceleration (Fig. 7-α), since boost pressure is closer to its steady state value throughout whole acceleration (Fig. 5) compared to faster accelerations. Therefore slow engine acceleration places higher demands on EM torque output than on high torque to mass moment of inertia ratio (angular acceleration), since in the limiting case it approaches steady state operation. It is obvious that the engine with the ISG+EMG again assures the fastest acceleration.

All engines are not able to reach 2400 rpm under these operating conditions, so a comparison was made only at 1600 rpm, corresponding to 79 km/h. The engine with the ISG requires 10.1%, the EM2 13.8%, the EMG 18.8%, and the ISG+EMG 25.7% less time than the MAN engine to reach 1600 rpm. The electric assisting system energy consumption was 219.5 kJ (1.45 Ah), 30.2 kJ (0.2 Ah), 37.3 kJ (0.25 Ah), and 233.2 kJ (1.54 Ah) of electrical energy or electric charge at 42 V, respectively.

Figure 8 presents improvement of dynamic response of a turbocharged diesel engine (and also the dynamic response improvement of a vehicle) by the electric assisting systems when accelerating from 800 to 1600 rpm in different gears (II.–VI. gear). Duration of the acceleration that is defined by the chosen gear defines time scale—abscissa in Fig. 8. It can be seen that ISG improves TC diesel engine dynamics nearly constantly with respect to the duration of the acceleration. This is the consequence of direct energy addition to the crankshaft. Considering the EM2, it is clear that the longer the acceleration the greater is the benefit by EM2, since angular acceleration of the turbocharger diminishes with increasing time needed for the acceleration. The benefit of EMG is greater than that of the EM2 due to its superior characteristic, but the difference diminishes with increasing time needed for the acceleration as already discussed in relation to Fig. 7. Dynamic response improvement of the engine with the EMG is minor in comparison to that of the engine with the ISG for fast engine accelerations, since there is not enough time for boost pressure to reach the value that enables the injection of added fuel quantity adequate to the ISG power. However, if the vehicle is in third gear or higher the improvement with the EMG assistance surpasses that achieved with ISG. Dynamic response of the engine with the ISG+EMG is the largest throughout the whole engine operation regime, since it combines the benefits of direct and indirect energy supply. It can be concluded that presented electric assisting systems improve the dynamic response of the baseline TC engine by up to 26%.

Vehicle Hill Climbing

Another realistic example presented in Fig. 9 shows engine parameters when propelling a fully loaded vehicle in sixth gear at 59 km/h (1200 rpm) on the flat, attaining a 3.5 deg inclination at time 0 s, and simultaneously pushing the fuel rack to its maximum. This gradient was chosen so that some engines equipped with electric assisting systems accepted the loading unlike the others, thus enabling insight into the features of a particular electric assisting system. The electric assisting systems were switched on for up to a maximum of 30 s. The rotational speed of all the engines initially falls slightly, but afterwards all except the baseline MAN engine accelerate up to 30 s (Fig. 9-v). The engine with the ISG accelerates slower than the engines with electrically assisted turbochargers since the power benefit of a larger quantity of injected fuel is greater than that of the ISG (Fig. 9-v and P). After 30 s, when the ISG is turned off, the engine with the ISG does not develop enough power to maintain vehicle speed. Similar deduction also holds for the engine with the EM2. After turning off the EM the CD, RCD, and engine power start to decrease (Fig. 9-RCD and P) due to lower boost pressure; therefore vehicle velocity also decreases (Fig. 9-v). Boost pressure and engine power as well as the speed of the vehicle (engine) with the EMG is only slightly higher than that of the EM2 engine, thus just enabling the injection of a larger fuel quantity (Fig. 9-RCD). As a result the vehicle accelerates up to a new steady state value of approximately 66 km/h (Fig. 9-v) avoiding the need for supplementary gear change. The engine with the ISG+EMG accelerates much faster than the engine with the EMG up to 30 s, but afterwards, when both electric assisting systems are switched off, vehicle speed decreases slowly to the same steady state value of 66 km/h. The observed electric assisting systems consumed 327.1 kJ (2.16 Ah) for ISG, 68.9 kJ (0.46 Ah) for EM2, 92 kJ (0.61 Ah) for EMG, and 352.2 kJ (2.33 Ah) for ISG+EMG of electric energy or electric charge at 42 V, respectively.

All the cases presented in the last two paragraphs indicate that the use of the electrically assisted systems enable better vehicle dynamics on the one hand, or allow the introduction of gearboxes with fewer gears, or the use of smaller displacement engines at the same engine dynamics on the other hand. Both of the latter cases reduce production costs, while the last case could lead to a reduction in fuel consumption.

Downloaded 02 Jun 2010 to 171.66.16.98. Redistribution subject to ASME license or copyright; see http://www.asme.org/terms/Terms_Use.cfm

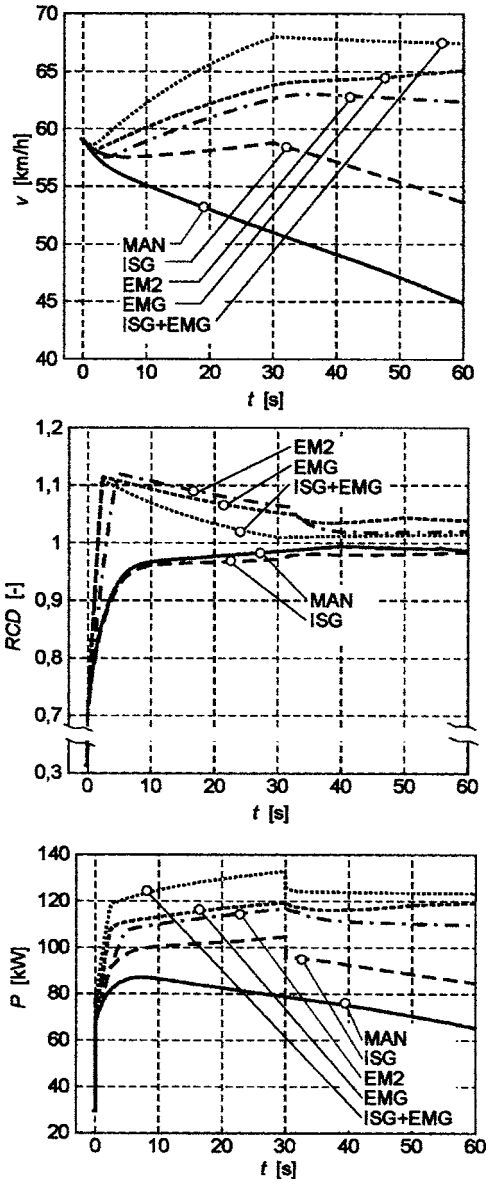

Fig. 9 Driving case: 0° road inclination to 3.5° road inclination in sixth gear

Parametric Study

The influence of the parameters of the electric assisting systems on dynamic response improvement of the vehicle is investigated in this chapter. It is evident from the results presented in the former chapter that the EMG outperforms the EM2. Therefore the shape of the EMG power to speed characteristics [7] was retained, whereas mass moment of inertia and maximum power output were changed when examining the influence of EMG parameters on vehicle dynamics. The same procedure was also applied when investigating the influence of the ISG parameters on vehicle dynamics; the shape of torque to speed characteristic (Fig. 3) was kept unchanged, whereas torque output was increased.

Figure 10 presents the influence of the EM mass moment of inertia, at the same power density, i.e., angular acceleration of the free EM (maximum value of $\alpha = 19\,860$ rad/s^2), on the dynamic response improvement of the vehicle when accelerating in different gears from 800 to 1600 rpm. It is obvious that all curves depart from the origin, since zero mass moment of inertia implies that no torque is added and therefore dynamics of the baseline turbocharged engine is observed.

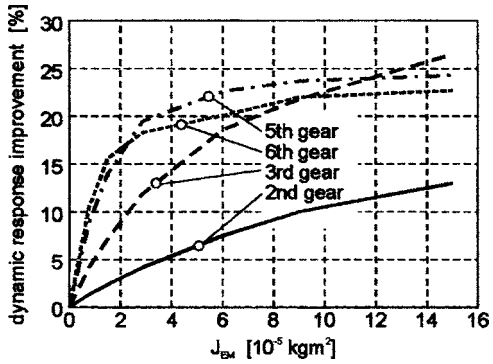

Fig. 10 Influence of EM mass moment of inertia at the same power density on dynamic response improvement of the baseline TC diesel engine

Dynamic response improvement of the vehicle accelerating in second gear is inferior to that observed in higher gears, since angular acceleration of the baseline turbocharger is higher when accelerating in second gear (maximum value of $\alpha = 5290$ rad/s^2); the ratio between left hand side (lhs) and right hand side (rhs) of Eq. (1) is therefore smaller, resulting in a smaller improvement in turbocharger dynamics due to the use of the EM. The value of RCD is lower than 1 throughout whole acceleration period when accelerating in second gear. Improved turbocharger dynamics therefore implies a larger amount of the injected fuel and consequently improved vehicle dynamics. The curve of the dynamic response improvement (Fig. 10; second gear) therefore resembles the ratio between lhs and rhs of Eq. (1) (=improvement in turbocharger dynamics) for constant angular acceleration of EM. Similar deduction is also valid for the dynamic response improvement of the vehicle accelerating in third gear up to $J_{EM} = 6 \times 10^{-5}$ kg m^2 (Fig. 10), where maximum fuel quantity is injected at 1530 rpm. Dynamic response improvement diminishes slightly thereafter, since maximum fueling is reached significantly before 1600 rpm; dynamic response improvement of the vehicle is not proportional to the improvement in turbocharger dynamics anymore. This phenomenon is observed more evidently in fifth and sixth gear, where the slope of the dynamic response curves diminishes after $J_{EM} = 3 \times 10^{-5}$ kg m^2. Explanation of this fact can also be seen from Fig. 4-CD and RDC and Fig. 7-RCD, from where it is seen that improvements in turbocharger dynamics do not result in a significant increase of injected fuel as it is limited by the characteristic of the fuel injection pump.

When interpreting Figs. 10 and 11 it should be noted that (as already presented in Figs. 4 and 6–8) acceleration from 800 to 1600 rpm in second gear lasts 0.87 s, in third 2.35 s, in fifth 10.1 s, and 22.3 s in sixth gear for the baseline engine. This

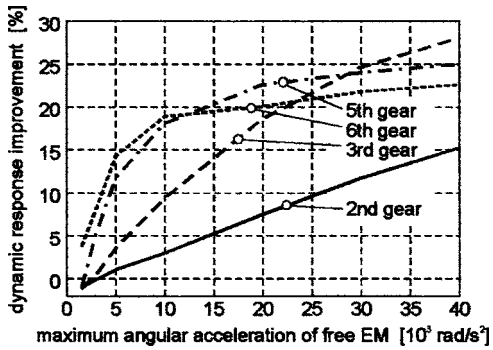

Fig. 11 Influence of maximum angular acceleration of EM at $J_{EM} = 6 \times 10^{-5}$ on dynamic response improvement of the baseline TC diesel engine

Downloaded 02 Jun 2010 to 171.66.16.98. Redistribution subject to ASME license or copyright; see http://www.asme.org/terms/Terms_Use.cfm

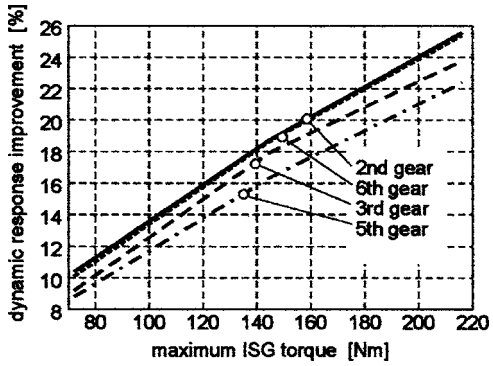

Fig. 12 Influence of maximum torque output of the ISG on dynamic response improvement of the baseline TC diesel engine

means that it is not advisory to enlarge EM beyond reasonable limit to assure faster acceleration in first, second and third gear, since benefits can reach up to approximately 0.5 s with the drawbacks in electric energy consumption and complicated controlling, since EM must be turned on at each, also very slow, turbocharger acceleration. EM with $J_{EM}=6\times10^{-5}$ kg m^2 (maximum value of $\alpha=19\,860$ rad/s^2) is the best choice considering all previously mentioned facts, since it enables satisfactory turbocharger dynamics for slow engine accelerations also with EM turned off [4,6].

Figure 11 presents the influence of EM power density, i.e., angular acceleration of the turbocharger at $J_{EM}=6\times10^{-5}$ kg m^2 on the dynamic response of the vehicle. Dynamic response improvement of the vehicle in second gear increases linearly with increasing maximum angular acceleration of free EM. This is again the consequence of RCD<1 throughout whole acceleration period (i.e., turbo lag affects the complete transient) and improvement in turbocharger dynamics, which increases linearly with increasing angular acceleration of the free EM at constant EM mass moment of inertia. The same conclusion is valid for the acceleration in third gear up to maximum EM angular acceleration of approximately 20 000 rad/s^2, where slope of the dynamic response improvement curve changes due to the facts mentioned when examining Fig. 10. Conclusions drawn for dynamic response improvement in fifth and sixth gear when analyzing Fig. 10 are also valid for Fig. 11. It is evident from Fig. 11 that EM with maximum angular acceleration of approximately 20 000 rad/s^2 is again the best choice considering the earlier mentioned criteria.

Figure 12 presents the influence of maximum ISG torque output on the dynamic response of the vehicle. It is evident that dynamic response increases nearly linearly with the increasing ISG torque output, which is somehow intuitive, since ISG adds power directly to the crankshaft. The differences in the dynamic response improvement in different gears are small and are nearly constant with increasing ISG torque output.

Summary

To efficiently assist the turbocharger an EM with 1/3 up to a maximum 1/2 of the turbocharger's mass moment of inertia should be applied. Angular acceleration of free EM should be approximately an order of magnitude larger than angular acceleration of the baseline turbocharger at the operating conditions where significant dynamic response is required. This fact is valid for all types of available turbochargers: free floating, waste-gated and VNT turbochargers. EM attached to the turbocharger shaft should operate up to the turbocharger speed that is equivalent to the maximum boost pressure still limiting full fuelling via fuel limiting device.

Appropriate EM attached to the turbocharger shaft ($J_{EM}=6\times10^{-5}$ kg m^2, maximum $\alpha=19\,860$ rad/s^2) consumes approximately 1 Ah (at 42 V) for a 30 s acceleration, and proportionally less when operating shorter. It is evident that a truck battery enables a series of consecutive electrically assisted accelerations without significant loss of electric charge.

ISG adds power directly to the crankshaft with no delay. It therefore improves dynamic response of the engine nearly constantly with respect to the duration of the acceleration. It is a promising technical solution since it combines starter, generator and booster. It therefore enables powerful and efficient electric generation, comfortable start/stop operation and energy recuperation (regenerative braking).

Baseline ISG used in this investigation consumes up to 2.2 Ah (at 42 V) for a 30 s acceleration, whereas the ISG with maximum torque output of 216 N m consumes up to 6.6 Ah. It is evident that compromise should be made between dynamic response improvement and electric energy consumption. Application of a large ISG would require a larger capacity battery. It should also be noted that ISG electric energy production is disabled when it operates in booster mode.

Conclusion

It is evident from the results presented that electrically assisted systems improve turbocharged engine dynamics. Reductions in production and operating costs can be achieved for the same requirements on engine dynamics due to the possible downsizing of electrically assisted engines.

The ISG is effective especially in the first phase of load increase, since it increases engine power without any delay, and after reaching full fueling, since thereafter engine power could only be increased with a direct power supply. A compromise considering engine applications should be made between the ISG power output, operational time, and electric energy consumption. The ISG is the best electrically assisted solution in cases of large instant engine load increase, enabling smaller deviations in the engine speed, whereas it does not outperform electrically assisted turbochargers in terms of electric energy consumption at the same engine dynamics improvement when operating for longer periods.

For vehicle application an electrically assisted turbocharger is superior to an ISG, since the typical operational times of electric assisting systems are longer than a few seconds, thus offering a better ratio of engine dynamics improvement to electric energy consumption, as well as greater potential for engine dynamics improvement, since the ISG power potential hardly competes with that of additional fueling. The higher the rating of the turbocharged engine the greater is the benefit of an electrically assisted turbocharger in comparison to ISG.

Acknowledgment

The financial support of the Ministry of Science and Technology of the Republic of Slovenia is greatly appreciated. The valuable support of ISKRA Autoelektrika d.d. (R&D) and MAN GV Slovenia is also gratefully acknowledged.

Nomenclature

CD = cyclic fuel delivery (kg/cycle)
J = mass moment of inertia (kg m^2)
M = torque (N m)
n_m = engine speed (rpm)
P = crankshaft power (kW)
p_2 = boost pressure (kPa)
RCD = relative cyclic fuel delivery
t = time (s)
α = angular acceleration (rad/s^2)
v = vehicle velocity (km/h)
λ = air–fuel ratio

Subscripts

C = compressor
EM = electric motor

Downloaded 02 Jun 2010 to 171.66.16.98. Redistribution subject to ASME license or copyright; see http://www.asme.org/terms/Terms_Use.cfm

T = turbine
TC = turbocharger

References

[1] Zellbeck, H., Friedrich, J., and Berger, C., 1999, "Electrically Assisted Turbocharger as the New Boosting Concept," (original title: "Die Elektrisch Unterstuetzte Abgasturboladung Als Neues Auflade Konzept") MTZ Motortechnische Zeitschrift, **60**(6), pp. 386–391.

[2] Zellbeck, H., and Friedrich, J., 2001, "Optimizing the Dynamic Behavior of Turbocharged Internal Combustion Engines," (original title: "Optimirung Des Dynamischen Verhaltens Aufgeladener Verbrennungsmotoren") MTZ Motortechnische Zeitschrift, **62**(6), pp. 474–480.

[3] Shahed, S. M., et al., 2000, "Turbocharging Systems with Electrical Assistance for Conventional, Hybrid and Fuel Cell Powertrain," 21, Internationales Wiener Motorensymposium 4–5 May 2000, Band 1, pp. 310–324.

[4] Katrašnik, T., 2001, "Analysis of Transient Process in a Turbocharged Diesel Engine," Master Sc. thesis No. M/1177, Department of Mechanical Engineering, University of Ljubljana, Slovenia.

[5] Katrašnik, T., et al., 2001, "Improvement of the Dynamic Characteristic of an Automotive Engine by a Turbocharger Assisted by an Electric Motor," in Proceedings of the 2001 Fall Technical Conference of the ASME Internal Combustion Engine Division, Argonne, Illinois, September 23–26, 2001.

[6] Katrašnik, T., et al., 2003, "Improvement of the Dynamic Characteristic of an Automotive Engine by a Turbocharger Assisted by an Electric Motor," ASME J. Eng. Gas Turbines Power, **125**(2), pp. 590–595.

[7] Hoecker, P., et al., 2001, "eBooster Key Component of a New BorgWarner Turbo Systems Charging System for Passenger Cars," Internationales Wiener Motorensymposium 2001, Wien, Band 2, pp. 333–352.

[8] Medica, V., 1988, "Simulation of Turbocharged Diesel Engine Driving Electrical Generator Under Dynamic Working Conditions," Dr. Sc. thesis, University of Rijeka, Croatia.

[9] Hribernik, A., 1994, "Modeling of Boundary Conditions for a Twin-Entry Automotive Diesel Engine Turbine," Dr. Sc. thesis, University of Maribor, Slovenia.

[10] Winterbone, D. E., et al., 1977, "Transient Response of Turbocharged Diesel Engines," SAE technical paper 770122.

Downloaded 02 Jun 2010 to 171.66.16.98. Redistribution subject to ASME license or copyright; see http://www.asme.org/terms/Terms_Use.cfm